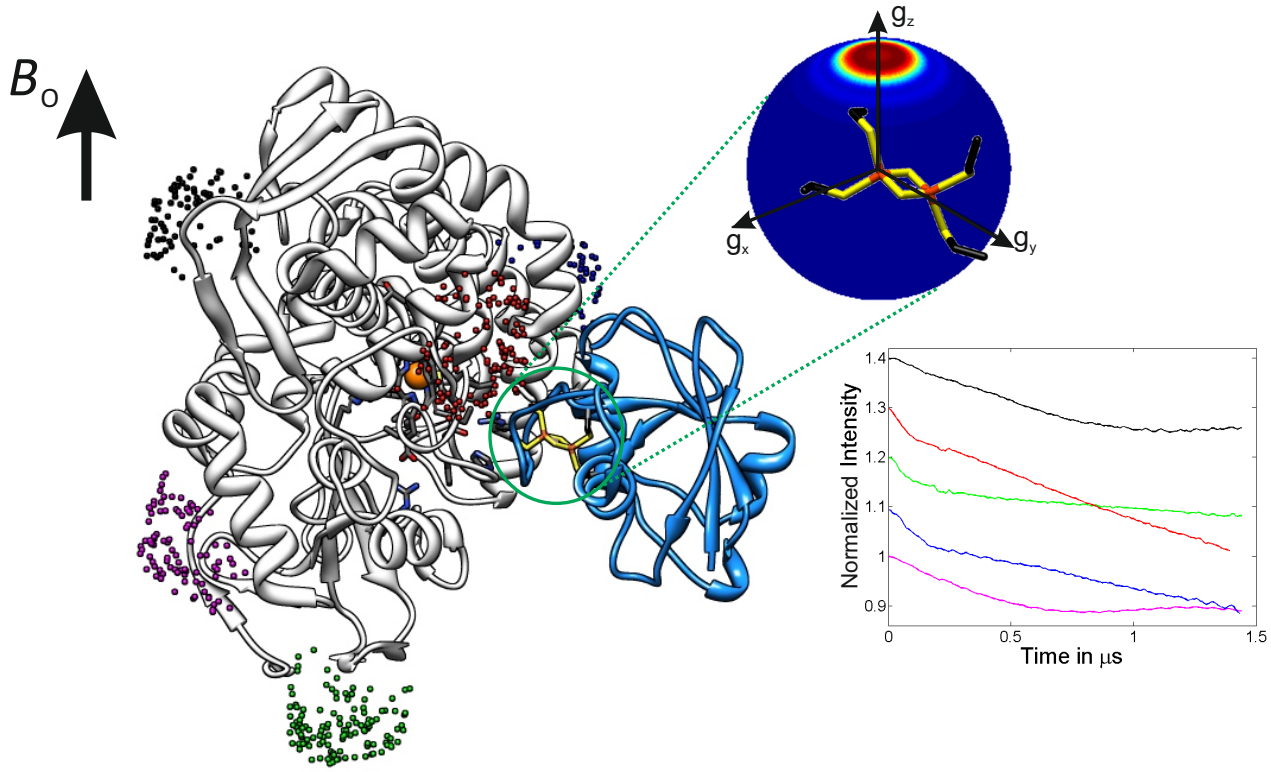
Magnetic Resonance Studies of Proteins and Model Systems



Alice M. Bowen

University College, Oxford

Michaelmas Term 2012

The image on the front cover represents the results of Chapter 4. It shows the final fitted structure for the protein−protein complex of ferredoxin (HaPux), shown in blue, and P450 (CYP199A2), shown in white. The $[Fe_2S_2]$ centre of HaPux is highlighted in green and the iron of the heme centre of P450 is shown in orange. The distributions of MTSL nitroxide spin labels attached to the P450 are indicated by coloured spheres, with the colours corresponding to the labelling sites as follows: 42−magenta, 226−blue, 315−lime green, 345−red and 404−black. These colours also correspond to the DEER data depicted which is measured between the nitroxide spin labels and the reduced $[Fe_2S_2]^+$ centre, primarily excited in the g_z orientation as shown by the excitation sphere.

"Dr Bloch and Dr Purcell! You have opened the road to new insight into the micro-world of nuclear physics. Each atom is like a subtle and refined instrument, playing its own faint, magnetic melody, inaudible to human ears. By your methods, this music has been made perceptible, and the characteristic melody of an atom can be used as an identification signal. This is not only an achievement of high intellectual beauty - it also places an analytic method of the highest value in the hands of scientists."

From Les Prix Nobel en 1952, Editor Göran Liljestrand, [Nobel Foundation], Stockholm, 1953

Thesis Abstract

Magnetic Resonance Studies of Proteins and Model Systems

Alice M. Bowen, University College, Oxford

Michaelmas Term 2012

This thesis discusses, employs and develops further applications of both Electron Paramagnetic Resonance (EPR) and Nuclear Magnetic Resonance (NMR) methodology in the study of a variety of biological systems.

Chemically Induced Dynamic Nuclear Polarization (CIDNP) is used to study the surface accessibility of Tryptophan and Tyrosine residues in the Equine Lysozyme-Oleic Acid complex (ELOA). It is believed that these amino acids may play a vital role in the interaction of this partially structured complex with cell walls leading to the apoptosis of the cell.

Double Electron-Electron Resonance (DEER) is an EPR technique that can be used to study the distance and, in some cases, the orientation between two paramagnetic centres on a nano-meter length scale. Attaching spin labels, such as Methane Thiosulphonate Spin Label (MTSL), to proteins, or by using spin active cofactors in proteins as innate spin labels, allows the measurement of distances within proteins or their complexes. In this thesis, model copper systems were initially studied in order to gain a better understanding of the orientational information obtainable from such spectra. The methodology developed from this project was applied to the protein−protein complexes of ferredoxin reductase−ferredoxin and ferredoxin−P450, three proteins that form a vital electron transport chain, leading to the catalytic hydroxylation of many small molecules. The structure of the docked P450−ferredoxin complex is the first experimentally determined structure of its type and thus is of considerable biochemical interest.

As part of the structural determination of the ferredoxin complexes, it was necessary to measure the relative orientation of the g-matrix with respect to the molecular structure. This was achieved using a combination of orientationally selective proton Electron Nuclear Double Resonance (ENDOR) and HYperfine Sublevel CORrElation (HYSCORE) spectroscopy.

The expansion of the DEER technique to measure an ever-increasing variety of systems has shown the limitations of the pulse sequences most frequently employed at present, particularly in relation to the measurement of many of the metal centres, which could be used as innate spin probes in protein systems. Methodological work has also been undertaken to examine possible solutions to circumvent some of these problems, namely low modulation depths and fast relaxation times. This has resulted in the development of two modifications to the existing techniques: Dead-time free three-pulse DEER and Repeated Excitations IN DEER (REINDEER). These techniques have been used to study of both synthetic model systems and also spin labelled proteins.

Acknowledgements

My thanks must firstly go to my supervisors Dr Christiane Timmel and Prof. Peter Hore, whose patient help and support has allowed me to complete this thesis. They are both inspirational scientists and I am honoured that they have allowed me to join their groups and work with them during my doctorate.

I am indebted to Dr Jeffrey Harmer; without whose expertise in EPR, both practical and theoretical, I would have fallen flat on my face many more times than I have done. Oxford's EPR community will miss him greatly and I wish him all the best for his new adventures down under!

I would like to thank Dr Arzhang Ardavan and Dr Kiminori Maeda for interesting and informative discussions and advice with respect to the theoretical aspects and pulse sequence development during the work on REINDEER and dead-time free three-pulse DEER. Furthermore, Dr Kiminori Maeda provided invaluable advice on the experimental aspects of the CIDNP experiment.

Dr Janet Lovett was as instrumental in allowing me to settle-in to research in EPR, she was responsible for teaching me how to set up my first EPR experiments. I am very grateful for the way I was taken under her wing during my first few years in doctoral research.

The body of work presented in this thesis could not have been accomplished without a great number of experimental collaborators; who have supported, encouraged and most importantly provided me with samples to work on! I am very appreciative of the skills and hard work of the following people:

- Dr Michael Jones and Prof. Jon Dilworth (Oxford University) – who synthesised and characterized the model Cu−Cu, Cu−$NO^{\bullet}$ and $NO^{\bullet}$−$NO^{\bullet}$ systems.
- Prof. Michael McPherson and Thembanikosi Grace Gaule (University of Leeds) – for the kind gift of the copper amine oxidase protein (AGAO).
- Prof Harry Anderson and William Peveler (Oxford University) – for providing the copper nanoring system.
- Dr Luet Wong and members of his research group particularly Dr Stephen Bell, Eachan Johnson and Nikki Hoskins (Oxford University) – who produced the large (and ever expanding) number of different samples required in the determination of the docked structures of the ferredoxin complexes.
- Bruker Biospin, in particular Dr Peter Höfer and Dr Pat Carl – for lending me the 2 mm resonator and samples used in the method development work and for answering my panicked emails when things wouldn't work.
- Dr Ludmilla Morozova-Roche (Umeå University, Sweden) – for supplying the ELOA and equine lysozyme samples studied by CIDNP.

Ribbon diagrams of protein structures shown in this thesis have been generated using the PDB viewer chimera.[1]

For funding I wish to acknowledge the support of the Biotechnology and Biological Sciences Research Council (BBSRC) which has provided me with my doctoral stipend and also University College, Oxford, for their generous scholarship towards conference attendance.

There are of course those in the lab who have shared this experience with me and without whose moral support my doctorate would have been a lot less enjoyable. In particular: Dr Kevin Henbest; who always helps you, with a smile, to find that piece of equipment which has gone walk-about. Kelly-Anne Ferguson; it has been lovely to have you as a friend over the last four years, I am sure you will be more organised with your thesis writing than I ever was with mine. Claudia Tait; thank you for all of your proof reading, your written English is no doubt better than mine. I hope that you enjoy your DPhil as much as I have mine and I feel sure that the CRT group EPR mantel is in safe hands with you. 'DPhil corner' and honorary/future members (Dr Christopher Wedge, Dr Alexander Robinson, Jonathan Storey, Neil Gunn and Emrys Evans); thank you for healthy doses of scepticism, cynicism and sarcasm, as well as dynamism and drinks. There are other many members of the CÆSR (Centre for Advanced Electron Spin Resonance) community who have contributed to an enjoyable working environment and I hope that the centre will continue in the same vein for many years to come.

Outside the lab I particularly want to recognise the contribution to my general well-being from Will, Elizabeth and Rachel. Having fiends to share the write-up process with has undoubtedly made it much more bearable. Thank you for all of your company in the library, coffee breaks and persuading me that there is life after the thesis. I hope that we have time now to do all of the things we have put on that 'when we've finished our theses' list!

Most importantly I owe a large debt of gratitude to my family and foremostly my parents, to whom this thesis is dedicated. Thank you for rescuing me when I've needed it. On several occasions you have picked me up, dusted me off then let me go back to the lab. I am eternally grateful for your love and support.

Finally, if only research were this simple:

"Begin at the beginning and go on till you come to the end: then stop."

The King of Hearts instruction to the White Rabbit,
from Alice's Adventures in Wonderland by Lewis Carroll.



Acknowledgements: rights and permissions

- Fig. 2.2 and Fig. 2.3 in Chapter 2 are adapted from a figure on a webpage from the University of Hamburg:
http://www.chemie.uni-hamburg.de/nmr/insensitive/tutorial/en.lproj/dipolar_coupling.html.[2]

- Fig. 2.7 in Chapter 2 is partially adapted and reproduced from *A Tutorial on Nitroxide Spectral Analysis* by E. Bordignon.[3]

- Fig. 2.11 in in Chapter 2 is adapted and reprinted from *Journal of Magnetic Resonance*, **216**, G. W. Reginsson, R. I. Hunter, P. A. S. Cruickshank, D. R. Bolton, S. T. Sigurdsson, G. M. Smith and O. Schiemann, W-band PELDOR with 1kW microwave power: Molecular geometry, flexibility and exchange coupling, 175–182. Copyright © 2012, with permission from Elsevier.[4]

- Fig. 2.12, Fig. 2.14 and Fig. 2.16 in Chapter 2 are reproduced from J. E. Lovett, A. M. Bowen, C. R. Timmel, M. W. Jones, J. R. Dilworth, D. Caprotti, S. G. Bell, L. L. Wong and J. Harmer, Structural information from orientationally selective DEER spectroscopy. *Physical Chemistry Chemical Physics*, 2009, **11(31)**, 6840–6848 with permission from the PCCP Owner Societies.[5]

- Fig. 2.13 in Chapter 2 is reproduced from *ESR Spectroscopy in Membrane Biophysics*, published by Springer,**27**, 1997, Chapter 2: Instrumentation and Experimental Setup, G. Jeschke, Figure 10. Copyright © Springer Science+Business Media, LLC 2007; with kind permission from Springer Science and Business Media.[6]

- Fig. 2.15 in Chapter 2 is reprinted from *Journal of Magnetic Resonance*, **178**, S. Stoll and A. Schweiger, EasySpin, a comprehensive software package for spectral simulation and analysis in EPR, 42–55. Copyright © 2006, with permission from Elsevier.[7]

- Fig. 3.3 **A)** in Chapter 3 is adapted with permission from *Journal of Physical Chemistry A*, **112(23)**, B. E. Bode, J. Plackmeyer, T. F. Prisner and O. Schiemann, PELDOR measurements on a nitroxide-labeled Cu(II) porphyrin: Orientation selection, spin-density distribution, and conformational flexibility, 5064–5073. Copyright © 2008 American Chemical Society.[8]

- Fig. 3.3 **B)** and **D)** in Chapter 3 are reprinted with permission from *Journal of Physical Chemistry B*, **114(18)**, Z. Yang, D. Kise and S. Saxena, An approach towards the measurement of nanometer range distances based on Cu^{2+} ions and ESR, 6165–6174. Copyright © 2010 American Chemical Society.[9]

- Fig. 3.3 **C)** in Chapter 3 is reprinted from *Journal of Magnetic Resonance*, **188**, Z. Yang, J. Becker and S. Saxena, On Cu(II)-Cu(II) distance measurements using pulsed electron electron double resonance, 337–343. Copyright © 2007, with permission from Elsevier.[10]

- Fig. 4.12 in Chapter 4 is adapted and reproduced from *http://bioinfo3d.cs.tau.ac.il/FireDock/firedock.html* and *Proteins: Structure, Function, and Bioinformatics*, 2007, **69(1)**, N. Andrusier, R. Nussinov and H. J. Wolfson, FireDock: Fast interaction refinement in molecular docking. Copyright © 2007 Wiley-Liss, Inc., with permission from John Wiley and Sons.[11].

- Fig. 4.13 in Chapter 4 is reproduced from *Journal of Biological Inorganic Chemistry*, published by Springer, **15(3)**, 2010, 315–328, Protein recognition in ferredoxin-P450 electron transfer in the class I CYP199A2 system from Rhodopseudomonas palustris, S. G. Bell, F. Xu, E. O. D. Johnson, I. M. Forward, M. Bartlam, Z. Rao and L. L. Wong, Figure 6. Copyright © SBIC 2009; with kind permission from Springer Science and Business Media.[12]

- Fig. 5.6 in Chapter 5 is adapted and reproduced from Springer, *Applied Magnetic Resonance*, **21(3–4)**, 2001, 287–297, High-Field ENDOR and the Sign of the Hyperfine Coupling, B. Epel, P. Manikandan, P. M. H. Kroneck and D. Goldfarb, Figure 2. Copyright © Springer-Verlag 2001; with kind permission from Springer Science and Business Media.[13]

- Fig. 5.10 in Chapter 5 is reproduced from *Helvetica Chimica Acta*, **89(10)**, 2006, 2495–2521, Pulse EPR methods for studying chemical and biological samples containing transition metals, C. Calle, A. Sreekanth, M. V. Fedin, J. Forrer, I. Garcia-Rubio, I. A. Gromov, D. Hinderberger, B. Kasumaj, P. Leger, B. Mancosu, G. Mitrikas, M. G. Santangelo, S. Stoll, A. Schweiger, R. Tschaggelar and J. Harmer. Copyright © 2006 Verlag Helvetica Chimica Acta AG, Zürich.[14]

- Table 5.1 in Chapter 5 is reproduced from the Supporting Information of J. A. B. Abdalla, A. M. Bowen, S. G. Bell, L. L. Wong, C. R. Timmel and J. Harmer, Characterisation of the paramagnetic $[Fe_2S_2]^+$centre in palustrisredoxin-B (PuxB) from Rhodopseudomonas palustris CGA009: g-matrix determination and spin coupling analysis, *Physical Chemistry Chemical Physics*, 2012, **14(18)**, 6526–6537 with permission from the PCCP Owner Societies.[15]

- Fig. 5.11, Fig. 5.12, Fig. 5.14, Fig. 5.15, Fig. 5.18, Fig. 5.19, Fig. 5.22, Fig. 5.23, Fig. 5.25, Fig. 5.26, Table 5.2 and Table 5.3 in Chapter 5 are reproduced from J. A. B. Abdalla, A. M. Bowen, S. G. Bell, L. L. Wong, C. R. Timmel and J. Harmer, Characterisation of the paramagnetic $[Fe_2S_2]^+$centre in palustrisredoxin-B (PuxB) from Rhodopseudomonas palustris CGA009: g-matrix determination and spin coupling analysis, *Physical Chemistry Chemical Physics*, 2012, **14(18)**, 6526–6537 with permission from the PCCP Owner Societies.[15]

- Fig. 7.6 from Chapter 7 is adapted and reproduced from Springer, *Applied Magnetic Resonance*, **41(4)**, 2011, 59–67, Effect of Pumping Pulse Duration on Echo Signal Amplitude in Four-Pulse PELDOR, A. D. Milov, Y. A. Grishin, S. A. Dzuba, and Y. D. Tsvetkov, Figure 5 and Figure 6. Copyright © Springer-Verlag 2011; with kind permission from Springer Science and Business Media.[16]

- Fig. 8.2 in Chapter 8 is reprinted from *Methods*, **34(1)**, K. H. Mok and P. J. Hore, Photo-CIDNP NMR methods for studying protein folding, 75–87. Copyright © 2004, with permission from Elsevier.[17] After a figure in *Progress in NMR Spectroscopy*, **25(4)**, P. J. Hore and R. W. Broadhurst, Photo-CIDNP of biopolymers, 345–402. Copyright © 1993.[18]

- Fig. 8.3 in Chapter 8 is adapted and reprinted from *Progress in NMR Spectroscopy*, **25(4)**, P. J. Hore and R. W. Broadhurst, Photo-CIDNP of biopolymers, 345–402. Copyright © 1993, with permission from Elsevier.[18]

- Fig. 8.4 and Fig. 8.8 in Chapter 8 and Fig. L.1, Fig. L.2, Fig. L.3 and Fig. L.3 in Appendix /refapp:ELOA are reprinted with permission from Lipoprotein Complex of Equine Lysozyme with Oleic Acid (ELOA) Interactions with the Plasma Membrane of Live Cells; V. Vukojevič, A. M. Bowen, K. Wilhelm, Y. Ming, Z. Ce, J. Schleucher, P. J. Hore, L. Terenius and L. A. Morozova-Roche, *Langmuir*, 2010, **26(18)**, 14782–14787. Copyright © 2010 American Chemical Society.[19]

- Fig. 8.5 in Chapter 8 is adapted and reprinted from *Methods*, **34(1)**, K. H. Mok and P. J. Hore, Photo-CIDNP NMR methods for studying protein folding, 75–87. Copyright © 2004, with permission from Elsevier.[17]

- Fig. 8.11, Fig. 8.9 and Table 8.3 in Chapter 8 are reprinted with permission from the Supporting Information of Lipoprotein Complex of Equine Lysozyme with Oleic Acid (ELOA) Interactions with the Plasma Membrane of Live Cells; V. Vukojevič, A. M. Bowen, K. Wilhelm, Y. Ming, Z. Ce, J. Schleucher, P. J. Hore, L. Terenius and L. . Morozova-Roche, *Langmuir*, 2010, **26(18)**, 14782–14787. Copyright © 2010 American Chemical Society.[19]

- Table 8.2 in Chapter 8 is adapted and reprinted from the Supporting Information of *Journal of Molecular Biology*, **268(5)**, L. A. Morozova-Roche, C. C. Arico-Muendel, D. T. Haynie, V. I. Emelyanenko, H. van Dael and C. M. Dobson, Structural characterisation and comparison of the native and A-states of equine lysozyme, 903–921. Copyright © 1997, with permission from Elsevier.[20]

- Fig. A.1 in Appendix A is reproduced from *www.wikipedia.org* and is licensed under the GNU Free Documentation License.

- Fig. A.2 in Appendix A is reprinted from *Physical Review*, **109(6)**, J. Blume, Electron spin relaxation times in sodium-ammonia solutions, 1867-1873.[21]

- Fig. A.3 in Appendix A is reprinted with permission from *The Journal of Chemical Physics*, **19(4)**, J. T. Arnold, S. S. Dharmatti and M. E. Packard, Chemical Effects on Nuclear Induction Signals from Organic Compounds, 507. Copyright © 1951, AIP Publishing LLC.[22]

- The image of Alice used in the Acknowledgments is after John Tenniel adapted from an image digitized by Project Gutenberg (*http://www.gutenberg.org/*).

For my parents.

Contents

1 Introduction **1**
- 1.1 The scope of this thesis . . . 2
- 1.2 Understanding spin . . . 3
  - 1.2.1 Spin angular momentum and the magnetic dipole . . . 4
  - 1.2.2 The electronic g-factor . . . 4
- 1.3 The resonance condition and energy levels in EPR and NMR . . . 6
  - 1.3.1 The Zeeman effect . . . 6
  - 1.3.2 The anomalous Zeeman effect and magnetic resonance spectroscopy . . . 7
- 1.4 Coupling in EPR and NMR for spin-$\frac{1}{2}$ particles . . . 10
  - 1.4.1 Coupling of unpaired electrons to an external magnetic field . . . 11
  - 1.4.2 Coupling of spin-$\frac{1}{2}$ nuclei to an external magnetic field . . . 11
  - 1.4.3 Electron-nuclear hyperfine interaction . . . 12
  - 1.4.4 Electron-electron exchange coupling . . . 14
  - 1.4.5 Nuclear-nuclear through bond coupling . . . 15
  - 1.4.6 Through space dipolar coupling . . . 15
- 1.5 The spin Hamiltonian in a static magnetic field . . . 17
- 1.6 Methods in modern NMR and EPR experiments . . . 18
- 1.7 The vector model . . . 19
  - 1.7.1 The application of pulses in the rotating vector frame . . . 20
  - 1.7.2 The frequency offset . . . 22
- 1.8 Relaxation in magnetic resonance . . . 23
  - 1.8.1 Spin-lattice or longitudinal relaxation, T_1 . . . 23
  - 1.8.2 Spin-spin or transverse relaxation, T_2 . . . 24
  - 1.8.3 Phase memory time, T_m . . . 25
  - 1.8.4 Spectral diffusion . . . 25
- 1.9 The structure of this thesis . . . 26

2 Double electron-electron resonance (DEER): an experimental, theoretical and computational approach **28**
- 2.1 The theoretical basis of DEER . . . 29
  - 2.1.1 The effect of exchange coupling on DEER spectra . . . 33
  - 2.1.2 The validity of the point dipole approximation . . . 35
  - 2.1.3 The dipolar coupled spectrum . . . 35
- 2.2 The DEER pulse sequences . . . 39

2.3 A description of DEER using the vector model . . . 41
2.4 Orientational selection and DEER . . . 43
2.4.1 Orientational selectivity in nitroxide - nitroxide DEER . . . 45
2.4.2 Orientational selectivity in DEER measurements on metal centres . . . 52
2.5 DEER at X-band: experimental considerations . . . 54
2.6 Simulating orientationally selective DEER . . . 57
2.6.1 Simulating the orientational dependence of the non-secular part of the dipolar interaction . . . 65
2.7 Analysis of experimental DEER traces . . . 65
2.7.1 The structure of the DEER trace . . . 66
2.7.2 The form of the background correction . . . 68
2.7.3 DEER distance analysis: the Tikhonov regularization . . . 69
2.7.4 DEER orientational analysis: pre-simulated libraries of spectra . . . 71

3 Orientationally selective DEER measurements on copper(II) systems 75
3.1 Introduction to EPR of copper systems . . . 75
3.1.1 Previous EPR studies on copper(II) systems . . . 78
3.2 EPR materials and methods . . . 81
3.2.1 Continuous wave EPR measurements . . . 81
3.2.2 Pulsed EPR measurements . . . 81
3.2.3 Simulation of orientationally selective DEER: background correction . . . 84
3.3 Copper-copper, copper-nitroxide and nitroxide-nitroxide rod-like model systems . . . 86
3.3.1 Model systems: design, synthesis and sample preparation for EPR . . . 86
3.3.2 Density Functional Theory (DFT) modelling to generate a molecular model for simulation of spectra . . . 91
3.3.3 Validation of the models generated via DFT by comparison to crystal structures 100
3.3.4 CW EPR on the model systems; results and analysis . . . 101
3.3.5 DEER experiments on model systems: choice of experimental parameters . . . 102
3.3.6 DEER experiments on the model systems: simulated and experimental results and analysis . . . 106
3.3.7 Summary of results for the $NO^{\bullet}-NO^{\bullet}$, $Cu-NO^{\bullet}$ and Cu−Cu model systems . . . 116
3.4 EPR measurements on the copper amine oxidase homo-dimer . . . 117
3.4.1 Sample preparation for copper amine oxidase . . . 117
3.4.2 The relative positions of the two copper centres in a copper amine oxidase homo-dimer . . . 118
3.4.3 CW EPR of AGAO: results and analysis . . . 120
3.4.4 DEER experiments on AGAO: choice of experimental parameters . . . 120
3.4.5 DEER experiments on AGAO: results and analysis . . . 122
3.5 The consequence of g-tensor axiality . . . 127
3.6 The effect of the model used in simulations of orientational DEER . . . 129
3.6.1 Analysis and conclusion on dependence of the model used . . . 131
3.7 Short range distance analysis on a copper nanoring . . . 133
3.7.1 Copper nanoring sample synthesis and preparation . . . 134

3.7.2 Dipolar convolution for analysis of short inter-spin distances and exchange contributions . . . 136
3.7.3 Orientational analysis of dipolar convolution . . . 138

4 Structural determination of the electron transport complexes formed by ferredoxin, ferredoxin reductase and cytochrome P450 using orientationally selective DEER 140
4.1 An introduction to ferredoxin reductase, ferredoxin and cytochrome P450 . . . 142
4.1.1 Existing crystal structures in the literature . . . 144
4.1.2 Sample preparation . . . 146
4.1.3 The importance of the binding constant . . . 149
4.2 EPR experiments . . . 153
4.3 Orientational DEER simulation . . . 155
4.3.1 Simulation of orientationally selective DEER libraries . . . 156
4.3.2 Simulating the nitroxide-nitroxide DEER for MTSL . . . 160
4.4 Calculation of spin label rotamer distributions . . . 161
4.4.1 Comparison of the spin label ensembles for PuxB and HaPux . . . 163
4.4.2 The reliability of MMM . . . 164
4.5 Generating initial starting structures for fitting . . . 167
4.5.1 PatchDock and FireDock . . . 168
4.5.2 Choosing parameters to direct the docking . . . 170
4.5.3 The use of biochemical information . . . 172
4.6 Fitting the simulated data to the experimental data . . . 175
4.6.1 The use of sparse distance constraints . . . 180
4.7 The fitted DEER traces and structures of the complexes . . . 183
4.7.1 Validation of the final structure for the HaPux-P450 complex . . . 187
4.7.2 Further refinement and analysis of the DEER fitted structures . . . 189
4.8 Reflection on the docked structures found . . . 196

5 Determination of the *g*-tensor orientation and spin distributions for the $[Fe_2S_2]^+$ cluster in *Plasutradoxin* B 201
5.1 A theoretical introduction to ENDOR and HYSCORE . . . 202
5.1.1 The ENDOR technique . . . 202
5.1.2 The HYSCORE technique . . . 211
5.2 Determination of the *g*-tensor orientation and the spin distributions within the $[Fe_2S_2]$ cluster in PuxB . . . 215
5.2.1 Existing *g*-tensor orientations for related $[Fe_2S_2]$ protiens . . . 215
5.2.2 Experimental details . . . 216
5.2.3 The method of analysis . . . 219
5.2.4 Devising a structural model for fitting to the experimental data . . . 220
5.2.5 Spin densities and spin projection factors . . . 225
5.2.6 Calculation of the ^1H hyperfine couplings . . . 230
5.3 Experimental results on PuxB to determine the *g*-tensor orientation . . . 234
5.3.1 Comparison of the EPR for PuxB alone and PuxB-PuR . . . 234

5.3.2 Assignment of the proton identities to individual hyperfine couplings 238
5.3.3 Simulation and fitting of the orientationally dependent ENDOR and HYSCORE spectra 242
5.4 Density Functional Theory Calculations on the $[Fe_2S_2]^+$ centre in PuxB 246
5.4.1 Comparison of DFT results with the experimental results 248
5.4.2 Variable mixing time ENDOR to determine the absolute sign of the hyperfine couplings 249
5.4.3 The optimal g-matrix orientation and the dependence on the structure 250
5.5 Discussion and conclusion 252
5.5.1 Use of $[Fe_2S_2]^+$ clusters as spin probes 255

6 Repeated Excitations IN DEER (REINDEER) 257
6.1 The need for modifications of DEER 257
6.2 Application of Repeated Excitations IN DEER (REINDEER) 258
6.2.1 Experimental conditions 259
6.2.2 Tuning the REINDEER experiment 261
6.3 REINDEER experimental data: results and analysis 264
6.3.1 The theoretical relationship between REINDEER and DEER traces with supporting simulations 266
6.4 Orientational selectivity and REINDEER 270
6.4.1 Conclusions on the applicability of REINDEER to reduce orientational selection 273

7 Dead-time free three-pulse DEER 275
7.1 Introduction to dead-time free DEER 275
7.1.1 The advantages of three-pulse DEER 277
7.1.2 Why do we need dead-time free DEER? 279
7.1.3 Other dead-time free EPR techniques 279
7.2 Initial experimental investigations 280
7.2.1 Experimental conditions 280
7.2.2 TWT non-linearity 281
7.2.3 The linear regime of the TWT 282
7.2.4 The dynamic phase shift 284
7.3 Experimental dead-time free three-pulse DEER 289
7.3.1 Experimental conditions for dead-time free three-pulse DEER 289
7.3.2 Dead-time free three-pulse DEER experimental results 290
7.3.3 Experimental determination of the zero-time for three-pulse DEER 292
7.3.4 Effects of the dynamic phase-shift when processing data 293
7.3.5 The best method of processing dead-time free three-pulse DEER data 297
7.4 Theoretical analysis of three-pulse DEER 298
7.4.1 Hamiltonians for simulation of DEER 298
7.4.2 Calculating DEER spectra 302
7.4.3 Parameters for the simulation 304
7.5 DEER simulation results 307
7.5.1 The origin of the dynamic phase shift 307

7.5.2 Determination of the zero-time, (t_0), using simulations . . . 311
7.5.3 The dynamic phase shift in simulations of three-pulse DEER . . . 313
7.5.4 The effect of the phase-shift on the modulation depth . . . 316
7.5.5 A theoretical method for correction of the dynamic phase shift in dead-time free three-pulse DEER . . . 322
7.6 Conclusions . . . 325

8 Application of chemically induced dynamic nuclear polarization to elucidate the surface structure of equine lysozyme with oleic acid complexes 327
8.1 An introduction to the theory and methods of CIDNP . . . 328
8.1.1 Radical pairs and spin chemistry . . . 329
8.1.2 The radical pair process in biological photo-CIDNP . . . 330
8.1.3 Representative CIDNP data . . . 333
8.2 A brief review equine lysozyme complexes with oleic acid (ELOA) as a model system and other related complexes . . . 336
8.2.1 Existing literature on the interaction of oleic acid complexes with cells and membranes . . . 338
8.2.2 Previous NMR studies of equine lysozyme and ELOA . . . 340
8.3 Experiments conducted on the equine lysozyme oleic acid complex (ELOA): experimental procedure and theory . . . 340
8.3.1 Production and characterization of ELOA complexes . . . 341
8.3.2 Fluorescence imaging and fluorescence correlation spectroscopy . . . 343
8.3.3 NMR and CIDNP experimental setup . . . 343
8.4 Experiments conducted on the equine lysozyme oleic acid complex (ELOA): experimental results, analysis and discussion . . . 348
8.4.1 Summary of the results from fluorescence experiments . . . 348
8.4.2 Results of NMR and photo-CIDNP to probe the surface and structure of ELOA in relation to the native and molten-globule states of equine lysozyme . . . 349
8.4.3 Solvent accessibility calculations . . . 355
8.4.4 Interpretation of the CIDNP data in light of the solvent accessibility data, hydrogen exchange data and protein structures . . . 355
8.5 Conclusions . . . 359

9 Conclusions and further work 360

Bibliography 365

Appendices

A A historical review of EPR and NMR i
A.1 A brief time-line of EPR and quantum mechanics . . . i
A.1.1 The Stern-Gerlach experiment, hydrogen fine structure and Zeeman splittings . . . ii
A.1.2 Progression towards modern EPR techniques . . . iv

A.2 A brief time-line of NMR and CIDNP v
A.2.1 Chemically Induced Dynamic Nuclear Polarisation vii

B The classical description of magnetic resonance ix
B.1 The magnetic dipole for orbital angular momentum x

C Experimental evidence for spin angular momentum xii
C.1 The interactions or coupling of angular momenta with one another and external magnetic fields xii
C.2 The quantum mechanics of hydrogen spectra fine structure xv
C.3 The quantum mechanics of the Zeeman effect xvi
C.4 The quantum mechanics of the Stern-Gerlach experiment xviii

D The Landé *g*-factor xx

E Interactions that contribute to the structure of magnetic resonance spectra for nuclei $S > \frac{1}{2}$ xxi
E.1 Nuclear quadrupole interaction xxi
E.2 Zero field splitting xxii

F The vector model for four-pulse DEER xxiii

G Synthetic schemes for copper and nitroxide model systems xxv

H The catalytic cycle of cytochrome P450 xxxi

I The experimental parameters used for DEER experiments on the ferredoxin reductase−ferredoxin and ferredoxin−P450 protein systems xxxii

J PatchDock and FireDock xxxv
J.1 PatchDock xxxv
J.2 FireDock xxxvi

K Derivation of the rotating frame Hamiltonians and the time-dependent Hamiltonians for the pump pulse in regions of pulse overlap xxxvii

L Fluorescence experiments performed on equine lysozyme with oleic acid bound (ELOA) xliv
L.1 Fluorescence experimental procedures and theory xliv
L.1.1 Fluorescence imaging xlv
L.1.2 Fluorescence correlation spectroscopy (FCS) xlv
L.2 Fluorescence results for ELOA and PC12 cells xlvii
L.2.1 Single colour fluorescence studies with fluorescently labelled ELOA xlvii
L.2.2 Single colour fluorescence studies with fluorescently labelled plasma membrane li

L.2.3 Dual colour fluorescence studies with fluorescently labelled ELOA and plasma membrane li

Chapter 1

Introduction

From the lodestones of the ancient world to applications in modern medical imaging, people have always found magnets both intriguing and useful in equal measure. Although the bulk properties of magnets have been known about for thousands of years and understood for several hundred, it is only in the last century that magnetism on a sub-atomic level has been studied. Magnetism on this scale arises from 'spin', an innate property possessed by electrons and some nuclei.

Arguably the two most important analytical techniques relying on the existence of spin are: Electron Paramagnetic Resonance (EPR), also known as Electron Spin Resonance (ESR), which probes unpaired electrons and Nuclear Magnetic Resonance (NMR) that can detect any nuclei with non-zero spin, such as ^{1}H, ^{13}C, ^{14}N, ^{15}N, ^{19}F, etc.

Although the first EPR measurement was recorded by Evgeny Zavoisky at Kazan State University in 1944,[23] the year before the first recognizable NMR measurements of water (Bloch et al.)[24] and solid paraffin (Purcell et al.),[25] the development of EPR has undoubtedly been slower than that of NMR, due to the requirement of higher operating frequencies and shorter timescales. This makes the hardware necessary for pulsed EPR techniques much more difficult to construct than that required for pulsed NMR techniques. Furthermore, whereas NMR can be used to study any nucleus with non-zero spin (although difficult for quadrupolar nuclei), EPR can only be applied to systems that have unpaired electrons.

NMR is now a routine technique used ubiquitously by synthetic chemists for substance analysis and identification, whereas EPR has remained a more specialized technique, with equipment far less

automated and at most institutes much less available. (In the Oxford Chemistry department at the time of writing this thesis, there are fifteen individual NMR spectrometers operating across the four sub-departments, all capable of running complex pulse sequences, compared to four EPR spectrometers, only one of which is capable of pulsed measurements).

In recent years, EPR has grown in popularity due to the availability of sophisticated hardware, a consequently expanding arsenal of measurement techniques and an increasing variety of spin probes. In particular, for protein systems with complex NMR spectra, the relative simplicity of the EPR spectra, which directly probe unpaired electrons and their immediate environments, offers an attractive alternative.

The history of magnetic resonance techniques is fundamentally tied to that of quantum mechanics, since the first experiments using magnetic transitions, such as the Stern-Gerlach experiment, provided evidence for previously unknown quantum mechanical properties. A historical perspective on the development of EPR and NMR is given in Appendix A.

1.1 The scope of this thesis

This thesis utilizes pulsed EPR to study a variety of biological systems. Most of the results have been obtained using the technique Double Electron-Electron Resonance (DEER) also known as Pulsed Electron DOuble Resonance (PELDOR). This technique measures both distances and relative orientations between spin centres and can be used to compute the frozen solution state structures of docked protein complexes (Chapters 2, 3 and 4). To understand orientational measurements, it is necessary to find the orientation of the electronic g-tensor within the structure of the protein being studied. This is achieved using Electron Nuclear DOuble Resonance (ENDOR) and HYperfine Sublevel CORrElation (HYSCORE) measurements (Chapter 5). EPR methodological development was performed by examining in detail the orientational effects on DEER measurements of copper model systems, resulting in the suggestion of two modifications of existing DEER techniques: Repeated Excitations IN DEER (REINDEER) and dead-time free three pulse DEER (Chapters 6 and 7). These techniques may afford better measurements to be taken on systems traditionally difficult to study using DEER. This thesis

also includes work on Chemically Induced Dynamic Nuclear Polarization (CIDNP), an NMR technique that uses the polarization of an unpaired electron to enhance the NMR intensities of the nuclei to which it is coupled; in effect, a reverse of the ENDOR EPR technique. The spectra produced from this technique are much simpler than those from most other NMR techniques, since the enhancements seen in the NMR spectra are limited to the nuclei near the site of the unpaired electron (Chapter 8).

1.2 Understanding spin

For magnetic resonance, the most important quantum mechanical property is the spin angular momentum, or spin, of a particle. This is denoted by the quantum number s for an electron (and the analogous i for a nucleus). The magnitude of the electronic spin angular momentum vector ($\|\mathbf{s}\|$) and the projection of this vector onto the z-axis (s_z) are quantized.[a]

$$\|\mathbf{s}\| = \sqrt{s(s+1)}\hbar \qquad (1.1)$$

$$s_z = m_s\hbar \qquad (1.2)$$

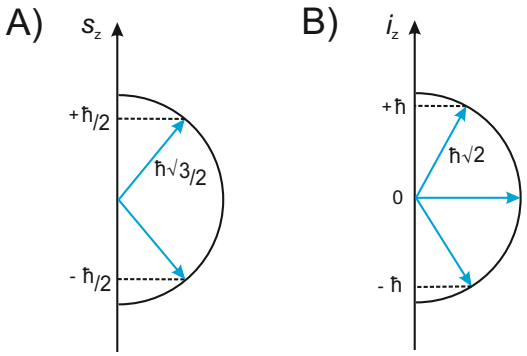


Figure 1.1: **Left:** Equations describing the spin magnitude and projection onto the z-axis. $\hbar$ is the reduced Planck constant and m_s is the spin angular momentum quantum number, which can take values from $-s$ to $+s$ in integer steps with a total of $2s+1$ values. **Right:** The spins can be represented in vector form. **A)** The spin vector projections for a spin-$\frac{1}{2}$ particle (such as an electron) onto an arbitrary z-axis. **B)** The spin vector projections for a spin-1 particle (such as a ^{14}N nucleus) onto an arbitrary z-axis.

In the presence of an external magnetic field to define the z-axis, the $2s+1$ components of m_s will possess different energies. It was the detection of transitions between these energy levels that provided the experimental evidence for the existence of spin angular momentum and it is the same

[a]The Heisenberg uncertainty principle prohibits the simultaneous specification of all components of an angular momentum and its magnitude.

energy transitions which form the basis of all analytical magnetic resonance techniques.

1.2.1 Spin angular momentum and the magnetic dipole

Associated with the spin is a magnetic dipole moment, the magnitude of which is denoted μ_s:

$$\mu_s = g_s \frac{-e}{2m_e}\sqrt{s(s+1)}\hbar = -g_s\sqrt{s(s+1)}\mu_{\mathrm{B}} \tag{1.3}$$

where e is the charge on an electron, m_e is the mass of an electron and μ_B is he Bohr magneton, $\mu_B = \frac{e\hbar}{2m_e}$. The g_s-factor is a correction to the classical analogue of magnetic dipole moments derived from the motion of charge in a magnetic field (See Appendix B). For a free electron, g_s is more commonly notated as g_e and takes a value of $g_e \sim 2.00232$. This value implies that the electron appears to be twice as effective in producing a magnetic moment compared to a corresponding classical body. More detail on g-factors is given in Section 1.2.2.

The spin magnetic dipole moment vector, $\boldsymbol{\mu}_{\mathbf{s}} = -\frac{g_s\mu_{\mathrm{B}}}{\hbar}\mathbf{s}$, lies anti-parallel to the corresponding spin angular momentum vector, $\mathbf{s}$. Likewise the z-components of both, $\mu_{s,z} = -g_s m_s \mu_{\mathrm{B}}$ and s_z respectively, are also anti-parallel. This is due to the negative charge on the electron. For nuclei, the nuclear spin magnetic dipole moment can either lie parallel or antiparallel to the nuclear spin angular momentum vector, $\mathbf{i}$. This is dependent on the sign of the gyromagnetic ratio (γ) of the nucleus, positive or negative respectively. More detail on the gyromagnetic ratio is given in Section 1.3.2.

In some EPR active systems, the paramagnetic centre comprises a system of strongly coupled electrons, as seen in Chapters 4 and 5. In these cases, s is replaced by S and m_s by M_S, where capitalization denotes the overall value for the coupled system.

1.2.2 The electronic *g*-factor

The Dirac equation, a relativistic wave equation, provides a description of spin-$\frac{1}{2}$ particles and predicts that the g-value for a free electron should be $g_e = 2$.[26,27] Experimentally, g_e is found to be slightly larger than this theoretical value, ~ 2.00232. This small correction to the theoretical value is known

as the anomalous magnetic dipole moment and has been accounted for theoretically using quantum electrodynamics.[b] However, discussion of this is beyond the scope of this application-driven thesis.

The electronic g-factor, g_e, is only applicable for free electrons. When an electron is found within an atom or molecule its g-factor will vary from g_e. The size of the variation, Δg, will depend on the coupling of the electron to its environment, in particular the spin-orbit coupling and the energy separation between ground and excited electronic states. The components of $\boldsymbol{\Delta g}$ are described by the equation:

$$\Delta g_{ij} \propto \lambda \sum_{n \neq 0} \frac{\left\langle \psi_0 \left| \hat{L}_i \right| \psi_n \right\rangle \left\langle \psi_n \left| \hat{L}_j \right| \psi_0 \right\rangle}{\epsilon_0 - \epsilon_n} \tag{1.4}$$

where ψ_0 is the ground state wave-function, ψ_n are the excited state wave functions, λ is the spin-orbit coupling constant, $\hat{L}$ is the orbital angular momentum coupling operator and $(\epsilon_0 - \epsilon_n)$ is the energy separation between ground and excited states.[29] The indices i and j denote the tensor or vector elements.

The g-factor is an anisotropic quantity, due to the anisotropic nature of the magnetic dipoles in the surrounding system and the directional nature of p, d, f and higher order orbitals.

Different electron environments can give rise to characteristic g-values and anisotropy. For example in organic radicals, such as carbon centred radicals, the deviation from g_e is small, since the level of spin-orbit coupling in such molecules is low, due to the small values of orbital angular momentum present in these systems. For systems where the orbital angular momentum is non-negligible, such as electrons close to metal centres, the coupling of the spin and orbital angular momentum causes variation in g.

In simple atomic cases that fall within the limit of Russell-Saunders coupling (where L and S are good quantum numbers), it is possible to predict the g-factor via the Landé formula to give the Landé g-factor, g_J.[c 30] However, for most spin systems quenching of the spin orbit coupling causes

[b] Classically, electrodynamics expresses the electromagnetic field as a collection of simple harmonic oscillators. Each of these possesses a zero-point energy, which causes fluctuating electric and magnetic fields within the electromagnetic vacuum. Interaction of these fluctuations with the electron prevents it from spinning smoothly and these "wobbles" increase the electronic magnetic moment over that which would be predicted for a smoothly spinning particle.[28]

[c] More detail on the Landé g-factor is given in Appendix D.

deviations from this predicted value. For metal centres in chemical compounds, the addition of ligands to the metal centre disrupts the symmetry of the orbitals quenching the spin-orbit coupling to varying degrees. This quenching of the spin-orbit coupling can cause a broad range of g-values to be observed for different systems. For example, electrons associated with an iron centre can have g-factors that vary from less than 1 to greater than 6, due to incomplete quenching of the spin-orbit coupling in the ground state.[31]

1.3 The resonance condition and energy levels in EPR and NMR

When a particle possessing non-zero spin angular momentum is placed in an external magnetic field, the magnetic spin dipole moment will interact with the external field. As the angular momenta states are quantized with respect to an arbitrary z-axis (see Fig. 1.1), when this z-axis is defined by an external magnetic field, the different orientations of the spin angular momentum dipole moment adopt different energy values. This interaction is known as the Zeeman effect.

1.3.1 The Zeeman effect

The original observation of the Zeeman effect was made in 1897 by Pieter Zeeman, who saw splitting of the visible lines in electronic excitation spectra upon the application of a magnetic field.[32–35] Although it was recognized at the time that the primary effect causing this was the coupling of the electronic orbital angular momenta to the external field, this did not explain all of the splittings observed. The remainder of the splittings were assigned to the anomalous Zeeman effect. This was finally understood almost 30 years later by Goudsmit and Uhlenbeck as resulting from the coupling of the electronic spin angular momenta to the external magnetic field.[36] Further information on the explanation of Zeeman's observations and the two other experiments, the Stern-Gerlach experiment and the observation of fine structure in hydrogen spectra, which allowed Goudsmit and Uhlenbeck to postulate the electron spin, are given in Appendix C

1.3.2 The anomalous Zeeman effect and magnetic resonance spectroscopy

Electrons within molecules are held in molecular orbitals which are delocalized over many nuclei, therefore the quantum number L is no longer valid to describe the electronic state. However, the spin angular momentum is localized to the electron(s) and therefore s (or S) is still a valid quantum number if the spin-orbit coupling is small. Considering a system with a single unpaired electron, the spin angular momentum interacts with the magnetic field to split the energy levels of the unpaired electron into two. It is the transition between these energy levels that is measured in EPR. NMR is also based on a Zeeman effect that splits the energy levels of the different nuclear spin states of an atom.

For a free electron in an external magnetic field the two possible energy states are $+m_s g_e \mu_B B_0$ and $-m_s g_e \mu_B B_0$, and the energy difference between the two is $\Delta E = g_e \mu_B B_0$.

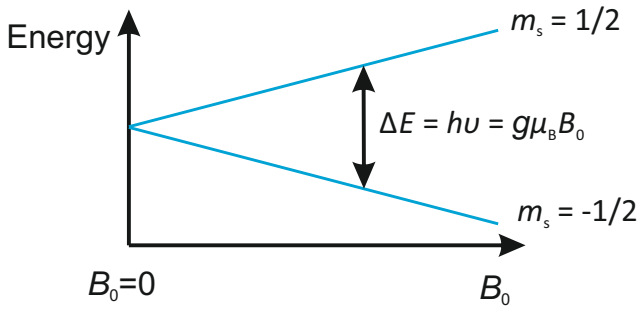


Figure 1.2: For unpaired electrons within molecules, only s is a valid quantum number, since orbital angular momentum is quenched and therefore it is only the coupling of the spin angular momenta to the applied magnetic field that causes splitting in the electronic energy levels.

The original observation of the electronic Zeeman effect was detected in electronic energy level transitions, where an electron moves between electron shells of different n quantum numbers. Thus, the different energy levels of spin-orbital angular momenta gave only small perturbations to the overall energies of the transitions. In contrast, both EPR and NMR detect the transitions between different spin states directly.

When electromagnetic radiation that has a photon energy ($h\nu$) corresponding to the energy difference between the spin levels is applied, the photons can interact with the magnetic moment of the

electron causing the electron's spin state to flip (see Fig. 1.2). This is known as the resonance condition and is fulfilled when:

$$h\nu = g_e \mu_\mathrm{B} B_0 \tag{1.5}$$

In NMR, the notation is usually slightly modified and the resonance condition for an isolated spin-$\frac{1}{2}$ nucleus is given by $h\nu = \gamma\hbar B_0$, where the upper and lower energy levels are $+\gamma m\hbar B_0$ and $-\gamma m\hbar B_0$ respectively. γ is the gyromagnetic ratio, an intrinsic property for a nucleus of a given type, defined as $\gamma = \frac{g_n \mu_n}{\hbar}$. Here, g_n is the nuclear g-factor and μ_n is the nuclear magneton.

For EPR conducted in magnetic fields of c. 0.35 T (X-band) to c. 3.5 T (W-band) the resonance condition lies in the microwave region of the electromagnetic spectrum, c. 9.5 GHz and c. 95 GHz respectively. The energy difference between nuclear spin states is even smaller, and for this reason NMR is generally conducted at higher magnetic field strengths. For example in a magnetic field of 14.1 T protons resonate in the radio frequency region of the electromagnetic spectrum at c. 600 MHz. In both cases, these are much smaller than the energy differences between electronic shells, which correspond to transitions typically in the infra-red to ultra violet region of the electromagnetic spectrum.

The small difference in energies between the two spin states lead to very small differences in population between the upper and lower energy state. At equilibrium, the ratio of the populations is given by the Boltzmann formula.

$$N_{upper}/N_{lower} = \exp\left(\frac{-\Delta E}{k_B T}\right) \tag{1.6}$$

where N_{upper} and N_{lower} are the number of molecules in the upper and lower energy states respectively. ΔE is the energy difference between the two states, k_B is the Boltzmann constant and T is the temperature. Magnetic resonance techniques are inherently insensitive, since the difference in populations between the different spin states is very small, due to the very small energy difference between the states.

The applied electromagnetic radiation is in the form of an alternating magnetic field, B_1. Inter-

actions between this field and the electronic dipole moment allow the energy transfer, which enables the electron to flip from one spin state to the other. This spin-flipping causes the populations of the different spin states to change so that the populations of the different states are no longer Boltzmann in distribution. Over time, the populations will return to the Boltzmann levels. Commonly this occurs via radiation-less relaxation processes rather than emission and thus detection is usually made in absorptive mode, measuring the photons absorbed by the sample.

The energy separation of the electronic or nuclear energy levels is dependent on the strength of the static magnetic field applied. Therefore, by moving to a higher magnetic field strength, the population difference increases and the techniques become more sensitive.

The interaction for the electronic or nuclear magnetic moment with the static magnetic field is described by a static Hamiltonian, $\hat{\mathbf{H}}_0$. For a free electron in a magnetic field, this has the form of Equation 1.7a and an isolated nucleus in a static magnetic field is described by Equation 1.7b.[d]

$$\hat{\mathbf{H}}_0 = \frac{\mu_\mathrm{B} g_e \tilde{\mathbf{B}}_0 \hat{\mathbf{S}}}{\hbar} \tag{1.7a}$$

$$\hat{\mathbf{H}}_0 = -\frac{\mu_n g_n \tilde{\mathbf{B}}_0 \hat{\mathbf{I}}}{\hbar} = -\gamma \tilde{\mathbf{B}}_0 \hat{\mathbf{I}} \tag{1.7b}$$

$\mathbf{B_0}$ is the external magnetic field vector.[e] To distinguish between electron spins and nuclear spins, the angular momentum operators for electrons are denoted by $\hat{\mathbf{S}}$ and nuclear spin angular momentum operators and indicated by $\hat{\mathbf{I}}$.

The picture of an isolated nucleus or free electron is, however, very unrealistic since electrons and nuclei in atoms and molecules do not exist in isolation. Instead, they couple to one another and to their surroundings, causing shifts in their energy levels. The resonance conditions and Hamiltonians for electrons and nuclei in atoms and molecules are thus much more complex. The couplings affecting the energy levels of the system and their contributions to the Hamiltonian are described in the following

[d] For Equation 1.7a, division by $\hbar$ yields a result in units of angular frequency. In Equation 1.7b, this is already taken into account through γ.

[e] The tilde on the magnetic field vector indicates that this is the transpose of this vector.

Section 1.4.

1.4 Coupling in EPR and NMR for spin-$\frac{1}{2}$ particles

The experimental measurements of the fine structure of hydrogen spectra, the Zeeman effect and the Stern-Gerlach experiment, could be explained using only couplings between the spin angular momenta and orbital angular momenta of an electron to each other and to an external magnetic field. Within atoms and molecules, there are many other types of coupling of magnetic dipole moments and, in order to interpret magnetic resonance spectra, it is necessary to understand these interactions. Furthermore, it is these interactions which are probed in EPR and NMR, the most important interactions contributing to magnetic resonance spectra are:

1. Coupling of electronic angular momenta to an external magnetic field − resulting in an EPR signal.

2. Coupling of nuclear angular momenta to an external magnetic field − resulting in an NMR signal.

3. Coupling of nuclear angular momenta to electronic angular momenta − resulting in hyperfine interactions. These can manifest as structure within an EPR spectrum and also form the basis for the CIDNP technique.

4. Coupling of electronic angular momenta to other electronic angular momenta, either due to orbital overlaps occurring through bonds (exchange coupling) or through space (dipole coupling) − resulting in structure within the EPR spectrum.

5. Coupling of nuclear angular momenta to other nuclear angular momenta, either through bonds (J-coupling/scalar coupling) or through space (dipole coupling) − resulting in structure within the NMR spectrum.

It should be noted that for particles with spin $> \frac{1}{2}$ there are other types of interaction, including nuclear quadrupole interactions and zero field splitting. These are detailed in Appendix E.

1.4.1 Coupling of unpaired electrons to an external magnetic field

As introduced previously, the g-factor for unpaired electrons in atoms and molecules is rarely isotropic and thus is not accurately described by a single number. Instead we must consider a g-tensor, $\boldsymbol{g}$, which describes the full anisotropy of this parameter in three-dimensional space. Hence, the interaction of an unpaired electron with a magnetic field is described by the Hamiltonian:

$$\hat{\mathbf{H}}_{EZ} = \frac{\mu_{\mathrm{B}} \tilde{\mathbf{B}}_0 \boldsymbol{g} \hat{\mathbf{S}}}{\hbar} \tag{1.8}$$

1.4.2 Coupling of spin-$\frac{1}{2}$ nuclei to an external magnetic field

Equation 1.7b described the interaction of an isolated spin-$\frac{1}{2}$ nucleus with an external static magnetic field. However, it does not take into account the effect of the electrons surrounding the nucleus on the magnetic field at the nucleus. The motion of the electrons is very fast on the nuclear timescale and this motion induces magnetic fields, which can be accounted for as perturbations to the static external magnetic field. Furthermore, the difference in the electronic and nuclear timescales means that electronic relaxation is too fast for individual couplings of nuclei to unpaired electrons to be resolved in NMR experiments.

For a spin-$\frac{1}{2}$ nucleus, in a molecule the resonance condition can be quantified as:

$$h\nu = \gamma \hbar B_0 (1 - \sigma) \tag{1.9}$$

where σ is the shielding constant, which gives a numeric correction to the applied static magnetic field, due to different electronic motion and distributions in the system.

The Hamiltonian for the nuclear Zeeman interaction can therefore be rewritten as:

$$\hat{\mathbf{H}}_{NZ} = \frac{\mu_n g_n \tilde{\mathbf{B}}_0 (1 - \sigma) \hat{\mathbf{I}}}{\hbar} = \gamma \tilde{\mathbf{B}}_0 (\mathbf{1} - \boldsymbol{\sigma}) \hat{\mathbf{I}} \tag{1.10}$$

For inclusion in the static Hamiltonian for EPR, the nuclear Zeeman interaction can usually be considered isotropic and represented by Equation 1.7b, unless the hyperfine couplings are very large or there are low lying excited states. The nuclear Zeeman interaction has little influence on the EPR spectrum. However, it is the primary source of interactions in NMR.

1.4.3 Electron-nuclear hyperfine interaction

Although the electronic relaxation may be too fast relative to the timescale of NMR to resolve the coupling of individual electrons to a nucleus in this experiment, the timescale of EPR is much faster. Therefore it is possible to measure individual couplings of nuclei to a unpaired electron using this experiment.[f] This coupling provides one of the major sources of structure in EPR spectra.

The Hamiltonian for the hyperfine interaction between a single electron and can be written as:

$$\hat{\mathbf{H}}_{HF} = \tilde{\hat{\mathbf{S}}}\mathbf{A}\hat{\mathbf{I}} \tag{1.11}$$

where $\mathbf{A}$ is the hyperfine interaction tensor. In a molecule, there may be numerous nuclei coupling to a single unpaired electron. In this case, the Hamiltonian for the hyperfine interaction must be summed over all the contributions from the different nuclei and thus becomes:

$$\hat{\mathbf{H}}_{HF} = \sum_{k=1}^{m} \tilde{\hat{\mathbf{S}}}\mathbf{A}_k\hat{\mathbf{I}}_k \tag{1.12}$$

where an electron couples to m different nuclei.

[f] The difference in the electronic and nuclear timescales is such that the motion of nuclei is very slow on the electronic timescale and thus the nuclei can be approximated as being stationary. This is the Born-Oppenheimer approximation and forms an important basis for the density functional theory calculations used later in this thesis.

The hyperfine tensor can be split into two components: an isotropic part, a_{iso}, resulting from a Fermi contact interaction and an anisotropic part, described by the tensor $\mathbf{T}$, arising from the electron-nuclear dipole-dipole interaction. Hamiltonians for these two interactions can be written respectively as:

$$\hat{\mathbf{H}}_{FC} = a_{iso}\tilde{\hat{\mathbf{S}}}\hat{\mathbf{I}} \tag{1.13}$$

$$\hat{\mathbf{H}}_{ENDD} = \tilde{\hat{\mathbf{S}}}\mathbf{T}\hat{\mathbf{I}} \tag{1.14}$$

a_{iso}, the isotropic hyperfine coupling constant, is given by:

$$a_{iso} = \frac{2}{3}\frac{\mu_0}{\hbar} g_e \mu_B g_n \mu_n \left|\psi_0\left(0\right)\right|^2 \tag{1.15}$$

$\left|\psi_0\left(0\right)\right|^2$ is the spin density at the nucleus. Since this is only non-zero for s orbitals, these orbitals form the basis for the Fermi contact interaction, a direct electron to nuclear interaction. The spherical symmetry of s orbitals leads to the isotropic nature of this interaction.

The dipolar component of the hyperfine interaction occurs through space (as for the other types of dipolar interaction discussed in section 1.4.6). Unlike the Fermi contact interaction, which requires non-zero electron density at the nucleus, the dipolar interaction can be arise for electrons in orbitals that have zero electron density at the nucleus. These orbitals, p, d, f, etc.,are not isotropic and thus give rise to the anisotropic nature of the electron-nuclear dipole-dipole interaction. The dipolar coupling tensor, $\mathbf{T}$, contains the elements:

$$T_{ij} = \frac{\mu_0}{4\pi\hbar} g_e \mu_B g_n \mu_n \left\langle \psi_0 \left| \frac{3r_i r_j - \delta_{ij} r^2}{r^5} \right| \psi_0 \right\rangle \tag{1.16}$$

ψ_0 is the ground state wave function, $\mathbf{r}$ is the vector linking the electron and the nucleus, and r is the distance between the two spins. The indices i and j denote the tensor or vector elements. Using a point dipole approximation, applicable when the electron is mainly localized to one nucleus, for the

hyperfine couplings to other nuclei in the system (where the distance, r, between the electron and these nuclei is ≥ 0.25 nm), the dipolar interaction tensor in the hyperfine principal axis system can be written:

$$\mathbf{T}^d = \frac{\mu_0}{4\pi\hbar}\frac{g_e\mu_B g_n\mu_n}{r^3}\begin{pmatrix} -1 & & \\ & -1 & \\ & & 2 \end{pmatrix} = \begin{pmatrix} -T & & \\ & -T & \\ & & 2T \end{pmatrix} \tag{1.17}$$

The anisotropy of the dipolar part of the hyperfine interaction is vital for the orientational ENDOR and HYSCORE analysis presented in Chapter 5. It should also be noted that hyperfine interactions are the root cause of the photo-CIDNP effect, this is described in detail in Chapter 8.

1.4.4 Electron-electron exchange coupling

Exchange coupling describes the interaction of electrons due to orbital overlap and can be described by the Hamiltonian:

$$\hat{\mathbf{H}}_{EX} = \tilde{\hat{\mathbf{S}}}_1\mathbf{J}\hat{\mathbf{S}}_2 \tag{1.18}$$

where $\mathbf{J}$ is the exchange coupling constant. A positive exchange interaction is described as *antiferromagnetic* coupling and the opposite is *ferromagnetic* coupling where a negative exchange interaction is present. The total exchange coupling is made up from both antiferromagnetic and ferromagnetic contributions. An antiferromagnetic contribution arises from the effect of the orbital overlap on the average kinetic energy of the system, while the Coulomb interaction of the two unpaired electrons, which shows a $\frac{1}{r}$ dependence with the distance between the electrons, causes a ferromagnetic interaction. Further polarization effects may lead to either an antiferromagnetic or a ferromagnetic contribution.[37]

In cases where the exchange interaction is strong, the spin vectors couple to give a total spin, S. An example of this type of system is seen in Chapter 5, which aims to elucidate the g-tensor orientation for a Fe_2S_2 cluster. In this cluster, two iron ions are antiferromagnetically coupled to give a ground state of $S = \frac{1}{2}$. Spin-orbit coupling can also give rise to an anisotropic contribution in the exchange

interaction. However, for organic radicals this is generally very small and can be neglected.

Since the exchange coupling mechanism is dependent on direct overlap between electronic orbitals, in systems without a large degree of electron delocalization, exchange coupling between two unpaired electrons can operate at distances of up to c. 1.5 nm. This is one of the factors providing the lower limit for the DEER experiment, which relies on measuring the longer range through space dipolar interaction (see Chapter 2). When the electrons are greatly delocalized, such as in extended aromatic systems, the exchange interaction can be significant over a much longer distance.[38]

1.4.5 Nuclear-nuclear through bond coupling

Nuclear-nuclear through bond coupling, known as J-coupling or scalar coupling, is characterized by the coupling constant, J, which can take either positive or negative values. J-coupling occurs via a combination of two different mechanisms: the Fermi contact interaction between electrons and nuclei, and Pauli exchange interactions between electrons. Considering two nuclei (A and X), J-coupling gives the following addition to the Hamiltonian:

$$\hat{\mathbf{H}}_J = \frac{\mathbf{J}}{\hbar^2}\tilde{\hat{\mathbf{I}}}_A\hat{\mathbf{I}}_X \tag{1.19}$$

The effect of the J-coupling is to cause shifts in the nuclear energy levels, causing a splitting in the lines of the NMR spectrum. In the case of a nucleus coupling to multiple chemically equivalent nuclei, this causes the familiar multiplet splitting patterns, which are a key feature in the NMR spectra of small molecules. In protein NMR, such as that considered in Chapter 8, the number of J-couplings becomes very large and thus they are not well resolved.

1.4.6 Through space dipolar coupling

Dipolar coupling describes the through space interaction of any two spins: electron-electron, nuclear-nuclear or electron-nuclear. The electronic and nuclear dipolar coupling interactions can be probed directly via experiment; the EPR technique DEER measures the dipolar (and exchange) coupling between two electrons. The experimental data can then be analysed to give information on the relative

positions of the two electrons in space. Dipolar coupling is also the primary mechanism behind the Nuclear Overhauser Effect (NOE),[39] which can be investigated using the NMR NOESY technique to give information on the relative positions of atoms in space.[40] The range over which the electron-nuclear dipolar interaction occurs is generally much smaller and it cannot be resolved explicitly. Instead it is treated as part of the hyperfine interaction as discussed in Section 1.4.3. The interaction for spins of the same type is very similar in form and the electronic dipole coupling contribution to the Hamiltonian of a two electron system and the nuclear dipole coupling contribution to a Hamiltonian describing two coupled nuclei are respectively:

$$\hat{\mathbf{H}}_{DD} = \tilde{\hat{\mathbf{S}}}_1 \mathbf{D} \hat{\mathbf{S}}_2 \tag{1.20a}$$

$$\hat{\mathbf{H}}_{NN} = \tilde{\hat{\mathbf{I}}}_A \mathbf{d}^{(A,X)} \hat{\mathbf{I}}_X \tag{1.20b}$$

$\mathbf{D}$ and $\mathbf{d}^{(A,X)}$ are the dipole interaction tensors for electronic and nuclear dipole interaction respectively. The dipole interaction considers the two spins to act as point dipoles, with localized spin density and a fixed distance between the two spins; $r_{1,2}$ for two electrons or $r_{A,X}$ for two nuclei.

Considering the electronic dipolar interaction, the dipolar Hamiltonian can be expanded to give:[g]

$$\hat{\mathbf{H}}_{DD} = \frac{1}{r_{1,2}^3} \frac{\mu_0}{4\pi\hbar} \boldsymbol{g_1 g_2} \mu_{\mathrm{B}}^2 \left[\tilde{\hat{\mathbf{S}}}_1 \hat{\mathbf{S}}_2 - \frac{3}{r_{12}^2} \left(\tilde{\hat{\mathbf{S}}}_1 \mathbf{r}_{12} \right) \left(\tilde{\hat{\mathbf{S}}}_2 \mathbf{r}_{1,2} \right) \right] \tag{1.21}$$

If the anisotropy of the g-tensors can be ignored under the high-field approximation, the dipolar coupling tensor in its principal axis frame is given by:

$$\mathbf{D}^d = \frac{\mu_0}{4\pi\hbar} \frac{g_1 g_2 \mu_{\mathrm{B}}^2}{r_{12}^3} \begin{pmatrix} -1 & & \\ & -1 & \\ & & 2 \end{pmatrix} = \begin{pmatrix} -\omega_{dd} & & \\ & -\omega_{dd} & \\ & & 2\omega_{dd} \end{pmatrix} \tag{1.22}$$

ω_{dd} is known as the characteristic dipolar interaction frequency and it is the frequency of oscillation

[g] The nuclear dipolar interaction can also be expanded in a similar form.

observed in the DEER experiment. A full introduction to DEER is given in Chapter 2, including treatment of the case when the anisotropy of the g-tensors is not negligible.

The nuclear dipole-dipole interaction is too small to be resolved in solid state EPR, but provides one of the main sources of information in solid state NMR.

1.5 The spin Hamiltonian in a static magnetic field

The Hamiltonian for a system in a static magnetic field is built up from the components described previously, the exact composition depending on which interactions are present. Frequently, the notation $\hat{\mathbf{H}}_0$ is used to describe the spin Hamiltonian in a static magnetic field, $\mathbf{B}_0$; such a Hamiltonian for an unpaired electron in a molecule coupled to the surrounding nuclei is given as:

$$\hat{\mathbf{H}}_0 = \frac{\mu_\mathrm{B}\tilde{\mathbf{B}}_0\boldsymbol{g}\hat{\mathbf{S}}}{\hbar} + \sum_{k=1}^{m}\tilde{\hat{\mathbf{S}}}\mathbf{A}_k\hat{\mathbf{I}}_k \tag{1.23}$$

In some cases for completeness, the nuclear terms ($\hat{\mathbf{H}}_{NZ}$, $\hat{\mathbf{H}}_J$ and $\hat{\mathbf{H}}_{NN}$) are also included, since these can cause slight shifts in the electronic energy levels. However, the effects are so small that they are frequently omitted.

When unpaired electrons are able to couple to other electronic spins (as is the case considered in the DEER experiment, one of the primary themes of this thesis), the through space dipole-dipole interactions ($\hat{\mathbf{H}}_{DD}$) and exchange interactions ($\hat{\mathbf{H}}_{EX}$) also contribute to the Hamiltonian. For two electrons the Hamiltonian for the system is:

$$\hat{\mathbf{H}}_0(S_1, S_2) = \hat{\mathbf{H}}_0(S_1) + \hat{\mathbf{H}}_0(S_2) + \hat{\mathbf{H}}_{EX} + \hat{\mathbf{H}}_{DD} \tag{1.24}$$

1.6 Methods in modern NMR and EPR experiments

The original NMR and EPR experiments were continuous wave (CW) experiments, where a sample in a static magnetic field was irradiated with a single frequency at a time. Different resonance conditions could be probed by sweeping the magnetic field strength with a constant excitation frequency or by changing the frequency of the electromagnetic radiation causing the excitations in a constant magnetic field.

Although CW methods have all but disappeared from NMR (where the bandwidth of frequencies contained in a spectrum is small), in favour of pulsed Fourier transform NMR (ft-NMR), they are still used in EPR for compound characterization. Fourier transform NMR uses microsecond pulses, which are approximately rectangular in the time domain. The finite time length means that each pulse excites over a range of frequencies which is broad enough to excite the entire NMR spectrum simultaneously.[41] The response of the spins to this pulse produces a free induction decay (FID) time domain trace that contains components oscillating at all the frequencies resonant with the sample.[h] The FID is Fourier transformed to give a frequency domain spectrum.

In comparison, pulsed EPR relies on detection of spin echoes (primary, refocused or stimulated), rather than collection of an FID. This is due to the significantly broader frequency range needed to excite many EPR spectra and technically it is very challenging to construct a microwave source that produces microwaves of constant amplitude at a broad range of frequencies. Pulsed EPR uses nanosecond pulses, which have frequency profiles with a width generally <100 MHz. EPR spectra of metal centres are frequently much broader than this. Furthermore, the excitation profiles follow *sinc*-like patterns rather than being equal at all frequencies.[i] Therefore the pulses do not excite equally at all frequencies. A spin echo occurs when the different magnetization components within the system are all refocused along the same axis. The simplest sequence to achieve this is the Hahn echo sequence ($\frac{\pi}{2}$ - τ - π - τ - *echo*). In order to understand the effects of pulses on the system, a simple pictorial method is the vector model (see Section 1.7).

[h] Free induction decay is the signal generated by a non-equilibrium spin-magnetization precessing about the static magnetic field.

[i] The sinc function takes the form: $\mathrm{sinc}(x) = \frac{\sin(x)}{x}$.

Spin echoes can be used to measure EPR field swept spectra. However, in many cases it is still preferable to measure these 'finger-print' spectra via CW methods. The primary reason for this is that measurement of these spectra via CW methods removes any distortions of the spectra due to relaxation processes, in particular spectral diffusion (see Section 1.8.4). Modern CW EPR uses field modulation to give a better signal-to-noise ratio in the spectrum detected. This also means that the spectra are detected in the first derivative.

1.7 The vector model

In magnetic resonance spectroscopy, the application of electromagnetic radiation on resonance with the spins in the system causes spin inversion of individual spins. However, in conventional EPR and NMR experiments the magnetic response is measured for a sample containing many spin systems. Therefore when understanding these experiments, we must consider an ensemble of spin systems. Considering an ensemble of spin-$\frac{1}{2}$ particles in a magnetic field, the z-component of the spin magnetic moment for each spin is well defined. However, without any radio frequency excitation, the orientation of the x/y-components is random. This bulk spin ensemble can be represented by a single magnetization vector, which lies parallel to the applied static field, $\mathbf{B}_0$ (see Fig. 1.3).

This depiction is known as the vector model. Every spin magnetization vector precesses about the external magnetic field at the Larmor frequency, ω:

$$\omega = \frac{g\mu_{\mathrm{B}}}{\hbar} B_0 \tag{1.25a}$$

$$\omega = -\gamma B_0 \tag{1.25b}$$

for an electron and a nucleus respectivly.

The vector model can be viewed in one of two frames: the laboratory frame, where the axes of the frame are stationary, or the rotating frame, where the axes rotate about the z-axis at a given frequency. Usually the frequency of rotation is chosen to coincide with the frequency of the applied

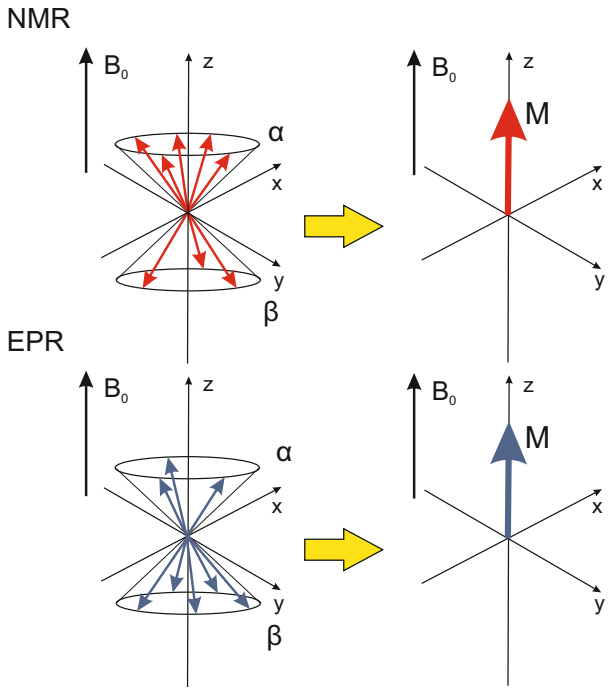


Figure 1.3: The spin angular momentum vectors of individual electrons or nuclei combine to form an overall magnetization vector, which will lie in the same direction as the applied magnetic field when the system is at equilibrium. In NMR (upper scheme), there is an excess of α spins, whereas in EPR (lower scheme), there is an excess of β spins. Both situations result in a magnetization vector that lies parallel to the applied magnetic field, as electrons have magnetization vectors which lie in the opposite direction to their spin vectors, due to the electrons negative charge. To aid viewing, the difference between the number of spins in the upper and lower states has been greatly exaggerated.

electromagnetic field (the pulses); however, sometimes other frequencies are chosen, such as the Larmor frequency of the spins.

1.7.1 The application of pulses in the rotating vector frame

In the laboratory frame, the B_1 field is a polarized linear field, $\mathbf{B}_1$, applied along the x-axis. The linearly polarized field, $\mathbf{B}_1$, can be split into two counter rotating components, which rotate at the same frequency as one another in opposing directions. When we consider the application of this field in the rotating frame, which rotates at the frequency of one of the components, the other component is generally considered so far off resonance that it can be neglected. The mathematical description of this is given in Chapter 7, where it is utilized for the simulations of three-pulse DEER.

The orientation of the x- and y-axes in the vector model can be defined arbitrarily within the plane perpendicular to the z-axis. Thus, in a rotating frame revolving at the frequency of the applied alternating magnetic field, $\mathbf{B}_1$, the orientation of this field with respect to the frame is usually chosen to coincide with the x-axis of the rotating frame.[j] When this is the case, the application of the $\mathbf{B}_1$ causes the magnetization vector to rotate about the x-axis. This induces phase coherence in the x-y plane (see Fig. 1.4).

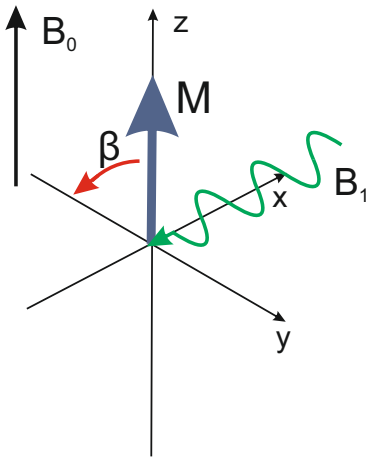


Figure 1.4: Application of an electromagnetic field, $\mathbf{B}_1$, along the x-direction causes a rotation of the magnetization around the x-axis away from the equilibrium position along the $+z$-axis towards the $-y$-axis.

The angle through which the magnetization vector rotates, β, is determined by the length of time the $\mathbf{B}_1$ field is applied for, t_p:[41]

$$\beta = -\omega_1 t_p \tag{1.26}$$

where ω_1 is the precession frequency of spins about the applied electromagnetic field, $\mathbf{B}_1$. Note that ω_1 is also known as the pulse strength.

[j] It should be noted that, experimentally, the angle at which two alternating fields act in the rotating frame is controlled by changing the phase of the linear fields applied in the laboratory frame. This control over the phase of the $\mathbf{B}_1$ fields is the basis of phase cycling used in magnetic resonance experiments to remove unwanted signals from the spectra collected.

1.7.2 The frequency offset

Within a sample, not all of the spins will possess the same Larmor frequency. The result of this is that when the spin ensemble is viewed in one rotating frame, not all of the spins will be static with respect to the frame. The difference in the Larmor frequency of a spin from the frequency of the rotating frame is described as the frequency offset and is quantified as Ω:

$$\Omega = \omega_{\text{Pulse}} - \omega_{\text{Larmor}} \tag{1.27}$$

where ω_{Pulse} is the frequency of the applied electromagnetic field and ω_{Larmor} is the Larmor frequency of a spin. In the rotating frame, this has the effect that when the magnetization vector is excited into the x-y plane, it does not remain as a single vector, but rather fans out into its individual components.

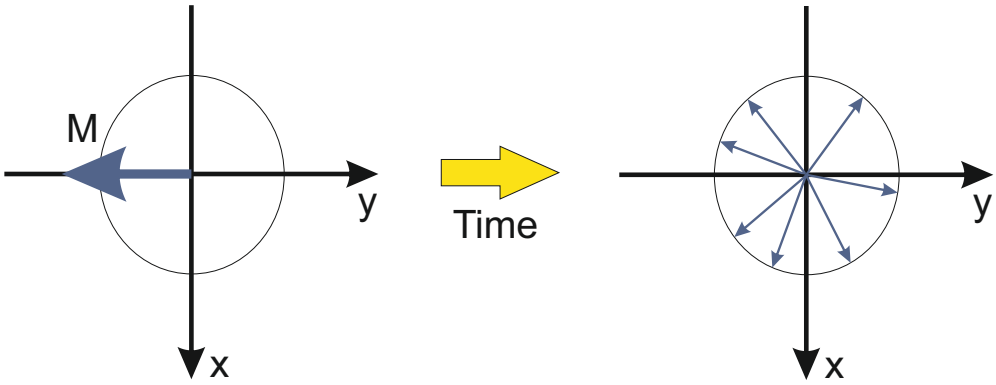


Figure 1.5: When the magnetization vector comprising spin packets of different Larmor frequencies is rotated away from the z-axis to lie in the x-y plane (left hand side of the figure, the z-axis is pointing out of the page), over time the magnetization vector dephases into these component spin packets (right hand side of the figure).

An alternative method to visualize this is to consider a rotating frame that rotates at a frequency just off-resonance with the applied field, $\mathbf{B}_1$. In this representation, the magnetization does not rotate about the x-axis, but rather about the vector sum of the two magnetic fields $\mathbf{B}_0$ and $\mathbf{B}_1$. In this case, the frequency offset is defined as:

$$\Omega = \omega_{\text{Larmor}} - \omega_{\text{Pulse}} \tag{1.28}$$

If the offset frequency, Ω, is smaller than the inverse of the duration of the pulse, a large component of the magnetization vector will still be excited by the correct flip angle. For this reason, a $\mathbf{B}_1$ pulse can excite a range of frequencies simultaneously. In addition, pulses are not comprised of a single frequency, due to their finite length and the Heisenberg uncertainty principle.[42] Thus an applied pulse will excite spins with a range of Larmor frequencies.

1.8 Relaxation in magnetic resonance[29]

Briefly, there are primarily two types of relaxation process:

1. Spin-lattice relaxation, characterized by a relaxation time T_1;

2. Spin-spin relaxation, characterized by a relaxation time T_2.

Relaxation as an umbrella term describes the mechanisms which return the spin populations to their equilibrium Boltzmann distributions after they have been perturbed. This is propagated by fluctuations in the magnetic field experienced by the spin, which either modulate its Larmor precession frequency or induce spin-flips.

Two other relaxation associated parameters are also considered in the following section: the phase memory time, since frequently this is more important in determining EPR experimental parameters than T_1 or T_2; and spectral diffusion as this is important in orientationally selective spectroscopy, when only a portion of a spectrum is excited.

1.8.1 Spin-lattice or longitudinal relaxation, T_1

Spin-lattice relaxation restores the z-component of the magnetization vector to thermal equilibrium. The mechanism occurs due to coupling of the spin to the surrounding lattice. Motion within the lattice causes magnetic field fluctuations to be experienced by the spin. When these fluctuations have a component that occurs at the same frequency as the resonance frequency of the particle, they will induce a spin-flip, the random nature of which restores the system to equilibrium.

This relaxation mechanism is characterized by a time constant, T_1, the spin-lattice relaxation time, which is defined as the time taken for the projection of the magnetization vector, $\mathbf{M}$, to return to $(1 - \frac{1}{e})$ of its original value after a $\frac{\pi}{2}$ pulse perturbation at time $t = 0$. The magnetization in the z-direction at time $= t$, $M_z(t)$, is given by:

$$M_z(t) = M_{z,equilibrium}\left(1 - e^{-\frac{t}{T_1}}\right) \tag{1.29}$$

In liquid state samples, the rate of T_1 relaxation is primarily dependent on the rotational correlation time of the molecules and is fastest when the molecular rotations have a component on resonance with the Larmor frequency of the spins. In frozen solution samples, the rotational correlation time of the whole molecule is necessarily very long. Instead, T_1 relaxation processes are induced by mechanisms such as molecular vibrations.

1.8.2 Spin-spin or transverse relaxation, T_2

Spin-spin relaxation causes dephasing of the x/y-components of the magnetization, this is also termed transverse relaxation. It is characterized by the spin-spin relaxation time, T_2. This is the time taken for the component of the magnetization vector in the x-y plane to decay to $\frac{1}{e}$ of its original value after a $\frac{\pi}{2}$ pulse applied in the x-direction aligns all of the magnetization with the $-y$-axis. The decay of the magnetization in the x-y plane, $M_{x/y}$, with time, t, is described by the following equation:

$$M_{x/y}(t) = M_{x/y}(0)e^{-\frac{t}{T_2}} \tag{1.30}$$

Fluctuations of the magnetic field at the spin being observed cause its precession rate to alter. When viewed over the large ensemble of spins, these small changes in Larmor frequency on an individual spin basis over time cause any phase coherence induced in the x-y plane by the application of pulses to be lost.

In liquid samples, the value of T_2 is also affected by the rotational correlation time, since the motion

of the molecules modulates the coupling between spins in the system. Molecular motions, in particular the rotations of methyl groups, also contribute to T_2 dephasing in both liquid and frozen samples. At cryogenic temperatures, T_2 is frequently the limiting factor for experimental acquisitions and the length of pulse sequences. Examples of this are given in Chapters 3 and 4, where the length of the DEER sequence used is limited by the fast T_2 relaxation times.

T_2 can be measured using a Hahn echo sequence ($\frac{\pi}{2}$ - τ - π - τ - *echo*) where the echo is monitored with different τ delay times. Monitoring the echo height gives a direct measure of the decoherence of the x/y-component of the magnetization with time.

1.8.3 Phase memory time, T_m

In reality, spins in solid samples and frozen samples couple to form a virtually infinite network of spins at fixed positions with respect to one another. In this situation, it is nearly impossible to separate a coherent finite spin system from its environment. In this case, the experiment described previously to measure the transverse relaxation time does not measure the absolute T_2 relaxation of a single spin. Instead the decay parameter measured is the phase memory time, T_m. This empirical parameter contains contributions not only from the spin-spin relaxation, but also lifetime broadening, due to the finite length of the longitudinal relaxation, and instantaneous diffusion, resulting from a change in the magnetic field at the spin being observed, due to the excitation of coupled spins by the pulses applied.

1.8.4 Spectral diffusion

In orientationally selective EPR experiments, only a small fraction of an overall spectrum is excited by an applied pulse (i.e. only those spins with frequencies that lie within the excitation bandwidth of the pulse). As we have already seen, magnetic fluctuations at the spin can change the precession frequency of the spin being observed. Consider a hypothetical pair of coupled spins, A and B, with different resonant frequencies. If spin A is excited and spin B is not, relaxation processes at spin B cause fluctuations in the magnetic field at spin A. This can cause an interchange in the resonant frequencies of the two spins and thus a transfer in the magnetization of spin A to parts of the spectrum that were

not directly excited. In return there is a transfer in magnetization from spin B to the part of the spectrum that is resonant with the pulses applied.[43]

This leads to spins with non-equilibrium magnetization being replaced by spins that are at thermal equilibrium. Although when only spin A is observed this appears to be a relaxation process, the non-equilibrium magnetization is still present in other parts of the spectrum.

1.9 The structure of this thesis

This thesis is primarily concerned with the EPR technique Double Electron-Electron Resonance (DEER), a further introduction to this technique is given in Chapter 2. Although DEER is frequently used to analyse the inter-spin distances between a pair of nitroxide labels, its application to other spin centres such as metal ions is currently much more limited. This is primarily due to the inherent problems associated with the broad spectra of such centres and the associated orientational selectivity. Chapter 2 also looks at the theoretical aspects of orientational selection with respect to the DEER experiment and Chapters 3 and 4 employ orientationally selective DEER for copper-based systems and an $[Fe_2S_2]^+$ cluster respectively.

Chapter 3 uses model systems, both a protein and chemical systems, where the structures are either known or can be modelled using Density Functional Theory (DFT) in order to validate the method of analysis for orientationally selective DEER. Chapter 4 uses the protocol established in the previous chapter and applies it to the determination of the frozen solution state docked protein complexes of ferredoxin with ferredoxin reductase and cytochrome P450. Ferredoxin contains a$[Fe_2S_2]$ cluster which can be prepared in the EPR-active $[Fe_2S_2]^+$ state which has an $S = \frac{1}{2}$ ground state. In order to fully understand the EPR properties of this cluster it was necessary to determine the orientation of the g-matrix with respect to the surrounding protein structure. This was achieved using a combination of Electron Nuclear DOuble Resonance (ENDOR) and HYperfine Sublevel CORrElation (HYSCORE) spectroscopy. The method, analysis and results for this procedure are presented in Chapter 5 and were

used in the analysis of the orientational DEER spectra recorded on the ferredoxin docked complexes. The ferredoxin-P450 structure is the first structure of its type to be determined (in spite of significant efforts to crystallize the structure which have thus far failed) and it is therefore of great biochemical interest.

The expansion of DEER to measuring new systems has highlighted some problems with the existing measurement techniques. Specifically with respect to low modulation depths and short relaxation times. The method development work described in Chapters 6 and 7 has been shown to provide improved results for these parameters by increasing the pump pulse excitation bandwidth (Chapter 6) and using a dead-time free three-pulse sequence (Chapter 7).

Finally CIDNP was used to investigate the surface accessibility of tryptophan, tyrosine and histidine residues in equine lysozyme and its aggregate with oleic acid, ELOA. ELOA has been shown to selectively induce apoptosis in cancer cells and therefore is of great interest as a potential anti-cancer treatment.

Chapter 2

Double electron-electron resonance (DEER): an experimental, theoretical and computational approach

The main pulse sequence used for the work in this thesis is the dual frequency Double Electron Electron Resonance (DEER) experiment, also known as Pulsed ELectron DOuble Resonance (PELDOR). This chapter introduces this technique and provides a theoretical description of the experiment in terms of the Hamiltonian basis and also the pictorial representation using the vector model, previously detailed in Section 1.7 of Chapter 1.

Experimental considerations are discussed and we begin to examine orientation selection and the effect that this can have on DEER spectra. The latter part of this chapter details the simulation of orientationally dependent DEER spectra, applications of this are demonstrated in Chapters 3 and 4.

The original DEER (or PELDOR) experiments were conducted using the three-pulse technique on paramagnetic centres in solids.[44] However, it was the introduction of the four-pulse technique and also the freely available MATLAB-based plug-in software DeerAnalysis (see Section 2.7.3)[45] that made the technique more accessibly to a broader community of scientists rather than just those who specialize in EPR. The new-found popularity of DEER can clearly be seen from the explosion of papers utilizing the technique published in recent years. DEER has found many applications, in particular within the field of structural biology,[46] due to the methodology originated by Berliner and co-workers,[47] following on from earlier work by Kenyon and Bruice,[48] which allowed nitroxide spin labels, in particular (l-oxyl-

2,2,5,5-tetramethyl-Δ^3-pyrroline-3- methyl) methane-thiosulfonate (better known as MTSL: methane-thiosulfonate spin label), to be chemically bound to the thiol group of cysteine residues in proteins. By attaching two spin labels to a protein or pair of proteins, intra- and inter-molecular distances can be measured. In combination with the technique of site-directed mutagenesis,[49,50] this allowed labels to be attached to proteins at known sequential positions and used to study protein structure and conformational flexibility. The first nitroxide-nitroxide DEER measurements were carried out on nitroxide centres distributed in a solid matrix by Larson and Singel in 1993.[51]

2.1 The theoretical basis of DEER

Double Electron-Electron Resonance exploits through space dipolar coupling between two unpaired electrons; as seen in Section 1.4.6 for a pair of electrons coupling can either take place via exchange coupling or dipolar coupling. In most cases for the analysis of DEER data only the dipolar coupling between electrons needs to be considered as the exchange coupling is a shorter range interaction, significant below about 1.5 nm (unless the electrons are delocalized), which is the general lower limit for the applicability of DEER.

DEER probes the coupling between two (or more) electrons and all variants of the DEER technique use a detection sequence on resonance with one of the electron spins; during this sequence a pump pulse on a second frequency resonant with the second electron of a spin pair is applied. The pump pulse inverts the magnetization of the spin with which it is resonant. When the two electrons are coupled to one another via a through space dipolar interaction this inversion of the magnetization of the so-called pump spin changes the magnetic environment of the first (detection) spin. This change in the overall magnetic field experienced by the detection spin causes the Larmor frequency of the detection spin to alter and therefore when the inversion of magnetization of the pump spin occurs during a detection sequence of the first spin this causes the size of the echo observed from the detection spin to change. The magnitude of the echo detected oscillates as the timing of the inverting pump pulse is altered throughout the experiment causing a characteristic oscillating DEER trace to be observed. The frequencies present in the DEER trace are dependent on the magnitude of the dipolar coupling

between the two spins which in turn is dependent on the relative distance and orientation between the two spins. Fig. 2.1 shows a pictorial representation of the classical magnetic dipolar interaction of two electron spins and how this changes under the application of a pump pulse.

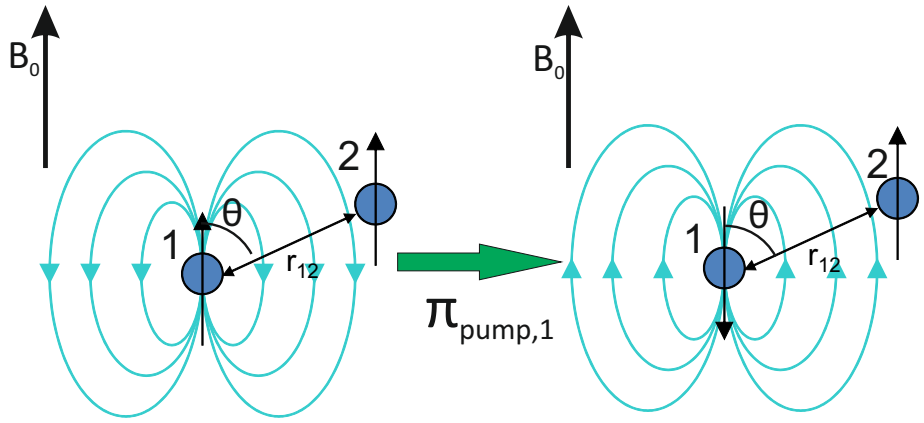


Figure 2.1: A schematic diagram of the classical representation of dipolar coupling between two spins denoted 1 and 2. Initially both spins have their magnetic moments aligned with the field in the lower energy state. The magnetic field projected by electron 1, couples to the static magnetic field (B_0) to give an overall magnetic field, that is experienced by electron 2. If a π pulse is applied on resonance with electron 1 the magnetization of this electron is inverted and as a result the magnetic field experienced by electron 2 is altered.

A typical Hamiltonian describing a DEER system made up from two electrons which interact via a through space dipolar interaction only is therefore:

$$\hat{\mathbf{H}}_0(S_1, S_2) = \hat{\mathbf{H}}_0(S_1) + \hat{\mathbf{H}}_0(S_2) + \hat{\mathbf{H}}_{DD} \tag{2.1}$$

where the different components of this Hamiltonian describe in turn the coupling of each of the electrons to the magnetic field (electronic Zeeman interaction) and also the dipolar coupling between the electrons.

$$\hat{\mathbf{H}}_0(S_1) = \frac{\mu_B \boldsymbol{g_1} \tilde{\mathbf{B}}_0 \hat{\mathbf{S}}_1}{\hbar} \tag{2.2a}$$

$$\hat{\mathbf{H}}_0(S_2) = \frac{\mu_B \boldsymbol{g_2} \tilde{\mathbf{B}}_0 \hat{\mathbf{S}}_2}{\hbar} \tag{2.2b}$$

$$\hat{\mathbf{H}}_{DD} = \frac{1}{r_{12}^3} \frac{\mu_0}{4\pi\hbar} \boldsymbol{g_1 g_2} \mu_B^2 \left[\tilde{\hat{\mathbf{S}}}_1 \hat{\mathbf{S}}_2 - \frac{3}{r_{12}^2} \left(\tilde{\hat{\mathbf{S}}}_1 \mathbf{r}_{12} \right) \left(\tilde{\hat{\mathbf{S}}}_2 \mathbf{r}_{12} \right) \right] \tag{2.2c}$$

$\hat{\mathbf{S}}_1$ and $\hat{\mathbf{S}}_2$ are the angular momentum operators of the two spins. For calculations involving this Hamiltonian in Liouville space, these are frequently represented by combinations of the Pauli spin operator matrices. Further detail on the application of density matrix calculations and the Pauli spin operators is given in Section 2.6.1 where calculations are used to consider the effect of the non-secular part of orientational DEER and also in Section 7.4.2 where calculations from first principles for dead-time free three-pulse DEER are used to study the zero-time of this technique.

The scalar products of the Hamiltonian for the dipolar interaction (Equation 2.2c) can be expanded to give six distinct terms, each of which involves a spin factor comprising components of the angular momentum operators of the two spins and a geometric factor.[52] The dipolar Hamiltonian can thus be rewritten as:

$$\hat{\mathbf{H}}_{DD} = \frac{1}{r_{12}^3} \frac{\mu_0}{4\pi\hbar} \boldsymbol{g_1 g_2} \mu_B^2 \left[A + B + C + D + E + F \right] \tag{2.3}$$

where:

$$A = -\hat{\mathbf{S}}_{1z}\hat{\mathbf{S}}_{2z}\left(3\cos^2\theta - 1\right) \tag{2.4a}$$

$$B = +\frac{1}{4}\left[\hat{\mathbf{S}}_{1+}\hat{\mathbf{S}}_{2-} + \hat{\mathbf{S}}_{1-}\hat{\mathbf{S}}_{2+}\right]\left(3\cos^2\theta - 1\right) \tag{2.4b}$$

$$C = +\frac{3}{2}\left[\hat{\mathbf{S}}_{1z}\hat{\mathbf{S}}_{2+} + \hat{\mathbf{S}}_{1+}\hat{\mathbf{S}}_{2z}\right]\sin\theta\cos\theta e^{-i\phi} \tag{2.4c}$$

$$D = -\frac{3}{2}\left[\hat{\mathbf{S}}_{1z}\hat{\mathbf{S}}_{2-} + \hat{\mathbf{S}}_{1-}\hat{\mathbf{S}}_{2z}\right]\sin\theta\cos\theta e^{+i\phi} \tag{2.4d}$$

$$E = -\frac{3}{4}\hat{\mathbf{S}}_{1+}\hat{\mathbf{S}}_{2+}\sin^2\theta e^{-2i\phi} \tag{2.4e}$$

$$F = -\frac{3}{4}\hat{\mathbf{S}}_{1-}\hat{\mathbf{S}}_{2-}\sin^2\theta e^{+2i\phi} \tag{2.4f}$$

The operators $\hat{\mathbf{S}}_{1Z}$ and $\hat{\mathbf{S}}_{2Z}$ represent the z-component of the complete angular momentum operators $\hat{\mathbf{S}}_1$ and $\hat{\mathbf{S}}_2$. $\hat{\mathbf{S}}_{1/2+}$ and $\hat{\mathbf{S}}_{1/2-}$ are termed the raising and lowering operators and are formed from a combination of the x and y-components of the complete angular momentum operators.

$$\hat{\mathbf{S}}_+ = \hat{\mathbf{S}}_x + i\hat{\mathbf{S}}_y \tag{2.5a}$$

$$\hat{\mathbf{S}}_- = \hat{\mathbf{S}}_x - i\hat{\mathbf{S}}_y \tag{2.5b}$$

Under the high field approximation, applicable for DEER experiments performed at X-band, only components A and B have significant contributions to the dipolar interaction. A is known as the secular part and B as the pseudo-secular contribution. The pseudo-secular contribution mixes the $|\alpha_1\beta_2\rangle$ and $|\beta_1\alpha_2\rangle$ states.[53] Its contribution is small when the difference in resonance frequencies is much larger than the dipolar interaction; this is known as the weak coupling case.

The dipolar Hamiltonian containing the secular and pseudo-secular contributions is:

$$\hat{\mathbf{H}}_{DD} = -\frac{1}{r_{12}^3}\frac{\mu_0}{4\pi\hbar}\boldsymbol{g_1 g_2}\mu_B^2\left[\hat{\mathbf{S}}_{1z}\hat{\mathbf{S}}_{2z} - \frac{1}{4}\left(\hat{\mathbf{S}}_{1+}\hat{\mathbf{S}}_{2-} + \hat{\mathbf{S}}_{1-}\hat{\mathbf{S}}_{2+}\right)\right]\left(3\cos^2\theta - 1\right) \tag{2.6a}$$

$$= \omega_{dd}\hat{\mathbf{S}}_{1z}\hat{\mathbf{S}}_{2z} - \frac{1}{4}\omega_{dd}\left(\hat{\mathbf{S}}_{1+}\hat{\mathbf{S}}_{2-} + \hat{\mathbf{S}}_{1-}\hat{\mathbf{S}}_{2+}\right) \tag{2.6b}$$

However, this is frequently approximated to contain only the secular part, it is this form that is used in the orientational DEER calculations.

$$\hat{\mathbf{H}}_{DD} = \omega_{dd}\hat{\mathbf{S}}_{1z}\hat{\mathbf{S}}_{2z} \tag{2.7}$$

ω_{dd} is the dipolar frequency which can be extracted from an experimental DEER trace, and contains a dependence on the distance between the two electrons, r_{12}, and on the angle between the vector linking the two electrons and the applied magnetic field, θ. Fig. 2.1 demonstrates r_{12} and θ. As the definition of ω_{dd} includes the g-values for the two electrons the frequency is also sensitive to the pump and probe positions used in a DEER experiment.

$$\omega_{dd} = -\frac{1}{r_{12}^3}\frac{\mu_0}{4\pi\hbar}g_1 g_2\mu_B^2\left(3\cos^2\theta - 1\right) \tag{2.8a}$$

$$= \omega_\perp\left(3\cos^2\theta - 1\right) \tag{2.8b}$$

$\omega_\perp$ is the non-orientationally dependent part of ω_{dd}, for a defined pair of radicals where the g-values are known; $\omega_\perp$ is solely dependent on this distance as shown in Table 2.1.

2.1.1 The effect of exchange coupling on DEER spectra

Exchange coupling occurs when the proximity of the two interacting electrons is close enough that the electronic wave-functions overlap and interact via a Pauli interaction (see Section 1.4.4). The magnitude of this interaction, $|J|$, for two isolated electrons is exponentially dependent on the distance

Table 2.1: The dependence of $\omega_\perp$ on the separation of two radicals both with $g_1,\ g_2 = 2.005$.

r_{12} in nm	$\lvert\omega_\perp.2\pi\rvert$ in MHz
0.5	417
1.0	52.2
2.0	6.52
5.0	0.417
10.0	0.0522

between them ($J = J_0 e^{-\beta r}$) and is usually negligible for inter-spin distances greater than *c.* 1.5 nm. In systems with extensive π-conjugation, the electronic wave-functions delocalize over many nuclei and thus the range over which the exchange interaction is active increases.

DEER measures both the exchange and dipolar coupling; however, most methods of analysis do not take into account the exchange coupling and thus it is usually desirable to minimize this component by using systems where there is no significant delocalization of the unpaired electrons. This concern influenced the design of the model systems used in Chapter 3.

The contribution of exchange coupling to the Hamiltonian for a two electron system, containing electrons denoted 1 and 2, takes the form:

$$\hat{\mathbf{H}}_{EX} = \frac{1}{2}\left(\hat{\mathbf{S}}_1.\mathbf{J}.\hat{\mathbf{S}}_2 + \hat{\mathbf{S}}_2.\mathbf{J}.\hat{\mathbf{S}}_1\right) \tag{2.9a}$$

$$= J\hat{\mathbf{S}}_{1z}\hat{\mathbf{S}}_{2z} + \frac{1}{2}J\left(\hat{\mathbf{S}}_{1+}\hat{\mathbf{S}}_{2-} + \hat{\mathbf{S}}_{1-}\hat{\mathbf{S}}_{2+}\right) \tag{2.9b}$$

It should be noted that assuming the interaction is isotropic it is allowable to substitute the J-tensor ($\mathbf{J}$) for a single value, J. Alternatively, Equation 2.9b is also valid for a single orientation of the two electrons with respect to one another where the value of the exchange coupling, J, is dependent on this orientation.

DEER measurements on exchange coupled systems have shown that the exchange coupling alters the oscillation frequency observed in DEER, which will in turn causes inaccuracies in the extracted distance distribution. It has been shown in some cases that, by performing DEER at different magnetic

fields, it is possible to separate the dipolar interaction (which is dependent on the field strength) from the exchange interaction (which does not depend on the field strength).[54] It has also been found that exchange interactions can significantly dampen DEER modulations reducing the quality of data collected.[38]

2.1.2 The validity of the point dipole approximation

As already stated, the exchange interaction is negligible for electronically isolated spin systems, except at small inter-spin separations. In these cases the point dipole approximation for the dipole-dipole interaction is valid; however, at small separations this approximation begins to break down. A theoretical study, where it was assumed that the spin density was localized at the mid point of the N-O bond, found that the point dipole approximation underestimated the dipolar coupling by 35% at 1.75 nm and 20% at 2.0 nm.[55] However, these predictions are at odds with experimental studies for compounds with approximate distances of 2.0 nm, where the deviation from the point dipole approximation was seen to be much less pronounced.[54,56]

Calculations with the spin density split approximately equally between the nitrogen (45%) and the oxygen (50%) in the nitroxide (the remainder distributed along the N-O bond) have shown that a distance is underestimated by <0.04 nm for a distance of 1.5 nm and by <0.03 nm for distances greater than 2.5 nm, which agree with the experimental findings.[57] For most spin labels these errors fall well within the uncertainty in labelling position due to conformational flexibility and thus use of the point dipole approximation in analysis is valid for these systems. For metal centres the spin density distribution is frequently spread over a larger number of atoms and to model this it is necessary to use point dipole interactions between each of the atoms over which the spin density is delocalized in order to calculate appropriate distances.

2.1.3 The dipolar coupled spectrum

Both the through space dipolar interaction and the exchange interaction cause shifts in the energy levels of a pair of radicals. The spectrum of a pair of coupled electron spins is dependent on the relative

magnitude of the dipolar and, if present, the exchange coupling frequencies compared to the Larmor frequencies, ω_1 and ω_2, of the two isolated electrons. As we have already seen in Equation 2.6b, the dipolar Hamiltonian can be written in terms of the dipolar frequency; likewise the static Hamiltonians (Equations 2.2a and 2.2b) can also be rewritten in terms of the Larmor frequencies:

$$\hat{\mathbf{H}}_0(S_1) = \omega_1 \hat{\mathbf{S}}_1 \tag{2.10a}$$

$$\hat{\mathbf{H}}_0(S_2) = \omega_2 \hat{\mathbf{S}}_2 \tag{2.10b}$$

Weak coupling

Weak coupling occurs when $\left|J - \frac{1}{2}\omega_{dd}\right| << |\omega_1 - \omega_2|$. In this case only the secular parts of the Hamiltonians, $\hat{\mathbf{H}}_{DD}$ (Equation 2.6b) and $\hat{\mathbf{H}}_{EX}$ (Equation 2.9b) need to be considered. When the Hamiltonians are written in matrix form this corresponds to the diagonal elements only; thus the eigenstates are simply the basis states of two electrons and the eigenvalues, corresponding to the energy of the eigenstates, are the diagonal elements.

$$\epsilon_i = +\frac{1}{2}(\omega_1 + \omega_2) + \frac{1}{4}(J + \omega_{dd}) \qquad |i\rangle = |\alpha_1\alpha_2\rangle \tag{2.11a}$$

$$\epsilon_{ii} = +\frac{1}{2}(\omega_1 - \omega_2) - \frac{1}{4}(J + \omega_{dd}) \qquad |ii\rangle = |\alpha_1\beta_2\rangle \tag{2.11b}$$

$$\epsilon_{iii} = -\frac{1}{2}(\omega_1 - \omega_2) - \frac{1}{4}(J + \omega_{dd}) \qquad |iii\rangle = |\beta_1\alpha_2\rangle \tag{2.11c}$$

$$\epsilon_{iv} = -\frac{1}{2}(\omega_1 + \omega_2) + \frac{1}{4}(J + \omega_{dd}) \qquad |iv\rangle = |\beta_1\beta_2\rangle \tag{2.11d}$$

The frequencies of the allowed EPR transitions are therefore:

$$\epsilon_{i-ii} = +\omega_2 + \frac{1}{2}(J + \omega_{dd}) \tag{2.12a}$$

$$\epsilon_{i-iii} = +\omega_1 + \frac{1}{2}(J + \omega_{dd}) \tag{2.12b}$$

$$\epsilon_{ii-iv} = +\omega_1 - \frac{1}{2}(J + \omega_{dd}) \tag{2.12c}$$

$$\epsilon_{iii-iv} = +\omega_2 - \frac{1}{2}(J + \omega_{dd}) \tag{2.12d}$$

For a single orientation of the two spins with respect to one another and the magnetic field, this results in two pairs of lines each centred about one of the Larmor frequencies and split by $|J + \omega_{dd}|$. Since ω_{dd} is dependent on the orientation between the magnetic field and the inter-spin vector (see Equation 2.8a), the average overall orientations yields a Pake pattern, where the shape is determined by the statistical distribution of the number of possible orientations. This is demonstrated in Fig. 2.2 and the splitting between peaks of the pattern is also shown.

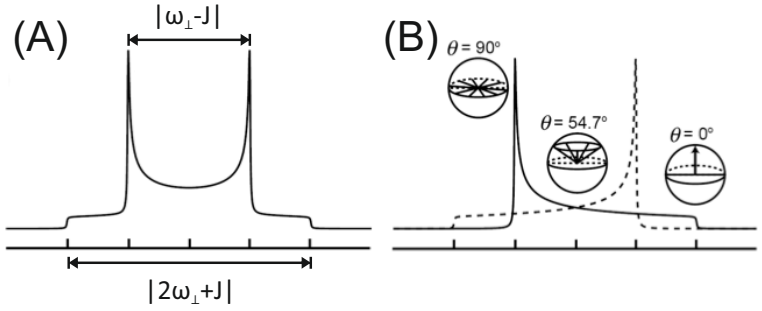


Figure 2.2: (A) The Pake pattern generated under a weak coupling regime. (B) Demonstrating the angular contributions to a Pake pattern. (This is valid under both the weak and strong coupling regimes.) This figure is adapted from a figure on a webpage from the University of Hamburg (*http://www.chemie.uni-hamburg.de/nmr/insensitive/tutorial/en.lproj/dipolar_coupling.html*).[2]

It should be noted that when $|J| << |\omega_\perp|$, as is usually the case for systems studied by DEER, the splitting between the central peaks and outer portions of the spectrum becomes $|\omega_\perp|$ and $|2\omega_\perp|$ respectively.

Strong coupling

The strong coupling limit corresponds to the case when $\left|J - \frac{1}{2}\omega_{dd}\right| >> |\omega_1 - \omega_2|$ and consequently $\omega_1 \approx \omega_2 \approx \omega$. In this case, off-diagonal terms cannot be ignored and they result in the mixing of the two central eigenstates (Equations 2.11b and 2.11c). Hence the eigenvalues and eigenstates for states $|ii\rangle$ and $|iii\rangle$ become:

$$\epsilon_{ii} = \frac{1}{4}J - \frac{1}{2}\omega_{dd} \qquad |ii\rangle = \frac{1}{\sqrt{2}}\left(|\alpha_1\beta_2\rangle + |\beta_1\alpha_2\rangle\right) \tag{2.13a}$$

$$\epsilon_{iii} = -\frac{1}{4}J \qquad |iii\rangle = \frac{1}{\sqrt{2}}\left(|\alpha_1\beta_2\rangle - |\beta_1\alpha_2\rangle\right) \tag{2.13b}$$

The differing symmetry of the states (providing singlet and triplet contributions, as seen in Chapter 8) only allows two possible transitions between the symmetric triplet states: $|i\rangle$ to $|ii\rangle$ and $|ii\rangle$ to $|iv\rangle$. The allowed energy transitions are therefore:

$$\epsilon_{i-ii} = \omega + \frac{3}{4}\left(\omega_{dd}\right) \tag{2.14a}$$

$$\epsilon_{ii-iv} = \omega - \frac{3}{4}\left(\omega_{dd}\right) \tag{2.14b}$$

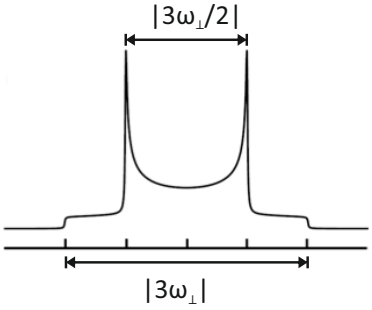


Figure 2.3: The Pake pattern generated under a strong coupling regime. This figure is adapted from a figure on a webpage from the University of Hamburg (*http://www.chemie.uni-hamburg.de/nmr/insensitive/tutorial/en.lproj/dipolar_coupling.html*).[2]

The spectrum at a single orientation therefore consists of a single doublet centred at ω with a separation between the lines of $\left|\frac{3\omega}{2}\right|$. Allowing for the orientational dependence of ω_{dd} yields the Pake pattern seen in Fig. 2.3.

The dipolar spectrum and DEER

Although the dipolar splitting is always present in the EPR of coupled systems usually the size of ω_{dd} is small compared to other splittings in the system such as hyperfine couplings and thus the Pake pattern is hidden beneath these larger couplings in continuous wave (CW) EPR spectra. A CW nitroxide spectrum is on the order of 180 MHz wide whereas, the dipolar coupling, even for a relatively short distance of 2 nm, is only c. 6.5 MHz (see Table 2.1). DEER, however, is designed to probe the dipolar coupling and a Fourier transform of the DEER time trace will yield the Pake pattern, or part of the Pake pattern if not all orientations are excited, in the frequency domain.

It should be noted that for very short distances, <1.5 nm, where the size of the dipolar coupling is very large, it is possible to see the effect of the coupling in the CW spectrum as a contribution to the line broadening.[58,59] Analysis of this broadening can allow determination of these short distances from CW EPR spectra; however, the analysis process is generally much less accurate than analysis of DEER spectra at longer distances due to the presence of exchange coupling at these short distances, which is difficult to quantify. An example of this type of analysis is given in Section 3.7.

2.2 The DEER pulse sequences

There are two primary variants of the DEER pulse sequences: the original three-pulse technique,[44] and a later modification using four-pulses.[60,61] Both pulse sequences involve the use of two microwave frequencies. The two pulse sequences are shown in Fig. 2.4 and Fig. 2.5 respectively.

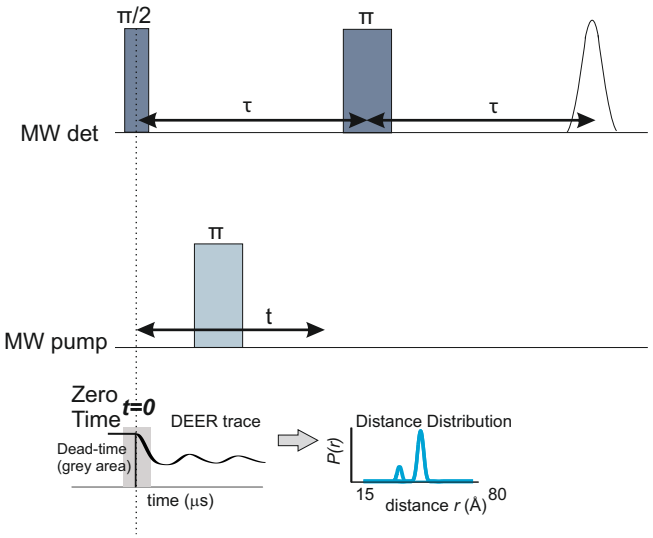


Figure 2.4: The pulse sequence for three-pulse DEER.

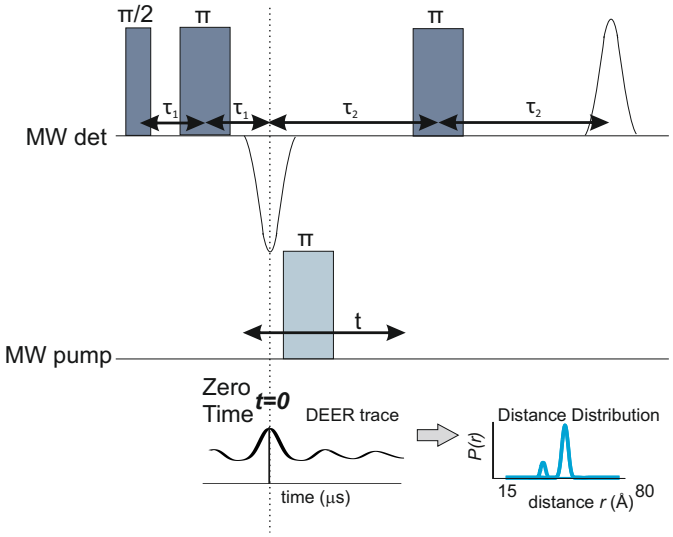


Figure 2.5: The pulse sequence for four-pulse DEER.

Both techniques provide a detection echo, either a direct Hahn echo (three-pulse) or a refocused echo (four-pulse), the amplitude of which oscillates as the timing of the pump pulse is stepped within a given window in the pulse sequence. Stepping the pump pulse over this time window yields a decaying oscillating trace.

Both the three- and four-pulse techniques have advantages and disadvantages; three-pulse DEER is a shorter pulse sequence and therefore has applications for the measurement of longer distances or in systems with unfavourable relaxation properties. However, the direct pulse overlap at the zero-time in three pulse DEER as shown in Fig. 2.4 distorts the data at the zero-time making the technique less reliable for determining accurate distances, particularly for distances with broad distributions and also prevents it from being used as an analysis technique for the determination of the average number of coupled spins in a sample. Chapter 7 includes a longer comparison of the two techniques and suggests a possible method for negating the loss of data from three-pulse DEER at the zero-time.

A new five-pulse DEER technique has recently been published, the pulse sequence mirrors that of the four-pulse experiment with an additional π pulse at the pump frequency at a fixed time interval after the final detection pulse.[62] This additional pulse is used to reduce the effect of nuclear spin-diffusion on the electron-spin phase relaxation, allowing the use of longer dipolar evolution times. This experiment therefore has the potential to measure longer inter-spin distances; however it is yet to be tested by the EPR community at large and thus the exact degree of the benefits are not clear.

2.3 A description of DEER using the vector model

In Chapter 1 it was demonstrated how the individual magnetic moments of spins in an ensemble could be combined into a representation of an overall magnetic vector, and shown how this vector behaves both under the application of microwave pulses (Fig. 1.4) and also evolution of the system without external perturbation (Fig. 1.5). This representation can be used to demonstrate the paths of the spin vectors during pulse sequences in order to provide a visual explanation for the oscillating echo observed in the DEER experiments. A vector model representation for the three-pulse DEER sequences is shown in Fig. 2.6 and a similar one for four-pulse DEER is given in Appendix F.

Figure 2.6: **Vector diagram for three-pulse DEER in the rotating frame**. Initially the magnetization is aligned with the z-axis (i), application with a $\frac{\pi}{2}$ pulse on resonance with spins moves the magnetization to the $-y$-axis (ii). As the magnetization is made up from components with different Larmor frequencies the spin packets corresponding to these different components spread out into the x-y plane (iii). considering a 'fast' component with a Larmor frequency greater than the rotational frequency of the frame (orange arrow) and a 'slow' component with a Larmor frequency less than that of the frame (green arrow), (iv). Application of a π pump pulse can have one of two effects; it will have no effect if it is off resonance from all of the spins to which the detection spin is coupled (v), in this case application of a final detection π pulse will turn the spins in the x-y plane about the x axis (vi) and after a the same length of time that occurred between the initial detection $\frac{\pi}{2}$ and π pulses (τ), the echo will refocus along the $+y$-axis (vii). Alternatively if the applied pump pulse is on resonance with a spin coupled to the detection spin this causes interconversion of the Larmor speeds for the 'fast' and 'slow' components previously described (viii). Application of a detection π pulse on resonance with the rotating frame turns the spins in the x-y plane about the x axis (ix). However, due to the new different Larmor speeds of the components they do not refocus completely along the $+y$ axis at a time τ after the π detection pulse. Thus the size of the echo observed is reduced, the degree of the reduction is dependent on when the π pump pulse occurs within the delay between the two detection pulses.

2.4 Orientational selection and DEER[5]

Orientational selection arises when only part of an EPR spectrum is excited by a given microwave pulse. In DEER the use of two different frequencies allows for the possibility of orientational selection if either one or both of the pulses excite a portion of the spectrum which does not correspond to all orientations of the electron with respect to the static magnetic field. Orientational effects in DEER manifest as changes in modulation depth of the spectra collected and as a change in the observable frequencies of the DEER trace. A change in modulation depth can be related to a change in the number of spins contributing to the DEER effect. The oscillation frequency may also be seen to change at different pump and probe positions as in all cases only part of the dipolar spectrum is excited.

One of the first records of orientationally selective DEER measurements is the measurement of $NO^{\bullet}-NO^{\bullet}$ DEER in a solid medium by Larsen et al in 1993.[51] Since then, orientationally dependent DEER measurements have been made on a number of different types of systems. These include systems containing organic radicals studied at high fields where the g-anisotropy is resolved; examples of such studies include nitroxide centres present in rigid bi-radical systems[63,64] and innate spin centres in photosynthetic membrane proteins.[65] Denysenkov et al. used PELDOR measurements at 180 GHz[66] to determine the structure of the tyrosyl bi-radical in mouse R2 ribonucleotide reductase.[67,68]

Orientational studies at lower fields generally involve metal centres, many of which have large g-anisotropy. Copper-copper distances have been estimated from DEER measurements in the engineered disulphide (S-S) bridged dimer of the protein azurin,[69] dicupric human serum transferrin and lactoferrin,[70] and a poly-proline peptide.[9,10,71] Other systems studied include nitroxide-terpyridine based copper complexes,[72] nitroxide labelled Cu(II) porphyrin complexes,[8,38] and a Mo(V)/Fe(III) state of sulfite oxidase.[73]

For the relatively few orientationally selective EPR and DEER measurements reported in the literature, the degree of analysis has varied. One of the first detailed orientational analyses was conducted by Savitsky et al., who reported a method for extracting distance and orientation information from the line-shape analysis of the echo-detected spin-polarized transient high-field (95 GHz) EPR spectra for disordered systems containing organic radicals, in their case bacterial photosynthetic reaction cen-

tres.[74] Two recent publications have attempted to use the Tikhonov regularization method on DEER spectra, currently the most common method of analysis for non-orientationally dependent DEER data to analyse orientationally dependent data sets.[75,76]

In some early studies of DEER measurements between two metal centres, apparent orientational effects were not clear to see (primarily due to poor data quality) and analysis was only considered in the frequency domain.[69] In others the effect of orientational selection is ignored completely.[70] A large proportion of the small number of orientational studies in the literature have used simulations of orientationally selective DEER data based on model of the relative orientation of the two centres and fitting of the simulated data to the experimentally collected data. Such an approach is used in Chapters 3 and 4. Model based approaches can either use precalculated models,[4,5,8,63] or adaptive models which are refined with the data fitting.[9]

A recent study comparing $NO^{\bullet}-NO^{\bullet}$ DEER for labelled proteins at both X-band, where orientational selection can usually be discounted, and W-band, where the pulses are selective, has shown that simple distance analysis of both traces can yield mean distances that do not vary from one another by more than 2 Å.[77] This surprising result arises when the pump pulse in the W-band is positioned at the maximum of the nitroxide spectrum, in this case the form factor is dominated by contributions from the $\theta = 90°$ orientation (perpendicular contributions), which allows the determination of the correct mean distance. Although pumping in the centre of the spectrum samples the majority of the $\theta = 90°$ orientations, the orientations from near $\theta = 0°$ are not present; this results in an incomplete Pake pattern. Distortions in the distance distribution from the lack of $\theta = 0°$ orientations can be suppressed through the use of a non-negativity constraint for the distance distribution, $P(r)$.[57] Although such an analysis disregarding orientational selection is far less complex than a full orientational analysis, it is only possible when a large degree of flexibility is present in the spin labels; the use of such analysis of W-band $NO^{\bullet}-NO^{\bullet}$ DEER data for conformationally restricted labelling sites will yield inaccurate mean distances. Therefore use of this type of analysis on orientationally selective measurements has the potential to set a dangerous precedent if applied to systems where the labels are conformationally restricted, which is frequently difficult to determine accurately (see Section 4.4.2).

2.4.1 Orientational selectivity in nitroxide - nitroxide DEER

A good proportion of the literature on DEER measures distances between two nitroxide spin labels. As we have already seen, to allow a DEER spectrum to be measured it is necessary to excite two spins independently. When two spin centres of the same type are used, the question must be asked how these centres can be excited independently. For nitroxides the answer to this lies in the hyperfine structure of the radical. ^{14}N has a nuclear spin of $I = 1$ and thus coupling between the unpaired electron and nitrogen occurs. Although usually pictured in molecular diagrams as being associated with the oxygen, the unpaired electron actually has electron density that is delocalized over both the oxygen, nitrogen and the carbon bonded to the nitrogen.[78] The coupling to the nitrogen causes a clearly defined structure in solution state nitroxide spectra of three lines which are easily associated with each of the hyperfine states; $m_I = +1,\ 0,\ -1$. In frozen solutions spectral broadening of the components, particularly $m_I = -1$ and $m_I = +1$, causes them to overlap (see Fig. 2.7). The broadening is greatest for $m_I = -1$ and $m_I = +1$ due to the anisotropy in the hyperfine interactions.[3] In spite of the overlap in the solid state spectrum it is still possible to apply pulses that will cause a larger degree of excitation of one component compared to another. Because a single nitroxide can only be observed occupying one of the hyperfine states at a time and nuclear relaxation is slow on the timescale of the experiment, by applying the detection pulses primarily to one hyperfine component (for example $m_I = -1$) and the pump pulses to another ($m_I = 0$), it is possible to independently excite two centres of the same chemical composition.

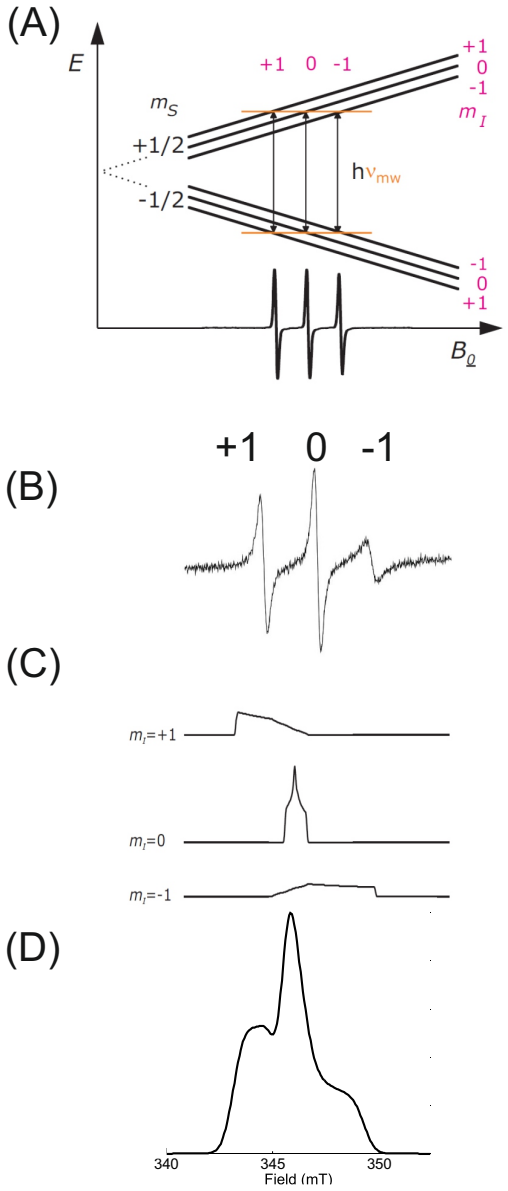


Figure 2.7: (A) A representation of the allowed EPR transitions for a nitroxide and the corresponding solution state CW nitroxide spectrum where the three hyperfine coupling components are easily resolved. (B) A frozen solution CW nitroxide spectrum where broadening of the +1 and −1 hyperfine components is seen. The spectrum is also considerably broader than the solution state spectrum. This is due to the absence of rotational averaging of the different hyperfine coupling constants (A_{xx}, A_{yy} and A_{zz}, the separation of the outer peaks correspond to A_{zz}). (C) Independent simulations for the different hyperfine components of a nitroxide spectrum. (D) An ESE spectrum of a frozen solution nitroxide sample, the integral of spectrum (B) and the sum of the components in (C) which overlap. (A) and (C) are adapted from *A Tutorial on Nitroxide Spectral Analysis* by E. Bordignon.[3]

For two nitroxide centres, if we consider a simplistic model where the detection pulses are applied to the $m_I = +1$ portion of the spectrum and the pump pulse to the $m_I = 0$ peak, this method of excitation has the result that only $\frac{2}{9}$ of the total possible combinations of the hyperfine states for two spins will contribute to the DEER effect. This is exemplified in Fig. 2.8. Although the remaining combinations of hyperfine states do not contribute to the DEER effect, they can contribute to the signal background either by direct detection for spins with $m_I = +1$ or by contributing to relaxation mechanisms within the sample. This model is over-simplified as it does not consider the overlap of the different hyperfine components or the fact that a pulse is not made up of a single frequency but rather a range of frequencies that can be modelled as sinc functions.[a] Therefore a pulse applied on the central nitroxide peak although primarily exciting the $m_I = 0$ will also excite contributions from $m_I = +1$ and $m_I = -1$.

m_I of spin 1	m_I of spin 2	Contributes to DEER effect
-1	-1	No
-1	0	No
-1	$+1$	No
0	-1	No
0	0	No
0	$+1$	Yes
$+1$	-1	No
$+1$	0	Yes
$+1$	$+1$	No

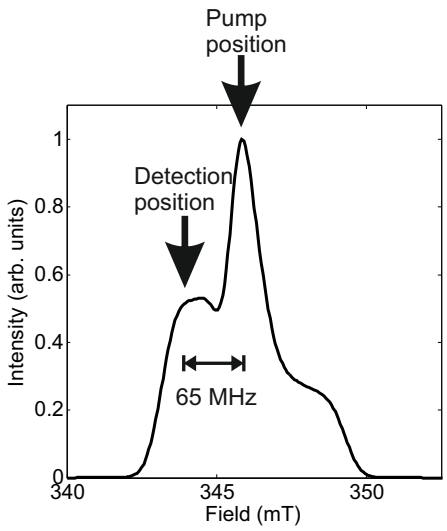


Figure 2.8: Left: Table showing the combinations of hyperfine states for two nitroxide spins contributing to the DEER effect for detection on $m_I = +1$ and pump on $m_I = 0$. Right: Nitroxide spectrum with the pump and detection pulse positions marked corresponding to those in the table.

[a]The normalized sinc function takes the form: $\mathrm{sinc}(x) = \frac{\sin(\pi x)}{\pi x}$.

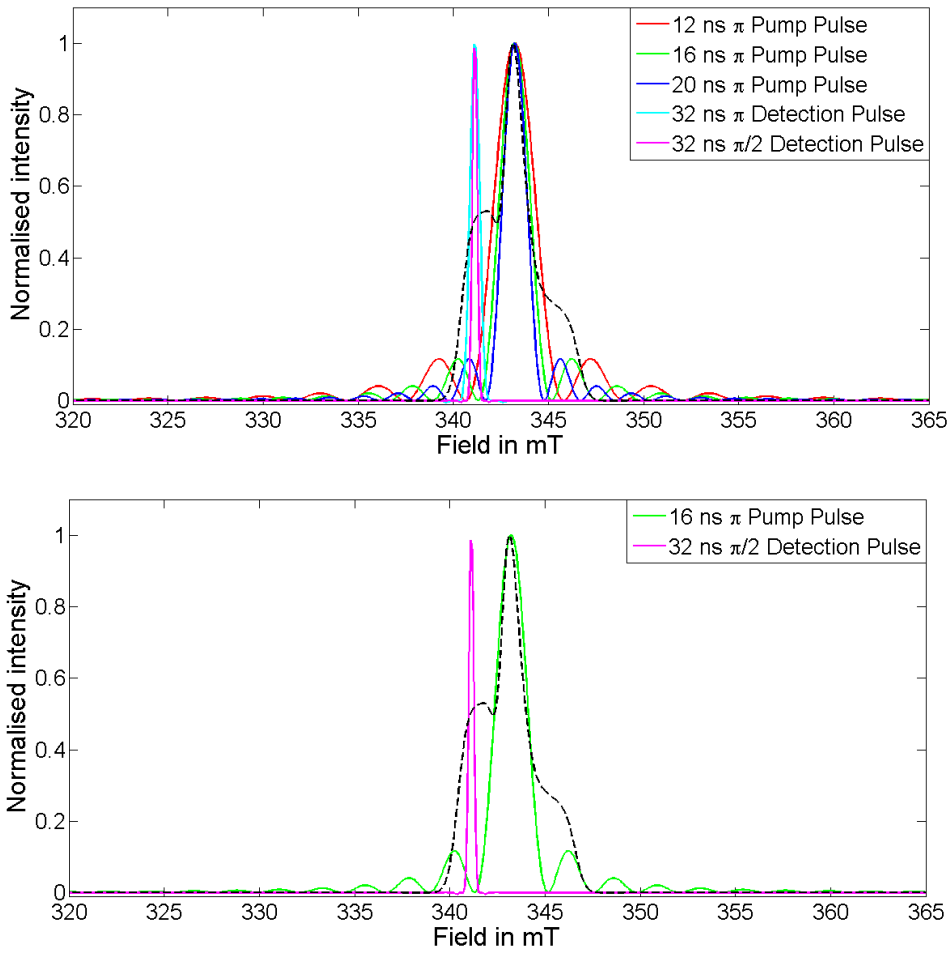


Figure 2.9: The frequency profile (truncated sinc function) for simulated pulses of different lengths overlaid on a nitroxide spectrum. The upper plot shows pump pulses, modelled by Equation 2.15, for pulse lengths 12 ns, 16 ns and 20 ns. The pulses become more selective as the pulse length increases; however, all three are able to excite all of the central transition mitigating orientational selectivity. The pulse profiles, modelled by Equation 2.16b, of typical matched length detection pulses, 32 ns π pulse and 32 ns $\frac{\pi}{2}$ pulse, are also shown. Comparing the profiles of both detection pulses demonstrates that the bandwidth of detection is governed by the matched $\frac{\pi}{2}$ pulse (see Section 2.5). The frequency offset between the detection and pump pulses is 65 MHz. The lower plot highlights the 32 ns $\frac{\pi}{2}$ detection pulse and the 16 ns pump pulse. At a pulse separation of 65 MHz the detection pulse occurs in one of the minima of the 16 ns pump pulse profile reducing pulse overlap and the effects associated with it such as spectral diffusion, Bloch-Siergert shifts (see Chapter 7), etc.

In order for a pulse to be orientationally unselective, it must simultaneously excite all orientations of a spin centre with respect to a magnetic field; to fulfil this condition the pulse must be broader in frequency distribution than the spectrum or portion of the spectrum it is exciting. Frequently the limiting factor for this is the achievable pulse width. For nitroxide spectra at X-band, pulses with 12, 16, or 20 ns are broad enough to excite the majority of the central ($m_I = 0$) transition of nitroxide spectrum and thus excite all orientations of the nitroxide with respect to the static magnetic field (see Fig. 2.9). Application of the same pulses to a region of the spectrum primarily composed of the $m_I = +1$ or $m_I = -1$ transitions will be unable to excite all of these transitions.

By considering the $m_I = +1$ hyperfine component of the nitroxide spectrum shown in Fig. 2.7 and the 32 ns detection pulse profile demonstrated in Fig. 2.9 it is clear that the detection pulse will not excite all g-matrix orientations of the $m_I = +1$ hyperfine component with respect to the static magnetic field. Furthermore the overlap of the different hyperfine components means that the pump pulse will not only excite the majority of the $m_I = 0$ hyperfine component but also orientationally selective portions of $m_I = +1,\ -1$ hyperfines (and the same is true of the detection pulse); this results in orientational selection for nitroxide centres which in some cases can be observed at X-band.[63,75,76] The observation of orientational effects in $NO^{\bullet}-NO^{\bullet}$ DEER measurements at X-band is limited to systems where the positions of the two nitroxide centres are very constrained with respect to one another. For the majority of $NO^{\bullet}-NO^{\bullet}$ systems measured experimentally, no discernible orientational effects are observed due to flexibility in the positions of the nitroxide labels with respect to each other. When the orientation of the two g-matrices approaches an isotropic limit, although each individual pair of nitroxides will show orientational selection when the total ensemble of spin centres is studied, these individual effects become buried in the overall signal.

Many of the rod-like $NO^{\bullet}-NO^{\bullet}$ model systems studied will show orientational effects at X-band due to the rigidity of the central linking moiety,[63,64,75,79] as will rigid spin labels attached to the backbone of DNA.[76,79] However, MTSL labels show large conformational freedom and thus, unless the labelling site constrains these significantly, MTSL labels will not show orientational selection in spectra recorded at X-band and in some cases limited orientational selection in spectra recorded at higher frequencies,

see Section 2.4.1.[77] The large conformational freedom of MTSL spin labels can be modelled by the program MMM,[80,81]. Use of this type of modelling in the analysis of docked protein-protein structures is described in Chapter 4.

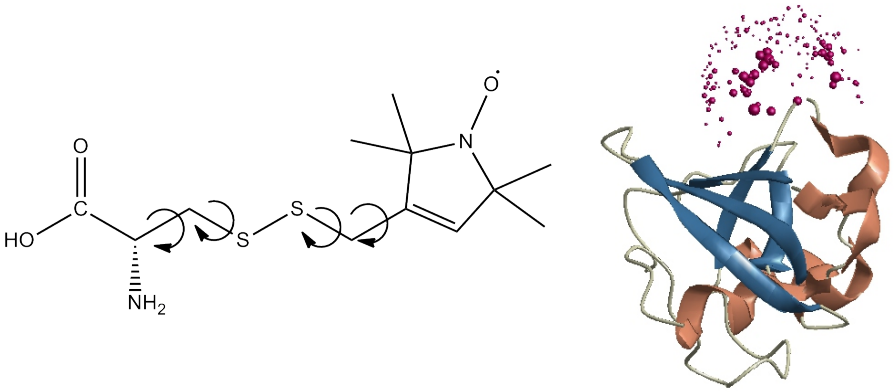


Figure 2.10: **Left**: Structure of the MTSL spin label with the rotational degrees of freedom marked. It should be noted that there is no rotation marked for the disulfide bond since at cryogenic temperatures (such as the freezing point of water glycerol mixtures) the energy barrier for the rotation of this bond is too large to be overcome; this bond is therefore fixed in either a cis- or a trans-configuration with the lower energy trans-configuration shown. **Right**: Structure of the Ferredoxin 3HUI used in Chapter 4 with the MTSL spin label spin-distribution for labelling site D54, calculated by MMM,[80,81] shown as magenta spheres. Their size is proportional to the predicted label occupancy of that site to demonstrate the near isotropic distribution possible when spin labels are attached at non-restricted sites.

Nitroxide-nitroxide DEER at W-band

At higher frequencies, the resolution of the g-values results in a broader nitroxide spectrum where the different portions of the g-matrix can be more easily independently excited with pulses (see Fig. 2.11). It is therefore possible to probe the orientational selection of nitroxide compounds much more efficiently at W-band.[4] DEER at high frequencies however, faces other problems. Most commercially available W-band spectrometers do not have the power required to create two pulses at a suitable frequency separation to run DEER experiments and require an upgrade to do so. For this reason, orientationally selective W-Band DEER has mainly been carried out on homebuilt instruments such

as the HiPER system,[b] a kilowatt pulsed 94 GHz EPR spectrometer of unique construction,[82] or on upgraded commercially available spectrometers, either with homebuilt upgrades,[83] or commercially available upgrades.[64]

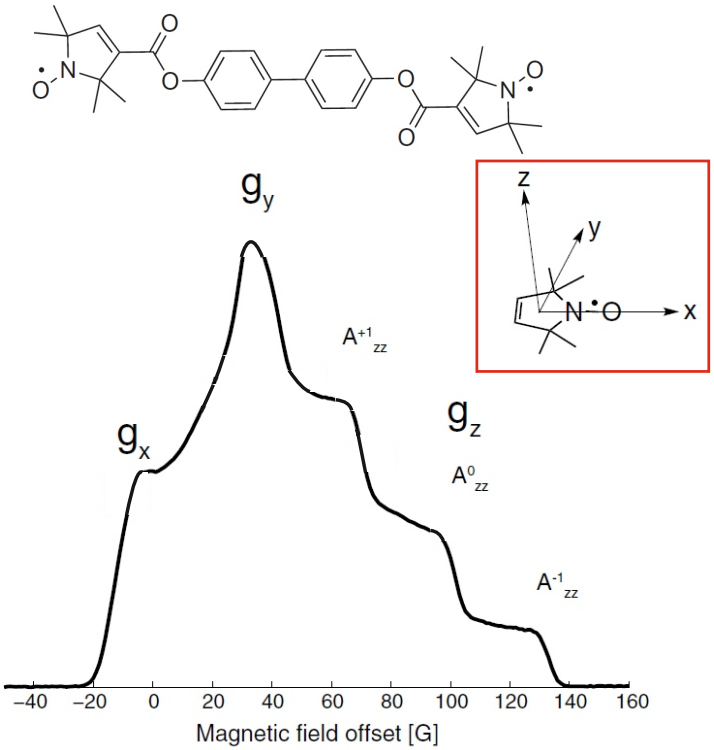


Figure 2.11: An echo-detected field sweep of the compound shown. The inset in the red box shows a nitroxide and the relative orientation of the g-tensor indicated by arrows. This figure is adapted and reprinted from *Journal of Magnetic Resonance*, **216**, G. W. Reginsson, R. I. Hunter, P. A. S. Cruickshank, D. R. Bolton, S. T. Sigurdsson, G. M. Smith and O. Schiemann, W-band PELDOR with 1kW microwave power: Molecular geometry, flexibility and exchange coupling, 175–182. Copyright © 2012, with permission from Elsevier.[4]

Although the orientationally selective DEER work presented in this thesis does not include data obtained at W-band frequencies, many of the considerations in the analysis and the experimental principles are common between both types of experiments.

[b] HiPER is a High-power Pulsed W-band EPR spectrometer

2.4.2 Orientational selectivity in DEER measurements on metal centres

In comparison to nitroxide spectra at X-band, which have a maximum width of c. 180 MHz and a maximum width for one hyperfine component ($m_I = -1$) of c. 100 MHz, the X-band EPR spectra for metal centres, and metal containing clusters, can be much wider, c. 500 MHz for both the copper centres and $[Fe_2S_2]^+$ clusters studied in Chapters 3 and 4. In most cases the additional broadening of the spectrum for metal centres is due to a larger anisotropy in the g-values, although hyperfine interactions, such as those seen for copper centres, can also provide structure to the spectrum.

As with the $NO^{\bullet}-NO^{\bullet}$ DEER, it is possible to measure DEER spectra between two centres of the same type of paramagnetic metal centre provided dipolar-coupled spins can be excited independently. This can be due to spins being present in different hyperfine states (as is the primary *modus operandi* in X-band $NO^{\bullet}-NO^{\bullet}$ DEER); however, it is more common when the g-anisotropy is large so that excitation at two different points on the EPR spectrum will occur due to the two spins having different g-matrix orientations with respect to the each other. Fig. 2.12 highlights the different contributions to a copper spectrum from two copper centres with different orientations to the external magnetic field, $\mathbf{B}_0$. For the orientation of two copper centres described in Fig. 2.12 A, in the external reference frame pictured in Fig. 2.12 B, when the orientation of $\mathbf{B}_0$ adopts that shown in Fig. 2.12 B, the portion of the overall powder averaged EPR spectrum (Fig. 2.12 C.1 and D.1) contributing at this orientation is detailed in Fig. 2.12 C.2 and D.2 of the A and B spins respectively.

As described in Section 2.4, orientationally selective DEER measurements have been recorded on many different types of metal centre. This thesis considers the orientational effects seen on Cu^{2+} centres in model systems and in a copper amine oxidase protein and an oxidized iron-sulphur cluster ($[Fe_2S_2]^+$) found in ferredoxin proteins.

Although most metal spin centres tend to show orientational selection particularly at high fields, one notable exception is Gadolinium. Gd^{3+} is a high spin ion ($S = \frac{7}{2}$) and its spin energy levels for a ladder with six possible transitions of $\Delta M_s = \pm 1$. The EPR spectrum of the $\left|-\frac{1}{2}\right\rangle \rightarrow \left|+\frac{1}{2}\right\rangle$ central transition of Gd^{3+} narrows with increasing external magnetic field, B_0. This has allowed high field DEER experiments with little orientational dependence to be carried out on Gadolinium labelled

systems; including model systems,[84] DNA,[85], proteins,[86] and protein complexes.[87]

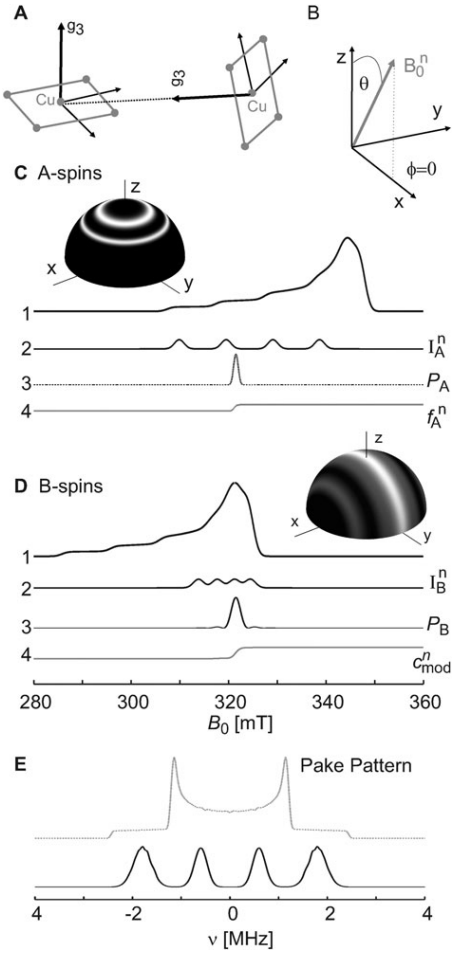


Figure 2.12: Dipolar spectrum calculation. **(A)** Model with two Cu(II) substituted tetra phenyl porphyrin centres oriented so that the two g_3-axes are perpendicular. **(B)** Orientation of the unit vector $\mathbf{B}_0^n(\theta = \frac{\pi}{10},\ \phi = 0)$ for the single orientation spectra shown in C.2 and D.2. **(C)** A-spins (detection spins) at ω_A showing: powder EPR spectrum (1), spectrum I_A^n at $\mathbf{B}_0^n(\theta = \frac{\pi}{10},\ \phi = 0)$ (2), detection pulse excitation profile P_A (3), and the integral of (2) $\times$ (3) giving the fraction of contributing A-spins f_A^n (4). **(D)** B-spins (pump spins) at ω_b showing: powder EPR spectrum (1), spectrum I_B^n at $\mathbf{B}_0^n(\theta = \frac{\pi}{10},\ \phi = 0)$ (2), pump pulse excitation profile P_B (3), and the integral of (2) $\times$ (3) giving the modulation depth c_{mod}^n (4). **(E)** Dipolar spectrum obtained by summing over the n contributions (black line), and the Pake pattern where all orientations are excited (grey dotted line). The two half spheres in (C) and (D) represent orientations resonant with the microwave pulses in the molecular frame (white: resonant, black: off resonance). Note that in C-D the frequency axis has been converted into a B_0-field axis. This figure is reproduced from J. E. Lovett, A. M. Bowen, C. R. Timmel, M. W. Jones, J. R. Dilworth, D. Caprotti, S. G. Bell, L. L. Wong, and J. Harmer. Structural information from orientationally selective DEER spectroscopy. *Physical Chemistry Chemical Physics*, 2009, **11(31)**, 6840–6848 with permission from the PCCP Owner Societies.[5]

2.5 DEER at X-band: experimental considerations

DEER experiments at X-band between two nitroxide centres are usually set up with a pump pulse (of length $\leq$ 20 ns) positioned at the centre of the nitroxide spectrum ($m_I = 0$), allowing the pump pulse to excite all orientations of the nitroxide with respect to the magnetic field. The detection pulses are usually c. $65 - 80$ MHz down-field on the maximum of the $m_I = +1$ portion of the spectrum. With a pump pulse of $\geq$ 12 ns and detection pulses of 32 ns, 65 MHz is considered to be a good separation between the pump and detection frequencies as there is negligible overlap between the pulses (see Fig. 2.9). This also corresponds to the detection pulse exciting the maximum of the $m_I = +1$ transitions allowing for a large number of detection spins to be excited giving the experiment good sensitivity.[57]

Any significant degree of overlap of the pulses will cause the appearance of artefacts in the spectrum as it will result in spins which are excited by both the pump and detection pulses. The most notable effect is the appearance of a growing dipolar oscillation, seen as the upwards bend of the DEER trace, towards the end of the time trace where the timing of the pump pulse and following detection pulses becomes close. It is reduced either through the use of longer pulses with narrower frequency profiles, greater frequency separation between the pulses or by increasing the time delay following the final position of the pump pulse before the following detection pulse.[57]

The overlap of pulses in frequency may also cause the excitation of forbidden electron-nuclear transitions of the detection spin by the pump pulse, which leads to the presence of nuclear modulations in the DEER trace.[60,61] In some cases, where the oscillation frequency corresponds to an extractable distance (for example proton modulation at X-band occurs at c. 14 MHz corresponding to a DEER distance of c. 1.55 nm), this can lead to an uncertainty in the analysis of the data.[57] These effects can be suppressed by varying the inter-pulse time delays.[88,89] For four-pulse DEER, the τ_1 time is typically varied from 160 ns in eight steps of 8 ns to remove proton modulations and from 400 ns in eight steps of 56 ns to remove deuterium modulations. This is commonly referred to as ESEEM (Electron Spin Envelope Echo Modulation) averaging.[89] Although three-pulse DEER is thought to be less affected by ESEEM modulations,[90] the τ time in the three-pulse sequence can also be 'ESEEM averaged'. In

both experiments this will result in a slight decrease in signal-to-noise on the overall spectrum due to the smaller echo detected for the longer times. This method was employed for some of the three-pulse DEER collected in Chapter 7.

Detection pulses are generally longer than the pump pulse; this makes the frequency profile narrower and thus they excite less of the EPR spectrum (see Fig. 2.9). The primary reason for the longer length of these pulses is the bandwidth profile of the resonators used, which is not equal at all frequencies (see Fig. 2.13). The usual experimental set-up places the pump pulse at the centre of the resonator bandwidth where the power conversion is highest and thus a short pulse can be used to cause a π turning angle. Away from this central position, where the detection pulses are set up, a longer pulse is required to achieve the same turning angle.

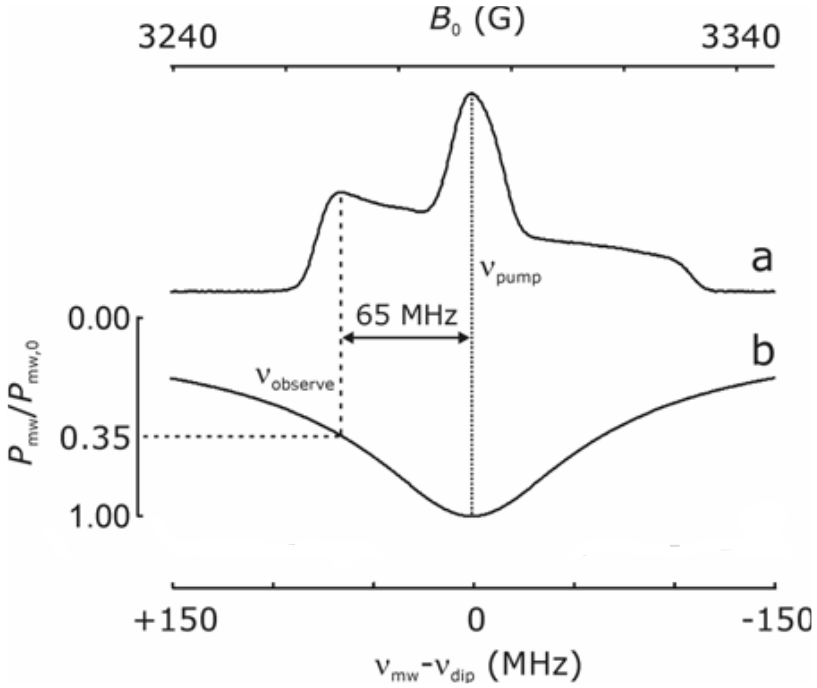


Figure 2.13: Optimum observer and pump pulse settings in the four-pulse DEER experiment. (a) Echo-detected field-swept ESR spectrum of a nitroxide bi-radical with a spin-to-spin distance of 5 nm (field abscissa). (b) Simulated idealized m.w. mode assuming $Q_L = 100$ (frequency abscissa power ordinate). This figure is reproduced from *ESR Spectroscopy in Membrane Biophysics*, published by Springer,**27**, 1997, Chapter 2: Instrumentation and Experimental Setup, G. Jeschke, Figure 10. Copyright © Springer Science+Business Media, LLC 2007; with kind permission from Springer Science and Business Media.[6]

The bandwidth of the resonator can be increased by over-coupling the system; however, this causes the power conversion to decrease and may require the use of longer pulses to achieve the desired turning angle. Furthermore it should be noted that for orientationally selective measurements on metal centres where the separation of the pulses is very large (100's of MHz), in order to achieve the required separation of the pulses within the bandwidth of the resonator it can be necessary to move the pump pulse away from the resonator's central frequency, which necessitates the use of both longer pump pulses and longer detection pulses.

On spectrometers with independently tuneable pulse channels, the detection pulses of the DEER sequence are frequently tuned to all have the same length and different powers to achieve the required π and $\frac{\pi}{2}$ turning angles rather than all having the same power and different lengths. This can be advantageous in preventing the frequency overlap of the two pulses, as the $\frac{\pi}{2}$ pulse of the same length (and half the power) as a π pulse will have a significantly narrower bandwidth compared to the π pulse. It is the bandwidth of the initial $\frac{\pi}{2}$ pulse that dictates which spins correspond to the DEER detection spins. Using a longer $\frac{\pi}{2}$ pulse, the bandwidth of excited detection spins is reduced without having to increase the length of the π pulses, see Fig. 2.9.

The majority of the DEER measurements in this thesis were carried out using an MS3 split-ring resonator from Bruker, which, for four-pulse DEER, is considered a good compromise between microwave field strength and filling factor, related to the sample volume and magnetic field strength.[53,91] The work in Chapter 7 is conducted using a 2 mm split ring resonator (MS2) where the smaller diameter of the resonator allowed a higher power conversion factor, thus allowing lower powered pulses to be used to achieve the same turning angle in the same time.[92] The relationship between the B_1 field and the bandwidth of the resonator is illustrated in Fig. 2.13.

In order to study orientational DEER of nitroxides at X-band, the pulses must have a narrow frequency bandwidth. For systems with short distances, this may become detrimental to the measurement if the required bandwidth of the pulses for orientational selection is smaller than the dipolar interaction. In these instances, an observer-selective pulse sequence, which uses a second pump pulses, can be used.[93]

All DEER traces were collected using phase cycling of the detection pulses; a two-step phase cycle was used for both the three- and four-pulse DEER measurements where the phase of the $\frac{\pi}{2}$ pulse was varied from positive to negative. In both cases, the pump pulse was incoherent, as the presence of a coherent pump pulse has been shown to be detrimental to the data recorded by allowing echoes from the pump and detection pulses to occur during signal accumulation. These echoes cancel if the pump pulse is incoherent with respect to the detection pulses.[6]

2.6 Simulating orientationally selective DEER[5]

Whereas for DEER simulations that are not orientationally selective, the angular dependence of the dipolar frequency is easily calculated by summing over all angles, this is not the case for orientationally selective DEER. The selective nature of pulses in orientationally selective DEER means that only a fraction of the EPR spectrum is excited and corresponding to the selection of a limited range of angles ψ_{ij}^n or spin-spin vectors.[c]

Simulations of DEER spectra can follow a full density matrix approach, where the spin density is propagated though the various pulses and time delays (such an approach is used in Chapter 7). Or alternatively, the DEER spectrum can be calculated from the analytical form of the dipolar frequency (see Equation 2.8a). The second method has the advantage of being much quicker computationally as it is not reliant on the calculation of multiple matrix exponentials.

Our algorithm to calculate orientation selective DEER time traces (or dipolar spectra) for a pair of paramagnets is outlined in Fig. 2.16. The experimental parameters needed for the calculation are the two microwave (mw) frequencies ω_A (detection) and ω_B (pump), pulse lengths for the DEER sequence, the measurement field position B_{obs}, the time trace increments and lengths, the A- and B-spin Hamiltonian parameters in the molecular frame sufficient to describe the field-swept EPR spectrum (g-values, line widths, hyperfine couplings, etc.), and the coordinates and spin densities (or spin projection factors) defining the two paramagnetic systems. Fig. 2.14 gives a representation of the geometrical parameters for an example system.

[c]The angle ψ_{ij}^n is the same as that described by θ in Section 2.1.

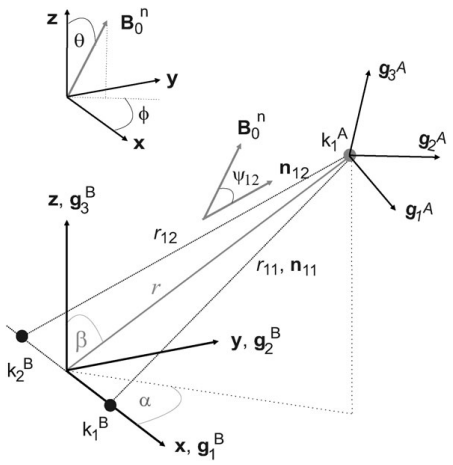


Figure 2.14: Geometric parameters in the molecular frame for an example where the spin density of the A-spins k_i^A is completely localized (i = 1), as in a nitroxide radical, and in the B-spin is distributed over two nuclei giving k_1^B and k_2^B. A- and B-spin Hamiltonian parameters are represented as only the g-matrix axes. The unit magnetic field vector $\mathbf{B}_0^n(\theta,\phi)$ is defined over the unit sphere and Ψ_{ij}^n are the angles between unit vectors $\mathbf{B}_0^n(\theta,\phi)$ and the spin-spin unit vectors $\mathbf{n}_{ij}$. Parameters r, α, β and Euler angles $(\alpha,\beta,\gamma)^B$ for the B-spin (not shown) are input variables to the algorithm used for fitting the simulation to experimental data. This figure is reproduced from J. E. Lovett, A. M. Bowen, C. R. Timmel, M. W. Jones, J. R. Dilworth, D. Caprotti, S. G. Bell, L. L. Wong, and J. Harmer. Structural information from orientationally selective DEER spectroscopy. *Physical Chemistry Chemical Physics*, 2009, **11(31)**, 6840–6848 with permission from the PCCP Owner Societies.[5]

The method of calculation proceeds as follows. Firstly, unit vectors n_{ij} and distances r_{ij} between the spin densities on A-spins (k_i^A) and B-spins (k_j^B) are defined and stored. Next, a grid of n vectors $\mathbf{B}_0^n(\theta,\phi)$ and solid angle weights w^n over a unit sphere or part thereof dependent on the symmetry of the system are generated and stored. For each orientation, the A-spin signal contributions excited by the detection pulses at ω_A at field position B_{obs} are calculated and stored. The resonances for the orientation $\mathbf{B}_0^n(\theta,\phi)$ are calculated from the A-spin orientation-selection Hamiltonian and used to generate an EPR spectrum with unit area, $I_A^n(\omega)$. The fraction of this spectrum contributing to the DEER echo is calculated from the integral of $I_A^n(\Delta\omega_A)$ with the detection pulse excitation profile $P_A(\Delta\omega_A)$ for a refocused echo.[60,61,94]

$$P_A(\Delta\omega_A) = \left(\frac{\omega_1}{\omega_{eff}}\right)^5 \sin^5\left(\omega_{eff}\frac{t_\pi}{2}\right) \tag{2.15}$$

where $\Delta\omega_A = \omega_A - \omega$ and $\omega_{eff} = \Delta\omega_A - \omega_1$, ω_1 is the microwave field strength for the applied B_1 field. t_π is the length of a π pulse. The form of the pulse profile is that of a truncated 'sinc' function ($\mathrm{sinc}(x) = \frac{\sin(x)}{x}$). The sinc frequency function corresponds to the Fourier transform of a square pulse in the time domain; however, due to the rise and fall time associated with pulse generation, real pulses are not truly square and instead have a more rounded shape, tending towards a Gaussian function. The Fourier transform of a Gaussian in the time domain is again a Gaussian in the frequency domain and thus real pulses are satisfactorily modelled as truncated sinc functions in the frequency domain. The level of truncation is not only dependent on the shape of the generated pulse (usually defined by the rise and fall time of pulse generation of the spectrometer) but also on the bandwidth of the resonator. Further functions used to model the frequency width of a pulse are sinc functions with smaller truncations (Equations 2.16a and 2.16b),[51,95] or Gaussian functions (Equation 2.16c):

$$P_A(\Delta\omega_A) = \left(\frac{\omega_1}{\omega_{eff}}\right)\sin\left(\omega_{eff}\frac{t_\pi}{2}\right) \tag{2.16a}$$

$$P_A(\Delta\omega_A) = \left(\frac{\omega_1}{\omega_{eff}}\right)^2\sin^2\left(\omega_{eff}\frac{t_\pi}{2}\right) \tag{2.16b}$$

$$P_A(\Delta\omega_A) = aexp\left(-\frac{(\omega-b)^2}{2c^2}\right) \tag{2.16c}$$

The presence of the 'sinc wings' causes a degree of overlap of the pump and detection pulses, which can cause distortions in the spectrum, see Section 2.5.

Once a form of the pulse profile has been selected the fraction of the A-spin spectrum excited at orientation $\mathbf{B}_0^n(\theta,\phi)$ is given by:

$$f_A^n = \int I_A^n\left(\Delta\omega_A\right) P_A\left(\Delta\omega_A\right) d\omega \tag{2.17}$$

The pulse excitation profile at the carrier frequency ω_A equals unity, $P_A(0) = 1$, so if the pulse bandwidth is much greater than the spectrum width the integral of Equation 2.17 is unity and there is no orientational selection by the pulse. This principle is illustrated in Fig. 2.12A-C for the example

of two Cu(II) ions with perpendicular g_3-axes. The DEER modulation depth c^n_{mod} will be calculated accurately provided the orientation selection Hamiltonian and line width parameters accurately simulate the intensity of the corresponding echo-detected field-sweep EPR spectrum, and the labelling of the sample used is close to complete as the modulation depth is dependent on the number of spins in the nanoobject, see Section 2.7.1. The resonance frequencies for radicals adequately described with an axial or rhombic g-matrix are easily calculated from analytical formulae,[29] and for more complicated systems with hyperfine (or zero field) interactions by diagonalization of the spin Hamiltonian.

For each excited A-spin orientation the corresponding B-spin resonances are determined and the spectrum $I^n_B(\Delta\omega_B)$ is calculated using the B-spin orientation-selection Hamiltonian and line width parameters, at field position B_{obs}. As with the detection pulses, the flip angles for the pump pulse, which are a function of the offsets $\Delta\omega_B = \omega_B - \omega$ from the carrier frequency ω_B, are generated. If the B-spin spectrum $I^n_B(\Delta\omega_B)$ is fully inverted by the pump pulse (π-pulse) then the modulation depth c^n_{mod} for this orientation $\mathbf{B}^n_0(\theta,\phi)$ will be 1, implying that all B-spins of the pairs are optimally excited. If the required B-spins are completely off resonance with the pump pulse then the modulation depth is 0. For flip-angles θ_B between 0 and π, the modulation depth is

$$c_{mod} = \frac{1-\cos(\theta_B)}{2} \tag{2.18}$$

This equation implies that the modulation depth is proportional to the z-component of the B-spin magnetization, $M_z = M_0\cos(\theta_B)$. This states that the greatest modulation depth will occur when the magnetization of the B-spins is fully inverted by the pump pulse.

Due to the shape of the pulse profile, not all of the spins excited by the pump pulse will be flipped by an angle of π; instead an effective flip angle, dependent on the frequency offset from the carrier frequency of the pump pulse ($\Delta\omega_B$) can be quantified:

$$\theta_B(\Delta\omega_B) = \cos^{-1}\left(1 - 2\left(\frac{\omega_1}{\omega_{eff}}\right)^2 \sin^2\left(\frac{\omega_{eff}t_\pi}{2}\right)\right) \tag{2.19}$$

The form of this equation is based on the pump pulse profile of the B-spins, in this case chosen to be:[51]

$$P_B(\Delta\omega_B) = \left(\frac{\omega_1}{\omega_{eff}}\right)^2 \sin^2\left(\frac{\omega_{eff} t_\pi}{2}\right) \tag{2.20}$$

The orientational selectivity of the modulation depth can be obtained from the integral of the B-spin spectrum ($I_B^n(\Delta\omega_B)$) and the pump pulse excitation profile, which can be related to the effective flip angle, $\theta_B(\Delta\omega_B)$.

$$c_{mod}^n = \int I_B^n(\Delta\omega_B) P_B(\Delta\omega_B) d\omega \tag{2.21a}$$

$$= \int I_B^n(\Delta\omega_B) \frac{1 - \cos\left(\theta_B(\Delta\omega_B)\right)}{2} d\omega \tag{2.21b}$$

It is now possible to calculate the DEER trace for the different orientations of the static magnetic field, $\mathbf{B}_0^n(\theta, \phi)$ with respect to the inter-spin vector. If a modulation depth of $c_{mod}^n = 0$ is calculated, a zero-frequency component is added to the spectrum with a weight; $w^n f_A^n$, the relative number of excited A-spins. f_A^n is the fraction of A-spins excited and w^n is the solid angle weight corresponding to the orientation. If $c_{mod}^n > 0$ is found, the corresponding dipolar oscillation at the given frequency is calculated, ω_{dd}, where, if appropriate, the calculation is summed over all the contributions from spin density delocalized over different atoms.

$$\omega_{dd}^n = \frac{\mu_0 \mu_B^2}{4\pi\hbar} g_A^n g_B^n \sum_i \sum_j k_i^A k_j^B \frac{3\cos^2\theta_{ij}^n - 1}{r_{ij}^3} \tag{2.22}$$

It should be noted that it is also possible to set cut-off values for the excitation fraction to further speed up the calculation so that, if the excitation at a particular level falls below a threshold value, no dipolar oscillation is calculated.

Where a dipolar frequency is calculated, its contribution to the overall spectrum is weighted by c_{mod}^n and the non-modulated part is weighted by $1 - c_{mod}^n$. Both components are added to the frequency

spectrum, $F(\omega)$, such that the overall frequency spectrum is calculated as:

$$F(\omega) = \sum_n \left\{ \left(\frac{1}{2} c^n_{mod} \left(\delta \left(\omega^n_{dd} + \omega \right) + \delta \left(-\omega^n_{dd} + \omega \right) \right) + \left(1 - c^n_{mod} \right) \delta(\omega) \right) w_n f^n_A \right\} \tag{2.23}$$

where δ is the Kronecker-delta and the index n represents the number of orientations of the static magnetic field, $\mathbf{B}^n_0(\theta, \phi)$, used in the calculation. It should be noted that this could also be achieved directly in the time-domain. Where the overall trace would be calculated as:

$$y(t)^{DEER}_{sim} = \sum_n \left\{ \left(1 - c^n_{mod} \left(1 - \cos(\omega^n_{dd} t) \right) \right) w^n f^n_A \right\} \tag{2.24}$$

However, computation in the time domain is much more expensive compared to the frequency binning procedure. In both methods of calculation, each contribution is weighted by the relative number of A-spins excited by the detection pulse, $w_n f^n_A$. The calculation must consider many different orientations of the static magnetic field $\mathbf{B}^n_0(\theta, \phi)$ with respect to a fixed molecular structure. The $\mathbf{B}^n_0(\theta, \phi)$ vectors are generated using a grid of knots, which can be calculated via EasySpin.[7,96] This is preferable to the alternative of using a $\sin\theta$ weighting, which under-weights orientations at the poles and also does not allow for a symmetry in the spin distribution of one centre. A sample grid of knots is illustrated in Fig. 2.15.

In some cases, the calculation is repeated for multiple molecular structures in order to model molecular disorder present within a sample in frozen solution. Fig. 2.16 outlines the orientationally dependent algorithm for calculating DEER traces.

It should be noted that this calculation method assumes that for each detection centre there is a corresponding pump centre that could be excited and it does not consider the homogeneous distribution of other spins surrounding the spin pair. For this reason the zero frequency component, the unmodulated part, calculated will be likely be smaller than that found experimentally. Furthermore, this calculation method does not make any consideration for relaxation. Therefore, in order to compare data simulated via this method to experimentally recorded data the simulation must be multiplied by an experimental background and in most cases a correction to the modulation depth. As such (unless

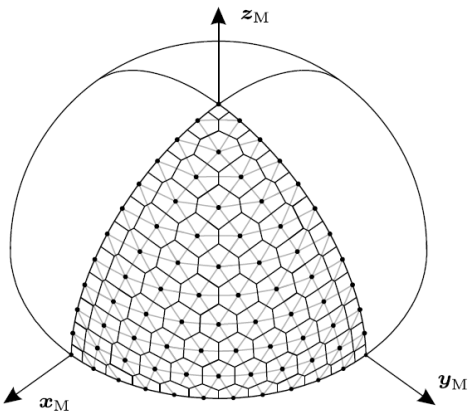


Figure 2.15: Orientational grid calculated by EasySpin over one octant for a spin system with D2h symmetry and 78 knots. Voronoi cells and Delaunay triangles are shown. Figure reprinted from *Journal of Magnetic Resonance*, **178**, S. Stoll and A. Schweiger, EasySpin, a comprehensive software package for spectral simulation and analysis in EPR, 42–55. Copyright © 2006, with permission from Elsevier.[7]

otherwise specified) all plots in this thesis comparing experimental data to data simulated using this method show the raw experimental data with simulated data that has been multiplied by a background correction and modulation depth correction, where the sizes of these corrections has been found by least squares fitting of these parameters to the experimental data. Section 3.2.3 provides further details on the background correction applied to the simulated data. All the DEER traces presented in this thesis are normalised to a signal maximum of 1.

DEER ALGORITHM

1. construct vectors $\mathbf{n}_{ij}$ and distances r_{ij} between A- and B-spin spin densities in molecular frame

2. generate a grid of n vectors $\mathbf{B}_0^n(\theta,\phi)$ over half the unit sphere defined by polar (θ) and azimuthal (ϕ) angles and the solid angle weights w^n

3. calculate for the A-spins the orientation set $\mathbf{B}_0^n(\theta,\phi)$ excited by detection pulses at the carrier frequency ω_A

$$f_A^n = \int I_A^n(\Delta\omega_A) P_A(\Delta\omega_A)\, d\omega$$

where P_A is the pulse excitation profile and I_A^n the A-spin spectrum at orientation $\mathbf{B}_0^n(\theta,\phi)$

4. delete all non-resonant $\mathbf{B}_0^n(\theta,\phi)$ vectors

5. generate the B-spin pump pulse profile $P_B(\Delta\omega_B)$ as a function of $\Delta\omega_B=\omega_B-\omega$ and store

$$P_B(\Delta\omega_B) = \left(\frac{\omega_1}{\omega_{eff}}\right)^2 \sin^2(\omega_{eff} t_\pi / 2)$$

Loop 'n' over all $\mathbf{B}_0^n(\theta,\phi)$ vectors where A-spins are excited

6. calculate the B-spin spectrum $I_B^n(\Delta\omega_B)$ which is centered around ω_B for orientation $\mathbf{B}_0^n(\theta,\phi)$

7. calculate the modulation depth, the fraction of B-spin signal at $\mathbf{B}_0^n(\theta,\phi)$ that is flipped by the pump π pulse

$$c_{\mathrm{mod}}^n = \int I_B^n(\Delta\omega_B) P_B(\Delta\omega_B) d\omega$$

Loop 'ij' over spin densities of the 2 paramagnets

$$\cos(\psi_{ij}^n) = \mathbf{n}_{ij} \quad \mathbf{B}_0^n(0,\phi)$$

$$\omega_{dd}^n = \omega_{dd}^n + \frac{\mu_0\beta^2}{2h} g_A^n g_B^n k_i^A k_j^B \frac{3\cos^2\psi_{ij}^n - 1}{r_{ij}^3}$$

next ij

$$F^n(\omega) = \frac{c_{\mathrm{mod}}^n}{2}\left(\delta(\omega_{dd}^n+\omega)+\delta(-\omega_{dd}^n+\omega)\right)+(1-c_{\mathrm{mod}}^n)\delta(\omega)$$

$$F(\omega) = F(\omega) + (w^n f_A^n) F^n(\omega)$$

next n

Figure 2.16: Algorithm outline to calculate a DEER time trace. The outermost loop (variable 'n') runs over all $\mathbf{B}_0^n(\theta,\phi)$ vectors which have A-spins excited by the detection pulses. Within each n-loop the corresponding single-orientation B-spin spectrum I_B^n is calculated and with the pump π-pulse profile P_B the modulation depth c_{mod}^n. If $c_{mod}^n > 0$ then the detection and pump pulses excite, at least partially, both spins of the pair at orientation $\mathbf{B}_0^n(\theta,\phi)$ and the weighted contribution to the DEER time trace is calculated and added. This figure is reproduced from J. E. Lovett, A. M. Bowen, C. R. Timmel, M. W. Jones, J. R. Dilworth, D. Caprotti, S. G. Bell, L. L. Wong, and J. Harmer. Structural information from orientationally selective DEER spectroscopy. *Physical Chemistry Chemical Physics*, 2009, **11(31)**, 6840–6848 with permission from the PCCP Owner Societies. [5]

2.6.1 Simulating the orientational dependence of the non-secular part of the dipolar interaction

The analytical equation for the dipolar frequency (Equation 2.22) only considers the secular part of the dipolar interaction. In order to consider the non-secular part the full Hamiltonian must be considered.

$$\hat{\mathbf{H}}_0 = \omega_A \hat{\mathbf{S}}_A^z + \omega_B \hat{\mathbf{S}}_B^z + \hat{\mathbf{H}}_{DD} \tag{2.25}$$

Equation 2.25 gives the form of the Hamiltonian in Liouville space. $\hat{\mathbf{H}}_{DD}$ is given in Equation 2.2c. The pulses were described by the following Hamiltonians:

$$\hat{\mathbf{H}}_{1,detection} = -\omega_1 \hat{\mathbf{S}}_A^x \tag{2.26a}$$

$$\hat{\mathbf{H}}_{1,pump} = -\omega_1 \hat{\mathbf{S}}_B^x \tag{2.26b}$$

The calculations used density matrix formalism and the integrated form of the Liouville-von-Neuman equation. More detail for this method of calculation is given in Chapter 7 where it is used extensively.

Comparison of the results for the orientationally dependent calculation using the analytical dipolar frequency formula and the full density matrix calculation including non-secular terms for the copper-copper systems studied in Chapter 3 and the iron-sulphur clusters in Chapter 4 the exclusion of the non-secular terms lead to distance errors well under 1 Å. This is as expected since the non-secular contributions only become significant in systems with large g-anisotropy.[97]

2.7 Analysis of experimental DEER traces

The majority of this thesis is concerned with the analysis of experimental DEER traces, the interpretation of the data, and the improvement in the experimental methods in order to improve the accuracy of this analysis.

Broadly, analysis for DEER spectra can be split into two main groups:

1. Distance analysis – for spectra where any orientational component is minimal; it is assumed that all orientations of the spins with respect to the magnetic field and each other are excited equally.

2. Orientational analysis – where both the distance and orientational components must be considered.

2.7.1 The structure of the DEER trace

As we have already seen for a simplified nitroxide model, not all of the spins detected will contribute to the DEER effect; if the paramagnetic centre to which they are coupled is not inverted by the pump pulse, the spin being detected will simply add to the background of the DEER trace. A DEER signal, $V(t)$, is therefore made up from a form factor, which contains the DEER oscillations, $F(t)$, and a background function, $B(t)$.

$$V(t) = F(t).B(t) \tag{2.27}$$

The form factor for a macroscopically disordered sample, such as a frozen solution, is given by the mathematical form and is the product of all the possible pair contributions for n spins:[57,98]

$$F(t) = \frac{1}{n} \sum_{det=1}^{n} \prod_{pump \neq det} 1 - \lambda_{pump} \left(1 - \cos \omega_{dd} t\right) \tag{2.28}$$

where the signal from a specific detection spin is the product of its interactions with all other spins affected by the pump pulse and the overall signal is the average of all of the signals from the individual detection spins. It should be noted that a detection spin cannot simultaneously be a pump spin. λ_{pump} is an inversion efficiency describing the proportion of spins excited by the pump pulse, it is orientation dependent. ω_{dd} is the dipolar oscillation frequency (see Equation 2.8b) for a particular pair of detection and pump spins; it is also orientation dependent due to the $(1-3\cos^2\theta)$ contribution and the g-values. In the case of $NO^{\bullet}-NO^{\bullet}$ DEER, the orientational dependence of λ_{pump} can generally be neglected when

the pump pulse is positioned to excite the $m_I = 0$ hyperfine component and thus a constant value of $\lambda \approx 0.5$ is appropriate for nitroxides.[57] Furthermore the average isotropic g-value for a nitroxide can be used in the calculation of ω_{dd}; thus the value of $\omega_\perp$ is now orientationally independent. Under these conditions the form factor becomes:

$$F(t) = 1 - \lambda \left[1 - \int_0^1 \cos\left(\omega_\perp \left(1 - 3\cos^2 \theta_i \right) t \right) d\cos\theta \right] \tag{2.29}$$

λ can be related to a modulation depth, Δ, via the following relation:[57]

$$\Delta = 1 - (1 - \lambda)^{n-1} \tag{2.30}$$

For a doubly-labelled nanoobject, $n = 2$ and thus $\lambda = \Delta$ if labelling of the system is incomplete so that there are some objects which are only labelled at one of the possible sites. This causes a reduction in the modulation depth to be observed as seen in the results of Chapter 3. For a system of two coupled spins ($n = 2$ in Equation 2.30), where there is only one pump spin in the sensitive DEER range of a detection spin, a labelling efficiency, f can be defined such that the modulation depth is equal to λf, the product of the inversion and labelling efficiencies.[57] Comparison of the predicted modulation depth for a system with only two spins, λf with the measured modulation depth, Δ allows prediction of the number of coupled spins, N, in a system:[99,100]

$$N = 1 - \frac{ln(1 - \Delta)}{ln(1 - \lambda f)} \tag{2.31}$$

When λf is very small this reduces to:

$$N = \frac{\Delta}{\lambda f} + 1 \tag{2.32}$$

Equation 2.30 also explains the orientational dependence of the modulation depth. As we have already seen, λ is only valid in systems where the pump pulse is not orientationally selective and thus in cases where this approximation cannot be made the orientationally dependent, λ_{pump} is used.

Factors affecting the modulation depth and its orientational dependence are considered in more detail in Chapter 6.

After suitable background correction the modulation depth can be found from the experimental form factor ($F(t)$) as the non-zero value to which it decays after a long time. Consequently at long dipolar evolution times after the dipolar oscillations have been damped (T_{dd}), the detected signal can be described as:

$$V(t > T_{dd}) = (1 - \Delta)B(t) \tag{2.33}$$

It should be noted that the modulation depth is only dependent on the inversion efficiency of the pumped spins and not on that of the detected spins. The excitation efficiency of the detected spins affects the size of the echo observed. Therefore when both the detected and the pumped spins show orientational selection, this can result in the observation of a very small echo and a signal with a very small modulation depth, respectively. Experimentally, this can mean that in order to collect analysable traces with good signal-to-noise the traces may have to be averaged for a long period of time. In some cases this results in measurements taking several days.

2.7.2 The form of the background correction

The form of the background used can greatly affect the analysis of the data;[101] in this work all the analysis uses a homogeneous background:

$$B(t) = \exp\left(-kt^{\frac{d}{3}}\right) \tag{2.34}$$

This form assumes a homogeneous distribution of all spins where k quantifies the density of spins and d is the dimensionality of the homogeneous distribution. In frozen solution samples of soluble proteins, the dimensionality of the background correction should be 3. In samples, such as membrane proteins, where there is a confinement of the sample distribution on a length scale of less than 10 nm, the dimensionality may be less; $d = 2$ is appropriate for samples confined to a two dimensional membrane

and $d = 1$ for those attached to a stretched polymer chain. The dimensionality may be a fractal number.

In many cases it may be more desirable to measure an experimental background, this is generally achieved using DEER measurements on singly-labelled samples, which are fitted to a polynomial or exponential function that can then be used as the background function for the double-labelled sample.

Ideally the DEER background should only result from the homogenous distribution of spins, other than the spin pairs, in the sample; leading to the exponential expression in Equation 2.34. However, as experimental DEER traces are not of infinite length in the time domain, longer distances between defined spin pairs, which give slow dipolar oscillations, can be difficult to distinguish from the background. This limits the distance information which can be extracted from a trace of a given length (see Equation 2.35 and Table 2.2).

2.7.3 DEER distance analysis: the Tikhonov regularization

When the excitation of two spins is isotropic, so that there is no orientational dependence, the Fourier transform of the DEER form factor (the resultant DEER signal after background correction) will yield a complete Pake pattern. From this Pake pattern the coupling frequency, $\omega_{\perp}$ can be extracted (see Fig. 2.2), and related to a separation distance between the two electron spins (Equation 2.8b). This method of finding a distance from direct measurement of $\omega_{\perp}$ (the peak to peak distance) will only yield a single distance. In biological and model systems, it is unlikely that a single distance can be fully representative of the sample due to the dynamic motion of the molecules present at room temperature, which will be frozen into the sample at cryogenic temperatures as a distribution of label positions. Instead it is much more desirable to extract a distance distribution from the data. This, however, is a very ill-posed problem, so small fluctuations in the input data from poor signal-to-noise or ill-fitted background corrections can cause large variations on the distributions extracted.[101]

The reliability of distance distribution extraction is highly dependent on the length of the time trace has been recorded; if a time trace is too short, longer distances present in the distribution may be removed from the distribution by a background correction. Equally the amount of time required to

build up the signal-to-noise of an experimental trace follows a square-root relationship and thus if a time trace is too long the level of signal-to-noise measured in a given experimental time will be worse for a longer time trace and poor signal-to-noise may introduce spurious distances into the extracted distance distribution, particularly at shorter distances. A general formula for predicting a reasonable time trace length with a little prior knowledge of the system being measured and the type of data that you wish to extract is given by:[102]

$$t_{max} = 2\ \mu\text{s}. \left(\frac{r_{exp}}{r_{max,i}} \right)^3 \tag{2.35}$$

where the length of the time trace is given by t_{max}, r_{exp} is the expected experimental distance to be measured and $r_{max,i}$ is given in Table 2.2.

Table 2.2: With a DEER trace length of 2 μs the maximum distances for which various properties of the distance distribution can be determined (shape, width, mean, detected) are given below:

$r_{max,i}$	Distance in nm
$r_{max,shape}$	3 nm
$r_{max,width}$	4 nm
$r_{max,mean}$	5 nm
$r_{max,detect}$	6 nm

The most common technique for the extraction of distance distributions from DEER data is Tikhonov regularization, which is considered to give the best compromise between artefact suppression and resolution. This is the method primarily used in DeerAnalysis.[45] The optimum distance distribution, $P(r)$, is found by minimizing an objective function $G_\alpha(P)$ for a given value of α known as the regularization parameter.[101]

$$G_\alpha(P) = \|S(t) - F(t)\|^2 + \alpha \left\| \frac{d^2}{dr^2} P(r) \right\|^2 \tag{2.36}$$

where $S(t)$ is a DEER form factor calculated from the trial distance distribution $P(r)$; $S(t) = K(t,r)P(r)$ where $K(r,t) = \int_0^1 \cos\left[(3x^2 - 1)\,\omega_{dd} t\right] dx$; and $F(t)$ is the experimentally derived form fac-

tor. The correct value of α to use is extracted from an L-curve, a plot of $log\left(\nu(\alpha)\right) = log\left(\left\|\frac{d^2}{dr^2}P(r)\right\|_\alpha^2\right)$ against $log\left(\rho(\alpha)\right) = log\left(\|S(t) - F(t)\|_\alpha^2\right)$, where the α value corresponding to the data point closest to the crook of the L is considered the best balance between smoothness and resolution.

In cases of noisy data, data with small modulation depths or broad distance distributions Tikhonov regularization may fail to produce an L-curve of appropriate shape.

Although Tikhonov regularizations have been used to analyse orientationally dependent DEER data sets through the use of two independent Tikhonov regularizations, one for the distance constraints and another for the angular constraints,[75,76] this is not the case in DeerAnalysis as the kernel uses a definition of ω_{dd} which uses a fixed g-value based on the average isotopic g-value for a nitroxide: $\omega_{dd} = 2\pi\frac{52.04\ \mathrm{MHz}^{-3}}{r^3}$.[101] There is currently no 'universal' program for orientational analysis of DEER spectra.

2.7.4 DEER orientational analysis: pre-simulated libraries of spectra

As already stated in Section 2.4, there have been a few different approaches taken for the analysis of orientationally selective DEER spectra. Unlike distance analysis, where there is only one parameter to be extracted, full orientational analysis of the position and orientation of one spin centre with respect to another requires six parameters: three positional, either Cartesian coordinates or a distance and two polar angles and three angular coordinates describing the rotation of one centre's g-frame with respect to the other spin centre. Each of these parameters will also have a distribution associated with it.

As with the extraction of a distance distribution extracting the six coordinates from experimental data is again an ill-posed problem mathematically. This can be seen in the analysis of a docked protein structure in Chapter 4 where there may be more than one set of coordinates which would provide a reasonable fit to the experimental data, although some of these can be ruled out using other sources of information; such as knowledge of binding interfaces, etc.

It is frequently not possible to extract reliably the relative coordinates of two centres directly from experimental data without considering the potential problem that this analysis may only find one of

many possible solutions. In order to make sure that all reasonable results for the system are found, an alternative to the complex problem of direct extraction of orientational data from orientationally selective spectra is instead to simulate data for the entire conformational space (or a given subset thereof) to provide a library of data to which the experimental data is fitted to provide a range of possible distances and angles, which match the experimental spectra.

This is the approach that we have undertaken in Chapters 3 and 4. The orientationally dependent DEER algorithm described above in Section 2.6 is used to simulate a library of possible DEER traces. The method uses spin distribution models of each centre which are defined from continuous wave EPR spectra, DFT, HYSCORE and ENDOR spectra, or otherwise, and contain information about the g-tensor, hyperfine interactions, EPR line widths and spin density distributions. The relative position of the two centres with respect to one another can then be specified and DEER traces calculated.

It is possible to pre-calculate DEER traces for all conformational space by generating a grid of knots about the detection centre and placing the pump centre at each knot on the grid. The excitation fraction of the detection and pump centres will not alter with the distance between the two centres and hence these parameters can be calculated and stored for a given angular orientation of the two centres with respect to one another and used to calculate the DEER spectra at multiple distances, effectively expanding and contracting the grid. This was the approach taken in Chapter 4 where orientational DEER data is used to study the orientation of one protein relative to another in a complex. In this case the pump label was a nitroxide, where the pump pulse was applied to the $m_I = 0$ transition; this was deemed to excite all orientations of the nitroxide and thus the orientational dependence of this centre did not need to be considered. In cases where this approximation cannot be made, in order to study the full conformational space for each grid point on the grid of knots surrounding the detection centre, the pump centre must also be rotated at that point through another grid of knots to allow for the orientational selectivity of this centre. The resulting calculation is very lengthy and may not be computationally practical in cases where there is orientational selection for both centres.

In some cases it may be possible to reduce the number of orientations sampled using symmetry of the centres being studied; however, in order for this to be possible not only must there be some symmetry

in the g-tensor and any hyperfine coupling but also in the spin density distributions, which is directly related to the molecular structure, and finally in the relative orientation of the g-tensor and hyperfine couplings to the spin density distributions, reducing the possibilities for making simplifications due to symmetry. It should be noted that although an increase in the symmetry of the system can reduce the calculation time, it may also cause inherent uncertainties in the position of spin labels as two or more orientations can become equivalent; this was observed in the case of orientationally selective DEER on the vinculin tail,[103] where 'a full grid search of parameter space revealed that the DEER experiment introduces parameter-space symmetry higher than the symmetry of the spin Hamiltonian. Thus, the number of equivalent parameter sets is twice as large as expected and the relative orientation of the two spin labels is ambiguous.'[103] In such instances it can be necessary to use other information about the system such as structural information in order to predict which of the equivalent orientations is most favourable.

Another approach is to use an alternative method to generate the input orientations of the two centres with respect to one another so that only the DEER traces for a relatively small number of orientations of the two centres need to be calculated. In Chapter 3, this is achieved using DFT calculations of the molecular structure. The calculated DEER traces are summed to create a total DEER trace and this is compared to the experimental data to evaluate the model used.

In Chapter 4, although the DEER traces were calculated for the entire conformational space in order to remove possible solutions that were not biochemically possible, protein docking simulations were used to generate potential structures for the complex, and the DEER traces for each of these structures generated using DEER traces from the pre-computed library. The use of the pre-computed library allowed the DEER traces for a given complex orientation to be calculated quickly using existing traces from the library; and finally the most promising orientations were refined using least squares fitting to provide the best possible orientation of the two proteins in the docked complex.

Both of these approaches are fundamentally model-based and require some prior knowledge of the system; it is vital to have information about the electronic structure of each of the centres. Knowledge of possible orientations of the two centres is useful for reducing the size of the calculation but not

absolutely necessary as calculations could search the entire conformational space. However, such calculations would be much more lengthy and computationally expensive.

Chapter 3

Orientationally selective DEER measurements on copper(II) systems

3.1 Introduction to EPR of copper systems

Copper(II) centres are of great interest for EPR studies of proteins due to their potential to constitute an innate spin label within the protein structure.[104] Many proteins have naturally occurring copper centres which can be prepared in the copper(II) ionization state by careful oxidation of the system and many more have other 2+ metal cations bound within their structures such as zinc (found in the zinc finger domains of many DNA binding proteins) or iron (present in the plethora of heme containing proteins) which, through careful protein preparation, can be replaced by copper.[a]

The use of innate spin probes such as copper can have some advantages over the currently predominant nitroxide spin labels, in particular *S*-(2,2,5,5-tetramethyl-2,5-dihydro-1H-pyrrol-3-yl)methyl methanesulfonothioate (MTSL, see Fig. 3.1), since there is a smaller degree of uncertainty in the position of the unpaired electron density for single metal centres in rigid environments compared to MTSL. Fig. 3.1 gives an example of how large the distribution of MTSL spin label positions can be for a single label attached to a small protein. In comparison, the location of the electron density on a copper ion that is tightly bound within a protein structure can be located to a much greater degree of accuracy. Furthermore, in most cases it is not known how the incorporation of the MTSL, particularly when site

[a] Although iron can also be EPR active, the spectrum of iron is usually much broader than that of copper. Thus, this makes pulsed EPR studies of iron systems more difficult as nanosecond pulses will only excite a very small portion of the iron spectrum and the resonator bandwidth limits the frequency separation to a very restrictive range.

directed mutagenesis is involved, affects the local and/or global structure of the protein, even when the activity of the protein is unaffected.

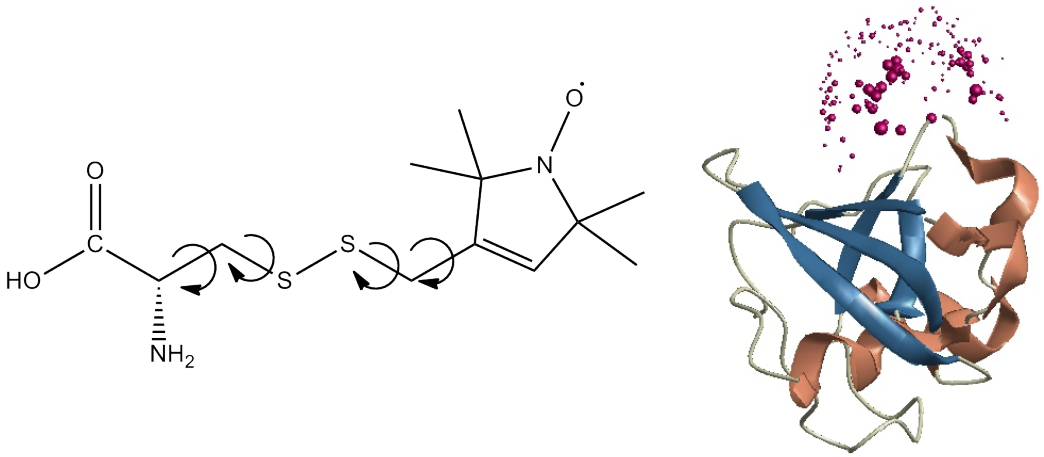


Figure 3.1: **Left:** The structure of the MTSL spin label with the flexible bonds marked. The sulphide (S–S) bond can adopt either a *cis-* or a *trans-* conformation. However, due to the relatively high polarisability of the sulphur electron density, there is partial double bond character in the S–S bond. Therefore, the *cis-* and *trans-* forms of the bond are predominant over any intermediate angles and interconversion between the two forms is slow. **Right:** A possible distribution of nitroxide positions calculated for an MTSL labelled ferredoxin protein (*3HUI.pdb*).[12]

Within the arsenal of EPR techniques available to assist in the determination of biomolecular structure, it is the DEER experiment that can be used to measure accurately inter-spin distances in the range 1.5 to 8+ nm. Indeed, it is frequently the uncertainty in the position of a nitroxide spin label that provides the greatest source of error in a DEER measurement. Therefore, the use of tightly bound innate paramagnetic centres, such as copper, in protein structures could reduce this error. The use of copper centres for this type of measurement has one further intriguing possibility: in addition to distance information, it may also be possible to extract orientational information from the measurements taken.

Unlike nitroxide spin labels, which at X-band (c. 9.5 GHz) can be approximated, and therefore modelled as having isotropic g-tensors (typical principal values being [2.001 2.003 2.009]), the g-tensor for an electron associated with a copper(II) centre under most symmetries is approximately axial

(typical values being [2.05 2.05 2.20]). In addition to this, the hyperfine splitting caused by coupling to the copper nucleus (both ^{63}Cu and^{65}Cu have nuclear spin $\frac{3}{2}$) results in an EPR spectrum for an electron associated with a copper centre that is several hundred MHz wide. Therefore, whereas a pulse at X-band applied at the centre of the nitroxide spectrum on the $m_I = 0$ transition can be considered to excite all orientations of the nitroxide with respect to the external magnetic field, the same pulse applied to an electron associated with a copper centre can only excite a small proportion of the EPR spectrum. This leads to orientational selection. This effect on DEER spectroscopy has previously been introduced and discussed in Chapter 2.

The shape of the copper EPR spectrum exhibits a g_z principal value feature (low field), where the signal can be described as 'single-crystal'-like, originating from molecules that have the g_z-axis aligned with the external static magnetic field. At higher field values towards the spectral maximum, there also exists a predominately *x/y*-region, originating from the g_x and g_y principal values, this region is denoted as arising from $g_{x/y}$. Each spin packet is split into four peaks due to hyperfine coupling to the spin-$\frac{3}{2}$ copper nucleus. Depending on the coordination environment of the copper nucleus, the spectrum may be split by further hyperfine couplings to ligating atoms such as nitrogen and also broadened due to unresolved smaller couplings (mainly from protons in the surrounding environment, which need not be directly coordinated to provide splitting due to the through space dipolar interaction). This structure of a typical copper(II) EPR spectrum is detailed in Fig. 3.2.

This chapter aims to provide a complete study of orientationally selective DEER between two copper(II) centres in the protein homo-dimer of copper amine oxidase from *Arthrobacter globiformis* (see Section 3.4) and also in five porphyrin-based rod-like model systems of differing lengths (see Section 3.3).

Orientationally selective DEER spectra were simulated using the MATLAB algorithm described in Chapter 2. In order to use this simulation program, a model of the system must be constructed so that the relative distance and orientation between the two centres may be defined. For the protein system, an X-ray crystal structure was used to give the position of the two centres relative to one another. The model systems are orientationally quite flexible, so it was not possible to use a single

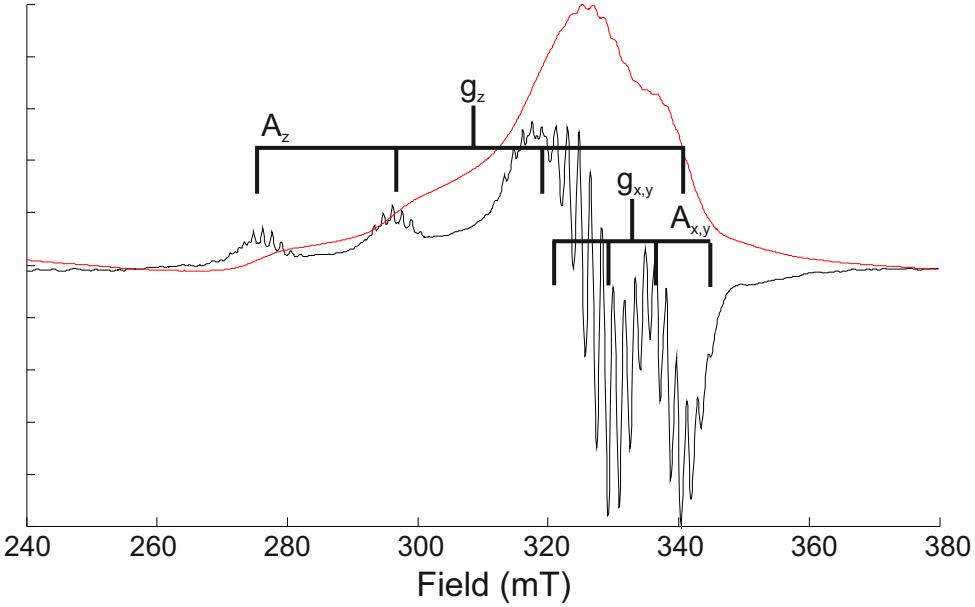


Figure 3.2: A copper(II) EPR spectrum shown in the differential (black) and integrated (red) forms, with the detailed g-values and hyperfine structure included for the x-,y-and z-components. The spectrum is that of the dicopper porphyrin 1-phenyl system illustrated in Fig. 3.5A.

orientation of the two centres for modelling. Instead a distribution of 1,000 possible conformers was generated using parameters defined from Density Functional Theory (DFT) calculations. Copper-nitroxide and nitroxide-nitroxide model systems of a similar form to the copper-copper model systems were also studied to verify the modelling procedure utilized for the copper-copper model systems, since the nitroxide containing systems can also be analysed using DeerAnalysis,[45] which analyses only the distance distributions also described in Chapter 2. The results of the two methods were compared.

Short copper-copper distances (<1.5 nm) were also studied using CW-spectral analysis for the copper centres in a porphyrin-based nanoring (see Section 3.7).

3.1.1 Previous EPR studies on copper(II) systems

As mentioned in Chapter 2, there are a small number of existing DEER studies of copper systems. The first copper-copper DEER measurement was carried out on a homo-dimer of the protein Azurin by

van Amsterdam et al.[69] As the data were very noisy, orientational information could not be extracted. Although analysis was attempted in the frequency domain, the results were ambiguous. Double Quantum Coherence (DQC) experiments on copper-copper systems have also been carried out; however, no orientational analysis was attempted in these studies.[105] In one further investigation, the effect of orientation selection is ignored completely.[70]

The first DEER studies that really attempted to tackle the problem of orientational selection were those of Bode et al.,[8,38] who investigated copper-nitroxide model systems. These papers used a geometric model as a basis for simulation of the orientationally selective DEER spectra. This model took into account the mean distance of 20.7 Å between the copper and the nitroxide, a single bending motion of $\pm 15^{\circ}$ centred at the mid-point of the biphenyl bridge and free rotation of the nitroxide group around the phenolic bond on a cone of 31.4°.[8] The inclusion of the nitroxide significantly simplified the problem since it required that only the orientational selection of the copper centre needed to be considered.

Yang et al.[9,10,71] have published work that studies the orientations of two copper centres attached to proline and aniline-based peptides. Their first work did not yield any change in the experimental results at different detection field positions, thus showing no orientational selectivity. This is likely to be an unfortunate result of the geometry of the system used in the study.[10] Through the use of a different model system, chemically similar but geometrically different, they were able to make an orientational analysis of two copper centres.[9,71] These papers aimed to provide model free fitting for orientationally selective spectra; however, the final approach required the use of a generic molecular model, based on a spherical distribution of each centre, where each centre can exist anywhere in a sphere of radius, ΔR, separated by a distance, R. This generic molecular model is not appropriate for the systems used in this study, as discussed in Section 3.3.2.

Fig. 3.3 shows structures of model systems which have been used to invistigate the orientational dependence of Cu−Cu and Cu−$NO^{\bullet}$ DEER measurements.

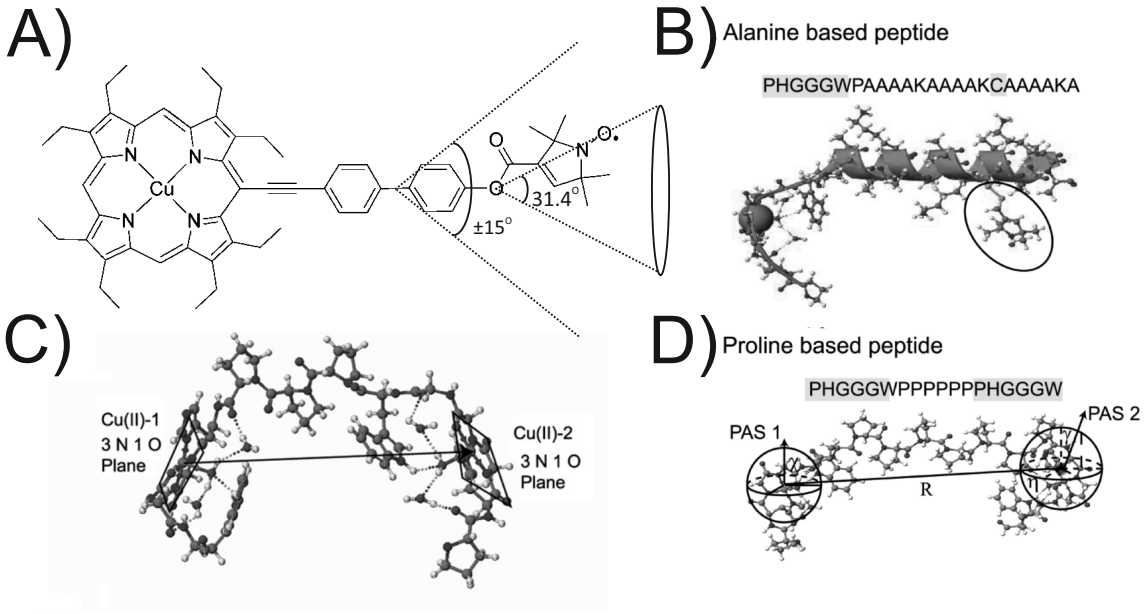


Figure 3.3: **A)** porphyrin-based Cu−NO$^{\bullet}$ model system used by Bode et al.[8,38] The alkyne-based linker allows rotation of the C-C single bonds within this linker. The bending mode ($\pm 15°$) and conical rotation (31.4°) used to generate a geometric model of the two centres in this system are marked. Figure adapted with permission from *Journal of Physical Chemistry A*, **112(23)**, B. E. Bode, J. Plackmeyer, T. F. Prisner and O. Schiemann, PELDOR measurements on a nitroxide-labeled Cu(II) porphyrin: Orientation selection, spin-density distribution, and conformational flexibility, 5064–5073. Copyright © 2008 American Chemical Society.[8] **B)** Cu−NO$^{\bullet}$ system with an analine-based peptide linker used by Yang et al.[9] Figure reprinted with permission from *Journal of Physical Chemistry B*, **114(18)**, Z. Yang, D. Kise and S. Saxena, An approach towards the measurement of nanometer range distances based on Cu^{2+} ions and ESR, 6165–6174. Copyright © 2010 American Chemical Society.[9] **C)** Cu−Cu system with a proline-based peptide linker used by Yang et al.[10] Unfortunately the orientation of the copper centres in this compound did not yield any measurable orientational selection. This figure is reprinted from *Journal of Magnetic Resonance*, **188**, Z. Yang, J. Becker and S. Saxena, On Cu(II)-Cu(II) distance measurements using pulsed electron electron double resonance, 337–343. Copyright © 2007, with permission from Elsevier.[10] **D)** Cu−Cu system with a proline-based peptide linker used by Yang et al.[9] Orentational selection was recorded for this compound. Figure reprinted with permission from *Journal of Physical Chemistry B*, **114(18)**, Z. Yang, D. Kise and S. Saxena, An approach towards the measurement of nanometer range distances based on Cu^{2+} ions and ESR, 6165–6174. Copyright © 2010 American Chemical Society.[9]

Currently, no generic method exists for the analysis of orientational spectra with a distribution of distances and orientations. In order to achieve orientational analysis, some prior knowledge of the system under study is still required.

3.2 EPR materials and methods

3.2.1 Continuous wave EPR measurements

Continuous wave (CW) frozen solution EPR measurements were taken for all of the systems studied. Data was collected on a Bruker EMX spectrometer at X-band (9.5 Hz) using an Oxford Instruments variable temperature cryostat. Cryogenic temperatures were reached by cooling the system with liquid helium.

These measurements were simulated using the EasySpin function '*pepper*', which allows the simulation of powder averaged solid state CW-EPR.[7,96]

3.2.2 Pulsed EPR measurements

Pulsed measurements were performed on a Bruker Elexsys E680 pulsed spectrometer with a 3 mm split ring Bruker resonator (EN 4118X-MS3) in an Oxford Instruments cryostat with a variable temperature control for pulsed experiments. Again, cryogenic temperatures were achieved using a continuous flow of liquid helium.

Copper centres have unfavourably fast relaxation times (in particular short T_m times), compared to many nitroxide centred radicals. This restricted the length of DEER traces that could be recorded, resulting in the loss of intelligible signal in the four-pulse DEER experiment to such a degree that it was not possible to record traces of sufficient length using this technique to measure the inter-spin distances for the two longest Cu−Cu rod systems (distances >3.5 nm). In order to allow DEER traces with longer τ_2 times to be recorded, and thus traces which could be used to measure longer distances, the shorter three-pulse DEER experiment was used. Traces recorded via this technique have a dead-time and are distorted about the zero-time, thus frequently this part of the trace is not recorded. Loss

of the zero-time results in an uncertainty in the modulation depth and can lead to spurious shorter distances in the analysis if the zero-time cannot be accurately predicted. (Further details about this are given in Chapter 7.) This causes a particular problem for orientationally selective spectral analysis as the subtle orientation effects can manifest as changes in the initial modulation depth.

In order to regain the information at the zero-time, shorter four-pulse DEER traces were also recorded, which include the zero-time. Four-pulse DEER is a dead-time free experiment and thus can be used to measure the modulation depth accurately.

The two data types were combined using the DEER-Stitch method of Lovett et al.[106] DEER-Stitch matches the three-pulse DEER data to the shorter four-pulse DEER trace, with corrections made for the potential different backgrounds and intensities for each of the two traces, to form a composite DEER trace.

In both the case of the copper-copper model systems and the protein dimer studied here, the ESEEM (Electron Spin Echo Envelope Modulation) traces (see Fig. 3.4) were used to help select an appropriate length for τ in the three-pulse experiment and τ_2 in the four-pulse experiment (as defined in Fig. 2.4 and Fig. 2.5), so that the signal observed was maximized. In cases where strong ESEEM is observed at early times, it is important to use this information to allow selection of a suitable τ_1 time for four-pulse DEER to ensure that a primary echo is formed, which can be refocused. For copper amine oxidase (Fig. 3.4b) no signal is observed in the Hahn echo-detected ESEEM experiment at $t = 600$ ns, so it would be very unwise to choose a τ_1 time of 300 ns, since this would result in no signal to form the first echo. Instead, a τ_1 of 120 ns was used, this forms a primary echo that corresponds to the signal intensity at 240 ns on the primary ESE plot.

For both the model systems and copper amine oxidase, the z-components of the EPR spectra relaxed faster than the x/y-components, so it was necessary to limit the overall pulse sequence length to c. 3000 ns in order to allow detection of both components. For both the Cu−Cu model systems and copper amine oxidase, four-pulse DEER with a τ_2 of 200 ns was collected and combined during the analysis with three-pulse DEER data, measured using a longer τ time, 1500 ns for the Cu−Cu model systems and 2000 ns for the copper amine oxidase.

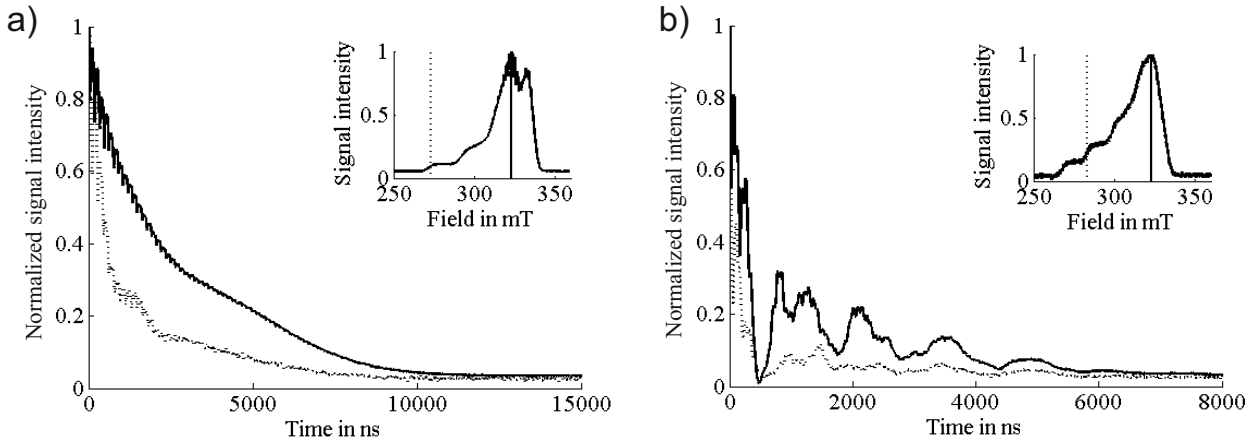


Figure 3.4: **a)** Two-pulse ESEEM spectra showing the T_m relaxation of the 5-phenyl Cu-Cu compound (see Fig. 3.5 for the structure of this compound). Data is shown for both the field maximum (solid line), which is primarily the $g_{x/y}$ contribution, and also at a lower field (dotted line), which is mainly g_z. The field positions with respect to the field sweep are shown in the insert. The sample was prepared in a 1:1:1 mixture of chloroform:toluene:THF at a concentration of 0.1 mM. **b)** Two-pulse ESEEM for the copper centre in the protein copper amine oxidase. Again, data is shown for both the field maximum (solid line) which is primarily the $g_{x/y}$ contribution, and also at a lower field (dotted line), which is mainly g_z. The field positions with respect to the field sweep are shown in the insert. The protein sample was prepared with a monomer concentration of 1.2 mM in 30% glycerol by volume.

DEER experimental parameters

Hahn echo-detected field sweeps and fixed field experiments, with variable τ times, to probe ESEEM were recorded with pulse lengths of 16 and 32 ns for the $\frac{\pi}{2}$ and π pulses respectively.

For all of the DEER experiments recorded on different systems, pulses of 32 ns were used for both the π and $\frac{\pi}{2}$ observer pulses. A pulse of 12 ns was used for the π pump pulse. For the Cu−Cu systems, three-pulse DEER was collected with a τ time of 1500 ns and four-pulse DEER used a τ_2 of 200 ns. These two types of traces were then combined using DEER-Stitch.[106] The Cu−NO$^\bullet$ and NO$^\bullet$−NO$^\bullet$ systems were studied using four-pulse DEER with a τ_2 time of 1 μs and 2 μs for the 1-phenyl and 3-phenyl Cu−NO$^\bullet$ systems respectively, and 1 μs for the NO$^\bullet$−NO$^\bullet$ system.

3.2.3 Simulation of orientationally selective DEER: background correction

The orientationally selective DEER simulation program calculates the dipolar spectrum arising from the interaction of two spin centres. The calculated trace contains both a modulated and unmodulated part. The program calculates a contribution to the dipolar spectrum for all orientations of the detection centre with respect to the magnetic field, which are on-resonance with the detection pulses. For each 'on-resonance orientation' of the detection centre, if the associated pump centre is on-resonance with the pump pulse a frequency contribution corresponding to the orientation of the two centres is added to the dipolar spectrum, giving rise to the modulated part of the spectrum. If the associated pump centre is not on-resonance with the pump pulse an unmodulated contribution is added to the spectrum.

The simulation program does not, however, include any contributions from the homogeneous distribution of spins surrounding the spin pair. Therefore, in order to allow comparison of the simulated data with experimentally recorded data, it is necessary to include a background feature to account for the contributions from these spins and relaxation.

As described in Section 2.7.2 the most common form of background correction in DEER experiments is the homogeneous background:

$$B(t) = \exp\left(-kt^{\frac{d}{3}}\right) \tag{3.1}$$

where k is the decay rate constant and d describes the dimensionality of the system. For the systems studied in this chapter, a dimensionality of approximately 3 would be expected, corresponding to homogeneous distribution of the molecules in three-dimensions with no long range order.

In addition to this, the simulated DEER assumes that the model is fully labelled with both copper and/or nitroxide, and that the spins pairs are isolated so that there is no aggregation. In reality, the labelling of the systems is not complete; hence both mono-labelled species and any aggregates present will contribute to the background and affect the modulation depth, which is related to the number of coupled spins (see Equation 2.31) and also the labelling efficiency.[57] In principle, assuming no aggregation, our simulation program could be calibrated to calculate the correct modulation depth

through careful parameterization of the resonator characteristics (e. g. bandwidth, B_1 inhomogeniety). However, in reality the spectrometer parameters change over time and with the coupling conditions used, to accurately calculate the modulation depth, it would be necessary to measure the resonator parameters before each experimental measurement. Instead, it is simpler to correct the modulation depth of the simulated data as part of the background correction.

The results of the DFT calculations defining the chemical structures and angle distributions with the compounds were used as input parameters to obtain simulations of DEER traces. Background correction is applied to the simulated data, $S(t)$, which is matched to the experimental data to provide the best parameters for the background correction.

The complete form of the background corrected simulation data, $D(t)$, including a correction to the modulation depth is:

$$D(t) = [(Y \times S(t)) + (1 - Y)] \,.\, \exp\left(-kt^{\frac{d}{3}}\right) \tag{3.2}$$

where $S(t)$ is the raw simulation data. Y is the correction to the modulation depth. Due to incomplete labelling, $Y \leq 1$ and the value is held constant between DEER measurements taken on the same sample at different pulse frequencies and field positions. In this chapter all of the figures presenting both experimental recorded data and data simulated using the simulation program described in Chapter 2 plot the raw experimental data with simulated data that has been multiplied by a background correction and a modulation depth correction. Where only simulated DEER traces are shown these are plotted without the addition of any background or modulation depth correction. In cases where experimental data is presented in comparison to a fit found by Tikhonov regularization analysis, the experimental form factor ($F(t)$) found by dividing the raw experimental DEER trace by a background correction, is shown. The reason for this is that Tikhonov regularization seeks to minimize the difference between the experimental form factor and one which is calculated for a given distance distribution ($S(t)$). Tikhonov regularization therefore does not use the raw experimental data directly in the fitting process.

3.3 Copper-copper, copper-nitroxide and nitroxide-nitroxide rod-like model systems

In order to make a systematic study of DEER measurements in copper systems, model systems of known length were synthesized by Dr Michael Jones in the laboratory of Prof. Jon Dilworth. These systems were designed to be rigid rods holding the two copper centres a fixed distance apart. Copper-nitroxide and nitroxide-nitroxide analogues were also prepared for some of the systems to provide benchmark measurements against which the accuracy of the modelling could be ascertained. Fig. 3.5 illustrates the structures of the systems. From this point forward, the model systems will be referred to by their type; Cu−Cu, Cu−$NO^{\bullet}$ and $NO^{\bullet}$−$NO^{\bullet}$ and the number of phenyl rings in the central linker; 1-phenyl to 5-phenyl.

3.3.1 Model systems: design, synthesis and sample preparation for EPR

Cu−Cu model system design

The rod structures were designed to be stable, rigid (to minimize the level of uncertainty for the distance) and with few degrees of freedom, although it was difficult to keep these to a minimum and DFT calculations show how large the angular flexibility can actually be. The amide functionality acts as a type of 'circuit breaker'; diminishing the through bond electronic exchange that could occur between the two paramagnetic centres impeding the determination of accurate distances.[38]

The tetraphenyl porphyrin (TPP) template offers a stable copper chelate and is also relatively easy to prepare, functionalize and purify, so this was duly selected as the copper-chelating moiety for this study. Attempts to use other bifunctional chelators were not successful, due to the formation of polymeric material during coordination to Cu(II) under a range of conditions; hence these approaches were abandoned.

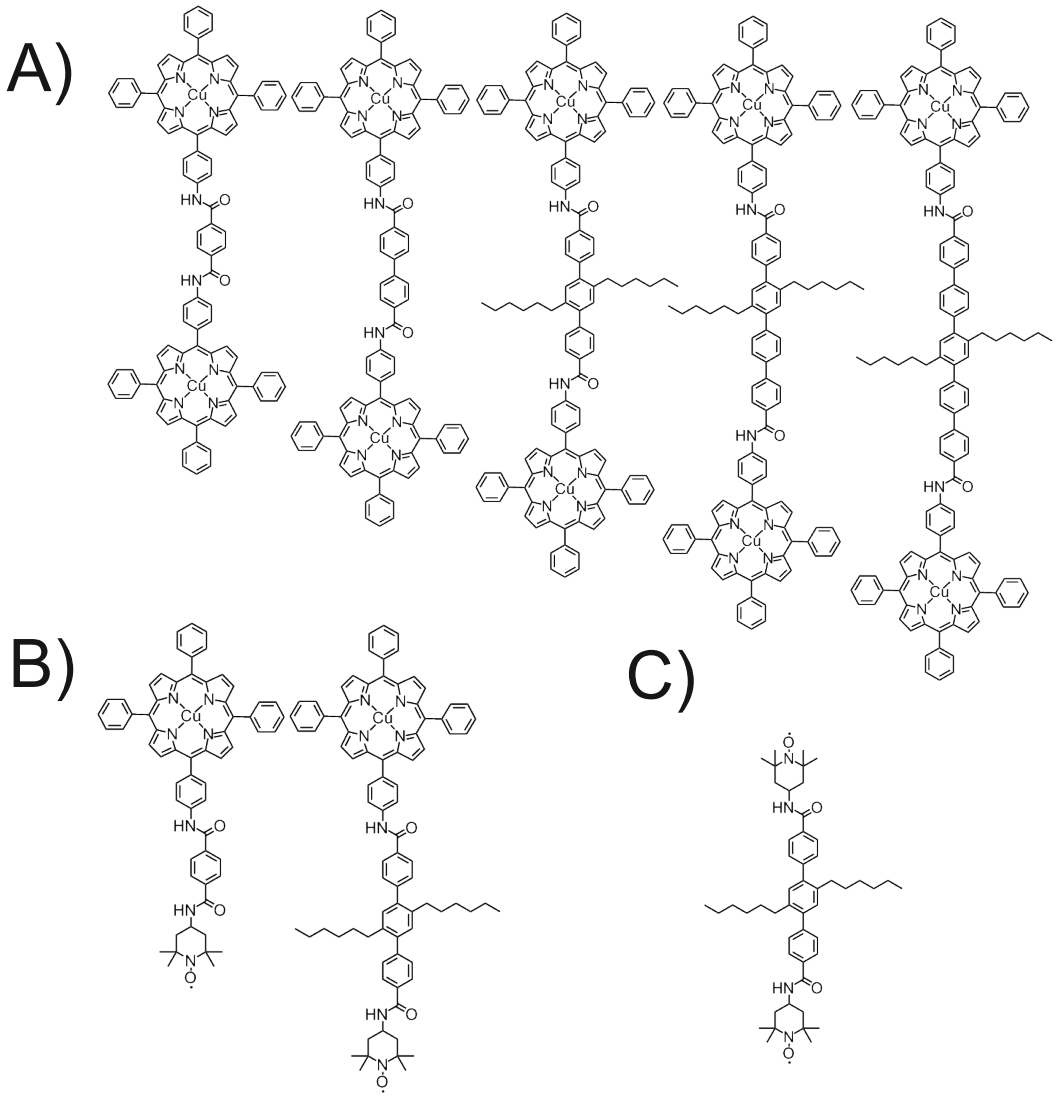


Figure 3.5: The chemical structures of the model systems used. **A)** Five copper-copper systems were made with 1-5 phenyl rings in the central linker. **B)** Analogous copper-nitroxide systems with 1- and 3-phenyl rings in the linker. **C)** Bisnitroxide system with 3-phenyl rings in the linker.

The linkers were made with one to five 1,4-disubstituted aryl rings, to give five compounds. Initially, these were not prepared with any substituents on the central phenyl group. However, to enhance the solubility of the larger compounds, those containing a central linker with greater than three phenyl rings, hexyl-groups were added in the 2- and 5-positions of one central phenyl ring. This also aided purification, since early synthetic attempts were thwarted by the insoluble nature of the polyaromatic compounds. The addition of aliphatic side-groups to polyaromatic systems to aid solubility has been previously reported in the work of Jeschke and co-workers, covering the production of similar model compounds for use in DEER methodology work.[72]

Compounds where one or both of the copper centres were replaced by a nitroxide were also synthesized for the 1- and 3-phenyl systems respectively, to allow study of the flexibility of the two rod-like building blocks forming the dicopper compounds: the tetraphenyl porphyrins and the phenyl linkers.

Cu−Cu model system synthesis

Synthesis of the model compounds was completed by Dr Michael Jones working in collaboration with Prof. Jon Dilworth in the Inorganic Chemistry Department of Oxford University.

The two smaller compounds (1- and 2-phenyl) did not suffer from solubility problems. Hence, simple 4,4-dicarboxylic acids were either commercially available or prepared without difficulty. The synthesis of the linker commenced from the previously reported dibromide, which was then subjected to Suzuki-Miyaura coupling reaction with the requisite aryl boronic acid (in the case of the 3- and 4-phenyl linkers) or aryl boronate (in the case of the 5-phenyl linker).[107] The synthesis of the 3- and 4-phenyl linker resulted in a mixture of products being formed, which were subsequently separated by chromatography. Even so, the products were isolated with a reasonable yield. The methyl ethers were readily saponified using lithium hydroxide to form the desired dicarboxylic acids. BOP ((Benzotriazol-1-yloxy)tris(dimethylamino)-phosphonium hexafluorophosphate) coupling with an excess of the $TPPNH_2$ (tetraphenylporphyrin amine) congener in all cases, afforded the diporphyrin species with phenyl linkers 1-5 in moderate yields after flash chromatography. Insertion of the metal was relatively trivial; a methanolic solution of copper(II) acetate was introduced to a stirred solution of

diporphyrin in chloroform and heated at reflux. Each copper species was formed cleanly, as evidenced by thin layer chromatography and MALDI analysis, UV-vis spectroscopy and CW-EPR at X-band. The copper-nitroxide species were prepared via the BOP coupling of one equivalent of $TPPNH_2$ to the requisite acid, followed by attachment of the $TEMPO{-}NH_2$ motif, also using a BOP mediated coupling procedure. This order of addition was employed to aid purification processes, since the porphyrin derivative is clearly visible (dark purple) on silica gel. Finally, the insertion of metal was achieved in the same way as for the symmetrical dicopper species. The Nitroxide-Nitroxide compound was prepared simply, again by BOP mediated coupling of the $TEMPO{-}NH_2$ motif to the 3-phenyl acid. Formal synthetic schemes for the syntheses are given in Appendix G.

The compounds were characterized using ^{1}H and ^{13}C NMR, mass spectrometry, UV and IR spectroscopy.

Cu−Cu model system EPR experimental conditions

Continuous wave EPR experiments were performed on 1 mM samples in chloroform to characterize the Cu−Cu model systems (Fig. 3.6a). The spectrum of the 3-phenyl compound is broadened compared to those for the other compounds. We attributed this broadening to π-stacking; the large, essentially planar porphyrin rings are known to have a propensity to π-stack with one another in non-aromatic solvents. The broadening of the 3-phenyl spectra was seen to significantly reduce on dilution (Fig. 3.6b). It is thought that this effect is only seen in the 3-phenyl compound, due to more efficient intercalation of the copper into the phorphyrin rings in this compound. To prevent this interaction between the porphyrin rings, an aromatic component can be introduced to the solvent. The degree of π-stacking was investigated by recording the T_1 relaxation times of the copper paramagnetic centre in different solvents for the 3-phenyl $Cu{-}NO^{\bullet}$ system recorded for 0.1 mM samples (Fig. 3.6c).

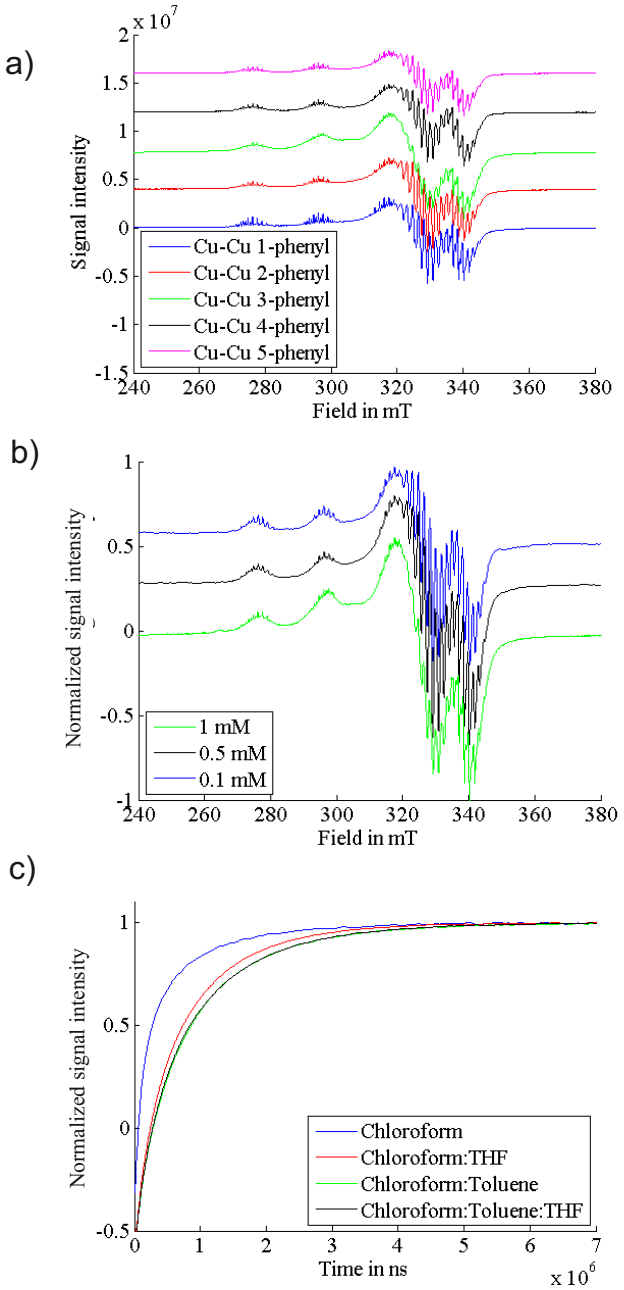


Figure 3.6: **a)** CW spectra of all Cu-Cu compounds in chloroform at 1 mM concentration; spectra were recorded at 15 K. **b)** CW spectra of 3-phenyl Cu−Cu model system in chloroform at different concentrations; spectra were recorded at 15 K. **c)** T_1 relaxation times measured for the 3-phenyl Cu−NO$^\bullet$ in different solvent mixtures recorded on the copper signal maximum; spectra were recorded at 25 K.

Using chloroform alone as the solvent gives the shortest T_1 relaxation time, followed by the 1:1 volumetric mixture of chloroform:THF[b] with the 1:1 mixture of chloroform:toluene and 1:1:1 mixture of chloroform:toluene:THF having equally long times. Since mixed solvents tend to form better glasses, it was decided to use a concentration of 0.1 mM and the 1:1:1 mixture of chloroform:toluene:THF for the DEER experiments.

To account for the different relaxation properties of copper and nitroxides; all EPR measurements on the Cu−Cu systems were conducted at 15 K, those on the Cu−$NO^{\bullet}$ systems at 25 K and those on the $NO^{\bullet}$−$NO^{\bullet}$ system at 50K.

3.3.2 Density Functional Theory (DFT) modelling to generate a molecular model for simulation of spectra

Two questions needed to be answered for the copper containing model systems:

1. Is it possible to predict the relative positions and orientations of the two centres for the model systems?

2. What is the orientation of the g-tensor with respect to the molecular frame and the distribution of spin density?

DFT determination of the relative positions of the two centres for the model systems

Initial predictions for the flexibility of the chemical systems followed the idea that adjacent phenyl rings would lie approximately at right angles to one another, to minimize steric interactions between the *ortho*-hydrogen on adjacent rings. This hypothesis, however, does not take into account any electronic effects, due to the aromaticity of phenyl rings. When two phenyl rings lie in the same plane, an extended conjugated π-electron system can be formed. This would lead to a reduction in the phenyl-phenyl torsional angle from 90°, which is the most sterically favourable orientation, towards 0°, which would allow for the largest degree of π-orbital overlap between adjacent phenyl rings. This leads to a broad distribution of bond angles being observed.

[b]THF is the solvent Tetrahydrofuran.

Previous rigid rod type systems have been modelled using a conical distribution of one centre with respect to the other.[8] This approach assumes full rotation is possible about all torsional bonds. In the case of acetyl linkers this is acceptable; however, this is not the case for the types of bonds present in the model systems studied here. Therefore, modelling the system in this way when trying to analyse the orientationally selective spectra may lead to false results. Another study from Yang et al.[9,71] looked at the relative orientation of two copper centres attached to short polypeptide chains. This used a ball model where each centre was modelled as a ball of spin density, where the radius of the sphere for each centre was defined as ΔR and the distance between the centres of the two spheres as R. For reasons that will be explored in the analysis, it is believed that this is an inappropriate model to use for the rod-like model systems employed in this study.

In order to gain the best understanding possible of the relative orientation of the two centres, a DFT study was carried out on the model systems, using the software package ADF.[108,109] In order to reduce the computational demands, a fragment analysis was performed, where the structures were broken up into smaller composite fragments (see Fig. 3.7a). For each of the marked bonds in each of the fragments, a linear transit over 180° in 10° steps was calculated using a BLYP functional (Becke-Lee-Yang-Parr), with a TZP basis set (triple-zeta polarization). The value of kT at the freezing point of a 1:1:1 volumetric mixture of chloroform, toluene and THF, measured to be 134.15 K, is 0.11547 eV. It was assumed that all angles occurring at an energy within the value of kT from the angle of lowest energy are equally accessible at the freezing point of the solvent mix and thus will occur with equal frequency in the frozen sample. Therefore, the maximum possible angles accessible for each type of bond were found (see Fig. 3.7b).

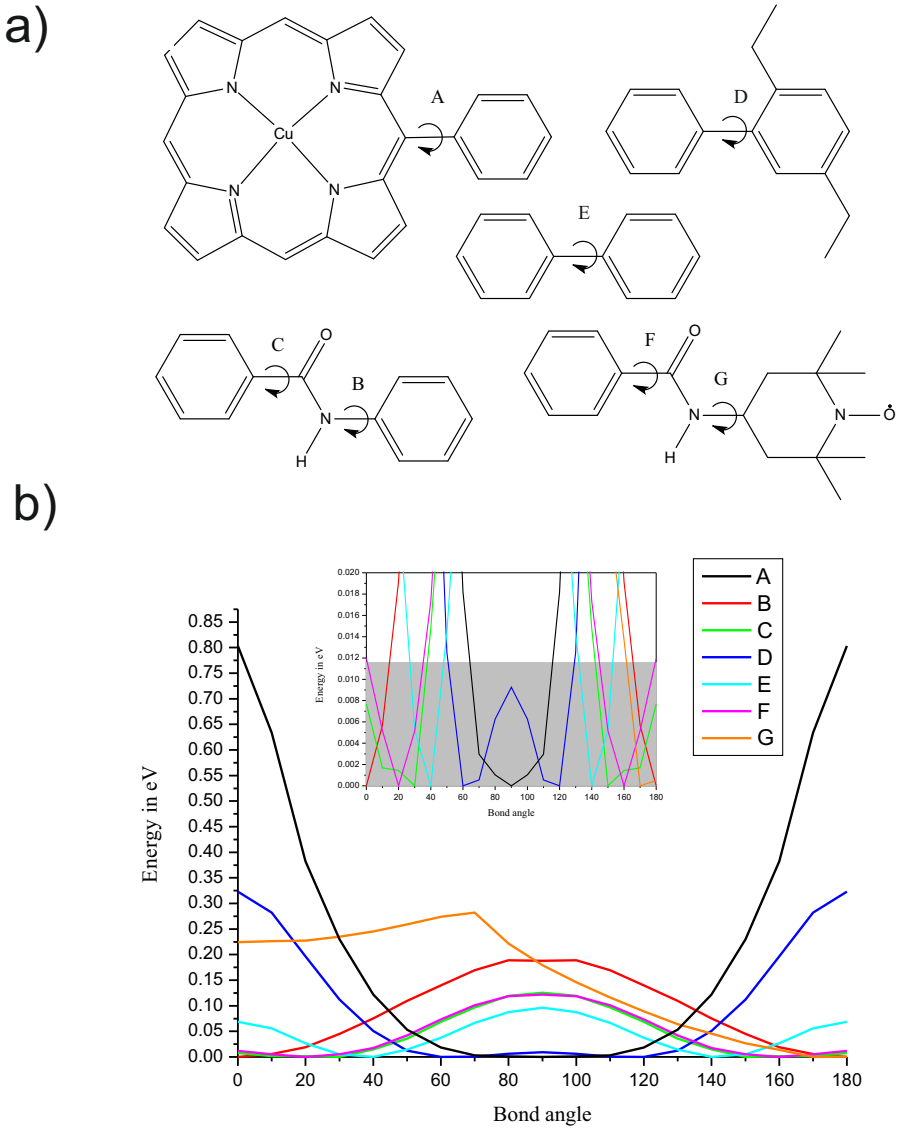


Figure 3.7: Rotation about dihedral bonds. **a)** Fragments used in the DFT analysis with the bonds used for linear transits of 0°–180° in 10° steps marked A–G. **b)** Results from DFT analysis calculated, with the BLYP GGA functional and a TZP basis set. The fragment with the copper porphyrin also used the zeroth-order regular approximation (ZORA) to correct the calculated energy, in order to account for relativistic effects. The inset depicts an enlargement of the main plot. The area marked in grey shows thermally accessible angles within the value of kT at the freezing point of the solvent mixture. It should be noted that the curves for angles C and F are almost coincident, since these both represent the same type of bond rotation.

The structures studied were broken up into 3 rods about which rotations can occur (see Fig. 3.8). From the allowed angles for each bond type an angle was selected at random and the total angles for each rod summed. The full structure was next rotated about the three defined rotation rods, to produce the relative orientation of the two centres for use in the DEER simulation. This was repeated to generate 1,000 random input structures for modelling the DEER spectra with a Monte-Carlo-like protocol.

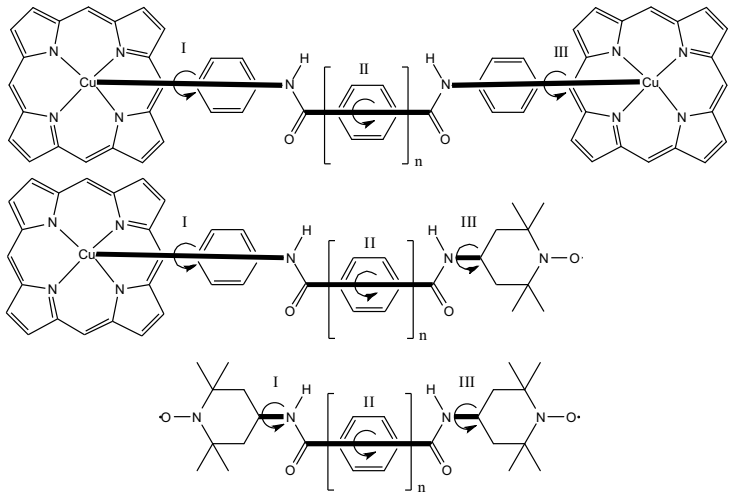


Figure 3.8: Simplified structures of the three types of molecule investigated, with the rigid rods used for rotation marked in bold and labelled I, II and III.

Once all of the rotations have been made, the position of the two centres relative to one another can be plotted, as shown in the Fig. 3.9. In each case, one centre is shown at the same point, plotted on the lower half of each graph in blue and circled in red. The other centre is displayed as a distribution of 1,000 points with respect to the first centre, plotted in blue on the upper half of each graph.

The model used here requires prior knowledge of the chemical structure of the molecular system being studied. When modelling spectra from molecular structures, it is important to use all the available information about the system, since use of an inadequate model would cause errors in the calculations.

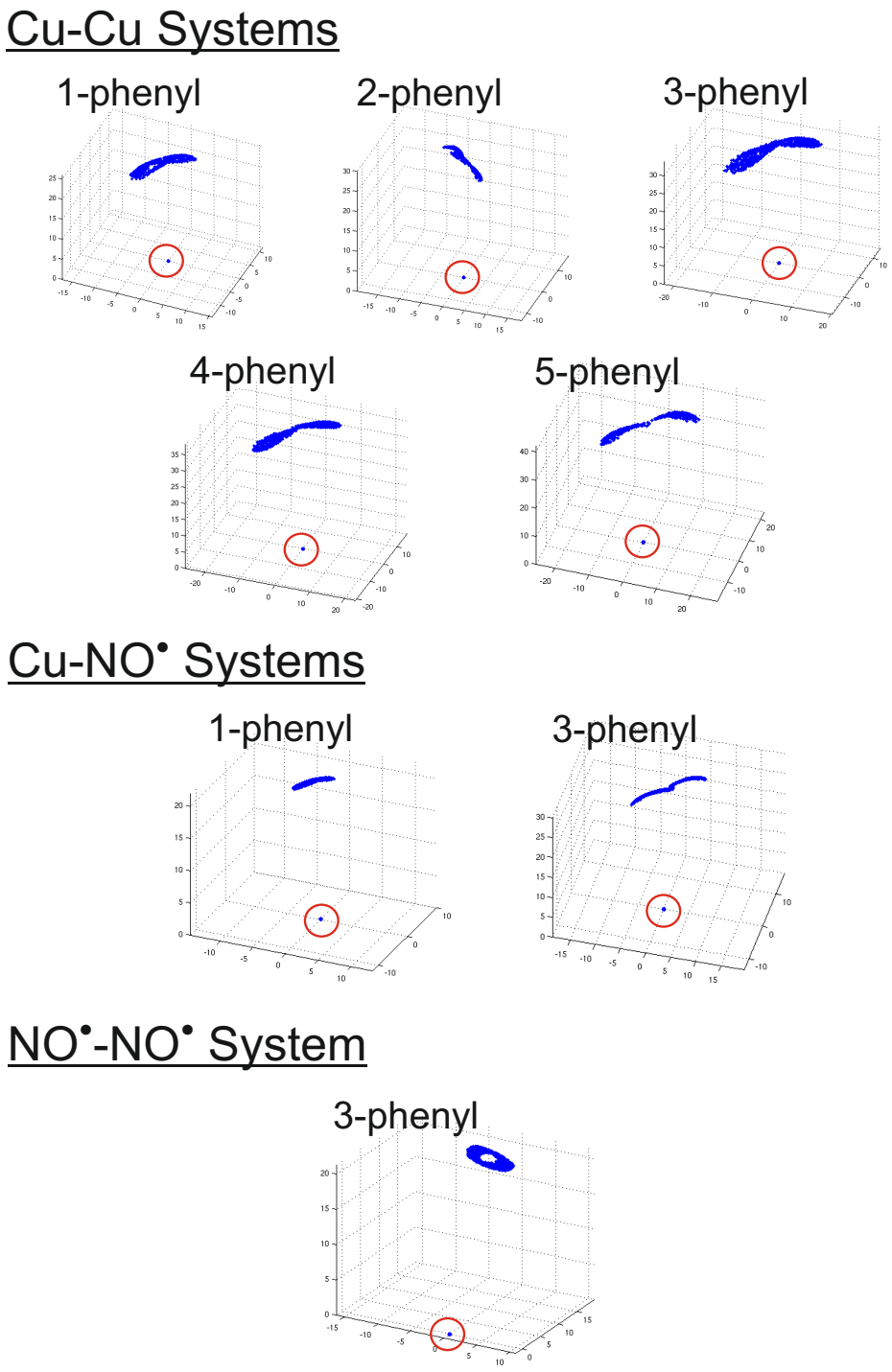


Figure 3.9: Plots of the distribution of the two centres with respect to one another in the models used. One centre is held static (centre 1), this is plotted in a red ring, and the other centre (centre 2) is plotted as a distribution of positions with respect to centre 1. All of the axes are scaled in Å.

The plots of the geometric distributions of the two centres shown in Fig. 3.9, are clearly different for each type of system under investigation. The Cu−Cu systems all display a characteristic 'double teardrop' shape distribution; the Cu−NO$^\bullet$ systems have a thinner 'double-arch' shape; and the NO$^\bullet$−NO$^\bullet$ system has a 'ring-like' distribution of the second centre with respect to the first. These distribution patterns could not be modelled exactly using a geometrical model based on a single bend and conical rotation, such as that used by Bode et al.[8,38] in their analysis. Furthermore, a spherical distribution, akin to the molecular model used by Yang et al.,[71] would be completely inappropriate.

A spherical model is only applicable for systems where equal movement of both centres in all directions can be assumed. For the model systems studied, the linking rod between the two centres allows more movement of the centres in directions perpendicular to the linking rod than it does in the direction parallel to the linking rod. If we consider the 5-phenyl Cu−Cu system, the average inter-copper distance is 4.18 nm and the difference between the maximum and minimum inter-copper distance is found to be 0.13 nm. If we consider the average structure for this system to have both copper centres lying in the x-y plane, the maximum displacement out of this plane in the z-direction, observed within total calculated distribution, is ±1.53 nm. Thus there is a greater degree of flexibility of the two copper centres out of the plane than within the plane. If a spherical model was to be used, in order to encompass all of the rotamers within the distribution, the radius of each sphere would need to be 0.765 nm. Using this spherical model would introduce many additional orientations of the two centres that are not actually accessible to the molecule and would most likely to provide very inaccurate results for this system. Further investigation into the importance of the model chosen for the relative position of the two centres is given in Section 3.6.

DFT determination of the orientation of the *g*-tensor with respect to the molecular frame and distribution of spin density

When attempting to model and interpret orientationally selective spectra, it is vital to know the orientation of the g-matrix with respect to the molecular frame. Copper in an approximately planar environment is well-known for having an axial g-matrix, which can be assumed to lie perpendicular to

the plane in which the equatorial ligands are bound. DFT calculations were used to corroborate this for the copper porphyrin fragment (see Fig. 3.10). The calculation of magnetic resonance parameters using the internal magnetic resonance calculation unit in ADF showed an axial g-tensor with principal g-values of $g_x = 2.0352,\ g_y = 2.0362,\ g_z = 2.1049$; aligned with the g_z-axis perpendicular to the plane of the porphyrin ring.

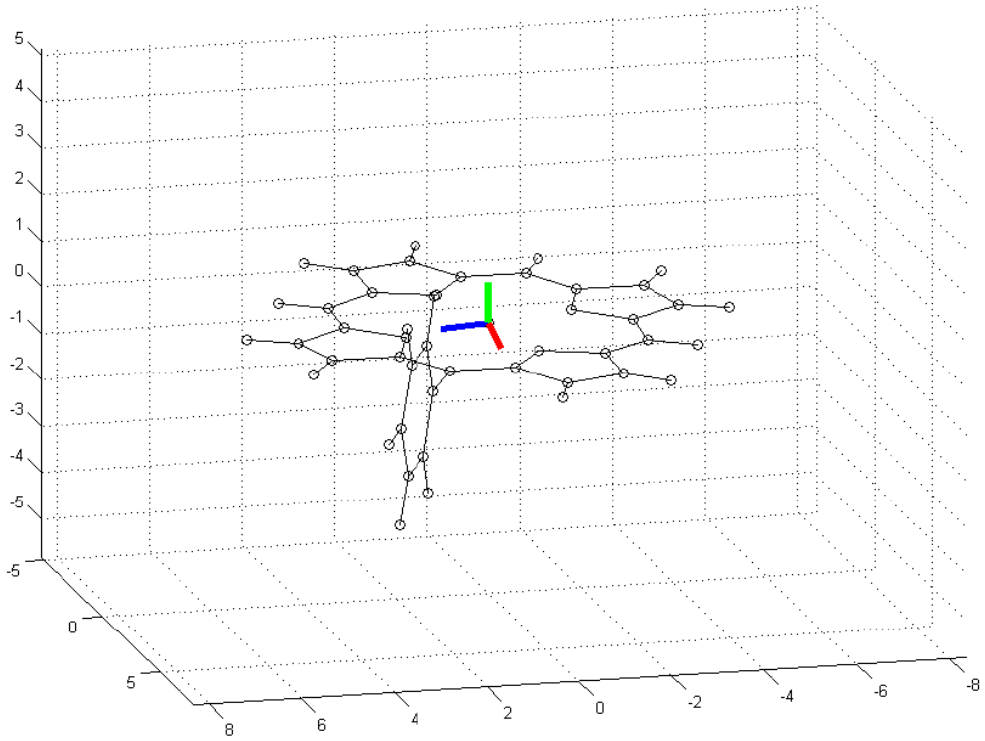


Figure 3.10: Diagram showing the orientation of the g-matrix on the porphyrin structure; green is the z-axis, blue the x-axis and the y-axis is red. The calculated g-values are: $g_x = 2.0352,\ g_y = 2.0362,\ g_z = 2.1049$. Deviations of these values from those measured are due to the truncated structure and also inadequacies in the DFT method for the calculation of magnetic resonance parameters.

The spin density of the unpaired electron can also be extracted from the DFT calculation (see Fig. 3.11). However, DFT is renowned for overestimating the degree of delocalization of electrons,[110,111] a result of DFT not taking into account the natural bond order. Therefore, it was decided not to use the calculated spin density, but instead to place 84% of the spin density on the copper atom and 4% on each ligating nitrogen in the simulation. These values were chosen in analogy with previously

successful spectral simulations for similar centres,[5] and are consistent with spin densities estimated from experimental hyperfine couplings.

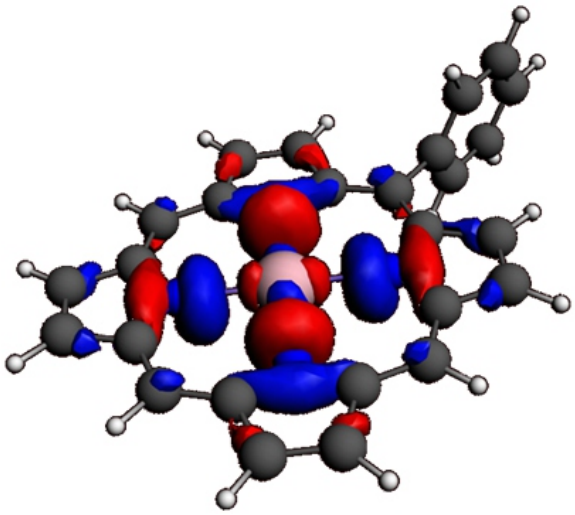


Figure 3.11: Pictorial representation of the highest occupied molecular orbital of the copper porphyrin fragment, calculated using DFT. This shows that a large degree of the electron density (coloured red and blue for the positive and negative portions) of this orbital containing the unpaired electron is delocalized onto the nitrogen ligating the copper centre.

Yang's previously mentioned approach for simulating Copper-Copper DEER spectra does not consider any delocalization of the electron density onto any atom other than copper, since the DEER traces are calculated between single points of spin density.[9,71] For systems such as copper porphyrins, this is unrealistic, as the spin density is shared between the copper and the chelating nitrogen. In cases where geometrical freedom of the system allows the orientation of the ligands to be considered as an isotropic distribution, or where the coordination environment tends towards isotropic (i.e. tetrahedral coordination symmetry or higher), this oversight is compensated for by allowing the single point of spin density to sit at any point within a sphere of radius ΔR. In the porphyrin systems presented here, the square planar coordination of the nitrogen to the copper means that the spin density lies in a plane so the spherical approximation will not compensate for the absence of spin delocalization in the model.

At X-band, the width of the $m_I = 0$ component of the spectrum is narrow (c. 2 mT). Therefore as described in Chapter 2, the application of a pulse at the maximum of the nitroxide signal on the $m_I = 0$ transition excites all orientations of the nitroxide with respect to the magnetic field, resulting in isotropic excitation. If excitation occurs on one of the wings ($m_I = \pm 1$), where the signal resulting from one hyperfine contribution is broader, one pulse does not excite all orientations of the nitroxide with respect to the magnetic field. This may result in orientationally selective spectra when the spatial distribution of the nitroxide centres is constrained. It is therefore important to characterize fully the g-tensor, A-tensor and spin density distributions of the paramagnetic centre.

It is known from the literature that for nitroxides the g-tensor and A-tensor are orientated with the z-component perpendicular to the plane formed by the N−O bond and the two N−C bonds.[112] Couplings along the x- and y-directions are almost equivalent, so these are chosen arbitrarily in the plane perpendicular to the z-component. The spin density in a nitroxide radical is known to be delocalized over both the nitrogen and the oxygen of the nitroxide (and to a small extent over the adjacent carbon atoms).[78,113] However, to simplify the picture, for the calculations in this study the point of spin density was selected to be the oxygen of the nitroxide. Any error introduced through the use of this approximation is likely to be much smaller than the error in the distribution.

The three-dimensional structure of the nitroxide moiety used in this study is given in Fig. 3.12.

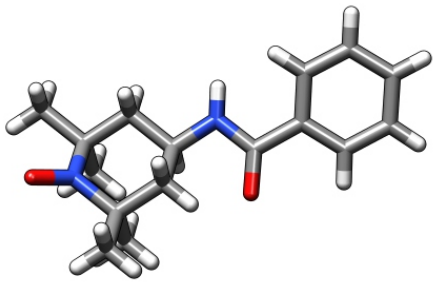


Figure 3.12: Model of the structure of the nitroxide linked via an amide bond to a phenyl group. It is coloured according to atom type H–white, C–grey, N–blue and O–red.

3.3.3 Validation of the models generated via DFT by comparison to crystal structures

Although it has not been possible to crystallize any of the complete model systems, the crystal structure of an intermediate in the synthesis of the 3-phenyl systems, a 3-phenyl linker with a carboxylic acid at either end, has been solved. Crystallization took place by slow evaporation of a solution of the 3-phenyl di-acid in DMSO and the crystals diffraction data was collected using an Enraf-Nonius Kappa CCD diffractometer with Mo Ka radiation (k = 0.71073 Å). The sample was held at 150 K with an Oxford Cryosystems Cryostream N_2 open-flow cooling device[114] and processed using the DENZO-SMN package,[115] including inter-frame scaling (which was carried out using SCALEPACK within DENZO-SMN). The structures were solved using SIR92 by Dr Michael Jones in association with the Oxford Crystallographic Centre.[116] Refinement was carried out using full-matrix least-squares within the CRYSTALS suite,[117] on F^2. All non-hydrogen atoms were refined with anisotropic displacement parameters. Hydrogen atoms on the oxygen atoms were visible in the difference map and together with the other hydrogen atoms, their positions and isotropic displacement parameters were refined using restraints prior to inclusion into the model with riding constraints. The crystal structure is shown in Fig. 3.13.

The torsional angles between two phenyl rings in the linker were found to be 82.8°. This agrees well with the DFT calculations (bond type D, see Fig. 3.7), since this value, although not the minimum calculated for this bond rotation (60°) occurs at an energy value that is accessible at the freezing point of the solution. The variation is most likely a result of the fact that the DFT calculation uses a truncated structure and also calculates for the structure *in vacuo*, thus omitting any crystal packing effects. The angle from one phenyl ring to the carboxylic acid is 12.6°. It is assumed that this angle should be similar to the minimum energy angle between the phenyl ring and the amide linker (bond types C and F, see Fig. 3.7), found to be between 20° to 30°. In this case, the DFT is also in fairly good agreement with the crystal structure and the deviation can be assigned to the differences in the bond type and the exclusion of the large copper porphyrin moieties from the crystal structure molecule.

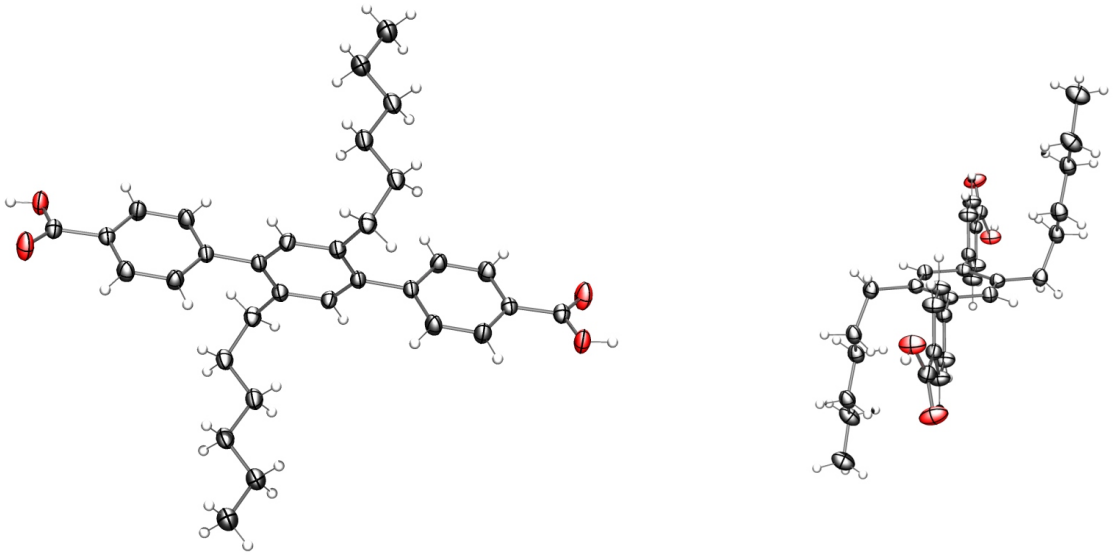


Figure 3.13: ORTEP depictions of the crystal structure of the 3-phenyl di-carboxylic acid linker with thermal ellipsoids shown at 50% probability from two different view points. The dimethyl sulphoxide (DMSO) of crystallization has been omitted for clarity.

3.3.4 CW EPR on the model systems; results and analysis

Simulation of the CW EPR spectra was achieved using the EasySpin program from Dr Stefan Stoll.[7,96]

The parameters gained from this are shown in Tables 3.1 and 3.2. These system parameters were used as input for the OriDEERSim program, a MATLAB-based program written in-house.[5]

Table 3.1: Fitting parameters extracted from X-band CW EPR spectra using EasySpin for the Cu−Cu model spectra. It should be noted that this fitting neglects coupling to the ligating nitrogen and simply models the large copper hyperfine coupling.

Parameter	x-component	y-component	z-component
g-values	2.05	2.05	2.19
A-values (Cu) [MHz]	87	87	600
H strain (line broadening) [MHz]	250	250	250

Table 3.2: Fitting parameters extracted from CW EPR spectra using EasySpin for the copper and nitroxide portions of the Cu−NO$^\bullet$ model spectra. It should be noted that the copper fitting neglects coupling to the ligating nitrogen and simply models the large copper hyperfine coupling. The same nitroxide parameters were also used found to fit the NO$^\bullet$−NO$^\bullet$ model system.[c]

Copper parameters			
Parameter	x-component	y-component	z-component
g-values	2.056	2.056	2.205
A-values (Cu) [MHz]	80	80	593
H strain (line broadening) [MHz]	221	173	238
Nitroxide parameters			
Parameter	x-component	y-component	z-component
g-values	2.01	2.01	2.009
A-values (N) [MHz]	20	20	100
H strain (line broadening) [MHz]	40	40	40

3.3.5 DEER experiments on model systems: choice of experimental parameters

The relative field and frequency positions measured in DEER were chosen after calculation of orientationally selective DEER simulations at a range of different field values. Simple arguments suggest that the best places to measure, for the Cu−Cu systems, in order to observe the two most orientationally different spectra using the same pump-probe separation of 200 MHz, would be at the top of the spectrum (where the signal originates predominately from $g_{x/y}$) and on the far left (which comprises exclusively g_z). However, in order to measure good signals, we must also choose positions that correspond to reasonable modulation depths. Thus test simulations to study this parameter were used to guide the measurement positions.

Using a small number of calculated structures (30 in total) for the 1-phenyl Cu−Cu system, the DEER traces at different positions across the CW EPR spectrum were calculated, to show the possible orientational selection and relative modulation depths. The 1-phenyl Cu−Cu is the shortest copper-copper model system and therefore should show the most orientational selection, since it has the fewest number of torsional bonds.

[c]Although the hyperfine splittings are listed in Table 3.2, they are not used as part of the orientational DEER simulation as the nitroxide centre is assumed to have isotopic excitation of all orientations.

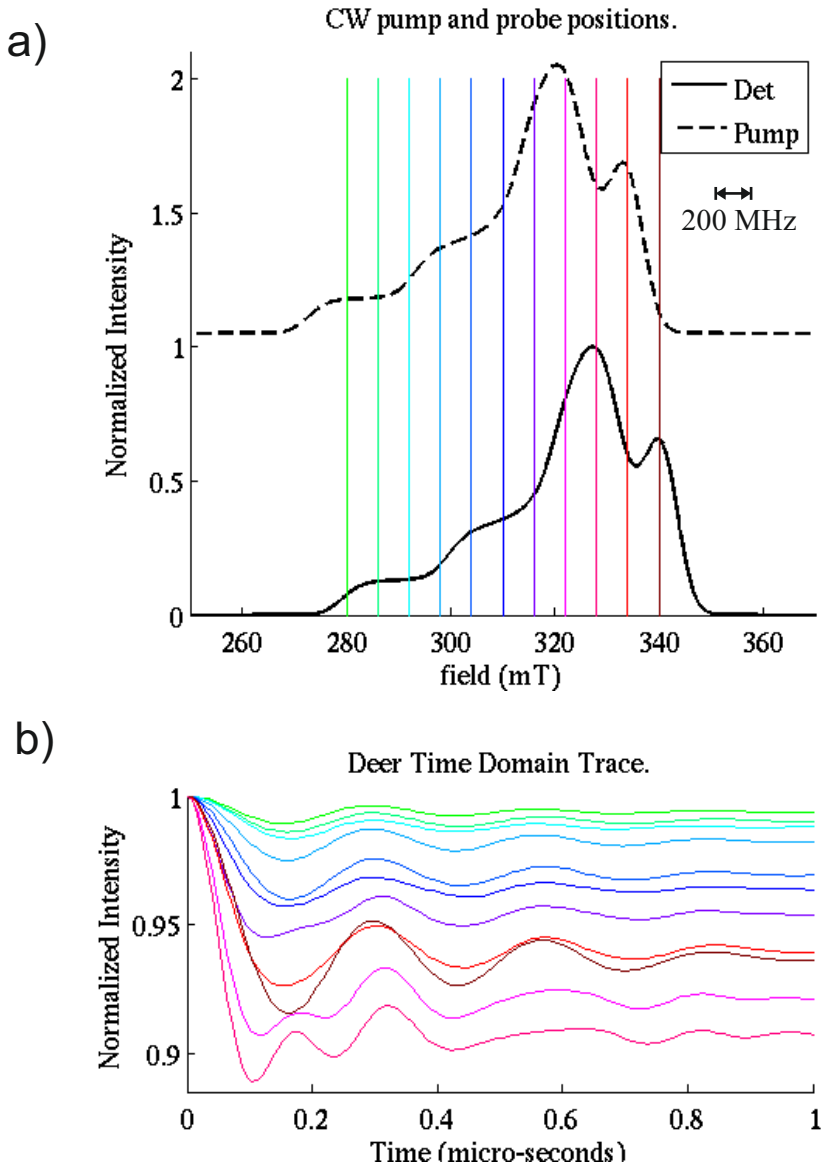


Figure 3.14: 1-phenyl Cu-Cu system, modelled for DEER spectra at different field positions, using a constant 200 MHz pump and probe pulse frequency separation. **a)** Pump and probe (Det) positions relative to the CW spectrum; a scale bar for the 200 MHz pulse separation is shown. **b)** Plot of the calculated DEER traces. It should be noted that the colours of the lines representing the field values in a) correspond to the DEER traces in b). The simulated DEER traces plotted here have not had a background correction or modulation depth correction applied to them.

From these results, it transpired that the differences in the spectra due to orientational selection were small and in many cases would remain within the noise of the experimental spectra measured. The predicted modulation depths for DEER traces, obtained using pulse positions on the far left of Fig. 3.14a) corresponding to the z-orientation, are too small to become distinct from the noise in a sensible length of measurement time. Thus, in order to measure contributions from the z-component for this system, we must measure the g_z feature at c. 320 mT, which corresponds to signals with Cu($m_I = +\frac{1}{2}$). The $g_{x/y}$ components also contribute at this field position, causing a slight loss in the amount of orientational selection resolution, but the gain in the modulation depth far outweighs this when trying to measure the orientational dependence of the spectra.

To ensure experimental continuity, it was decided to use a consistent set of field and frequency values for the 1-, 2-, 3- and 5-phenyl systems; the pump and detection frequency positions were 9.33 GHz and 9.53 GHz respectively, with fields of 316.5 mT and 323.5 mT for the two data sets. In the 4-phenyl case, it should be noted that it was not possible to collect data at these frequencies due to the observation of a large ESEEM effect. Instead, the frequencies 9.40 GHz and 9.60 GHz were used and the field values changed accordingly, to 318.9 mT and 325.9 mT, so that the same regions of the spectrum were probed.

The Cu$-$NO$^\bullet$ and NO$^\bullet-$NO$^\bullet$ systems are used in this study for calibration of the method. Therefore, assessment of the pulse positions likely to provide the most visible orientational selection in the spectra, prior to recording the DEER measurements, was not as important. Instead, pulse positions were chosen to be those where the most signal and largest modulation depths would be detected, while preventing pulse overlap. For the Cu$-$NO$^\bullet$ system the pump pulse is located on the nitroxide maximum and the probe pulse on the Copper maximum. Experiments on the NO$^\bullet-$NO$^\bullet$ system used a pump pulse located on the nitroxide maximum, exciting the $m_I = 0$ transition. Two different probe pulses are used (see Fig. 3.15) with separations from the pump pulse of 80 MHz and -108 MHz respectively, to avoid pulse overlap.

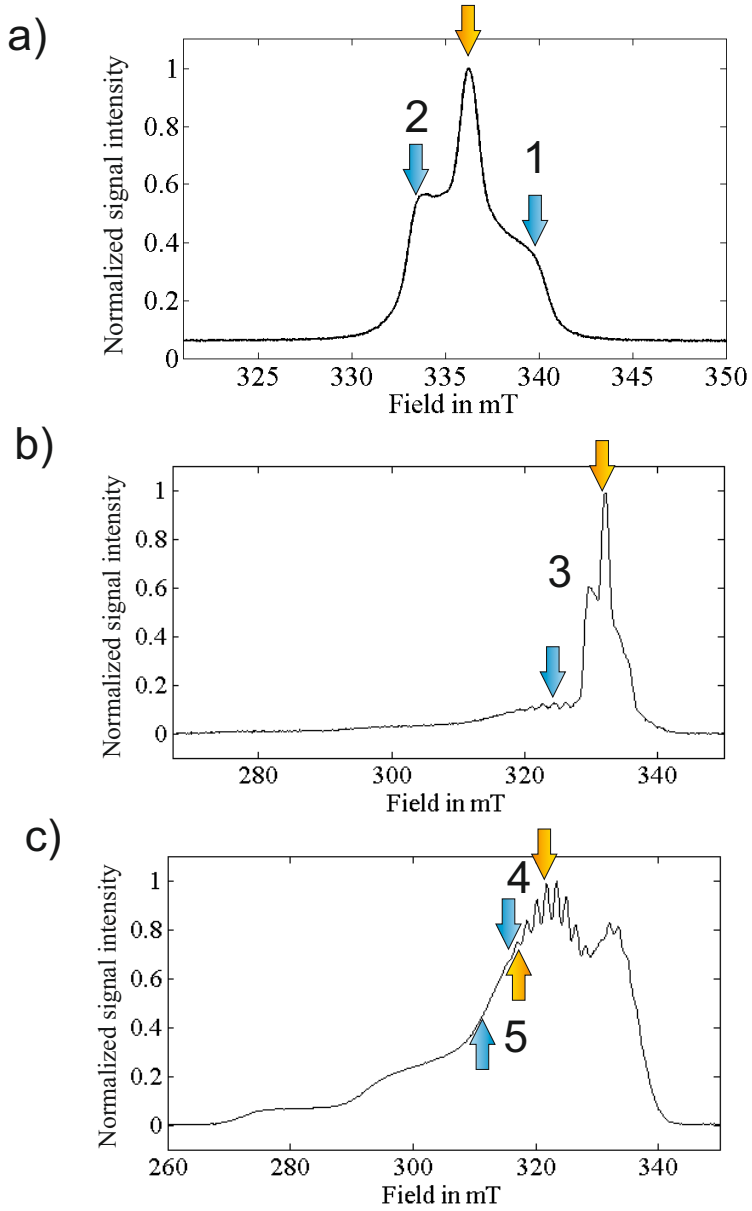


Figure 3.15: Pump and detection positions for each of the model systems studied. In all cases, the gold arrow represents the pump position and the blue arrow the detection position. **a)** 3-phenyl $NO^{\bullet}-NO^{\bullet}$: two sets of measurements were taken. In each case the pump pulse was applied at the nitroxide spectral maximum and the data sets have different pump-probe separations. **b)** $Cu-NO^{\bullet}$ systems (1- and 3-phenyl): the data shown is that of the 3-phenyl system. In each case, the pump pulse is applied on the nitroxide maximum and the detection down-field on the copper maximum. **c)** Two field positions were used for the analysis of the Cu−Cu systems (1- to 5-phenyl). The spectrum shown is that of the 3-phenyl system. In both cases, a 200 MHz separation was used and the positions 4 and 5 correspond to the fields 323.5 mT and 316.5 mT.

The pump pulses do not excite all orientations of the nitroxide, due to the broader $m_I = \pm 1$ transitions, which leads to a slight orientation selection at X-band for the nitroxide radicals in rod-like molecules. In most systems, using flexible nitroxide labels such as MTSL, the inherent flexibility of the spin label means that this orientation selection is not seen.

3.3.6 DEER experiments on the model systems: simulated and experimental results and analysis

The general scheme for the generation of the simulated DEER traces and their analysis with respect to the experimental DEER traces is given in Fig. 3.16.

Nitroxide-nitroxide system

Initially, data was fitted for the $NO^{\bullet}-NO^{\bullet}$ 3-phenyl rod, to check the validity of the DFT calculations for the distance between the spins, since this could be compared to the result from DeerAnalysis.[45] The simulated orientationally selective data was background corrected to match the experimental data using Equation 3.2 and the parameters in Table 3.3. The fitting of the experimental DEER traces to the simulated DEER traces is shown in Fig. 3.17.

Table 3.3: The scaling factors necessary in order to fit the data for the $NO^{\bullet}-NO^{\bullet}$ system. The parameters correspond to those in Equation 3.2. The same Y value is used in each case, since this is a system-dependent parameter. Y takes into account the labelling efficiency of the system and also the pump pulse inversion efficiency. A dimensionality of $d = 3$ was used in all simulations.

Pulse separation	Y	k
80 MHz	0.7	0.045
−108 MHz	0.7	0.02

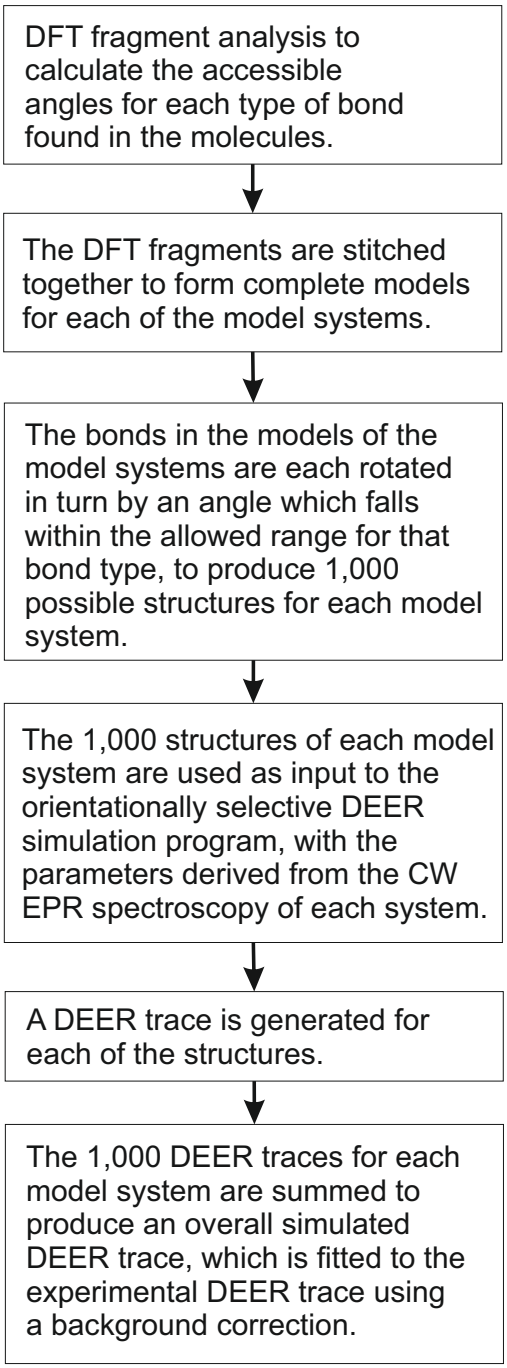


Figure 3.16: A flowchart demonstrating the method used to generate simulated DEER spectra and their analysis, with respect to the experimental DEER data.

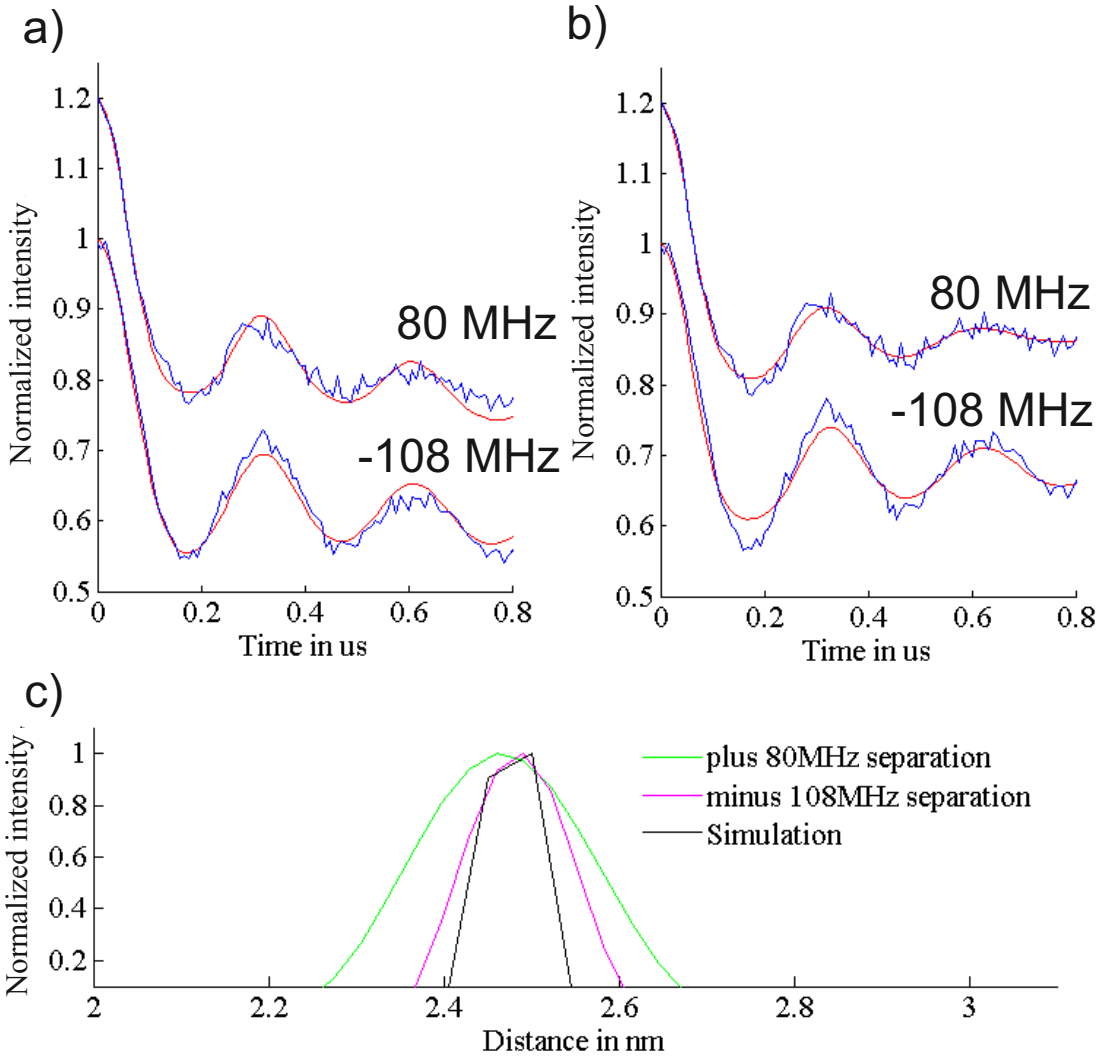


Figure 3.17: Spectral results for the 3-phenyl bisnitroxide ($NO^{\bullet}-NO^{\bullet}$) system. **a)** Raw experimental DEER traces with no background correction (blue) plotted with DEER traces simulated using the orientationally selective DEER simulation program that have been multiplied by a homogenous background correction and a modulation depth correction (red). **b)** Background corrected experimental DEER traces (blue) with Tikhonov regularization fits from DeerAnalysis (red). The experimental data has been background corrected to allow the Tikhonov fitting. **c)** Distance distribution derived from the 1,000 structures formed from the DFT calculations and used as input for the orientationally selective simulations, in a) (black curve). Also, the distance distributions extracted by Tikhonov regularization in DeerAnalysis from the experimental (magenta [−108 MHz] and green [+80 MHz] curves). Table 3.4 gives the sum of the least squares residuals between the experimental and simulated or fitted data traces in a) and b).

The experimental traces for the NO$^{\bullet}$−NO$^{\bullet}$ system show a little orientational selectivity at X-band. This can be seen in the broader U-shaped first oscillation for the 80 MHz separation, compared to the narrower V-shaped first oscillation for the −108 MHz spectrum, which has a greater degree of orientational selection. This phenomenon is not usually considered in analysis of X-band nitroxide spectra, since it is normally not observed. In the spectra recorded here, the orientational selectivity is seen due to the restricted motion of the nitroxide out of the plane of the rod and the rigidity of the spin labels. MTSL, a commonly used nitroxide spin label, is much more flexible, due to the aliphatic linker between the nitroxide moiety and the protein backbone where it is incorporated (see Fig. 3.1). This flexibility 'washes out' the orientational selectively in the spectra, since the EPR spectrum observed is a composite of many different orientations of the spin label. The lack of orientational selectivity is also supported by the calculated sums of the least squares residuals between the experimental and simulated or fitted DEER traces shown in Fig. 3.17 a) and b), which are given in Table 3.4. The sums of the least squares residuals calculated between the raw experimental DEER data and the orientaionally dependent simulations with background and modulation depth corrections and also between the background corrected experimental DEER data (form factor, $F(t)$) and the Tikhonov regularization of this form factor are very similar for both the 80 MHz and the −108 MHz pulse separations. This shows that for DEER between two nitroxides the data can be modelled equally well with and without orientational analysis.

As can be seen from Fig. 3.17 and Table 3.4, comparison of the Tikhonov regularization derived fits and orientational simulations with the experimental data, and also the distance distributions calculated using DeerAnalysis with that obtained from the 1,000 structures calculated from the DFT results, both give fairly good agreement. This validates the model that is being used. For the 3-phenyl bisnitroxide (NO$^{\bullet}$−NO$^{\bullet}$), the average distance from the generated structures is 2.48 nm, with a full-width half-maximum distribution of 0.12 nm. This compares well to the average distances measured using DeerAnalysis, which are 2.50 nm and 2.49 nm for the 80 MHz and −108 MHz separations respectively. However, these show broader full-width half-maximum distributions of 0.25 nm and 0.17 nm respectively. The slight variations between the two Tikhonov distance distributions and the

Table 3.4: The least squares residual calculated between the experimental and fitted or simulated traces from Fig. 3.17a) and b).

Plot in Fig. 3.17	Pulse separation	Experimental data type	Simulated or fitted data type	Sum of least squares residual
a)	80 MHz	Raw experimental data	Simulated data with background and modulation depth correction	1.4431
a)	−108 MHz	Raw experimental data	Simulated data with background and modulation depth correction	1.6656
b)	80 MHz	Background corrected experimental data	Tikhonov regularization fitted data	1.0184
b)	−108 MHz	Background corrected experimental data	Tikhonov regularization fitted data	1.6457

calculated distribution lie well within what might be expected as reasonable experimental error of the DFT calculations. They can also be accounted for by the fact that DeerAnalysis does not perform any orientational analysis.

Copper-nitroxide systems

Experimental data for the Cu−NO$^\bullet$ systems were fitted to the simulated data, giving very good agreement (see Fig. 3.18).

As with the bisnitroxide (NO$^\bullet$−NO$^\bullet$) samples, the simulated spectra were background corrected. The parameters used in the background correction are given in Table 3.5.

Table 3.5: The scaling factors necessary in order to fit the data for the Cu−NO$^\bullet$ system. The parameters correspond to those in Equation 3.2. The same Y value is used in each case as this is a system-dependent parameter. A dimensionality of $d = 3$ was used in all simulations.

Model system	Y	k
Cu−NO$^\bullet$1-phenyl	0.9	0.4
Cu−NO$^\bullet$3-phenyl	1.0	0.72

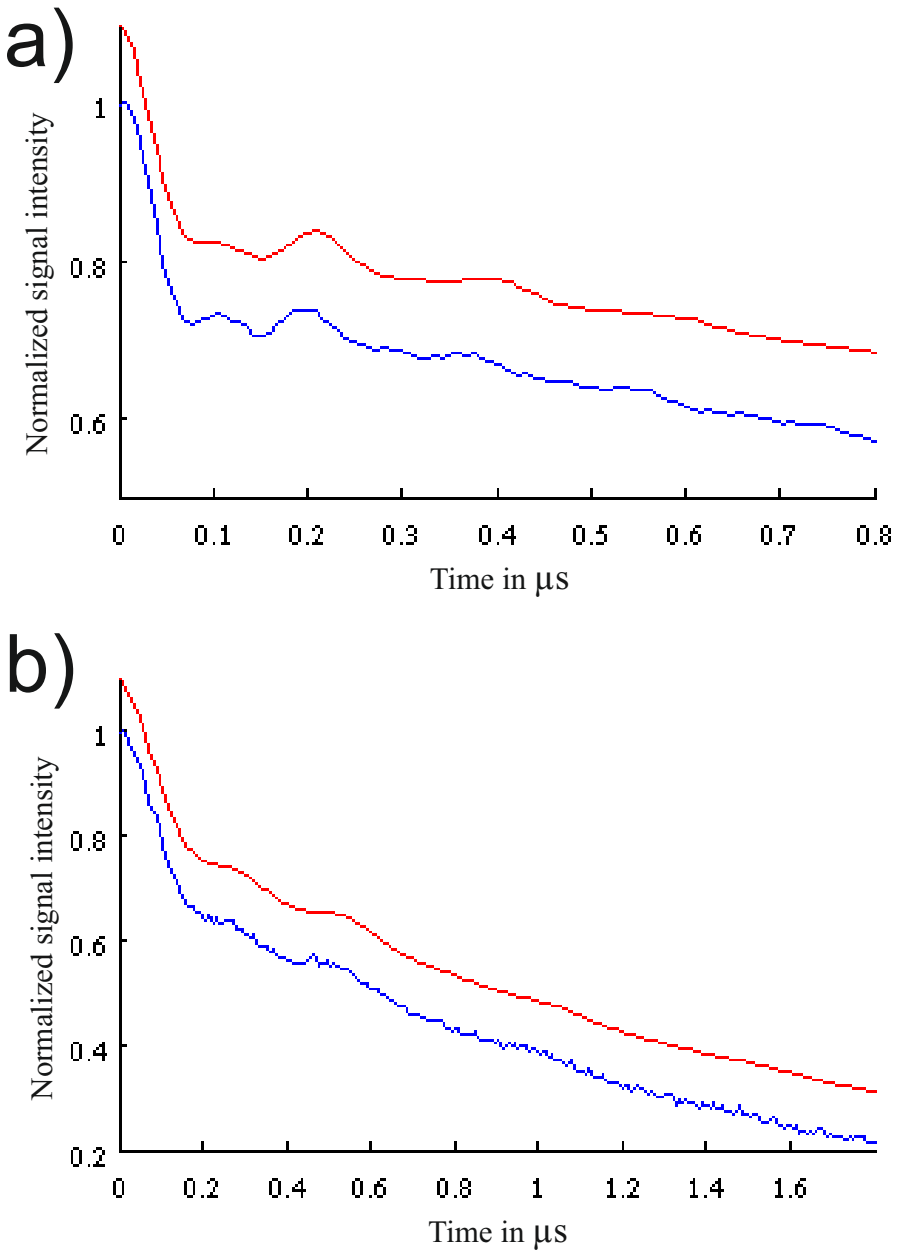


Figure 3.18: Raw experimental data (blue) with simulated data that has been multiplied by both a background correction and a modulation depth correction (blue) for **a)** the 1-phenyl Cu−NO$^{\bullet}$ system and **b)** the 3-phenyl Cu−NO$^{\bullet}$ system. In both cases the data sets have been normalized. The fitted simulated data are offset from the experimental data for clarity.

Excitation at the nitroxide radical spectral maximum means that the nitroxide moiety can be considered to have been excited isotropically. Furthermore, the axiality of the Cu tensors (both g-tensor and hyperfine tensor) means that when both Cu spins are excited within their perpendicular components, there will always be an intersect of these $g_{x/y}$ planes involving both paramagnetic centres. Therefore the dipolar spectrum produced by these excitations will always include the central peaks corresponding to $\omega_{\perp}$, allowing the extraction of the correct distance. DeerAnalysis can be used to extract an approximate distance from the data. However, as DeerAnalysis is designed for the extraction of distance distributions from two nitroxide centres, this distance must be corrected to allow for the variation in g-values from the isotropic nitroxide g-value to the copper $g_{x/y}$ component.

The distance is related to the dipolar frequency and the g-values using the following equation:

$$r_{12} = \sqrt[3]{\left| -\frac{1}{\omega_{dd}} \frac{\mu_0}{4\pi\hbar} g_1 g_2 \mu_B^2 \left(3\cos^2\theta - 1\right) \right|} \tag{3.3}$$

In DeerAnalysis, both g-values are taken to be 2.005 ($g_{NO,iso}$). For the analysis of the Cu−NO$^{\bullet}$ systems, one of the g-values must be replaced with that of the $g_{Cu,x/y}$ copper component, 2.056, and the mean distance corrected accordingly:

$$r_{12,real} = r_{12,DeerAnalysis} \sqrt[3]{\frac{g_{Cu,x/y}}{g_{NO,iso}}} \tag{3.4}$$

The average distances obtained from the DFT simulations and DeerAnalysis method are given in Table 3.6.

Table 3.6: Measured and calculated distances and distance distributions for the Cu−NO$^{\bullet}$ systems.

Model system	Cu−NO$^{\bullet}$ 1-phenyl	Cu−NO$^{\bullet}$ 3-phenyl
Average distance from simulated distribution (nm)	2.17	2.99
Overall distribution of simulated distances (nm)	0.15	0.15
Raw distance calculated from DeerAnalysis (nm)	2.03	2.89
Corrected distance calculated from DeerAnalysis (nm)	2.05	2.91
$\omega_{\perp}$ measured from the dipolar spectrum (MHz)	5.60	2.04
Distance corresponding to $\omega_{\perp}$ (nm)	2.12	2.97

As with the NO$^\bullet$−NO$^\bullet$ system, there is reasonable agreement between the experimental, simulated and DeerAnalysis fitted data. DeerAnalysis is attempting to fit a complete Pake pattern to an incomplete dipolar spectrum . Thus the small deviations seen for the distances extracted using DeerAnalysis are not unexpected. Making a correction of the free electron g-value (2.002) used in the kernel of DeerAnalysis,[101] to that of the copper $g_{x/y}$ (2.056, see Table 3.2) gives a small improvement in the agreement of the mean distances extracted through DeerAnalysis compared with those gained from the models based on DFT calculations. These g-value corrected distances are referred to as 'Corrected distance calculated from DeerAnalysis' in Table 3.6. However, better agreement is seen between the DFT derived distance and that measured directly from $\omega_\perp$, taken from the incomplete dipolar spectrum. Extracting the distance in this way yields only a single distance and provides no information on the distribution of distances present in a sample.

The simulations for both the 1-phenyl and the 3-phenyl Cu−NO$^\bullet$ system fit the experimental data very well. For the 1-phenyl Cu−NO$^\bullet$ system, the distance predicted by the DFT was found to be slightly longer than that obtained using DeerAnalysis and the corrected DeerAnalysis method. However, the agreement between the distance extracted directly from the dipolar spectrum and the distance predicted by the DFT model was better. The discrepancy between the data extracted using DeerAnalysis and the distance found directly from the dipolar spectrum is likely to be due to inaccuracies in the DeerAnalysis method of analysis, which is not designed for orientationally dependent spectra.

The difference in the distances calculated for the 3-phenyl NO$^\bullet$−NO$^\bullet$ and Cu−NO$^\bullet$ systems is measured at 0.5 nm, corresponding roughly to the difference in the length of the rod from the amide linker to the nitroxide or copper spin density.

Copper-copper systems

The Cu−Cu data was also fitted in a similar form and the fitting factors are given in Table 3.7. The fitted data is shown in Fig. 3.19.

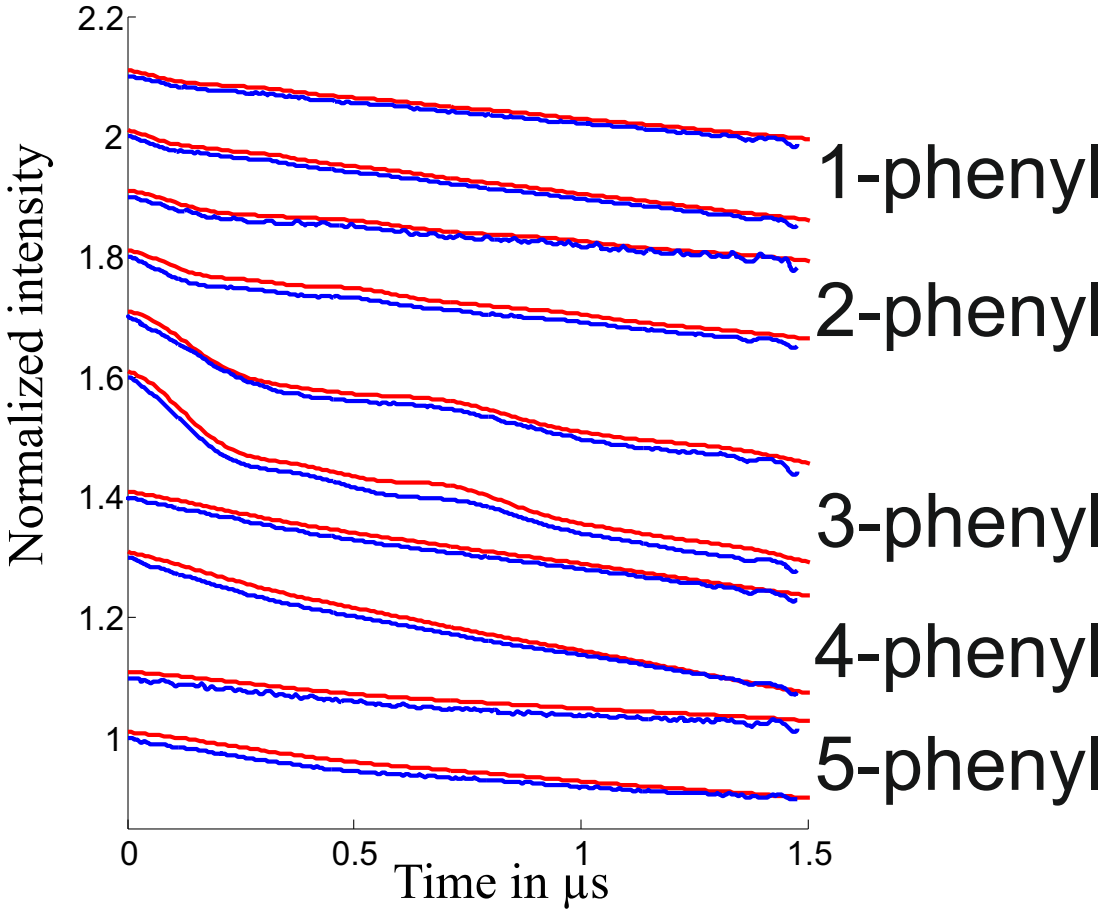


Figure 3.19: **DEER traces for the Cu−Cu model systems.** Experimental data (without background correction) are shown in blue and simulated data multiplied by a homogeneous background and modulation depth correction that has been optimized to fit the experimental data are plotted in red. It should be noted that all of the data sets have been normalized and offset from one other for clarity. Furthermore, in each case the simulated data has been offset from the experimental data by 0.01. The data sets are arranged in pairs, corresponding to the different Cu−Cu systems. For each system, the upper data set corresponds to a field of 316.5 mT (318.9 mT for the 4-phenyl system) and the lower data set to a field of 323.5 mT (325.9 mT for the 4-phenyl system).

Table 3.7: The scaling factors used in the simulation of the Cu−Cu systems. The parameters correspond to those in Equation 3.2. The same Y value is used in each case, since this is a system-dependent parameter. A dimensionality of $d = 3$ was used in all simulations.

Model system	Field of experiment (mT)	Y	k
Cu−Cu 1-phenyl	316.5	0.12	0.075
	323.5	0.12	0.1
Cu−Cu 2-phenyl	316.5	0.26	0.07
	323.5	0.26	0.09
Cu−Cu 3-phenyl	316.5	0.9	0.15
	323.5	0.9	0.2
Cu−Cu 4-phenyl[d]	316.5 (318.9)	0.13	0.12
	323.5 (325.9)	0.13	0.17
Cu−Cu 5-phenyl	316.5	0.16	0.05
	323.5	0.16	0.07

As previously stated, one possible explanation for the variation in the parameter needed to fit the modulation depth of the experimental data, Y, is incomplete labelling of the porphyrin rings with copper, resulting in contributions from mono-copper molecules. This can be probed using a spin counting technique. For this purpose the CW EPR spectra of the Cu−Cu compounds were recorded under the same experimental conditions, with the same concentrations in each sample. It is assumed that in each case that the volume of solution in the resonator was the same and thus calculating the double integral of these spectra gives a measure of the relative number of spins in the each system (see Table 3.8).

Table 3.8: Cumulative integral values of the CW spectra for the Cu-Cu systems given in arbitrary units.

Model system	Cumulative integral value
Cu−Cu 1-phenyl	529.88
Cu−Cu 2-phenyl	523.67
Cu−Cu 3-phenyl	566.55
Cu−Cu 4-phenyl	535.67
Cu−Cu 5-phenyl	540.33

The larger value for the 3-phenyl system suggests that it is more fully labelled than the other

[d]The actual field values at which the 4-phenyl experiments were performed are shown in brackets.

spectra and thus, this may explain the need for a scaling factor in the other systems' DEER spectra. However, the difference in sizes of the cumulative integral values alone is not enough to explain the large differences in the scaling factors needed to correct the modulation depth. Instead, we must invoke the argument that the most likely cause is due to the spectrometer itself and the amount of power it can place in the ELDOR channel, which is known to be variable over time. The results for the 3-phenyl system were taken several months before those of the other systems.

The average Cu−Cu distance between the two copper centres is recorded for all five compounds in Table 3.9. In addition, the difference between the maximum and minimum inter-copper distance for each system is also given, termed '*overall distribution of simulated distances*'.

Table 3.9: Showing the average Cu-Cu distance and overall distribution of the second centre from the 1,000 DFT structures used to generate the simulated DEER traces.

Model system	Average distance from simulated distribution (nm)	Overall distribution of simulated distances (nm)
Cu−Cu 1-phenyl	2.52	0.16
Cu−Cu 2-phenyl	2.95	0.12
Cu−Cu 3-phenyl	3.32	0.16
Cu−Cu 4-phenyl	3.79	0.11
Cu−Cu 5-phenyl	4.18	0.13

3.3.7 Summary of results for the NO$^{\bullet}$−NO$^{\bullet}$, Cu−NO$^{\bullet}$ and Cu−Cu model systems

For all three types of model system studied, NO$^{\bullet}$−NO$^{\bullet}$, Cu−NO$^{\bullet}$ and Cu−Cu, there is good agreement between the experimental DEER data and that simulated using our MATLAB-based orientational DEER simulation program, with inter-spin distances and distributions generated from the DFT fragment analysis. Not only are the average distances seen in the experimental data and predicted by the DFT analysis in line with one another, where orientational features are seen in the experimental data, these are also reproduced in the simulations with a high fidelity. This agreement of the experimental results with the simulated results validates the methods used in the simulations to model the distance and orientational distributions observed in the model systems.

It was, however, necessary to scale the modulation depth of the simulated DEER traces to match those of the experimental data. This was to account for fluctuations in the labelling efficiency for each system and variations over time in the pump pulse power (which dictates the pump pulse efficiency). For DEER traces measured within a short period of time on one sample, the correction to the modulation depth required was the same. In these cases, the relative modulation depths were consistent with those of the simulation.

3.4 EPR measurements on the copper amine oxidase homo-dimer

Having validated the simulation method using synthetic model systems, it is also important to demonstrate the applicability of the method to a biological system, since it is in biological systems where the use of innate metal centres as spin labels has the potential to have the greatest impact. The copper-containing protein, copper amine oxidase from *Arthrobacter globiformis* (AGAO) was selected as a suitable model protein. AGAO is known to form tightly bound homo-dimers in solution, each of which has a single copper (II) bound. Furthermore, there are published X-ray structures of the AGAO homo-dimer from which the relative position and orientation of the two copper centres can be found.

Whereas the flexibility of the model system required the modelling of a large distribution of the two centres with respect to one another, in the AGAO homo-dimer the surrounding protein structure makes the positions of the two copper centres rigid with respect to one another. It is therefore possible to sample a single orientation in the DEER experiments.

3.4.1 Sample preparation for copper amine oxidase

The copper amine oxidase from *Arthrobacter globiformis* (AGAO) was a kind gift from the group of Prof. Michael McPherson at the University of Leeds, prepared by Thembanikosi Grace Gaule according to the method of Juda et al.[118] The sample of strep-tagged copper amine oxidase was prepared for EPR by making a stock solution of 120 mg/ml (1.7 mM concentration of the protein monomer) in 50 mM HEPES buffer at pH 7.2.[e] This was diluted, adding 30% glycerol by volume to produce the

[e]HEPES, 4-(2-hydroxyethyl)-1-piperazineethanesulfonic acid, is a zwitterion organic buffer.

EPR sample containing c. 1.2 mM concentration of the protein monomer. It is necessary to add the glycerol, since it ensures the formation of a good glass when the protein is frozen.

3.4.2 The relative positions of the two copper centres in a copper amine oxidase homo-dimer

For copper amine oxidase, the crystal structure *1IU7.pdb* was used as a basis for the relative positions and orientations of the two centres.[119] Each copper centre comprises a Cu^{2+} ion, ligated by three nitrogen from the histidines at positions 431, 433 and 592 of the monomer. The copper is also ligated by two water molecules that will most likely be in dynamic exchange with the bulk water in liquid solution (see Fig. 3.20c).

Although DFT calculations were attempted on one extracted centre (Fig. 3.20b) these calculations did not converge; this is most likely due to the fact that the centre geometry is unstable outside the cage-like protein structure that supports it. In accordance with the general rule for axial copper spectra, it was decided to place the g-tensor and copper A-tensor (hyperfine tensor) on the structure, so that the z-axis is perpendicular to the plane formed by the three ligating nitrogen nuclei of the histidine ligands.

For the calculation of the DEER spectra, 85% of the spin density assigned to the copper and 5% is placed on each of the ligating nitrogen. These values were chosen to mirror those used for the porphyrin model systems.

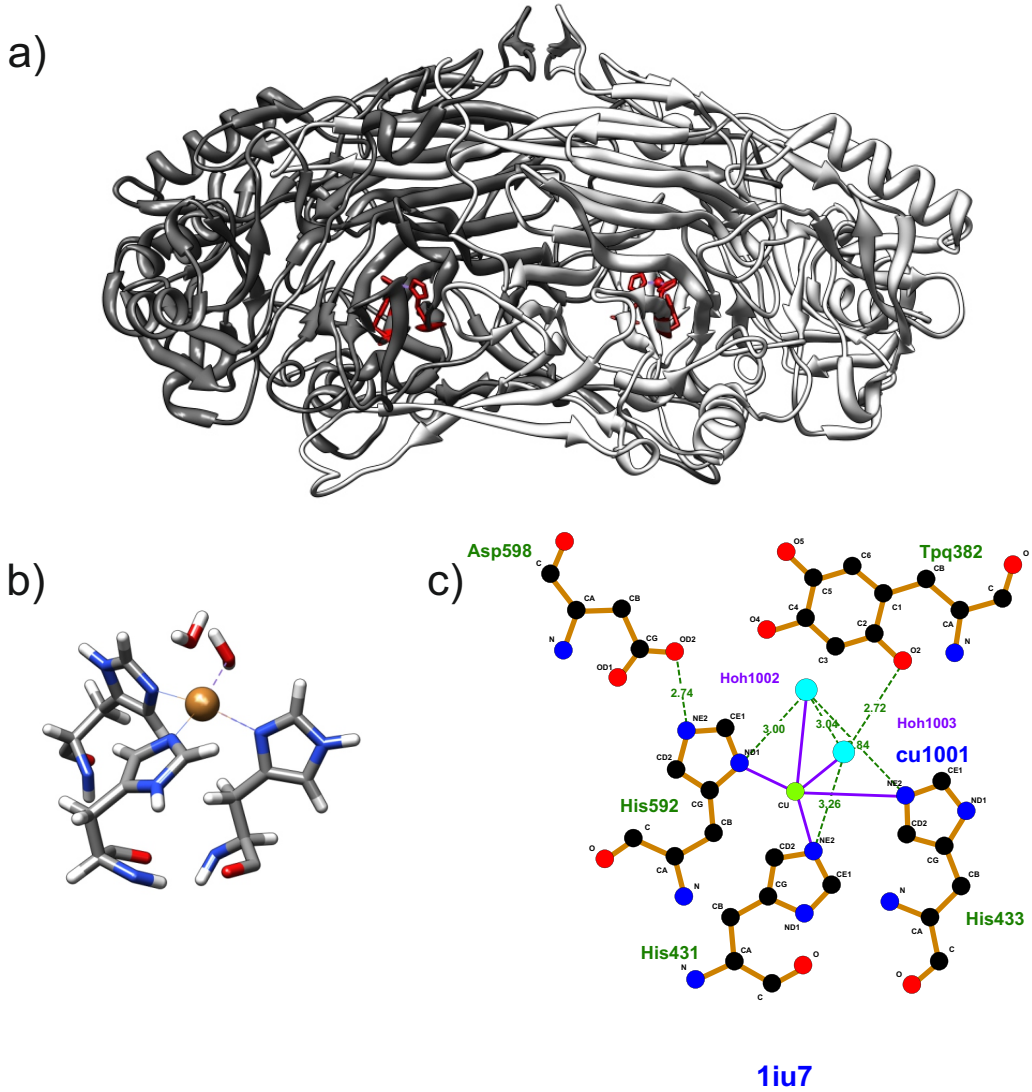


Figure 3.20: **a)** Copper amine oxidase (AGAO) crystal structure (*1IU7.pdb*).[119] This homo-dimeric structure has two protein monomer units in complex with one another. Each monomeric unit contains a Cu^{2+} centre that is ligated by three nitrogen from surrounding histidines (431,433 and 592) and two water molecules. One monomer is shown in grey and the other in white. The copper centres and their ligating histidines are highlighted in red. **b)** An expanded structure from one of the copper centres coloured according to atom type; H–white, C–grey, N–blue, O–red and Cu–orange. **c)** The coordination of one of the copper centres plotted using LigPlot^{+}.[120,121]

3.4.3 CW EPR of AGAO: results and analysis

As for the model systems, the CW EPR spectrum was simulated using EasySpin.[7,96] The parameters gained from this are shown in Table 3.10. These system parameters were used as input for the OriDEERSim program.[5]

Table 3.10: Fitting parameters extracted from X-band CW EPR spectra using EasySpin for the copper paramagnetic centres present in copper amine oxidase. In this case no hyperfine coupling is resolved in the spectra to any nuclei other than the copper. This is due to 'strain' in the system, which increases the EPR line width such that it is greater than the splitting due to hyperfine couplings to the nitrogen and protons in the immediate environment. This strain is likely to be a result of flexibility in the protein structure when in solution, such that when the sample is frozen a distribution of structures is formed. The hyperfine couplings in each of these structures will be slightly different and when all the different contributions from each of the structures is measured this causes strain which broadens the EPR line widths.

Parameter	x-component	y-component	z-component
g-values	2.0675	2.0675	2.290
A-values (Cu) [MHz]	57.5	57.5	515
H strain (line broadening) [MHz]	180	180	160

3.4.4 DEER experiments on AGAO: choice of experimental parameters

As with the Cu−Cu model systems, initial simulations to isolate the spectral positions that are likely to give the best quality DEER data, which should show discernible effects due to orientation selection, were carried out. These initial simulations used the *1IU7.pdb* crystal structure as a template for the relative position and orientation of the copper centres.[119] The inter-copper distance is 3.60 nm and an orientation of the g-matrix, which puts the g_z axis perpendicular to the plane of the nitrogen of the three ligating histidine ligands, was chosen. Following the simulations for the model systems, 5% of the electron spin density was delocalized onto each of the ligating nitrogen. Experimentally, it was found that the observed modulation depth was very small. Therefore, in order to maximize the signal seen, it was necessary to limit the pulse separation to 100 MHz. This allowed both pulses to be placed close to the resonant frequency of the over-coupled resonator, where the power conversion is highest,

allowing the use of short pulses. The trial simulations generated are shown in Fig. 3.21.

All EPR measurements on the AGAO system were conducted at 15 K.

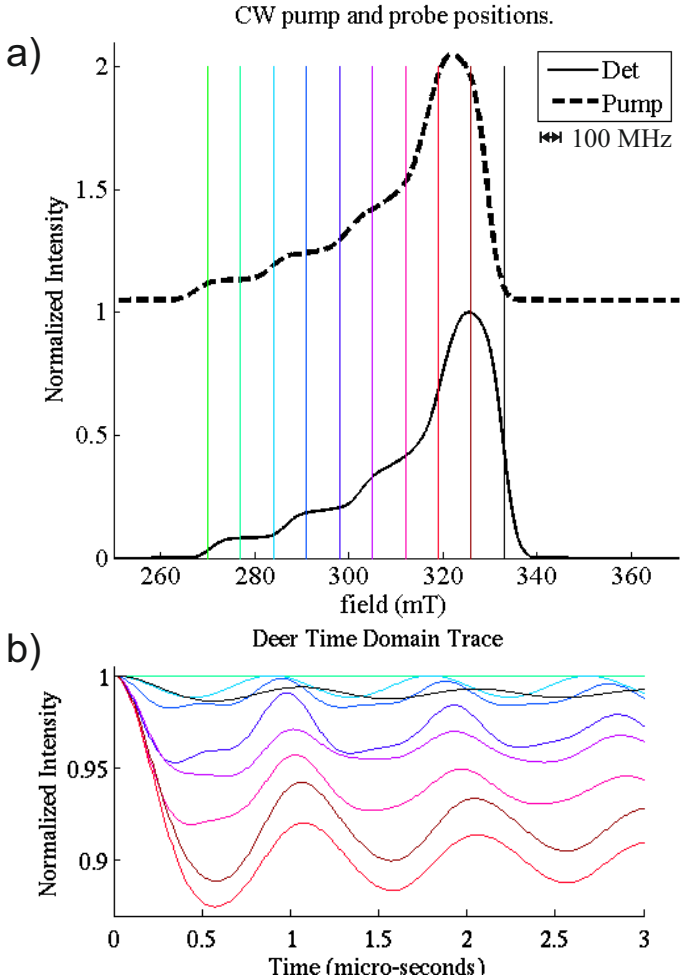


Figure 3.21: DEER spectra modelled at different field positions for the copper amine oxidase using a constant 100 MHz pump and probe pulse frequency separation. **a)** The pump and probe (Det) positions relative to the CW spectrum. A scale bar for the 100 MHz pulse separation is shown. **b)** Plot of the DEER traces calculated. It should be noted that the colours of the lines representing the field values in a) correspond to the DEER traces in b). The DEER traces corresponding to pump and detection pulses at low field have very little modulation depth, since the excitation fraction of the overall copper spectrum is very small and thus the inversion efficiency of the pump pulse is also small. It should be noted that the DEER traces for the two lowest field positions overlap. The simulated DEER traces plotted here have not had a background correction or modulation depth correction applied to them.

3.4.5 DEER experiments on AGAO: results and analysis

From the trial simulations, four sets of pump and detection pulse positions were chosen and DEER data were recorded for each with 100 MHz separation between the pump and detection pulse frequencies. The four pump and detection pulse positions chosen are highlighted in Fig. 3.22. Although ideally a further position sampling more of the g_z orientations would have been useful, experimentally it was not possible to detect a suitable DEER echo that would average to give a trace of reasonable signal-to-noise ratio with both pump and detection pulses located on g_z components.

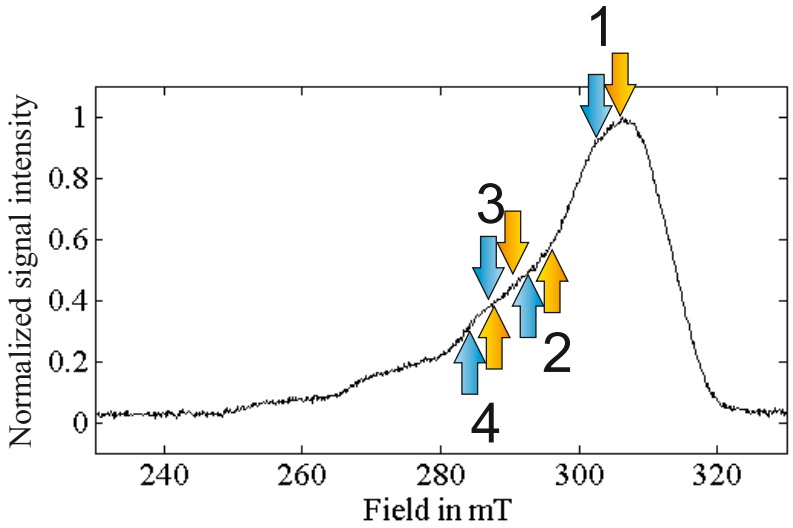


Figure 3.22: Pump and detection pulse positions, each separated by 100 MHz used in the acquisition of DEER spectra on the AGAO system. The numbers 1 to 4 correspond to the data sets presented in Fig. 3.23. The gold arrows represent pump positions and the blue arrows detection positions.

Simulations were made with pump and probe frequencies and field positions that matched used those used for the experimental DEER acquisitions. The system parameters (g-tensor, spin density distribution etc.) utilized were the same as those used for the simulation of the initial test data. Comparison of the simulated and experimental data is shown in Fig. 3.23. In each case, the simulated traces had a background correction applied.

Pulse positions	Y	k
1	0.82	0.010
2	0.82	0.012
3	0.82	0.007
4	0.82	0.006

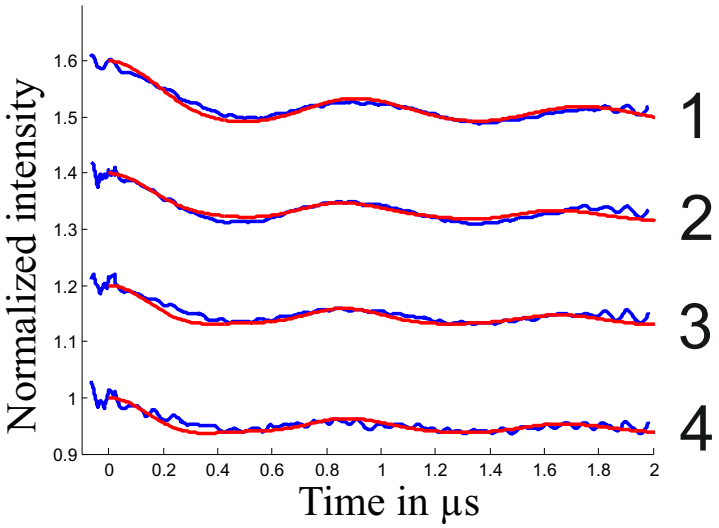


Figure 3.23: Comparison of simulated traces with a homogeneous background and modulation depth correction (red) and normalized experimental (blue) data with no background correction for AGAO. Simulations use only one orientation of the two centres, taken directly from the crystal structure *1IU7.pdb*.[119] The spectra all use 100 MHz separation and correspond to the pump and probe positions 1–4 in Fig. 3.22, from top to bottom. The table on the left shows the parameters used for the background correction applied to the simulated data. A dimensionality of $d = 3$ was used in all simulations.

Fig. 3.23 shows a good fit of the simulated data to the experimental data. The relative modulation depths are accurately reproduced. However, in order to understand the system fully it is necessary to see if the fit of the simulated data can be improved, by altering the model used to generate it.

In the original model, the delocalization of 5% of the electron density onto each of the chelating nitrogen is rather arbitrarily chosen to be similar to the parameters that gave good results for the Cu−Cu model systems. Therefore, the simulations were repeated with, in turn. 5%, 10% and 20% of the spin density delocalized onto each of the nitrogens. The results for these simulations are shown in Fig. 3.24. Due to the nature of the model, which has the positions of the nitrogen fairly evenly placed around the copper centre, the effect of delocalizing more of the spin density onto the ligating nitrogens did not have any significant effect on the simulated spectra.

1IU7.pdb is not the only published X-ray structure for the AGAO protein. Some show the protein present as a monomer (e.g. *1W6G.pdb* and *1W6C.pdb*).[122] However, a good proportion of the reported

structures give the structure as a homo-dimer (i.e. *2YX9.pdb*,[123] *1RJO.pdb*,[124] *1IVU-V-W-X.pdb*,[125] *1AV4,L.pdb*,[126] and *2CWT-U-V.pdb*[127]). Several of these structures have a point mutation at D298 or have been formed as intermediates in topaquinone biogenesis. *1IU7.pdb* provides a high resolution structure of the wild-type enzyme and, for this reason, this structure was chosen as the basis for the simulations presented previously in Fig. 3.23.

Table 3.11: The inter-copper distances measured from a range of AGAO homo-dimer crystal structures crystallized under a range of conditions.

PDB structure code	Cu−Cu distance (nm)
1IVW.pdb	3.559
2YX9.pdb	3.561
1IVV.pdb	3.567
1RJO.pdb	3.568
2CWU.pdb	3.574
2CWV.pdb	3.579
1AVL.pdb	3.587
1IVU.pdb	3.593
2CWT.pdb	3.595
1IU7.pdb	3.602
1IVX.pdb	3.602
1AV4.pdb	3.615

There is some variation within the crystal structures for the inter-copper distance; the full composite of the Cu−Cu distances are given in Table 3.11. In order to consider how these observed variations could impact on the DEER traces, the spectra were re-simulated using the longest and shortest inter-copper distances found in the crystal structures. As can be seen from the data in Fig. 3.24, altering the distance inter-copper distance by the small variation observed in the crystal structures does not significantly change the shape of the simulated spectra. AGAO forms a tightly bound homo-dimer and it appears that the structure of this dimer found in solution is likely to be similar to that observed by X-ray crystallography.

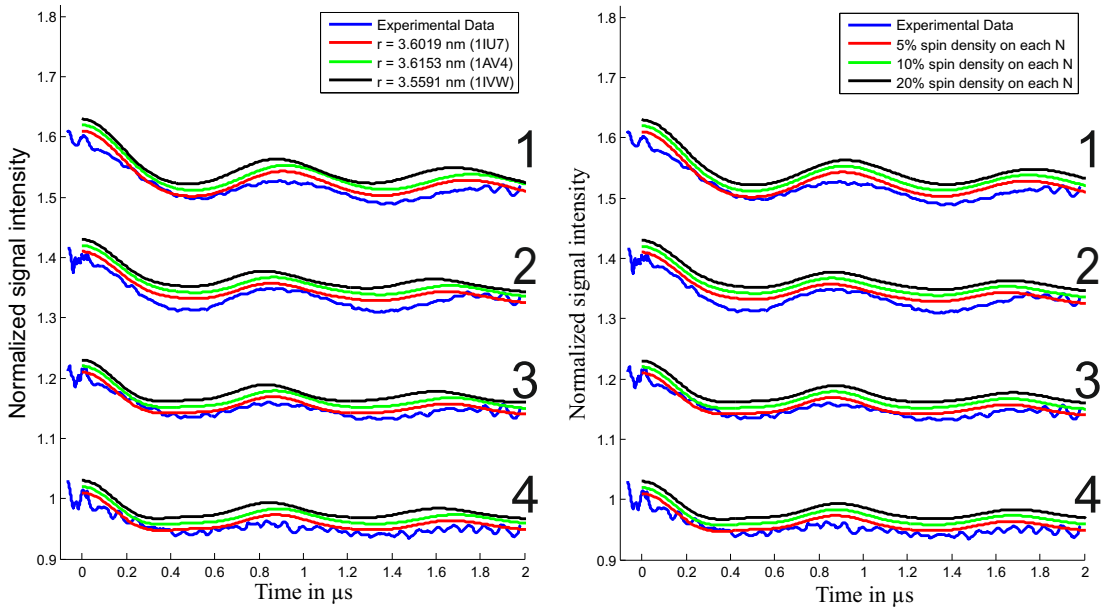


Figure 3.24: **Left:** Plot showing the change in the simulated data for different inter-copper distances taken from the maximum and minimum distances found in AGAO crystal structures. **Right:** Plot showing the variation in the simulated data for different degrees of delocalization of spin density onto the chelating nitrogen. Both data sets are simulated for the four pump and detection pulses given in Fig. 3.22. The simulated data multiplied by a homogeneous background and modulation depth correction, the parameters used are the same as those given in Fig. 3.23. In all cases the experimental and simulated data sets are offset from one another by 0.01 and each data set corresponding to a different set of pulse positions is offset by 0.2.

The orientation of the g-tensor in AGAO

The exact orientation of the g-matrix in relation to the molecular frame is unknown. As seen in Chapter 5, the orientation of the g-matrix in proteins is sensitive to the surrounding structure. Although the g-tensor is likely to lie with the g_z axis approximately perpendicular to the plane of histidine coordination triad, it was decided to vary the orientation of the g-matrix within the molecular frame, to test how much effect this had on the spectra produced. Since the protein forms a homo-dimer, we can reasonably expect that the orientation of the g-matrix with respect to the molecular structure of each unit will be the same. The results of these calculations for pump and detection position 1, keeping the original Cu−Cu distance of 3.602 nm from 1IU7, are shown in Fig. 3.25.

Although it is clear that changing the relative g-matrix orientation with respect to the protein

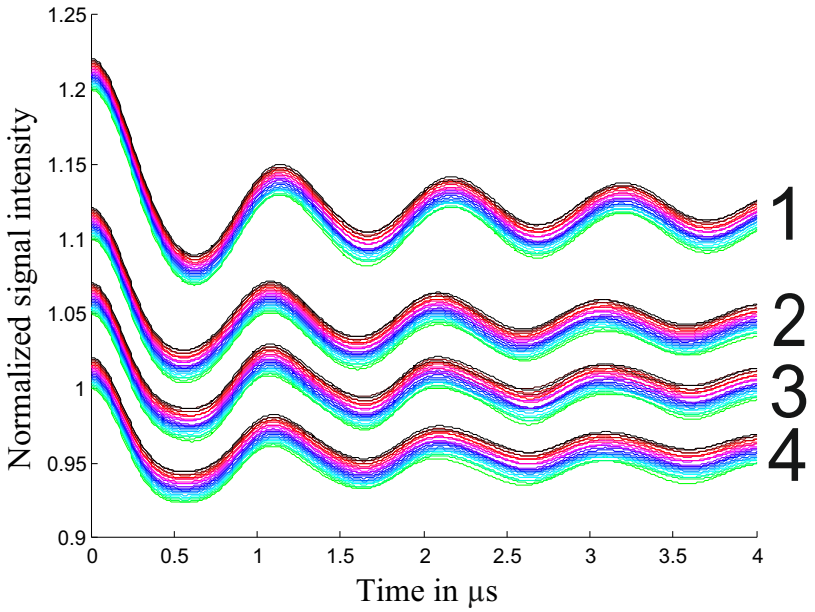


Figure 3.25: Simulated data for different orientations of the g_z axis with respect to the molecular frame. The numbers 1 to 4 represent data sets for the pump and detection positions labelled 1 to 4 in Fig. 3.22. Within each data set, each trace of a different colour represents a different orientation of the g_z axis with respect to the molecular frame. Traces within a data set are off-set from one another by 0.01 for clarity and different data sets are off-set by 0.1. As the two copper centres are identical, when the orientation of g_z with respect to the molecular structure is changed for one centre, the same change in orientation must occur with respect to the molecular structure at the second centre. In order to model multiple different orientations of the g_z axis a grid of knots was used where each knot represents one g_z axis orientation. The simulated data presented in this figure has not had a background correction or modulation depth correction applied.

structure results in a change to the shape of the trace produced for the AGAO system, this change is very subtle. This apparent lack of orientational selection is most likely due to the axiality of the g-tensor; further details on the consequences of the axiality of the g-tensor are given in Section 3.5.

Conclusions for the validity of the AGAO orientationally selective DEER simulations

The simulated data provides a good fit to the experimental data, confirming that AGAO forms a homo-dimer in solution and that the structure of the homo-dimer is likely to be very similar to that found by X-ray crystallography.

Small deviations between the simulated and experimental data are likely to be due to the fact

that the analysis portrayed here only takes account of one relative orientation of the two centres. Although the surrounding protein structure holds the two centres relatively rigidly with respect to one another, it is still possible that a small distribution of inter-copper distances and orientations remains. It would be possible to model a distribution of the two centres, taking into account the surrounding protein structure, using molecular dynamics simulations of the homo-dimer and using 'snap-shots' of the relative copper positions at small time intervals. However, overall the fit of the experimental data to the simulated data for the single Cu−Cu orientation taken from the crystal structure is satisfyingly close, without further need for more cumbersome simulations.

3.5 The consequence of *g*-tensor axiality

For the all the copper systems studied here, the g-tensor was taken to be axial. This has an intriguing result on the spectra: when the pump and detection pulses are positioned at frequencies where both excite a portion of the spectrum containing a contribution from $g_{x/y}$, the dipolar spectrum formed will contain a contribution from $\omega_{\perp}$, no matter what the orientation of the two centres is with respect to one another. This is because when the g-tensor for two centres is axial, there will always be a component of the $g_{x/y}$ plane of one centre that is co-directional with a component of the $g_{x/y}$ plane of the other centre. Simulations of this phenomenon are shown for two hypothetical copper porphyrin centres in Fig. 3.26.

In Fig. 3.26, the upper plot shows three possible orientations of two copper centres (shown as orange circles), ligated by four nitrogen (shown as white circles or coloured stars) with respect to one another. In all cases, the g_z axis was chosen to lie perpendicular to the plane of the ligating nitrogen. The first centre was fixed in all simulations, while the orientation of the second centre was varied. Initially it shared the same orientation as the first centre (red stars for nitrogen). The remaining two orientations were formed by rotations of 90°, so that g_z lies in one instance along the vector linking the two centres and perpendicular to the orientation of the first centre (blue stars for nitrogen), with the final orientation (green stars for nitrogen) having the g_z axis perpendicular to those of the first two orientations. DEER was simulated using a pump pulse at the copper spectral maximum, with

detection pulses 100 MHz downfield. Both copper centres were modelled using the spectral parameters determined for the Cu−Cu model systems, as presented in Table 3.1. The lower part of the figure shows the DEER spectra in the frequency domain (dipolar spectra), with colours corresponding to the orientation of the second centre in the upper figure. In all cases, there are peaks corresponding to the

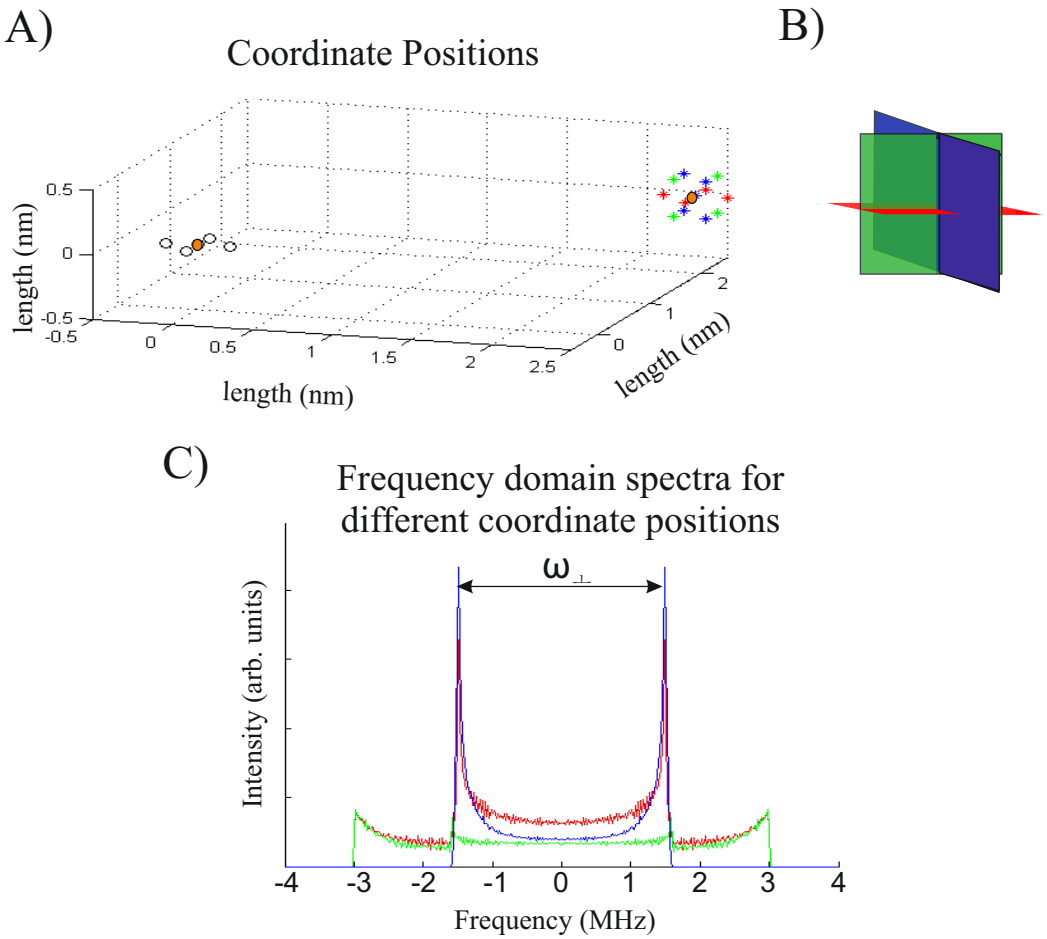


Figure 3.26: **A)** Three possible orientations of two copper centres (shown as orange circles), ligated by four nitrogen, (shown as white circles or coloured stars) with respect to one another. This is the model for a copper centre ligated in a porphyrin ring. The axes are in nm. **B)** An expansion of the three intersecting planes of the porphyrin nitrogen depicted as stars in A). The three simulations in C) each correspond to one of these orientations. **C)** The dipolar spectrum calculated for the interaction between the centres in different orientations. The noise on this spectrum is a result of the use of discrete angles for the orientation of the molecule with respect to the external magnetic field, $\mathbf{B}_0$.

perpendicular frequency, $\omega_{\perp}$, which will allow extraction of the correct distance. This is a feature of the axiality of the copper g-tensor and the pump and detection pulse positions, both exciting on the copper $g_{x/y}$ component.

3.6 The effect of the model used in simulations of orientational DEER

The method of orientational analysis shown here relies on the use of a chemical model to generate the simulations, which are compared to the experimental data. For the porphyrin-based synthetic systems, the initial model was generated using DFT to specify the allowed torsional angles of each bond in the linking rod and a Monte-Carlo simulation method to choose random angles within the specified bounds. AGAO was modelled using the relative positions of the copper centres extracted from an X-ray crystal structure of the protein homo-dimer, *1IU7.pdb.*[119] All these models were found to give good fits to the experimental data.

The question must therefore be posed: how strongly are the simulations dependent on the model used? To investigate this, simulations relying on a number of different models (see below) were performed using the Cu-Cu distance determined for the 3-phenyl Cu−Cu system, so that the simulated results can be compared not only to one another, but also to experimentally recorded data. Furthermore, each copper(II) centre was ligated by four nitrogen atoms as found in the copper porphyrin moiety and 4% of the spin density was delocalized onto each nitrogen; the g_z axis was chosen to lie perpendicular to the plane of the chelating nitrogen. Several models were then constructed in order to test what effect they had on the simulated data produced; the results are detailed below (the colours given in brackets refer to Fig. 3.27).

Model 1: DFT derived model (red)

This is the 'default', DFT-based model described in detail above (Section 3.3.2), for which simulated data has been shown to agree well with the data collected experimentally.

Model 2: All angles (green)

Model 2 uses the same rigid rods as for model 1 above. However, rather than using the DFT calculations of the structural fragments to determine the allowed rotations about the rods, all angles were allowed for all three rods. The simulated data is very similar to that simulated for model 1. We believe that this is most likely a result of the high flexibility of the system rather than inaccuracies in the DFT calculations, since for the Cu−Cu 3-phenyl system the allowed rotations in model 1 cover almost 360°. Therefore it is as expected that the results for model 1 and model 2 are very similar.

Model 3: Sphere (cyan)

Keeping the distance between the centres fixed and, instead, allowing the angles between the g-matrices to vary without restriction yields a spherical distribution of one centre around the other. This model corresponds to an isotropic angular distribution of the copper centres and thus yields a DEER trace that does not possess any angular weighting.

Model 4: Point average (magneta)

In model 1, 1,000 structures were used to form a distribution of the two centres, not only in their geometric positions, but also in the relative orientation of the two centres. In contrast, for model 4, the average of the geometric positions and relative orientations of the two centres was used. The simulation for model 4, while sharing some features with the experimental data, does not accurately reproduce all the oscillation frequencies. This ill-fitting model shows that when a distribution of centres is present, it is necessary to fit the full distribution rather than just an average. This information prompted the decision to use the statistically significant part of the MMM calculated distribution when fitting the DEER traces for the protein complexes described in Chapter 4.

Model 5: Ball (black)

Similar to the model described by Yang et al.,[9,71] who used a spherical distribution of points to fit their data, in model 5 two spheres of radius 0.5 nm are defined, centred at the point average derived

from model 1. The radius of the spheres was chosen so that it would encompass both the maximum and minimum distances found in the DFT derived model 1. However, the larger degree of positional and orientation freedom is seen to 'wash out' much of the structure, showing that this model is a poor choice for the rod-like systems. Yang et al. studied copper centres attached to poly-peptide chains and it is likely that the larger degrees of freedom in their systems made a ball-like model applicable for their systems.[9,71]

3.6.1 Analysis and conclusion on dependence of the model used

The simulated data from the different models is plotted in Fig. 3.27. The experimental data also shown in Fig. 3.27 has undergone a three-dimensional homogeneous background correction in DeerAnalysis. Therefore no background correction is applied to the simulated data for the different models. It can be seen that only two models accurately predict the form of the experimental data: the DFT derived model (model 1), which was used in the original analysis, and a related model (model 2), where the same rotational rods are used, but the angles through which these rods are rotated are not restricted. Given the flexibility of the rod-like systems (even when the rotations in the 3-phenyl system are restricted the rotational angles about the copper−amide rod covers c. 260° and the amide−amide rod covers the whole 360°) it is not entirely surprising that the two models produce very similar results.

The simulation of data using different models highlights the need to use a model that is appropriate for the system being studied, especially when modelling orientationally selective DEER spectra; the average position of the two centres seems to be as crucial as the distribution of the centres.

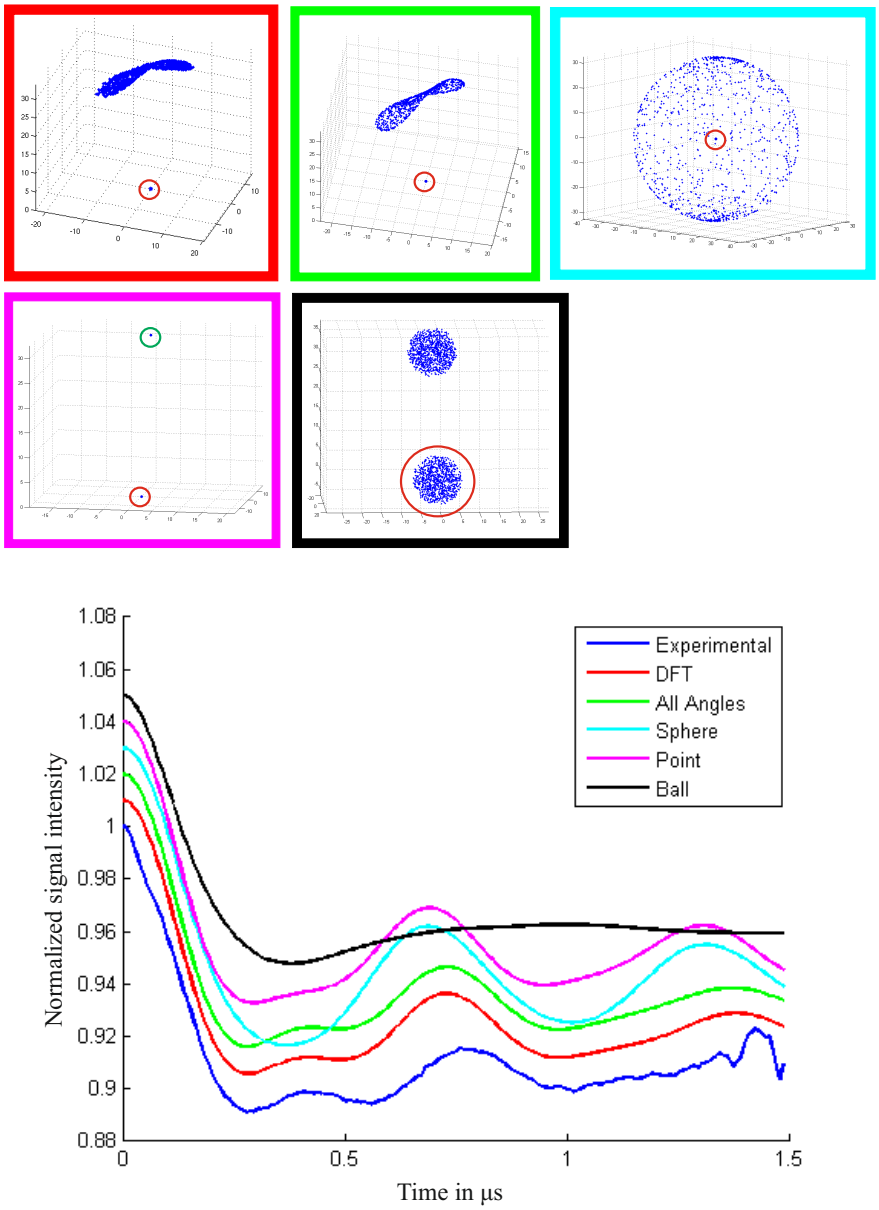


Figure 3.27: **Upper figure:** This details the different models trialled; the surrounding box colour corresponds the DEER traces in the lower part of the figure. In each case, the average distance between the two copper centres is held constant to that of the 3-phenyl system. The simulation parameters are the same as those used for the 3-phenyl simulations in Section 3.3.6, so each centre is ligated by four nitrogens, each with 4% of the electron density associated with it and the g_z axis is chosen to lie perpendicular to the plane formed by these nitrogens. In each case, the detection centre(s) is(are) highlighted in red and were represented by only one point for clarity; the pump centre is highlighted in green. **Lower figure:** Plots to compare the simulated data with the experimentally recorded data for the 3-phenyl system. The experimental data has had a background correction removed and the simulated traces have not had any corrections made to them. The traces are offset from one another by 0.01 for clarity.

3.7 Short range distance analysis on a copper nanoring

Although DEER is very useful for distance measurements in the range 1.5–c. 8 nm, it has a lower limit imposed on it by the point at which the width of a pulse is unable to excite the spectral extent of the dipolar spectrum. Although this problem can be overcome via observer-selective DEER,[93] another method of analysis for short distance biradicals, at the borderline of accessibility for DEER, is dipolar convolution of continuous wave spectra.[58]

Dipolar convolution requires CW spectra to be measured for a system containing coupled spins and also for a similar system containing only one spin, which is used as a reference. The degree of broadening observed in the spectrum of the coupled spins compared to that for the single spin system can be related to coupling between the spins. When dipolar convolution is used to extract distances, it is assumed that the exchange coupling in the system is negligible; the same assumption is usually made in the analysis of DEER data. For a system where the inter-spin distances between coupled spins are known, it is possible to use dipolar convolution as a probe into the level of exchange coupling, the extent of exchange interactions between two unpaired electrons in a system. This is achieved by simulating the spectrum, which should result from a system with only dipolar coupling, by broadening the spectrum of the uncoupled spin and comparing this spectrum to the experimental spectra for the coupled system.

This study used a hexaporphyrin nanoring, fully intercalated with copper (see Fig. 3.28), and a monomer unit derived from an intermediate produced during the synthesis. Due to the rigidity of the nanoring structure, it is possible model the inter-copper distances to a reasonable degree of accuracy using DFT, as shown in Fig. 3.28. In addition, DEER distance measurements have been carried out on related nitroxide labelled structures and these have shown that for porphyrin wires, a 'worm-like' chain model can be used to predict the end-to-end distance of the wires. When these are templated to form half a nanoring, the structure becomes much more rigid.[128]

The aim of this study was therefore not to extract inter-copper distances, but rather to investigate the exchange coupling between the copper paramagnetic centres, from examination of the CW EPR broadening. By analysing the samples using dipolar convolution, a technique that does not take into

account any exchange contribution, deviations in the spectral width of the nanoring spectra from that predicted through a purely dipolar model will provide an estimate for the size of the exchange coupling.

	Copper-copper distances (Å)		
	Nearest	Two away	Opposite
	12.497	21.683	24.897
	12.509	21.601	25.071
	12.490	21.576	25.049
	12.498	21.647	
	12.489	21.713	
	12.485	21.642	
Mean Average:	12.495	21.644	25.006
Standard Deviation:	0.00860	0.0505	0.0947

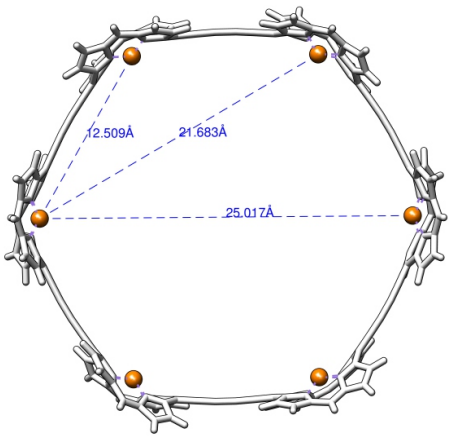


Figure 3.28: **Left:** Table showing the inter-copper distances for the nanoring; their averages and standard deviations have been calculated. **Right:** The structure of the copper nanoring, as modelled by TurboMole,[129] with the inter-copper distances marked.[f] It should be noted that the structure from TurboMol is not completely symmetric and therefore six different distances are measured between adjacent copper centres; likewise, there are six different distances between copper centres two away and three between opposite copper centres.

3.7.1 Copper nanoring sample synthesis and preparation

The system was synthesized by William Peveler of Prof Harry Anderson's group. The copper nanoring was formed from the corresponding templated zinc nanoring, the synthesis of which has been published by Sprafke and co-workers.[130] The templated zinc ring was treated with TFA for 15 minutes at room temperature, followed by the addition of pyridine at room temperature for 15 minutes, which gave the metal-free nanoring in 86% yield. This metal-free nanoring was treated with 120 molar equivalents of copper acetate in dichloromethane and a small amount of methanol. The mixture was then passed over a short silica plug to remove the excess metal salts. A colour change from green to yellow/brown was observed and the yield calculated to be 85%. The synthetic scheme is shown in Fig. 3.29.

The monomer samples were produced by replacing zinc with copper, following a similar procedure

[f]The TurboMole modelling was completed by William Peveler, who synthesized the compound.

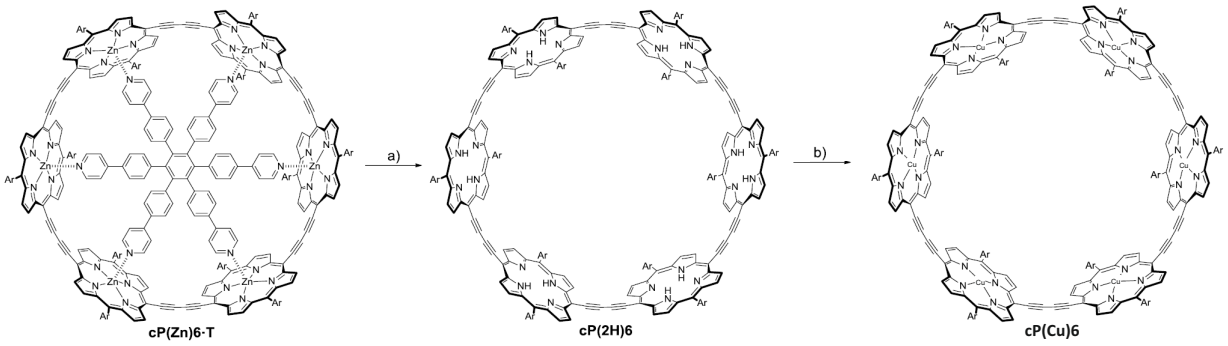


Figure 3.29: Synthesis of copper nanorings. Experimental conditions: **a)** TFA, 15 min, RT then pyridine, 15 min, RT, 86%. **b)** $Cu(OAc)_2 \cdot H_2O$, 12hrs, RT, 85%.

to that outlined above, using one of the monomeric units utilized for the initial synthesis of the zinc templated ring. The synthesis of the monomer units is described in detail by Sprafke and co-workers. [130] Fig. 3.30 shows the structure of one monomer unit.

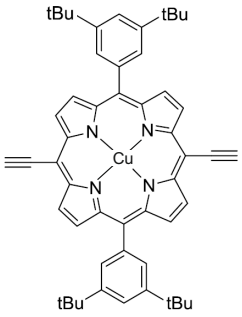


Figure 3.30: The structure of one monomer unit, used as a comparison to the hexaporphyrin copper nanoring.

Samples were prepared for EPR investigation at 100 μM for the Cu(6) ring and 200 μM for the monomer, in a 1:1:1 mixture of chloroform:toluene:THF, and placed in 4 mm Wilmad quartz EPR tubes. CW EPR measurements were recorded at 15 K.

3.7.2 Dipolar convolution for analysis of short inter-spin distances and exchange contributions

Dipolar convolution is a method of predicting the spectral changes caused by the interaction of two spins, via dipolar coupling only, from comparison of the uncoupled spectrum of one of the spins with the spectrum of the coupled system. As previously stated, at short distances the dipolar coupling is large and can manifest in the CW spectra as a broadening of the spectral lines. The method assumes that there is negligible exchange coupling and that the dipolar broadening term is formed from a distribution of Pake patterns. The Pake, or dipolar coupling, pattern is formed from isotropic orientation distributions of dipole-dipole interacting spins, as seen in Fig. 2.2 (B).[131] If a large degree of exchange coupling is present, this will be apparent through the measurement of a coupled spectrum, which is significantly broader than that calculated via dipolar convolution for the known inter-copper distances.

Initially, both the monomer and nanoring spectra were baseline corrected (using a 4th order polynomial), integrated and frequency matched so that the spectral maximum occurred at the same field value. The spectrum of the monomer is then convolved using three Gaussian functions of Pake patterns, one for each distance present in the system (see Fig. 3.28). The distances used to generate the Gaussian distributions of Pake patterns were the average of those measured from the TurboMole model, shown in Fig. 3.28. The standard deviations of these distances were also used to define the width of the Gaussian distributions.

The dipolar convolution was achieved using MATLAB-based software, DipCon, written by Dr Janet Banham and co-workers.[58] This method was extensively tested by Banham et al. using nitroxide labelled peptides. The agreement between experimentally extracted distances and those predicted from models was found to be fairly reliable.[58]

The EPR data and the dipolar convolution results are shown in Fig. 3.31. The monomer in frozen solution is extremely well resolved (Fig. 3.31 A) and was simulated with a g-matrix and hyperfine couplings of one copper and four nitrogen (Fig. 3.31 B). The spectra were fitted using the MATLAB-based EasySpin simulation package; the parameters are shown in Table 3.12.[7,96]

Table 3.12: EPR parameters of the copper nanoring and corresponding monomer.

Species	g-values	A(^{65}Cu) [MHz]	A(^{14}N) [MHz]	Line widths [MHz]
Monomer (D in Fig 3.31)	2.0460, 2.0530, 2.2100	64, 64, 570	46, 46, 50 46, 46, 50 46, 46, 50 46, 46, 50	20, 20, 40
Nanoring (E in Fig 3.31)	c. 2.0620, c. 2.0620, 2.190	c. 50, 50, 590	Not resolved	-

By comparison, the copper nanoring in frozen solution was poorly resolved (Fig. 3.31 C) and only broad features due to copper hyperfine couplings could be resolved. This lack of resolution, particularly of the nitrogen hyperfine couplings, is due to the additional electron-electron dipolar interactions between the copper paramagnetic sites. Also, the formation of the ring causes some distortions of the porphyrin moieties and the loss of symmetry will also cause broadening of the spectrum.

The convolution of the monomer spectrum, using the three copper-copper distances, is shown in Fig. 3.31 D. This indicates that the broadening of the copper nanoring spectrum can at least be accounted for by the through space dipolar interactions. However, it is clear from comparison of the experimental copper nanoring spectrum and the convolved monomer spectrum that the g-values and copper hyperfine coupling are not the same in the monomer and the nanoring. This is perhaps not surprising since these parameters are very sensitive to the local geometry of the paramagnetic site. An improved simulation was thus attempted by adjusting the g-values and copper hyperfine values; parameters for this are given in Table 3.12. Using these g- and A- values to simulate a monomer-like spectrum, with the experimentally derived line widths and nitrogen couplings, this spectrum was broadened via a dipolar convolution and the resulting spectrum is shown in Fig. 3.31 E. Again, the broadening of the EPR spectrum is well accounted for by just the through space dipolar interactions. This analysis thus indicates that any exchange interaction, if present at all, is relatively small.

It is possible that the lack of exchange coupling between the copper centres is a result of the distortion of the porphyrin rings, as seen in Fig. 3.28. Similar zinc substituted rings have been prepared

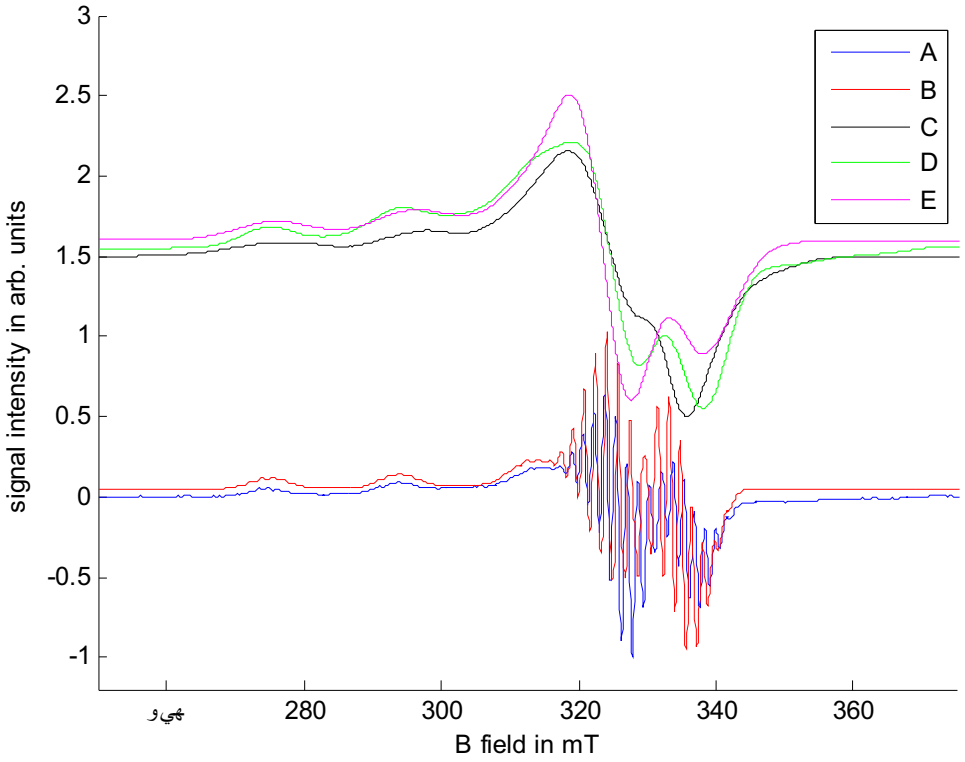


Figure 3.31: EPR spectra in frozen solution (20K) of monomer (A) and its simulation (B), and the Cu(6)-ring (C) and its simulation with a through space dipolar broadening model (D/E). The difference between D and E are the g-matrix and copper hyperfine values used (see Table 3.12).

in an EPR active state and via reduction of the system and DFT modelling of these systems has provided structures where the porphyrins have a much higher propensity to remain planar.[g]

3.7.3 Orientational analysis of dipolar convolution

The dipolar convolution method used did not take into account any of the orientational information of the copper locations with respect to one another. The fixed orientations of the copper would mean that only part of the dipolar coupling Pake patten would be present for each relative orientation of the copper centres. However, since the g-values were seen to change between the nanoring and the

[g]Work on the electronic structure of the reduced zinc rings is currently being conducted by other members of the Anderson and Timmel research groups.

monomer, this limited any analysis that could be carried out. Also, the inclusion of three different types of distance constraints, each of which would also have a different orientational constraint, meant that even had the g-values remained constant between the monomer and the nanoring, it is unlikely that any meaningful orientational analysis could be performed on this sample. Instead, samples labelled with only one of the different copper-copper interactions would be required; the remaining sites would be filled using an EPR silent metal such as zinc (see Fig. 3.32). Unfortunately, the synthesis of such samples was beyond the scope of this research.

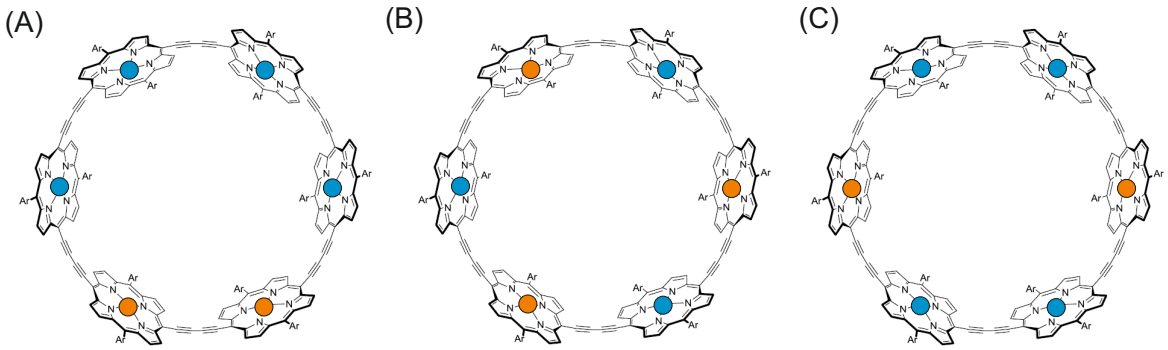


Figure 3.32: Hypothetical structures of mixed copper and zinc nanorings for orientational analysis. Orange circles represent copper centres and blue circles represent zinc centres. **(A)** Adjacent copper sites occupied. **(B)** Copper sites two away occupied. **(C)** Opposite copper sites occupied.

Chapter 4

Structural determination of the electron transport complexes formed by ferredoxin, ferredoxin reductase and cytochrome P450 using orientationally selective DEER

Most of the recent applications of X-band DEER in proteins have involved the use of DEER between two nitroxide spin labels. Generally, the spin labels are bound to cysteine residues, either naturally present or added via site-directed mutagenesis. Distance information gained through DEER can provide insight into the protein structure and dynamics, including conformational changes.[132] Where two molecules are known to form tightly bound complexes, the DEER methodology is not limited to measuring intra-molecular distances, in which two spin labels are placed on the same molecule, but can also probe inter-molecular distances, when one spin label is attached to each partner in the bound complex. The transient nature of many such complexes means that the structure of the docked complex frequently eludes structural determination via X-ray crystallography. However, in many cases it is possible to solve the X-ray structure of the two binding partners independently. In such cases, if experimental information from another source, such as DEER, Double Quantum Coherence (DQC), electron microscopy, etc., can provide information about the docked structure, a model of the docked complex can be built from the X-ray structures of the component proteins. Such studies have been

undertaken for both protein homo- and hetero-dimers using distance constraints between pairs of nitroxide labels defined using DEER (or DQC).[133–136]

Thus far, models of protein complexes built from EPR constraints have been produced using distance constraints only. As seen in the previous chapters, X-band DEER measured using either a metal centre with a nitroxide, or two metal centres, where the metal centres are held in a rigid conformation, is not only sensitive to the distance between the two paramagnetic centres but also their relative orientation. Here, we present an original methodology for the use of orientationally selective DEER traces in the determination of protein-protein docked complexes in frozen solution. Measurements have been performed by utilizing an iron-sulphur cluster ($[Fe_2S_2]$) in the protein ferredoxin, which can be prepared in an S=$\frac{1}{2}$ ground state as an innate spin probe ($[Fe_2S_2]^+$). DEER traces were measured between this cluster and a nitroxide (MTSL) spin labels added to the ferredoxin binding partner (either ferredoxin reductase or cytochrome P450) at known location within the protein sequences. These experimental DEER traces have been fitted using a library of pre-simulated orientationally dependent DEER traces to determine the distance and orientation between the two centres. This allows a three-dimensional map of the relative positions of the spin pairs to be constructed. The X-ray structures of the two proteins are then superimposed on these sets of spin pair constraints to provide a model of the docked structure.

Iron-sulphur clusters are well studied and characterized by EPR,[137] and have been used in previous DEER studies. For example, DEER measurements were used to assign the different EPR signals from the multiple iron-sulphur centres in complex I, by measuring the relative position of the clusters in the system and comparing the distances and angles gained from analysis of the DEER data to those found in the X-ray crystal structure of the complex.[138]

This chapter represents the results of an investigation into the structures of the electron transfer complexes from the Cytochrome P450 electron transport chain in *Rhodopseudomonas palustris*.[a] Two docked complexes were investigated, ferredoxin–ferredoxin reductase and ferredoxin–P450. For both systems, the X-ray structures of the individual binding partners are available. However, it has proved

[a]Rhodopseudomonas palustris is a gram-negative purple non-sulphur bacteria, notable for its ability to switch between four different modes of metabolism.

impossible thus far to crystallize either of the docked complexes from the native state proteins. A tethered structure has been published for the ferredoxin–ferredoxin reductase complex, with a short tether link between the two proteins. The short length of the tether severely biases the possible docked structures that are accessible, and thus there is doubt on the validity of this structure for the native proteins.[139] Since the structure of the individual binding partners are known independently, distance and angular restraints from DEER can be used to build models of the docked complexes. It is hoped that these models will help add further insight into the mechanism of electron transport within this system and in the wider context.[12,139–141]

Measurements on the ferredoxin–ferredoxin reductase complex commenced before this doctorate was started; DEER measurements between MTSL labels and the iron-sulphur cluster for this system were recorded by Dr Janet Lovett in Oxford and Mülheim. The measurements between pairs of nitroxide labels on the ferredoxin–ferredoxin reductase complex and all measurements on the ferredoxin–P450 system were conducted at Oxford University as part of my doctoral research. All samples have been prepared by Dr Luet Wong and members of his research group, specifically Dr Stephen Bell, Eachan Johnson, Nikki Hoskins and Dominic Caprotti. I am further indebted to Dr Jeffrey Harmer who wrote the initial fitting routine for the DEER traces and for his help with further development of the code in order to complete this research.

4.1 An introduction to ferredoxin reductase, ferredoxin and cytochrome P450

The superfamily of cytochromes P450 is comprised of a wide variety of heme *b* enzymes, where their most common function is the activation of atmospheric oxygen, leading to the catalytic hydroxylation of C–H bonds and the formation of water with the concomitant oxidation of NAD(P)H.

$$2H^+ + R\text{–}H + O_2 + 2e^- \rightarrow R\text{–}OH + H_2O$$

P450 cytochromes are almost ubiquitous throughout the different kingdoms of life and they have even been found in some viruses. Their catalytic properties are biologically necessary for the Phase

I metabolism of xenobiotics, hormone synthesis and calcium regulation, amongst many others.[142–146] More recently, interest has been piqued by the application of this family of proteins in industrial environments, where they can provide clean and efficient activation of classically inert substrates, obviating the need for heavy-metal based catalysts.[147–149]

P450 enzymes rarely work alone; class I P450s, such as the CYP199A2 studied here, form the terminal proteins of an electron transport chain involving a ferredoxin and a ferredoxin reductase. Ferredoxin reductase contains a flavin cofactor, which can be doubly reduced by NAD(P)H. This in turn passes the electrons one at a time to the ferredoxin, containing a variable oxidation state [Fe_2S_2] cluster (+2 or +1). Finally, the singly reduced ferredoxin transfers an electron to the heme centre in P450 (see Fig. 4.1). The second electron from the NAD(P)H oxidation also travels down the same transport chain, since both are needed in the catalytic cycle of P450 (see Appendix H).

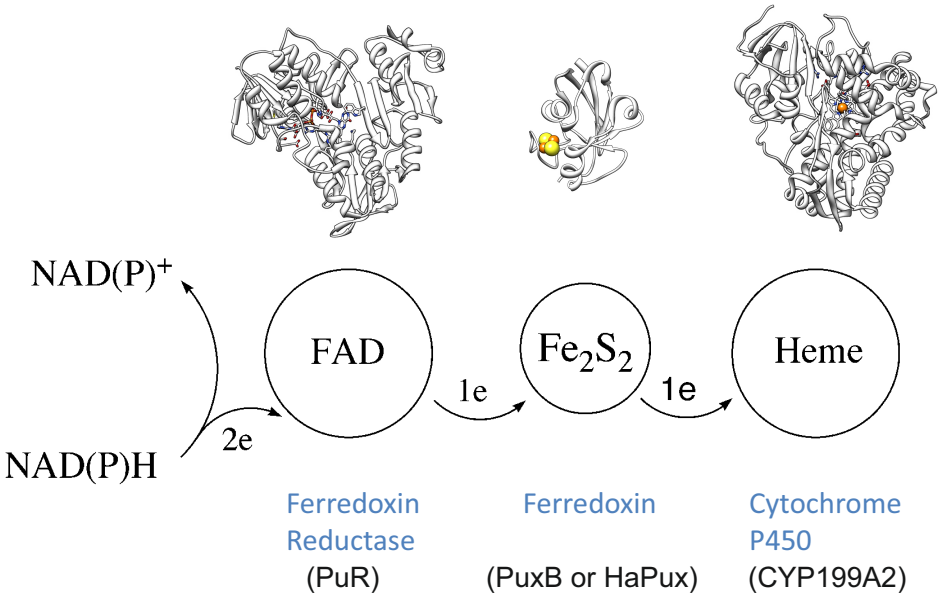


Figure 4.1: A schematic of the electron transport chain containing ferredoxin reductase, ferredoxin and P450. The structures above are the proteins used in the EPR experiments. (PDB codes left to right; *3FG2.pdb*, *3HUI.pdb*, *4DNJ.pdb*.)

Electron transport occurs via docked complexes of the proteins and knowledge about the structures of these complexes is vital to the understanding of the electron transport chain. This research has allowed the determination of the structures of the docked complexes, using the X-ray structures of the

independent protein partners and orientationally selective DEER.

Class I cytochrome P450 systems are primarily found in prokaryotic cells; and all three proteins are water soluble, making them suitable for study in frozen water/glycerol solutions. In total, four proteins were used in this study: palustrisredoxin reductase, Palustrisredoxin-B, Ha-palustrisredoxin and CYP199A2. Palustrisredoxin reductase (PuR)[150] is the ferredoxin reductase from *Rhodopseudomonas palustris* CGA009.[151,152] CYP199A2 is a P450 protein and forms part of the same electron transport chain as PuR.[151,153] Palustrisredoxin (Pux) is the natural binding partner of PuR and the P450, CYP199A2. However, this protein was replaced in the DEER experiments by two different ferredoxin proteins, also from *Rhodopseudomonas palustris* CGA009, which have been shown *in vitro* to substitute for Pux in the electron transport chain described above. The first was palustrisredoxin-B (PuxB)[12] and the second was Ha-palustrisredoxin (HaPux). HaPux is not associated with a CYP gene and therefore does not have a natural cytochrome binding partner. The reason for these substitutions was the low yields of Pux from recombinant *Escherichia coli* expression systems, compared to PuxB and HaPux,[154] which were produced in much larger quantities, making the volumes and concentration required for DEER experiments comparatively readily attainable. In addition, there is currently no crystal structure of Pux available. This would mean that any experiments using Pux would rely on the use of a homology model in the analysis, which could introduce errors into the final results.

4.1.1 Existing crystal structures in the literature

The formulation of a structure for a docked protein complex using DEER determined constraints requires knowledge of the independent structures of the two binding partners. The fitting procedure using the DEER constraints only produces possible positions in space of two paramagnetic centres with respect to one another. Therefore, in order to produce a model of the docked protein complex, it is necessary to map the positions of these pairs of paramagnetic centres onto the crystal structures of the two constituents.

Crystal structures of the proteins forming the electron transfer complexes are available from the Protein Data Bank (*http://www.rcsb.org/pdb*) in the following deposited files: PuR (*3FG2.pdb*)[150],

P450 CYP199A2 without a cofactor bound (*2FR7.pdb*)[151] and with a cofactor bound (*4DNJ.pdb*)[153] and PuxB (*3HUI.pdb*)[12]. The crystal structure of HaPux has recently been solved by Dr Wong and collaborators. Although not yet published, the structure was available to our laboratory for use in the fitting procedure.

A tethered structure (*3LB8.pdb*) formed between the putidaredoxin (Pdx) and NADH-dependent putidaredoxin reductase (PdR) proteins of the camphor monooxygenase system from *Pseudomoanas putida* has been published.[139] The PdR and Pdx are chemically cross-linked via the Lys 409 Pdr–Glu 72 Pdx pair (see Fig. 4.2). Both PdR and Pdx have very similar structures and amino acid sequences to PuR and PuxB respectively.[b] It could therefore reasonably be expected that, if the published tethered structure is the same as that found naturally for the untethered Pdx-PdR complex, the PuxB-PuR complex might show some similarities to this structure. The tethered structure is shown in Fig. 4.2.

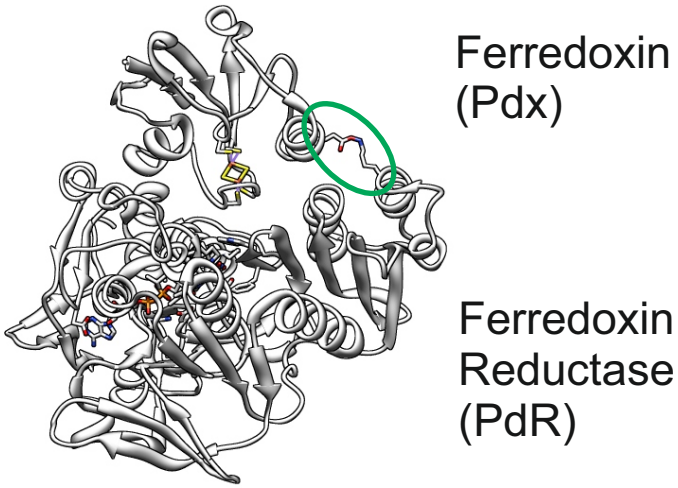


Figure 4.2: Tethered structure (*3LB8.pdb*) formed between ferredoxin (upper protein) and ferredoxin reductase (lower protein). The tether between Lys 409 Pdr–Glu 72 Pdx is highlighted in the green ring.

[b]PdR and PuR have a 38.61% sequence identity with an RMSD of 0.903 Å. Pdx and PuxB have a 43.30% sequence identity with an RMSD of 0.781 Å.

There is no such tethered structure for a ferredoxin–P450 system; and in general there is less published information about the binding interaction between ferredoxin and P450. This lack of information would make the process of choosing a suitable tether location, which would not significantly bias the binding away from the native state, almost impossible.

4.1.2 Sample preparation

All the samples studied were prepared at Oxford University by members of the Wong group. The method of protein expression for all four proteins that were used in the experiments followed published protocols.[12,150]

Initial experiments to probe the docked ferredoxin-ferredoxin reductase complex used the PuR-PuxB system with the PuxB prepared in a reduced state ($[Fe_2S_2]^+$). The reduced iron-sulphur cluster has an $S = \frac{1}{2}$ ground state making it paramagnetic and allowing its use as a spin probe. PuR was mutated to place one cysteine at a time at the following sites: 82, 135, 164, 196, 249, 281, 303 (wild type), 309 and 347, which were spin labelled with MTSL.

Experiments to probe the ferredoxin–P450 complex used the HaPux ferredoxin. The change in ferredoxin type was necessitated as no DEER signal was observed during initial experiments on a PuxB-P450 system. It is believed that this is a result of the lower binding constant for this system. Further detail is given in Section 4.1.3. P450 was spin labelled at the wild type cysteine, at site 226, and following site-directed mutagenesis at sites 42, 315, 345 and 404.

For structural determination in both the ferredoxin–P450 and ferredoxin–ferredoxin reductase systems, a further $NO^{\bullet}-NO^{\bullet}$ restraint was needed. This additional restraint was required due to the axiality of the g-tensor and symmetry constraints associated with the electron on the $[Fe_2S_2]^+$ cluster, which allowed two possible configurations of bound structure to be modelled that were found to be equally probable from fitting of the $[Fe_2S_2]^+$-nitroxide restraints alone. Hence, samples of HaPux were prepared where a cysteine was added at site 54 and spin labelled with MTSL. It proved impossible to mutate the same residue in PuxB, as the protein produced was found to be unstable and unfolded. Thus, the $NO^{\bullet}-NO^{\bullet}$ measurements needed for the ferredoxin-ferredoxin reductase system

used the HaPux-PuR complex. The high sequence and structural similarity between the two ferredoxin proteins indicates that the binding of the two proteins is likely to occur via the same docking motifs.

CYP199A2 P450 possesses a heme cofactor. Although the iron in this centre can be prepared in an EPR active state, DEER experiments attempted between this iron centre and the $[Fe_2S_2]$ cluster in the ferredoxin did not yield interpretable results, due to the fast relaxation of both centres and the very small modulation depth, a consequence of the broad spectra of both centres.[155] Instead, the iron centre was silenced by capping with carbon monoxide, as shown in step 10 of Fig. H.1 in Appendix H.

The PuR and P450 prepared in phosphate buffered saline (PBS) with 1% DMSO were spin labelled by treatment with an excess of MTSL: 10-fold for PuR from a 10 mM stock solution in DMSO and 100-fold for P450 from 100 g/L solution in DMSO, for c. 2 hours at 4 °C in both cases. Excess MTSL was removed by eluting twice on de-oxygenated G25 columns using 50 mM Tris, pH 7.4, 1 mM $Na_2 \cdot EDTA$ for PuR and the same buffer with an additional 1 mM of p-methoxybenzoic acid, a substrate of P450 CYP199A2, or by using the same buffers. It should be noted that $Na_2 \cdot EDTA$ was included to remove Fe^{3+} or other metal ions that might be present in any of the buffer components. The unlabelled PuxB and HaPux were also similarly eluted.[c]

For the labelling of HaPux E54C, the addition of the MTSL to the HaPux alone was found to cause degradation of the $[Fe_2S_2]$ centre. The MTSL not only reacted with the surface accessible cysteine at site 54, but also with the four cysteines ligating the $[Fe_2S_2]$ cluster. To reduce the level of accessibility of the $[Fe_2S_2]$ cluster to MTSL during the labelling procedure, the HaPux E54C was initially mixed with a pre-labelled binding partner, either PuR or P450, and the MTSL required to label the HaPux added to this solution where the HaPux was already in complex. Furthermore, the number of equivalents of MTSL was reduced to two and the reaction time decreased slightly.

All the proteins were concentrated separately using Millipore Amicon Ultra-4 centricons, which were flushed with nitrogen, sealed, and centrifuged at 7000 $\times g$, 4 °C. Once concentrated to a small volume (<50 μL), deoxygenated buffer TE was added to the protein solutions in a glove-box (<4 ppm O_2) and the centricons were sealed and centrifuged again at 7000 $\times g$, 4 °C. After three cycles of concentration

[c]Some of the later samples had the excess MTSL removed, using the same buffer mixtures in centricons rather than on columns.

and dilution, the proteins were quantitated by UV/Vis spectroscopy.

The centricons were transferred into the glove box where 0.5 equivalents of NADH were added to the PuxB and HaPux samples. The final volume of the protein solution for EPR samples was 50 μL, at a protein concentration of 0.5–1 mM. Volumes of the two proteins required to form the complex were mixed in an approximate 1:1 molar ratio. The presence of the NADH allowed the reduction of the ferredoxin and a colour change to give a pink solution was observed for ferredoxin samples with both PuR and P450 on the addition of NADH, although the colour is much more intense for solutions containing P450. De-oxygenated glycerol (50 μL) was added to make a 50% v/v glycerol/H_2O or D_2O solution at a final sample volume of 100 μL and a final protein concentration of 0.25–0.5 mM.[d] The samples were finally transferred to an EPR tube and sealed with para-film. The EPR tube was removed from the glove box and the sample immediately frozen by slowly lowering the tube into liquid nitrogen. Samples were stored in a liquid nitrogen dewar prior to measurement.

Samples containing the labelled HaPux and PuR were not prepared with NADH since DEER measurements on these systems used two nitroxide spin labels and thus it was not necessary to prepare the $[Fe_2S_2]$ in an EPR active state. For the sample of labelled HaPux with CYP199A2 P450 a catalytic amount of PuR with an equivalent of NADH was added to initiate the electron transfer chain reactions and carbon monoxide was used to silence the heme group in the P450. The samples were also prepared in D_2O and in phosphate buffer, rather than Tris (since the phosphate buffer contains fewer protons) and with deuterated glycerol of 5% v/v glycerol/D_2O. The reason for these changes in sample conditions was an attempt to increase the signal-to-noise ratio and length over which the DEER traces could be measured. Samples prepared in deuterated buffers have longer relaxation times than the corresponding samples in protonated buffers. This allows longer precession times to be used in the DEER sequence and thus the detection of lower frequency oscillations corresponding to longer inter-spin distances. The initial salt used to prepare the buffer was not deuterated. Therefore, using phosphate salt with fewer protons than tris reduced the residual number of protons from the buffer

[d]Some early samples were prepared in H_2O solutions; however, subsequently it was found that the quality of the recorded data was significantly improved by preparation of the samples in D_2O, which increased the relaxation times of the samples significantly.

salt in the final EPR sample. Analysis for an initial model of the HaPux-PuR system indicated that one of the $NO^{\bullet}-NO^{\bullet}$ pairings was expected to show an inter-spin distance of c. 5.3 nm, requiring a trace of >2.7 μs in order to determine the mean distance with any degree of confidence. Reduction in the glycerol content of the solutions allowed a greater protein concentration within the sample leading to larger EPR signals. We believe that the low DEER echo intensity and thus the poor signal-to-noise ratio seen for these systems is most likely due to incomplete labelling of the HaPux, a result of the reduced reaction time allowed for this labelling reaction to prevent destruction of the $[Fe_2S_2]$ centre.

4.1.3 The importance of the binding constant

Protein-protein complexation can be quantified in terms of a binding constant (K_a), the equilibrium constant for the formation of the complex, or a dissociation constant (K_d), the equilibrium constant of the reverse reaction.

$$\text{Protein1} + \text{Protein2} \underset{k_{-1}}{\overset{k_1}{\rightleftharpoons}} \text{Complex}$$

k_1 and k_{-1} are the rate constants for the forward and backward reactions. Therefore, the dissociation constant and the association constant (binding constant) can be defined as:

$$K_a = \frac{[\text{Complex}]}{[\text{Protein1}]\,[\text{Protein2}]} = \frac{k_1}{k_{-1}} \tag{4.1}$$

and

$$K_d = \frac{[\text{Protein1}]\,[\text{Protein2}]}{[\text{Complex}]} = \frac{k_{-1}}{k_1} \tag{4.2}$$

The dissociation constant is an inverse measure of the affinity for two binding partners to form a complex.

When considering enzyme kinetics, usually complex formation is considered to result in some reaction occurring within the complex. This can be generalized to:

$$\text{Enzyme} + \text{Substrate} \underset{k_{-1}}{\overset{k_1}{\rightleftharpoons}} \text{Complex} \xrightarrow{k_{cat}} \text{Enzyme} + \text{Product}$$

k_{cat} is the rate constant for the catalytic second step. The kinetics for this system are described by the Michaelis-Menten equation.

$$rate = \frac{V_{max}\,[\text{Substrate}]}{K_M + [\text{Substrate}]} \tag{4.3}$$

V_{max} is the maximum rate of reaction, equivalent to $k_{cat}\,[\text{Enzyme}]_0$, where $[\text{Enzyme}]_0$ is the total enzyme concentration. K_M is the Michaelis constant, which is given by:

$$K_M = \frac{k_{-1} + k_{cat}}{k_1} \tag{4.4}$$

If we were to consider the complex to be in a pre-equilibrium with the enzyme and the substrate, implying that k_{cat} becomes negligibly small, K_M can be approximated to the dissociation constant K_d. The constant K_M, although always larger than K_d, is therefore also considered to be an inverse measure of the binding affinity for two molecules, which form a complex.

For the pairs of proteins studied here, transfer of an electron in the complex is the 'catalytic step', as shown in the following scheme:

$$\dot{FdR} + Fdx + Cyt \rightleftharpoons [FdR \dot{-} Fdx] + Cyt$$
$$[FdR \dot{-} Fdx] + Cyt \overset{k^1_{cat}}{\rightarrow} FdR + \dot{Fdx} + Cyt$$
$$FdR + \dot{Fdx} + Cyt \rightleftharpoons FdR + [Fdx \dot{-} Cyt]$$
$$FdR + [Fdx \dot{-} Cyt] \overset{k^2_{cat}}{\rightarrow} FdR + Fdx + \dot{Cyt}$$

where FdR is a ferredoxin reductase, Fdx is a ferredoxin and Cyt is a cytochrome. The dot above a protein indicates the electron that is transferred and thus a protein with a dot above it is in a reduced

state. Square brackets indicate an electron transport complex. k^1_{cat} and k^2_{cat} are the rate constants for the two catalytic steps of electron transfer. In all cases, the initial reduced ferredoxin reductase, $F\dot{d}R$, is reformed by reaction of the oxidized enzyme with NAD(P)H. This reaction is always very fast and therefore not rate limiting. If the system can be engineered through choice of proteins so that the relative sizes of k^1_{cat} and k^2_{cat} are different, then the above scheme reduces to Michaelis-Menten type kinetics.

For the systems studied in this chapter, when the cytochrome, Cyt, used is cytochrome C, the rate limiting step of the reaction is the electron transfer from the ferredoxin reductase to the ferredoxin. All other steps can be considered to be very fast, so the measured K_M value becomes an indication of the binding affinity of the ferredoxin and the ferredoxin reductase. On the other hand, when the cytochrome used is a P450 enzyme, the rate limiting step is the electron transfer from the ferredoxin to the P450. Thus the measured K_M value provides information about the binding affinity of these two enzymes.

K_M is found experimentally by measuring the rate of consumption of NAD(P)H, which is required to re-reduce the oxidized ferredoxin reductase.

The K_M for each of the pairs of the protein in the native state, without any spin labels added, have been measured and are given in Table 4.1.

Table 4.1: K_M and k_{cat} values for the protein systems used in the DEER experiments.

Protein system	Ref.	k_{cat} in s^{-1}	K_M in μM
PuR-PuxB(wt)-Cyt *c*	[12]	110.1 ± 1.1	1.03 ± 0.05
PuR-PuxB(A105R)[e]-Cyt *c*	[12]	114.7 ± 2.0	0.25 ± 0.02
PuR-HaPux-Cyt *c*	[154]	226.0 ± 3.9	2.00 ± 0.13
HaPuR-HaPux-CYP199A2	[154]	48.4 ± 1.9	0.53 ± 0.10

[e]The PuxB protein used in this study is the mutant PuxB(A105R), since this is the protein from which the crystal structure was derived. The values for the PuxB wild type are included here for completeness.

Although the electron transport chain in all cases contains three proteins reacting via two electron transport complexes, the systems exemplified in Table 4.1 are engineered such that one of the electron transport steps is much slower than the other and is thus rate limiting. K_M for these systems is therefore dependent on the formation of and the electron transfer within only one of the docked protein complexes. It is therefore possible to use the approximation $K_M \approx K_d$ and Equation 4.1, which considered the reaction between only two proteins. If we set [Protein1] = [Protein2] = [Total Protein], at equilibrium K_M is approximately:

$$K_d \approx K_M = \frac{[\text{Free Protein}]^2}{[\text{Complex}]} \tag{4.6}$$

where [Free Protein] = [Total Protein] − [Complex]. The DEER samples had an approximate concentration of 300 μM for each of the proteins used. Hence, substituting this and rewriting the expression in terms of a quadratic equation based on [Complex], allows us to calculate the approximate amount of complex present in the sample under equilibrium conditions, by solving the quadratic equation (see Table 4.2).

Table 4.2: The predicted concentrations of each complex present in solutions with an initial concentration of 300 μM for each of the binding partners, calculated from the K_M values given in Table 4.1.

Protein complex	Concentration of complex in μM
PuR-PuxB(wt)	282.9
PuR-PuxB(A105R)[f]	291.5
PuR-HaPux	276.5
P450-HaPux	288.0

The K_M values were measured for proteins without spin labels attached. However, since the spin label sites were chosen so that they did not lie on the expected binding interfaces of the proteins, it is anticipated that they should not interfere with binding to prevent complex formation. Therefore, it is an acceptable approximation to use the K_M values of the unlabelled protein systems in this calculation.

[f]The PuxB protein used in this study is the mutant PuxB(A105R), since this is the protein from which the crystal structure was derived. The values for the PuxB wild type are included here for completeness.

A process of trial and error in recording the DEER measurements of these complexes has demonstrated that relative values of K_M greatly affect the quality of the DEER results recorded. It was very difficult to measure DEER data on the PuR-HaPux complex, which has the highest K_M value, and proved impossible on other similar complexes that were measured to have even higher K_M values. When K_M is set to be equal to K_d, the calculated concentrations of complexed protein present do not vary greatly. This indicates that setting $K_M = K_d$ may not be an appropriate approximation to make. K_d is a purely thermodynamic property, whereas K_M also considers the rate of reaction occurring in the complex. Setting $K_M = K_d$ requires that $\frac{k_{cat}}{k_1}$ is negligible with respect to $K_d = \frac{k_{-1}}{k_1}$ which may not be a valid assumption to make.

4.2 EPR experiments

DEER was measured in the first instance between the reduced $[Fe_2S_2]^+$ centre of the ferredoxin and spin labels attached to its binding partners, namely ferredoxin reductase and cytochrome P450. For measurements between an MTSL nitroxide and the reduced $[Fe_2S_2]^+$ centre, three to five DEER experiments with different pump-detection pulse separations were performed on each sample. This allowed the orientational selectivity provided by the $[Fe_2S_2]^+$ centre to be probed. It was generally found that the best signal-to-noise ratio for the spectra could be gained by detecting on the centre of the nitroxide signal and moving the pump pulse to sample different regions of the $[Fe_2S_2]^+$ spectrum, although some of the initial experiments using the PuR-PuxB system have the pump pulse positioned on the nitroxide maximum and detect at different positions across the $[Fe_2S_2]^+$ spectrum. The pulse frequencies and field positions used for the experiments on both systems are given in Appendix I, Table I.1 and Table I.2. A schematic diagram showing the pump and probe pulse positions in relation to the spectra of the HaPux-P450 system is depicted in Fig. 4.3.

The DEER experiments used detection pulses of 24–40 ns length, with a 12–24 ns pump pulse. The range in values originated from the fact that results were recorded at different times and on different spectrometers; power requirements vary both over time and between spectrometers.[g] Although, ideally,

[g]All of the data on the HaPux-P450 system was recorded as a consistent set in Oxford using detection pulses of 40 ns

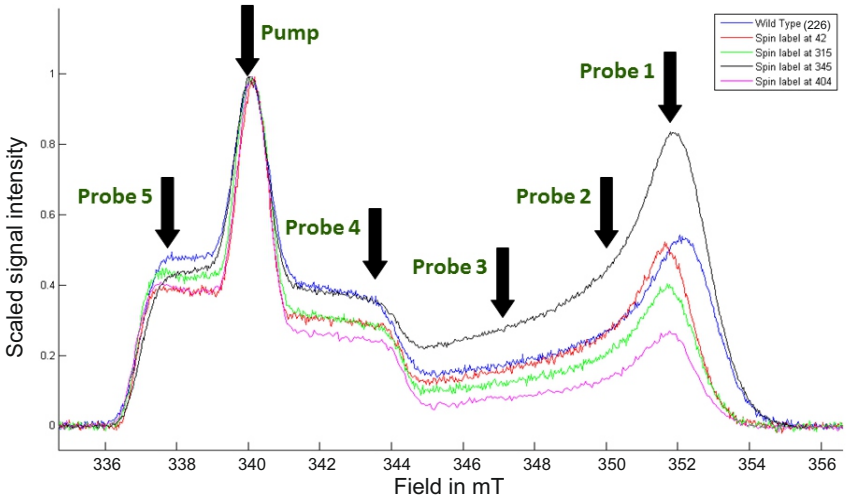


Figure 4.3: Hahn echo-detected field sweep spectra for the five differently labelled HaPux-P450 systems, with the positions of the pump and probe pulses highlighted. The overlaid spectra are normalized to the nitroxide maximum and show how the relative concentrations of the active $[Fe_2S_2]^+$ centre and nitroxide vary between samples. This is likely to have many sources, including incomplete labelling with MTSL, reduction of the spin labels by the reducing agent used to reduce the $[Fe_2S_2]$ centre (NAD(P)H in most experiments), incomplete reduction to form $[Fe_2S_2]^+$ and oxidation of this centre prior to freezing of the sample.

all of the experiments would use the same pump and detection frequencies and field values, in reality this is not possible, mainly due to the shape of the bandwidth of the resonator, which is not symmetric and varies with the degree of over-coupling used. Therefore, the pump and probe positions were shifted to ensure that the pulse length used could be consistent and also, in some instances, to avoid large ESEEM effects in the collected DEER traces resulting from pulse overlap. The frequency profile of the pulses is dependent on the resonator bandwidth. Therefore, experiments using different microwave frequencies and resonator coupling can result in pulses with slightly different profiles (particularly in terms of the extent of the 'sinc-wings'[h]).

Experimentally, it was found that the best temperature to record the DEER spectra was 25 K.

and pump pulses of 20 ns.

[h] A rectangular pulse in the time domain produces a sinc profile in the frequency domain ($\mathrm{sinc}(x) = \frac{\sin(x)}{x}$). True sinc functions will oscillate indefinitely and have an infinite bandwidth, the parts of the function oscillating outside the central peak are referred to as the 'sinc-wings'. However, as the pulse shape in the time domain tends towards a Gaussian function, the pulse profile also tends towards a Gaussian resulting in truncation of the 'sinc-wings' (a truncated sinc function). Although all pulses applied in the EPR experiments here are approximately rectangular in the time domain, the exact nature of the pulse is dependent on experimental conditions.

However, some of the early experiments were conducted at 50 K or 20 K, which, although having no effect on the modulated part of the DEER spectrum will affect the experimental background and also the signal-to-noise ratio of the traces. In particular, for experiments recorded at 50 K, T_1 relaxation during the DEER sequence is pronounced.

Initially, it was hoped that the orientationally selective DEER traces alone would be sufficient to define the docked complexes. However, initial fitting for the PuR-PuxB system, using only the orientationally selective $[Fe_2S_2]^{+}-NO^{\bullet}$ DEER traces, identified two possible conformations of the complex. As mentioned previously, in order to distinguish between these conformations, it was necessary to measure an additional DEER constraint between the two systems (see Fig. 4.4). To this end, HaPux was spin labelled at position 54 and two $NO^{\bullet}-NO^{\bullet}$ DEER experiments were performed for the HaPux-PuR[i] system [HaPux(54)-PuR(164) and HaPux(54)-PuR(303)], together with a single experiment for the HaPux-P450 system [HaPux(54)-P450(226)].[j] In all three cases, experiments were recorded at 50 K with an inter-pulse separation of 65 MHz, with the pump pulse applied in the centre of the $m_I = 0$ transition and detection occurring on $m_I = 1$.

4.3 Orientational DEER simulation

There are many parameters that affect the orientational effects in DEER spectra, namely the six spatial degrees of freedom: three positional ($x,\ y,\ z$ or $\theta,\ \phi,\ r$) and three angular ($\alpha,\ \beta,\ \gamma$; the Euler angles). The most computationally efficient method of analysis is to pre-compute a large library of simulated orientationally dependent DEER traces, the bounds of the library were determined by reference to the size of the protein-protein complex being analysed. Comparison of the experimental DEER data with the simulated traces allowed the determination of the relative orientations of the spin centres and the proteins with which they are associated. The procedure for generating a final docked structure is described in Section 4.6 and outlined in the flowchart presented in Fig. 4.14.

[i]Nitroxide labelling of PuxB was not possible due to poor expression of the protein with an additional cystein, thus it was necessary to use the structurally similar HaPux to partner PuR.

[j]For both the HaPux-PuR system and HaPux-P450 system, the numbers in the round brackets indicate the position of a cysteine that is spin labelled with the nitroxide MTSL.

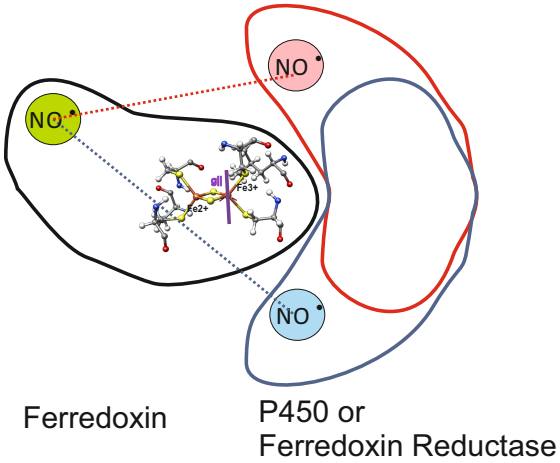


Figure 4.4: The $[Fe_2S_2]^+$ has an axial g-tensor, which is orientated with the $g_{||}$ component (shown as a purple line with relation to the $[Fe_2S_2]$ cluster) approximately perpendicular to the plane of the central $[Fe_2S_2]$ cluster (see Chapter 5 for determination of this orientation). This has the result that for a spin labelled protein docking to a reduced ferredoxin (black outline), the DEER spectra measured can be matched to many different orientations of the two proteins. Some of the possible orientations can be discounted by measuring multiple $[Fe_2S_2]^+$-nitroxide distances for different nitroxide labelling sites. Others can be discounted when the surrounding protein structure is considered, since the structures of the two proteins cannot penetrate into one another significantly. However, using only the $[Fe_2S_2]^+$-nitroxide restraints, it was found that two possible configurations of the proteins with respect to one another were found. These are represented schematically in the diagram by the red and blue outlines, where the pink and pale blue circles labelled $NO^\bullet$ represent two nitroxide labelling sites on each docking configuration. The two docking configurations can be distinguished by adding a labelling site to the ferredoxin (green circle labelled $NO^\bullet$) and measuring the distance between this label and one of the labelling sites on the binding partner, which is different for the two possible docked configurations (red and blue dashed lines).

4.3.1 Simulation of orientationally selective DEER libraries

The orientationally selective DEER traces were simulated using OriDEERSim, a MATLAB-based program that was written in-house. Details of this program are given in Chapter 2 and its application to copper centres detailed in Chapter 3. To calculate orientation selection, the program uses as inputs the parameterized information from the CW spectra of the two centres: g-values, hyperfine values and line widths.

The spin density for the nitroxide was localized on the nitrogen of the MTSL spin labels, the positions of which were calculated using MMM, as described in the following section. For the $[Fe_2S_2]^+$

Table 4.3: Fitting parameters extracted from CW spectra using EasySpin for the $[Fe_2S_2]^+$ cluster and nitroxide portions of EPR spectra for the HaPux-P450 and PuxB-PuR complexes. It should be noted that for the $[Fe_2S_2]^+$ centre, hyperfine interactions could not be resolved, but still contribute to the line broadening (HStrain). For the nitroxide, the hyperfine coupling to the nitrogen is resolved in the CW spectrum. However, this is neglected in the orientational DEER simulations, where isotropic excitation of the nitroxide centre is assumed.[k]

$[Fe_2S_2]^+$			
Parameter	x-component	y-component	z-component
g-values	1.934	1.934	2.025
H strain (line broadening) [MHz]	65	65	25
Nitroxide parameters			
Parameter	x-component	y-component	z-component
g-values	2.009	2.009	2.009
H strain (line broadening) [MHz]	25	25	25

cluster, the distribution of spin density is more complex as there is delocalization of the magnetic orbitals over not only the two iron and two sulphur centres in the cluster but also over the sulphurs of the four ligating cysteines. A detailed ENDOR and HYSCORE study was required to specify the correct location of the spin density within the structure and also the orientation of the $[Fe_2S_2]^+$ cluster with respect to its g-matrix. This study is described in Chapter 5 and the main results for all the models trialled in this study are given in Table 5.3. The results used as input for the orientational DEER simulations, the relative positions of the atoms within the $[Fe_2S_2]^+$ in the orientatiomnal frame of the g-tensor and the spin densities on each atom, are summarized in Table 4.4. The orientation of the g-tensor with respect to the molecular structure is shown in Fig. 5.11. (The results shown in Table 4.4 and Fig. 5.11 correspond to Model 3.)

In the simulations, the nitroxide centre was isotropically excited by a non-selective pulse to remove any orientation selection for this spin. In reality, the pulses exciting this centre would be narrower than that used in the simulation. However, it is assumed experimentally that by setting the frequency of the pulses equal to that of the centre of the nitroxide signal on $m_I = 0$, the pulse will excite the

[k]When isotropic excitation is used, all contributions are excited equally and as such the hyperfine splittings do not affect which portions of the spectrum are excited, therefore the hyperfine coupling can be neglected from the calculation to simplify the model.

Table 4.4: Relative positions and spin densities of the component atoms in the $[Fe_2S_2]^+$ cluster and the ligating sulphurs, given in the orientational frame of the g-tensor.[15]

Atom	Positional coordinates [x,y,z]	Spin density
Fe^{3+}_{ox}	[0,0,0]	+1.5554
S_{ox}	[-1.3677,0.4579,-1.9555]	+0.0894
S_{ox}	[-1.6729,-0.6980,1.6465]	+0.0894
Fe^{2+}_{red}	[2.6869,0,0.1505]	−0.841
S_{red}	[3.9069,-0.8986,2.0111]	−0.030
S_{red}	[4.2024,0.7678,-1.4739]	−0.030
S_{FeS}	[1.3851,-1.6040,-0.7058]	+0.0834
S_{FeS}	[1.2979,1.6148,0.8541]	+0.0834

entirety of this component and as such all orientations of the flexible nitroxide spin will be excited and the orientational information will be removed.

A truncated sinc function was used to model the frequency domain pulse shape for the pulses applied to the $[Fe_2S_2]^+$ centre. This pulse causes only partial excitation of this centre, corresponding to a few orientations of the $[Fe_2S_2]^+$ g-tensor with respect to the static magnetic field vector. A plot of this pulse selectivity is shown in Fig. 4.5.

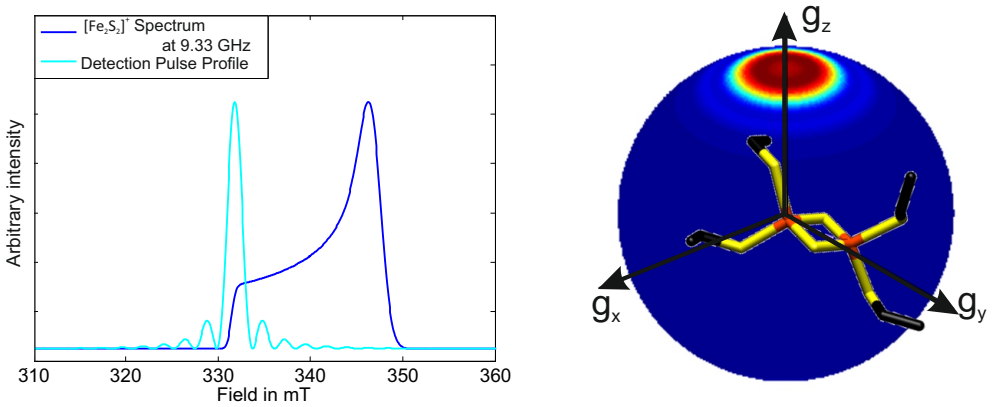


Figure 4.5: Left: A plot of the sinc function (light blue) used to represent the frequency profile of a pulse superimposed on the CW EPR spectrum (dark blue) of the $[Fe_2S_2]^+$ paramagnetic centre. Right: A sphere representing the orientations of the g-tensor field with respect to the B_0 excited by the pulse given in the figure on the left. Red regions demonstrate high excitation and blue regions low excitation. This pulse primarily excites the z-portion of the g-tensor. The structure of the $[Fe_2S_2]$ cluster is shown with respect to the g-tensor axis system.

The final parameters required by the simulation program were the relative frequencies of the pump and probe pulses for each experiment, the magnetic field strength used in the experiment and the pulse lengths. Although the experiments were not all recorded with the same frequencies and fields, using standardized gaps between the two frequencies reduced the number of DEER traces that needed to be calculated, and allowed a standardized look up library to be used. Provided that the frequencies and fields are chosen such that the pulses are applied at the same positions relative to the EPR spectrum, in each case, the DEER spectra collected will probe the same orientations of spins for each type of experiment. The field and frequency values used in the calculation of the standardized look up libraries for the orientationally selective measurements taken on each of protein system are listed in Tables 4.6 and 4.5.

Table 4.5: Pulse frequencies and fields used in the simulation of the DEER library for the PuR-PuxB complex.

Experiment number	Pump frequency (GHz)	Detection frequency (GHz)	Static field value (mT)	Pulse separation (MHz)
1	9.1800	9.5150	338.4	+335
2	9.1800	9.4200	335.0	+240
3	9.1800	9.3300	331.8	+150
4	9.2550	9.3300	331.8	+75
5	9.3950	9.3300	331.8	−65

Table 4.6: Pulse frequencies and fields used in the simulation of the DEER library for the HaPux-P450 complex.

Experiment number	Pump frequency (GHz)	Detection frequency (GHz)	Static field value (mT)	Pulse separation (MHz)
1	9.2355	9.5650	340.2	+330
2	9.2355	9.4829	337.2	+248
3	9.2855	9.4500	336.1	+165
4	9.3800	9.4603	336.4	+80
5	9.3800	9.3151	331.3	−65

For the PuR-PuxB system, some of the frequency separations used in the experiments did not

conform exactly to the simulated library data.[1] However, due to the line broadening of the $[Fe_2S_2]^+$ spectrum and the fact that the applied pulses have widths of several tens of MHz, these small deviations will have no significant effect on the final data fitting.

4.3.2 Simulating the nitroxide-nitroxide DEER for MTSL

Unlike DEER measured between the electron localized on the $[Fe_2S_2]^+$ spin centre and that in the nitroxide of MTSL, when two MTSL labels are used, the flexibility of these centres and the relatively narrow width of the nitroxide spectrum in relation to the applied pulses means that no angular contribution to the DEER trace needs to be considered. The modulated part of the DEER trace can simply be modelled using the analytical expression for the dipolar frequencies averaging over all angles. This produces a complete Pake pattern for each distance considered.

Orientationally dependent spectra simulated using the MATLAB-based program, described previously in Chapter 2, include both a modulated and an unmodulated contribution to the DEER spectrum. The modulated part arises from orientations of the spin centres where both spins are excited and the unmodulated contribution comes from orientations where only the detection spin is excited. The simulation program is therefore able to predict relative modulating depths for different spectra collected on the same sample. However, it is still necessary to calibrate these modulation depths to the experimental conditions used; resonator bandwidth, labelling efficiency, etc., in order to predict the experimentally observed modulation depths. Calculations using the analytical dipolar formula, which assumes isotropic excitation of the two centres, do not include an unmodulated part, since all detection spins are assumed to have a corresponding pump spin that is excited. In order to fit data simulated using the dipolar formula alone to experimental data, it is necessary to add an unmodulated part to the spectrum (see Section 4.6), whereas the modulation depth for spectra calculated using the orientationally selective calculations can be corrected by multiplying the spectra by a constant factor (see Equation 3.2).

[1]The spectra on the PuR-PuxB system were collected prior to the development of the analysis method. At the time the measurements were recorded it was not apparent how intensive the analysis methodology would be and therefore the requirement for all of the traces to correspond to a standard set of experimental frequency separations was not identified until part way though the experimental process.

4.4 Calculation of spin label rotamer distributions

The program MMM from the Jeschke laboratory at ETH, Zürich,[80,81] was used to calculate the spin label rotamer distributions from the crystal structures of the proteins. The PDB structures were prepared for the MMM calculation by removing the His-Tag from the PuxB (*3HUI.pdb*) structure, removing the Glycerol (GOL) cofactors from the PuR (*3FG2.pdb*) structure and the solvent molecules in all cases.[m] It should be noted that MMM does not take into account any hydrogen in the structure; the scoring parameter for the Lennard-Jones potential of all hydrogens is set to zero. This may in part be the cause for the overly broad MMM distributions that appear to be observed in many cases.

MMM works by attaching a library of pre-computed MTSL spin label configurations from a short peptide chain, containing the MTSL spin label, to the specified labelling sites. The MTSL conformers are scored at the attached site using Lennard-Jones potentials to produce a library of possible MTSL configurations that are given an occupation number corresponding to the probability of finding a spin label in a particular site. The probability of finding a given rotamer is determined by Boltzmann distribution: $p_i = \frac{g_i \exp\left(-\frac{\epsilon_i}{kT}\right)}{\sum_j g_j \exp\left(-\frac{\epsilon_j}{kT}\right)}$, where the calculated energy of the most populated rotamer (with population p_{max}) is set to zero and the relative energies of the remaining rotamers (ϵ_x) are used to calculate the probability that a nitroxide label occupies these rotamers (p_x). The statistically significant conformers are said to be those that are in the top 99.5%; it is only these conformers that were considered in the DEER fitting procedure.

Fig. 4.6, Fig. 4.7 and Fig. 4.8 show the results of the MMM modelling for the PuR and P450 proteins. MMM calculations were performed on the two P450 crystal structures, with and without substrate bound. Comparison of the results for the two structures does not show any significant differences between the two data sets.

[m] Although it is not strictly necessary to remove the solvent molecules from protein structures used for MMM calculations, since solvent molecules are discounted from MMM calculations by the program itself, removal of the bound solvent molecules at this point allowed the same structure files to be used in the protein docking calculations, where the solvent molecules were not required.

PuR labelling site	Colour
82	Magenta
135	Blue
164	Lime Green
196	Red
249	Black
281	Cyan
303	Orange
309	Purple
347	Dark Green

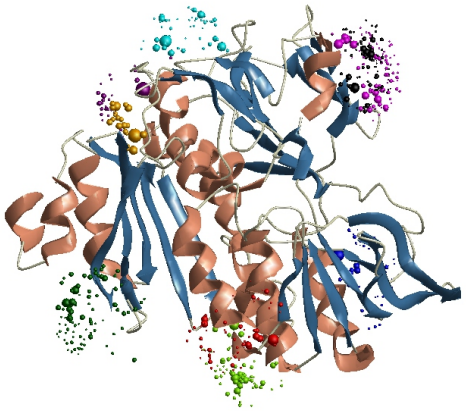


Figure 4.6: Spin label locations predicted by MMM for PuR (*3FG2.pdb*); the coloured balls represent the spin density location and the size of the ball is proportional to the occupation of the nitroxide rotamer. The different colours of the spin densities correspond to different labelling sites.

P450 labelling site	Colour
42	Magenta
226	Blue
315	Lime Green
345	Red
404	Black

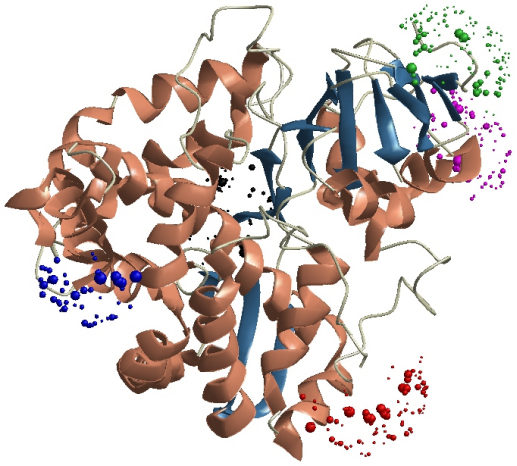


Figure 4.7: Spin label locations predicted by MMM for cytochrome P450, CYP199A2 (*2FR7.pdb*); the coloured balls represent the spin density location and the size of the ball is proportional to the occupation of the nitroxide rotamer. The different colours of the spin densities correspond to different labelling sites.

P450 site	labelling	Colour
42		Magenta
226		Blue
315		Lime Green
345		Red
404		Black

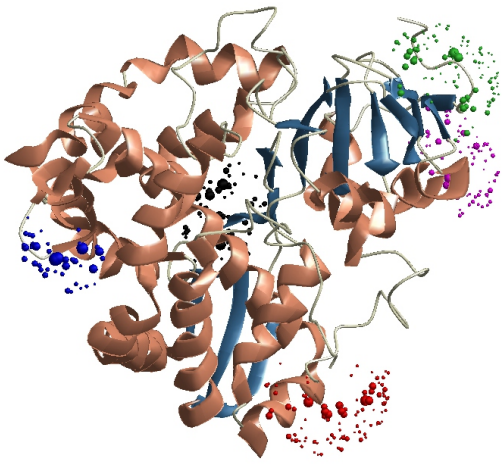


Figure 4.8: Spin label locations predicted by MMM for cytochrome P450, CYP199A2, with a methoxybenzoate substrate bound and a chloride ion blocking the substrate access channel (*4DNJ.pdb*); the coloured balls represent the spin density location and the size of the ball is proportional to the occupation of the nitroxide rotamer. The different colours of the spin densities correspond to different labelling sites. The colours used are the same as for the P450 without substrate bound.

4.4.1 Comparison of the spin label ensembles for PuxB and HaPux

Since it proved impossible to produce PuxB with a cysteine mutagenesis at an appropriate site, it was necessary to use HaPux to provide the nitroxide-nitroxide restraints for the ferredoxin-ferredoxin reductase system. The $NO^{\bullet}-NO^{\bullet}$ HaPux-PuR data was analysed in conjunction with the PuxB-PuR orientationally selective DEER traces. Modelling the spin label distribution at site 54 for both HaPux and PuxB shows that small differences between the two protein structures lead to different rotamer distributions for labelling at the same residue (see Fig. 4.9).

There is a difference in the weighted average spin label position of 0.0676 nm between the spin label libraries for PuxB and HaPux when the locations of the two iron sulphur centres are superimposed. In order to analyse the data recorded on the PuxB-PuR and HaPux-PuR systems simultaneously, it was necessary to generate a single model to be used in the protein-protein docking fitting procedure. To generate this model, it was assumed that the $[Fe_2S_2]$ cluster for the HaPux and PuxB would adopt

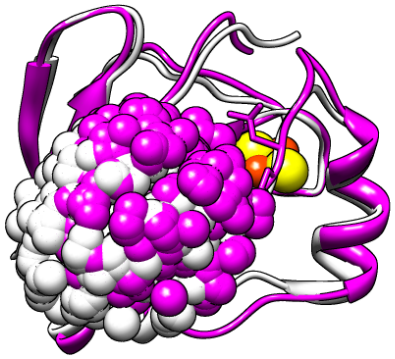


Figure 4.9: Comparison of the spin label libraries generated for the proteins PuxB (in white) and HaPux (in purple), labelled at site 54. The position of the nitroxide oxygen's are marked with spheres in the same colour as their corresponding structure. The position of the $[Fe_2S_2]$ cluster (shown in orange (Fe) and yellow (S)) in each structure were overlapped and it can be seen that the PuxB has a skew of nitroxide positions to the right and similarly for the HaPux to the left.

the same relative position with respect to the PuR in both complexes and therefore the calculated spin label positions for the HaPux in the reference frame of the PuxB $[Fe_2S_2]$ were used for the fitting procedure.

It should be noted that the difference in weighted average spin label position between PuxB and HaPux is relatively small. Therefore, any error caused by using the HaPux value for the determination of the PuxB docked structure is unlikely to be as significant as the uncertainty in the spin label positions themselves, which is modelled by the distribution of spin labels generated by MMM.

4.4.2 The reliability of MMM

Recent work at Oxford University by Lillington et al. has shown that MMM is not always accurate for predicting the most likely conformation for the MTSL spin label in sites where the spin label can adopt a conformation that is stabilized significantly by interactions with the protein surface.[156] These types of surface interactions are generally more important for labelling sites that are less solvent accessible. Therefore the probability of the MMM calculation result being wildly inaccurate is greatly reduced by selecting sites for MTSL labelling that are solvent accessible. Although imperfect, MMM provides

a computationally very affordable and fast option to generate a distribution of the spin labels with respect to the protein structures. Another possibility is to use the C_α positions directly from the crystal structure. However, these will be much closer to the protein backbone than the actual position of the nitroxide spin density. Alternatively, Molecular Dynamics (MD) simulations could be used for the MTSL label attached to the surface of the protein. In order to sample enough of the conformational space, these simulations would need to be very long and if the simulations are atomistic the cost of running such calculations would be significant. The computational time could be reduced through the use of coarse-grain or fixed backbone calculations. However, this could potentially introduce some inaccuracies into the results.

For these experiments, as a method of checking the reliability of the MMM distributions, two doubly-labelled mutants of PuR (with MTSL labels attached at 82-303 and 249-303) in complex with PuxB, in the oxidized EPR silent state, were prepared and DEER measured. The data from these mutants was analysed with DeerAnalysis,[45] and the results compared to the distributions generated using MMM calculated for the PuR crystal structure (*3FG2.pdb*). The results are shown in Fig. 4.10. In both cases, the distribution predicted by MMM was far broader than that measured experimentally, and thus the DEER modulations in the MMM predictions die off far faster than those observed experimentally.

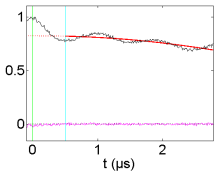
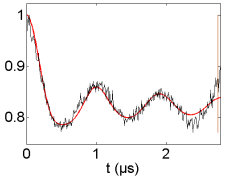
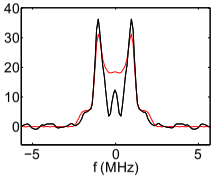
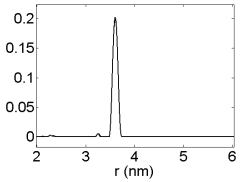
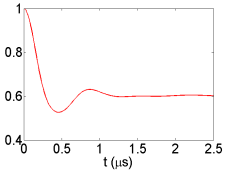
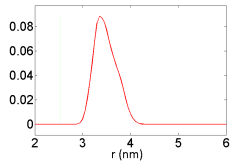
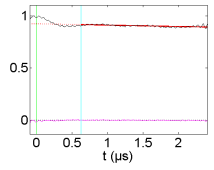
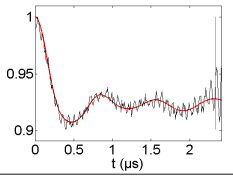
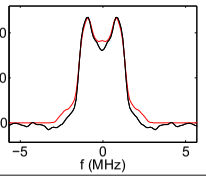
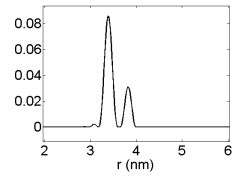
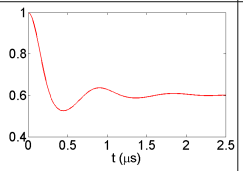
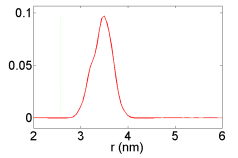
Mutant	Raw DEER data	Background corrected DEER	Experimental frequency domain data	Experimental distance distribution	MMM predicted DEER trace	MMM predicted distance distribution
82-303						
249-303						

Figure 4.10: Comparison of experimental DEER traces with those predicted by MMM for the PuR mutants with MTSL labelled cysteines at 82-303 and 249-303. In both instances, the MMM predicted distribution, although occurring at the same average distance, is much broader than that extracted from the experimental data by Tikhonov regularization. In addition the experimental results for 249-303 show a bimodal distribution, which is not well resolved in the MMM predictions.

A second sample of the doubly-labelled PuR 82-303 in complex in the absence of any Ferredoxin was also prepared in order to investigate whether any changes in the nitroxide distance distribution occurred on binding of the PuR to PuxB, since the DEER on the complexed and uncomplexed samples could be compared. Any changes in the measured distance distributions would indicate structural changes on binding, which would render the rigid-body technique used for docking invalid with respect to these systems. No significant changes in the distance distribution were seen; the results are shown in Fig. 4.11. Therefore, it appears to be appropriate to use rigid-body docking as a first approximation in the formation of the complex structure for these systems.

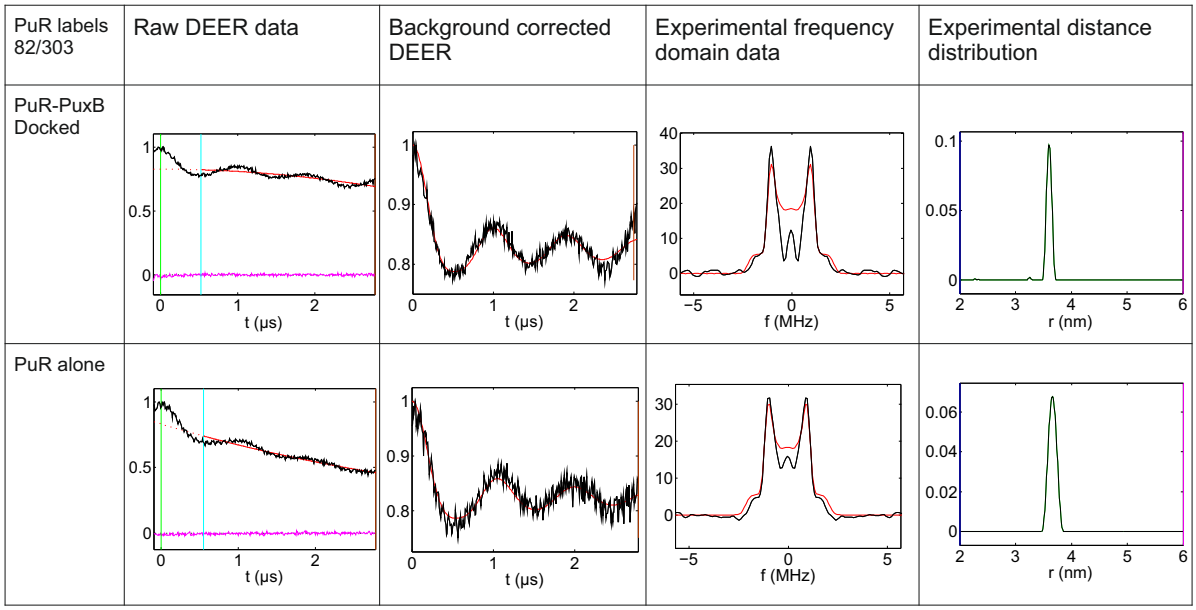


Figure 4.11: Comparison of DEER data collected for the PuR mutant 82-303, doubly-labelled with MTSL, for the PuR protein alone in solution and also docked to EPR silent oxidized PuxB.

4.5 Generating initial starting structures for fitting

Fitting the multiple experimental data sets to simulated data using fixed relative orientations of the labelling sites within each protein, but variable positions of the two proteins with respect to one another in order to produce a docked protein complex structure is a complicated problem. Many local minima will exist in the space spanned by the fitting parameters (three positional (θ, ϕ, r) and three angular

(α, β, γ)). In order to find the global minimum, it is initially necessary to generate starting structures for the docked complex that are likely to be close to the global minimum structure and also which are reasonable in terms of the protein complex (i.e. the proteins cannot be overlapping in space or the electron transfer centres must be in close contact). In previous studies of this type, the whole parameter space has been sampled in order to find appropriate solutions for the docked complex.[136] Although that would be possible, in this case we are also privy to biochemical data, in particular mutagenesis data, which can help to define the docking interfaces of the proteins in the complex. In order to make use of this data to reduce the conformational subspace that must be searched for an appropriate solution, protein-protein docking software was used to generate possible starting structures for refinement using the DEER data, as described in the following section.

4.5.1 PatchDock and FireDock

There are many programs available that are designed to produce models of docked protein complexes, such as those formed between two proteins, proteins and small molecules, proteins and nucleic acid structures, etc. Some docking programs are available as online servers to which users can submit structures of the binding partners and in some cases parameters to guide the docking program, such as interfacial residues or distance constraints. The unpublished nature of the HaPux structure prohibited the use of such servers, where information can be seen by other users. Therefore, the freely downloadable PatchDock[157,158] and FireDock[11,159] suite was used to calculate structures of the docked complexes on a local computer and to refine the initial docked structures. All of the complex structures generated, both the initial and refined, were used as starting points for fitting to the DEER data.

PatchDock is used initially to generate structures via rigid-body docking, where the structures of the two proteins are held constant and the shapes of the surfaces fitted together like a jigsaw puzzle. The output structures from PatchDock can be refined using FireDock, which tackles the problem of flexibility by performing side chain optimizations where the positions of the side chains can be modelled using pre-calculated rotamers in order to reduce side chain–side chain clashes. Either a restricted interface side-chain optimization (RISCO) or a more computationally intensive full interface

side-chain optimization (FISCO) can be used. Once the clashes have been removed, the positions of the backbones with respect to one another are re-optimized.

For this research, both the initial output from PatchDock and the outputs from the restricted and full side-chain optimizations were used as starting structures for the analysis of the experimental DEER data (see Fig. 4.12). Further information of the processes used by PatchDock and FireDock are given in Appendix J.

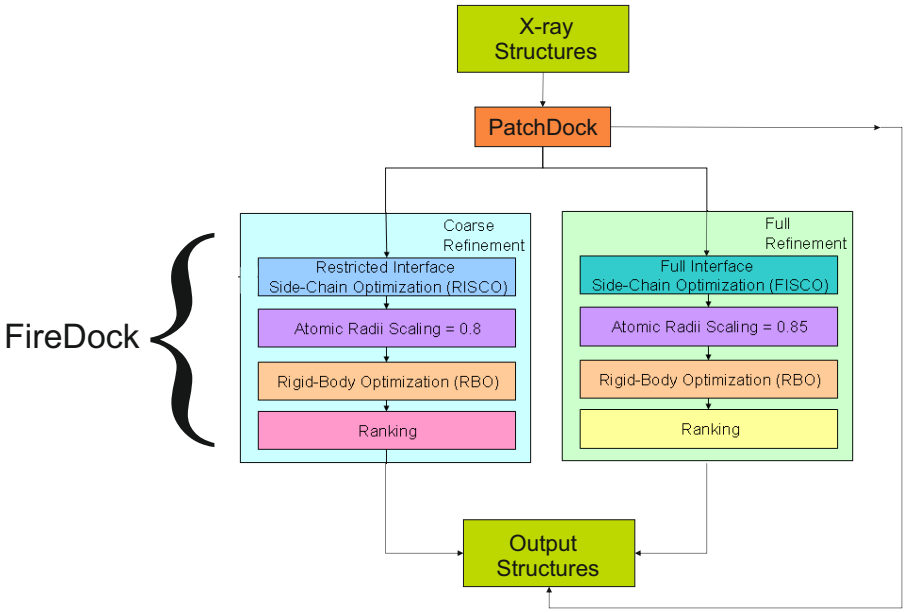


Figure 4.12: A schematic flowchart showing the procedure for generating the docked structures, defined as the output structures in the diagram above, that were used as initial inputs for analysis based on the experimental DEER data. PatchDock is used initially to dock the two proteins (using biochemical data to specify the docking interfaces, see Section 4.5.3). The initial structures are then refined using either a coarse Restricted Interface Side-Chain Optimization (RISCO) or a Full Interface Side-Chain Optimization (FISCO). The output from all three calculations form the output structures that are used as the input for further analysis and refinement utilizing the experimental DEER data. This figure is adapted and reproduced from *http://bioinfo3d.cs.tau.ac.il/FireDock/firedock.html* and *Proteins: Structure, Function, and Bioinformatics*, 2007, **69(1)**, N. Andrusier, R. Nussinov, H. J. Wolfson, FireDock: Fast interaction refinement in molecular docking. Copyright © 2007 Wiley-Liss, Inc., with permission from John Wiley and Sons.[11]

Both programs rank the output structures based on an internally calculated binding score, which takes into account softened Van der Waals interactions, short-range and long-range Coulombic electrostatic forces, atomic contact energies,[160] hydrogen and disulphide bond formation, cation$-\pi$ and

$\pi - \pi$ stacking, aliphatic interactions, an 'insideness' measure that considers how deeply one protein penetrates into the other and the internal energy of the system. However, this ranking was not used in analysing the structures for agreement with the DEER experimental data.

The decision not to be influenced by the binding score rankings of the docked structures was taken in order not to bias the experimentally derived complex, since the docking and the scoring method are not parameterized for the cofactors within the proteins. Hence, the cofactors are ignored in the docking process; in terms of changing the shape of the protein surface, this does not have a great effect since the cofactors have little surface accessibility. However, as the cofactors are known to be the electron transport centres for the proteins, it is likely that these cofactors will be close to or even on the binding interface and their presence will most likely influence the electronic properties of the binding interface. Since the cofactors features are not included in the binding score, the accuracy of the score for these proteins is likely to be low and it was not possible to rank the structures produced with any certainty. Therefore, all of the structures generated from the restricted docking procedures (those where the binding interface was specified) were used as potential starting structures for fitting and analysed in comparison to the DEER data. The structures were then ranked in accordance with their ability to reproduce the DEER traces.

Neither PatchDock nor FireDock is parameterized to include the spin labels. Therefore the structures used for the docking did not include the spin labels. The label rotamer distributions were calculated for the input protein structures using MMM and the positions of the spin label distributions rotated to match the final positions of the proteins in the docked complex.

4.5.2 Choosing parameters to direct the docking

Unconstrained docking of PuR to PuxB or HaPux to P450 in PatchDock produced c. 30,000 structures in each case. Although it would be possible to calculate the DEER traces for each structure and compare all of them to the experimental data, this process would be lengthy. Furthermore, many of the structures formed from docking of the two proteins when no restraints are supplied could not possibly be responsible for the electron transport as the distance between the two redox centres is too

great. Since the parameter space in which the final docked complex must exist is much smaller than the parameter space used in unconstrained docking (which itself is smaller than the complete parameter space of positioning two proteins close to one another when the solid nature of the proteins is not considered) it is wise to use constraints in the docking process to control the size of the parameter space searched and thus limit the number of docked complexes produced, such that those found are reasonable with respect to experimental knowledge.

PatchDock allows both distance constraints and interfacial residues to be defined in the docking process. Previous docking studies using DEER data to define the structure of a protein-protein complex have only used nitroxide labelling and thus it was possible to extract distances directly from the DEER data, which could then be used to generate a structure.[136] However in this study, the use of the $[Fe_2S_2]^+$ as an innate spin label with its orientational dependence means that extraction of a distance without considering any angular dependence will not be reliable. PatchDock does not allow for angle constraints and thus if the DEER information was used to directly construct the docked complexes utilizing PatchDock, this information would be lost. More importantly, PatchDock does not have parameterization for MTSL spin labels, therefore it would only be possible to consider the distances between the backbone or side chains of the amino acids present at the labelling sites.

There are some docking programs available, notably HADDOCK v.2.1 onwards,[161] which allow the explicit inclusion of spin labels. However, it is only possible to consider one rotational conformation of each label per docking procedure, rather than the overall distribution present which gives rise to the observed DEER spectra. In order to model the rotamer distribution using this approach, it would be necessary to include uncertainties in each of the distance restraints that are large enough to cover the range of the distribution of distances between two centres. The use of distance constraints without uncertainties could result in structures that are closely related to the correct docked structure being discounted as incompatible with the supplied constraints, as frequently it is the position of the MTSL spin label that provides the largest source of error in DEER distance measurements.

Due to the problems specified above, it was decided not to employ distance restraints in the docking calculations which produced the library of initial 'starting-guess' docked complexes. The experimental

DEER data is still the primary source of information allowing the identification of the correct complex structure for the systems studied, and the pre-docked complexes from PatchDock were used as a comprehensive set of initial guesses, which were refined with respect to the experimental DEER data (see Section 4.6).

Instead of using distance restraints to in generation of the starting-guess library, it was decided to specify residues that were likely to form interface contacts. These residues have been identified from a large number of mutagenesis experiments that have been carried out on the systems used in this DEER study and other closely related systems. Using the interfacial contacts as a method to direct the docking in PatchDock reduced the number of possible structures from c. 30,000 to c. 2,000. This method also allowed biological information derived from a second source, which alone could not define the binding structure, to influence the eventual structure formed as a result of the orientationally selective DEER traces. The use of this information improves the likelihood of any obtained structure being biologically relevant.

4.5.3 The use of biochemical information

The X-ray structures of all the proteins used in this work are known (see Fig. 4.13). From these structures it is possible to calculate the electrostatic surface charges. PuR and P450 both have large areas of positive potential close to their prosthetic groups and the ferredoxin has a region of negative potential surrounding the $[Fe_2S_2]$ cluster (see Fig. 4.13 b-d, where the prosthetic groups are highlighted in green). It is likely that these areas of opposite charge will be involved in the binding interactions in the PuR–ferredoxin and ferredoxin–P450 complexes. Thus these charged areas can aid in the identification of the binding sites.

In order to investigate the contribution of specific residues to the protein-protein interactions involved in complex formation, biochemical studies have been conducted in which specific residues thought to lie on the binding interface have been mutated and the rates of protein turnover (K_M) measured for proteins with and without mutations. These experiments have shed light on those residues that appear to stabilize the docked protein complexes.

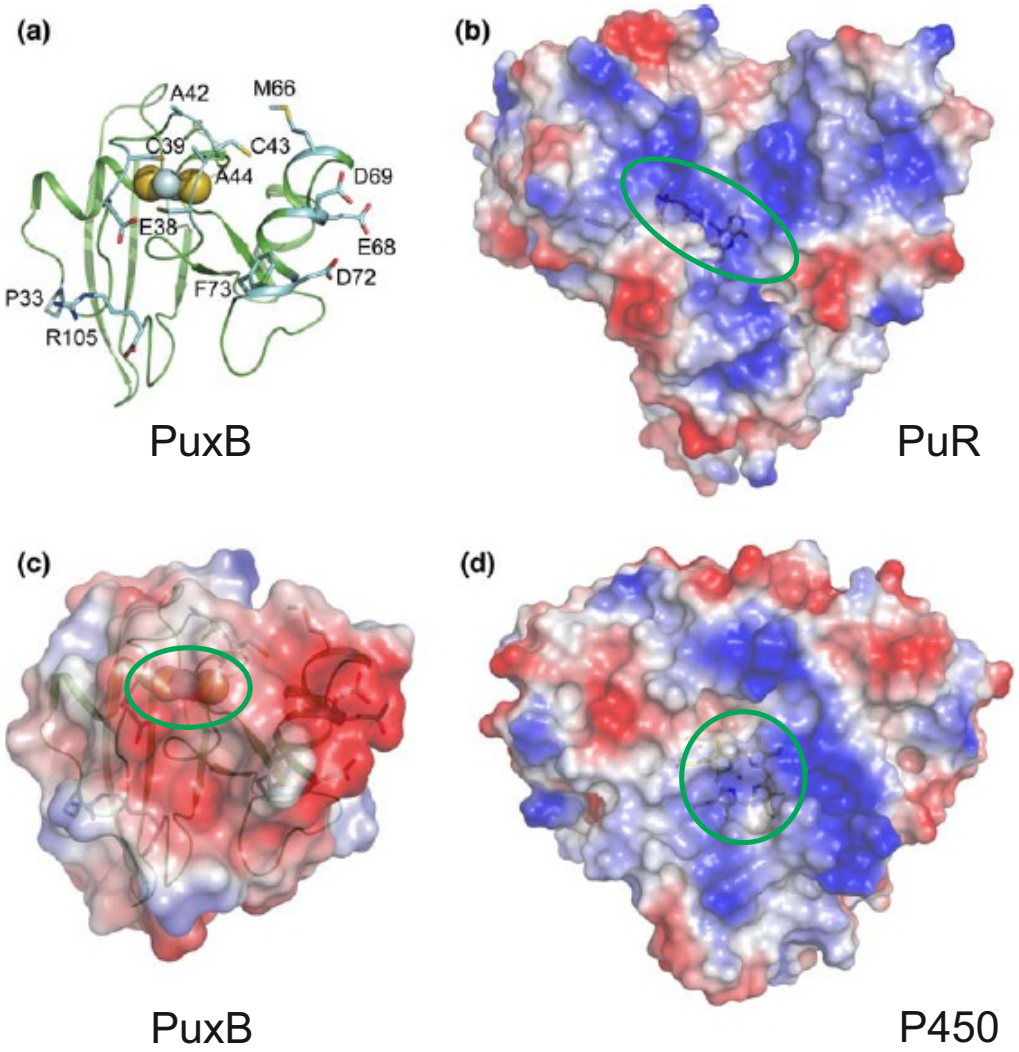


Figure 4.13: **(a)** The structure of PuxB showing some surface residues that may be involved in protein recognition. **(b)** The vacuum electrostatic potential surfaces of the FAD *si*-side surface of PuR (*3FG2.pdb*) where the FAD prosthetic group (circled in green) is closest to the surface. **(c)** The vacuum electrostatic potential surfaces of PuxB in the same orientation as in (a). The $[Fe_2S_2]$ cluster is highlighted in green. **(d)** The vacuum electrostatic potential surfaces of the heme proximal surface of CYP199A2 P450(*2FR7.pdb*).[12] The heme centre is circled in green. For the electrostatic potential surfaces, areas of negative potential are shown in red and areas of positive potential in blue. This figure is reproduced from *Journal of Biological Inorganic Chemistry*, published by Springer, **15(3)**, 2010, 315–328, Protein recognition in ferredoxin-P450 electron transfer in the class I CYP199A2 system from Rhodopseudomonas palustris, S. G. Bell, F. Xu, E. O. D. Johnson, I. M. Forward, M. Bartlam, Z. Rao and L.-L. Wong, Figure 6. Copyright © SBIC 2009; with kind permission from Springer Science and Business Media.[12]

A lot of mutagenesis work has been carried out on the protein PuxB.[12] The mutagenesis sites leading to changes in the observed K_M values for complexes with PuR and CYP199A2 P450 are detailed in Fig. 4.13 a. Thus, those residues important for the binding can be confidently identified. These are the residues labelled in the structure shown in Fig. 4.13. HaPux has a very similar structure; therefore, by mapping the two structures and sequences onto one another, as seen in Fig. 5.28, it is possible to identify residues or types of residues that occur at the same points in the protein structure. From this comparison, the likely interfacial residues in PuxB can be identified.

Relatively little is known about the binding interfaces of PuR and P450. The mutation K328G (Lys328) on PuR has been shown to significantly increase the K_M value for the binding of PuR to Pux, by almost a factor of 10 from 4.2 μM to 36.2 μM.[150] Furthermore, an almost opposite decrease in the K_M value for the complex PuR-Pdx is observed for the same mutation. It is therefore a fair assumption that in order for this residue to affect the K_M value of complex formation in both cases, in spite of the effect being opposite, this residue is likely to lie in or close to the PuR binding site for both Pux and Pdx. Pux and Pdx are structurally similar to HaPux and PuxB; therefore, there is a high probability that the binding site on PuR for all proteins will be similar. Recent mutagenesis work by members of the Wong group has also indicated that for P450 CYP199A2, the mutation of the residue R285 (Arg285) leads to changes in the K_M value of the P450 CYP199A2 complex formed with HaPux. (This work is currently unpublished.) It is therefore likely that Arg285 lies on the binding interface of P450 CYP199A2.

From mutagenesis experiments on PuR and P450 CYP199A2, it is only possible to identify one residue involved in the interaction with ferredoxins. Although specific information on additional residues that are important for binding is not known, the approximate binding interface itself can be identified as the face of PuR or P450 where the redox active cofactor is closest to the protein surface. It is therefore possible to specify residues on this surface in order to define the binding interface. Due to the greater uncertainty of the information in both PuR and P450, two sets of interfacial residues were specified for both proteins, which defined slightly different binding surfaces, in order to generate a larger number of possible starting structures for refinement using the distance and angular information

from the DEER traces. The residues used to specify the binding interfaces for the initial PatchDock calculations are given in Table 4.7

Table 4.7: The residues used to specify the binding interfaces for the initial PatchDock calculations.

Protein system	PuxB	HaPux	PuR		P450	
			A	B	A	B
Interface residues	33	36	41	41	111	285
	38	38	44	44	285	360
	39	42	301	321	360	364
	42	43	321	328	364	
	43	44	328	378		
	44	66				
	66	69				
	68	72				
	72	105				
	73					
	105					

The various calculations using PatchDock and FireDock with different interfacial residues specified occasionally brought up repeated structures. These were removed prior to the use of the structures in the analysis of the experimental DEER traces.

4.6 Fitting the simulated data to the experimental data

The overall method for finding the docked complexes used here is similar to that utilized by Hilger and co-workers. They used sparse distance constraints and rigid-body docking to form a model of the structure of the Na^+/H^+ antiproter dimer.[136] However, there are a few key differences in the methods; whereas Hilger et al. used model free extraction of the spin label to spin label distances, and then used these distances to search the parameter space for possible docked structures. In this study, initial starting structures were generated using PatchDock and FireDock, and the parameter space of possible docked structures was limited by the inclusion of biochemical data, as described in the previous Section 4.5. In both the Hilger study and this work, the initial structures were refined using direct fitting to the dipolar evolution traces from the experimental data set. A flowchart detailing the

methodology used in this study is given in Fig. 4.14.

For each starting structure complex, the pre-calculated spin label distributions were added. Using this starting orientation of the two proteins, the DEER traces were calculated for both the orientationally selective traces measured between nitroxide and $[Fe_2S_2]^+$ and the non-orientational $NO^\bullet - NO^\bullet$ trace(s). For the orientationally selective DEER data, the position of each nitroxide rotamer within the distribution of a single spin label was calculated with respect to the $[Fe_2S_2]^+$ cluster and the corresponding pre-calculated DEER trace was retrieved from the library of traces. The contribution of each rotamer to the overall simulated DEER trace was weighted by the rotamer probability calculated by MMM.[n] In the case of the non-orientational $NO^\bullet - NO^\bullet$ traces, the distance between all the pairs of rotamers and the probability was used to construct a weighted DEER trace.

All the simulated DEER traces (both $NO^\bullet - NO^\bullet$ and $[Fe_2S_2]^+$-$NO^\bullet$) were fitted to the experimental traces with a background correction, which was optimized using a Marquardt-Newton-Gauss algorithm for non-linear least squares fitting. For the orientationally selective DEER traces, the form of the background correction was the same as that used previously for fitting the orientationally dependent copper DEER traces (Equation 3.2). A satisfactory background function was obtained when the dimensionality of all of the background corrections was set to three and only the exponential decay rate constant, k, and the correction to the modulation depth, Y were fitted.

The need to adjust the modulation depth can be seen by examining the EPR field sweep spectra for the HaPux-P450 system given in Fig. 4.3. It is obvious that the relative intensities of the signals of the two paramagnetic centres, and thus their concentration, vary between samples, indicating that in the majority of cases, if not all, there is incomplete spin labelling or reduction of one or both sites. The DEER traces will therefore include contributions from 'mono-labelled' complexes, which will cause the intensity of the unmodulated part of the DEER trace to alter with the sample. The modulation depth is directly related to the labelling efficiency of the spins being pumped,[57] in this case the $[Fe_2S_2]^+$ cluster, and the pump pulse inversion efficiency.

[n] Only those rotamers considered to be significant, those covering 99.5% of the population at a given site were considered in the analysis.[80]

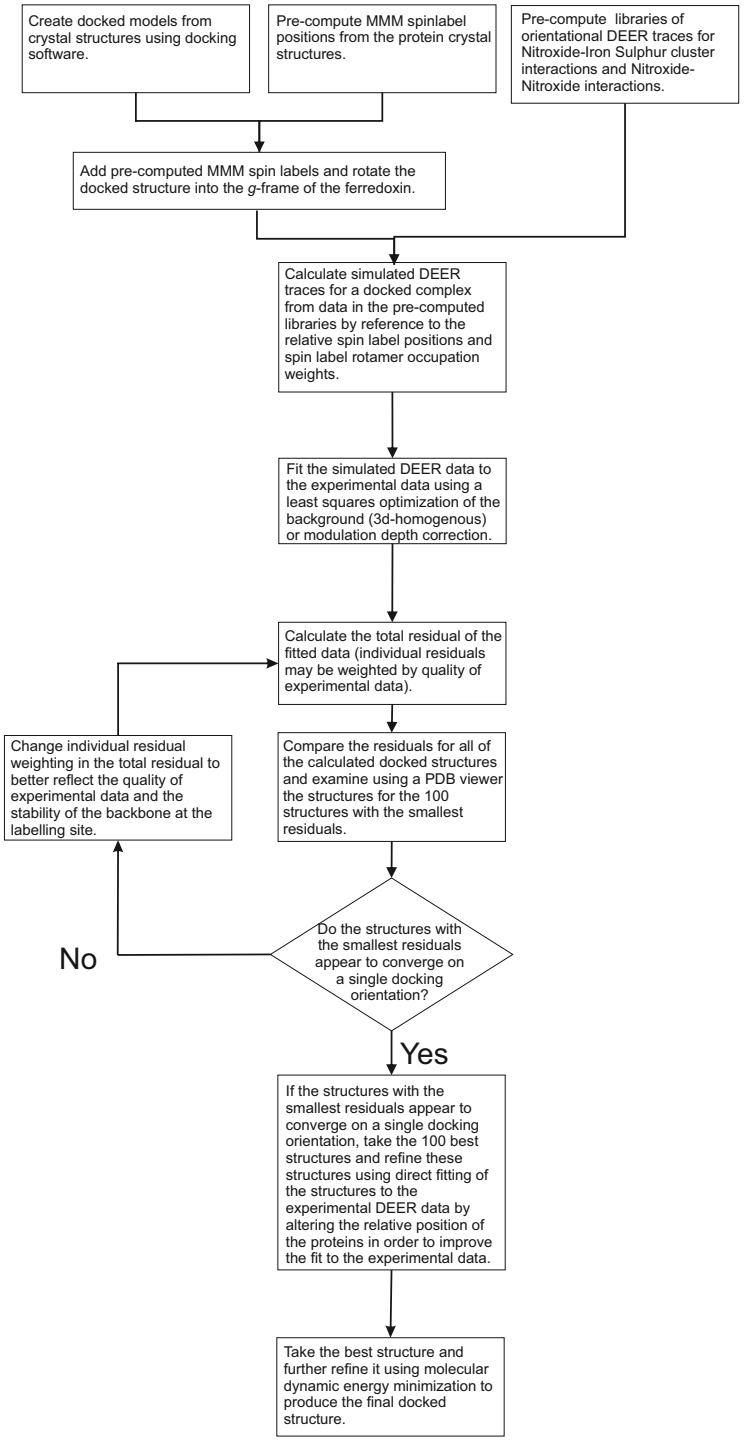


Figure 4.14: A flowchart showing the procedure for generating the final docked protein complex by fitting simulated DEER data for trial docked structures to the experimental DEER data, scoring the structures accordingly and then refining the best structures. The PDB viewer used for examining the protein structures was Chimera.[1]

In the case of the $NO^{\bullet}-NO^{\bullet}$ DEER traces, the experimental data was initially background corrected using DeerAnalysis to obtain the form factor (consisting of the reduced form factor and an unmodulated part). This meant that the simulated data only needed to be scaled by a constant modulation depth correction, p, to allow it to be compared to the background corrected experimental data. The form of the modulation depth correction is given in Equation 4.7:

$$D_{bc}(t) = \frac{S(t) + p}{max\,(S(t)) + p} \tag{4.7}$$

The division by $max\,(S(t)) + p$ is a normalization factor to allow the background corrected DEER trace, $D_{bc}(t)$, to start from 1. $S(t)$ is the simulated DEER trace containing both a modulated and an unmodulated part.

The least squares residual between each simulated DEER trace and the corresponding experimental DEER trace to which it was fitted was calculated and the residuals for all the available traces for the complex summed. This process was repeated for each of the starting structures (about 4,000 for each system). The different starting structures were then ranked based on these equally weighted DEER residuals.

It is also possible to use different weighting factors for the residuals of individual traces to account for the different qualities of experimental DEER data collected. Some of the DEER data was significantly more noisy than other sets, due to differing sample concentrations, labelling efficiencies, data acquisitions times, etc. Noisier data will automatically have a larger residual. When different weighting factors were trialled, it was found that this had little overall effect on the structures which had the lowest overall residuals and were therefore ranked highest.

Once the structures had been ranked (using equally weighted residuals), the top 100 progressed to the direct fitting stage of refinement. Here, the points of spin density within a protein structure were fixed, but the structures of the two proteins were allowed to move with respect to one another. Since there were six parameters to optimize, three positional (θ, ϕ, r) and three angular (α, β, γ), the optimization took place in two types of cycle. Initially, the positional restraints were optimized followed by the angular ones. The two cycles were repeated twice with 20 fitting iterations for each cycle. In most cases, this was found to be sufficient for the algorithm to reach a stable solution.

The optimization used a grid-search based algorithm, optimizing three parameters at a time. Hence, for each iterative step, a grid of 27 points was calculated $(27 = 3^3)$ with three possible values for each parameter being fitted, the central one corresponding to the value in the starting structure, the other two placed equidistant on either side of this value. Each one of these points corresponded to a different orientation of the two proteins with respect to one another and, for each of these orientations, the DEER traces were calculated, fitted to the experimental data using least squares fitting of the background correction and the least squares residual between the experimental and simulated data calculated. If one of the points was found to have a smaller residual than the initial orientation of the proteins with respect to one another, the orientation was changed to match the orientation with the lowest residual and the grid re-calculated with the new lowest residual structure at the centre.

After the top 100 structures had been refined by direct fitting to the experimental DEER traces and the structures were re-ranked by the least squares residual calculated for the refined structures; the top 20 of these structures were studied in detail. For both types of protein complex, PuR-PuxB and HaPux-P450, it was found that there was a smooth continuum in the residuals calculated between experimental and simulated DEER data, with no obvious cut-off to indicate structures that fitted the data and those that did not. However, in both cases the top-ranked structures clustered together in terms of their positional and orientational constraints. This indicates that the top-ranked structures are likely to be at or very close to the global minimum for the docked structure.

When calculating the final residual between the experimental and the simulated data, the tail portions of some of the experimental data traces were ignored. There were two reasons for this.

Firstly, in the case of some of the experimental DEER traces, the tail end of the trace rises, a result of pulse overlap. This feature is not part of the dipolar function and therefore it is correct that it should be ignored. Secondly, for shorter distances, where the oscillations die out quickly, all of the dipolar information is contained within the early portion of the DEER trace and the latter part of the trace is only required for accurate fitting of a background function. The different portions of the traces used are shown in Fig. 4.15 and Fig. 4.16, where the green parts of the fitted simulated data were used for the calculation of the residual to the trace and the magenta parts were not.

4.6.1 The use of sparse distance constraints

In the research described in this chapter the number of distance and angular restraints provided from the experimental DEER data falls into the sparse regime. However, as the methodology used to form and refine the docked complexes assumes a rigid-body model of both proteins, such that the individual structures are fixed and only the relative positions of the two proteins with respect to one another can be altered, only sparse constraints are required to define the relative positions of the proteins.

However, if there was a large change in conformation of the protein backbone for one or both proteins on formation of the docked complex, many more restraints would be required in order to model this change. Such modelling is very labour intensive; however, it has been attempted on other protein systems.[57] In this work doubly-labelled PuR was used to investigate the validity of a rigid-body model for this system (see Section 4.4.2).

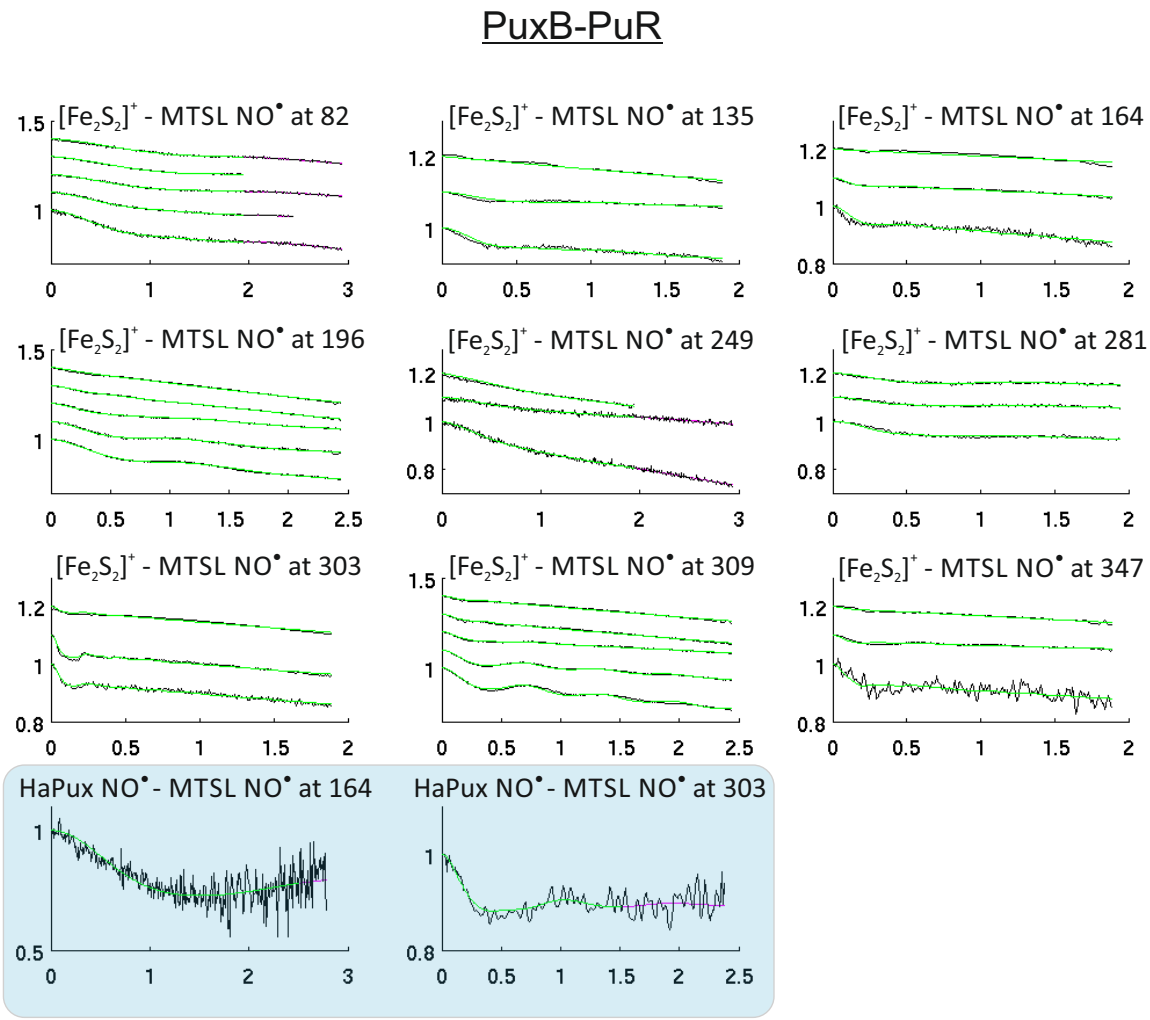


Figure 4.15: The experimental DEER traces with the fitted simulated traces for the top fitting structure of the PuxB-PuR complex. The experimental data is shown in black and the fitted data in green and magenta. The green parts correspond to those used to calculate the least squares residual between the experimental and simulated traces; the magenta parts are removed from this analysis. Most traces are measured between the $[Fe_2S_2]^+$ of PuxB and an MTSL label added to the PuR. In these cases the experimental data has not been background corrected and a modulation depth correction and background correction are added to the simulated traces. The DEER traces highlighted in blue are measured using PuR in complex with HaPux, where an MTSL label has been added to the HaPux at site 54. These traces are therefore measured between two nitroxide labels and in these cases the experimental data has had a background correction removed and the simulated data is only scaled by a modulation depth correction. The noise in the experimental data for the DEER traces measured between two nitroxides is a result of a low glycerol concentration in these samples.

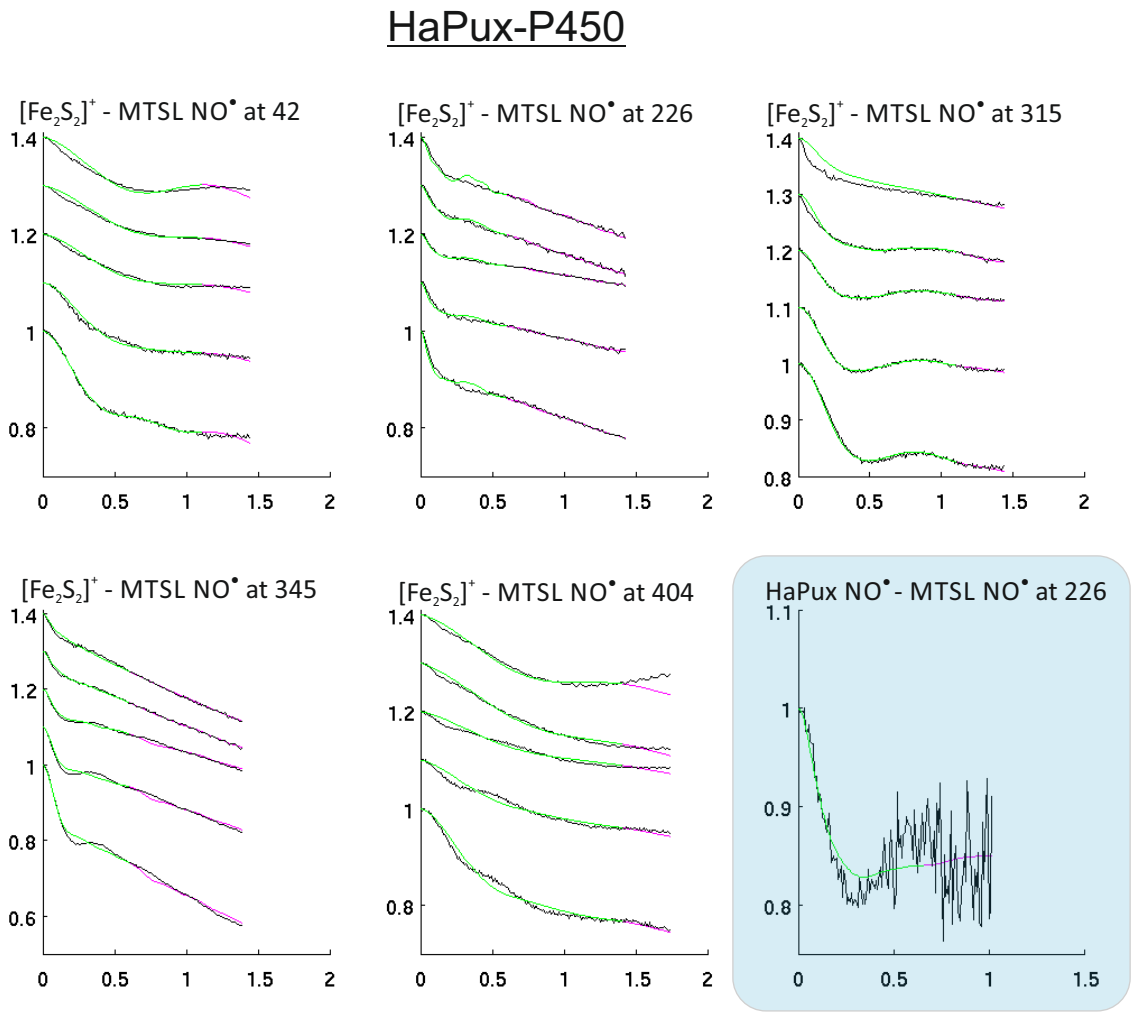


Figure 4.16: The experimental DEER traces with the fitted simulated traces for the top fitting structure of the HaPux-P450 complex. The experimental data is shown in black and the fitted data in green and magenta. The green parts correspond to those used to calculate the least squares residual between the experimental and simulated traces; the magenta parts are removed from this analysis. Most traces are measured between the $[Fe_2S_2]^+$ of HaPux and an MTSL label added to the P450. In these cases the experimental data has not been background corrected and a modulation depth correction and background correction are added to the simulated traces. The DEER trace highlighted in blue was measured using P450 in complex with HaPux, where an MTSL label has been added to the HaPux at site 54. This trace is therefore measured between two nitroxide labels and in this case the experimental data has had a background correction removed and the simulated data is only scaled by a modulation depth correction. The noise in the experimental data for the DEER trace measured between two nitroxides is a result of a low glycerol concentration in this sample.

4.7 The fitted DEER traces and structures of the complexes

The fitted DEER traces for the top-ranked structures found to give the lowest residuals after direct fitting are shown in Fig. 4.15 and Fig. 4.16. The average distances between all of the MTSL rotamers included in the fitting model and the $[Fe_2S_2]^+$ found for the top-ranked final models of the two protein systems are given in Table 4.8.

Table 4.8: The average distances found between paramagnetic centres in the top two models.

PuxB-PuR		
MTSL spin label position(s)	Average inter-spin distance (nm)	Type of measurement
82(PuR)	5.0	$[Fe_2S_2]^+$–$NO^\bullet$
135(PuR)	3.9	$[Fe_2S_2]^+$–$NO^\bullet$
164(PuR)	2.9	$[Fe_2S_2]^+$–$NO^\bullet$
196(PuR)	3.9	$[Fe_2S_2]^+$–$NO^\bullet$
249(PuR)	4.9	$[Fe_2S_2]^+$–$NO^\bullet$
281(PuR)	3.7	$[Fe_2S_2]^+$–$NO^\bullet$
303(PuR)	2.1	$[Fe_2S_2]^+$–$NO^\bullet$
309(PuR)	3.2	$[Fe_2S_2]^+$–$NO^\bullet$
347(PuR)	2.6	$[Fe_2S_2]^+$–$NO^\bullet$
164(PuR) - 54(HaPux)	5.1	$NO^\bullet$–$NO^\bullet$
303(PuR) - 54(HaPux)	3.4	$NO^\bullet$–$NO^\bullet$
HaPux-P450		
MTSL spin label position(s)	Average inter-spin distance (nm)	Type of measurement
42(P450)	4.0	$[Fe_2S_2]^+$–$NO^\bullet$
226(P450)	2.3	$[Fe_2S_2]^+$–$NO^\bullet$
315(P450)	3.5	$[Fe_2S_2]^+$–$NO^\bullet$
345(P450)	2.7	$[Fe_2S_2]^+$–$NO^\bullet$
404(P450)	4.3	$[Fe_2S_2]^+$–$NO^\bullet$
226(P450) - 54(HaPux)	3.0	$NO^\bullet$–$NO^\bullet$

The overlay of the top six ranked protein complexes for the two systems; PuR-PuxB and HaPux-P450, are shown in Fig. 4.17 and Fig. 4.18 respectively. These figures demonstrate the clustering of the structures described previously.

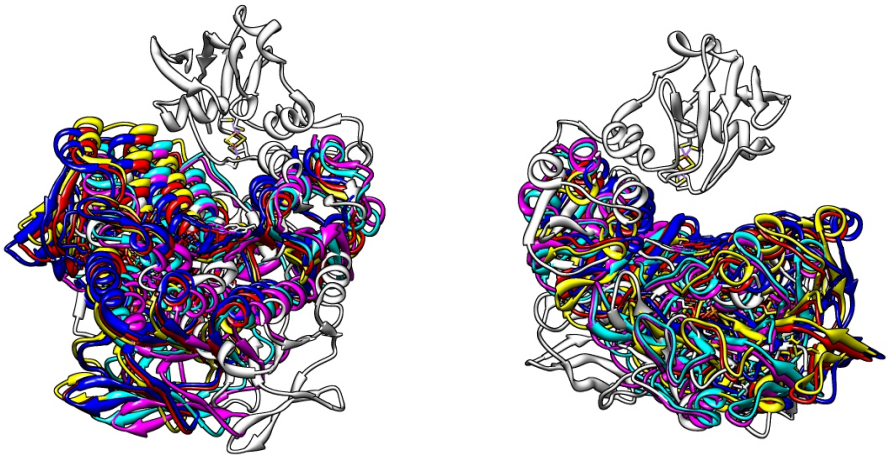


Figure 4.17: The top six structures for the PuxB-PuR complex, after direct fitting to the experimental DEER data. The orientation of PuxB (upper protein) is the same for all complexes and the relative positions of the PuR (lower protein) are ranked in the order white, magenta, cyan, yellow, red, blue by increasing least squares residual calculated between the experimental and simulated DEER data. It can be seen that the structures form a cluster. The two views are related by a c. 180° rotation about the z-axis.

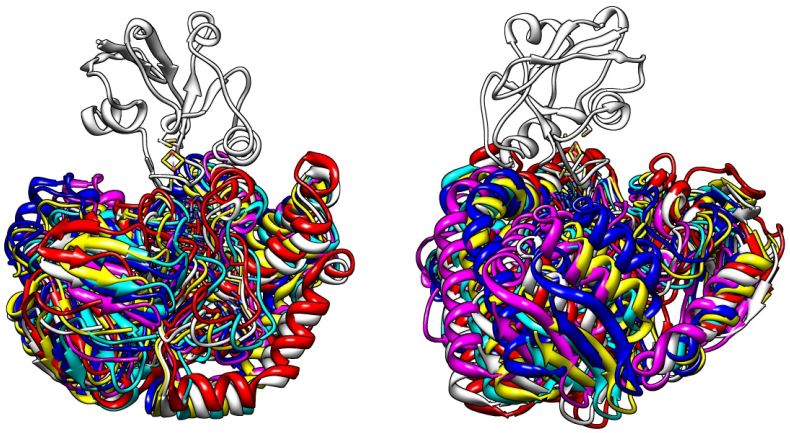


Figure 4.18: The top six structures for the HaPux-P450 complex, after direct fitting to the experimental DEER data. The orientation of HaPux (upper protein) is the same for all complexes and the relative positions of the P450 (lower protein) are ranked in the order: white, magenta, cyan, yellow, red, blue by increasing least squares residual calculated between the experimental and simulated DEER data. It can be seen that the structures form a cluster. The two views are related by a c. 180° rotation about the z-axis.

For the PuxB-PuR complex, the highest ranked structure (that with the lowest residual between the experimental and simulated DEER data) lies at a slightly different orientation to the other structures within the cluster shown in Fig. 4.17. Examining this structure with respect to the next highest ranked structure from the cluster shows that they are related by a small rotation (see Fig. 4.19).

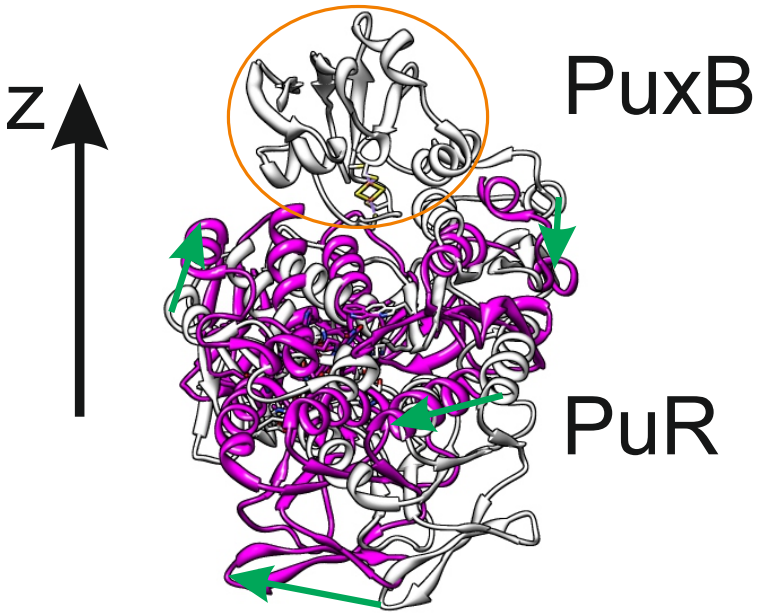


Figure 4.19: The top two ranked structures for the PuxB-PuR complex, after direct fitting to the experimental DEER data. The white structure is the highest ranked structure; it is related to the next highest ranked structure (magenta) by a small rotation detailed by the green arrows, approximately about the z-axis shown. Both structures have the same orientation of the PuxB (detailed in the orange circle).

The least squares residuals calculated between the fitted simulations and the experimental DEER data for the top-ranked structures are given in Table 4.9. This table also lists the relative cofactor separation distance for the top-ranked structures and the root mean squared deviation (RMSD) between the backbone C_α atoms for each of the structures in the cluster and the structure with the smallest least squares residual.

Chimera was used to calculate the RMSD,[1] by the following equation:

$$RMSD = \sqrt{\frac{1}{N}\sum_{i=1}^{N}\left(r_i^{model} - r_i^{min}\right)^2} \tag{4.8}$$

where r_i^{model} are the Cartesian coordinates for an atom in the model being considered and r_i^{min} are the Cartesian coordinates for the corresponding atom in the calculated structure with the lowest residual. For the calculation of the RMSD, the ferredoxin coordinates were overlaid and therefore the RMSD records the deviation in the position of the PuR or P450.

Table 4.9: The least squares residuals (DEER fit residuals) calculated between the experimental DEER data and the simulated DEER traces for the top six structures in their raw and normalized forms. The RMSD for the structures relative to the top two ranked structures are also given to demonstrate the clustering of the top six structures.

PuxB-PuR				
Complex residual ranking	Calculated DEER fit residual ($/10^{-4}$)	Normalized DEER fit residual	RMSD between this structure and the structure with the lowest residual, structure 1 (Å)	RMSD between the structure and the structure with the second lowest residual, structure 2 (Å)
1	1.059	1.000	0	-
2	1.066	1.007	10.766	0
3	1.071	1.011	12.717	2.365
4	1.079	1.019	15.982	8.060
5	1.081	1.021	15.272	7.397
6	1.086	1.025	15.854	9.305
HaPux-P450				
Complex residual ranking	Calculated DEER fit residual ($/10^{-4}$)	Normalized DEER fit residual	RMSD between the structure and the structure with the lowest residual, structure 1 (Å)	RMSD between the structure and the structure with the second lowest residual, structure 2 (Å)
1	0.5243	1.000	0	-
2	0.5345	1.020	5.699	0
3	0.5350	1.020	4.554	4.804
4	0.5365	1.023	5.094	5.046
5	0.5405	1.031	3.933	9.236
6	0.5406	1.031	7.904	4.857

The normalized residuals are calculated as a ratio of the calculated residual to the smallest residual found. For comparison of the relative sizes of the residuals given in Table 4.9, the largest residuals

calculated for the initial starting structures of the two complexes were 0.1862 for PuxB-PuR and 0.2634 for HaPux-P450. Each of these is several orders of magnitude larger than that found for the highest ranked structures. Given that the method of forming the docked starting structures, by defining the docking interface, should provide a set of structures which cover the entirety of the biochemically feasible parameter space, we can have reasonable confidence that the structures with the lowest residuals are the global minima for the docked structures.

4.7.1 Validation of the final structure for the HaPux-P450 complex

For the PuR-PuxB complex, the final structure found is similar to the published tethered ferredoxin-ferredoxin reductase complex,[162] (see Fig. 4.27), providing a degree of confidence that the tethered structure is likely to be close to the native docked structure, and that docking is not influenced by the restrictions of the short tether employed.

For the HaPux-P450 structure, there is no existing structure against which the docked complex refined from the experimental DEER measurements can be compared. Therefore it was necessary to test whether the top-ranked structure after direct fitting to the DEER data was at or close to the global minimum. This was achieved by using the relative orientation of the two proteins for the top-ranked structure and rotating the P450, through an angle β, with respect to the HaPux about an axis which linked the active sites of the two proteins, the Fe^{3+} of the [Fe_2S_2] cluster and the iron centre of the P450 Heme. For each rotation made about this axis, the position of the two proteins was re-optimized with respect to the distance between the active sites and two tilt angles orthogonal to the β axis linking the original location of the two active sites.

The overall sum of the residuals for fitting of the simulated data to the experimental DEER data is plotted against the angle β in Fig. 4.20. This plot shows an overall trend, with a minima located at approximately at 0°. The structure within this trend is to be expected, due to fitting noise and the large number of parameters that are considered. The level of structure also illustrates the complex energy surface involved for docking of these two proteins using the DEER data set.

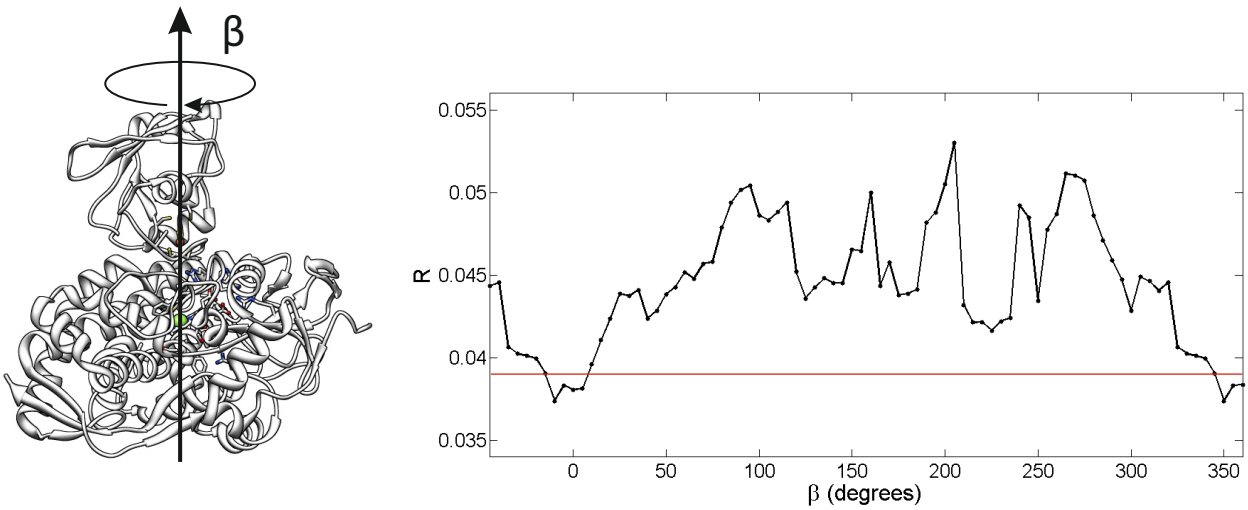


Figure 4.20: **Left:** The HaPux-P450 complex, used as the structure with 0° β rotation, with the axis about which the β rotations occur marked. **Right:** A plot for the HaPux-P450 complex of the overall least squares residual (R) calculated from fitting simulated DEER data to the experimental DEER data for structures with a fixed angle of rotation (β) between the electrochemically active centres. The red line is included in order to demonstrate the minima in the curve existing between $-10°$ and $+5°$.

Fig. 4.20 shows that a minimum in the curve occurs between $-10°$ and $+5°$. A comparison of the structures found between $-10°$ and $+5°$ shows that although there is some movement, all the structures have the same basic protein-protein orientation and the distance between the redox centres changes by less than 0.1 nm. Fig. 4.18 details the structures corresponding to β angles of 0° and $-10°$. Comparison of Fig. 4.21 with Fig. 4.18 shows that the deviations seen between the structure at 0° and that at $-10°$ are very similar to those seen between the original six lowest residual structures.

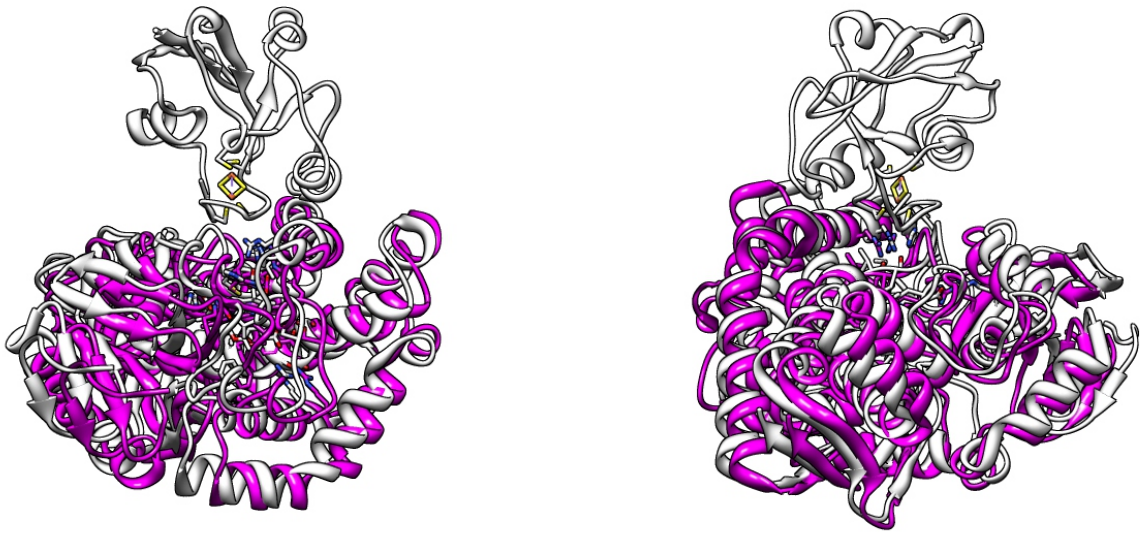


Figure 4.21: The structures for the HaPux-P450 complex with beta angles of 0° (white) and −10° (magenta). The orientation of HaPux (upper protein) is the same for both complexes and shown only in white. The structures are closely related and lie within the cluster formed by the six structure of lowest residual shown in Fig. 4.18. The two views are related by a c. 180° rotation about the z-axis.

Furthermore, performing a LigPlot[120,121] analysis on the same structures to visualize the residues forming interactions at the binding interface (see Fig. 4.22) shows a large degree of similarity between the binding interfaces in the two structures.

4.7.2 Further refinement and analysis of the DEER fitted structures

While the top-ranked structure for the HaPux-P450 system from the original structural fitting to the experimental DEER data did not have any backbone clashes, some of the residue's side chains were considered to be too close to define a stable structure. Furthermore, the top-ranked PuR-PuxB structure had a small backbone clash. These models are currently undergoing further refinement using molecular dynamics simulations using explicit water molecules. However, these calculations are lengthy and at this time they are incomplete.

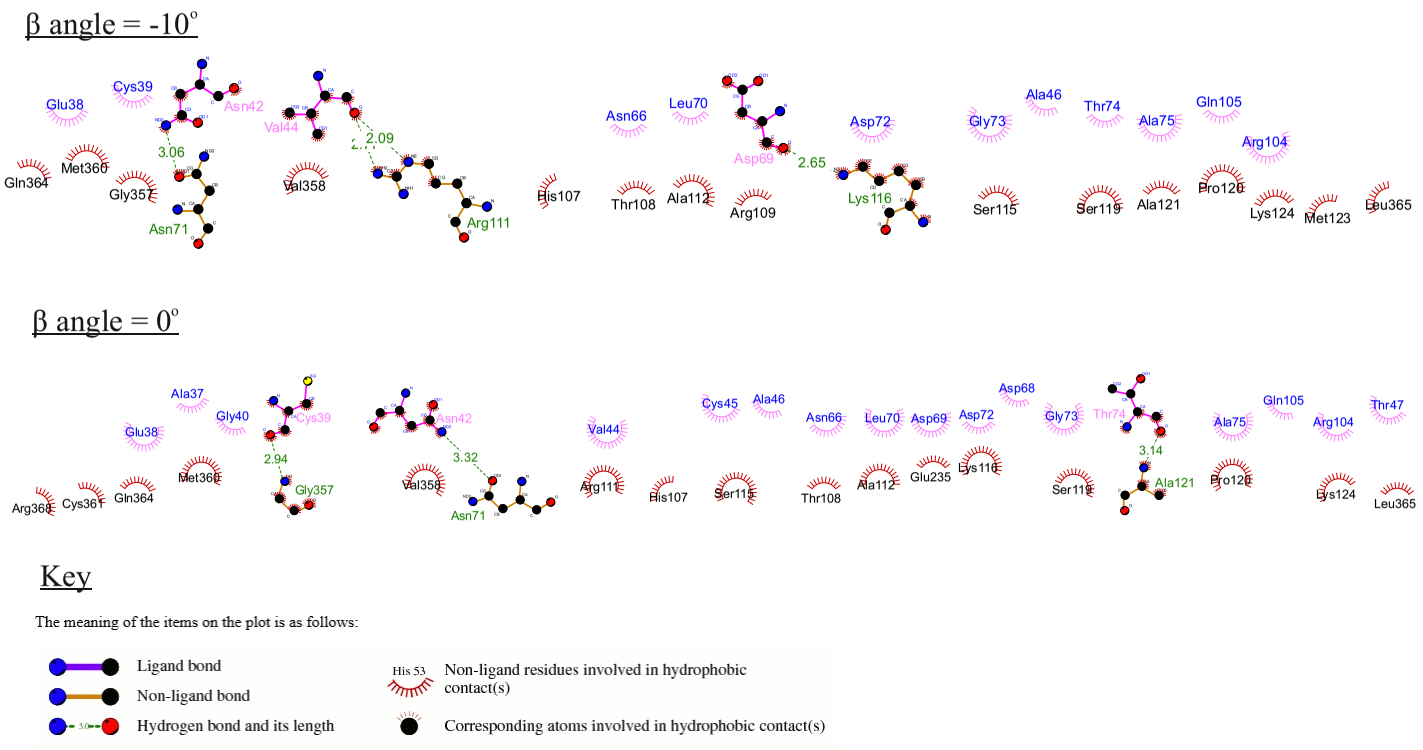


Figure 4.22: LigPlot[120,121] analysis for the HaPux-P450 complex structures, with beta angles of $-10°$ (top) and $0°$ (bottom).[120,121] In both cases the HaPux residues are shown in pink and the P450 residues are shown in red. There is a large degree of similarity in the residues forming interactions in both structures, indicating that the binding interfaces are very similar.

Therefore as a first approximation to allow further analysis of the two top-ranked complex structures found through DEER fitting, the steric clashes were removed using the 'clean geometry' function in the program Accelrys Discovery Studio.[163] The resulting 'geometrically clean' structures were analysed in more detail to give an insight the mechanism of binding.

PuxB-PuR structure and interactions

In the highest ranked structures, there is a persistent motif of close interactions between the helix-3 of PuxB and two helices on PuR, the terminal helix (helix-10) and the geometrically close helix-8. This interaction is indicated by the green circle in the left panel of Fig. 4.23. Examining the side chains in this region seems to show a hydrogen bond between Leu 71 in PuxB and Ala 404 in PuR. Furthermore, there are likely favourable interactions between the side chains of Glu 68 in PuxB and the two adjacent Lysines 400 and 401 in PuR. If the charged surface of the two proteins is calculated, the two protons appear to have some complementary regions of positive and negative charge, highlighted by the green circle in the central panel of Fig. 4.23. Taking a closer look at the binding site reveals a distance between the $[Fe_2S_2]$ cluster of PuxB and the flavin cofactor in PuR of 17.3 Å. This distance is a too long for direct electron transfer. However, there is some evidence that the electron transfer may occur via the ligating cysteine sulphurs of the $[Fe_2S_2]$ cluster. Taking the closest distance between the ligating sulphurs and the flavin gives 15.7 Å, which is also a little long for electron transfer. Looking at other residues present in the binding site, Trp 321 of PuR is seen to lie directly in the path of the electron transfer between the $[Fe_2S_2]$ and the flavin. The distance between the closest ligating cysteine to the Trp side chain is 12.3 Å, which is in an acceptable range for electron transfer. It is therefore plausible that the electron transfer between the $[Fe_2S_2]$ cluster and the flavin occurs via Trp 321. A detailed picture of the binding site is given in the right panel of Fig. 4.23.

In order to further investigate the activity of Trp 321 as part of the electron transport chain mutagenesis studies could be carried out and the activity of the protein measured via the consumption of NAD(P)H (see Section 4.1.3).[12] It should also be noted that a similar proposal involving the Trp 330 of PdR was also invoked for the tethered structure formed between Pdx and PdR.[139]

Figure 4.23: **Left:** Ribbon diagram of the highest ranked complex of PuxB-PuR. **Centre:** charge surface for the same PuxB-PuR complex (blue is positive, red is negative). **Right:** Close-up of the binding site, showing the $[Fe_2S_2]$ centre of PuxB and the Trp321 of PuR located in the centre of the binding site.

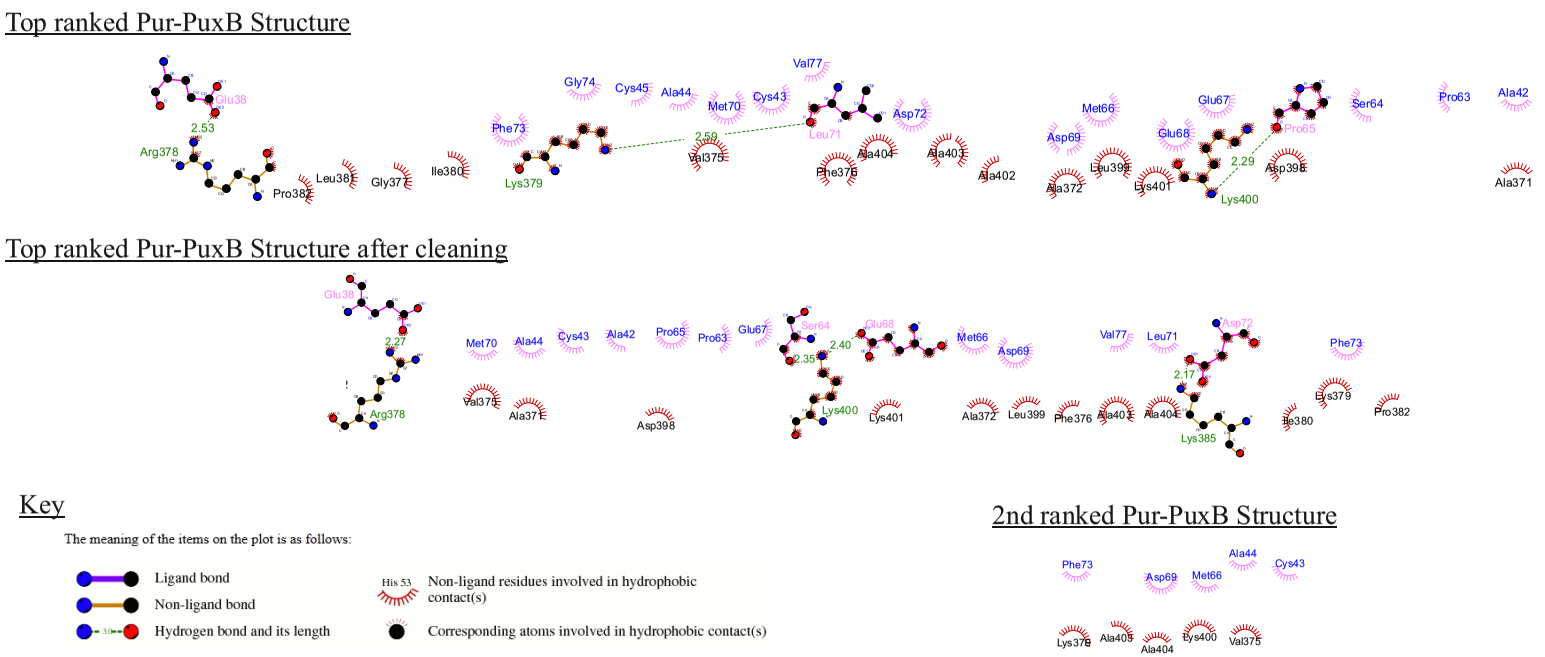


Figure 4.24: Ligplot analysis for the PuR-PuxB complex structures, in all cases PuxB residues are shown in pink and PuR residues in red. *Top:* top-ranked structure with the lowest residual. *Centre:*top-ranked structure after geometrical cleaning. *Bottom:* 2nd ranked structure.[120,121]

LigPlot analysis was performed (see Fig. 4.24) for the top-ranked Pur-PuxB structure with the lowest residual both before and after geometrical cleaning and also for the 2nd ranked Pur-PuxB structure, since there is a large discrepancy in the RMSD between these two structures (see Table 4.9). There is a large degree of similarity in the plots for the top-ranked structure and the same structure after geometrical cleaning showing that no significant movement of the protein has occurred during the geometrical cleaning. The plot for the second ranked structure is different to that for the top-ranked structure; there are far fewer interactions in this structure. This shows that the second ranked structure is significantly less tightly bound than the top-ranked structure.

HaPux-P450 structure and interactions

As with the PuxB-PuR structure, it seems that helix-3 of the ferredoxin is important for protein recognition and docking for the HaPux-P450 complex. As seen in the left panel of Fig. 4.25, there are close interactions between helix-3 of HaPux and helix-3 of P450. The charge surfaces for the docked complex are also shown in the central panel of Fig. 4.25. Close examination of the binding site reveals two intermolecular hydrogen bonds between the backbone carbonyl of Val 44 on HaPux and the side chain of Arg 111 on P450. This allows for the formation of a tight complex with a $[Fe_2S_2]$ ligating cysteine to heme edge distance of 11.3 Å. This lies well within the range where electron transport can occur at a reasonable rate, so it seems that in this complex the electron transfer may occur directly from one cofactor to the other, without the need for mediation via an amino acid side chain. The hydrogen bonds in the binding site are shown in the right panel of Fig. 4.25.

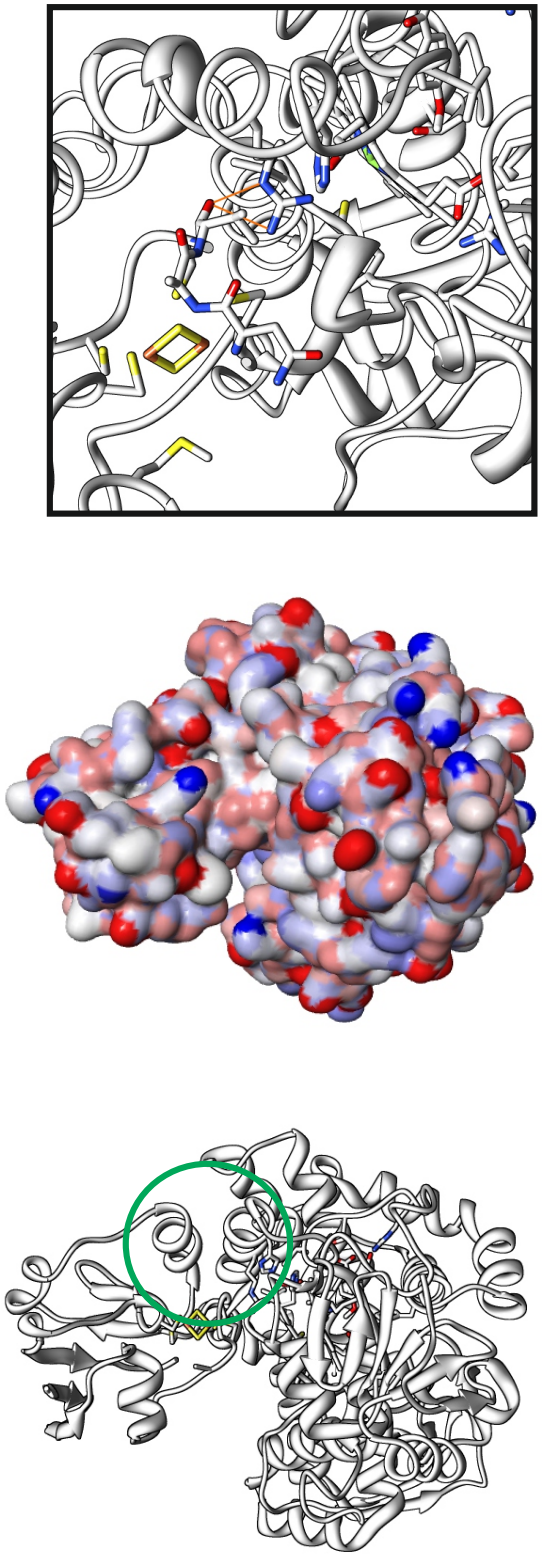


Figure 4.25: **Left:** Ribbon diagram of the highest ranked complex of HaPux-P450. **Center:** Charge surface for the same HaPux-P450 complex (blue is positive, red is negative). **Right:** Close-up of the binding site showing the $[Fe_2S_2]$ centre of HaPux and the two hydrogen bonds (orange) formed between backbone carbonyl of Val 44 on HaPux and the side chain of Arg 111 on P450.

Comparing the structures before and after fitting to the experimental DEER data

Comparing the top-ranked structures after direct fitting to the DEER data and the structure that was the input shows an interesting feature; in both cases, the binding between the two structures becomes tighter, particularly around the interacting helices. This is demonstrated in Fig. 4.26. This result is not unexpected, since the docking programs used to generate the starting structures are primarily based on rigid-body docking (with side chain refinement in some cases) and the limited or complete lack of flexibility in the side chains is likely to make the proteins appear more bulky than in reality, where full flexibility of the side chains allows a closer distance of approach.

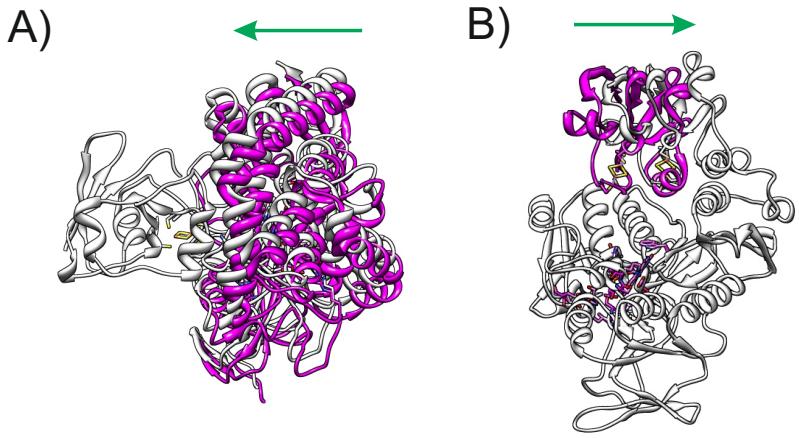


Figure 4.26: **A)** HaPux-P450 complex; the magenta structure is before fitting to the experimental DEER data and the white structure is the output after the fitting. The HaPux (protein on the left) is common to both structures and the position of the P450 can be seen to move towards the HaPux (green arrow) after the direct fitting to the DEER data. **B)** PuxB-PuR complex; the magenta structure is before fitting to the experimental DEER data and the white structure is the output after the direct structural fitting to the experimental DEER data. The PuR (lower protein) is common to both structures and the position of the PuxB can be seen to move to the right (green arrow), decreasing the separation between the interacting helices and also bringing the $[Fe_2S_2]^+$ centre into alignment with the tryptophan shielding the flavin cofactor.

4.8 Reflection on the docked structures found

In both complexes, the interaction of helix-3 on the ferredoxin with helical regions on the binding partner appears to be an important motif in the protein recognition. It therefore becomes apparent

that the sequence of amino acids in these helical regions may shed light on the relative stability of the complexes, as determined by the binding constants.

Comparison of the sequence of CYP199A2 (*4DNJ.pdb*)[153] with that of the structural homologue P450cam (*2ZAX.pdb*)[162] revealed differences in the residues on the interacting helix-3, listed from 119 to 133 in the aligned sequences in Fig. 4.28. Of particular note are the substitutions of Ala 106, Thr 108 and Thr 110 in CYP199A2, with the residues Glu, Arg and Phe respectively in P450cam, since these have significantly different hydrophobicity. These variations provide a potential reason why HaPux will form a tight complex with CYP199A2, while such a complex does not seem to be formed with P450cam.

Comparing the DEER defined structure of the PuR-PuxB complex to the crystal structure of the tethered complex (*3LB8.pdb*)[139] shows some similarities between the two. Both seem to involve interactions of helix-3 on ferredoxin with the helical bundle of helices-8 and 10 on ferredoxin reductase. However, the tethered structure appears to have the ferredoxin rotated further into the binding site (see Fig. 4.27).

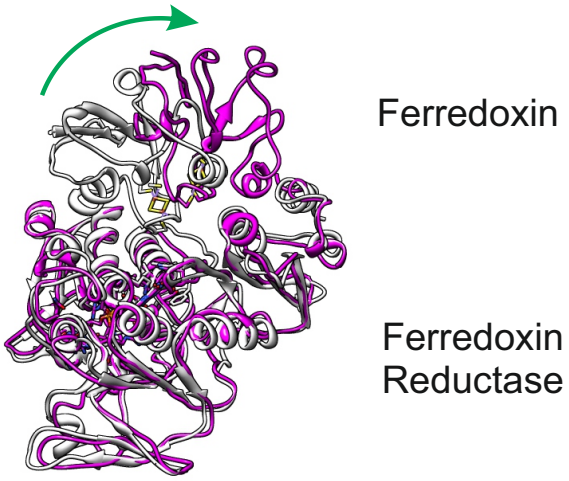


Figure 4.27: An overlaid plot of the X-ray determined tethered structure (*3LB8.pdb*),[139] in white, and the DEER defined structure, in magenta, for the ferredoxin–ferredoxin reductase complex. The DEER structure appears to show a rotation in the binding site from the tethered structure, this is indicated by the green arrow.

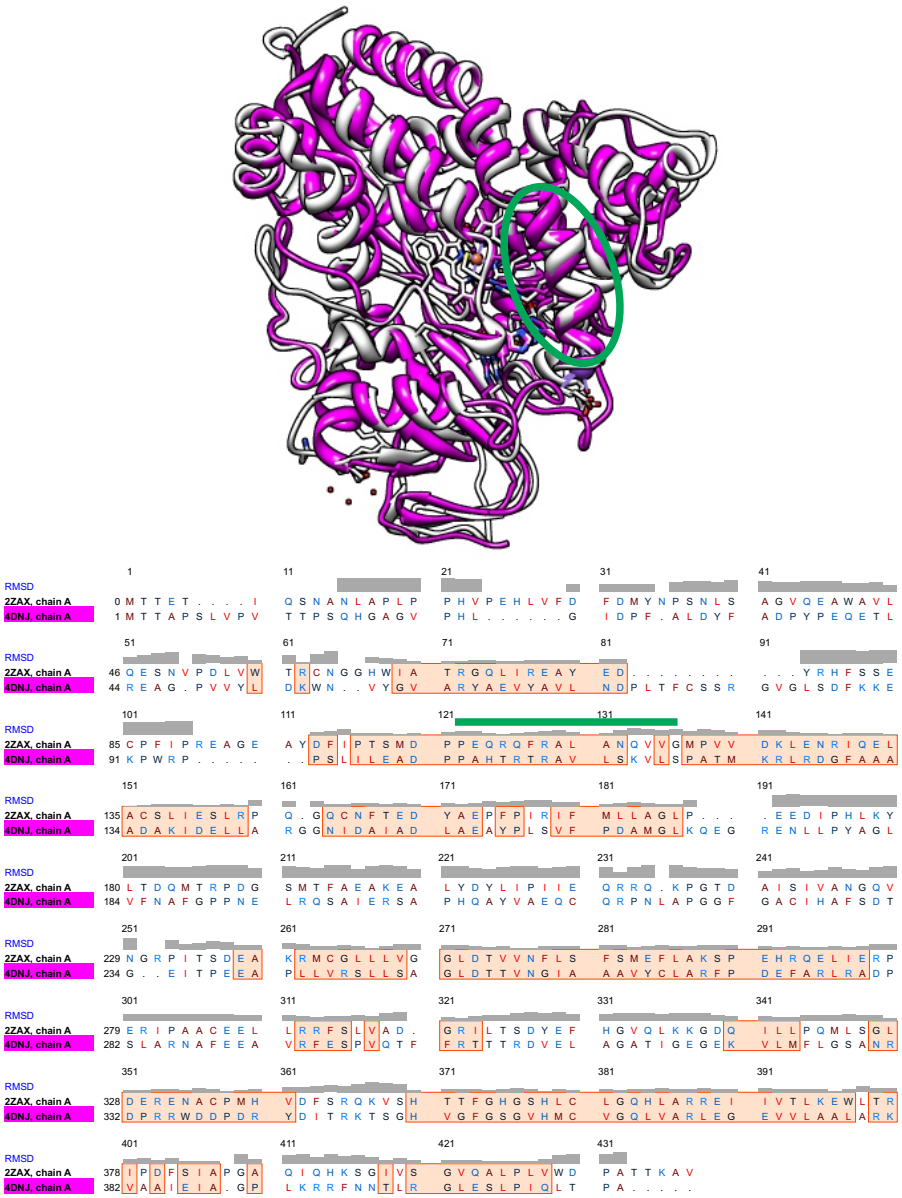


Figure 4.28: An overlay of the structure of P450 from *Rhodopseudomonas palustris*, CYP199A2, in magenta (*4DNJ.pdb*)[153] and the P450cam protein, in white(*2ZAX.pdb*)[162] and a comparison of the amino acid sequences. The structural similarity is striking and the helix-3 involved in interactions with HaPux for CYP199A2 is marked by the green ring on the structure and the green line on the sequence alignment.

Also the tethered structure, which is known to be active as an electron transfer protein complex, has an edge-to-edge distance between the $[Fe_2S_2]$ cluster in the ferredoxin and the flavin cofactor in the ferredoxin reductase of 11.9 Å, which is considerably shorter than that found in the DEER defined complex (17.3 Å).

One possible explanation for the observation of the longer distance in the DEER defined structure is the use of the HaPux-PuR complex to provide the $NO^{\bullet}-NO^{\bullet}$ distance restraints. Fig. 4.27 indicates that the tethered and DEER structures are related by a rotation of the ferredoxin away from the ferredoxin reductase. It is therefore possible to imagine that a structure, similar to the tethered structure, could be the activated complex in which electron transfer can occur and a structure, more similar to the DEER derived structure, could be an inactive complex in which no electron transfer can occur. The tethered structure is known to be electrochemically active and, due to the short nature of the tether, the electrochemically active complex must be very similar to the complex observed by X-ray crystallography.[139] A high K_M value could thus indicate a predominance of the inactive complex in solution.[o]

Comparing the K_M values for the HaPux-PuR and PuxB(A105R)-PuR complexes (see Section 4.1.3) shows that the value observed for HaPux-PuR is eight times larger than that seen for PuxB(A105)-PuR. It can therefore be hypothesised that a greater degree of the inactive structure may be present in the HaPux-PuR system, compared with PuxB-PuR. Inclusion of the $NO^{\bullet}-NO^{\bullet}$ distance restraints from the HaPux-PuR complex may have caused the complex structure predicted from the direct structural fitting to the DEER data to favour an inactive complex form, rather than the active form, which is likely to have a higher concentration in the PuxB-PuR system.

The docked structures analysed in this chapter, even after geometrical 'cleaning', still show some atom-atom intra-molecular distances that are considered to be too close. Further refinement will therefore be necessary, using a fully parameterized molecular dynamics simulation. These calculations are on-going at present.

Overall the research in this chapter has shown that it is possible to use orientational DEER re-

[o]Given the noisy nature of the DEER data for the HaPux-PuR complex which has a high K_M value this is likely to be in addition to a generally lower concentration of complex present in solution

straints in combination with rigid-body docking to formulate likely protein-protein docked complexes with an overall structural confidence of c.<1 nm, as defined by the RMSD between the top six structures found. The proposed structures of the two complexes both indicate that helix-3 of the ferredoxin is important for interactions with binding partners and in protein recognition.

The ferredoxin–ferredoxin reductase structure shows some similarities with the tethered structure found by X-ray crystallography, particularly in the interaction of ferredoxin helix-3 with the ferredoxin reductase helices 8 and 10. As the types of ferredoxin and ferredoxin reductase studied here vary from those used in the tethered structure, it is reasonable to imagine that the structures might differ slightly from one another. The distance between the electronic cofactors in the PuR-PuxB structure is further than is ideal for electron transfer, suggesting that the electron transfer is likely to take place via the cysteines ligating the $[Fe_2S_2]$ centre and Trp 321. The long distance may also be a result of the $NO^{\bullet}-NO^{\bullet}$ distance restraints measured on the HaPux-PuR complex, which has a higher K_M value and thus may favour an inactive form of the complex, with a longer distance between the electron transfer centres.

In the ferredoxin–P450 complex, helix-3 of the ferredoxin is seen to interact with helix-3 of the P450. The distance between the electronically active cofactors is within the range where direct electron transfer could occur and it seems likely that intermolecular hydrogen bonds in the binding site may stabilize the complex formation. The structure proposed for the ferredoxin–P450 complex is the first such experimentally derived structure for a docked complex between these classes of proteins; thus it will be of great interest to the biochemical research community.

Chapter 5

Determination of the *g*-tensor orientation and spin distributions for the $[Fe_2S_2]^+$ cluster in *Plasutradoxin* B

Until this point we have only considered the orientational dependence of DEER spectroscopy. However, as this orientational dependence arises from the fact that, for a species with a broad EPR spectrum, pulses can only excite a small portion of the spectrum corresponding to a small number of orientations; other forms of EPR spectroscopy will also exhibit orientational dependencies.

As we have seen in the previous chapter, the *g*-tensor orientation and the spin distribution for the ferredoxin proteins used in the structural determination for the docked complex with ferredoxin reductase and cytochrome P450 was needed for the interpretation of the orientationally selective DEER measurements. The orientation used for these calculation had the *z*-axis of the *g*-tensor tilted towards one of the ligating sulphur molecules.[164,165]

In order for the orientation dependent DEER to be fitted correctly to a structure of the docked protein complex, it was necessary to determine the orientation of the *g*-tensor and the spin distributions in the ferredoxin proteins used for this work.

Previous work to determine the *g*-tensor of ferredoxin proteins has used only continuous wave (cw) ENDOR experiments.[164–169] In this work we aim to improve on this protocol through the use of both pulsed ENDOR and HYSCORE orientationally selective experiments to determine the orientation of the *g*-matrix with respect to the $[Fe_2S_2]$ cluster and surrounding protein structure. Orientationally

dependent couplings of the paramagnetic centre on the $[Fe_2S_2]$ cluster to protons in the surrounding protein structure were measured and making the assumption that the proton positions can be predicted by adding them to the X-ray structure via geometric analysis. This information can be used to extract the *g*-matrix orientation and spin distributions.

This work has been published: J. A. B. Abdalla, A. M. Bowen, S. Bell, L. L. Wong, C. R. Timmel and J. Harmer, *Physical Chemistry Chemical Physics*, 2012, **14**, 6526–6537.[15] Some of the results figures in this chapter are taken from this publication. The fitting of the orientation dependent HYSCORE and ENDOR was done in collaboration with Dr Jeffrey Harmer, who wrote the fitting regimes and was instrumental in the development of the theoretical ideas in this chapter, and Mr Joseph Abdalla.

5.1 A theoretical introduction to ENDOR and HYSCORE

Electron Nuclear DOuble Resonance (ENDOR) and HYperfine Sublevel CORElation Spectroscopy (HYSCORE) are two EPR techniques used to study hyperfine interactions between nuclei of non-zero spin and electrons.[29] Although measuring the same interactions, the two techniques operate in quite distinct ways: ENDOR is usually a one-dimensional technique, which uses radio frequency excitation to cause nuclear spin flips within an electron detection sequence. As such ENDOR is sometimes described as EPR-detected NMR. HYSCORE, on the other hand, is a two-dimensional technique that relies on the excitation of forbidden EPR transitions via the use of hard pulses to probe the hyperfine couplings.

5.1.1 The ENDOR technique

There are two flavours of the ENDOR experiment:[170] Mims ENDOR originated from Bell Labs. and the group of W. B. Mims in 1964.[171] The technique however, does suffer from blind spots in the spectra, which are dependent on the length of the delays between pulses. Almost ten years later in 1974, a second variant of the ENDOR technique, Davies ENDOR, was introduced.[172] This pulse sequence is absent of blind spots (apart from one central one); however, it is less sensitive than Mims ENDOR as it requires selective pulses. The choice of which technique to use must be tailored to the system being studied. The work in this chapter uses both two pulse sequences in tandem.

Mims ENDOR

Mims ENDOR relies on the generation of a stimulated echo via a train of three $\frac{\pi}{2}$ pulses (see Fig. 5.1 for the pulse sequence). A long radio frequency (RF) pulse is used to excite the nuclear transitions and the experiment is repeated multiple times using different frequency RF to excite different nuclei with different hyperfine couplings to the electron being probed.

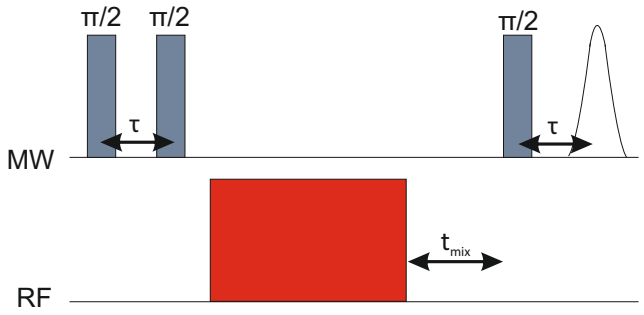


Figure 5.1: The pulse sequence for Mims ENDOR; microwave pulses exciting electron transitions are shown in blue and the radio frequency pulse exciting the nuclear transitions is shown in red. The three microwave $\frac{\pi}{2}$ pulses form a stimulated echo, detailed in Fig. 5.2. The t_{mix} time is usually constant; however, it can be varied when variable mixing time EMDOR is used to determine the absolute sign of the hyperfine coupling.

The action of three consecutive $\frac{\pi}{2}$ pulses is shown in Fig. 5.2 using the vector model. This pulse sequence is also used for the three-pulse ESEEM (Electron Spin Echo Envelope Modulation) experiment.

The maximum hyperfine coupling for which Mims ENDOR gives an undistorted spectrum is approximately $A_{max} \approx \frac{1}{2\tau}$, the upper bound of which is limited by the dead-time of the spectrometer.

Figure 5.2: **Vector diagram for the Mims ENDOR pulse sequence.** (i) Initially the magnetization vector, **M**, is aligned with the static field; (ii) Application of a $\frac{\pi}{2}$ pulse along the x-axis causes rotation of the magnetization to the $-y$-axis. (iii) During the initial delay period, τ, the magnetization vector fans out in the x-y plane due to components with different Larmor precession frequencies. (iv) Application of a second $\frac{\pi}{2}$ tilts the magnetization from the x-y plane into the x-z plane. (v) The magnetization vectors continue to precess about the z-axis changing the x/y-components but effectively freezing the z-component (ignoring the effects of relaxation). (vi) When a third $\frac{\pi}{2}$ pulse is applied at a time, T, after the previous pulse the z-components of the magnetization vectors are rotated back along the y-axis and a stimulated echo forms at time τ after this pulse.

The blind spots in Mims ENDOR can be removed through the use of selective pulses. However, this significantly reduces the sensitivity of the technique. The three $\frac{\pi}{2}$ pulses used in the Mims experiment are generally non-selective, the first two pulses prior to the application of the extended radio frequency pulse act to generate a grated polarization pattern, which is dependent on the delay time between the pulses (τ). This is the source of the blind spots, the position of which can be predicted using the following formula for the efficiency of the experiment, F_{ENDOR}.

$$F_{ENDOR} = \frac{1}{4}\left(1 - \cos\left(a_{iso}\tau\right)\right) \tag{5.1}$$

a_{iso} is the isotropic hyperfine coupling constant. The Mims ENDOR signal is therefore at a maximum when $\tau = \frac{(2n+1)\pi}{a_{iso}}$ and zero when $\tau = \frac{2n\pi}{a_{iso}}$. It should be noted that three-pulse ESEEM also displays a similar blind spot behaviour; however, the dependence on a_{iso} is replaced by a dependence on the nuclear frequencies in the α and β electron spin manifolds. Mims ENDOR is generally used for the measurement of systems with small hyperfine couplings and where an increased sensitivity due to the use of short, non-selective microwave pulses is advantageous.

Davies ENDOR

Davies ENDOR uses the pulse sequence shown in Fig. 5.3.

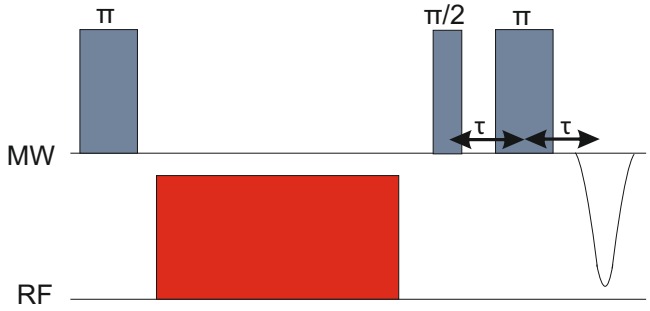


Figure 5.3: The pulse sequence for Davies ENDOR; microwave pulses exciting electron transitions are shown in blue and the radio frequency pulse exciting the nuclear transitions is shown in red. The initial microwave π pulse must be selective for only one of the electronic transitions and thus the technique is better for systems with large hyperfine couplings.

The coupling of an unpaired electron to one spin-$\frac{1}{2}$ nucleus generates four separate energy levels

due to the Zeeman splitting of the electron and the nucleus in the magnetic field. The energies of these levels are also affected by the hyperfine interaction between the coupled electron and nucleus. As can be seen from the energy level diagram for an electron coupled to a single spin-$\frac{1}{2}$ nucleus (Fig. 5.4), this results in the two EPR transitions having different energies.

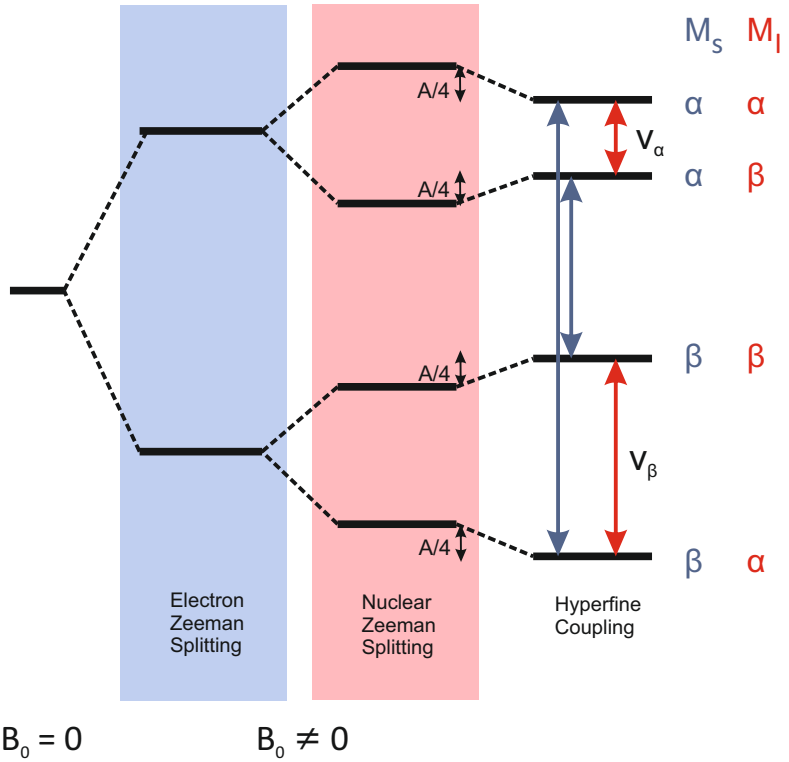


Figure 5.4: A schematic diagram illustrating the energy levels for a system of a single unpaired electron coupled to a single spin-$\frac{1}{2}$ nucleus. There are four possible allowed transitions between the energy levels involving the flip of one spin. Two are EPR transitions (blue arrows) and two are nuclear spin-flips (red arrows). The spin states of the electron and nucleus in each energy level are denoted. The lowest energy state occurs when the two spins are paired anti-parallel and the electrons magnetization vector is aligned with the magnetic field. A is the hyperfine coupling constant.

The Davies ENDOR technique relies on the selective excitation of only one of these transitions by the first π pulse. Initially the populations of the levels follow a Boltzmann distribution, where the lower two energy states are more highly populated than the upper two. The Davies ENDOR pulse sequence moves the spin populations between the four different levels, manipulating it until one nuclear spin manifold is more highly populated than the other (see Fig. 5.5).

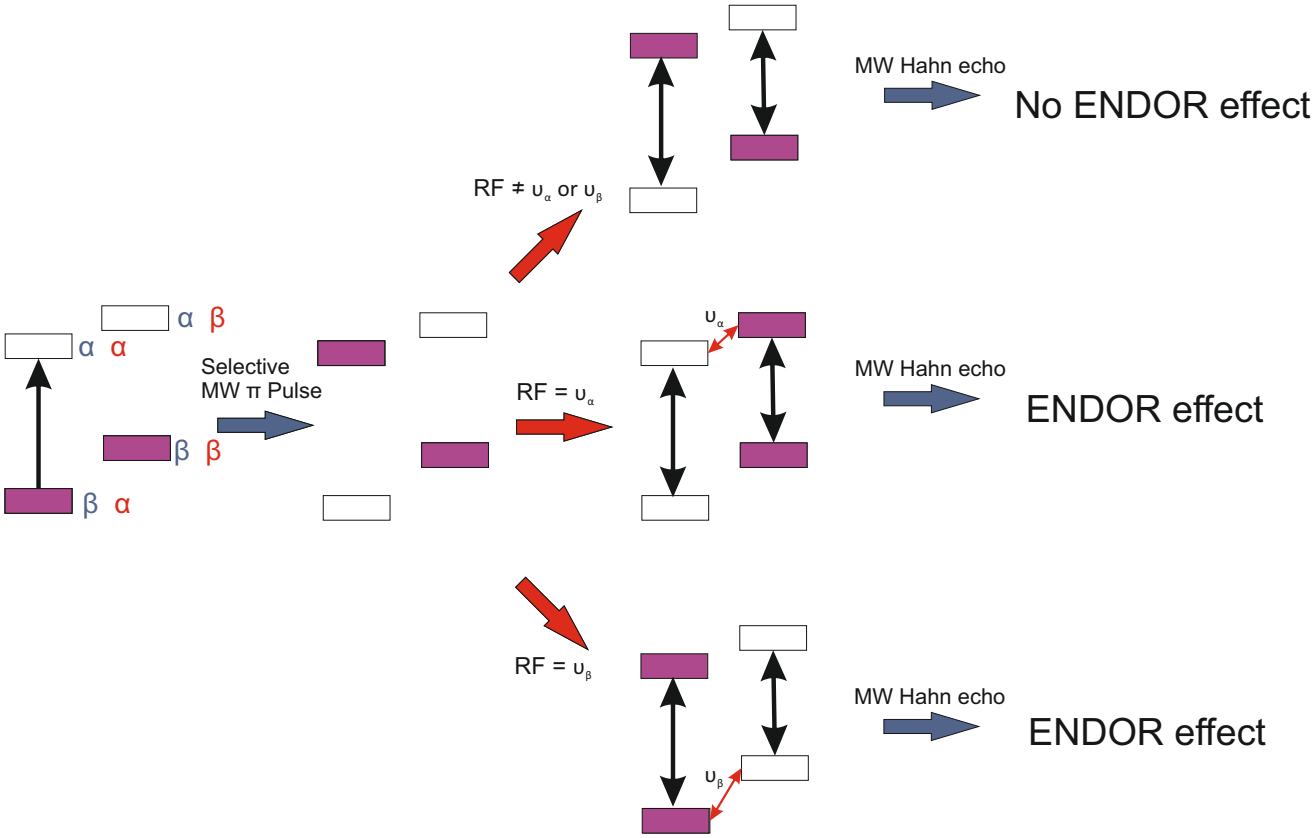


Figure 5.5: **Population manipulations in Davies ENDOR**. The electronic spin states are shown in blue and the nuclear spin states in red, black arrows show the electronic transitions excited by the microwave pulses. The initial selective π pulse excites electron transitions in the β nuclear spin manifold only. If the applied RF pulse is on resonance with either of the nuclear spin flips (ν_α or ν_β), this results in more population in one of the nuclear spin manifolds than the other, this can be detected by the Hahn echo-detection pulse sequence, which may be non-selective.

As with Mims ENDOR, the experiment is performed multiple times with the RF frequency being altered. Often data is collected stochastically with the frequency of the RF pulse being selected randomly within a given range until all points within the range have been measured. This technique can help to minimize experimental distortions such as crooked baselines and asymmetric peak intensities. Bad baselines can occur as a result of sample heating and asymmetric peak intensities from the interplay of various spin-lattice relaxation processes.[173]

The ENDOR effect is detected as a decrease in the inverted echo intensity which can be calculated according to the following formula.

$$V = \frac{1}{4}V_0\,(1 + \cos\beta) \tag{5.2}$$

where β is the radio frequency pulse nutation angle. The ENDOR efficiency is calculated from this in the following form.

$$F_{ENDOR} = \frac{1}{2}\frac{V_{echo}(RF_{off}) - V_{echo}(RF_{on})}{V_{echo}(RF_{off})} \tag{5.3}$$

The Davies ENDOR efficiency varies in the range 0 to 1. Davies ENDOR is the primary ENDOR method used for measuring systems with large hyperfine couplings as it is blind spot free. Also, as it is necessary for the first π pulse to be selective, which is achieved by increasing the length of this pulse relative to other pulses in the sequence, when the couplings are small it is necessary for this first pulse must be more selective (longer) than when the couplings are large, thus fewer spins are excited by this pulse and the sensitivity is decreased for small couplings. In this body of work Davies ENDOR is the technique used for accruing most of the spectra, since the couplings between the unpaired electron located on the $[Fe_2S_2]$ cluster to the protons in the surrounding protein structure are relatively large.

Variable mixing time ENDOR

Both Mims and Davies ENDOR allow the determination of the magnitude of a hyperfine coupling. However, the absolute sign of these couplings is not determined. One way to measure the sign of a hyperfine coupling is to compare two ENDOR spectra recorded with different mixing times, i.e. the delay time left after the RF pulse before the following microwave pulse (see Fig. 5.1). This introduces a controlled asymmetry into the spectrum, which allows specific lines to be assigned to a specific m_s manifold. Thus the sign of the hyperfine coupling, A, can be determined.[13]

The determination of the sign of the hyperfine coupling is necessary for this work since it leads to an unambiguous determination of the iron oxidation states and this allows the determination of the

isotropic and anisotropic parts of the hyperfine interaction. This is vital for predicting the orientation of the g-tensor as it allows the assignment of areas of positive and negative spin density.

The original variable mixing time ENDOR experiments used the Davies ENDOR sequence.[174] However, for the experiments presented in this thesis, a Mims type sequence was used to allow for greater sensitivity in the measurement. Three spin-lattice relaxation processes can occur during the mixing time, t_{mix}. These are: electronic relaxation (T_{1e}), nuclear relaxation (T_{1n}) and cross relaxation (T_{1x}). When the relaxation processes occur at different rates, this can lead to asymmetry in the spectrum (for example if $T_{1n}, T_{1x} >> T_{1e}$ and $t_{mix} >> T_{1e}$). Relaxation of the electrons into the lower energy (β) state during the delay time results in an excess in population of a single state. This causes the intensity of the echo from one of the spin manifolds being much greater than that from the other, giving a change of sign of the ENDOR signals (efficiency) observed in one of the manifolds as the time allowed for mixing increases. This is demonstrated in Fig. 5.6, which shows a plot of the ENDOR efficiency at different mixing times.

ENDOR spectra

The spectrum observed in ENDOR is dependent on the size of the hyperfine coupling in the system, A, in comparison to the nuclear Larmor frequency, ν_I. The weak coupling condition is characterized by:

$$\left|\frac{A}{2}\right| < |\nu_I| \tag{5.4}$$

and the strong coupling condition is given by:

$$\left|\frac{A}{2}\right| > |\nu_I| \tag{5.5}$$

Weak coupling (to a first order approximation) results in a spectrum centred about the nuclear Larmor frequency with peaks occurring at the nuclear frequencies of the α and β spin manifolds, separated by the hyperfine coupling constant, A. Strong coupling gives a spectrum (to a first order approximation)

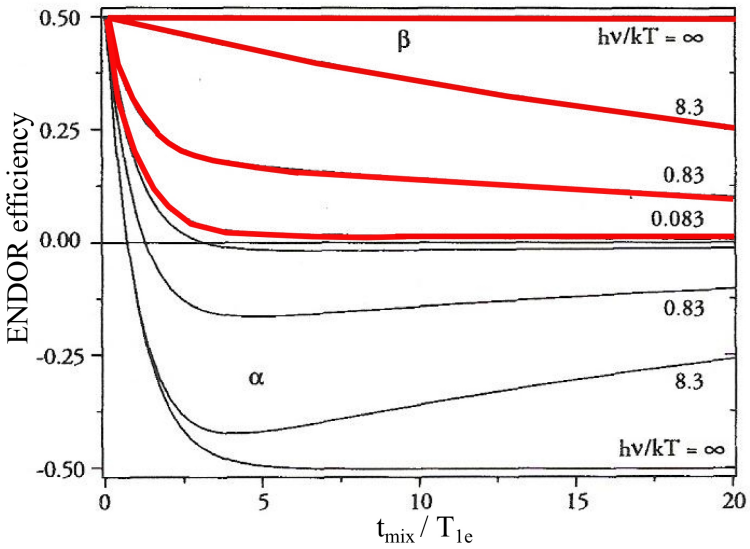


Figure 5.6: The dependence of the ENDOR efficiency on temperature and the ratio of $\frac{t_{mix}}{T_{1e}}$, for values of $\frac{h\nu}{kT}$ are indicated in this plot. Red lines correspond to F^{β}_{ENDOR} and black lines to F^{α}_{ENDOR}. $T_{1n} = T_{1e} = 30$; t_R, $T_{1x} = 1$. This figure is adapted and reproduced from Springer, *Applied Magnetic Resonance*, **21(3–4)**, 2001, 287–297, High-Field ENDOR and the Sign of the Hyperfine Coupling, B. Epel, P. Manikandan, P. M. H. Kroneck and D. Goldfarb, Figure 2. Copyright © Springer-Verlag 2001; with kind permission from Springer Science and Business Media.[13]

centred about $\frac{A}{2}$, with a peak separation of $2\nu_I$. These two cases are given in Fig. 5.7. $\left|\frac{A}{2}\right| = |\nu_I|$ is the cancellation condition, and in this case only a single peak is observed in the ENDOR spectrum at $2A$, a second peak at 0 is not observed as the hyperfine enhancement factor ($E = \left|1 + \frac{m_s A}{\nu_I}\right|$) at this point is zero. The experimental ^{1}H data collected in this chapter fall into the weak coupling limit.

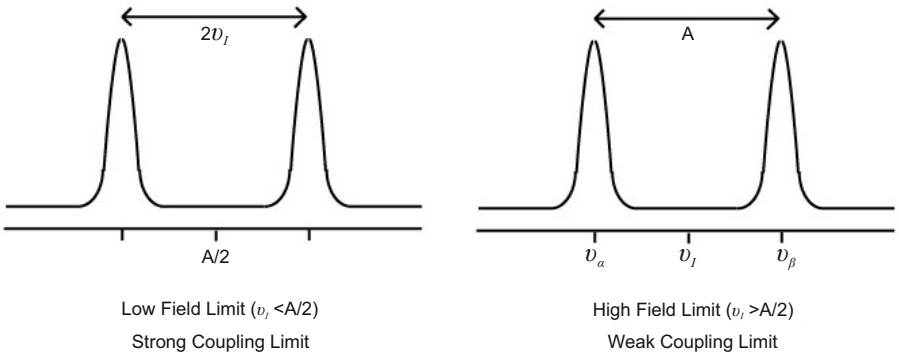


Figure 5.7: Two possible ENDOR spectra are shown. **Left:** The ENDOR spectrum in the strong coupling limit. **Right:** The ENDOR spectrum in the weak coupling limit.

5.1.2 The HYSCORE technique

Hyperfine Sublevel CORrElation (HYSCORE)[175] spectroscopy is effectively a two-dimensional ESEEM technique. It was introduced by Peter Höfer and colleagues in 1986.[176] The pulse sequence for HYSCORE is given in Fig. 5.8.

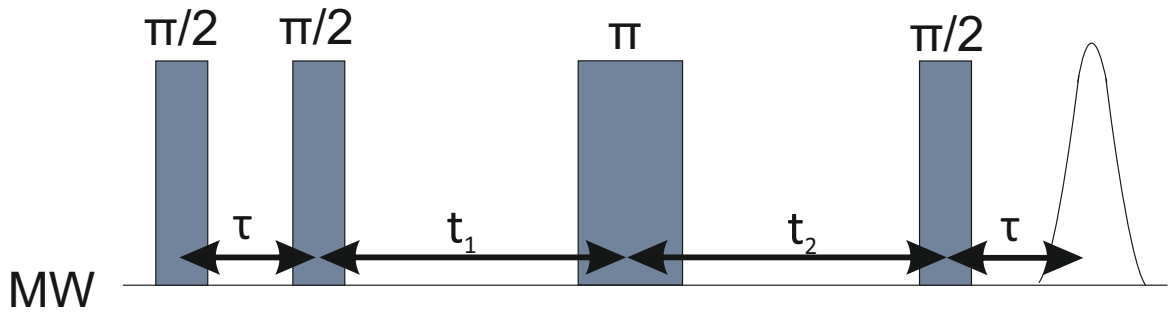


Figure 5.8: The pulse sequence for HYSCORE.

As with ESEEM, the first two $\frac{\pi}{2}$ pulses act as a nuclear coherence generator. The first pulse generates electronic coherence by exciting either the allowed transitions (only the electron spin-flips) or forbidden transitions (both the electron and the nucleus undergo a spin-flip). The second pulse also excites the same electronic transitions, which either causes the electron to return back to its original energy level, if the same type of transition (allowed or forbidden) is excited by both pulses, or revert back to its original electronic spin state with the inverted nuclear spin state, if the two pulses excite opposite types of transitions. Hence the two $\frac{\pi}{2}$ pulses separated by a time delay, τ, generate nuclear coherence. The π pulses mixes the nuclear coherence states by inverting the electronic states and the final $\frac{\pi}{2}$ pulse converts the nuclear coherence back to electronic coherence for detection. This is shown pictorially in Fig. 5.9.

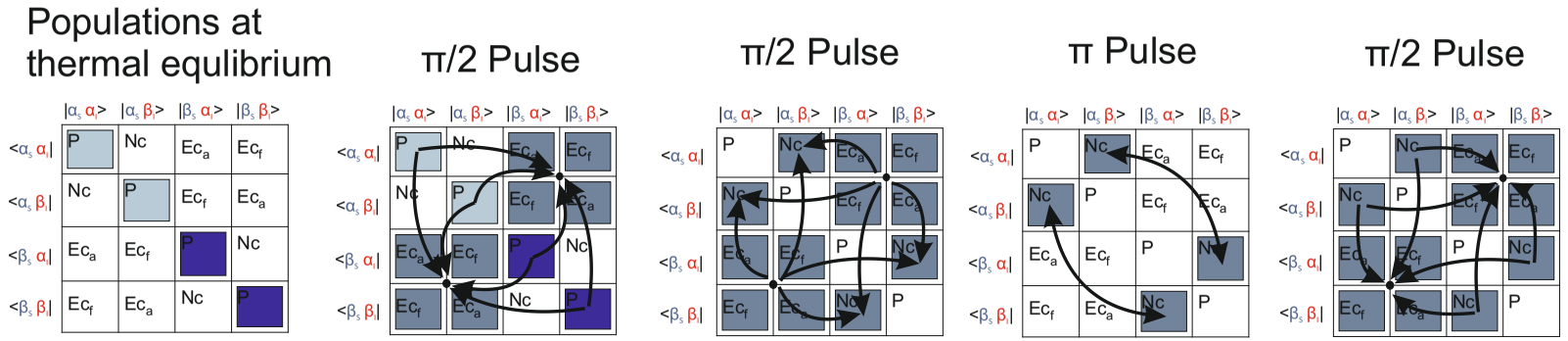


Figure 5.9: A pictorial representation of the coherences generated in HYSCORE for a system of a single unpaired electron coupled to a single spin-$\frac{1}{2}$ nucleus. The arrows represent the movement of population caused by each of the pulses and the blue blocks represent the population of the spin states, (the deeper the blue colour the greater the population of the state). P shows the coherences causing polarization of the electronic states, Ec_a are allowed electron coherences, Ec_f are forbidden electron coherences and Nc are nuclear coherences.

HYSCORE spectra are measured in the time domain and give a two-dimensional trace, which is the recorded echo intensity for the pulse sequence with variable t_1 and t_2 time delays. For a fixed τ time, the echo intensity ($V(\tau, t_1, t_2)$) for a system of a single electron coupled to a single spin-$\frac{1}{2}$ nucleus is given by:

$$V(\tau, t_1, t_2) = 1 - \left(\frac{k}{2}\right)(V_I + V_{IIa} + V_{IIb} + V_{IIIa} + V_{IIIb}) \tag{5.6}$$

where the five components $V_I,\ V_{IIa},\ V_{IIb},\ V_{IIIa}$ and V_{IIIb} are dependent on the action of the π pulse. V_I corresponds to the pulse changing from one polarization state to another, V_{IIa} and V_{IIb} correspond to the π pulse changing polarization to nuclear coherence or vice versa, and V_{IIIa} and V_{IIIb} are the echo contributions from changing from one nuclear coherence to another. V_{IIIa} and V_{IIIb} are the main two contributions which give oscillations in the time domain over the course of the experiment. All of the different contributions to the echo intensity can be modelled as a combination of cos functions, which vary with $t_1,\ t_2$ and τ.

HYSCORE spectra are analysed in the frequency domain (the Fourier transform of the time domain signal). The V_{IIa} and V_{IIb} contributions to the echo give rise to peaks on the x and y-axes; for a the system of a single electron coupled to a single spin-$\frac{1}{2}$ nucleus these occur at $(\nu_\alpha, 0),\ (\nu_\beta, 0),\ (0, \nu_\alpha)$ and $(0, \nu_\beta)$. In comparison, the V_{IIIa} and V_{IIIb} contributions give rise to cross peaks at $(\pm\nu_\alpha, \pm\nu_\beta)$ and $(\pm\nu_\beta, \pm\nu_\alpha)$. Since ν_α and ν_β are orientationally dependent for a frozen solution, a powder pattern is observed, such as that seen in Fig. 5.10, where each of the combinations of ν_α and ν_β give rise to an arc of points.

In the strong coupling regime ($|A| > 2\,|\nu_I|$), peaks appear in the $(-,+)$ quadrant, whereas in the weak coupling regime they occur in the $(+,+)$ quadrant. In this work, all of the spectra fall into the weak coupling regime and in this case it is the curvature of the arcs behind the anti-diagonal that can be used to estimate the magnitude of the anisotropic dipolar interaction.

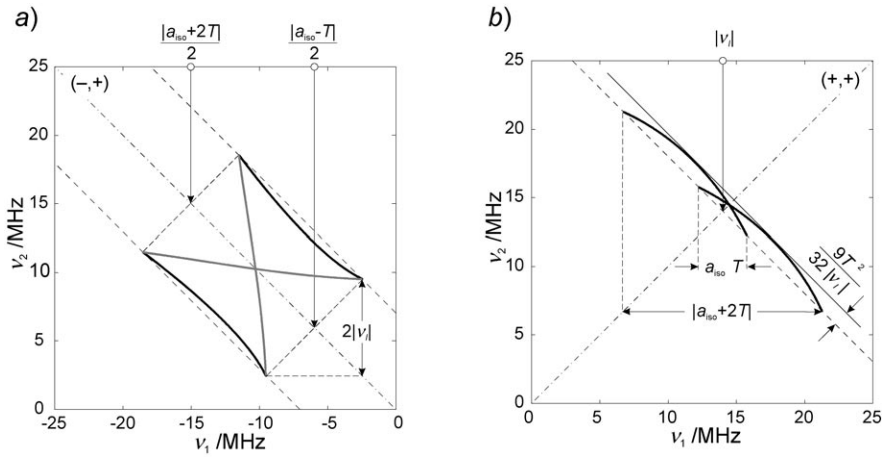


Figure 5.10: Theoretical HYSCORE powder patterns for an $S = \frac{1}{2}$, $I = \frac{1}{2}$ spin system with an axial hyperfine matrix: **(a)** Strong-coupling case with $\nu_I = 3.5$ MHz, $a_{iso} = 18$ MHz and $T = 6$ MHz (black curves), $a_{iso} = 2$ MHz and $T =$14 MHz (grey curves), **(b)** weak-coupling case with $\nu_I = 14$ MHz, $a_{iso} =$ 2.5 MHz and $T = 6$ MHz. This figure is reproduced from *Helvetica Chimica Acta*, **89(10)**, 2006, 2495–2521, Pulse EPR methods for studying chemical and biological samples containing transition metals, C. Calle, A. Sreekanth, M. V. Fedin, J. Forrer, I. Garcia-Rubio, I. A. Gromov, D. Hinderberger, B. Kasumaj, P. Leger, B. Mancosu, G. Mitrikas, M. G. Santangelo, S. Stoll, A. Schweiger, R. Tschaggelar and J. Harmer. Copyright © 2006 Verlag Helvetica Chimica Acta AG, Zürich.[14]

The maximum distance behind the anti-diagonal, $\Delta\nu_{max}$ is dependent on the dipolar coupling, T. When T is given in units of frequency, the relationship is:

$$\Delta\nu_{max} = \frac{9T^2}{32\,|\nu_I|} \tag{5.7}$$

The positions of the ends of the arcs also give information about the values of the dipolar coupling contribution to the hyperfine interaction, T and the isotropic part, a_{iso} (see Fig. 5.10).

Although HYSCORE spectra can provide a lot of information, their acquisition is generally time-consuming since two-dimensions are required. Due to the use of the three $\frac{\pi}{2}$ pulses in the sequence, HYSCORE suffers from blind-spots in the same manner as three pulse ESEEM and Mims ENDOR. Therefore it may be necessary to record more than one HYSCORE spectrum with different τ times. In most circumstances, to understand the hyperfine coupling within a system, a combination of ENDOR and HYSCORE measurements are used.

5.2 Determination of the *g*-tensor orientation and the spin distributions within the $[Fe_2S_2]$ cluster in PuxB

In order to facilitate the determination of the orientation of the *g*-tensor, it is first necessary to understand the environmental asymmetry of the $[Fe_2S_2]$ cluster. Density functional theory (DFT) calculations on symmetrized and native state structures show a fairly large deviation in terms of the energy levels calculated (see Section 5.4). Since the magnitude of the *g*-tensor, and thus in turn its orientation, are dependent on the energies of the excited states (see Section 1.2.2), these changes in energy levels will necessarily cause changes to the *g*-tensor calculation (value and orientation).

However, it is the asymmetry in the $[Fe_2S_2]$ environment, in particular the spatial distribution of protons to which the $[Fe_2S_2]$ cluster couples via hyperfine interactions, that facilitates the determination of the orientation of the *g*-tensor with respect to the surrounding protein structure. In the work presented here, the ^1H couplings to the $[Fe_2S_2]$ cluster are used to specify the orientation of the *g*-matrix with respect to the protein structure.

5.2.1 Existing *g*-tensor orientations for related $[Fe_2S_2]$ protiens

Over the last decade there has been a steadily building body of work on the applications of orientationally selective hyperfine spectroscopy to determine *g*-matrix orientation. Some of the most notable contributions are from Kappl and co-workers, who pioneered the approach of using the ^1H hyperfine couplings to determine the *g*-tensor for several related proteins containing Iron-Sulphur clusters. Their work has examined not only $[Fe_2S_2]$ cluster containing proteins but also those with $[Fe_4S_4]$ clusters and $[FeNiS_2]$ containing hydrogenases.[164–169]

$[Fe_2S_2]$ clusters in ferredoxins generally exist in one of two types of coordination environment depending on the protein ligands to the two iron centres. Clusters ligated by the thiol groups from two cysteines and nitrogen from two histidine amino acids are termed 'Rieske clusters'. Alternatively the $[Fe_2S_2]$ cluster may be ligated by four cysteine thiol groups. Both PuxB and HaPux, used for the DEER work in the previous chapter, fall into the second category. The $[Fe_2S_2]$ cluster class ligated by four

cycteines can be further subdivided into two categories: 'plant type', which have a rhombic g-matrix, and 'vertebrate type' (e.g. adrenodoxin (Adx)), which have an axial, or almost axial, g-matrix.[177] Rarer intermediate types with three ligating cysteine and one ligating histidine are also known.[178] The broad variation of g-matrix composition seen for relatively small structural changes again highlights how sensitive the g-matrix is to the extended structure of the protein around the $[Fe_2S_2]$ cluster.[179]

Under atmospheric conditions, the $[Fe_2S_2]$ clusters have both irons present in the Fe^{3+} oxidation state. In this case antiferromagnetic coupling makes the cluster EPR silent, all of the electrons are paired. In order to study the $[Fe_2S_2]$ clusters by EPR, it is necessary to reduce the cluster to the $[Fe_2S_2]^+$ form, with an $S = \frac{1}{2}$ ground state, where one iron is present as Fe^{3+} and the other as Fe^{2+}. Therefore EPR determination of the g-matrix orientation has been performed on the reduced form of the protein in frozen solution. Assessing orientations of the g-tensor published for different types of $[Fe_2S_2]$ protein shows that vertebrate type $[Fe_2S_2]^+$ clusters consistently appear to show structures with the unique $g_{||}$ axis almost perpendicular to the $[Fe_2S_2]^+$ plane but with a tilt towards one of the sulphur atoms of a ligating cysteine residue.[164,165,169,180] A nickel containing hydrogenase with a $[FeNiS_2]$ cluster also showed a rhombic g-matrix with a principal axis tilted towards a ligating cysteine of the nickel.[167] Rieske clusters, with their rhombic g-matrices, have shown a wider range of different orientations.[164,165,181,182] Rarer variants exist, such as human mitoNEET containing three ligating cysteines and one histidine, this has been reported to have a g-matrix orientation similar to several Rieske proteins.[178]

PuxB (and HaPux) both fall into the vertebrate class of ferredoxins and thus it is only necessary to determine the unique direction of the $g_{||}$ component of the g-tensor. This considerably simplifies the problem to be solved, since assigning the orientation of a single vector requires significantly fewer variables than assigning the orientation of a system of x,y,z-axes.

5.2.2 Experimental details

In this investigation, W-band EPR is employed to determine the principal g-values. W-band (94 GHz) pulse ENDOR and X-band (9.7 GHz) HYSCORE experiments allow the full ^1H hyperfine matrix

(principal values and axes) of the protons closest to the paramagnetic $[Fe_2S_2]^+$ centre to be determined. The experimental data are then modelled with the aid of the X-ray crystal structure and a dipolar model for the protons to allow the magnetic moment and orientation of the g-matrix to be evaluated.

Two samples were investigated: firstly a sample of the frerredoxin (PuxB) in complex with the ferredoxin reductase (PuR) and secondly a sample containing PuxB alone. The use of two samples was to establish whether there was any change in the g-tensor environment, and thus on the structure of the PuxB, on docking to the PuR as this would put into doubt the validity of using the independently determined X-ray crystal structures for the determination of a docked structure.

Sample preparation

The preparation for the mixed PuxB-PuR sample was very similar to the procedure described for the preparation of those used in the DEER experiments in Chapter 4 (see Section 4.1.2). The proteins used were the same as those used for the DEER measurements; the wild-type PuR and the PuxB(A105R) mutant. No spin labelling was required. Samples for this investigation were produced by Mr Eachan Johnson and Dr Stephen Bell, members of Dr Luet Wong's research group.

Both proteins were expressed in *E. coli* and then concentrated by centrifugal filtration using Millipore Amicon Ultra-4 centricon filters with 30 kDa and 10 kDa cut off for PuR and PuxB respectively. The protein concentrations were determined using $\epsilon_{414} = 10.8$ $mM^{-1}cm^{-1}$ for PuxB and $\epsilon_{454} = 10.0$ $mM^{-1}cm^{-1}$ for PuR.[12,150] Both proteins were prepared to a concentration of c.1 mM in TE buffer.[a] The two samples were reduced in a Belle Technology glove box (O_2<5 ppm). PuxB alone was reduced using an excess of sodium dithionite until the sample turned pink. This method was not suitable for the mixed sample, where the PuR might also be reduced. Instead half an equivalent of the physiological reducing agent NADH was used. The samples were diluted with 50% glycerol by volume, placed in EPR tubes and temporarily sealed with nescofilm in the glove box, before being flash frozen in liquid nitrogen directly on removal from the glove box.

[a]TE buffer is made from a combination of Tris (tris(hydroxymethyl)aminomethane, $(HOCH_2)_3CNH_2$) and EDTA (Ethylenediaminetetraacetic acid, $((HO_2C(CH_2))_2N(CH_2))_2$).

EPR setup

X-band CW EPR measurements were carried out on a Bruker EMX micro spectrometer and pulse measurements at X-/W-band on a Bruker ELEXSYS 680 spectrometer. Both spectrometers were equipped with a helium gas-flow cryostat from Oxford Instruments. X-band CW EPR spectra were recorded with a microwave power of 2 mW and a modulation amplitude and frequency of 0.2 mT and 100 kHz respectively, using a Bruker ELEXSYS super high sensitivity cavity. The field was calibrated with a 2,2-diphenyl-1-picrylhydrazyl (DPPH) sample with $g = 2.0036$.

The echo-detected field-sweep W-band EPR spectra at 20 K were recorded by integrating over the echo created with the microwave (MW) pulse sequence $\frac{\pi}{2}$ - τ - π - τ - *echo*, with MW pulse lengths $t_{\frac{\pi}{2}} = 32$ ns, $t_\pi = 64$ ns, and $\tau = 200$ ns. The field was calibrated using the two central lines from a CaO sample containing manganese ions. The ^{1}H Davies-ENDOR spectra were obtained at 20 K with a 500 W radio-frequency (RF) amplifier with the MW pulse sequence π - T - ($\frac{\pi}{2}$ - τ - π - τ - *echo*), with MW pulses of length $t_{\frac{\pi}{2}} = 32$ ns, $t_\pi = 64$ ns, $\tau = 200$ ns, and a shot repetition time of 1.5 ms. A RF pulse of length 23 ms of variable frequency (νRF) was applied during time $T = 24$ ms. Due to magnetic hysteresis effects in setting the field of each ENDOR experiment, the field was corrected so that the ^{1}H Larmor frequency is in the middle of the symmetric W-band trace. A variable mixing time ENDOR experiment using a Mims-type sequence to measure the absolute sign of the hyperfine interaction was carried out with the sequence $\frac{\pi}{2}$ - τ - $\frac{\pi}{2}$ - t_1 - RF - t_{mix} - $\frac{\pi}{2}$ - τ - *echo*, where $t_{\frac{\pi}{2}} = 32$ ns, $\tau = 200$ ns, $t_1 = 200$ ns, with a shot repetition time of 60 ms at 5 K. RF indicates a radio-frequency pulse of length 23 ms and variable frequency, ν_{RF}. Two t_{mix} times of 400 ns and 16 ms were used. All W-band measurements were conducted using an EN600-1021H TeraFlex W-band pulsed ENDOR-resonator.

X-band hyperfine sublevel correlation (HYSCORE) experiments were recorded at 15 K in a 4 mm dielectric resonator (EN 4118X-MD4). These measurements employed the pulse sequence $\frac{\pi}{2}$ - τ - $\frac{\pi}{2}$ - t_1 - π - t_2 - $\frac{\pi}{2}$ - τ - *echo* with MW pulses of lengths $t_{\frac{\pi}{2}} = t_\pi = 16$ ns, $\tau = 116$, 120 or 124 ns, and starting times $t_{1,0} = t_{2,0} = 64$ ns with increments $\Delta t = 16$ ns (data matrix 350 × 350). The shot repetition time was 1.5 ms. An eight-step phase cycle was used to remove unwanted echoes.

5.2.3 The method of analysis

Whereas previous approaches have used only CW-ENDOR measurements to determine the position of the g-matrix with respect to the protein structure, the approach reported here uses W-band ^{1}H Davies ENDOR measurements, to provide highly orientation dependent spectra, in combination with X-band ^{1}H HYSCORE, which is very sensitive to the dipolar part of the ^{1}H hyperfine coupling.

Hyperfine couplings are distance dependent; the hyperfine coupling constant increases as the distance between the electron and nucleus decreases. For this reason it is only necessary to consider the couplings of the protons nearest to the paramagnetic $[Fe_2S_2]^+$ cluster in the analysis, as these will have the largest splittings in the ENDOR and HYSCORE spectra.

Within the $[Fe_2S_2]^+$ cluster, the two iron centres in oxidation states Fe^{2+} and Fe^{3+} are antiferromagnetically coupled to one another to give the cluster an $S = \frac{1}{2}$ ground state. This requires a strong exchange coupling between the two iron centres and as a consequence we must consider spin projection factors. These quantify the strength of the magnetic moment at points in the antiferromagnetically coupled cluster.

As an initial model the spin projection factors appropriate for an ionic model of antiferromagnetically coupled Fe^{3+} ($S_A = \frac{5}{2}$) and Fe^{2+} ($S_B = 2$); $K_A(Fe^{3+}) = +\frac{7}{3}$ and $K_B(Fe^{2+}) = -\frac{4}{3}$ were used.[183] However, results from this model showed that it was not representative of the real system (see Section 5.2.5) and, by optimizing the spin density distribution, the resulting delocalized spin projection factors were shown to give much better fits to the experimental data.

The spin projection factors allowed the calculation of the dipolar parts of the hyperfine interaction, as detailed in Section 5.2.6. Once this was done, the isotropic parts of the hyperfine couplings were adjusted to give the best fit of the ENDOR and HYSCORE simulations to the set of orientationally dependent experimental data. A search over all molecular orientations relative to the g-matrix frame identifies the unique best fit.

Key to the analysis is the assignment of the two Fe ion oxidation states; it is believed that the Fe ion nearest to the surface of the protein is the one that is reduced (Fe^{2+}). Further evidence for this was afforded by a variable mixing time ENDOR experiment to determine the absolute sign of the

hyperfine interaction; positive hyperfine values are expected around the Fe^{3+} ion, which has an excess of electrons in the β spin manifold.

Curve fitting and EPR simulation

The HYSCORE data were processed with MATLAB 7.10.0 (The MathWorks, Inc.). The time traces were baseline-corrected with an exponential function, apodized with a Gaussian window and zero filled. After a two-dimensional Fourier transformation, absolute-value spectra were calculated. The field-sweep EPR, Davies-ENDOR, and HYSCORE spectra were simulated with the program EasySpin.[7] HYSCORE simulations of just the cross-peak positions were simulated with a program written in-house that diagonalizes the spin Hamiltonian.

Simulated ENDOR spectra generated with EasySpin were fitted to the experimental spectra using the Gauss-Newton algorithm, with the Levenberg-Marquardt extension which was written in-house. The non-linear parameters are the isotropic hyperfine couplings and the linear parameters are the amplitudes of the spectra for each component.

5.2.4 Devising a structural model for fitting to the experimental data

Just as the fitting of the orientationally selective DEER spectra to determine the docked protein structures requires prior knowledge of the individual protein structures and the distribution of the spin centres within them, in order to utilise the ENDOR and HYSCORE data to find a relative orientation of the g-tensor of the $[Fe_2S_2]^+$ with respect to the protein structure, a model of the protein structure surrounding this centre is needed. The crystal structure of PuxB is available, PDB accession code *3HUI.pdb.*[12] The program 'Chimera', a graphical user interface protein visualization and manipulation program developed by researchers at UCSF,[1] was used to add protons to the carbon backbone and heteroatoms. Proton positions are calculated using the atom types specified in the PDB file and by taking into account steric interactions and hydrogen bonding interactions.

It is a good assumption that any protons lying within three bonds from an iron in the $[Fe_2S_2]^+$ cluster will have a significant isotropic hyperfine coupling component conducted via the Fermi contact

interaction. For a $[Fe_2S_2]^+$ cluster ligated by four cysteine residues, such as that found in PuxB, these protons correspond to those bound to the β-carbon of the ligating cyesteines. These protons are referred to as β-protons. In addition any protons close in spatial terms to the $[Fe_2S_2]^+$ cluster will have a though-space, dipolar, anisotropic hyperfine coupling to the unpaired electron on the cluster. In our model, any proton lying within 3.5 Å from one of the Fe ions in the cluster was considered to have a considerable dipolar hyperfine component. Protons further away have hyperfine interactions that are too small to be resolved in either ENDOR or HYSCORE spectra and therefore these cannot be used to provide information about the g-matrix orientation or the spin projection factor values. In total, 13 protons comprised the model of the protein structure surrounding the $[Fe_2S_2]^+$ cluster; these are listed in Table 5.1.

Due to the antiferromagnetic nature of the coupling in the $[Fe_2S_2]^+$ cluster, protons closest to Fe^{3+} will possess a_{iso} values of opposite sign to those for the protons closest to Fe^{2+}.

Examination of the protein structure and knowledge of the function of the protein indicated that the Fe ion closest to the surface of the protein, designated *Fe1* in the PDB structure (*3HUI.pdb*)[12] was likely to be in the reduced oxidation state, Fe^{2+}, and therefore possess a negative spin projection factor. The protons close in bonding terms to this Fe centre will therefore have negative a_{iso} values. They are the protons on Cysteine 39 and 45 (numbers 3, 4, 7 and 8 in the model). In contrast, those close in bonds to the Fe^{3+}, the β protons of Cysteines 48 and 85 (numbers 1, 2, 5 and 6 in the model), will have positive a_{iso} values due to the positive spin projection factor associated with the Fe^{3+} centre. The assignment of the oxidation states of the two Fe ions in $[Fe_2S_2]^+$ was confirmed by means of the variable mixing-time ENDOR experiment (see Section 5.4.2).

Table 5.1: Showing the hyperfine parameters for all 13 protons in the EPR model 3. The columns correspond to residue and reference number, the distance from the nearest Fe ion, the experimental isotropic hyperfine couplings, a_{iso}, the principal values of the dipolar hyperfine couplings, T_i, and the full matrix of the dipolar hyperfine couplings, **T**, relative to the '*3HUI.pdb*' frame. All dipolar couplings are given in MHz and the error on the principal values of these couplings is estimated to be ±0.2 MHz. This table is reproduced from the Supporting Information of J. A. B. Abdalla, A. M. Bowen, S. G. Bell, L. L. Wong, C. R. Timmel and J. Harmer, Characterisation of the paramagnetic $[Fe_2S_2]^+$centre in palustrisredoxin-B (PuxB) from Rhodopseudomonas palustris CGA009: g-matrix determination and spin coupling analysis, *Physical Chemistry Chemical Physics*, 2012, **14(18)**, 6526–6537 with permission from the PCCP Owner Societies.[15]

Residue	Proton No.	Distance Fe−H (Å)	a_{iso} (MHz)	T_1 (MHz)	T_2 (MHz)	T_3 (MHz)		**T** (MHz)	
Cys85	1	2.825	2.90	9.67	−4.28	−5.43	4.7249	−4.6777	4.939
							−4.6733	−1.868	−2.7118
							4.9323	−2.7153	−2.8879
Cys48	2	3.200	3.29	7.02	−4.46	−2.55	−2.545	3.0104	−2.4732
							2.985	3.828	−3.3986
							−2.423	−3.3669	−1.2739
Cys39	3	3.780	−4.10	−1.79	0.69	1.03	0.6029	−0.1785	−0.5619
							−0.1811	0.9567	−0.2976
							−0.5312	−0.2697	−1.6243
Cys45	4	3.853	−3.22	−1.69	0.60	1.03	−0.9435	0.2219	−1.0456
							0.2497	0.8553	0.3883
							−1.0846	0.369	0.0335
Cys85	5	3.889	3.28	4.31	−1.80	−2.52	3.861	−1.5518	0.4163
							−1.5395	−1.3811	−0.1209
							0.4007	−0.1279	−2.4927
Cys48	6	4.048	2.80	3.96	−2.27	−1.69	−2.0792	0.0225	−0.4264
							0.0148	0.8107	−2.8995
							−0.4079	−2.8867	1.2636
Cys45	7	4.527	−3.81	−1.11	0.38	0.72	−1.0596	0.2561	−0.0024
							0.2972	0.4346	0.1674
							−0.0413	0.1568	0.6193
Cys39	8	4.555	−2.46	−1.05	0.55	0.49	0.41	−0.0044	0.4078
							0.0043	0.4968	−0.116
							0.4424	−0.0771	−0.9195
Gly41	9	3.406	n/a	5.95	−4.04	−1.92	2.2336	−1.5932	−4.4065
							−1.5377	−1.3549	1.3438
							−4.4514	1.3369	−0.8897
Leu83	10	3.447	n/a	5.55	−3.03	−2.54	−2.7522	−0.9246	−0.9657
							−0.9261	2.2071	3.8799
							−0.9689	3.8759	0.5233
Cys39	11	3.005	n/a	−4.01	1.42	2.52	1.5944	−1.0069	0.0534
							−1.0663	−2.4738	−2.4932
							−0.032	−2.614	0.8042
Ala44	12	3.232	n/a	−3.69	0.75	3.08	0.5937	−0.9502	0.9043
							−1.0631	−2.9136	1.555
							1.0037	1.5768	2.4645
Gly41	13	3.361	n/a	−4.46	−0.39	4.77	−2.8685	1.0023	−2.2945
							1.0783	−0.5236	2.2761
							−2.3169	2.3042	3.3136

Protons close to the $[Fe_2S_2]^+$ cluster in space but distant in terms of bonds have hyperfine couplings to the electron on the $[Fe_2S_2]^+$ cluster, which have much larger dipolar contributions than isotropic contributions. Therefore for these protons only the dipolar contributions need to be considered in the modelling. This class of proton encompasses protons numbered 9, 10, 11, 12 and 13 in the model.

The location of the protons included in the model are shown in Fig. 5.11.

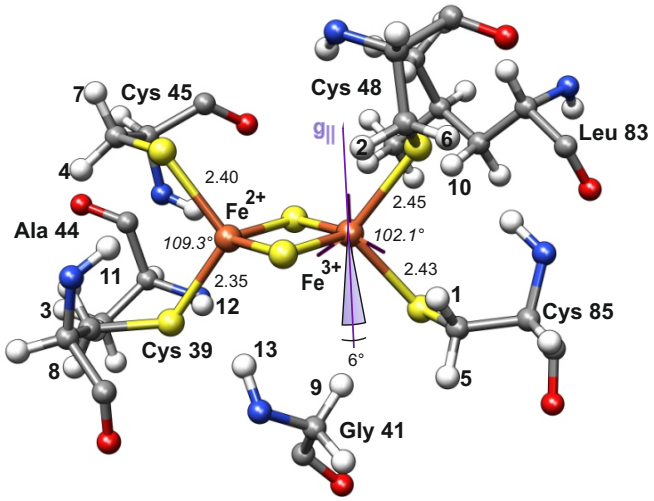


Figure 5.11: X-ray structure of oxidized PuxB. The 13 protons used in the model to simulate the ENDOR and HYSCORE data are numbered 1 to 13 (see Table 5.1). The axis vector placed on the Fe^{3+} ion (labelled `Fe2` in PDB file *3HUI.pdb*) shows the orientation of the $g_{||}$-axis relative to the molecular frame of the protein. The cone indicates the uncertainty in the $g_{||}$-axis direction (as derived later). This figure is reproduced from J. A. B. Abdalla, A. M. Bowen, S. G. Bell, L. L. Wong, C. R. Timmel and J. Harmer, Characterisation of the paramagnetic $[Fe_2S_2]^+$centre in palustrisredoxin-B (PuxB) from Rhodopseudomonas palustris CGA009: g-matrix determination and spin coupling analysis, *Physical Chemistry Chemical Physics*, 2012, **14(18)**, 6526–6537 with permission from the PCCP Owner Societies.[15]

The validity of the crystal structure

As we have already seen for the work using DEER to generate structures of the docked complexes of PuxB-PuR and HaPux-P450, it is clear that the crystal structures, while providing a good indication of the structure of the proteins in solution and in the docked complexes, do not provide a completely accurate depiction of the solution state structures as they are not dynamic. This necessitated the opti-

mization of the final docked protein structures by geometrical relaxation and also the use of molecular dynamic calculations to minimize the energy of the structures (see Section.4.8).

The crystal structure *3HUI.pdb* was measured using PuxB in an oxidized state, where the cluster is found as diamagnetic $[Fe_2S_2]^{2+}$. A handle on the structural changes between the oxidized and reduced forms can be quantified from the vertebrate-type $[Fe_2S_2]$ ferredoxin putidaredoxin (Pdx) from *Pseudomonas putida* for which there are X-ray structures of both oxidized and reduced forms.[184] A comparison of the localized $[Fe_2S_2]$ structures in the oxidized and reduced forms of Pdx are shown with important bonds lengths marked in Fig. 5.12. There appears to be a very small redox-dependent conformational change in Pdx causing contraction of the Fe-S_{cys} bonds by up to 0.05 Å upon reduction.[185]

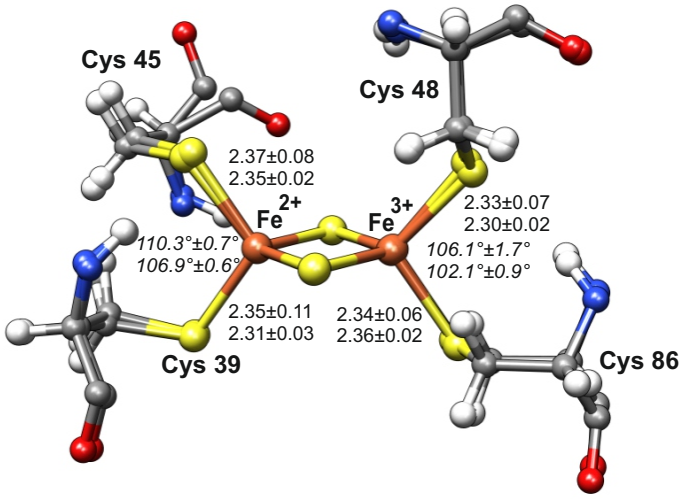


Figure 5.12: Overlay of the X-ray structure of the oxidized (*1XLP.pdb*) and reduced (*1XLQ.pdb*) C73S mutant of Pdx.[184] Selected bond distances and angles are shown to highlight the similarity between the oxidized and reduced forms (upper and lower numbers, respectively). This figure is reproduced from J. A. B. Abdalla, A. M. Bowen, S. G. Bell, L. L. Wong, C. R. Timmel and J. Harmer, Characterisation of the paramagnetic $[Fe_2S_2]^+$centre in palustrisredoxin-B (PuxB) from Rhodopseudomonas palustris CGA009: g-matrix determination and spin coupling analysis, *Physical Chemistry Chemical Physics*, 2012, **14(18)**, 6526–6537 with permission from the PCCP Owner Societies.[15]

Comparison of the both Pdx structures with the oxidized PuxB structure (see Fig. 5.13) demonstrates that all three structures are very similar. This indicates that use of the PuxB crystal structure

coordinates without modification in the analysis of the EPR data should not introduce an unreasonable margin of error. Notwithstanding this, we tested this assertion by modifying four bond lengths and two angles of the oxidized $[Fe_2S_2]^{2+}$ structure of Pux in line with the changes found between the oxidized and reduced forms of Pdx and analysis of the EPR data using this 'reduced PuxB' as the structural model made no significant different to the orientation of the g-matrix found or the experimentally determined spin projection factors.

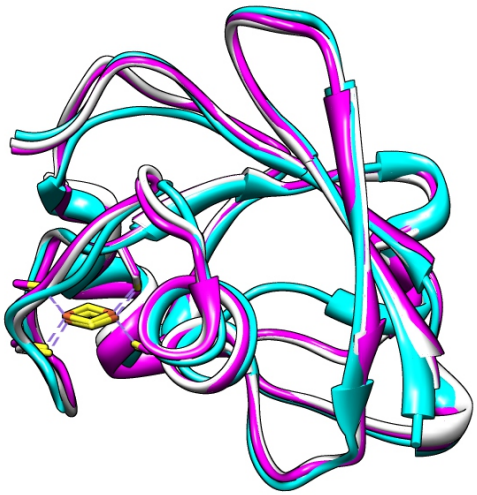


Figure 5.13: Comparison of the oxidised (*1XLP.pdb*) and reduced (*1XLQ.pdb*) structures of the C73S Pdx mutant, shown in white and magenta respectively, with the oxidised structure of PuxB (*3HUI.pdb*), shown in cyan. The orientation of the $[Fe_2S_2]$ cluster corresponds to those in Fig. 5.11 and Fig. 5.12.

5.2.5 Spin densities and spin projection factors

The reduced $[Fe_2S_2]^{+}$ cluster contains one Fe^{3+} ion ($S_A = \frac{5}{2}$) and one Fe^{2+} ion ($S_B = 2$), which couple antiferromagnetically to give an $S = \frac{1}{2}$ ground state. Using the strong-exchange limit assumption between the two spins, the spin projection factor, K_i, giving the projection of the total spin, S, onto the local spin site, S_i, can be calculated for the two iron centres.[183,186,187]

$$K_A\left(Fe^{3+}\right) = \frac{\langle S_{AZ}\rangle}{\langle S_Z\rangle} = \frac{S\left(S+1\right) + S_A\left(S_A+1\right) - S_B\left(S_B+1\right)}{2S\left(S+1\right)} = +\frac{7}{3} \tag{5.8}$$

$$K_B\left(\mathrm{Fe}^{2+}\right) = \frac{\langle S_{BZ}\rangle}{\langle S_Z\rangle} = \frac{S\left(S+1\right) - S_A\left(S_A+1\right) + S_B\left(S_B+1\right)}{2S\left(S+1\right)} = -\frac{4}{3} \tag{5.9}$$

Equations 5.8 and 5.9 bear a striking parallel to the Landé formula for the calculation of an isolated atom in the gas phase (see Appendix D). They are valid for a Hamiltonian that is block-diagonal in the spin coupled representation. It can be assumed that the energy difference between the isolated lowest $S = \frac{1}{2}$ ground state manifold and the excited state spin manifolds is such that only the $S = \frac{1}{2}$ ground state manifold needs to be considered in the Hamiltonian. The spin projection factors result from the Clebsch-Gordan coefficients that transform the Hamiltonian between its coupled and uncoupled representation. Under these conditions, the total spin vector of the system is calculated as: $\boldsymbol{S} = \boldsymbol{S_A} + \boldsymbol{S_B}$; and furthermore, S, S_A and S_B are good quantum numbers.

Mössbauer spectroscopy of ^{57}Fe labelled $[Fe_2S_2]^+$ clusters in ferredoxins has been used to verify the picture of the localized spins or valence trapped states to form Fe^{2+}/Fe^{3+} ions, rather than the delocalized electronic state $Fe^{2.5+}/Fe^{2.5+}$.[188,189] This implies that for ferredoxins, S, S_A and S_B are good quantum numbers. Hence that the Heisenberg exchange parameter J, which defines the energy between the two spin manifolds, is greater than the zero field splitting, parameterized by D. When J becomes comparable to D small corrections may be applicable.[190,191]

Although Mössbauer measurements have indicated the localized arrangement of electron density, the reduced $[Fe_2S_2]^+$ cluster in ferredoxins other EPR studies have reported spin projection factors significantly smaller than those determined from Equations 5.8 and 5.9.[165,166] It will therefore be necessary to determine the spin projection factors in the reduced PuxB $[Fe_2S_2]^+$ cluster experimentally.

To this end, three models for the delocalization of the spin projection factors will be examined by considering the spin density delocalized on to the Fe ions and bridging sulphurs within the $[Fe_2S_2]^+$ cluster and the ligating cysteine sulphurs.

Model 1: A purely ionic model

In a purely ionic picture (model 1 in Table 5.2), the spin densities and spin projection factors are entirely localized on the Fe ions. There are two spin projection factors and just one independent

variable as their sum should total 1 for an $S = \frac{1}{2}$ ground state. In simulations of the ENDOR and HYSCORE data, the value of the spin projection factor for the Fe^{3+} ion, K^A_{exp}, was varied to best fit the data. The spin projection factor for the Fe^{2+} ion is $(1 - K^A_{exp})$. Absolute values less than those given in Equations 5.8 and 5.9 are expected as delocalization of the magnetic orbitals onto the bridging sulphurs and cysteine ligands is ignored in this ionic picture. A purely ionic model gives five unpaired α-spins and four β-spins on Fe^{3+} and Fe^{2+} respectively, with delocalization factors $d^A_{Fe^{3+}} = d^B_{Fe^{2+}} = 1$ (see Equations 5.10 to 5.12). The spin densities and delocalization factors for this model are shown in Table 5.2.

Model 2: A DFT based model

Using density functional theory (DFT), spin density distributions were extracted from a calculation on $[Fe_2S_2(SCH_3)_4]^{3+}$, see Section 5.4.[192] These calculations show that the 3p orbitals of the sulphur atoms are sufficiently low in energy to mix with the 3d orbitals of the irons. Hence a significant amount of spin density, ρ, can be delocalized from the iron centres onto the sulphur atoms, both in the cluster and from the ligating cysteines. To account for this, spin density delocalization factors $d^{A/B}_j$ were calculated from the DFT spin density distribution over the Fe and S atoms and the corresponding spin projection factors for each nucleus were scaled for each atom over which the spin was delocalized in accordance with this distribution. The DFT calculations also show a very small delocalization of the spin density onto the cysteine β carbons; however, the contribution is very minor and can be ignored. Eight delocalization coefficients for the two Fe and six S atoms in the cluster and the ligating cysteines are therefore used; these are given in Table 5.2.

The absolute spin densities ρ^A (ferric site) and negative ρ^B (ferrous site) from the DFT calculation sum together to give $\rho^A = +4.033$ and $\rho^B = -3.033$. These are smaller than $\rho^A = +5$ and $\rho^B = -4$, as predicted for the ionic picture in model 1, where there is no overlap of the magnetic orbitals. The spatial overlap of the ferric α-spin and ferrous β-spin magnetic orbitals cancel out $|0.966|$ of the spin densities in both α-spin and β-spin magnetic orbitals.

Table 5.2: Two models for the distribution of spin densities, ρ, used to calculate the delocalization factors, d, associated with the ferric A and ferrous B sites. Model 1 is the ionic limit with all unpaired spins on the Fe ions. Model 2 uses the DFT ρ values directly and the corresponding delocalization coefficients d^A and d^B are normalized to 1. S* refers to a bridging sulphur; S_{ox} and S_{red} refers to cysteine sulphurs ligating Fe^{3+} and Fe^{2+} respectively. This table is reproduced from J. A. B. Abdalla, A. M. Bowen, S. G. Bell, L. L. Wong, C. R. Timmel and J. Harmer, Characterisation of the paramagnetic $[Fe_2S_2]^+$centre in palustrisredoxin-B (PuxB) from Rhodopseudomonas palustris CGA009: g-matrix determination and spin coupling analysis, *Physical Chemistry Chemical Physics*, 2012, **14(18)**, 6526–6537 with permission from the PCCP Owner Societies.[15]

	Model 1		Model 2		
Atom	ρ^A	d^A	ρ^A	$\rho^{A,sum}$	d^A
Fe^{3+}	5	1	+3.256		0.819
S*		0	+0.174	+4.033	0.044
S_{ox}		0	+0.187		0.047
	ρ^B	d^B	ρ^B	$\rho^{B,sum}$	d^B
Fe^{2+}	−4	1	−2.847	−3.033	0.934
S_{red}		0	−0.100		0.033

Model 3: Experimentally determined model

The third model uses the spin delocalization parameters, $d_j^{A/B}$ from the DFT (model 2) as a starting point. However, during the fitting of the spectra, in addition to optimizing the spin projection factors and g-matrix orientation, the spin delocalization parameters are also optimized.

Parameterising the spin density distribution

In order to allow for the delocalized nature of the spin density distribution in models 2 and 3, the DFT derived distribution, used as a starting point for both models, was normalized. The positive DFT spin densities associated with the Fe^{3+} centre were normalized to sum to 1, while the negative spin densities associated with the Fe^{2+} centre were normalized to -1 to give the delocalization coefficients, $d_j^{A/B}$. This analysis assumes that all of the spin density contributing to the paramagnetic centre is located on the $[Fe_2S_2]$ cluster and its ligating sulphurs.

The positive and negative spin densities were treated separately in order to allow their relative contributions between the two Fe centres to be varied with just one parameter: K_A^{exp}.

$$K_A^{exp}\left(d_{Fe^{3+}}^A + 2d_{S_{ox}}^A + 2d_{S*}^A\right) + (1 - K_A^{exp})\left(d_{Fe^{2+}}^B + 2d_{S_{red}}^B\right) = 1 \tag{5.10}$$

where S* refers to a bridging sulphur, S_{ox} and S_{red} refers to cysteine sulphurs ligating Fe^{3+} and Fe^{2+} respectively. This equation holds true for all three models. However, for model 1 the spin delocalization factors associated with the sulphur atoms are set to 0.

For model 2, the eight delocalization factors, $d_j^{A/B}$, are fixed by the DFT spin densities and the ENDOR and HYSCORE experiments are used to determine the value of K_A^{exp}. In model 3, the values of $d_j^{A/B}$ are allowed to vary as part of the experimental fitting process. Note that j labels the iron and sulphur atoms included in the models.

The spin projection factors resulting from the spin density distributions are given by:

$$k_j^{del} = K_A^{exp} d_j^A \tag{5.11a}$$

$$k_j^{del} = (1 - K_A^{exp})\, d_j^B \tag{5.11b}$$

for the Fe^{3+} and Fe^{2+} centres respectively. Note that:

$$\sum_j^8 k_j^{del} = K_A^{exp} \sum_{(j=1)}^{5} d_j^A + K_B^{exp} \sum_{(j=6)}^{8} d_j^B = 1 \tag{5.12}$$

which is required for an $S = \frac{1}{2}$ ground state.

In models where the electron density is delocalized, the $k_{Fe^{3+}}^{del}$ and $k_{Fe^{2+}}^{del}$ values will be lower than the corresponding $K_A(Fe^{3+})$ and $K_B(Fe^{2+})$ values, as a result of the delocalization of the unpaired spins.

5.2.6 Calculation of the ^{1}H hyperfine couplings

As we have already seen, hyperfine couplings consist of an anisotropic dipolar part, $\mathbf{T}$, and an isotropic scalar contribution, a_{iso}, to give an overall hyperfine matrix, $\mathbf{A}$. It is the anisotropic part of these couplings, $\mathbf{T}$, that allows them to be used to orientate the g-matrix relative to the $[Fe_2S_2]^+$ cluster. Each $\mathbf{T}$ can be accurately calculated from the position of the proton and the magnetic moment of the unpaired spins through the k_j^{del} values. The overall hyperfine coupling matrix is therefore defined as:

$$\mathbf{A} = a_{iso}\mathbf{I} + \sum_{(j=1)}^{8} \mathbf{T}_j \tag{5.13}$$

$\mathbf{I}$ is the identity matrix and the $\mathbf{T}_j$ matrices are easily calculated from the eight k_j^{del} values.

$$\mathbf{T}_j^0 = k_j^{del}\left(\frac{\mu_0\mu_B\mu_N g_e g_N}{4\pi\hbar}\right)\frac{(3\mathbf{n}_j\tilde{\mathbf{n}}_j - 1)}{r_j^3} \tag{5.14}$$

$\mathbf{T}_j^0$ is in radians, and $\mathbf{n}_j$ and r_j are the unit row vector and distance describing the relative position of one of the protons included in the model with respect to one of the atoms of the $[Fe_2S_2]$ cluster, designated j. The tilde indicates the matrix transpose.

The effect of the spin-orbit coupling on the dipolar hyperfine interaction

The effect of spin-orbit coupling on $\mathbf{T}$ can be included via the g-matrix anisotropy, $\boldsymbol{\Delta g} = \boldsymbol{g} - g_{iso}\mathbf{I}$, where $g_{iso} = \frac{1}{3}(g_1 + g_2 + g_3)$ and g_1, g_2 and g_3 are the principal g-values. This allows the dipolar coupling to be formulated as:

$$\mathbf{T}_j = \mathbf{T}_j^0 + \frac{\boldsymbol{\Delta g}\mathbf{T}_j^0}{g_e} \tag{5.15}$$

The experimentally observed g-matrix in the valence-localized $[Fe_2S_2]$ cluster can be described within a local spin model,[193,194] where the observed deviation of the g-matrix from the free electron value g_e is given by:

$$\boldsymbol{\Delta g} = K_A(\mathrm{Fe}^{3+})\boldsymbol{\Delta g}^{\mathrm{Fe}^{3+}} + K_B(\mathrm{Fe}^{2+})\boldsymbol{\Delta g}^{\mathrm{Fe}^{2+}} \tag{5.16}$$

This is applicable for the ionically derived model 1. However, for models 2 and 3, a covalency corrected spin-orbit correction including the k_j^{del} is necessary.[195]

$$\boldsymbol{\Delta g} = \left(k_{Fe^{3+}}^{del}\boldsymbol{\Delta g}^{\mathrm{Fe}^{3+}} + 2k_{S_{ox}}^{del}\boldsymbol{\Delta g}^{S_{ox}} + 2k_{S*}^{del}\boldsymbol{\Delta g}^{S*}\right) + \left(k_{Fe^{2+}}^{del}\boldsymbol{\Delta g}^{\mathrm{Fe}^{2+}} + 2k_{S_{red}}^{del}\boldsymbol{\Delta g}^{S_{red}}\right) \tag{5.17}$$

Fe^{3+} has an orbital contribution that is essentially zero and thus $\boldsymbol{\Delta g}^{\mathrm{Fe}^{3+}} \cong 0$. As described in Section 1.2.2, the source of the anisotropy of g-tensors is spin-orbit coupling. The deviations from g_e observed in the g-values of sulphur radicals, such as cysteine thiyl radicals, are also relatively small ($g^S = [2.23, 2.00, 1.95]$, giving $\Delta g^S = [0.23, 0.00, -0.05]$).[196b] Furthermore, when these are weighted by the small $k_S^{del} < 0.27$ values, their overall effect on the calculation of $\mathbf{T}$ is further diminished. For example, for proton 1, $\boldsymbol{T} = [-5.43, -4.28, 9.67]$ MHz, which comprises a contribution from the nearest S cysteine of $\boldsymbol{T}^0_{S_{red}} = [-0.52, -0.52, 1.04]$ MHz (Equation 5.14), or with the spin-orbit correction included $\boldsymbol{T}_{S_{red}} = [-0.43, -0.43, 0.84]$ MHz (Equation 5.15). The difference between the non-spin-orbit coupled case ($\boldsymbol{T}^0_{S_{red}}$) and the spin-orbit corrected case ($\boldsymbol{T}_{S_{red}}$) is very small compared to the total coupling $\boldsymbol{T}$.

The primary contribution to the g-matrix anisotropy arises from the Fe^{2+} ion. Experimentally determined estimates for the principal g-values of $g^{Fe^{2+}}$ for $[Fe_2S_2]^+$ cluster in related ferredoxins can be found in the literature: $g^{Fe^{2+}} = [2.11, 2.19, 2.00]$ for rubredoxin (*Clostridium pasteurianum*)[197] and $g^{Fe^{2+}} = [2.08, 2.02, 2.02]$ for desulforedoxin (*Desulfovibrio gigas*).[198] It is therefore vital that the

[b]For cysteine thiyl radicals the g-tensor is orientated so that the g_x-axis points along the $S_\gamma - C_\beta$ bond.[196]

deviation from the electronic g-value and the anisotropy of the g-tensor of the Fe^{2+} ion is used in the calculation of the dipolar contribution to the hyperfine interaction between the protons and Fe^{2+}.

Experimental g-values for the $[Fe_2S_2]^+$ cluster are easily measured using W-band EPR and are found to be $g_\perp = 1.9328$ and $g_{||} = 2.0233$, providing an axial g-tensor. Considering the ionic model (model 1) and using Equation 5.16, these principle values give an estimated contribution from the Fe^{2+} of $g^{Fe^{2+}} \cong [2.0842, 2.0842, 1.9776]$, broadly in agreement with the values seen for the rubredoxin and desulforedoxin.

Closer examination of the contribution of the g-tensor anisotropy from the Fe^{2+} centre on the values of the dipolar part of the hyperfine couplings show that for proton 1 $\boldsymbol{T}_{Fe^{2+}} = [0.39, 0.41, -0.82]$ MHz and $\boldsymbol{T}^0_{Fe^{2+}} = [0.40; 0.40; -0.81]$ MHz for the contributions with and without the spin-orbit correction respectively. Although these values are on the same order of magnitude as those given for S_{red} for proton 1 ($\boldsymbol{T}^0_{S_{red}} = [-0.52, -0.52, 1.04]$ MHz and $\boldsymbol{T}_{S_{red}} = [-0.43, -0.43, 0.84]$ MHz), the difference between them is in fact smaller. This is a little surprising considering the larger relative size of $k^{del}_{Fe^{2+}}$ compared to k^{del}_S.

The effect of the spin-orbit coupling and the resulting g-value anisotropy is increased for protons closer to the Fe^{2+} centre. Proton 3 is closest to the Fe^{2+} centre and thus has the largest orbital contribution, with a maximum value of $|0.25|$ MHz. The overall dipolar contribution hyperfine coupling is $\boldsymbol{T}^0 = [-1.59, 0.67, 0.92]$ MHz without the spin-orbit coupling correction (Equation 5.14) and with the spin-orbit coupling correction $\boldsymbol{T} = [-1.61, 0.92, 0.65]$ MHz (Equation 5.15). Calculations show that for protons close to Fe^{3+}, the size of the spin-orbit coupling correction is much smaller (< 0.02 MHz) since the dipolar coupling for these protons is largely determined by the Fe^{3+} ion.

During the fitting of the experimental data, it was discovered that the protons closest to the Fe^{3+} centre have significantly larger hyperfine couplings compared to those close to the Fe^{2+} centre. This is primarily due to the relative sizes of the spin projection factors; the spin projection factor associated with the positive spin density originating from the Fe^{3+} centre (K^{exp}_A), was found to be almost twice the size of that associated with the negative spin density on Fe^{2+} (K^{exp}_B). It is therefore the protons close to the Fe^{3+} centre that provide the main source of information to orientate the g-matrix and

adjust the spin projection factors. Consequently the spin-orbit correction to $\mathbf{T}_j$ does not make a large difference to the results. However, it is easily included and thus the dipolar couplings were calculated using Equation 5.15.

The calculated anisotropy of the hyperfine tensors are shown in Fig. 5.14.

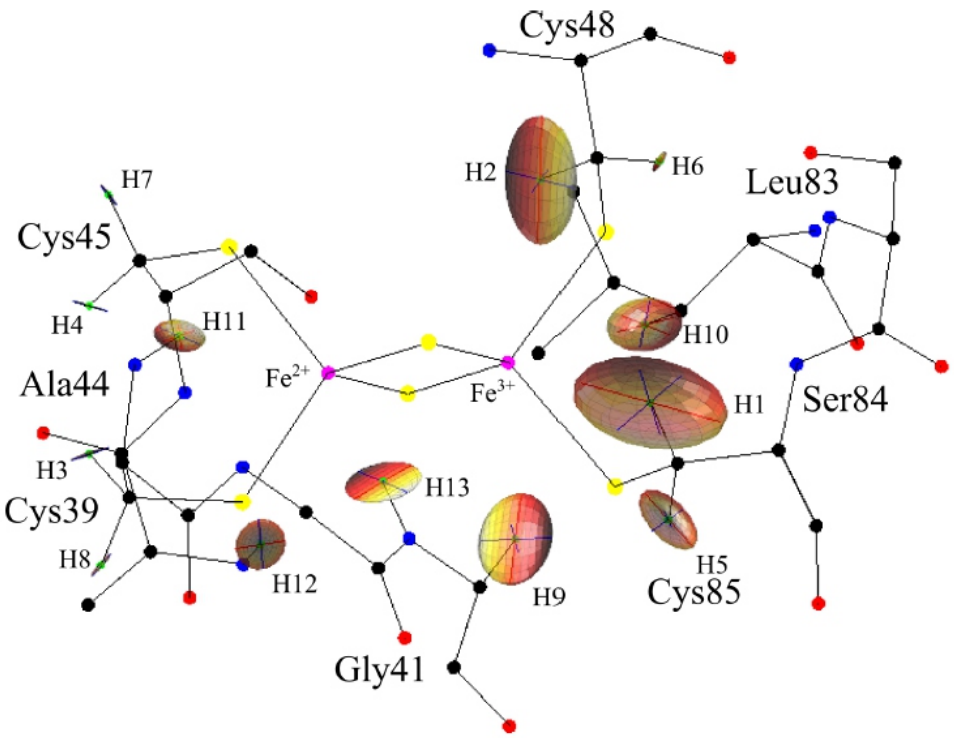


Figure 5.14: The hyperfine tensors of all protons included in the model plotted on the molecular structure. The isotropic part has been scaled by $\frac{1}{100}$ to show the anisotropy of the hyperfine tensors more clearly. This figure is reproduced from J. A. B. Abdalla, A. M. Bowen, S. G. Bell, L. L. Wong, C. R. Timmel and J. Harmer, Characterisation of the paramagnetic $[Fe_2S_2]^+$centre in palustrisredoxin-B (PuxB) from Rhodopseudomonas palustris CGA009: g-matrix determination and spin coupling analysis, *Physical Chemistry Chemical Physics*, 2012, **14(18)**, 6526–6537 with permission from the PCCP Owner Societies.[15]

The isotropic part of the hyperfine interaction

Although the dipolar matrices, $\mathbf{T}$, for each of the 13 protons included in the model at a given orientation of the g-matrix can be calculated, the a_{iso} values must be found experimentally. In all three models, the

eight β-protons have non-zero a_{iso} values and these are found by matching ENDOR and HYSCORE simulations to the experimental spectra. Since the a_{iso} values are found directly from the experiment, there is no need to consider the effect of spin-orbit coupling on this value explicitly.

The a_{iso} values, along with the polar angles (θ, ϕ) defining the g-matrix orientation with respect to the molecular frame and the scaling factor, K_A^{exp}, are all optimized in the fitting process for all models. In the case of model 3 the delocalization parameters, $d_j^{A/B}$ are also optimized.

5.3 Experimental results on PuxB to determine the *g*-tensor orientation

The g-tensor orientational analysis was performed on two distinct samples: a sample of the Ferredoxin protein PuxB alone without a binding partner and a second sample of PuxB in complex with a ferredoxin reductase, PuR. Both proteins were expressed in *E. coli* and the EPR samples were prepared as described in Section 5.2.2. The PuxB in both cases was prepared in the reduced state, so that it had a ground spin state of $S = \frac{1}{2}$. A 1 mM concentration of each protein was used in the samples.

5.3.1 Comparison of the EPR for PuxB alone and PuxB-PuR

Initially CW measurements were taken at both X- and W-band under cryogenic cooling to a temperature of 20 K. The spectra are shown in Fig. 5.15. Both samples have virtually identical CW spectra, indicating that there is no change in the paramagnetic $[Fe_2S_2]$ cluster and coordinating ligand geometry when PuR binds. The experimental and simulated CW spectra as shown in Fig. 5.15

W-band ^{1}H ENDOR spectra (at 20 K) and X-band ^{1}H HYSCORE spectra (at 15 K) were measured at different positions across the EPR spectrum for both the PuxB alone and PuxB in complex with PuR. The field positions of these measurements (corrected to the same frequency) are shown in Fig. 5.16

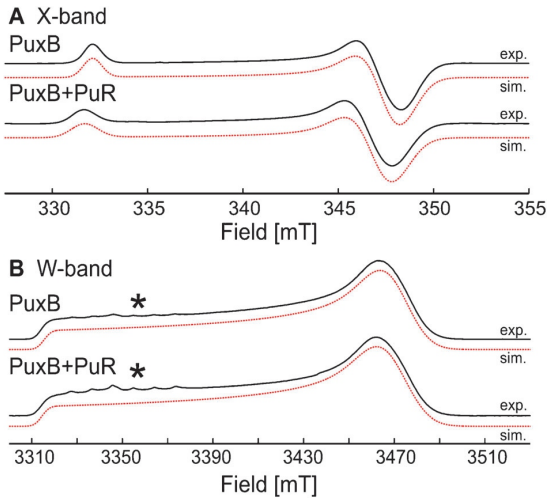


Figure 5.15: **(A)** X-band (9.3947 GHz) CW EPR spectra of PuxB and PuxB-PuR measured at 20 K. **(B)** W-band (93.799 GHz) echo-detected EPR spectra of PuxB and PuxB-PuR measured at 20 K. The black lines shows the experimental data, and the red lines EasySpin[7] simulations using for PuxB: $g_{\perp} = 1.9328$, $g_{||} = 2.0233$, and Gaussian line widths at X-band (W-band) of $L_{\perp} = 64(605)$ MHz, $L_{||} = 32(178)$ MHz; and for PuxB-PuR: $g_{\perp} = 1.9324$, $g_{||} = 2.0227$, and Gaussian line widths at X-band (W-band) of $L_{\perp} = 69(615)$ MHz, $L_{||} = 47(179)$ Hz. The $*$ indicates the resonator background signal from Mn^{2+}. This figure is reproduced from J. A. B. Abdalla, A. M. Bowen, S. G. Bell, L. L. Wong, C. R. Timmel and J. Harmer, Characterisation of the paramagnetic $[Fe_2S_2]^{+}$centre in palustrisredoxin-B (PuxB) from Rhodopseudomonas palustris CGA009: g-matrix determination and spin coupling analysis, *Physical Chemistry Chemical Physics*, 2012, **14(18)**, 6526–6537 with permission from the PCCP Owner Societies.[15]

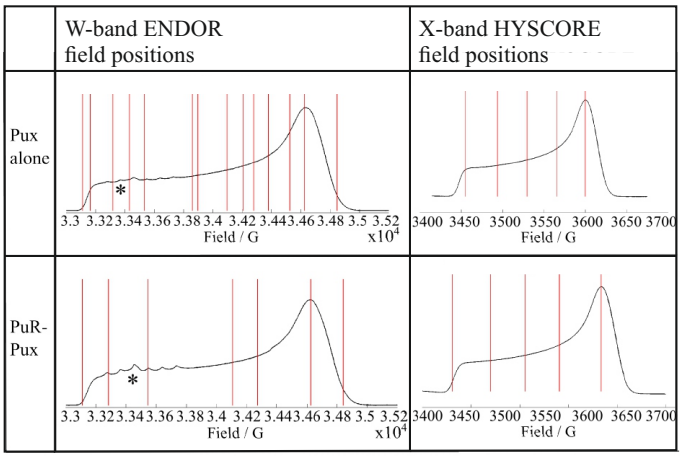


Figure 5.16: Field positions marked by red vertical lines at which W-band ENDOR and X-band HYSCORE spectra were recorded. The weak sextets, denoted by $*$, in the W-band field sweep spectra are due to a Mn^{2+} impurity in the resonator.

Due to the broad width of the $[Fe_2S_2]^+$ EPR spectrum, the pulses applied only excite a small proportion of the spectrum. As with the orientationally selective DEER discussed in the previous chapters, this means that only a few orientations of the g-tensor with respect to the magnetic field are excited. The orientational dependence of the excitation profiles is shown in Fig. 5.17.

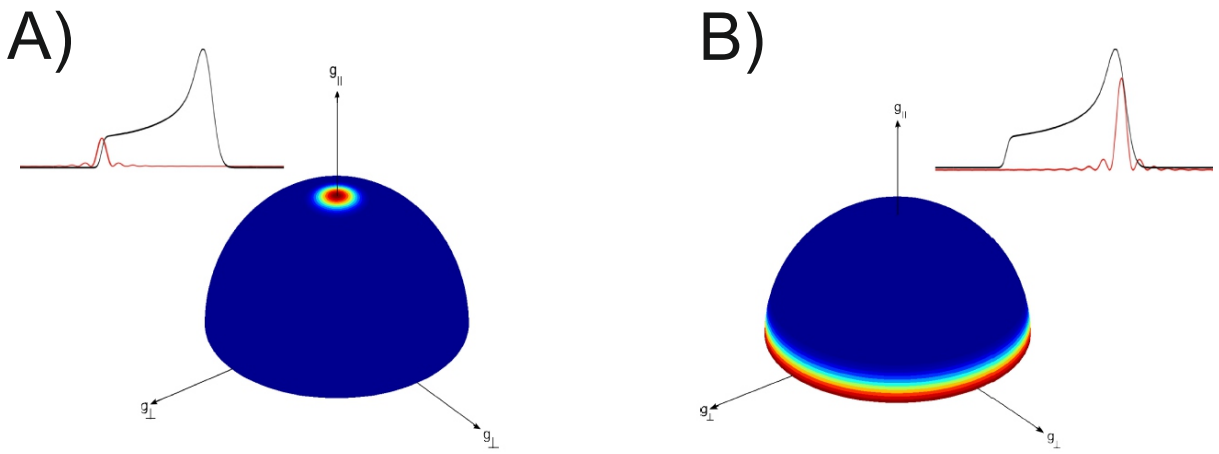


Figure 5.17: Spheres showing the orientations which are resonant with the selective microwave pulses applied at **(A)** the lowest W-band ENDOR field position B_0 = 3311.4 mT, microwave frequency = 93.8065 GHz and **(B)** highest W-band ENDOR field position B_0 = 3348.48 mT, microwave frequency = 93.8065 GHz.

Some of the ENDOR and HYSCORE spectra for the PuxB and PuxB-PuR samples were collected at field positions and frequencies, which resulted in the same portion of the spectrum being excited. Thus for these spectra, it is possible to compare them directly to highlight any differences between the spectra. Examples of such HYSCORE and ENDOR spectra are shown in Fig. 5.18 and Fig. 5.19 respectively.

No significant difference between the spectra can be seen, further supporting the hypothesis that there is no large structural or electronic change in the $[Fe_2S_2]^+$ centre on formation of the protein-protein complex.

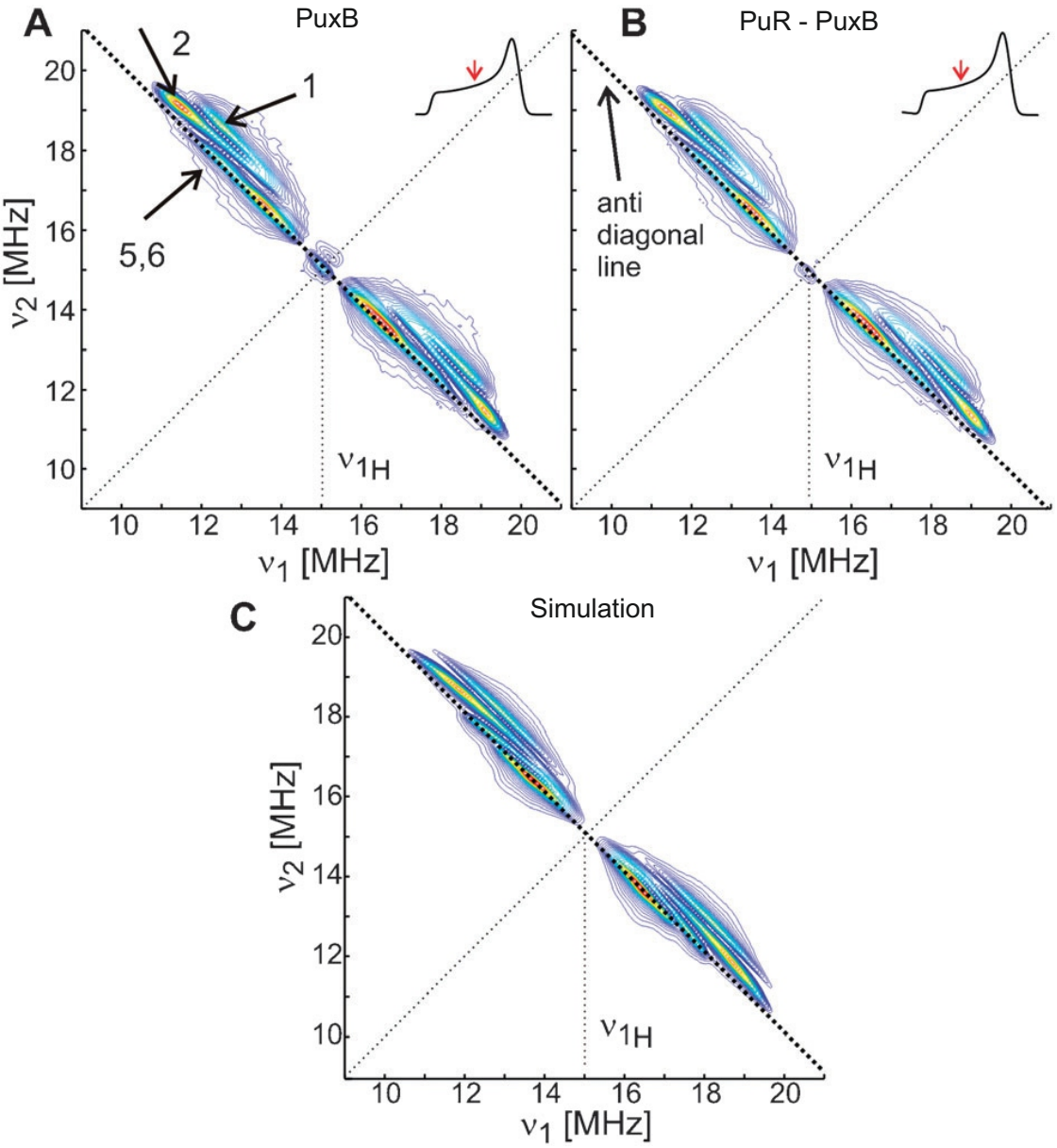


Figure 5.18: X-band ^{1}H HYSCORE spectra of PuxB **(A)** and the PuR-PuxB complex **(B)**, and a simulation **(C)**. Inset: position of the HYSCORE experiment at $g = 1.976$ (9.7833 GHz, 353.7 mT). The numbered arrows refer to peaks assigned to this proton number; see Fig. 5.11 for the proton numbering scheme. This figure is reproduced from J. A. B. Abdalla, A. M. Bowen, S. G. Bell, L. L. Wong, C. R. Timmel and J. Harmer, Characterisation of the paramagnetic $[Fe_2S_2]^+$centre in palustrisredoxin-B (PuxB) from Rhodopseudomonas palustris CGA009: g-matrix determination and spin coupling analysis, *Physical Chemistry Chemical Physics*, 2012, **14(18)**, 6526–6537 with permission from the PCCP Owner Societies.[15]

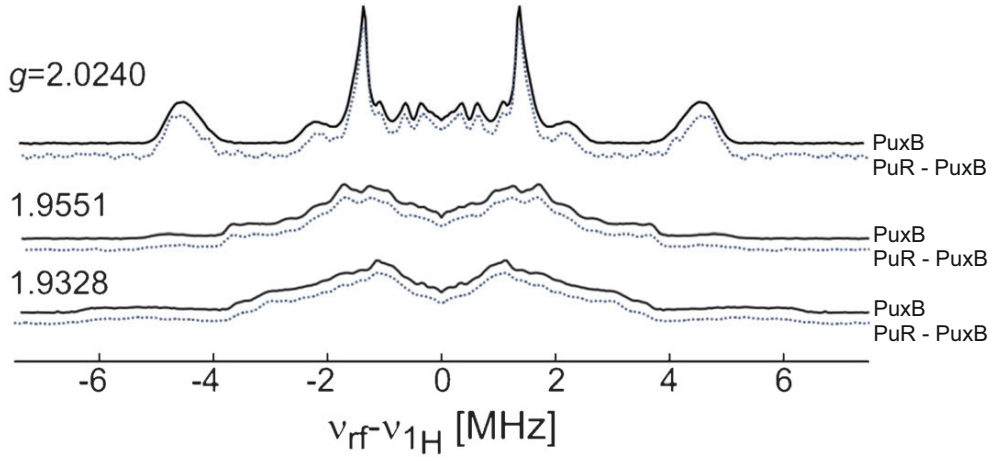


Figure 5.19: W-band ^{1}H Davies ENDOR spectra at 20 K of PuxB (black lines) and of the PuxB-PuR complex (dashed blue lines) at the g-value positions indicated. The spectra of PuxB and PuR-PuxB are essentially identical, which implies the local structure around the reduced $[Fe_2S_2]^+$ cluster is unchanged by formation of the PuxB-PuR complex. This figure is reproduced from J. A. B. Abdalla, A. M. Bowen, S. G. Bell, L. L. Wong, C. R. Timmel and J. Harmer, Characterisation of the paramagnetic $[Fe_2S_2]^+$centre in palustrisredoxin-B (PuxB) from Rhodopseudomonas palustris CGA009: g-matrix determination and spin coupling analysis, *Physical Chemistry Chemical Physics*, 2012, **14(18)**, 6526–6537 with permission from the PCCP Owner Societies.[15]

5.3.2 Assignment of the proton identities to individual hyperfine couplings

Since the spectra recorded for PuxB and PuxB in complex with PuR are identical, the figures in the following results section only show data for the PuxB protein alone. However, all of the analysis and discussion presented is also applicable to the PuR-PuxB sample.

The initial stage of the fitting process involved determining which protons were responsible for the largest splittings at the high and low field spectra (shown in Fig. 5.20). As we have seen from the excitation profiles in Fig. 5.17, pulses applied at the low field portion of the spectrum primarily sample, $g_{||}$, and pulses at high field, $g_{\perp}$. The largest proton couplings at the lowest and highest field positions show clearly discernible peaks, which can be traced through several ENDOR and HYSCORE spectra collected at consecutive field positions. See Fig. 5.23 for the ENDOR spectra sampling different g-values.

Using an initial guess for the orientation of the g-tensor with respect to the molecular frame, high

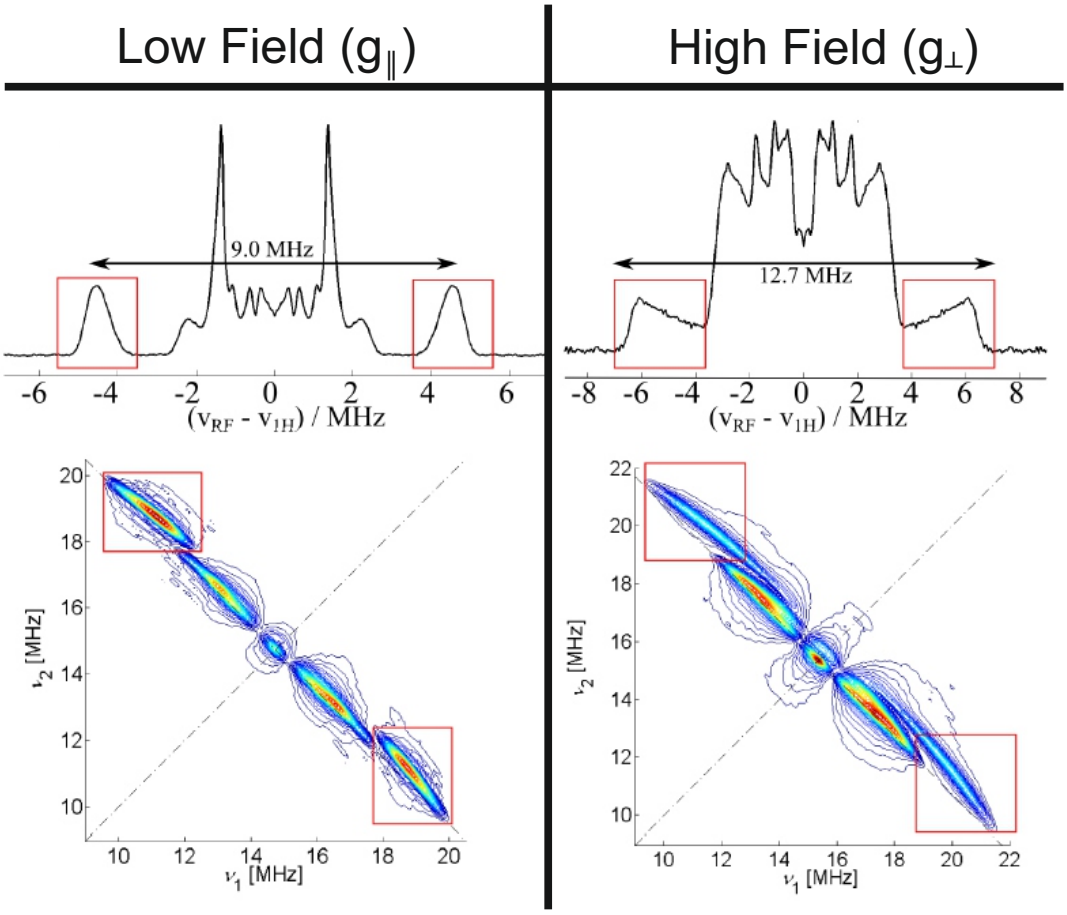


Figure 5.20: The largest coupling in the high and low field W-band ENDOR (3311.4 mT and 3484.8 mT) and X-band HYSCORE (345.5 mT and 360.0 mT).

and low field positions were simulated in turn for each proton in the model using the calculated dipolar part of the hyperfine coupling, the DFT derived spin densities and the DFT derived spin projection factors. The value of a_{iso} was varied until the best fit between the experimental and simulated peak shapes was found. For the low field position, which is sampling predominately $g_{||}$ orientations:

$$A_{zz}^{exp} = T_{zz}^{dip} + a_{iso} = 9.0\ MHz \tag{5.18}$$

The fitting procedure was then repeated at a different orientation of the g-matrix with respect to the molecular frame; in total 3121 orientations were trialled.

For each proton the a_{iso} value and g-matrix orientation corresponding to the best fit to the ENDOR and HYSCORE experimental spectra at high and low field values was established. Each set of parameters was used to simulate spectra at the field positions adjacent to the high and low field positions in order to investigate whether the peak movements seen between the experimental data sets could be correctly simulated.

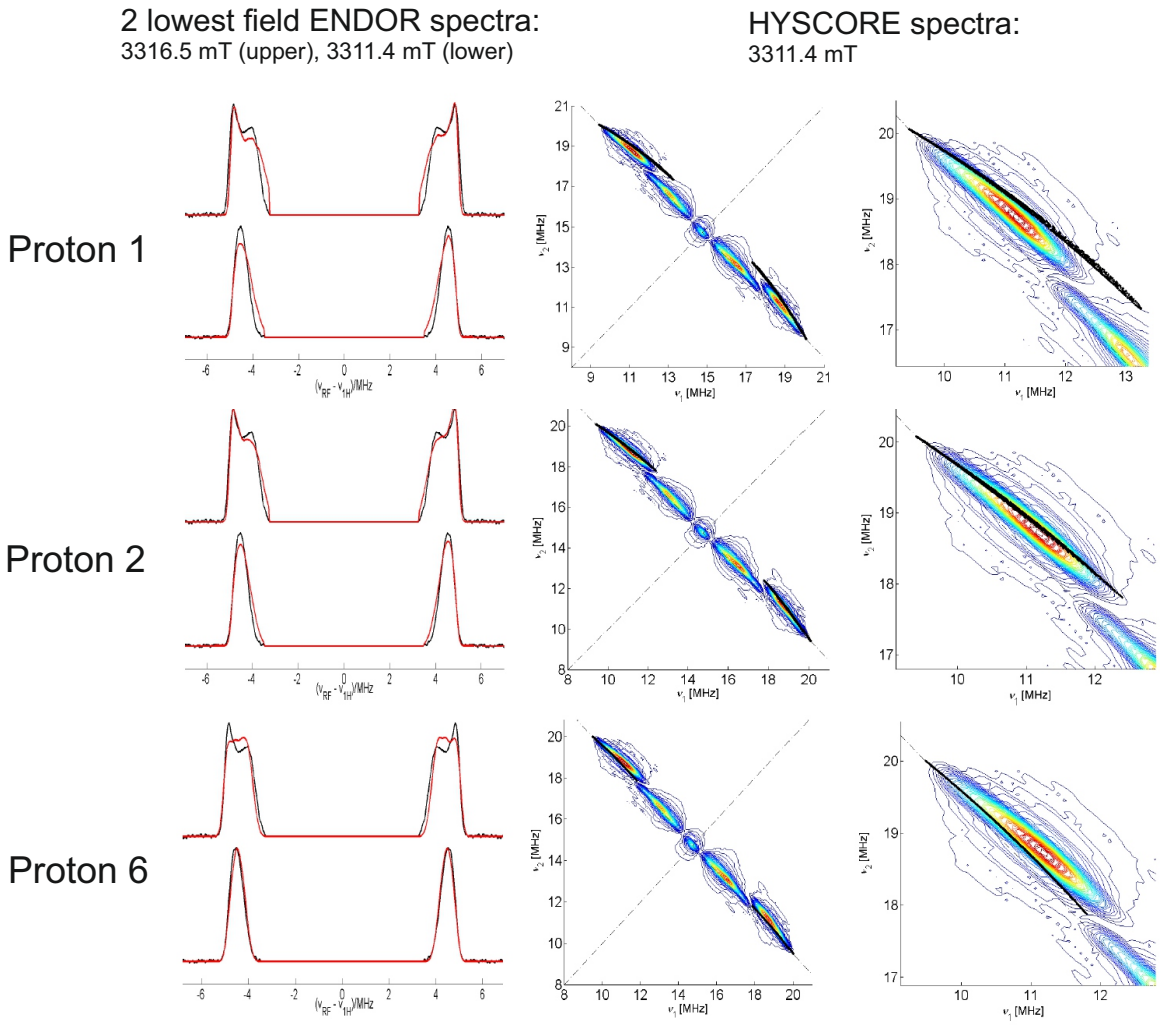


Figure 5.21: Comparison of the best initial W-band ENDOR and X-band HYSCORE simulations for protons 1, 2 and 6 at the low field positions. ENDOR spectra (left column) are recorded at 3311.4 mT (bottom) and 3316.5 mT (top) with the experimental data in black and the simulation in red; HYSCORE with the whole spectrum (central column) and a detail of the largest coupling (right column) is recorded at 345.5 mT, with the simulation shown as a black line.

For all ENDOR spectra the 'goodness' of fit between experimental and simulated data sets was evaluated using the sum of the square of the point-to-point residuals, χ^2, between the experimental spectrum and the simulation across multiple spectra at different field values.

Protons 1, 2 and 6 (see Fig. 5.11) appeared to show a good fit in the low field ENDOR spectra. The value of the a_{iso} found for each proton to give the best fit in the ENDOR spectra, was further evaluated by using this parameter to simulate HYSCORE spectra. In HYSCORE the curvature of the signal line behind the anti-diagonal is dependent on the value of a_{iso}. A comparison for the low field fits for protons 1, 2 and 6 are given in Fig. 5.21.

Clearly it is the simulation for proton 2 which most accurately predicts the experimental HYSCORE curvature at low field and thus the largest low field hyperfine coupling must originate from proton 2. The same technique was employed for the high field splitting and using this initial trial-and-error method it was found that the protons that gave the best fits at the low and high field positions were protons 2 and 1 respectively. These two protons are the two cysteine β-protons found closest to the Fe^{3+} centre.

The fact that the outer peaks observed in the low and high field spectra can be traced through several spectra at different field positions provides unambiguous information on the orientation of the g-matrix with respect to the proton hyperfine matrices of protons 1 and 2.

Finding the a_{iso} values for the remaining protons

The assignments of the largest coupling to protons 1 and 2 were further corroborated and the orientations refined by calculating full ENDOR and HYSCORE spectra including all of the β-protons (listed 1 to 8 in Table 5.1 and depicted in Fig. 5.11).

Assigning values of a_{iso} for the remaining β-protons responsible for the smaller couplings was more difficult since many peaks overlap in the crowded inner regions of the ENDOR and HYSCORE spectra. Upper and lower bounds could be assigned by finding the values at which the proton couplings began to infringe on the largest hyperfine couplings observed at high and low field. These coupling had already

been attributed to protons 1 and 2 alone. Within these bounds, the isotropic couplings were assigned using a Monte-Carlo style approach as part of the fitting process.

5.3.3 Simulation and fitting of the orientationally dependent ENDOR and HYSCORE spectra

During the assignment of the low and high field coupling to protons 1 and 2 the HYSCORE spectra were also used to refine the spin projection factors; K_A^{exp} was adjusted until the curvature behind the anti-diagonal of the simulations for protons 1 and 2 matched the experimental ridges (see Fig. 5.22). The initial orientation of the g-matrix from these first fittings was next further refined using a finer grid of molecular orientations around the above solution and inclusion of the remaining protons via the Monte-Carlo method, where the a_{iso} values were assigned randomly within the upper and lower limits previously defined. This allowed the sampling of a range of a_{iso} values for each proton using fewer simulations than would be required if each a_{iso} values had been sequentially changed.

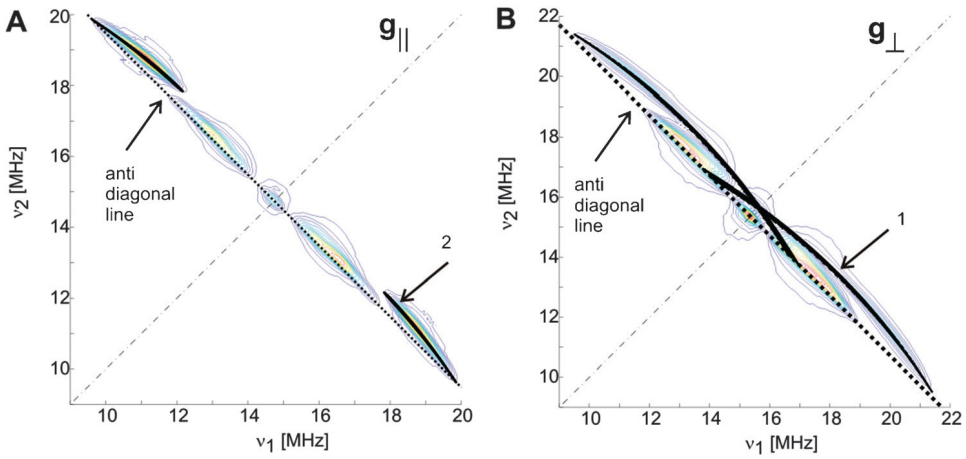


Figure 5.22: X-band HYSCORE spectra recorded at 15 K at **(A)** the low field ($g = 2.019$, 9.7828 GHz, 346.2 mT) and **(B)** high field ($g = 1.938$, 9.7847 GHz, 360.7 mT) positions. The simulations for protons 2 and 1, at low and high field respectively, are shown by the solid black lines. The curvature of the ridge behind the anti-diagonal line is sensitive only to the dipolar part of the hyperfine coupling. This figure is reproduced from J. A. B. Abdalla, A. M. Bowen, S. G. Bell, L. L. Wong, C. R. Timmel and J. Harmer, Characterisation of the paramagnetic $[Fe_2S_2]^+$centre in palustrisredoxin-B (PuxB) from Rhodopseudomonas palustris CGA009: g-matrix determination and spin coupling analysis, *Physical Chemistry Chemical Physics*, 2012, **14(18)**, 6526–6537 with permission from the PCCP Owner Societies.[15]

Subsequently, proton 6 was assigned to have the second largest coupling at $g_{||}$ (low field) and proton 5 to have the second largest coupling at $g_{\perp}$ (high field). It is reassuring to discover that proton 6 and proton 2, which give rise to the two largest couplings in the low field spectra are both bound to the same carbon on Cys48 and hence share a similar orientation dependence with respect to the g-matrix. The same applies for proton 1 and 5, which have their largest couplings at the high field position and are both assigned to Cys85.

The experimental W-band ENDOR spectra at a range field positions across the $[Fe_2S_2]^+$ spectrum and the corresponding simulations for the individual protons 1, 2, 5 and 6 are given in Fig. 5.23.

The remaining four β-protons are all closer to Fe^{2+}, which has a much lower spin density than the Fe^{3+}, K_B^{exp} or k_j^{del} values. This results in smaller dipolar interactions from these protons, as calculated in Section 5.2.6, and the hyperfine couplings from these protons contribute primarily to the central crowded region of the spectrum. Several sets of the a_{iso} values for these four protons gave reasonable fits to the spectra; the best fit as judged by the square sum of the residuals is given in Table 5.1. The unique axes of all the proton hyperfine matrices all point generally towards Fe^{3+}, which is associated with the largest component of the magnetic moment of the reduced $[Fe_2S_2]^+$ cluster.

The experimentally derived model 3 also used the fitting to the spectra to optimize the spin density distribution. The spin density was adjusted around the ferric (Fe^{3+}) iron under the constraint that $\sum d_j^A = 1$. No independent adjustment of the ferrous site was possible as its influence on the experimental data is not sensitive enough, as discussed previously. This analysis yielded the ranges (given in Table 5.3) for the delocalization factors and spin projection factors. The optimal g-matrix orientations for the extremes of these spin density distributions did not vary significantly and the $g_{||}$ axes were all found to be within ± 3 degrees of the mean value. This demonstrates that the method is not critically sensitive to small changes in the spin density distribution.

Table 5.3 lists the $d_j^{A/B}$ and spin projection factors found for all three models. In all cases, the spin projection factors at the Fe^{3+} ion are very similar, $k_{Fe^{3+}}^{del} \cong 1.50$ to 1.56. This is not unexpected since the analysis is dominated by the large Fe^{3+} ion contribution. Fig. 5.23 shows the calculated ENDOR spectra for these best sets of parameters for model 3, which, as expected, was found to give the most

accurate fit to the experimental data.

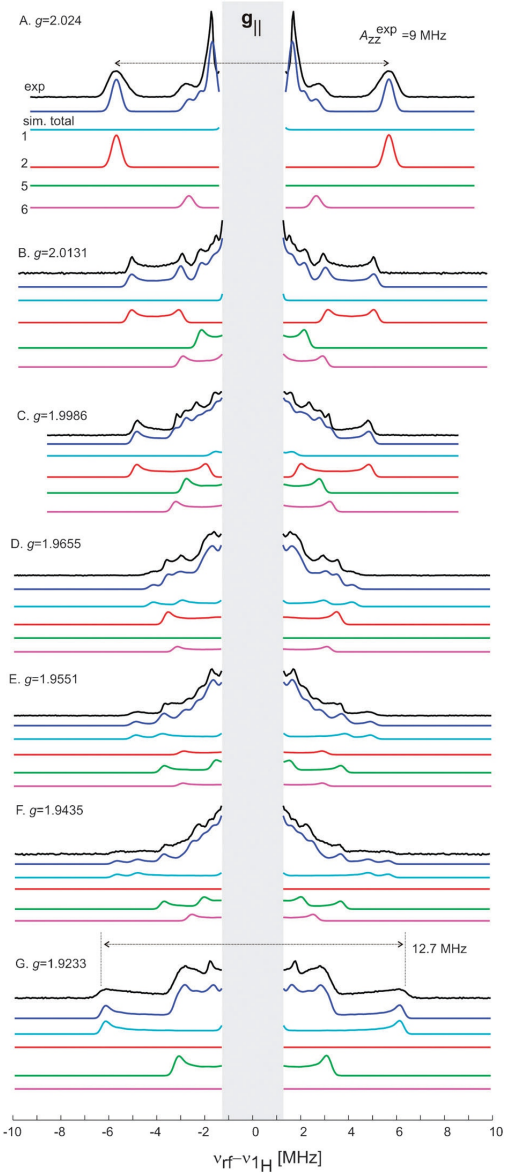


Figure 5.23: W-band (c.93.83 GHz) ^{1}H Davies ENDOR spectra recorded at 20 K of PuxB at the g-value positions indicated. At each field, the traces from top to bottom are: experiment, total simulation (sum of the 13 protons), and individual simulations for protons 1 (turquoise), 2 (red), 5 (green) and 6 (magenta). The hyperfine couplings for the simulations are given in Table 5.1. This figure is reproduced from J. A. B. Abdalla, A. M. Bowen, S. G. Bell, L. L. Wong, C. R. Timmel and J. Harmer, Characterisation of the paramagnetic $[Fe_2S_2]^{+}$centre in palustrisredoxin-B (PuxB) from Rhodopseudomonas palustris CGA009: g-matrix determination and spin coupling analysis, *Physical Chemistry Chemical Physics*, 2012, **14(18)**, 6526–6537 with permission from the PCCP Owner Societies.[15]

Table 5.3: Spin projection factors for the three models considered in the text. For each model the first column gives K_A^{exp} and $K_B^{exp} = 1 - K_A^{exp}$, the summed spin projection factors associated with the ferric site (α-spins) and ferrous site (β-spins). The k^{del} values give the contributions located at the Fe ions, the bridging sulphurs S* and the cysteine sulphurs S_{ox} and S_{red} ligating Fe^{3+} and Fe^{2+} respectively. $d^{A/B}$ are the delocalization factors for the ionic model 1, from DFT model 2, and from experimental model 3, where a range of values are given. This table is reproduced from J. A. B. Abdalla, A. M. Bowen, S. G. Bell, L. L. Wong, C. R. Timmel and J. Harmer, Characterisation of the paramagnetic $[Fe_2S_2]^+$centre in palustrisredoxin-B (PuxB) from Rhodopseudomonas palustris CGA009: g-matrix determination and spin coupling analysis, *Physical Chemistry Chemical Physics*, 2012, **14(18)**, 6526–6537 with permission from the PCCP Owner Societies.[15]

	Model 1		Model 2			Model 3		
Atom	K_A^{exp}	d^A	K_A^{exp}	k^{del}	d^A	K_A^{exp}	k^{del}	d^A
Fe^{3+}	1.50 ± 0.05	1		1.555 ± 0.041	0.819		1.56 to 1.51	0.66 to 0.83
S*		-	1.90 ± 0.05	0.083 ± 0.002	0.044	2.33 to 1.85	0.27 to 0.08	0.12 to 0.04
S_{ox}		-		0.089 ± 0.002	0.047		0.11 to 0.08	0.03 to 0.06
	K_A^{exp}	d^A	K_A^{exp}	k^{del}	d^A	K_A^{exp}	k^{del}	d^A
Fe^{2+}	-0.50 ± 0.05	1	-0.90 ± 0.05	-0.841 ± 0.047	0.934	-1.33 to -0.85	-1.24 to -0.79	0.939
S_{red}		-		-0.030 ± 0.002	0.033		-0.04 to -0.03	0.033

5.4 Density Functional Theory Calculations on the $[Fe_2S_2]^+$ centre in PuxB

Density Functional Theory (DFT) calculations were carried out in order to gain a measure of the electron delocalization over the $[Fe_2S_2]$ cluster. The calculations were used to construct model 2, used in the fitting, and also to provide starting values for model 3, which was fitted to the experimental ENDOR and HYSCORE data (see Section 5.2.5).

Calculations were performed using the software package ADF [109] using the BLYP functional and the TZ2P basis set. Calculations were made on four structures: i)the PuxB crystal structure with truncated SCH_2CH_3 ligands; $[Fe_2S_2(SCH_2CH_3)_4]^{3+}$, ii) $[Fe_2S_2(SCH_2CH_3)_4]^{3+}$ symmetrized to D_{2h} structural symmetry iii) $[Fe_2S_2(SCH_2CH_3)_4]^{3+}$ with the D_{2h} symmetry partially broken and iv) a D_{2h} symmetrized structure with shorter SCH_3 ligands.

Use of the four structures was necessary to allow identification of the iron-based magnetic orbitals. These could be easily identified in the symmetrized structure with the methyl ligands by comparison with existing calculations on similar structures in the literature. [192] The asymmetry of the crystal structure made identification of the magnetic orbitals directly from the calculation on this structure impossible. Instead it was possible to trace the molecular orbitals, constituting the magnetic orbitals from the symmetrized $[Fe_2S_2(SCH_3)_4]^{3+}$ structure into the symmetrized $[Fe_2S_2(SCH_2CH_3)_4]^{3+}$ structure, then to the $[Fe_2S_2(SCH_2CH_3)_4]^{3+}$ structure with partially broken symmetry, and finally in the crystal structure. Identification of the magnetic orbitals was based on the orbital energy, relative order and, where applicable, symmetry.

Figure 5.24: The orbital energy level diagrams for magnetic orbitals of the four structures used in calculations. In each case the β spins are shown in blue and the α spins in red. The iron d-orbital giving the largest contribution to the magnetic orbital is marked. **A** is the symmetrized $[Fe_2S_2(SCH_3)_4]^{3+}$ structure. **B** is the symmetrized $[Fe_2S_2(SCH_2CH_3)_4]^{3+}$ structure. **C** is the partially non-symmetrized $[Fe_2S_2(SCH_2CH_3)_4]^{3+}$ structure. **D** is the truncated crystal structure; $[Fe_2S_2(SCH_2CH_3)_4]^{3+}$.

Fig. 5.24 shows the orbital energy level diagrams for the magnetic orbitals in the four structures used in calculations. In each case, the β spin manifold is lower in energy than the α spin manifold. Differences in the energy levels of the magnetic orbitals between the systems are due to structural and symmetry changes which cause the relative proportions of each atomic orbital contributing to the molecular orbitals to change. The orbitals in Fig. 5.24 are labelled with their largest d-orbital contribution.

For all four structures studied, initial calculations were carried out on the high-spin structure and the electronic orbitals from these calculations were used to start the low-spin broken symmetry calculation using the '`spinflip`' keyword to invert the spins associated with one of the iron centres. Both of the symmetrized structures had geometric symmetry of group D_{2h}; however, this is reduced to C_{2v} symmetry in the calculation due to the asymmetry of the electronic distribution on the two iron centres.

5.4.1 Comparison of DFT results with the experimental results

The spin densities for each of the calculations were obtained from a Mulliken analysis. In each case, the spin densities and the electronic orbitals calculated were similar for all four structures. Since the calculation on the crystal structure should theoretically yield results closest to the state of the protein in the PuxB protein analysis, we concentrated on these results. The broken symmetry calculation yielded spin densities for the different centres of $\rho(\mathrm{Fe}^{2+}) = -2.838$, $\rho(\mathrm{S}_{red}) = (-0.1164, -0.0822)$; and $\rho(\mathrm{Fe}^{3+}) = 3.2421$, $\rho(\mathrm{S}^*) = (0.1636, 0.1938)$ and $\rho(\mathrm{S}_{ox}) = (0.2901, 0.1293)$. These spin densities are in good agreement with those in the literature calculated for a $[\mathrm{Fe_2S_2(SCH_3)_4}]^{3+}$ structure, which were initially used as the basis for the DFT-derived model 2 used in the spectral fitting.[192] The DFT spin densities yield delocalization factors that lie within the experimentally derived limits found for model 3 (the experimentally derived model). The iron covalency factors ($c_{Fe^{3+}} = 0.65$ and $c_{Fe^{2+}} = 0.71$) are similar to those calculated by Mouesca for $[\mathrm{Fe_2S_2}]^{+}$ clusters.[186] The calculations also show positive and negative spin densities for the β-protons belonging to the Fe^{3+} and Fe^{2+} ions respectively, in agreement with the experimental assignments. An examination of the broken symmetry α- and β-iron centred

orbitals show that they are significantly delocalized onto the bridging S atoms and adjacent Fe ions. This is clearly seen in Fig. 5.25, where the DFT calculated magnetic orbitals for the crystal structure are plotted.

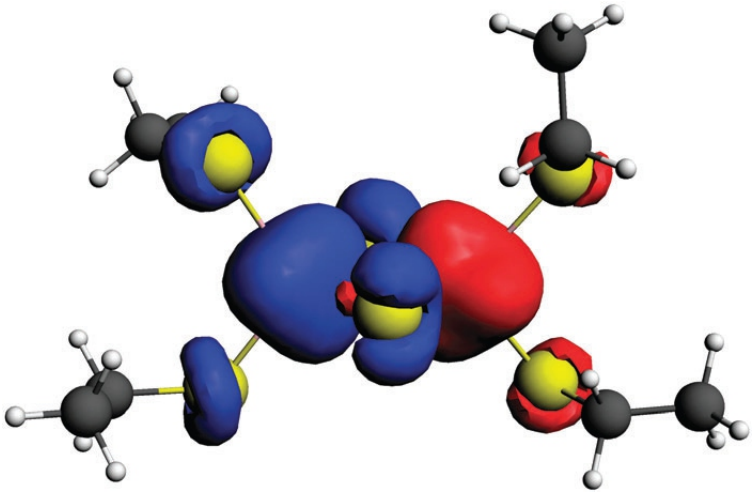


Figure 5.25: Broken symmetry DFT spin density (positive blue, negative red) calculated for the model $[Fe_2S_2(SCH_2CH_3)_4]^{3+}$, taken from the PDB crystal structure *3HUI.pdb*. This figure is reproduced from J. A. B. Abdalla, A. M. Bowen, S. G. Bell, L. L. Wong, C. R. Timmel and J. Harmer, Characterisation of the paramagnetic $[Fe_2S_2]^+$centre in palustrisredoxin-B (PuxB) from Rhodopseudomonas palustris CGA009: g-matrix determination and spin coupling analysis, *Physical Chemistry Chemical Physics*, 2012, **14(18)**, 6526–6537 with permission from the PCCP Owner Societies.[15]

5.4.2 Variable mixing time ENDOR to determine the absolute sign of the hyperfine couplings

Although it has been assumed that the reduced iron centre is likely to be located closest to the protein surface (*Fe1* in the PDB structure *3HUI.pdb*), this assignment can be tested via a variable mixing time ENDOR experiment to measure the absolute sign of a hyperfine coupling. For this purpose, the sharp low field peaks from proton 2, a proton closely associated with the Fe^{3+} centre that is denoted 'Fe2' in the crystal structure and is in possession of a positive k^{del} value, were selected.

With t_{mix} = 16 ms (Fig. 5.26), a notable decrease in intensity of the low radio frequency peak of proton 2 relative to the corresponding high frequency peak is observed. As we have already seen in Section 5.1.1 and Fig. 5.6, in variable mixing time ENDOR the magnitude of the ENDOR efficiency

corresponding to the β is reduced compared to that for the α spin manifold. Therefore the low frequency side of the proton Larmor frequency, ν_{1H}, corresponds to the β electron spin manifold and hence the hyperfine coupling must be positive.[13,199] This confirms the initial assignment of valence states, where the iron atom furthest from the protein surface is Fe^{3+}, since only in this case is A_{zz} positive for proton 2.

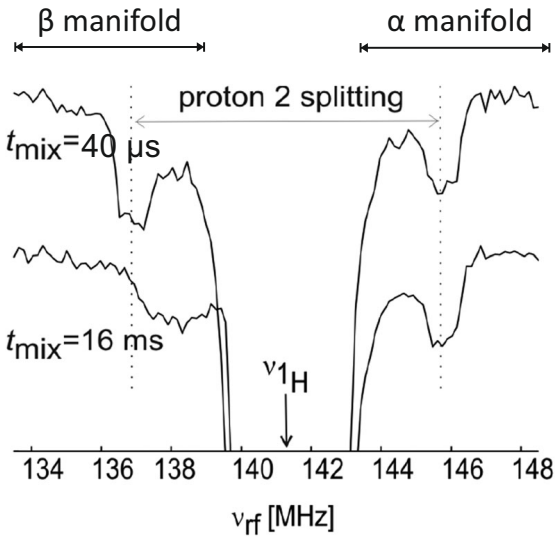


Figure 5.26: Variable mixing time W-band Mims ENDOR of PuxB alone, recorded at 3319.8 mT, T=5.5 K. For the long t_{mix} = 16 ms time, the low frequency peak of proton 2 decreases relative to the t_{mix} = 40 μs ($\cong$ 0) reference spectrum. This figure is reproduced from J. A. B. Abdalla, A. M. Bowen, S. G. Bell, L. L. Wong, C. R. Timmel and J. Harmer, Characterisation of the paramagnetic $[Fe_2S_2]^+$centre in palustrisredoxin-B (PuxB) from Rhodopseudomonas palustris CGA009: g-matrix determination and spin coupling analysis, *Physical Chemistry Chemical Physics*, 2012, **14(18)**, 6526–6537 with permission from the PCCP Owner Societies.[15]

5.4.3 The optimal *g*-matrix orientation and the dependence on the structure

The optimal g-matrix orientation for model 3 is shown in Fig. 5.11. The orientations found from models 1 and 2 are very similar and fall within the 6° error limits shown. The axis $g_{||}$ makes an angle of $\varphi = 48.51°$ with the `Fe2`$-$Cys48.Sγ (ligating cysteinyl sulphur) bond and the $g_\perp$ plane is inclined at an angle $\chi = 26.11°$ to the $[Fe_2S_2]$ plane. If the oxidized X-ray structure is replaced with calculated reduced structure (as discussed in Section 5.2.4), then there is a modest decrease, in particular in the

Fe−S_{cys} distances of < 0.05 Å, and a corresponding decrease in the proton distances to the cluster.

This results in a small increase in the dipolar part of the hyperfine interaction. The two S_{cys}−Fe−S_{cys} angles are also reduced by $< 4°$, which impacts on the determination of the *g*-matrix orientation. For example, the unique principal hyperfine axis for proton 1 changes by approximately 2° in going from the oxidized to reduced structure. It is estimated that these errors in the proton positions total ±0.075 Å.

The final error in our *g*-matrix orientation for PuxB was estimated by simulating the ENDOR spectra at a range of orientations around the best model 3 orientation calculated above and simultaneously considering an uncertainty in the proton positions of ±0.075 Å. Molecules were thus rotated relative to the *g*-matrix in all directions until the simulations of the outer wings of the ENDOR spectra no longer matched the experimental spectra satisfactorily. The acceptable range of orientations of the $g_{||}$ axis are depicted in Fig. 5.11 and are tightly clustered around the best solution, indicating that simulations of the data are very sensitive to the orientation. In the PDB reference frame of PuxB (*3HUI.pdb*) the optimized $g_{||}$ axis vector is:

$$g_{||} = [-0.6524 \pm 0.0248, -0.6269 \pm 0.0115, 0.4259 \pm 0.0405].$$

All three models give similar *g*-matrix orientations. For example, the unique axis of the dipolar hyperfine coupling for proton 1 changes by 3.5° between the ionic model 1 and model 3, and by only 0.3° between models 2 and 3. The fit of the ENDOR simulations to the data is similar between model 2 and 3, with the fits of model 1 being significantly worse. The *g*-matrix orientation is determined principally by the spin projection factor on the Fe^{3+} ion and to a lesser extent by the cysteine sulphurs ligating the ferric centre. The bridging sulphurs have little influence since they are further away from the important protons close to the ferric site. A more accurate description could be obtained from a single-crystal study; data exist for Rieske $[Fe_2S_2]^+$,[181] and $[Fe_4S_4]^+$ clusters,[200,201] but there are no such studies for vertebrate-type $[Fe_2S_2]^+$ clusters. The relatively small number of published single crystal studies gives an indication of the difficulty of obtaining suitable single crystal samples.

5.5 Discussion and conclusion

The g-matrix orientation determined for PuxB and PuR-PuxB complex is in general agreement with the previous findings by Kappl et al.[165] for the vertebrate-type ferredoxin (Adx). In Adx, the axis $g_{||}$ was found to have an angle of $\varphi = 33°$ with the `Fe2`$-$Cys55.Sγ bond direction, and to be inclined at $\chi = 21°$ to the $[Fe_2S_2]^+$ plane. For PuxB we find $\varphi = 48.5°$ and $\chi = 26.1°$. The similarity of Adx and other vertebrate-type ferredoxin systems to PuxB suggests that this is a relatively general result, which is not entirely surprising given the structural similarity.

Importantly it was found that the $g_{||}$ axis orientation is not critically sensitive to the model employed; models 1, 2 and 3 all gave very similar results. This indicates that, if only the g-matrix orientation is required, then it can be experimentally obtained with good accuracy from orientation dependent ENDOR data of the cysteine β-protons and spin projection factors for the two Fe ions. Numerous theoretical studies have been undertaken to explain the size of the three g-values and the axes orientation, which are shown to be sensitive to the ligands, their orientation, and the charge distribution.[202–205] This experimental study contributes to this experimental picture since it provides indisputable evidence that the ionic picture of model 1 with $K_A(Fe^{3+}) = +\frac{7}{3}$ and $K_B(Fe^{2+}) = -\frac{4}{3}$ will not describe the dipolar part of the proton hyperfine couplings. Values of $K_A^{exp} = +1.50 \pm 0.05$ gave a reasonable fit to the experimental data. A good fit to the data was achieved with model 2 using a spin density distribution calculated directly from DFT and yielding $K_A^{exp} = +1.90 \pm 0.05$, also significantly smaller than the theoretical value $K_A(Fe^{3+}) = +\frac{7}{3}$. In model 3, both the spin density distribution and spin projection factors around the ferric ion were varied and yielded experimentally derived upper and lower limits for the value of K_A^{exp} from 1.85 to 2.33 (the theoretical value). The simulations for all three models are critically sensitive to $k_{Fe^{3+}}^{del}$, which yields acceptable values that lie between 1.50 to 1.56. As spin density is moved from the Fe^{3+} ion onto the bridging S atoms in models 2 and 3, the K_A^{exp} value increases to keep $k_{Fe^{3+}}^{del} \approx 1.53$. Our experiments cannot accurately determine K_B^{exp} independently of K_A^{exp} because K_B^{exp} is significantly smaller than K_A^{exp}. Thus the proton dipole couplings to the ferrous ion are relatively small and their ENDOR and HYSCORE signals contribute to the many overlapping proton signals comprising a broad and poorly resolved central region in the spectra.

The theoretical value of $K_A(Fe^{3+}) = +\frac{7}{3}$ could be used to simulate the experimental data, as is evident by the upper limit given for model 3 in Table 5.3. However, employing $K_A^{exp} = +\frac{7}{3}$ requires the assignment of a large spin density at the bridging sulphurs with the delocalization coefficient of $d(S*) = 0.12$. This value yields a spin density per bridging sulphur atom of $\rho(S*) \cong 0.12 \times 5 = +0.6$; a spin density of +5 is expected for a magnetically isolated Fe^{3+} ion. Density functional theory (DFT) calculations of a symmetrized $[Fe_2S_2]^+$ centre with truncated $SCH_3{}^-$ ligands found in the literature report $\rho(S*) = +0.174$.[192] Since the magnetic orbitals in the local spin site model should only be very weakly mixed, the valid use of the strong-exchange spin coupling scheme here would require that the β-spin magnetic orbital delocalization (from the Fe^{2+} site) onto the bridging sulphurs is negligibly small. If this were not the case, the negative (β) and positive (α) spin density at the bridging sulphurs would cancel out to an extent depending upon their respective contributions. Consequently, the associated contributions to the magnetic moment from the α-spins and β-spins would also be reduced; K_A and K_B would then be less than $+\frac{7}{3}$ and $-\frac{4}{3}$ respectively. A picture of delocalized positive spin density at the ferric site and very localized negative spin density at the ferrous site is not compatible with the electronic structure and thus is hard to rationalize chemically. Hence, the arguments presented point to a limitation of employing a coupling scheme valid in the strong exchange coupling limit in this $[Fe_2S_2]^+$ cluster with delocalized magnetic orbitals.

Alternatively, the lower limit on our experimental K_A^{exp} of 1.85 would indicate that the spin projection factors calculated from a local site spin coupling model using $S_A = \frac{5}{2}$ and $S_B = -2$ are significantly too high. It is reasonable to assume that this is a consequence of spatial overlap of the α-spin and β-spin magnetic orbitals. Indeed the DFT calculations of $[Fe_2S_2(SCH_3)_4]^{3+}$ from the literature yield positive and negative spin densities that sum to +4.034 and −3.033 respectively,[192] whereas there are five and four unpaired electrons associated with the high-spin Fe^{3+} and Fe^{2+} ions respectively. Spatial overlap of the α-spin with the β-spin magnetic orbitals cancels out positive and negative spin density contributions of $|0.966|$. The lower $K_A^{exp} = 1.85$ value could thus be interpreted as a cancellation of the spin density and the associated magnetic moment contribution due to the overlap. Given that the spatial overlap of magnetic orbitals calculated by DFT cancels out the spin density of approximately one

α-spin and one β-spin, it is interesting to consider the case where $S_A = \frac{(5-1)}{2} = \frac{4}{2}$ and $S_B = \frac{(4-1)}{2} = \frac{3}{2}$. Application of Equations 5.8 and5.9 then yields $K_A = +2$ and $K_B = -1$, which agrees well with our mean K_A^{exp} value determined experimentally.

The strong-exchange spin coupling limit considers the five ferric α-spin magnetic orbitals to be coupled to form a spin vector S_A and likewise for the ferrous β-spin magnetic orbitals to form S_B. The local spin site model is valid when these orbitals are only very weakly mixed. The experimental data indicates considerable delocalization of the magnetic orbitals and the analysis quantifies the error that may be introduced by employing a strong-exchange spin coupling scheme in $[Fe_2S_2]^+$ clusters. The delocalized or 'effective' spin projection factors for models 2 and 3 can be compared to those calculated by Mouesca et al.:[186,201]

$$k_{Fe^{3+}}^{del} = c_{Fe^{3+}} K_A^{exp}(\mathrm{Fe}^{3+}) = 0.66 \times \frac{7}{3} = +1.50 \tag{5.19}$$

$$k_{Fe^{2+}}^{del} = c_{Fe^{2+}} K_B^{exp}(\mathrm{Fe}^{2+}) = 0.75 \times -\frac{4}{3} = -1.00 \tag{5.20}$$

where $c_{Fe^{2+}}/c_{Fe^{3+}}$ are covalency factors and have been defined as the ratio of the spin density at the ion to the maximum expected spin density in the valence-bond limit (i.e., -4 for Fe^{2+} and $+5$ for Fe^{3+}). The numerical values for $c_{Fe^{2+}}/c_{Fe^{3+}}$ are based on experimental ^{57}Fe isotropic hyperfine coupling constants determined from Mössbauer measurements. The $k_{Fe^{3+}}^{del}$ and $k_{Fe^{2+}}^{del}$ values calculated in this way agree well with our experimental values given in Table 5.3. The covalency factors account for the lower than predicted experimental ^{57}Fe hyperfine coupling constants due to spin delocalization. The reduced spin projection factors $k_{Fe^{3+}}^{del}$ and $k_{Fe^{2+}}^{del}$ in Equations 5.19 and 5.20 are thus due to delocalization. Furthermore, overlap of the α-spin with β-spin magnetic orbitals cancels out local spin density and hence the ferric and ferrous site covalency factors ($c_{Fe^{2+}}$ and $c_{Fe^{3+}}$) presumably sum to less than unity. Consequently, the total α-site and β-site spin projection factors must sum to less than $+\frac{7}{3}$ and $-\frac{4}{3}$ respectively.

5.5.1 Use of $[Fe_2S_2]^+$ clusters as spin probes

Accurate knowledge of the magnetic moment of the $[Fe_2S_2]^+$ cluster and the g-matrix orientation is essential if this paramagnetic centre is to be used as a spin probe. The work in the previous chapter (Chapter 4) gave a demonstration of this in relation to DEER spectroscopy. It should be noted that in this work, both PuxB and the closely related protein HaPux were used. The g-tensor orientation devised in this chapter was used for both proteins in determination of their docked complexes. This is a reasonable approximation to make since the g-matrix orientation found for PuxB was very similar to that found for the vertebrate-type ferredoxin (Adx), suggesting that there is a generalized orientation of the g-matrix for all ferredoxins of this class.

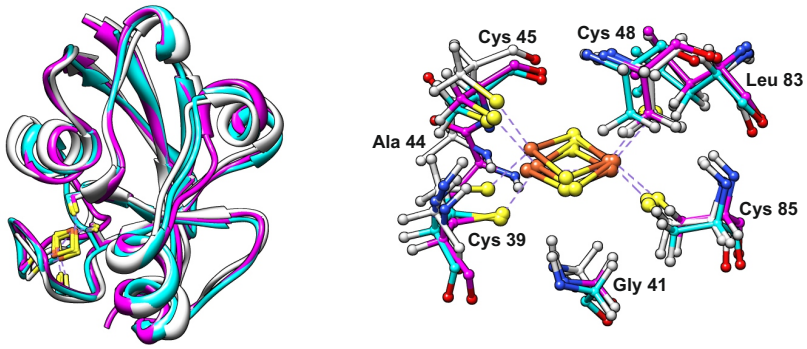


Figure 5.27: Figure showing the overlaid PDB structures for Adx (*1CJE.pdb*) shown in white; PuxB (*3HUI.pdb*) shown in magenta and HaPux (structure currently unpublished) shown in cyan. The overlay of the whole structure is shown on the left and the detail of the residues close to the $[Fe_2S_2]$ cluster on the right.

Comparing the sequence alignments (Fig. 5.28) and crystal structures (Fig. 5.27) for HaPux, PuxB and Adx, the structures are very similar and there is a high degree of sequence conservation, particularly in the region close to the $[Fe_2S_2]$ cluster. Furthermore, as we have seen from the ENDOR and HYSCORE analysis of the comparative oxidized crystal structure with a hypothetical reduced structure (see Section 5.2.4), small movements in the coupled proton positions and in relative bond lengths make little difference to the derived g-matrix orientation. This also lends support for the idea of a generalized g-matrix orientation for the vertebrate-type ferredoxins.

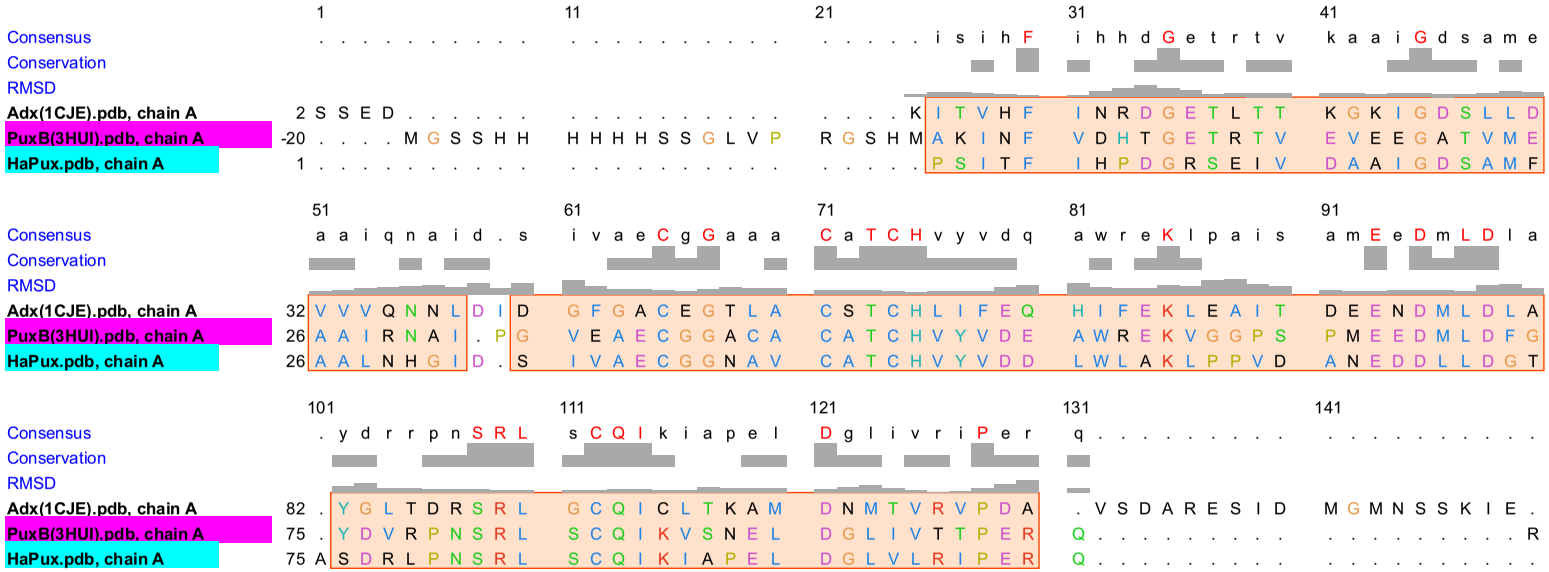


Figure 5.28: The sequence alignment for Adx (*1CJE.pdb*), PuxB (*3HUI.pdb*) and HaPux (structure currently unpublished), generated in Chimera.[1] The numbering is not the same as that given in Fig. 5.27 due to the inclusion of the polyhistidine-tag (His-tag) at the start of the PuxB amino acid sequence in the numbering scheme. The four conserved ligating cysteine residues are numbered 65, 71, 74 and 112.

Chapter 6

Repeated Excitations IN DEER (REINDEER)

6.1 The need for modifications of DEER

As we have seen in the previous chapters, which detailed DEER measurements on copper(II) systems and iron-sulphur centres in ferredoxin proteins, one disadvantage to these measurements is the small modulation depth of the spectra that can result. This is due to the broad EPR spectra of these metal centres with respect to the excitation width of a pulse applied at X-band and higher frequencies. This scenario results in a pulse that only excites part of the EPR spectrum. Thus, both the inversion efficiency of the applied pump pulse and the modulation depth λ are low (see Equation 2.30).

Although orientation selection can lead to more information being gained from the DEER data through orientational analysis, it also poses problems experimentally in the recording of DEER traces, since the modulation depth can be very small. This chapter investigates a method to increase the excitation range of the pump spins by using more than one pump pulse. As previously described, experimentally recorded DEER spectra comprise an oscillating form factor, $F(t)$, containing a modulated and unmodulated part, $1 - \lambda$ (see Equation 2.29), and a background decay, $B(t)$. Thus, increasing the modulation depth λ increases the signal-to-noise ratio of the modulated part of the spectrum (the reduced form factor) for the same detection spin signal intensity. This has many advantages; faster measurement times and better separation of the modulated and unmodulated parts of the DEER trace

are to be anticipated.

This chapter describes a modification of the DEER sequence using multiple pump pulses to excite a broader range of frequencies, a technique we call REINDEER (Repeated Excitations IN DEER). The new pulse sequence was applied using a commercially available external microwave source, in addition to the two sources already built into the Bruker ELEXSYS 680 spectrometer. It is thus a three-frequency pulse sequence. A 2 mm split-ring resonator is employed, which has an exceptional B_1 conversion factor and when fully over-coupled has a bandwidth of c. 800 MHz. A similar multi-frequency DEER experiment was recently also attempted by Asada and co-workers.[206] When REINDEER is applied to nitroxide spins, we show that a very clear benefit results, since a significantly larger fraction of the spins in the sample now contribute to the experiment, either as detection or pump spins. Hence the experimental sensitivity increases to become closer to the theoretical maximum. This broader excitation also helps to remove orientation effects on the DEER trace, which is usually highly desirable, for example when using MTSL spin labels attached to proteins. We are also able to define a general relationship between a REINDEER form factor and that for multiple individual DEER traces collected with the same pulse positions.

Further studies were carried out on a copper-nitroxide system. In this case, the copper EPR spectrum is too broad to be excited in its entirety by the REINDEER sequence. However, measuring this system using the 2 mm resonator allowed us to exploit the very broad bandwidth and high B_1 conversion factor of this resonator, so that standard DEER experiments could be implemented with an unprecedentedly large frequency separation between the detection and pump pulses of up to 550 MHz. This set-up facilitated the collection of a number of DEER traces that sample a satisfactory number of orientations of the bi-radical with respect to the field allowing the distance between the two paramagnetic centres to be measured with confidence.

6.2 Application of Repeated Excitations IN DEER (REINDEER)

The ELEXSYS 680 spectrometer used in these experiments has an inbuilt ELDOR source, which can operate at a different frequency to that of the primary source. In order to introduce a third frequency,

an external microwave source was added and allowed to operate through the +/− x and +/− y channels. The main source to these channels was disconnected and a load added to prevent reflections in the bridge. The main frequency source was used through the tuneable microwave pulse forming unit (MPFU) channels, which can all be tuned independently for phase and amplitude, allowing greater flexibility compared to the +/− x and +/− y channels, The +/− x and +/− y channels have fixed relative phases and are all controlled only via one main high power attenuator. The set-up used is shown in Fig. 6.1.

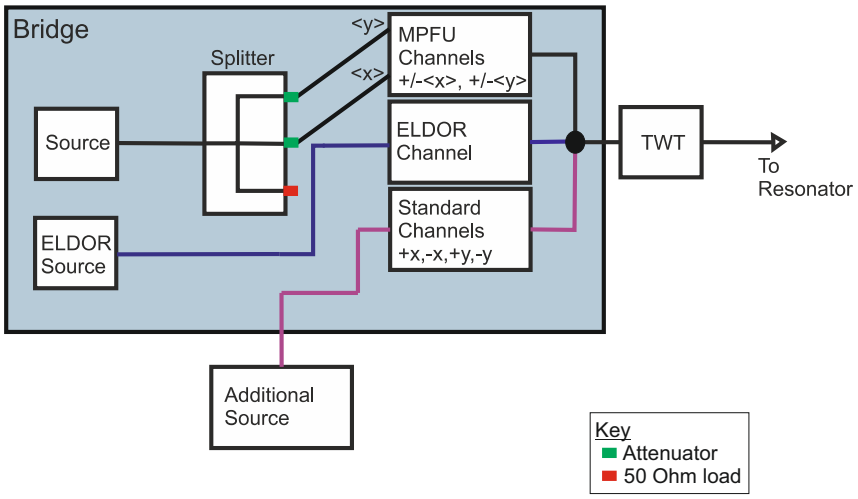


Figure 6.1: A schematic diagram of the bridge with an additional source added.

6.2.1 Experimental conditions

All experiments were performed using a Bruker ELEXSYS 680 spectrometer fitted with an Oxford Instruments cryostat. Experiments were conducted at X-band using a Bruker flexline 2 mm split-ring resonator (ER 4118X-MS2). The external source used to provide a third microwave frequency was an Agilent Technologies E8257D 25 KHz–20 GHz PSG analogue signal generator. All microwave signals were amplified using only one 1 kW travelling-wave tube (TWT) amplifier from Applied Systems Engineering.

Experiments were carried out on two nitroxide-nitroxide systems at 50 K: a model system with

an inter-spin distance of c. 2.1 nm, provided by Bruker and prepared in the solvent ortho-tertphenol (see Fig. 6.2 (A)). Secondly, a doubly-labelled Ferredoxin Reductase (PuR) protein of the CYP199A2 system from *Rhodopseudomonas palustris* (*3FG2.pdb*) was prepared according to the protocol from Xu and co-workers and spin labelled with MTSL at the sites S81C and C302 (see Fig. 6.2 (C)).[150] This protein was donated by the group of Dr Luet Wong. In addition, a copper-nitroxide model system was studied (see Fig. 6.2 (B)), in Chapter 3), which has an inter-spin distance of c. 2.05 nm. The sample was prepared in a 1:1:1 mixture of chloroform, THF and toluene to a concentration of 200 μM. Experiments on the copper system were carried out at 20 K in order to increase the T_m of the copper containing paramagnetic centre sufficiently to allow DEER measurements to be recorded. This sample was kindly provided by Dr Michael Jones and Prof. Jon Dilworth.

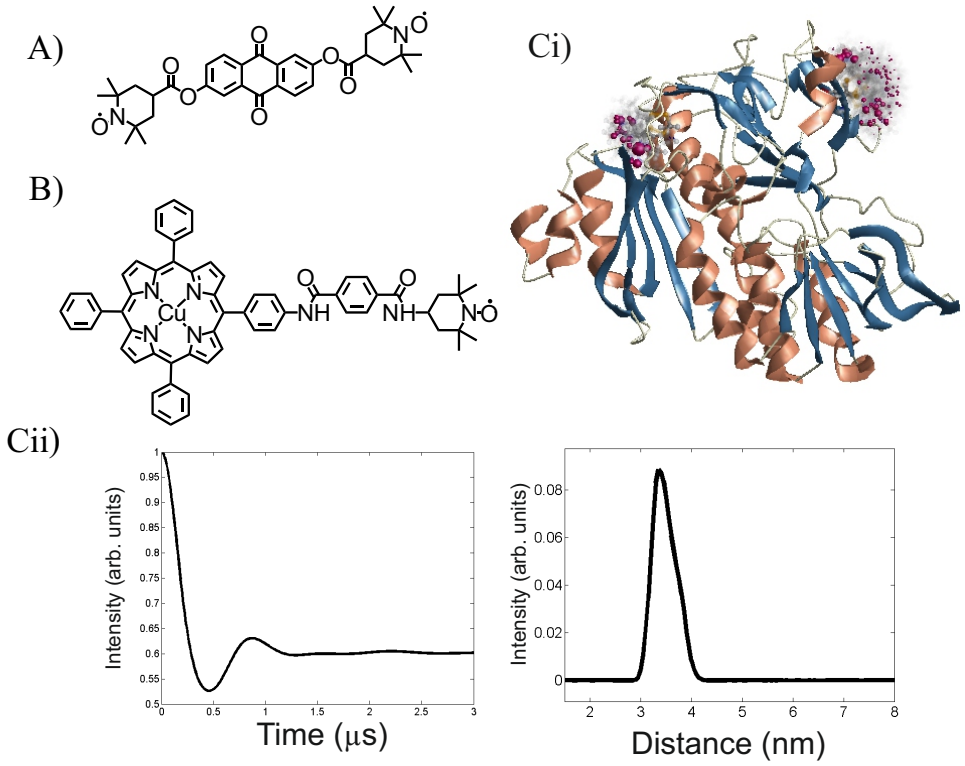


Figure 6.2: **A)** Structure of the 2.1 nm nitroxide-nitroxide model system; **B)** Structure of the 2.2 nm copper-nitroxide model system; **C)** Structure of the protein Ferredoxin Reductase (PuR) from the CYP199A2 system found in *Rhodopseudomonas palustris* (*3FG2.pdb*)) with spin labels distributions for MTSL spin labels at the sites S81C and C302, calculated using MMM;[80,81] the predicted DEER trace and distance distribution from MMM are also shown.

6.2.2 Tuning the REINDEER experiment

The pulse sequence used for the REINDEER experiment is shown in Fig. 6.3. The two pump pulses are coincident and move in unison through the precession time, τ. The pump pulses are approximately square in the time domain, thus their frequency profiles can be assumed to be sinc functions, the 'wings' of which cover a broad range of frequencies. The frequency range covered by the actual pulses is dependent on not only the shape of the input pulse but also on the resonator bandwidth. When the difference between the two frequencies at which the two pump pulses applied is small, the 'wings' of the pulses will overlap, causing the pulse at one frequency to have an effect on the spins at the second frequency. This phenomenon is also observed as the source of the phase shift in three-pulse DEER (see Chapter 7).

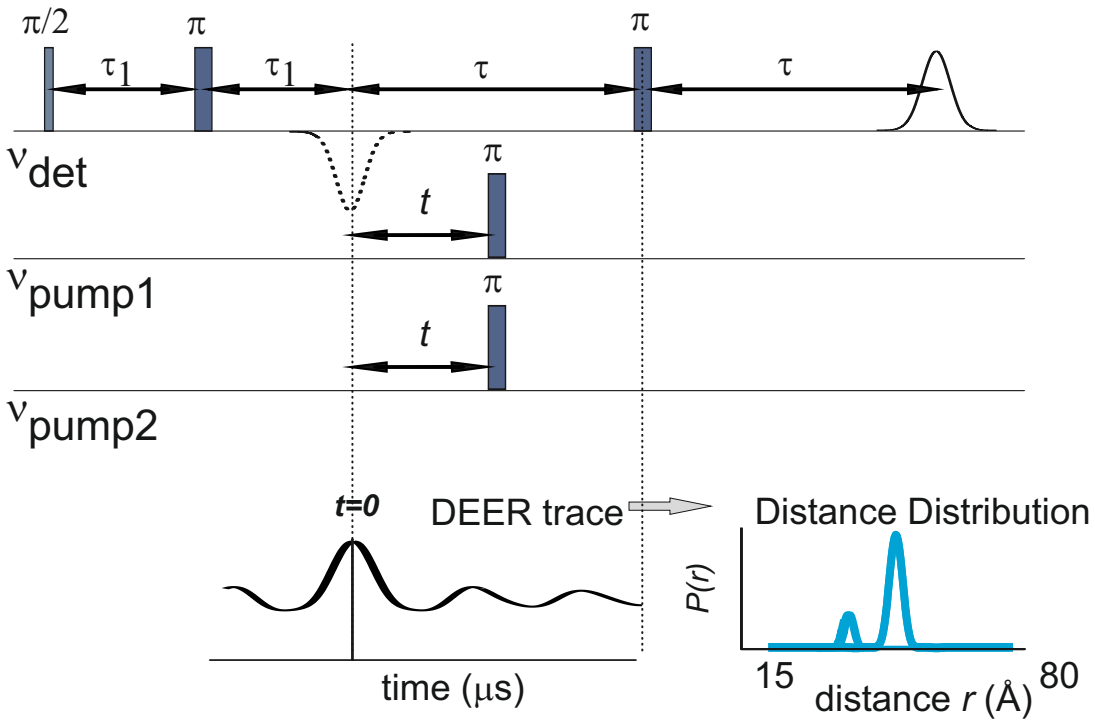


Figure 6.3: The pulse sequence used in REINDEER. The sequence resembles a standard four-pulse DEER sequence with an additional pump frequency, where the two pump pulses move coincidentally within the same time window. The lower part of the figure illustrates the experimentally collected time trace from which a distance distribution can be extracted.

Since it is important that the pump pulses have a turning angle of π at the centre frequency of the applied pulse, the two pump pulses must be tuned at the same time. This was achieved by tuning the pulses iteratively using a Hahn echo sequence preceded by a π inversion pulse (π-t-π/2-τ-π-τ-*echo*), as described in Fig. 6.4.

In order to ensure that the concurrent pump pulses still lay within the linear regime of the TWT, both pump pulse lengths were selected to be 24 ns. Pulse crossing experiments such as those described in Section 7.2.3 were undertaken with the two pump pulse frequencies used for the experiments. For the case where the pump pulses were separated only by 67 MHz, slight deviations from the linear regime were noted. The linear regime of the TWT is defined for input powers such that there is a linear relationship between the power input and power output for the amplifier.

The size of the inversion of the Hahn echo at one of the pump frequencies was also seen to decrease slightly when both pump pulses were applied at the same time, compared to the case when only the pump pulse at the frequency of the Hahn echo pulses was applied. This is a result of spectral diffusion, since the second pump frequency excites some spins coupled to those observed at the detection frequency. This changes the resonance frequency of the detection spins.[43]

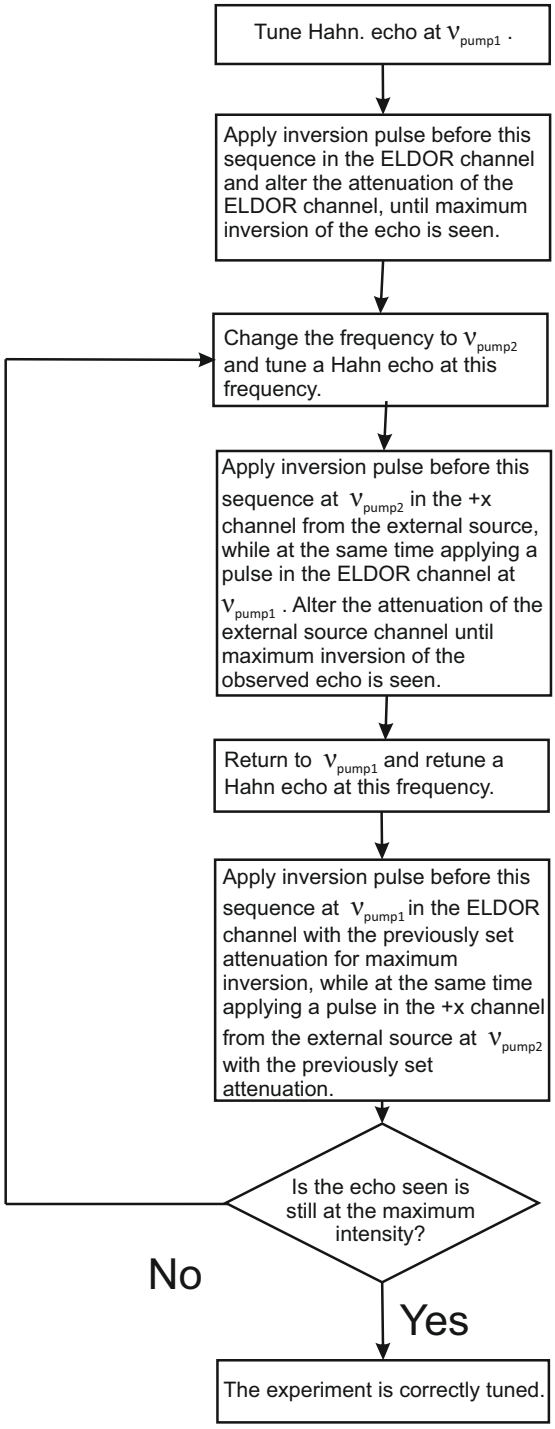


Figure 6.4: A schematic representation of the iterative process used to tune the attenuation required to produce π pulses at both pump frequencies, in the presence of the other pump frequency.

6.3 REINDEER experimental data: results and analysis

The experiment was performed on the 2.1 nm bisnitroxide model system and on the doubly MTSL labelled Ferredoxin Reductase protein (PuR). In each case, the three frequencies used corresponded approximately to the three hyperfine peaks forming the nitroxide spectrum ($M_I = -1, 0, +1$). The three pulses had the relative spacing of 0, −67 MHz and +128 MHz. For PuR, the detection frequency was selected such that it corresponded to excitation on the left of the spectrum on the $m_I = +1$ hyperfine (see Fig. 6.5).

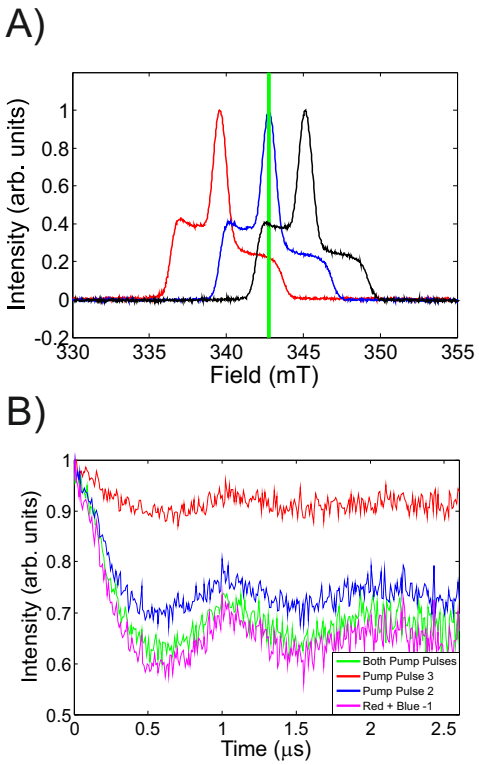


Figure 6.5: **A)** Normalized ESE detected field sweeps collected at each frequency, used in the experiments on PuR, are overlaid and the field value used in the final REINDEER and DEER experiments is highlighted (green line). **B)** Background corrected REINDEER results for the PuR protein with the relative detection and pump frequencies corresponding to A); the REINDEER trace (green) is shown with the individual DEER traces recorded for each pump frequency (red and blue) and also the combination of these DEER traces (magenta) according to Equation 6.1. **Key to data:** with reference to the three frequency positions defined in Fig. 6.6 A). *red trace:* detection frequency–frequency 1; pump frequency–frequency 3. *blue trace:* detection frequency–frequency 1; pump frequency - frequency 2.

For the 2.1 nm model system, the experiment was repeated so that, in turn, each of the frequency positions was used as the detection frequency and the remaining two as pump frequencies. The relative positions and the experimental results are shown in Fig. 6.6 (A). Experiments were also repeated on the 2.1 nm model system where the pump pulse positions from the different sources were swapped with the same detection position to verify that this had no influence on the data collected, no differences were observed (data not shown).

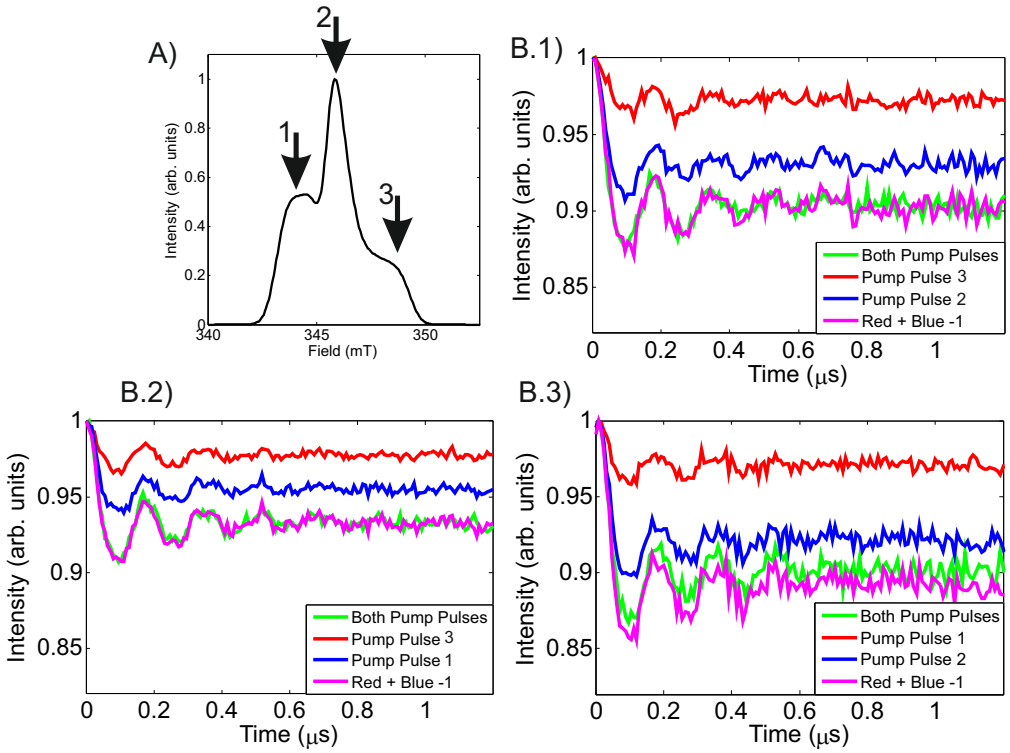


Figure 6.6: **A)** Relative positions of the three pulse frequencies used (1, 2, 3) shown on a CW nitroxide spectrum. **B.1,2,3)** Background corrected REINDEER results (green traces) for the 2.1 nm model system with the detection frequency at all three different frequency positions, 1, 2 and 3. In each case, the data presented are; the individual DEER traces (red and blue traces) and the combined DEER trace (magenta trace) in accordance with Equation 6.1. **Key to data:** with reference to the three frequency positions defined in A). B.1) *red trace:* detection frequency–frequency 1; pump frequency–frequency 3. *blue trace:* detection frequency–frequency 1; pump frequency–frequency 2. B.2) *red trace:* detection frequency–frequency 2; pump frequency–frequency 3. *blue trace:* detection frequency–frequency 2; pump frequency–frequency 1. B.3) *red trace:* detection frequency–frequency 3; pump frequency–frequency 1. *blue trace:* detection frequency–frequency 3; pump frequency–frequency 2.

6.3.1 The theoretical relationship between REINDEER and DEER traces with supporting simulations

For the case where the combination of both pump π pulses are within the linear regime of the TWT and the frequencies of the two pump pulses are separated, so that there is little overlap between the two pulses in frequency, the REINDEER form factor, $F_R(t)$, can be calculated from the DEER form factors, $F_D^i(t)$, for each of the pump positions separately, using the formula:

$$F_R(t) = \left[\sum_{i=1}^{n} F_D^i(t)\right] - (n-1) \tag{6.1}$$

n is the number of DEER traces being combined. (For all of the data presented here $n = 2$.) To examine this relationship further, it is instructive to consider the possible m_I values for each of the two spins and which of the possible combinations of the two m_I values contribute to the spins detected and, of these, which contribute to the observed DEER form factor when different pump and detection pulse positions are used. If we consider a very simplistic model, where the detection frequency lies in the centre of the nitroxide spectrum, exciting all of the spins with $m_I = 0$, but none with $m_I = +1$ or -1, and a pump frequency that can either be applied at a higher frequency, exciting only spins with $m_I = -1$, or at lower frequency, exciting only spins with $m_I = +1$.

Table 6.1 details the combinations of spins from a biradical that would contribute to the DEER effect under different experimental conditions for DEER and REINDEER. In each case, if the detection occurs on the $m_I = 0$ component, only combinations of the two spins where one or more of the m_I values is 0 will contribute to the measured signal. When the pump pulse frequency corresponds to the $m_I = -1$, only those where the other spin has $m_I = -1$ will contribute to the DEER form factor, i.e. $\frac{2}{6}$. The same argument can be applied to the situation where the detection pulse on $m_I = 0$ and the pump pulse on $m_I = +1$; the number of contributions to the DEER form factor of the total configurations detected is again $\frac{2}{6}$.

In the REINDEER experiment with detection on $m_I = 0$ and pump pulses on $m_I = -1$ and $m_I = +1$ the number of m_I configurations contributing to the detected signal is also six but the number of these contributing to the DEER form factor is four, thus the fraction which give rise to the DEER form factor is $\frac{4}{6}$. This can be calculated from:

$$P_R(t) = \left[\sum_{i=1}^{n} P_D^i(t)\right] - (n-1) \tag{6.2}$$

where P_R and P_D are the proportion of detected configurations contributing to the DEER effect for the REINDEER experiment and the standard DEER experiments respectively. The $n-1$ component is effectively a normalization factor, since with only one detection frequency the number of configurations of two spins that are detected in both the DEER and REINDEER experiments is constant. This equation is of the same form as Equation 6.1, demonstrating the validity of this method for combining spectra.

Table 6.1: Combinations of m_I values for two spins contributing to a DEER effect for a very simplistic model where the detection frequency lies in the centre of the nitroxide spectrum, exciting all of the spins with $m_I = 0$, but none with $m_I = +1$ or -1 and a pump frequency that can either be applied at a higher frequency, exciting only spins with $m_I = -1$, or at lower frequency, exciting only spins with $m_I = +1$.

m_I of spin 1	m_I of spin 2	Number of spins detected ($m_I = 0$)	Number of spins contributing to DEER form factor for pump pulse on $m_I = -1$	Number of spins contributing to DEER form factor for pump pulse on $m_I = +1$	Number of spins contributing to REINDEER form factor for pump pulses on $m_I = +1, -1$
-1	-1	0	0	0	0
-1	0	1	1	0	1
-1	$+1$	0	0	0	0
0	-1	1	1	0	1
0	0	2	0	0	0
0	$+1$	1	0	1	1
$+1$	-1	0	0	0	0
$+1$	0	1	0	1	1
$+1$	$+1$	0	0	0	0
	Total	6	2	2	4

Using the orientational DEER simulation program utilized earlier in this thesis (see Chapter 2),[5] it is possible to simulate both REINDEER and DEER data to further validate Equation 6.1 (see Fig. 6.7). The first step in the simulation program is the calculation of pulse profiles for both the detection and pump pulses used in the experiment. These profiles are used to calculate the portions of the spectrum and thus the orientations of a molecule with respect to the external static field, which are resonant with the pulse being considered. For cases where both pulses are resonant, one with each of the two centres in the biradical, a frequency contribution to the DEER trace is calculated. The frequency contributions for all contributing molecular orientations are summed to give the dipolar spectrum. This is Fourier transformed to give the time trace, which can be compared directly to background corrected experimental data (experimental form factor). Using this simulation method, it is possible to define the pump pulse profile to be a Gaussian for individual DEER experiments and a combination Gaussians for REINDEER experiments (see Fig. 6.7).

Experimentally, deviations from the expected relationship can occur for a number of reasons. Firstly, one such deviation occurs when the two pulses are close together in frequency, so that the profiles of the two pump pulses overlap and the 'sinc-wings' of one pump pulse cause significant excitations at the other pump pulse frequency. This means that when one of the pump pulses is applied alone in a normal DEER experiment without retuning its amplitude, the turning angle of the pulse is altered and this affects the modulation depth obtained in the DEER trace compared to the same pulse's contribution to the REINDEER trace. Secondly, deviations will also occur when the combination of the two pump pulses falls outside the linear regime of the TWT. Although both pulses are tuned to have a turning angle of π in the presence of the other pulse, this angle will be different for the pulses acting together and separately if the single pulses fall into the linear regime of the TWT, but the combined pulses do not. Thirdly, the use of two pulses at the same time also promotes spin-spin diffusion effects. This is observed when tuning the pump pulses via the inversion method; the inverted echo observed when both pulses are acting is much smaller than that with only one pulse acting. All three of these effects can cause a reduction in the modulation depth observed in the REINDEER experiment, compared to that predicted by summing the individual DEER traces.

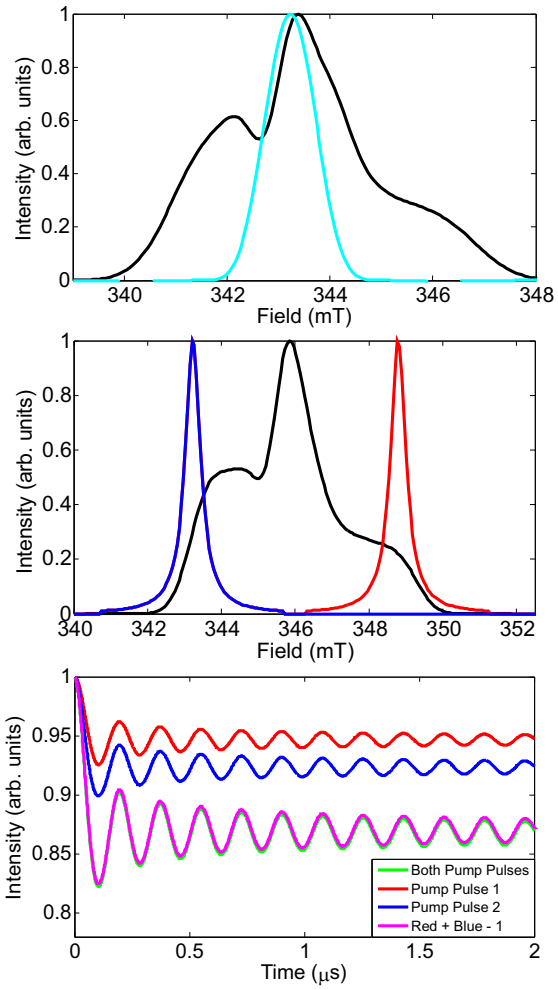


Figure 6.7: **Upper plot:** A plot of the detection pulse profile, shown in cyan, relative to a simulated nitroxide spectrum. **Central plot:** The Gaussian pump pulse profiles relative to the same simulated nitroxide spectrum in red and blue. These are used individually for DEER and together for REINDEER. **Lower plot:** The simulated DEER, combined DEER and REINDEER time traces. No background correction or modulation depth correction had been added to these traces.

As expected from an effect related to pulse overlap, the greatest deviation from the predicted relationship of DEER and REINDEER modulation depths are seen when the pulses are closest together. This is demonstrated in Fig. 6.6 where the difference between the REINDEER spectrum and the combined sum of the DEER spectra is greatest in Fig. 6.6 B.3, where the two pump frequencies are only separated by 67 MHz and least in Fig. 6.6 B.2, where the pump pulse separation frequency is 195 MHz. Fig. 6.6 B.1 has an intermediate pump pulse separation of 128 MHz.

The results from the PuR MTSL doubly-labelled system (see Fig. 6.5 B) show that for this system, deviations of the modulation depth can occur with a separation of 128 MHz between the pulses. With this frequency separation between the pulses, the degree of overlap is likely to be small. Therefore in this case, the deviation in the modulation depth of the REINDEER trace from the expected result is most likely a result of the combined pulses being outside the linear regime of the TWT. The large separation causes the pump pulses to lie in less favourable positions within the resonator bandwidth and therefore greater pulse powers are required to cause a turning angle of π. This pushes the combination of the two pulses outside the TWT linear regime. The pulse powers required could be reduced by employing longer pump pulses.

6.4 Orientational selectivity and REINDEER

For DEER experiments involving electron spins, particularly those associated with metal centres, which have broad spectra in relation to the frequency bandwidth of pulses used, orientational selection must be considered in the analysis of DEER traces. The use of two or more pulses in a REINDEER experiment allows the excitation profile of the pump pulses to be broader, exciting more of the spectrum and hence more orientations. Asada and co-workers have already explored the possibility of studying the dipole interaction between a tyrosine radical and a manganese cluster in Photosystem II using five pump pulse frequencies, created by combining different oscillating sources with the aim to remove any orientational effects and to increase the modulation depth of the spectra observed.[206] Thomas Prisner and co-workers have also published a paper demonstrating how the bandwidth of frequencies excited by a single pulse can be increased through the use of optimal control pulses.[207]

There have also been attempts to suppress the effects of orientational selectivity from EPR spectra via the averaging of DEER traces recorded at multiple field positions (field averaging).[208] However, this generally results in the majority of the DEER traces being recorded under non-optimal conditions, particularly when the procedure is automated.[209] Generally, orientation selection is not completely cancelled by such field averaging.[210] Averaging over different pump and observer frequency positions has also been proposed and it is this method that will be investigated here.[75]

We have used a copper-nitroxide model system with an inter spin distance of c. 2.05 nm (see Fig. 6.2) to examine how the use of multiple pump pulses affects the modulation depth and degree of orientational selection observed. For the copper-nitroxide system, applying a short detection pulses to the centre of the nitroxide spectrum causes uniform excitations of all orientations of the nitroxide. Therefore, any orientational dependence will arise solely from the copper paramagnetic centre. The EPR spectrum of the copper porphyrin studied here is axial and thus described by the principle values g_z and $g_{x/y}$. Measuring normal DEER with a single pump pulse frequency at various different pump-detection pulse separations shows how the DEER spectrum changes across the copper EPR spectrum as different combinations of orientations from $g_{x/y}$ and g_z are excited (see Fig. 6.8). With prior knowledge of the g-tensor and copper hyperfine coupling, it is possible to calculate which portions of the EPR spectrum will be excited by pulses applied at different frequencies (Fig. 6.8).

Due to the overlap of the nitroxide spectrum with the copper spectrum, it would be impossible to apply a pump pulse or combination of pump pulses to excite the entirety of the copper EPR spectrum uniformly. Using two pump frequencies, it is possible to excite both x/y and z components simultaneously. However, due to the large anisotropy of the copper EPR spectrum, and the fact that the copper hyperfine coupling along g_z is much larger than that in the $g_{x/y}$ direction, applying a pulse of a given length in the predominantly g_z region of the spectrum will excite far less of the z-component, compared to the portion of the x/y-component excited by a pulse of the same length applied to a region of the spectrum rich in components from x/y.

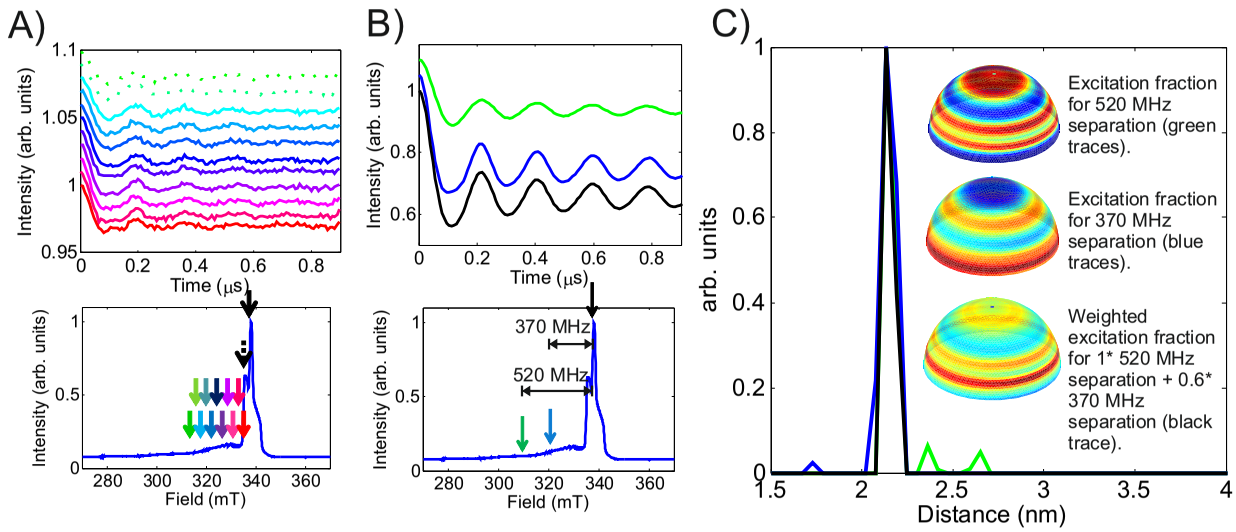


Figure 6.8: **A)** *Upper plot:* Background corrected experimental DEER traces measured on the copper-nitroxide model system with the detection pulses applied to the centre of the nitroxide spectrum (solid lines) and on the $m_I = +1$ peak (dotted lines) for different separations of pump and detection frequencies. *Lower plot:* The pulse positions represented by coloured arrows are shown with respect to the CW EPR spectrum of the copper-nitroxide system . Moving the pump pulse across the copper EPR spectrum samples the orientational selectivity. **B)** Simulated orientationally selective DEER traces using isotropic excitation of the nitroxide centre, with a single orientation of the nitroxide, placed at a distance of 2.05 nm from the copper centre along the x-axis. *Upper plot:* Plots of simulated orientationally dependent time-domain traces for two different pump pulse separations, 520 MHz (green) and 370 MHz (blue).[5] The black trace is the weighted sum of these two traces; 1×520 MHz(green) + 0.6×370 MHz (blue). The weighting factors (1 and 0.6) are defined by finding the combination of the two pump pulses that gives the most isotropic excitation in all orientations. This is found by combining the excitation fractions in different ratios and taking the combination with the lowest standard deviation of these orientationally dependent excitation fractions. No background correction or modulation depth correction has been applied to these traces. *Lower plot:* The position of the detection pulses (black arrow) and the two pump positions on relative to the EPR spectrum of the copper-nitroxide system (blue and green arrows).**C)** Distance distributions extracted from the simulated traces using DeerAnalysis (the colours correspond to those in the upper plot of B)). The inset coloured half spheres show the excitation fractions for different orientations of the magnetic field with respect to the copper centre, which is oriented with the porphyrin ring in the x-y plane. In these plots, red corresponds to an area of high excitation and blue to an area of low excitation, non-resonant spins. It can be seen that for the combined excitation fraction the excitation over the whole half sphere is more uniform than those for either of the individual traces.

Interestingly, when orientations of each paramagnetic centre excited can be predicted by simulations, it is possible to reduce the orientational effects observed in the form factor by using the weighted sum of two independently collected DEER traces. The weighting factors can be found by examining the orientational form of the portion of the spectrum excited by each pulse (see Fig. 6.8) and trailing combinations of the excitations in different ratios, until the standard deviation of the excitation fractions across the all orientations is minimized. Using simulated data for one orientation of the copper with respect to the nitroxide and assuming uniform excitation of the nitroxide, this method is seen to reduce the orientational effects observed the spectra. The data sets were combined using the relation:

$$F_{CD}(t) = \left[\sum_{i=1}^{n} K^i.F_D(t)\right] - \left[\left(\sum_{i=1}^{n} K^i\right) - 1\right] \tag{6.3}$$

where K^i is the constant weighting factor found for each trace, determined by the combination of the excitation fractions giving the most uniform excitation in all orientations.

6.4.1 Conclusions on the applicability of REINDEER to reduce orientational selection

The orientational simulations in Section 3.6 of Chapter 3, highlighted the importance of using the correct model in orientationally dependent simulations and also showed that for the Cu−NO$^\bullet$ 3-phenyl rod-like system used here, in order to correctly reproduce the orientational effects in the DEER spectra a large distribution of the two centres with respect to one another was required (see Fig. ref-fig:CuModelSystemReltaivePositions). The orientational simulations detailed in Fig. 6.8 used only one orientation of the nitroxide centre with respect to the copper centre, therefore this is a poor model of the real experimental system. Furthermore, the excitation of the nitroxide centre is also likely to be non-uniform, due to the presence of the 'sinc-wing' features in the frequency profile of the pulse that will excite portions of the $m_I = +1$ and/or $m_I = -1$ which may cause orientational selection for the nitroxide centre in addition to that observed for the electron associated with the copper centre. Both of these experimental factors would make determination of the weighting factors required to combine

experimentally recorded DEER spectra, such that orientational selectivity for the Cu−$NO^{\bullet}$ system is minimized, very difficult.

For this reason, the primary benefit of using REINDEER on such metal systems is not to remove or reduce orientational selectivity, but rather the value of the experiment lies in the excitation of a greater proportion of the spectrum, leading to a greater modulation depth. Since the signal-to-noise ratio for DEER is often measured with respect to the modulation depth for a normalized DEER trace, a larger modulation depth allows the collection of a DEER trace with a suitable signal-to-noise ratio within a shorter time period. The increase in modulation depth for the data collected on this system is shown in Fig. 6.9

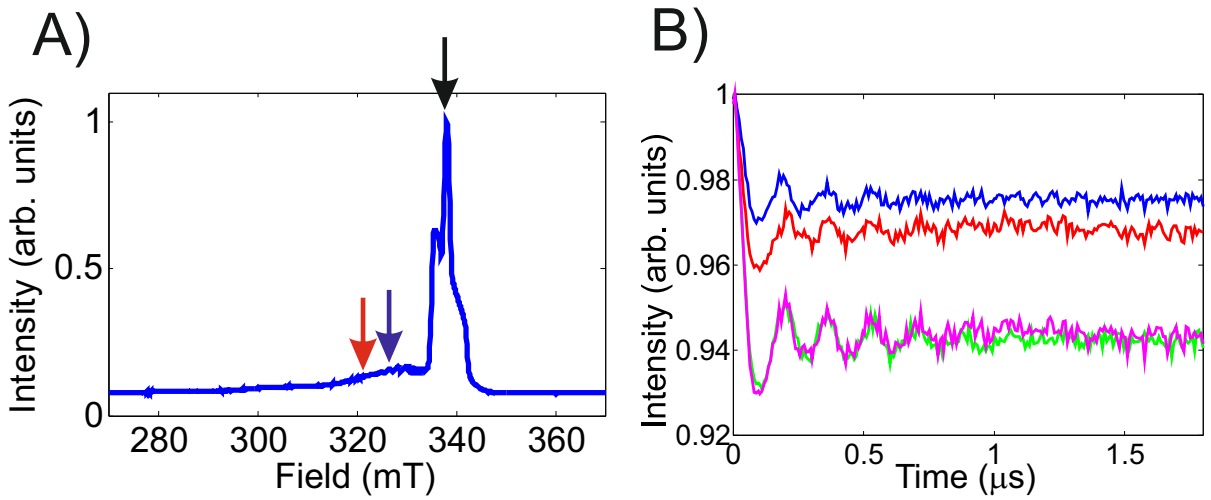


Figure 6.9: **(A)** CW spectrum for the copper-nitroxide model system showing the detection (black arrow) and probe positions (red and blue arrows) used in DEER and REINDEER. **(B)** DEER (red and blue traces with the single pump frequencies), combined DEER (magenta trace) and REINDEER (green trace using both pump frequencies). All of these experimental traces have been background corrected.

It is possible that REINDEER could have a greater impact for removal of orientational selectivity in the measurement of geometrically constrained nitroxide-nitroxide systems at X-band. Here, application of three pulses covers almost all of the spectrum and thus will have a good probability of significantly exciting all orientations.

Chapter 7

Dead-time free three-pulse DEER

7.1 Introduction to dead-time free DEER

Pulsed ELectron DOuble Resonance (PELDOR) was initially developed by Salikhov and co-workers in the early 1980s as a three-pulse technique that uses a simple Hahn echo-detection sequence at one frequency (ν_{DET}) and a pump pulse at a second frequency (ν_{PUMP}), which is moved within the precession delay of the Hahn echo.[44] The three-pulse technique does, however, suffer from the problem of a dead-time at the start of the trace. The dead-time is defined as the distorted part of the data occurring around the zero-time. This arises from the crossing of the pump and detection pulses.

The distortion of the data points detected when the pulses are overlapping in time is caused by two distinct effects. Firstly, the TWT used in these experiments has an upper limit on its power output, such that when two hard pulses act simultaneously this limit is surpassed, with the result that the pulses in the crossover region each have a lower power compared to the application of the two pulses independently. When pulses cross causing very high input power, such that the output power is lower than that expected from the sum of the pulses acting independently, the TWT is said to be operating in its non-linear regime. Secondly, the broad frequency profile of the pulses used and the finite separation of the pulse carrier frequencies mean that the detection pulse can cause excitations at the frequency of the pump spins and the pump pulse can cause excitations at the frequency of the detection spins. The additional excitation of the detection spins causes a Bloch-Siegert phase shift,[a 211] also referred to

[a] A traditional definition of the Bloch-Siergert shift considers the effect of the counter-rotating off-resonance component

as a dynamic phase shift.[212]

The dead-time causes data analysis problems, see Section 7.3.4. It was these issues that drove the development of the four-pulse technique by Jeschke, Spiess and co-workers in 2000.[60,61] The four-pulse Double Electron-Electron Resonance (DEER) sequence contains an additional π refocusing pulse in the detection sequence, allowing the zero-time (t_0) of the sequence to occur at a point when detection and pump pulses do not overlap (see Fig. 7.1).

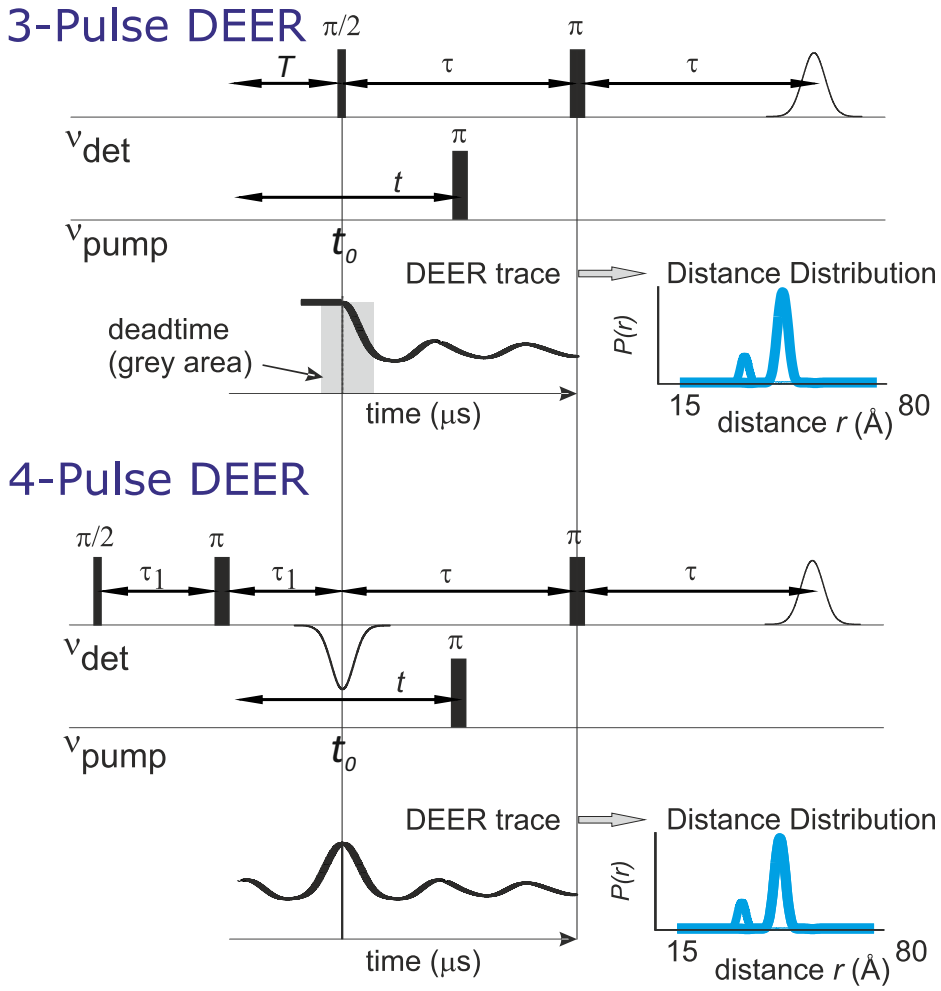


Figure 7.1: Schematic diagrams of the three- and four-pulse DEER sequences.

of a linearly polarized field when it is implemented in the rotating frame such that, of the two counter rotating components forming the linearly polarized field, one is on-resonance with the rotating frame and the other is off-resonance. The Bloch-Siergert shift as defined in this chapter considers the effect of the B_1 field of the off-resonance pump pulse on the detection spins.

This chapter investigates the factors that cause the dead-time in three-pulse DEER and examines possible methods to remove their effects in the three-pulse technique, either during the experimental acquisition, where possible, or by post-processing of the experimental data. The TWT non-linearity is addressed in Sections 7.2.2 and 7.2.3, and can be removed by careful tuning of the experiment, in conjunction with the use of a resonator with a high power to B_1 conversion factor. The dynamic phase shift is also examined; both experimentally (Section 7.2.4) and theoretically (Section 7.5.1). To allow for accurate analysis of the data, the zero-time, t_0, must be determined. This was achieved using both experimental comparisons between three- and four-pulse data and theoretical simulations (see Sections 7.5.2 and 7.3.3 respectively).

7.1.1 The advantages of three-pulse DEER

In spite of the dead-time, three-pulse DEER has one significant advantage over the four-pulse technique, namely the lower number of pulses in the pulse sequence. This leads to a significantly increased echo intensity for a three-pulse experiment compared to a four-pulse DEER sequence of the same overall length. As the types of systems being studied by DEER has expanded from measurements on $NO^{\bullet}-NO^{\bullet}$ model systems,[51] nitroxide labelled soluble proteins, polypeptides,[213] and DNA,[79] to nitroxide labelled membrane proteins,[214] systems containing metal centres,[70] and other prosthetic groups,[65] problems with the experimental signal-to-noise ratio have become more critical.

Membrane proteins are often prepared in detergent or other dense media, this replaces the phospholipid bilayer in which the protein is naturally present.[215] Stabilizing membrane proteins in this way brings the proteins into closer contact with one another as compared to proteins prepared in a glycerol/water frozen-glass. This results in an increase in the local spin concentration in the region of the detergent or bilayer and a reduced average intermolecular radical-radical separation, causing the spin relaxation times to be much shorter and thus limiting the overall length of the pulse sequences that can be used to study these samples. Metal paramagnetic centres on average also have T_m relaxation times that are much shorter than those for nitroxides in solutions of similar concentration.

In such cases, the use of a three-pulse DEER sequence is advantageous since the echo intensity for

a four-pulse sequence with τ_2 equal to the τ values of a three-pulse sequence will be smaller due to the longer overall length of the four-pulse DEER sequence and the inclusion of an additional π refocusing pulse.[106] The greater echo intensity observed in the three-pulse experiment allows longer τ times to be used in the experiment, while still detecting an acceptable signal. In turn, these longer evolution times in which the π pump pulse can be applied allow longer distances to be measured using the three-pulse technique.

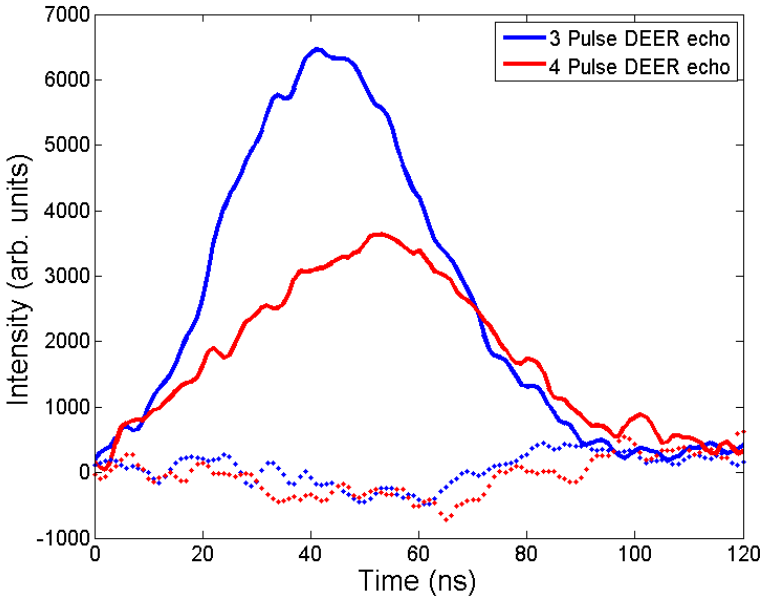


Figure 7.2: Plot showing the difference in the echo intensity detected for a three-pulse and a four-pulse DEER detection sequence (i.e., with no π pump pulse), where both pulse sequences have the same overall length. The real part of the echo is shown with a solid line and the imaginary part with a dotted line. The echos were measured using the 2.1 nm $NO^{\bullet}-NO^{\bullet}$ model system (see Fig. 6.2).

7.1.2 Why do we need dead-time free DEER?

At present the most common method of analysis for three-pulse DEER is simply to remove the distorted data points at the beginning of the trace. This can provide satisfactory results when certain conditions are met:

1. The pulses used are short, so that the time period of the distortion is minimal (only a few data points need to be discarded).

2. The distance being measured is sufficiently long, so that removal of these points does not truncate the first oscillation too severely.

3. The oscillations are not dampened too quickly, so that strong second, third or latter oscillations are observed; i.e., there is a narrow distance distribution and the signal is not affected too severely by relaxation.

When the above conditions are not met, deletion of the distorted data causes the detection of spurious shorter distances in a fitted distance distribution or broadening of the detected distance distribution.

In addition to affecting the distances extracted from the spectrum, truncation of the first oscillation of the DEER trace removes any information contained in the modulation depth. Although this information is not required to extract the distance distribution for centres that are isotropically excited, the modulation depth contains important information on the number of coupled spins in the system. Accurate measurement of the modulation depth allows the labelling efficiency to be calculated by comparison to a calibration.[101] Furthermore, for systems where orientation dependence plays a role, such as those presented in previous chapters, modulation depth is an important parameter in determining orientational information from the experimental data.[4 5]

7.1.3 Other dead-time free EPR techniques

Double quantum coherence (DQC) experiments can also generate dead-time free dipolar oscillations.[216] The application of DQC, however, requires the use of very short pulses of high-power, which are not

achievable on most commercially available spectrometers. In addition, there is an uncertainty in the form of the background correction that should be applied to DQC data, as it is highly dependent on the form of the excitation profile of the pulses and on the EPR line shape. This complicates the extraction of a reliable form factor and thus of the width and shape of the distance distributions.[57]

7.2 Initial experimental investigations

Initial studies into the sources of the zero-time distortion of three-pulse DEER, the TWT non-linearity and dynamic phase shift, were designed and conducted as follows. Further detail on the dynamic phase shift is given in Section 7.4.

7.2.1 Experimental conditions

The experimental data presented in this chapter were recorded using a Bruker ELEXSYS 680 spectrometer with a 1 kW TWT. A 2 mm split-ring resonator (MS2) with a conversion factor of 2.5 G / $\sqrt{W}$ at $Q_L = 30$ was used. (Some experiments were also repeated using a 3 mm split-ring resonator (MS3) with a conversion factor of 2 G / $\sqrt{W}$ at $Q_L = 150$ for comparison.) The two resonators therefore have different power requirements for a 16 ns $\frac{\pi}{2}$ pulse at room temperature with $Q \approx 200$,[b] the MS2 uses an attenuation of 22 dB and the MS3 requires a lower attenuation of 18 dB. Use of the 2 mm resonator allows the application of lower-powered pulses. Therefore, in order to reduce the power of the pulses, additional attenuation was added into the detection channels in the bridge before amplification by the TWT. 6 dB attenuation was added to the $<y>$ channel, through which ran the 32 ns π detection pulse, and 12 dB attenuation was added to the $<x>$ channel, through which ran the 32 ns $\frac{\pi}{2}$ detection pulse.

Although the 2 mm resonator has advantages in terms of power requirements, it should be noted that the lower sample volume may make this resonator unsuitable for measuring systems where only low concentration samples can be produced.

[b] The Q factor is defined as the ratio of energy stored/energy lost.

7.2.2 TWT non-linearity

TWT amplifiers display deviations from a linear gain at high input powers; a plot showing the extent of the linear and non-linear behaviour of the TWT amplifier used for the experiments is shown in Fig. 7.3. For the 3 mm split ring resonator in an over-coupled configuration such as that used for DEER experiments, the amount of power required to cause a 16 ns π pump pulse is frequently towards the upper limit of the linear regime (c. 70% +<x> power). It is therefore not unexpected that for this resonator, although the single pulses fall into the linear regime of the amplifier, the combination of a 20 ns π pump pulse and a 32 ns $\frac{\pi}{2}$ pulse pushes the TWT into a non-linear regime. Thus the effective excitation power (B_1 field in resonator) of both pulses is reduced during the crossover period.

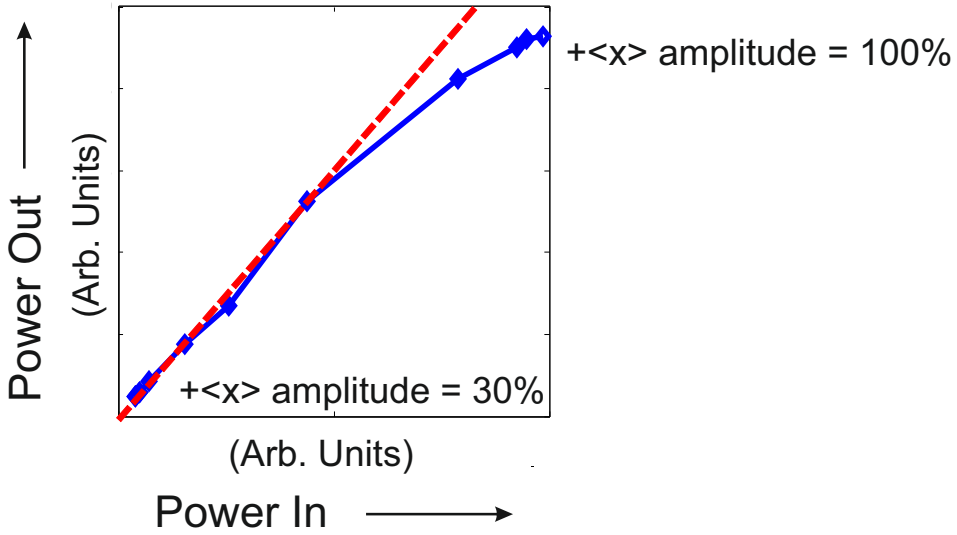


Figure 7.3: A plot of output against input power for a 1 kW TWT, experimentally measured data is shown in blue and the linear line of best fit at low values of input power is shown in red (the linear regime). The experimental data was measured using the height of the pulse observed in transmission mode (power input) and receiver mode (power output) using different amplitudes of the MPFU +<x> channel from 30% to 100% with measurments taken at approximately equal increments, the graph therfore also demonstates the nonlinerarity of the MPFU atenuator.[c] Measurements were made with a transmitter level of 72% and a high power attenuation of 0 dB.

It is therefore possible to remove the distortion of data points due to the TWT non-linearity by reducing the input power of the pulses and thus working within the linear regime. This can be achieved

[c]It should be noted that the attenuation and phase on the MPFU channels are co-dependent and this can affect the amount of power in the pulses, which may cause an increased uncertainty in this plot.

either by increasing the length of the pulses or by using a resonator with a high power conversion factor, such as the 2 mm split-ring resonator used in this work. Increasing the length of the pulses significantly is not a viable method of decreasing the pulse power since it leads to a broader echo. In these cases, the zero-time is more ambiguous. Longer pulses also have narrower frequency profiles. This may lead to additional orientational selection and for sufficiently long pulses the frequency profile of the pulse becomes narrower than the dipolar splitting for the very shortest distances prohibiting the measurement of these smaller distances.

Another alternative would be to use two TWT amplifiers, one for each frequency applied and to combine the pulses once they had been amplified to high power. In addition to requiring two TWT amplifiers, a waveguide capable of combining two high powered signals and strong isolators are also needed to prevent the signals feeding back from one TWT to the other and causing instrumental damage. The expense of acquiring a second TWT amplifier prevented this mode of experiment being utilized in this study.

7.2.3 The linear regime of the TWT

In order to measure the extent of the linear regime of the TWT for pulse crossings, a Hahn echo-detection sequence was set up with an initial delay time, T, (T - $\frac{\pi}{2}$ - τ - π - τ - *echo*). The experiment used a τ value of 200 ns and a pump pulse with an offset of 65 MHz from the Hahn echo pulses. The position of the pump pulse was initially placed 200 ns prior to the first $\frac{\pi}{2}$ detection pulse ($T = 200$ ns). The length of the pulse sequence was kept constant and the pump pulse was moved in time steps of 8 ns through the $\frac{\pi}{2}$ detection pulse to the start of the π detection pulse (see Fig. 7.4 A). The detection pulses used were both 32 ns in length and the π pump pulse was 20 ns long.

The field of the experiment was selected so that the detection pulses excited the $m_I = -1$ portion of the nitroxide spectrum and the pump pulse was off-resonance. In this way, the DEER effect was removed from the data, as the pump pulse does not excite any spins, and all effects seen in the measured trace were either due to TWT saturation or a result of the pump pulse causing a small rotation of spins at the detection frequency, the dynamic phase shift.

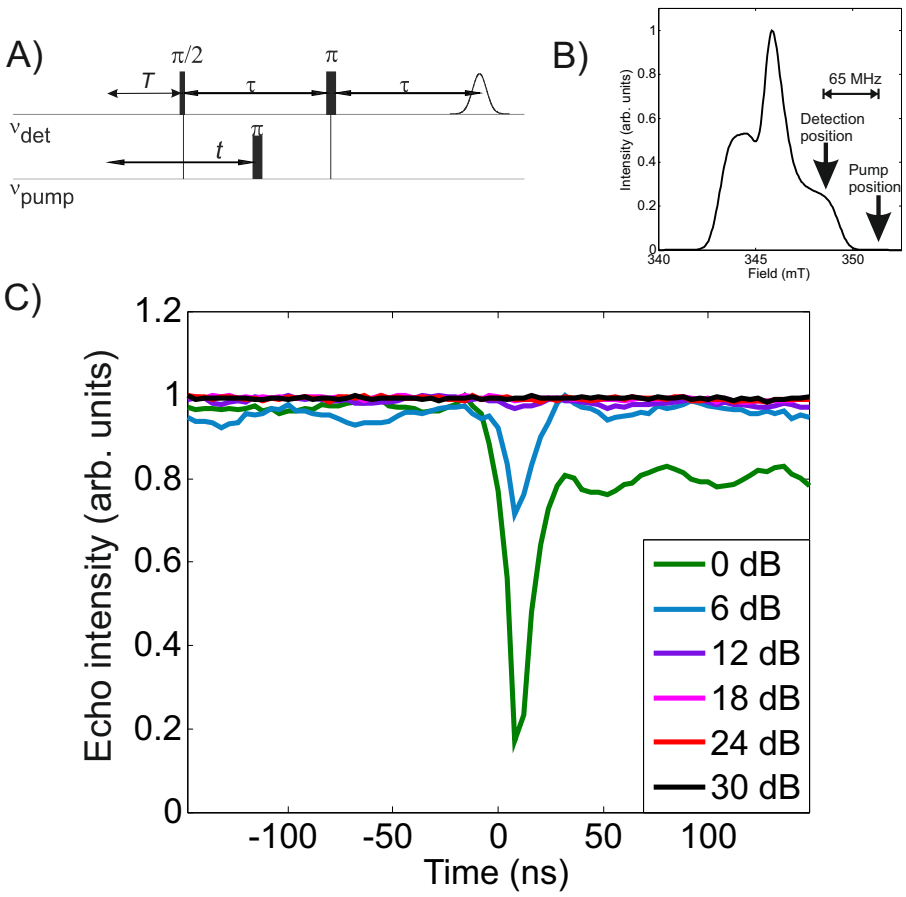


Figure 7.4: **(A)** Pulse sequence used for three-pulse DEER and for determining a linear operational region of the TWT when pulses cross. **(B)** EPR spectrum showing the pump and detection positions used for determining the linear operational region or linear regime of the TWT with a nitroxide sample. **(C)** Data traces gained for different values of input power for the pump pulse set with the ELDOR attenuator. The τ value used is 200 ns and the detection pulses were all 32 ns in length with a 20 ns pump pulse. The signal shown is the absolute of the quadrature detection used.

The echo intensity was recorded at each point in quadrature detection (see Fig. 7.4). The absolute of the signal is plotted to remove any phase shift in the x-y plane. Any remaining offset between the signal level before and after the $\frac{\pi}{2}$ detection pulse at 0 ns must be due to the rotation of the magnetization out of the z-direction (see Section 7.2.4). The reduction in signal intensity at the pulse-crossing (0 ns) at high pump pulse power is due to the TWT non-linearity; it is apparent that for the experimental setup described with the 2 mm resonator, the pulse crossing enters the linear regime of

the TWT when the attenuation of the ELDOR channel is 12 dB or greater.

It was found that under these conditions, a pump pulse of 20 ns achieved a turning angle of π with an attenuation of 13 dB, which is within the linear regime. It can also be seen that for an attenuation of 6 dB or more, there is no significant rotation of the magnetization away from the z-direction by the pump pulse applied before the Hahn echo sequence, which would lead to a loss of magnetization in the x-y plane during detection. Therefore by taking the absolute value of the quadrature signal, an essentially undistorted DEER trace can be detected.

7.2.4 The dynamic phase shift

Unlike the discontinuity from the TWT, the dynamic phase shift results directly from excitation of the detection spins by the pump pulse (see Section 7.4 for more details). The first experimental report of such a phase shift in EPR was made by Nechtschein and Hyde for pulsed ELDOR on a $^{\bullet}CH(CO_2H)_2$ radical ($S = \frac{1}{2}, I = \frac{1}{2}$)).[217] Similar phase shifts have also been reported experimentally for NMR.[218]

Studying a Hahn echo at ν_{DET}, the phase shift occurring between the signals detected when an off-resonance pump pulse at ν_{PUMP} is placed both before and after the initial $\frac{\pi}{2}$ detection pulse is clearly demonstrated in Fig. 7.5. The pump pulse is applied off-resonance so that the intensity of the echo is not distorted by a DEER effect.[d]

Studying the real and imaginary parts of the Hahn echoes, formed with the pump pulses before and after the initial $\frac{\pi}{2}$ pulse in the Hahn echo-detection sequence, it becomes apparent that there is a large phase shift. In some cases the absolute intensity, $\left(\sqrt{Re^2 + Im^2}\right)$, of the echo also changes. This is due to a rotation of the magnetization induced by the B_1 field of the off-resonance pump pulse. This effect results from excitations of the spin system and is dynamic with respect to the pulses applied; hence, it is difficult to remove experimentally. Some suggestions of experimental methods to remove, reduce or correct the shift are provided later in this section and a theoretical method for removal of the dynamic phase-shift is given in Section 7.5.5.

[d]For a similar experiment using fixed pump pulses before and after the zero-time in a four-pulse sequence, a small change in amplitude in the echoes might be seen, resulting from relaxation of the system; however, a change in phase would not be expected.

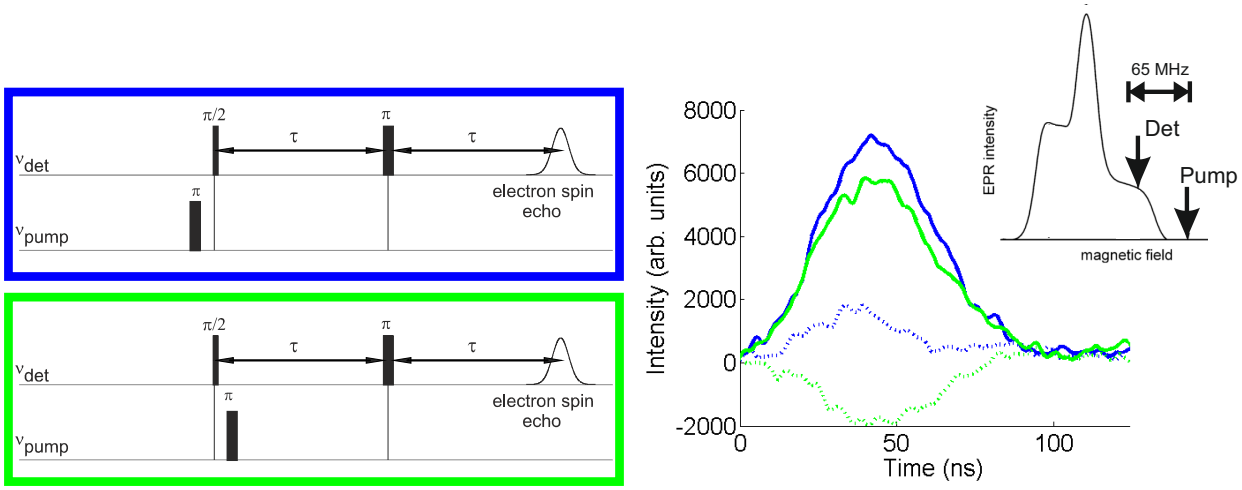


Figure 7.5: If two pulse sequences with two fixed pump pulse positions equally spaced before (blue) and after (green) the zero-time at the initial $\frac{\pi}{2}$ detection pulse is investigates, a dramatic change in the phase of the echoes is observed. Under certain experimental conditions there is also a change in the magnitude of the echo. The pump pulse is applied off-resonance, so the amplitude of the echo is not affected by DEER modulations.

For now it is useful to construct a reliable method to correct the data once it is recorded. Milov, Tsvetkov and co-workers have studied the effect of pulse duration in four-pulse DEER.[16] As part of their study, they examined the distortion when two pulses cross during a four-pulse trace by recording two traces, one with both the pump and detection pulses on-resonance with the spin system (although exciting different hyperfine components) and a second trace with the same separation between the pump and detection pulses but at a shifted magnetic field position, so that only the detection pulses are resonant with the spin system. Dividing the first trace by the second can remove the effects caused solely by the pulses overlapping. A third trace with both pulses off-resonance was recorded as an experimental background. This is not required if phase cycling of the first detection $\frac{\pi}{2}$ pulse is used. The traces were combined using the following relation:

$$V(t) = \frac{(trace1 - trace3)}{(trace2 - trace3)} \tag{7.1}$$

This technique has several drawbacks: it can only be used for EPR spectra with a sharp edge that is narrower than the separation between the pulses, the time taken to record the spectra will

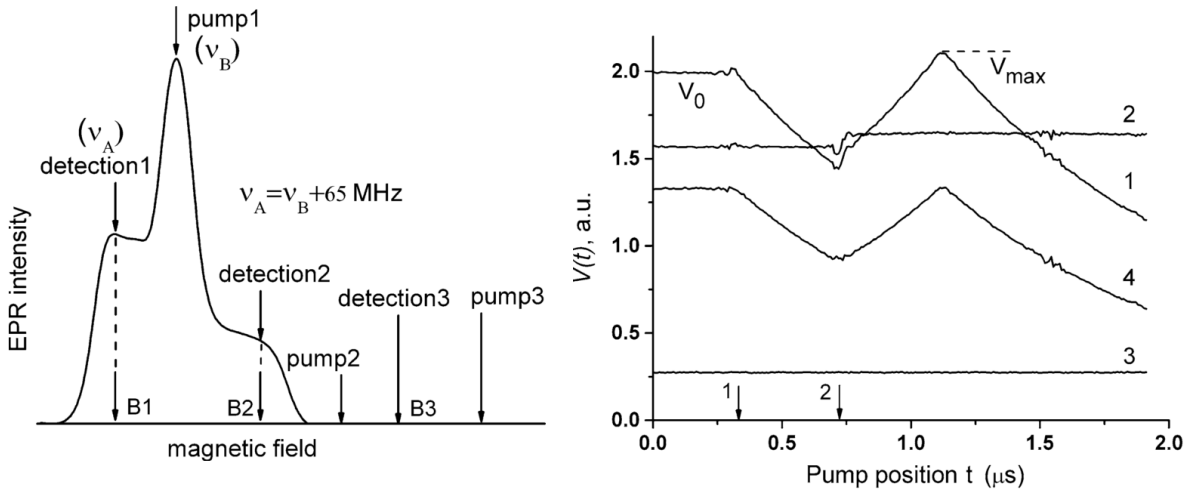


Figure 7.6: The relative pump and probe positions used by Milov to collect three traces, which were combined by Equation 7.1 in order to correct the pulse crossing discontinuities for an expanded four-pulse DEER trace, where the pump pulse starts before the detection sequence and passed through both the first two detection pulses. Traces 1–3 correspond to the DEER data collected at the three sets of pump and detection pulse positions specified, trace 4 is the combination of traces 1–3 using Equation 7.1. This figure is adapted and reproduced from Springer, *Applied Magnetic Resonance*, **41(4)**, 2011, 59–67, Effect of Pumping Pulse Duration on Echo Signal Amplitude in Four-Pulse PELDOR, A. D. Milov, Y. A. Grishin, S. A. Dzuba, and Y. D. Tsvetkov, Figure 5 and Figure 6. Copyright © Springer-Verlag 2011; with kind permission from Springer Science and Business Media.[16]

be doubled (or tripled) as two (or three) spectra of equivalent signal-to-noise ratio are required, and finally dividing one EPR trace by another leads to increased noise on the calculated signal. Using a correction technique that requires the measurement of multiple time traces is not ideal since it requires longer acquisition times. In a limited acquisition time, this may negate any increase in signal-to-noise ratio that could be afforded by using a three-pulse DEER experiment over a four-pulse experiment, where such multiple measurements are not required.

Ideally, any solution to the 'dynamic phase shift' problem should not require the measurement of multiple complete DEER traces. Taking the absolute value of the quadrature signal (M, see Equation 7.2) gives the magnitude of the magnetization in the x-y plane and thus removes the dynamic

phase shift in this plane. Taking the absolute of the signal does not, however, make any correction for rotation of the magnetization out of this plane towards the z-axis.

$$M = \sqrt{M_x^2 + M_y^2} \tag{7.2}$$

Examination of the data presented in Fig. 7.7 B (which is a repeat of that presented in Fig. 7.4 C) shows that for ELDOR attenuations of c. 6 dB or greater the loss of signal due to rotation of the detected magnetization out of the x-y plane is small. The phase shift in the z-direction becomes larger, resulting in a smaller absolute value of the magnetization in the x-y plane, as the power in the ELDOR channel is increased (attenuation is decreased). Increasing the power of the fixed length (20 ns) pump pulse increases the B_1 field of the pulse and thus it will have a greater turning angle. Fig. 7.7 A shows both the raw data from the same data set for comparison of the relative sizes of the two effects. A phase shift is observed in all the raw data recorded with attenuation of 18 dB or less. As the phase shifts for the data sets recorded with attenuation 6-18 dB are absent in the absolute of the signals, it can be considered that the phase shifts for these data sets are limited to occurring primarily within the x-y plane rather than out of it.

The small oscillations seen in the time traces in both Fig. 7.4 and Fig. 7.7 for the pulse crossing experiments, particularly at high pump power, are attributed to Electron Spin Echo Envelope Modulations (ESEEM). The pump pulse will excite forbidden transitions in the detection spins leading to the observation of the ESEEM.

Given that under the conditions of this experiment, a 20 ns pump pulse in the ELDOR was found to require 13 dB attenuation in order to cause a turning angle of π at the frequency of the pulse, the rotation of the detected magnetization out of the x-y plane for this attenuation is negligible (see Fig. 7.7 B). These conditions also fall within the linear regime of the TWT, thus it is possible to record a three-pulse DEER trace in which the distortions seen around t_0 can be removed by taking the absolute of the signal. This provides an undistorted (dead-time free) three-pulse DEER trace.

The experiments to test the linear regime and the extent of the phase shift in the z-direction are very quick to tune and run. They are far less time-consuming than acquisition of a complete three-

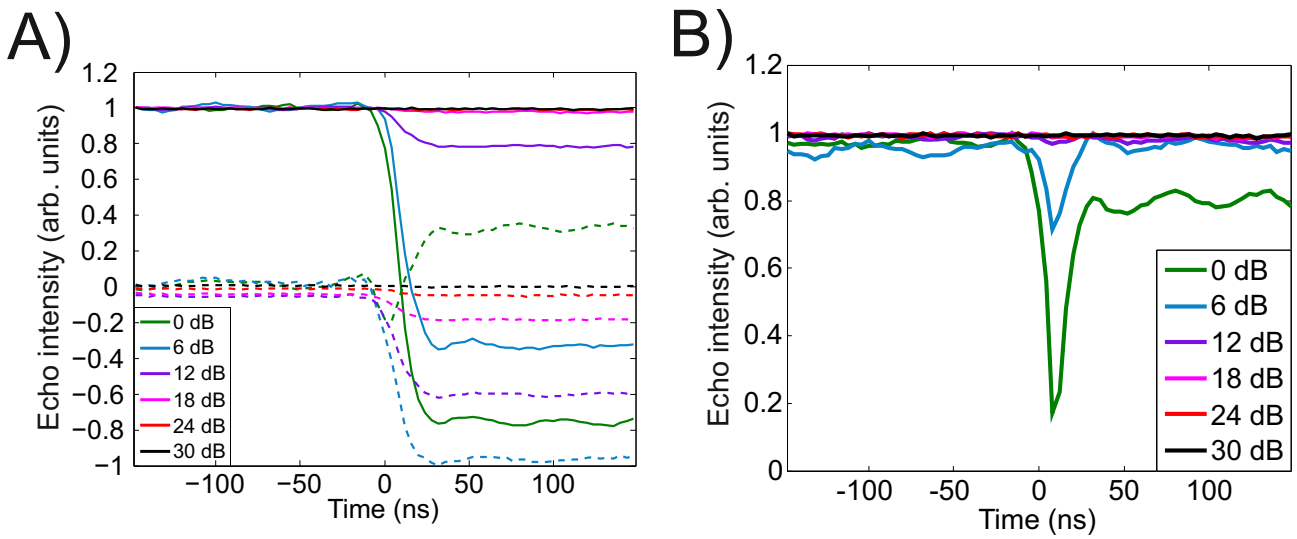


Figure 7.7: **A)** Normalized data from the pulse crossing experiments described in Fig. 7.4. Solid lines show the real portion of the data and dashed lines show the imaginary part. **B)** The normalized absolute value of the data shown in A). For both plots, the values in the key correspond to the attenuation used in the ELDOR channel. In order to clearly see the discontinuity in the signal due to the TWT non-linearity, it is necessary to view the absolute of the signal.

pulse DEER trace at a second field position. Therefore, tuning the three-pulse DEER experiment, such that the pulse crossing lies within the linear regime of the TWT and the rotation of the detected magnetization out of the x-y plane is negligible, is an attractive option. The remaining dynamic phase shift is satisfactorily confined to the x-y plane and corrected simply by taking the absolute value of the experimental trace recorded in quadrature.

In order to fully remove the dynamic phase shift experimentally, it would be necessary to eliminate the spectral overlap between the pulses completely. The pulses produced by the ELEXSYS 680 spectrometer have an approximate truncated sinc form in the frequency domain with 'wings' that can extend several hundred MHz on both sides of the carrier frequency of the pulse (see Fig. 7.13).[e] The pulse overlap could be removed by placing the pulses far enough apart, so that no overlap between the wings occurs. Experimentally this would not be possible for most systems, since the separation of the two pulses for a DEER experiment is limited by the width of the EPR spectrum and also by the resonator bandwidth. Furthermore, increasing the frequency separation between the two pulses

[e] A sinc function has the form: $\mathrm{sinc}(x) = \frac{\sin(x)}{x}$.

necessarily increases the power required for each pulse, due to the shape of the resonator bandwidth. This is likely to push the pulses into the non-linear regime of the TWT, causing a discontinuity around the zero-time from this source.

An alternative would be to use shaped pulses.[207,219] For example, a Gaussian pulse in the time domain possesses a Gaussian frequency profile and hence the 'sinc-wings' are absent. This technique is widely used in NMR. However, at present most commercial EPR spectrometers do not have the ability to produce shaped pulses. Shaped pulses can be achieved using external pulse generators, such as that used for the external frequency source in the REINDEER work (see Chapter 6).

7.3 Experimental dead-time free three-pulse DEER

7.3.1 Experimental conditions for dead-time free three-pulse DEER

The conditions used for recording dead-time free three-pulse DEER experimentally were very similar to those used for the initial investigations, described in Section 7.2.1. The pump frequency was chosen to be at the centre of the resonance dip and the 16 ns π pump pulse attenuation was selected to give the largest inversion in the echo using the following sequence with all pulses at the pump frequency (π_{ELDOR} - t - $\frac{\pi}{2}$ - τ - π - τ - *echo*).

The detection frequency was set to be +65 MHz and the field of the experiment chosen so that the pump pulse is applied to the centre of the $m_I = 0$ maximum of the nitroxide spectrum and the detection pulses fall on the $m_I = +1$ portion. The experiment was run using a two-step phase cycle on the initial $\frac{\pi}{2}$ detection pulse to remove the need for a baseline correction. The presence of ESEEM modulations in the DEER trace was reduced by averaging over different τ times. In four-pulse DEER, ESEEM averaging to remove proton modulations is achieved by changing the length of τ_1 in 8 steps of 8 ns from c. 160 ns. Three-pulse DEER only has one τ time. Therefore ESEEM averaging is carried out by stepping over eight different τ values each 8 ns apart.

For both three-pulse data sets, initial pulse crossing experiments were carried out to ensure that the overlapping pulses lay within the linear regime of the TWT and also that no significant dynamic

phase shift affecting the z-direction occurred. This is verified in the data sets given in Fig. 7.8, as there is no discontinuity around the zero-time and the modulation depths of the three- and four-pulse experiments are the same.

7.3.2 Dead-time free three-pulse DEER experimental results

Data was collected for the 2.1 nm model system and for the PuR protein system introduced in Chapter 6. The structures of the systems are given in Fig. 6.2 A and C. In each case, three- and four-pulse DEER traces were collected under the same experimental conditions. In the three-pulse experiment τ was set equal to τ_2 in the four-pulse experiment. The data recorded and pump and detection positions are shown in Fig. 7.8.

Plots on the left of Fig. 7.8 B and C show the normalized real and imaginary parts of the three-pulse DEER trace in relation to the absolute of the data. From inspection of the data for the 2.1 nm model system (Fig. 7.8 B), it is clear that there is an apparent change in modulation depth between the real and absolute traces. This is due to the signal phase used during the acquisition of the data; for the 2.1 nm model system, the acquisition signal phase was adjusted in an effort to minimize the imaginary component with the pump pulse acting *before* the detection sequence. Taking the absolute value of the quadrature signal when the phase shift is localized to the x-y plane corrects the modulation depth. This can be seen in the comparison of the three- and four-pulse DEER traces for this system. There are small ESEEM oscillations visible in the three-pulse DEER trace as a result of incomplete τ averaging.

In order to show that the phase change was independent of the signal phase used during the acquisition; for the experiments on the PuR acquisition system, the signal phase was set to minimize the imaginary contribution when a pump pulse was placed after the first $\frac{\pi}{2}$ detection pulse. In this case, the modulation depth of the absolute value of the quadrature detected signal appears to be the same as the real part, for $t > 0$. However, taking the absolute of the signal is necessary to correct the amplitude of the portion of the trace collected with the pump pulse before the detection sequence. As with the 2.1 nm sample, the absolute value of the three-pulse trace matches the four-pulse DEER trace collected under the same conditions.

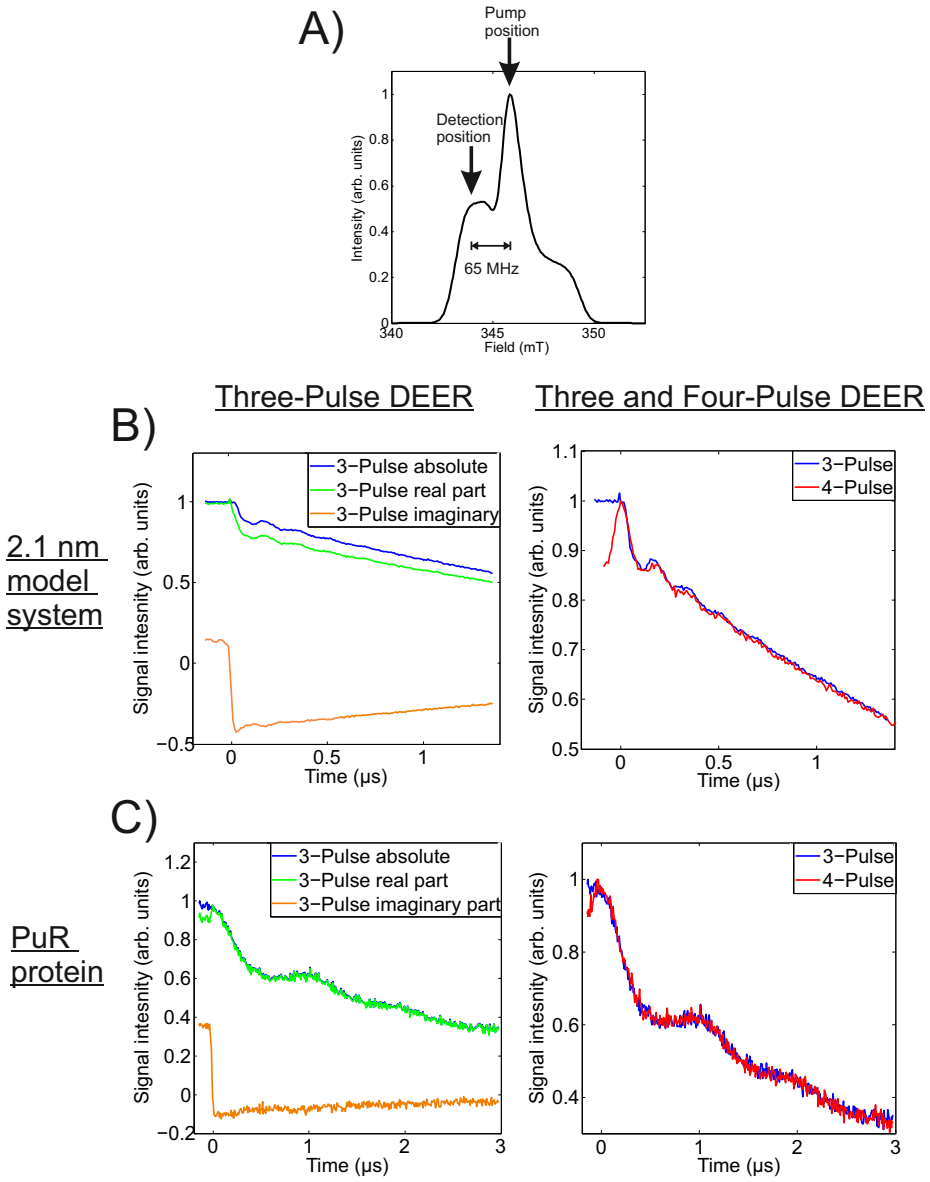


Figure 7.8: **A)** Idealized EPR spectrum of a nitroxide, showing the approximate pump and detection positions used in both three- and four-pulse DEER experiments for both systems described below. **B)** DEER results for the 2.1 nm model system. The plot on the left shows the normalized real (green) and imaginary (orange) parts of the three-pulse DEER trace. The absolute value is plotted in blue. The plot on the right shows the absolute value of the three-pulse DEER signal (five scans) overlaid with a four-pulse DEER trace (five scans) measured under the same conditions. **C)** DEER results for the PuR protein spin labelled at site 82 and 303 ($r_{mean} \approx 3.65$ nm): The plot on the left shows the normalized real (green) and imaginary (orange) parts of the three-pulse DEER trace. The absolute value is plotted in blue. The plot on the right shows the absolute value of the three-pulse DEER trace (nine scans) overlaid with a four-pulse DEER trace (twenty-eight scans), measured under the same conditions. The DEER traces plotted here do not include background corrections.

For both the 2.1 nm model system and the PuR system, a second set of four-pulse DEER data was acquired using a four-pulse DEER sequence in which the overall length of the time delays used was equal to those used in the three-pulse DEER sequence; i.e., $\tau_{(3-pulse)} = \tau_{1(4-Pulse)} + \tau_{2(4-Pulse)}$. In these cases, the four-pulse data also matched the absolute value of the three-pulse data sets. However, the signal-to-noise ratio on the four-pulse data was significantly worse than that for the corresponding three-pulse DEER (data sets not shown).

The three- and four-pulse experiments on the 2.1 nm model system (with $\tau_{(3-pulse)} = \tau_{2(4-Pulse)}$, shown in Fig. 7.8B) were both collected using five scans. Examination of the data reveals that the signal-to-noise ratio on the four-pulse data is worse than that for the three-pulse data by a factor of c. 2. For the results on the PuR system (with $\tau_{(3-pulse)} = \tau_{2(4-Pulse)}$, shown in Fig. 7.8 C), the three-pulse data was collected in nine scans and the four-pulse data in twenty-eight scans, and in these experiments the signal-to-noise levels of the spectra collected are comparable to one another.

7.3.3 Experimental determination of the zero-time for three-pulse DEER

In order to analyse three or four-pulse DEER data correctly, it is vital to locate the zero-time (t_0) accurately. For four-pulse DEER, t_0 is easy to find as the peak of the signal collected. This corresponds approximately to the point at which the centre of the pump pulse aligns with the centre of the primary echo.

From comparison of the experimental three- and four-pulse data collected on the same system with the same pulse lengths and $\tau_{(3-pulse)} = \tau_{2(4-Pulse)}$ it appears that the t_0 for the three-pulse data occurs when the centre of the pump pulse coincides with the centre of the first $\frac{\pi}{2}$ detection pulse.

This definition of the t_0 is at odds with the definition frequently used for three-pulse DEER, where t_0 corresponds to the point in the trace where the rising edge of the pump pulse and the falling edge of the first detection pulse are coincident.[220] Three-pulse DEER is often recorded without the pulse crossing region in order to avoid the dead-time problem. In these cases, the first pump pulse position occurs directly after the initial $\frac{\pi}{2}$ detection pulse (i.e., there is no overlap of the pulses) and the start of the trace is taken to be t_0.

It is well known that for four-pulse DEER experiments the exact position of t_0 seen in the time trace is dependent on the temporal resolution of the spectrometer, c. 4 ns, which is dependent on delays within the spectrometer and resonator. The most accurate method of finding t_0 is to measure four-pulse DEER on a strong sample to produce a spectrum with agood signal-to-noise ratio and determine t_0 for this spectrum from the signal maximum. This t_0 will be applicable for any other samples measured on the same spectrometer with the same experimental setup.[101] Likewise, the position of t_0 in three-pulse DEER will also vary slightly within the temporal resolution of the spectrometer. It is therefore also necessary to find the t_0 time for three-pulse DEER traces experimentally by measuring three-pulse DEER on a model system with a strong signal, then comparing the three-pulse data to four-pulse data measured under the same conditions and aligning background corrected time traces. Comparison of the experimental three- and four-pulse data measured on the 2.1 nm model system showed that the difference in t_0 for the two traces lay within the 4 ns temporal resolution of the spectrometer.

7.3.4 Effects of the dynamic phase-shift when processing data

Many in the EPR community, including our group at Oxford University, now routinely use DeerAnalysis to process DEER data and to extract distance distributions.[45,101] As described in Chapter 2, this program uses a Tikhonov regularization to fit the experimental time trace and determine the distance distribution. DeerAnalysis is designed specifically to analyse data from the four-pulse technique, which has a consistent phase and is also symmetric about t_0. However, it is also desirable to use DeerAnalysis to process three-pulse data, which is not symmetric about t_0 and has raw data that has two distinct phases. This can pose problems for analysing the data using DeerAnalysis, some of which are described in the following section.

Figure 7.9: Analysis of DEER spectra for the 2.1 nm model bisnitroxide system using DeerAnalysis. [45] **Column 1:** Four-pulse DEER. **Column 2:** Absolute value of quadrature detected three-pulse DEER, where the dynamic phase shift is limited to the x-y plane, t_0 is selected to be the point at which the centres of the pump pulse and the first $\frac{\pi}{2}$ detection pulse coincide. **Column 3:** Three-pulse DEER data with the real and imaginary parts analysed independently, the phase of the imaginary part during the main part of data acquisition is set to zero. t_0 is chosen to be at the signal maximum. **Column 4:** Three-pulse DEER data where the phase for the imaginary signal before t_0 is selected to be zero. t_0 is chosen to be the point at which the centres of the pump pulse and the first $\frac{\pi}{2}$ detection pulse coincide. **Column 5:** Three-pulse DEER data, where the phase for the imaginary signal after t_0 is selected to be zero. t_0 is selected to be the point at which the centres of the pump pulse and the first $\frac{\pi}{2}$ detection pulse coincide. In the first row, the green line represents the chosen zero time, the blue line the point at which the background correction begins, the red dotted line is the background correction used and the horizontal dashed magenta line shows the zero line. In most analysis, the imaginary component is phased to this zero line in order to minimize its contribution.

In Fig. 7.9 column 1 demonstrates the results of applying DeerAnalysis to a four-pulse DEER trace for the 2.1 nm model system. As seen in Fig. 7.8 when data is measured in the linear regime of the TWT and the dynamic phase shift is limited to the x-y plane, taking the absolute value of the quadrature signal for three-pulse DEER gives a time trace that does not have any appreciable phase shift at t_0 and is thus distortion free. The data is comparable to four-pulse data measured under the same experimental conditions in terms of modulation depth, but exhibits a superior signal-to-noise ratio for acquisitions recorded in the same number of scans. The higher signal-to-noise ratio for the three-pulse DEER allows the extraction of a marginally 'cleaner' distance distribution, as seen by comparing row 3 of columns 1 and 2 in Fig. 7.9.

For four-pulse data, DeerAnalysis will automatically find t_0, selected on the assumption that the data should be symmetric about the time origin. Three-pulse DEER, however, is not symmetric about t_0. To allow analysis of three-pulse traces in DeerAnalysis, it is therefore vital that the position of t_0 used in the analysis is verified in relation to the pulses in the experiment, since it should coincide with the crossing of the centre of the pump and first detection pulse. As discussed in Section 7.3.3, in the experimental data for three-pulse DEER, a difference of less than 4 ns was observed from the predicted zero-time with respect to that found from comparison with an experimental four-pulse DEER trace. However, even in the case of the relatively short 2.1 nm model system, this was not significant enough to cause large changes in the distance distribution calculated in DeerAnalysis, and thus using the predicted t_0 (where t_0 is selected to be the point at which the centres of the pump pulse and the first $\frac{\pi}{2}$ detection pulse coincide) appears to be a reasonable approximation.

The two-phase nature of the raw three-pulse DEER data (with one phase for the region of the trace when the pump pulse position is before the initial $\frac{\pi}{2}$ detection pulse and another when the pump pulse is after the initial $\frac{\pi}{2}$ detection pulse) can cause the real part of the data to exhibit a 'false' maximum, which could be easily mistaken for t_0. Column 3 of Fig. 7.9 shows analysis of three-pulse DEER, where t_0 is incorrectly chosen as the signal maximum of the real portion of the trace. In this example, the first oscillation is truncated, resulting in spurious shorter distances being found in the Tikhonov fitting. Use of an incorrect t_0 will cause either truncation or elongation of the first oscillation and will lead to

spurious distances in the distance analysis or broadening of the distance distribution, depending on the degree of the error. If necessary, the position of t_0 can be manually adjusted in DeerAnalysis before the distance distribution is extracted. The degree by which a DEER trace is affected by incorrect selection of the t_0 is directly related to the frequency of the DEER oscillations and thus is dependent on the inter-spin distance.

Since the phase in conventional four-pulse DEER, where the pump and detection pulses are assumed not to overlap, is constant, there is usually no need to correct multiple phases. For this reason, the phase correction used in DeerAnalysis is not designed to take into account two different phases within the data. Thus care should be taken when processing any three-pulse DEER data that is recorded with the pump pulse both before and after the initial detection pulse, since this data necessarily contains two regions of different phases (see Fig. 7.9 columns 4 and 5).

For the data shown in Fig. 7.9, when the phase before t_0 is set to zero, this causes an artificial increase in the modulation depth observed and also a sharper drop in the start of the first modulation, which leads to artefacts at short distances in the distance distribution (column 4). When the phase after t_0 is set to zero, the result is a small hump at the start of the first modulation (column 5). The frequency of this dip corresponds to a very short distance (< 0.5 nm). This distance is neglected from the Tikhonov regularization in DeerAnalysis, which has a minimum lower bound of 0.5 nm, although usually this lower bound is set at 1.5 nm corresponding to the lower limit of the technique. The inclusion of a lower bound is to prevent noise on the spectrum being fitted as part of the distance distribution. With the lower bound set at 1.0 nm as in Fig. 7.9, the dip at the start of the trace (column 5) does not cause any visible artefacts in the distance domain; however, it does alter the distance found by DeerAnalysis which corresponds to the first modulation. (An expansion of the fitting around the zero time is shown in Fig. 7.10.)

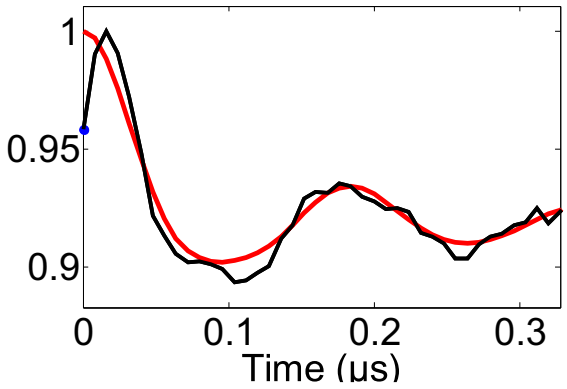


Figure 7.10: An expansion of the Tikhonov regularization fit for the spectrum in Column 5 of Fig. 7.9, showing the distortion at t_0 in the experimental data, which is not fitted by the Tikhonov regularization, due to the parameters imposed by the choice of allowed distances. In this case, the shortest distance for analysis is set to 1.0 nm. It should be noted that in order for the Tikhonov regularization to be calculated the experimental DEER data must first have a background correction removed, the experimental DEER data shown in this figure is therefore background corrected.

7.3.5 The best method of processing dead-time free three-pulse DEER data

From the analysis performed in the previous section (Section 7.3.4), it can be seen that the best approach when processing three-pulse DEER using DeerAnalysis, in order to produce a time trace that is dead-time free, is to use the absolute to of the signal collected. In this case, for accurate analysis, it is necessary to know the zero-time and to set this manually prior to the distance analysis using a Tikhonov regularization. The zero-time can be found by comparison of three- and four-pulse background corrected data collected on a sample with a strong signal and under the same experimental conditions as the spectrum in question. Alternatively, the zero-time can be approximated from the raw three-pulse DEER data (the data before an absolute value is taken), as occurring half-way through the phase change observed.

It is possible to process the raw three-pulse data to extract an accurate distance distribution, if the lengths of the pulses used are short enough, so that the distortion at the start of the spectrum is small. In this case, the phase should be set to zero during the main portion of trace and the zero-time selected either from the phase change or by comparison with four-pulse DEER data as described previously.

The DEER data will still be distorted at the start of the time trace; however, when the pulses are short this distortion will be small and if a sensible lower bound is set for the Tikhonov analysis, this distortion will not be fitted and will be treated simply as noise.

7.4 Theoretical analysis of three-pulse DEER

The dynamic phase-shift in three-pulse DEER has been studied by Bowman et al. using analytical formulae.[212] These calculations allowed the prediction of the dynamic phase shift when the pump pulse was placed before and after the initial $\frac{\pi}{2}$ detection pulse, but did not describe the region of actual pulse crossing. In order to study this region, full numerical density matrix simulations were performed using the product operator formalism.[f]

7.4.1 Hamiltonians for simulation of DEER

The simulations performed for DEER experiments consider two spins: 'a' and 'b', which have resonance frequencies ω_a and ω_b. To simplify matters, the calculation is performed in the rotating frame of one of the spins such that:

$$\Omega_a = \omega_a - \omega_{rot} \tag{7.3a}$$

$$\Omega_b = \omega_b - \omega_{rot} \tag{7.3b}$$

where ω_{rot} is the frequency of the rotating frame and Ω_a and Ω_b are the frequency offsets of the a and b spins respectively.

[f] Density matrix simulations using product operator formalism were originally described by Ernst et al. for use in NMR pulsed experiments.[221]

The time-independent Hamiltonian in the rotating frame for a spin system consisting of the coupled two spins, a and b, is given by:

$$\hat{H}_{0,rot} = \Omega_a \hat{S}_a^z + \Omega_b \hat{S}_b^z + \omega_\perp (3\cos^2\theta - 1)\hat{S}_a^z \hat{S}_b^z \tag{7.4}$$

This formulation assumes the two spins interact only via a dipolar coupling. Furthermore the pseudo-secular term has been dropped since it is assumed that $|\omega_a - \omega_b| >> |\omega_\perp|$. Here, $\omega_\perp$ is the dipolar coupling constant between the spins, which is proportional to $\frac{1}{r^3}$, where r is the inter-spin distance (see Equation 2.8b). No through bond coupling (J-coupling) was included in the model since for the experimental systems studied, this contribution is negligibly small. In the calculation, a range of frequency offsets Ω_a and Ω_b were used. Experimentally this corresponds to excitations of a range of frequencies by a single pulse. Rectangular pulses were used in the simulations. These possess a sinc-shaped frequency profile and thus excite a range of frequencies, all of which will contribute to the DEER trace if they overlap the electronic spectrum.

For pulses applied at a frequency resonant with the rotating frame (here selected to coincide with the frequency of the detection pulses), the Hamiltonian is given by:

$$\hat{H}_{1,rot_{det}} = -\omega_1(\hat{S}_a^x + \hat{S}_b^x) + \hat{H}_{0,rot_{det}}. \tag{7.5}$$

where $\hat{H}_{0,rot_{det}}$ is the time-independent Hamiltonian in the rotating frame of the detection pulse carrier frequency.[g] The form of $\hat{H}_{0,rot_{det}}$ is thus that of Equation 7.4, where Ω_a and Ω_b are defined by Equations 7.3a and 7.3b, with $\omega_{rot} = \omega_{det}$. ω_1 is the strength of the detection pulse. As the detection pulse carrier frequency coincides with the rotating frame frequency, there is no time-dependence for this pulse.

[g]From this point onwards the subscript on Hamiltonian operators of rot_{det} denotes that the Hamiltonian is acting in the rotational frame coincident with the detection pulse carrier frequency.

To model a pulse applied at a different frequency to the rotating frame, a time-dependent Hamiltonian is needed. The Hamiltonian below describes the effect of a pump pulse in the rotating frame of the detection spins.

$$\hat{H}_{2,rot_{det}} = -\omega_2((\hat{S}_a^x + \hat{S}_b^x)\cos(\xi t + \alpha) + (\hat{S}_a^y + \hat{S}_b^y)\sin(\xi t + \alpha)) + \hat{H}_{0,rot_{det}} \quad (7.6)$$

ξ is the frequency difference between the carrier frequencies of the detection and pump pulses; i.e. $\xi = \omega_{det} - \omega_{pump}$. In the experiment the pump pulse is not coherent with the detection pulses. To allow for this in the simulations, a variable phase offset between the pump and detection pulses, α, was included in the Hamiltonian.

For the region where the pump and detection pulses are applied simultaneously, the Hamiltonian in the rotating frame of the detection pulses is the sum of the time-independent Hamiltonian for the detection pulse and the time-dependent part of the Hamiltonian for the pump pulse.

$$\hat{H}_{overlap,rot_{det}} = -\omega_2((\hat{S}_a^x + \hat{S}_b^x)\cos(\xi t + \alpha) + (\hat{S}_a^y + \hat{S}_b^y)\sin(\xi t + \alpha)) + \hat{H}_{1,rot_{det}} \quad (7.7)$$

In the simulations, Equation 7.7 is solved using average Hamiltonian theory. This assumes that the time-dependence of the Hamiltonians over a short time step is negligible and therefore the overall time-dependence can be modelled by multiple small regions that are effectively time independent. The definition of a 'short' time step will vary between different systems and is dependent on the size of the highest frequency interaction in the system.

It should be noted that when the pump pulse is active in the absence of the detection pulse, the simulation speed can be increased significantly by completely removing the time-dependence of the pump pulse. This is achieved by changing into the rotating frame of the pump pulse for the portion of the calculation when the pump pulse is applied separately to the detection pulses.

The Hamiltonian during the pump pulse in the rotating frame of the pump pulse is therefore given by:

$$\begin{aligned}\hat{H}_{2,rot_{pump}} &= -\omega_2((\hat{S}_a^x + \hat{S}_b^x)\cos(\alpha) + (\hat{S}_a^y + \hat{S}_b^y)\sin(\alpha)) \\ &\quad +\Omega_{a,pump}\hat{S}_a^z + \Omega_{b,pump}\hat{S}_b^z + \omega_\perp(3\cos^2\theta - 1)\hat{S}_a^z\hat{S}_b^z \end{aligned} \tag{7.8}$$

where $\Omega_{a,pump}$ and $\Omega_{b,pump}$ are the frequency offsets from the pump pulse carrier frequency defined by Equations 7.3a and 7.3b, with $\omega_{rot} = \omega_{pump}$.

The portion of the Hamiltonian given by $-\omega_2((\hat{S}_a^x + \hat{S}_b^x)\cos(\alpha) + (\hat{S}_a^y + \hat{S}_b^y)\sin(\alpha))$ accounts for the application of the pump pulse at an angle α within the x-y plane of the rotating frame. The α angle is required to model the non-coherent nature of the pump pulse compared to the fixed phase of the detection pulses and the value of α varies randomly from 0 to 2π. This can be understood in terms of the vector model, where inclusion of this in the Hamiltonian moves the direction along which the pulse is applied within the x-y plane. An alternative but equally valid method is instead to use a fixed position for the pulse and to rotate the spin vectors by a random angle about the z-axis prior to the pulse application. In the calculations conducted here, the spin system is described by a density matrix, $\hat{\rho}$, and thus this rotation is achieved by a rotation of this matrix about the z-axis prior to the application of the Hamiltonian above with α consistently set to 0.[h] It should be noted that this rotation is independent of the rotation required to return to the detection frame after propagation in the pump frame. The application of this rotation to change frames is described in Section 7.4.2.

The four different Hamiltonians given in Equations 7.5, 7.4, 7.7 and 7.6 correspond to the time periods during the pulse sequence and their application with respect to the dead-time free three-pulse DEER pulse sequence is given in Fig. 7.11. A derivation of the time-dependent Hamiltonians is given in Appendix K.

[h] Given the Euler formula ($e^{ix} = \cos x + i\sin y$) it is possible to see how the part of the Hamiltonian given by $-\omega_2((\hat{S}_a^x + \hat{S}_b^x)\cos(\alpha) + (\hat{S}_a^y + \hat{S}_b^y)\sin(\alpha))$ can also be modelled by a rotation of the density matrix of the form $e^{-i\alpha}\hat{\rho}e^{+i\alpha}$ about the z-axis followed by application of the Hamiltonian including $-\omega_2(\hat{S}_a^x + \hat{S}_b^x)$.

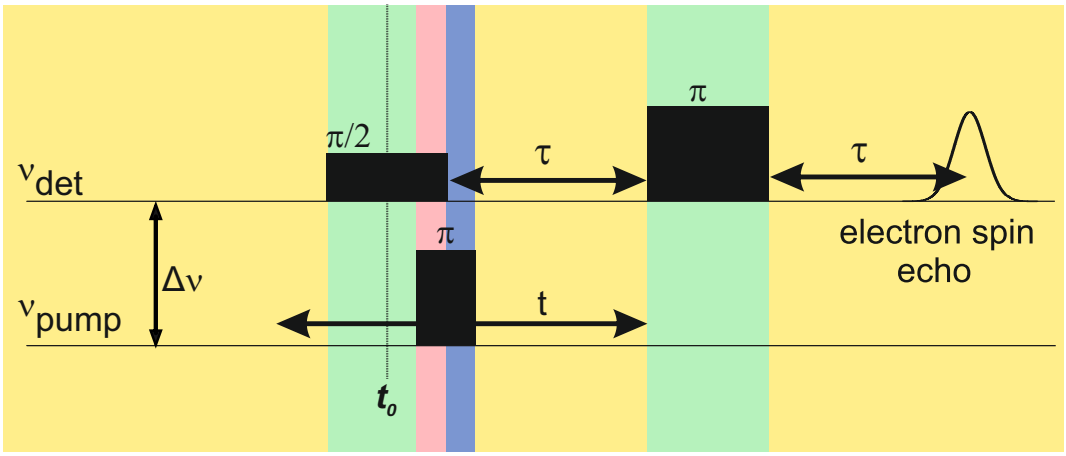


Figure 7.11: Diagram showing when each of the four Hamiltonians is used in the pulse sequence. The yellow region is described by the Hamiltonian given in Equation 7.4. The green region where only the detection pulses act is described by Equation 7.5. When both pulses act together in the pink region, the Hamiltonian becomes time-dependent and is given by Equation 7.7. Finally the blue region, where the pump pulse acts alone, can either be described by the time-dependent Hamiltonian, Equation 7.6, in the rotating frame of the detection pulses or by the time-independent Hamiltonian, Equation. 7.8, in the rotating frame of the pump pulse.

7.4.2 Calculating DEER spectra

The simulation uses the analytical solution (Equation 7.10) of the Liouville-von Neumann equation (Equation 7.9).

$$i\hbar\frac{\partial\hat{\rho}}{\partial t} = [\hat{H}, \hat{\rho}] \tag{7.9}$$

$$\hat{\rho}(t) = e^{\frac{-i\hat{H}t}{\hbar}}\hat{\rho}(0)e^{\frac{+i\hat{H}t}{\hbar}} \tag{7.10}$$

The initial state of the system, $\hat{\rho}(0)$ is given as $\hat{S}^z$, with an excess of spins in the $|\alpha\alpha\rangle$ state and a corresponding depletion in $|\beta\beta\rangle$.

As stated in Section 7.4.1, the speed of the calculation can be significantly increased by changing into the rotating frame of the pump pulse, ω_{pump}, for calculations where the pulses do not overlap. The majority of the calculation is carried out in the rotating frame of the detection pulse, ω_{det}, and only changes frame during the application of the pump pulse.

Changing from the detection frame into the pump frame is easily achieved by simply considering the time-independent Hamiltonian in the rotating frame of the pump pulse, $\hat{H}_{0,pump}$, for the period of time in which propagation in the pump frame is desired.[i] The change in frame corresponds to a change in speed of the rotating frame therefore when changing back into the original rotating frame of the detection pulse carrier frequency a rotation must be made to correct the propagation of the coherences. The size of the rotation necessary to unwind the coherences back into the original frame can be calculated from the difference in frequencies of the two frames (ξ), as defined in Equation 7.11, and the length of time (t_p) that the system was propagated in the pump rotating frame.

The difference between the Hamiltonians in the rotating frames of the pump and detection pulses is given by:

$$\hat{H}_{0,det} - \hat{H}_{0,pump} = \xi \hat{S}^z \tag{7.11}$$

Therefore the rotation required to correct for the propagation in the rotating frame is defined as:

$$\hat{\rho}^{rot_{det}}(t + t_p) = e^{-i\xi\hat{S}^z t_p} \hat{\rho}^{rot_{pump}}(t + t_p) e^{+i\xi\hat{S}^z t_p} \tag{7.12}$$

where t is the time at which propagation in the rotating frame of the pump pulse began.

[i] This effectively sets the coordinates of the two axis systems equal at the point when the change in frame occurs.

7.4.3 Parameters for the simulation

The parameters of the simulation were carefully chosen and are detailed in Table 7.1. Simulations were carried out in a custom-written MATLAB-based program.

Table 7.1: Parameters used in the simulation for dead-time free three-pulse DEER

Simulation parameter	Range of values used
θ	0 to $\frac{\pi}{2}$ in $\pi/90$ steps
α	randomly chosen value between 0 and 2π
Ω_a	-31.5 MHz to +31.5 MHz in 0.5 MHz steps
Ω_b	40 MHz to 90 MHz in 5 MHz steps
ξ	65 MHz
$\omega_\perp$	2 MHz
$\frac{\pi}{2}$ detection pulse length	32 ns
π detection pulse length	32 ns
π pump pulse length	16 ns
τ, precession time	2250 ns
time step for time-dependent portion	0.1 ns
d_0, echo integration	-8 ns to +8 ns in 4 ns steps

Density matrix simulations were utilized to calculate the excitation profiles of rectangular $\frac{\pi}{2}$ and π pulses as a function of the resonance frequency offset, Ω (see Fig. 7.12).

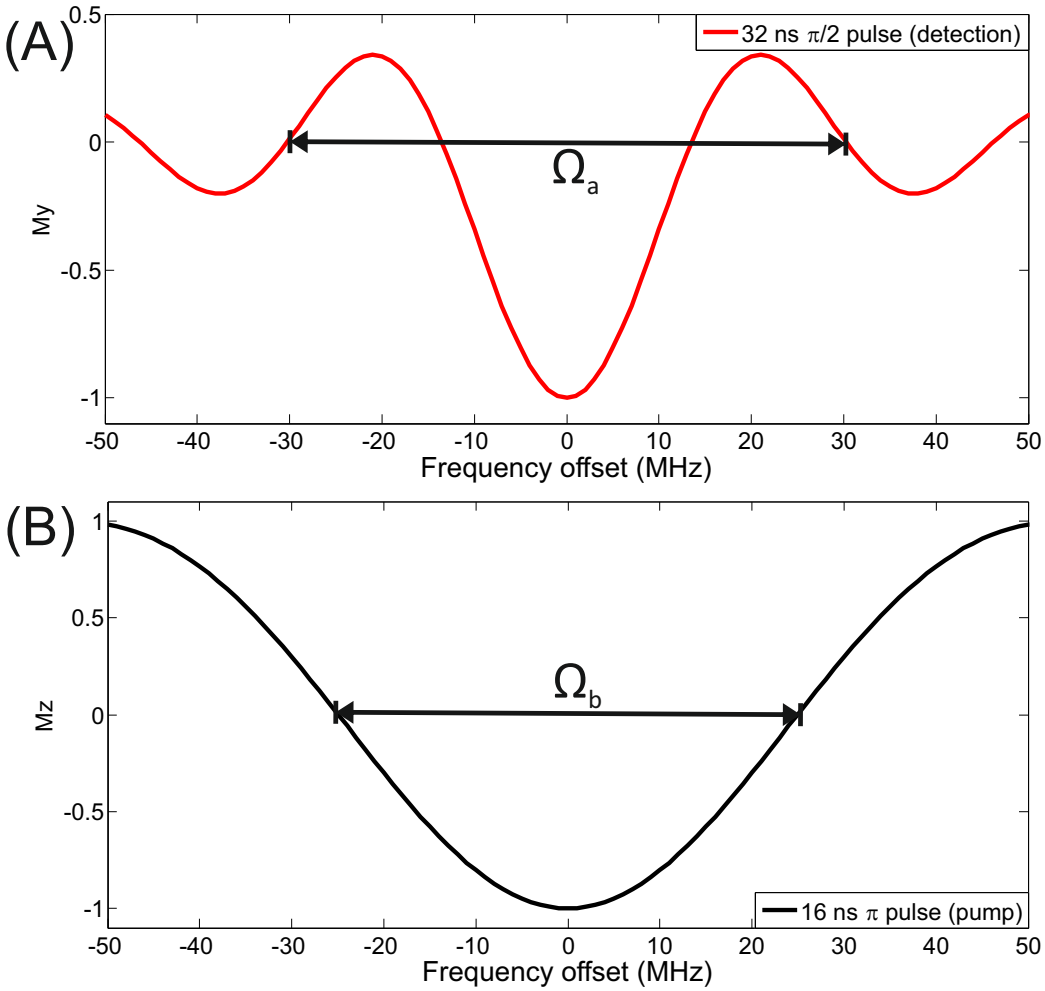


Figure 7.12: **(A)** M_y components for spins both on- and off-resonance with the pulses used in the DEER-simulations. This gives the frequency profile of the pulses as they are detected along the y-direction for a pulse applied along the $+x$-axis. Marked on this plot are the frequency offsets used in the simulation for detection spins (Ω_a). **(B)** M_z components for spins both on- and off-resonance with the pulses used in the DEER-simulations. This gives the frequency profile of the pulses in the z-direction, as the action of the pump pulse is to invert the z-magnetization of the pump spins, the integration width was chosen from the profile in this direction. The frequency offsets used in the simulation for pump pulses (Ω_b) are marked.

The range of Ω_a (a spins are primarily effected by the detection pulse) was chosen from the spin response in the y-direction, as the detection pulses are applied along the $+x$-direction, and the range of Ω_b (b spins are primarily effected by the pump pulse) was chosen from the response in the z-direction. This distinction was made as the detection pulses applied primarily affect the on-resonance detection spins, which provide a signal in the x-y plane with the real part being detected along the y-direction, whereas the largest effect from the pump pulses on the detected signal is due to the inversion of the z-magnetization of the pump spins. Initial investigations showed that the use of different pump-pulse offsets had a smaller effect on the resulting calculated DEER trace than the offsets of the detection pulse. For this reason a finer grid and broader range, corresponding to the second zero crossing of the M_y signal, was selected for Ω_a (detection-pulse offset, see Fig. 7.12A) than for Ω_b (pump-pulse offset, see Fig. 7.12B), where only the full-width half-maximum (FWHM) of the central feature was used. The plots in Fig. 7.12 are generated by applying the Hamiltonian for a pulse to the $\hat{\rho}(0)$ density matrix. The resulting density matrix is multiplied by one of the Pauli spin operators, $\hat{S}_y$ or $\hat{S}_z$, and the trace of the resulting matrix taken to give the response in the y and z directions respectively.

Calculations were carried out at all θ values from 0 to $\frac{\pi}{2}$, in steps of $\frac{\pi}{90}$ and the resultant traces weighted by $\sin\theta$, in order to produce a powder averaged dipolar spectrum.

In the acquisition of experimental DEER traces the signal detected is an integral of the echo formed along the $-y$-direction by the detection sequence. This is replicated in the simulations by taking the trace of the propagated density matrix with the Pauli spin operators at different time steps, defined by d_0, around the theoretical echo maximum, such that $d_0 = 0$ corresponds to the theoretical echo maximum. The Pauli spin operator in the y-direction ($\hat{S}_y$) is used to give the real part of the signal and the Pauli spin operator in the x-direction ($\hat{S}_x$) is used to give the imaginary part of the signal. The z part of the signal is not observed in the experiment. However, it is calculated in the simulation using the Pauli spin operator in the z-direction ($\hat{S}_z$). Also, in replication of the experiment where the applied pump pulse is not coherent for each DEER trace calculated, a randomly generated pump-pulse phase (α) was used.

The dynamic phase shift (Bloch-Siegert shift) induced in the phase of the detection spins by the off-

resonance pump pulse results in the observation of two clear regions of different phases in the resulting traces. In order to analyse the effect of this phase shift more thoroughly, the DEER traces were phased after calculation to minimize the imaginary component, as is the norm with experimentally recorded DEER data.

7.5 DEER simulation results

Simulations have been completed to model the cross-excitation effect due to non-selective pulses and to allow a better understanding of the dynamic phase shift. The results of simulations are presented in the following sections, which are structured as follows. Initially, time-independent simulations including pulses on-resonance with the rotating frame and time-dependent simulations using average Hamiltonian theory for pulses off-resonance with the rotating frame were carried out using single pulses in order to show the effect of these pulses for spins both on- and off-resonance with the pulse (see Section 7.5.1). Next, full DEER simulations for both the three- and four-pulse techniques were carried out so that the position of the zero-time for the two experiments could be accurately determined (Section 7.5.2). The three-pulse DEER simulations clearly show a change in phase as the pump pulse crosses the first $\frac{\pi}{2}$ detection pulse (Section 7.5.3) and the effect of this change of phase, particularly in connection with the modulation depth of the trace, are considered (Section 7.5.4). Finally, a theoretical technique for correction of the phase shift is discussed (Section 7.5.5). It should be noted that none of the simulations shown in the following sections have background corrections applied.

7.5.1 The origin of the dynamic phase shift

Time-independent calculations (considering only pulses on-resonance with the detection carrier frequency) of the effect of the different pulses used in DEER show that a rectangular pulse in the time domain gives a frequency profile, which can cause excitation of spins hundreds of MHz off-resonance with the pulse. A plot of the response of the *x, y* and *z*-components of the magnetization (M_x, M_y and M_z) against frequency offset ($\frac{\Omega}{2\pi}$) for pulses of different lengths and turning angles, corresponding to those used in the DEER simulations presented in later sections, is given in Fig. 7.13. The profile of

M_z follows a sinc-like, function as expected for a rectangular π pulse.

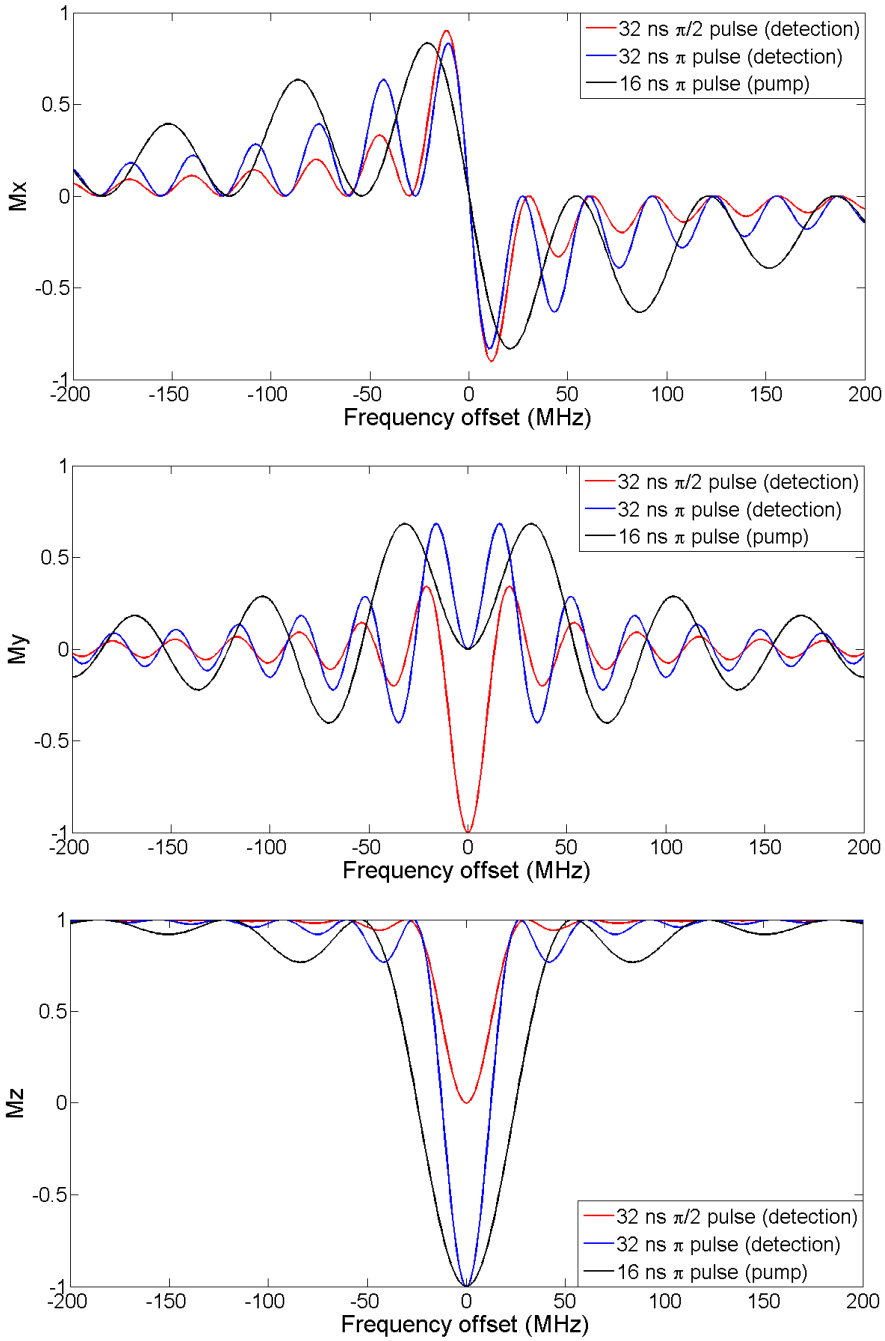


Figure 7.13: Plots of the magnetization response in the x, y and z-directions for spins both on- and off-resonance with the pulses used in the DEER simulations.

With a typical DEER pump and detection pulse separation of 65 MHz, it is clear from Fig. 7.13 that any pump pulse applied will also affect the detection spins. It is the excitation of detection spins (those on-resonance with and primarily excited by the detection pulses) by the pump pulse that is applied off-resonance with respect to these spins, which is the origin of the dynamic phase shift in the three-pulse DEER experiment.

Consider a system with two spins, a detection spin and a pump spin, which have a variable offset (ξ) between their resonance positions. The detection spin is always on-resonance with the detection pulses and the pump spin is always on-resonance with the pump pulses, such that the separation between the pulses is also ξ. Visualizing these spins as vectors gives pictures such as those plotted in Fig. 7.14.[j] This figure shows the effect of a 16 ns π pulse applied on-resonance with the pump spins. Examining the effect this pulse has on the detection spins, 65, 80, 100 and 500 MHz off-resonance from the pump spins, shows that the closer the two pulses are in frequency, the greater the effect of the pump pulse on the relative phase of the detection spins after the pump pulse has been applied. All of the visualizations are made in the rotating frame of the detection spins.

[j] An animated version of this figure is available on the CD of appendices.

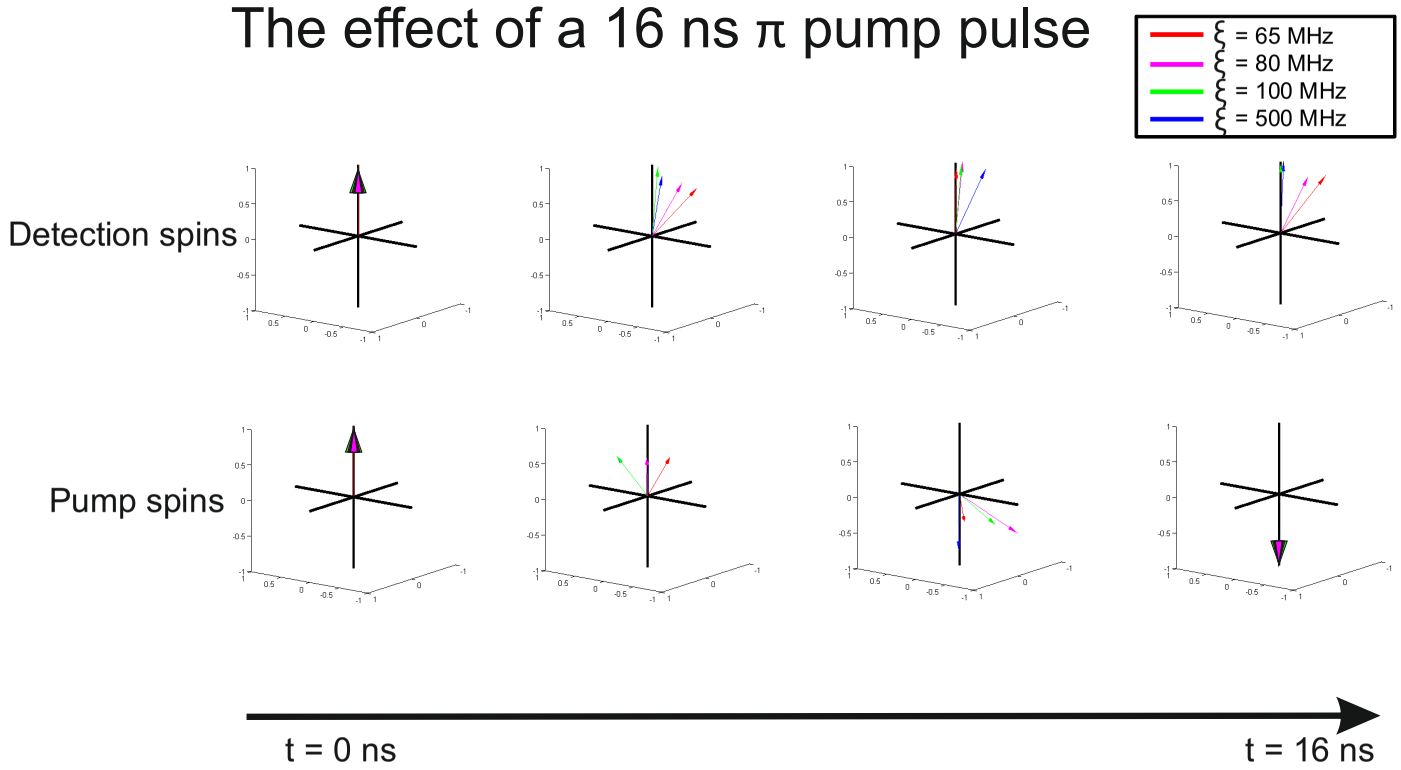


Figure 7.14: Vector diagrams showing the motion of the magnetization vector for detection and pump spins over the duration of a pulse applied on-resonance with the pump spins. ξ is the offset between these spins, calculation were carried out for four values of ξ corresponding to the differently coloured arrows. All diagrams are shown in the rotating frame of the detection spins. If there was no excitation of the detection spins by the pump pulse the magnetization vector for these spins would remain aligned with the z-axis. The applied π pump pulse causes inversion of the pump spins in all cases. Where the arrows coincide with each other and the axes, the size of the arrow-heads have been increased for ease of viewing. (An animated version of this figure is available on the CD of appendices.)

7.5.2 Determination of the zero-time, (t_0), using simulations

For four-pulse DEER, a good estimate of t_0 corresponds to the time when the centre of the pump pulse coincides with the point of maximum intensity of the primary echo, when all of the magnetization is refocused. Under these circumstances, the application of the pump pulse is having the least effect on the detection spins echo. This t_0 time can be reproduced in simulations of a delta pump pulse acting only on B-spins.[k] The exact position of the t_0 with finite pulses is dependent on the length of the pulses used.[220,222] Simulations of four-pulse DEER are shown in Fig. 7.15.

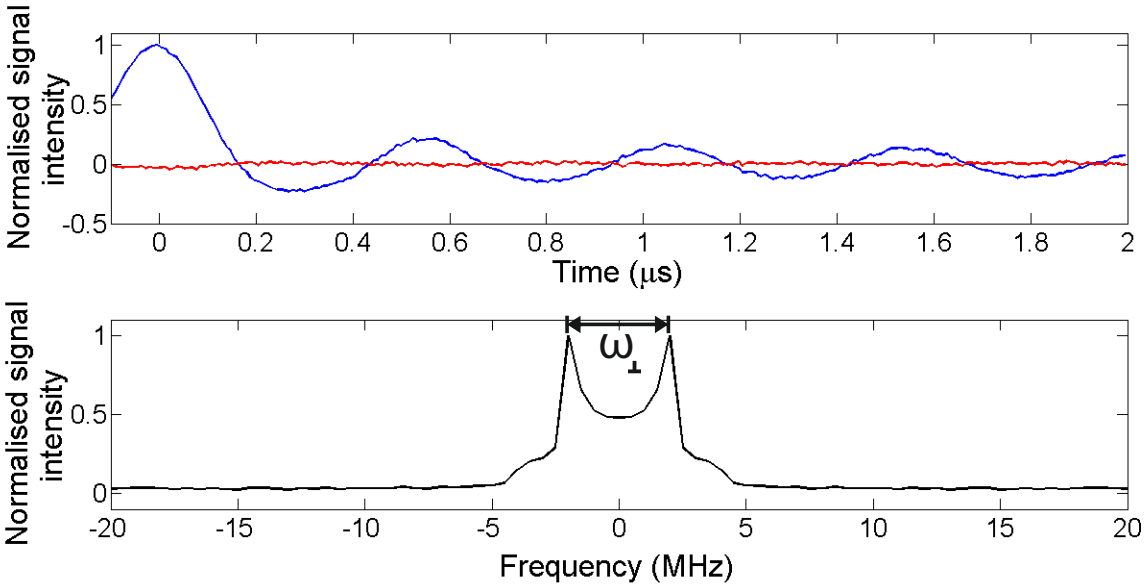


Figure 7.15: **Simulations for four-pulse DEER.** *Upper plot:* The blue trace is the real part and the red trace is the imaginary part of the signal. The phase has been chosen such that the imaginary part is minimized. *Lower plot:* The Fourier transform of the real part of the trace. The dipolar coupling constant, $\omega_\perp = 2$ MHz, is marked.

Although the t_0 can be defined from the pulse lengths, this does not correspond exactly to the signal maximum calculated in the simulations that did not use an ideal delta pulse acting only on the B-spins. (There is a discrepancy of c. 7 ns.) This discrepancy persists even when selective pulses are used and is independent of the width of the echo integration and sampling rate. It is therefore apparent that this discrepancy is a result of the finite lengths of the pulses used.[220] Furthermore, it was found

[k] A delta pulse is defined by a dirac delta function in the time domain.

that when the signal maximum was used as the zero-time rather than the idealized t_0, corresponding to the centre of the pump pulse coinciding with the centre of the first echo, a very small shift was observed in the positions of the perpendicular features of the dipolar spectrum. When the idealized t_0 is used, the value of $\omega_\perp$ extracted from the dipolar spectra is identical to that used as input in the simulation.

It appears that a similar effect also occurs in three-pulse DEER. Unlike four-pulse DEER, three-pulse traces do not go through a symmetric maximum and therefore, to find t_0 experimentally, it was necessary to compare experimental three- and four-pulse DEER traces. This analysis indicated that t_0 for the three-pulse sequence occurs when the centres of the pump and first $\frac{\pi}{2}$ detection pulse coincide (see Section 7.3.3). However, a small shift was seen between the idealized t_0 for three- and four-pulse DEER. This difference is within the 4 ns temporal resolution of the spectrometer and therefore it is not possible to tell from the experimental data if this shift is real.

Comparison of simulations for three- and four-pulse DEER traces calculated using finite pulses and plotted with their idealized t_0 times also showed a small shift of the two traces with respect to one another of c. 4 ns, similar to that observed experimentally (see Fig. 7.16, upper plot). This shift is removed when selective delta pulses are used in the simulations (see Fig. 7.16, lower plot).

The shift in t_0 observed experimentally between three- and four-pulse data sets is therefore likely to be a result of the finite pulse lengths used. However, the shift may also contain an additional component, due to the temporal resolution of the spectrometer. In both the three- and four-pulse calculations and experimental data, the shifts in the observed zero-times from the idealized t_0 are small and thus their impact on the distance analysis for the extraction of an average distance will be minimal. They may, however, cause a marginal change the shape of the distance distribution extracted. Since it is not possible to use infinitely short pulses experimentally, the most appropriate methods of finding t_0 for dead-time free three-pulse data are still those described in Section 7.3.5.

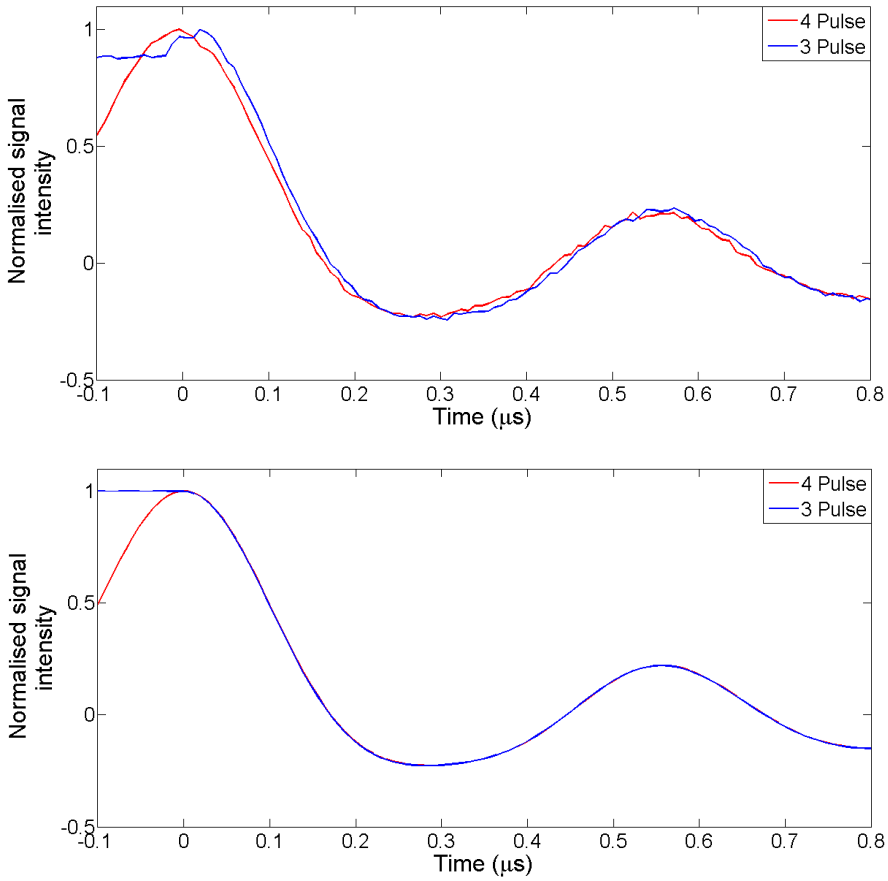


Figure 7.16: **Comparison of the absolute of the three-pulse (blue trace) and four-pulse (red trace) simulated data.** For all traces, t_0 is set to the idealized value predicted from the pulse lengths. *Upper plot:* This shows the results from simulations using non-selective pulses with detection pulses of 32 ns and a 16 ns π pump pulse. There is a very small shift of the two data sets with respect to one another. *Lower plot:* This shows the results from calculations using selective delta pump pulses. In the four-pulse simulation, all pulses were set to be delta pulses. By contrast in the three-pulse simulation, the detection pulse lengths were maintained at 32 ns length; this allowed the zero-time to be defined with respect to the detection pulse positions. The small shift seen when finite pulses are used is removed when selective delta pulses are used.

7.5.3 The dynamic phase shift in simulations of three-pulse DEER

Non-selective pulses used in the calculation of the upper plot of Fig. 7.16 mean that the detection pulses affect the pump spins and vice versa, as is the case in the experimental results. Plotting the individual magnetization components for the three-pulse DEER simulation using non-selective pulses shows that

the phase shift in the x-y plane is accurately reproduced (red and blue lines of Fig. 7.17). However, this simulation also shows that the M_z magnetization is not constant (green trace in Fig. 7.17); this is the result of a component of the dynamic phase shift which is not limited to the x-y plane, and rotates the magnetization into the z-direction.

As described in Section 7.2.4, taking the absolute of the three-pulse trace corrects any phase shift within the x-y plane. However, it does not make any corrections for phase shifts out of this plane. Examination of the absolute of the data for the three-pulse DEER simulation using non-selective pulses (blue line in the upper plot of Fig. 7.16 and black line in Fig. 7.17) shows that there is a small maxima around the zero-time as a result of the phase shift into the z-direction.

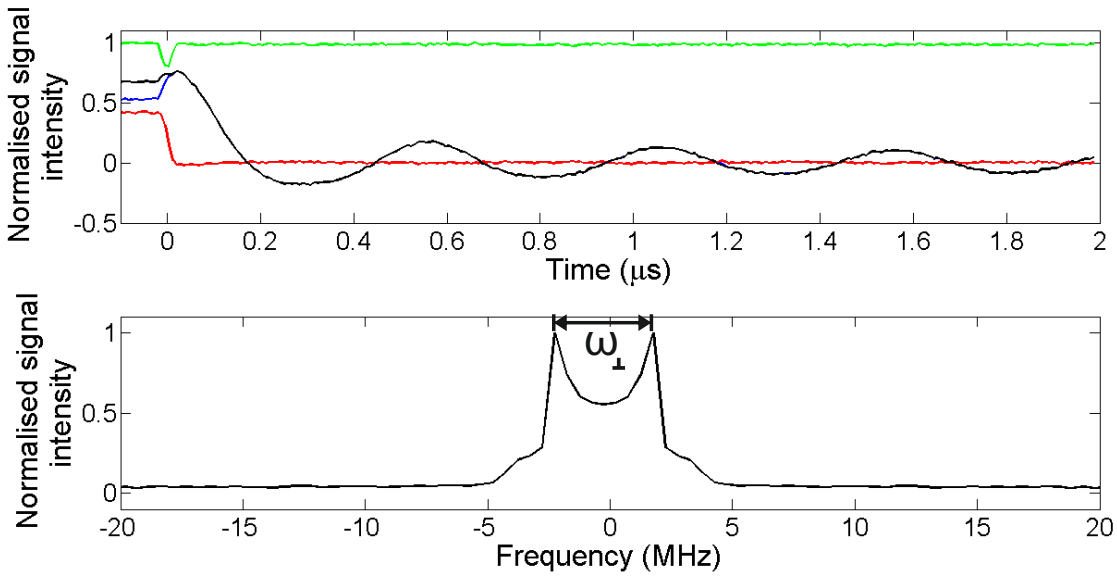


Figure 7.17: **Simulations for three-pulse DEER.** *Upper plot:* The blue trace is the real part and the red trace is the imaginary part of the signal. The phase has been chosen such that the imaginary part is minimized for $t > t_0$. The green trace is the M_z magnetization and the black trace is the absolute of the red and blue traces. The simulations accurately reproduce the dynamic phase shift observed in the experiment (see Fig. 7.8). *Lower plot:* The Fourier transform of the real part of the trace. The dipolar coupling constant, $\omega_\perp = 2$ MHz, is marked.

Experimentally, the phase shift out of the x-y plane could be reduced by lowering the power of the pump pulse (see Fig. 7.7). In these simulations, the same effect can be achieved by increasing the length of the pump pulse (see Fig. 7.18). The longer pump pulse has a narrower excitation profile and

thus the excitation of detection spins by this pulse is reduced. This reduces the overall dynamic phase shift and, as seen experimentally, the phase shift component out of the x-y plane can be reduced to a point at which the phase shift is satisfactorily confined to the x-y plane.

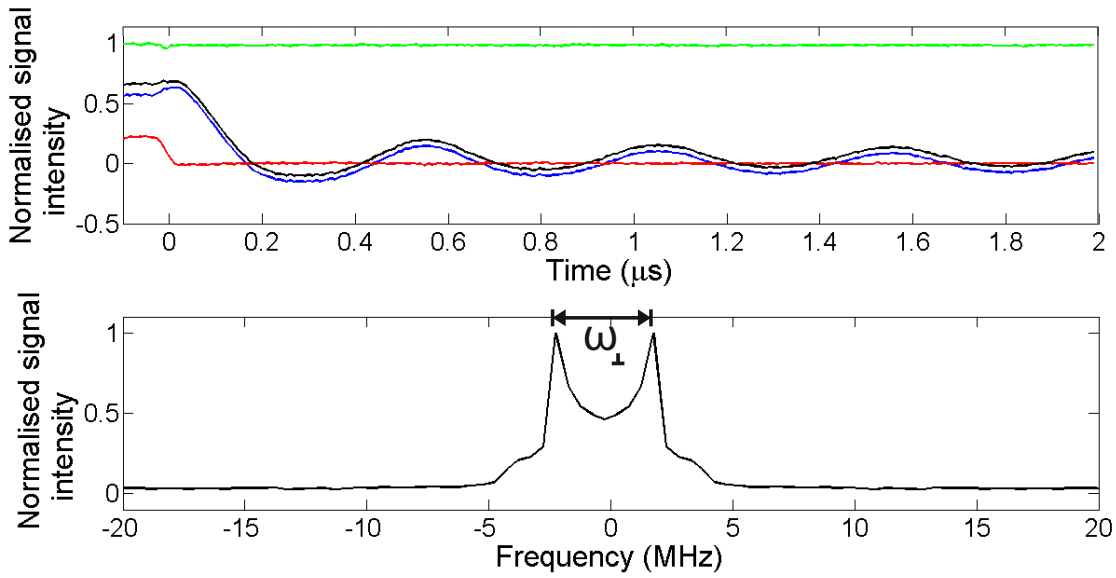


Figure 7.18: **Simulations for three-pulse DEER using longer pump pulse (32 ns detection pulses and 30 ns pump pulse).** *Upper plot:* The blue trace is the real part and the red trace is the imaginary part of the signal. The phase has been chosen such that the imaginary part is minimized for $t > t_0$. The green trace is the M_z magnetization and the black trace is the absolute of the red and blue traces. The black trace is offset from the blue trace by 0.1 units for clarity. The simulations accurately reproduce the dynamic phase shift observed in the experiment. The longer π pump pulse reduces the dynamic phase shift. *Lower plot:* The Fourier transform of the real part of the trace. The dipolar coupling constant, $\omega_\perp = 2$ MHz, is marked.

The dynamic phase shift can be completely removed by using selective pulses, which only excite either the detection or pump spins. Data from a simulation using selective pulses is shown in Fig. 7.19. This also corresponds to the lower plot of Fig. 7.16.

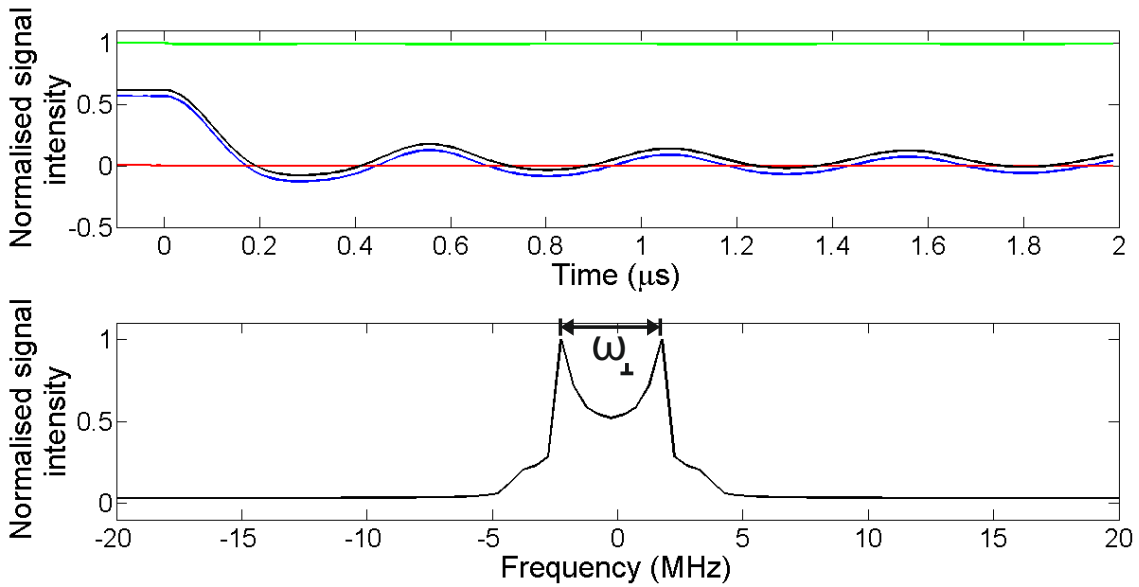


Figure 7.19: **Simulations for three-pulse DEER using selective pulses.** *Upper plot:* The blue trace is the real part and the red trace is the imaginary part of the signal. The phase has been chosen such that the imaginary part is minimized for $t > t_0$. The green trace is the M_z magnetization and the black trace is the absolute of the red and blue traces. The black trace is offset from the blue trace by 0.1 units for clarity. The use of selective pulses, where detection pulses only act on A-spins and pump pulses only act on B-spins, removes any dynamic phase shift in all directions. *Lower plot:* The Fourier transform of the real part of the trace. The dipolar coupling constant, $\omega_\perp = 2$ MHz, is marked.

7.5.4 The effect of the phase-shift on the modulation depth

As described in Chapter 2, a DEER signal in the time domain consists of two contributions: a decaying background of the trace, $B(t)$, which is multiplied by the form factor, $F(t)$, oscillating at the dipolar frequency. The form factor contains both a modulated and unmodulated part. The modulation depth (Δ) is measured from $F(t)$, as the vertical drop from the intensity at t_0 to the point at which the modulations are fully damped.

Since the form factor is orientationally dependent due to its $(1 - 3\cos^2\theta)$ contribution, it is not surprising that the modulation depth also displays orientational selectivity. In the orientationally dependent DEER calculations (see Chapter 2), the modulation depth was shown to be dependent on $1 - \cos(\theta_B)$, as in Equation 2.18. As such, the modulation depth is proportional to the z-component of the flipped B-spin (pump spins) magnetization, $M_z = M_0 \cos(\theta_B)$. Hence the greatest modulation

depth will occur when the magnetization of the B-spins is fully inverted by the pump pulse.

Simulation and experiment have shown that the pulse crossing in dead-time free three-pulse DEER causes a dynamic phase-shift in the observed signal due to the excitations of the detection spins by the pump pulse. It can therefore also be deduced that the detection pulses will also excite the pump spins. Excitation of the pump spins by the detection pulse(s) prior to the application of the pump pulse will cause a change in the alignment of the pump spin magnetization. This will reduce the z-component magnetization of the pump spins.

In the four-pulse experiment, there is the detection pulse sequence $\frac{\pi}{2}$ - τ - π prior to the first pump pulse position, whereas in the three-pulse sequence there is a single $\frac{\pi}{2}$ detection pulse that occurs prior to the pump pulse position which induces a DEER oscillation. The effects of the $\frac{\pi}{2}$ pulse and $\frac{\pi}{2}$ - τ - π pulse train on the M_z component of the magnetization at different excitation offsets from the pulse carrier frequency have been simulated and are shown in Fig. 7.20. 32 ns $\frac{\pi}{2}$ and π detection pulses were used with a τ time of 200 ns, corresponding to the detection pulses used in the three- and four-pulse DEER simulations shown previously. Also shown in Fig. 7.20 is the pulse profile of a 16 ns π pump pulse at an offset of +65 MHz from the detection pulses.

Taking the full-width half-maximum of the pump pulse, corresponding to the Ω_b offsets used in the full DEER simulations and integrating the area under the M_z, allows the average rotation from the z-axis to be calculated in each case, since the area under the graph is proportional to the average projection of the vector along z-axis. The maximum M_z component is 1 when all the magnetization is aligned with the z-axis. A single 32 ns $\frac{\pi}{2}$ pulse reduces the average M_z component to 0.9793 corresponding to a deviation from the z-axis of 11.7°, whereas the $\frac{\pi}{2}$ - τ - π sequence gives an average M_z component of 0.9030, a deviation of 25.4°. An increase in the modulation depth on the order of 8% could therefore potentially be expected for three-pulse DEER compared to four-pulse DEER with these parameters.

Experimentally, however, the size of any difference in the modulation depths could be very different. In the calculation above, the excitation across the whole of the frequency offset range was considered to be equal, corresponding to a rectangular pulse in the frequency domain (shown by the blue region

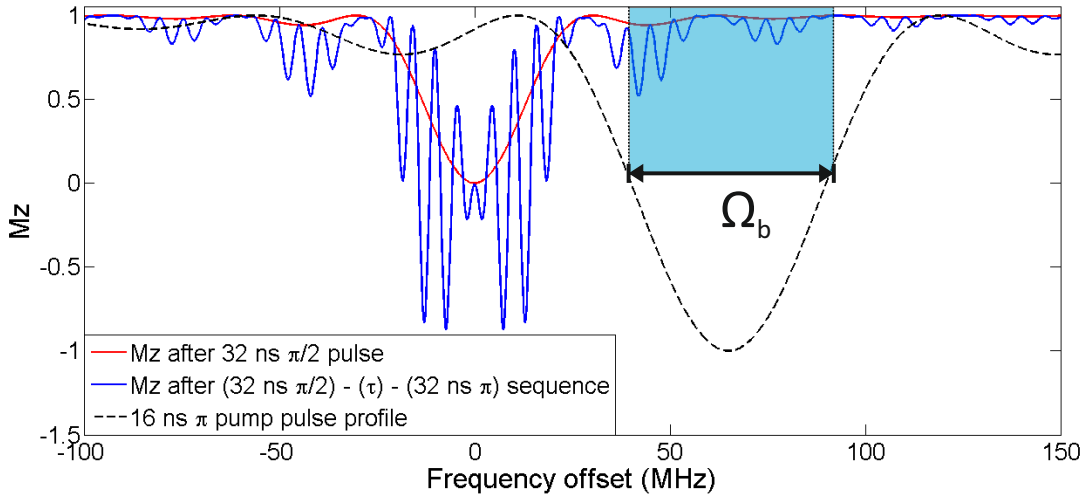


Figure 7.20: The M_z excitation profiles of a 32 ns $\frac{\pi}{2}$ pulse (red line) and the sequence $\frac{\pi}{2}$ - τ - π using 32 ns pulses and a τ delay time of 200 ns (blue line). Also plotted is the pulse profile of a 16 ns π pump pulse at a frequency offset of 65 MHz (dashed black line) with the offset range used for the simulations (Ω_b) marked. The blue region corresponds to the rectangular pulse in the frequency domain used in the analysis.

in Fig. 7.20), which is not the case experimentally. Therefore, in order to take into account the pump pulse profile in the frequency range, it would be necessary to weight each M_z offset by the pump pulse excitation profile at each frequency. Furthermore, experimentally there is no sharp cut-off in the pump pulse profile such as that used in the simulations. Instead the pump pulse profile is dependent on the bandwidth of the resonator. It is the convolution of the pump pulse profile with the resonator bandwidth profile that dampens the 'sinc-wings' of the pulse profile.

In order to compare the modulation depths of the simulated three- and four-pulse data, it is necessary to normalize the traces with respect to the signal collected for the pulse sequences in the absence of the pump pulse. This is different to the treatment of the experimental data, which are normalized to the signal maxima. This difference arises due to the absence of a large unmodulated contribution to the data, which is a result of the idealized nature of the spectrum considered in the

calculations.[1] Comparison of the normalized traces shows that the oscillation amplitude for the three-pulse DEER is c. 18% larger than that for the four-pulse DEER (see Fig. 7.21).

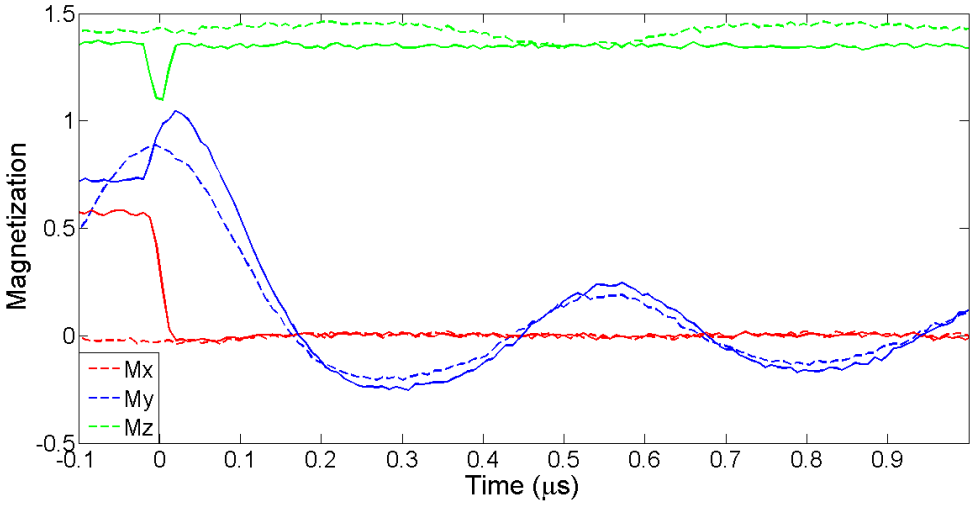


Figure 7.21: M_x (red), M_y (blue) and M_z (green) components from the four-pulse (dashed lines) and three-pulse (solid lines) simulations shown in Fig. 7.15 and Fig. 7.17, which have been normalized with respect to the signal observed in the absence of a pump pulse. Due to the phase shift in the three-pulse data, it is not possible to directly compare the first modulation depth of the three- and four-pulse data. However, it is possible to compare the modulation amplitudes of subsequent oscillations. No relaxation was considered in the simulations, so these amplitudes are directly comparable. The oscillation amplitude for the three-pulse DEER is c. 18% larger than that for the four-pulse DEER.

Examination of the experimental data collected, such as that presented in Fig. 7.8, shows the modulation depths for the three- and four-pulse DEER traces are measured to be the same. This result is not unexpected, since in order to bring the pulse overlapping region into the linear regime of the TWT, low-power pulses, which have narrow excitation profiles, must be used. Furthermore, as no phase shift is observed in the z-direction for the detection pulses due to the action of the pump pulse, it is a reasonable assumption that, similarly, there will be little to no rotation of the magnetization away from the z-axis for the pump pulse as a result of the detection pulses.

For DEER traces collected outside the linear regime of the TWT using stronger pulses, a difference in modulation depth between three- and four-pulse DEER becomes apparent. Fig. 7.22 shows data

[1]The simulations use an idealized spectrum which has equal intensity at all frequencies without any hyperfine couplings or g-tensor asymmetry. Also, the simulations assume that the labelling efficiency is 1.

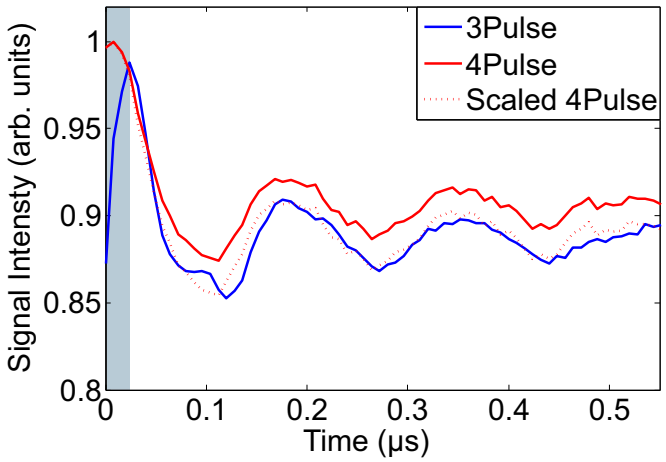


Figure 7.22: Background corrected three-pulse (blue) and four-pulse (red) DEER data measured on the 2.1 nm model system with a 12 ns pump pulse with an ELDOR attenuation of 9 dB. The three-pulse DEER trace is clearly not in the linear regime of the TWT, therefore in order to extrapolate the three-pulse data back to the zero time it is matched to four-pulse data scaled in the ordinate by 1.16 (dotted red trace). Under these experimental conditions the three-pulse DEER trace appears to have a larger modulation depth than the corresponding four-pulse trace. The exact degree of this difference is difficult to calibrate as the start of the three-pulse trace has been lost due to the TWT non-linearity. The blue box corresponds to the region of pulse overlap, where the three-pulse DEER trace is affected by distortions.

collected on the 2.1 nm model system using a 12 ns pump pulse with 9 dB ELDOR attenuation. This should be compared to the data in Fig. 7.8B, which was collected on the same system, using a 20 ns pump pulse with 13 dB ELDOR attenuation. In Fig. 7.22, both the three- and four-pulse data sets have been phased and background corrected in DeerAnalysis. The three-pulse data presented here was not recorded in the linear regime of the TWT as demonstrated by the large downward spike at the start of the trace. For the three-pulse data, the phase of the main portion of the trace, with the pump pulse after the first detection pulse, was corrected such that the imaginary part was set to zero. This left a phase discontinuity at the start of the trace; however, this fell within the region of the TWT non-linearity and therefore it is not possible to distinguish the two effects. Since the first few points of the three-pulse data, highlighted by the blue shading in Fig. 7.22, must be discarded in order to interpolate the three-pulse DEER back to the zero-time to give an accurate modulation depth, the four-pulse trace was scaled along the ordinate until it matched the three-pulse data. There are slight

deviations due to ESEEM present in the three-pulse data. The scaling showed that the modulation depth of the three-pulse data is 1.16 times that for the four-pulse trace. The slightly different gradients observed between the three-pulse data and the scaled four-pulse data at the very start of the traces are likely to be a result of the small shift in t_0 seen both experimentally and in simulations of three- and four-pulse DEER data due to the use of finite pulses (see Section 7.5.2).

The modulation depth (Δ) can be an important parameter in the analysis of orientationally dependent DEER. In addition, it can an also be used to give information on the degree of labelling and number of coupled spins within a system, since it is related to the labelling efficiency, f, number of spins per nanoobject, n, and the inversion efficiency, λ, of the pulses. For a system of two coupled spins, a doubly-labelled nanoobject, $n = 2$ and:[101]

$$\Delta = f\left[1 - (1 - \lambda)^{n-1}\right] \tag{7.13}$$

In order to obtain a consistent set of measurements either for orientational analysis or for determination of the labelling efficiency or average number of coupled spins per nanoobject, the experimental set-up must be kept consistent. The modulation depth of three-pulse DEER data should not be compared directly to that of four-pulse DEER data unless the pulse powers are low, so that the detection pulse does not induce a phase shift for the pump spins. In addition, if the modulation depths of data sets collected by the same technique are to be directly compared, the data sets should be measured under the same coupling conditions and with a constant detection and pump pulse offset and at the same positions with respect to the resonator bandwidth, so that the degree of cross-excitation between the detection pulse and pump spins is constant. This applies equally to three- and four-pulse DEER. In many ways, it is more important for four-pulse data, where the presence of two detection pulses prior to the pump pulse will have a larger effect on the pump spins than the single $\frac{\pi}{2}$ detection pulse in the three-pulse methodology.

The DEER-Stitch program by Lovett et al.[106] allows for the option to either match the three-pulse data onto the four-pulse data or vice versa. When several stitched DEER traces are to be compared;

only one matching method should be used, so that the modulation depth from either the three or four-pulse DEER traces are preserved.

7.5.5 A theoretical method for correction of the dynamic phase shift in dead-time free three-pulse DEER

Calculations of the three-pulse DEER using pump pulses of equal power and equal but opposite frequency offsets of the pump frequency from the detection frequency result in traces that have equal but opposite changes in phase, while maintaining the same real DEER signal (see Fig. 7.23). Addition of these two spectra would eliminates the dynamic phase shift in the x-y plane. However, it is possible to remove the phase shift from the data within one acquisition if two pump pulses at equal but opposite frequency offsets are applied in tandem. This is shown in Fig. 7.23 and also more clearly in Fig. 7.24.

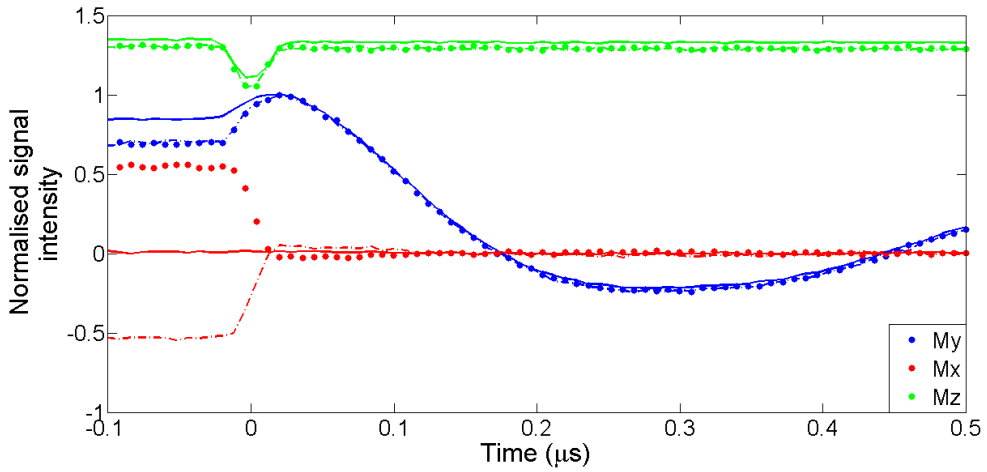


Figure 7.23: A comparison of three-pulse DEER data calculated with a 16 ns pump pulse at a frequency offset of +65 MHz (dotted lines), −65 MHz (dotted, -.-, lines) and with two coincident pump pulses each of 16 ns, one with a frequency offset of +65 MHz and the other with a frequency offset of −65 MHz (solid lines). In each case, blue lines show the real part of the DEER spectrum (M_y), red lines give the imaginary part (M_x) and green lines give the magnetization in the z-direction (M_z). The dotted and dashed lines overlap completely for the M_y and M_z components. In all cases, the phase has been chosen to minimize the imaginary component for $t > t_0$.

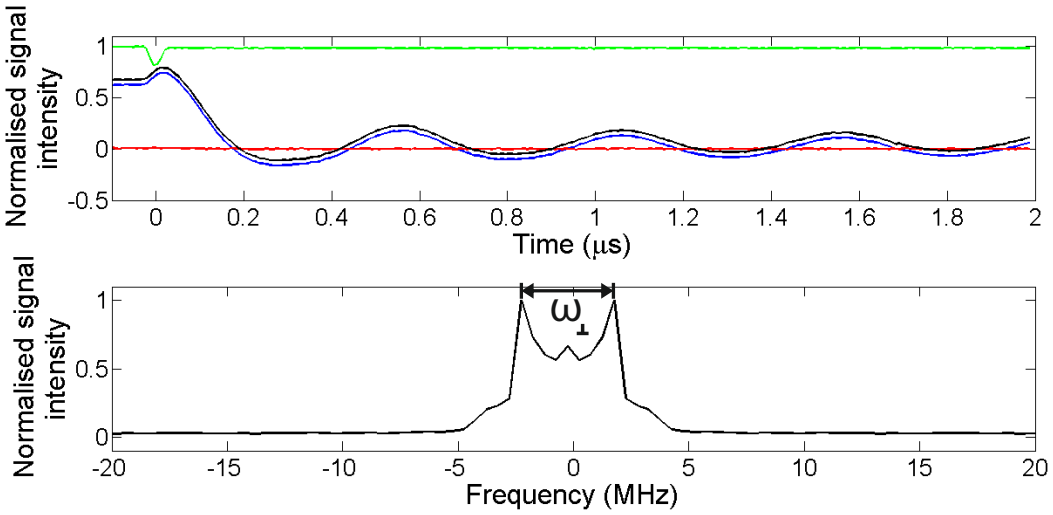


Figure 7.24: **Simulations for three-pulse DEER using two pump pulses of the same power with equal but opposite offsets from the detection frequency.** *Upper plot:* The blue trace is the real part and the red trace is the imaginary part of the signal. The phase has been chosen such that the imaginary part is minimized for $t > t_0$. The green trace is the M_z magnetization and the black trace is the absolute of the red and blue traces. The black trace is offset from the blue trace by 0.1 units for clarity. The simulation shows that use of two pump pulses of equal power and equal but opposite frequency offset from the detection frequency removes the dynamic phase shift in the x-y plane. There is still a small phase shift in the z direction which manifests as a dip in M_z at t_0 and a phase shift in the real part (and absolute) of the DEER trace. *Lower plot:* The Fourier transform of the real part of the trace. The dipolar coupling constant, $\omega_\perp = 2$ MHz, is marked.

Application of two pump pulses removes the shift in between the real and imaginary portions of the data. However, it is limited to the x-y plane and does not remove the shift in the z-direction, which also affects the total signal intensity detected in the x-y plane. When 16 ns pump pulses are used, as in Fig. 7.24, there is still a small dynamic phase shift in the z-direction, which results in a small dip in M_z at t_0, and also in a small residual phase shift in the real part of the data. The shift in the z-direction can be reduced by using a longer pump pulse, as seen in Fig. 7.25, where a 30 ns pump pulse is used.

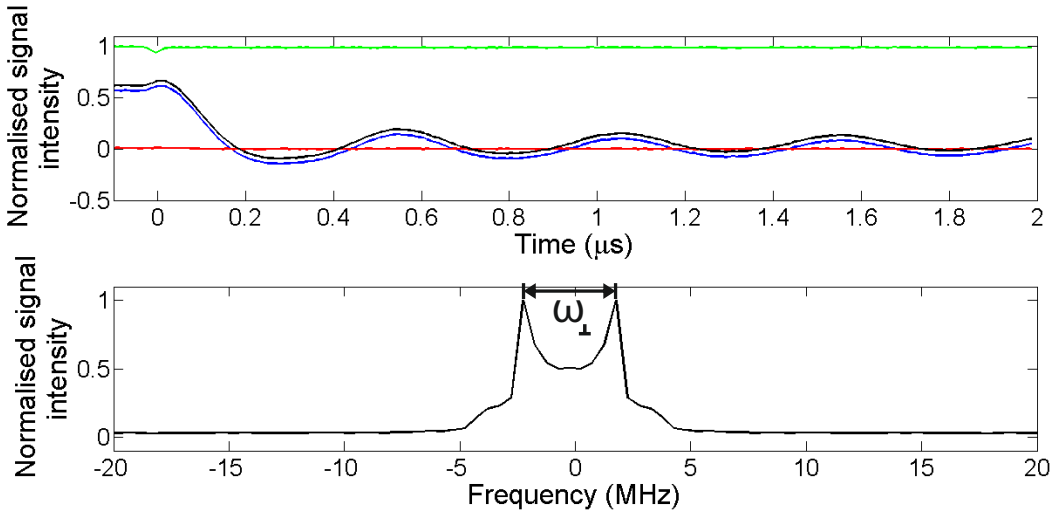


Figure 7.25: **Simulations for three-pulse DEER using two longer pump pulses (30 ns) of the same power with equal but opposite offsets from the detection frequency.** *Upper plot:* The blue trace is the real part and the red trace is the imaginary part of the signal. The phase has been chosen such that the imaginary part is minimized for $t > t_0$. The green trace is the M_z magnetization and the black trace is the absolute of the red and blue traces. The black trace is offset from the blue trace by 0.1 units for clarity. The simulation shows that use of two pump pulses of equal power and equal but opposite frequency offset from the detection frequency removes the dynamic phase shift in the x-y plane. The phase shift in the z direction seen in Fig. 7.24 is reduced through the use of a longer, lower-powered pump pulse. *Lower plot:* The Fourier transform of the real part of the trace. The dipolar coupling constant, $\omega_\perp = 2$ MHz, is marked.

Although it is apparent that direct correction of the dynamic phase shift in the x-y plane is possible theoretically, application of this correction experimentally poses several problems. In the idealized simulations the resonator bandwidth is considered to be infinite. Therefore the application of two pulses of equal strength at equal but opposite frequency offsets generates two opposing B_1 fields at the central detection frequency, which cancel one another. In a spectrometer, the resonator bandwidth is not infinite and indeed it is not even generally symmetric. Fig. 7.26 shows an experimentally measured resonator bandwidth for the MS2 resonator used for this work. Therefore, in order to apply two pulses at equal but opposite frequency offsets that have the same turning angle at the frequency at which they are applied, it may be necessary to use different pulse powers. Pulses of different powers will no longer have the same effect at the detection pulse carrier frequency and thus the effects of the pulses

at this frequency will not cancel. In order to allow the two pump pulses to cancel one another at the detection pulse carrier frequency, it may be necessary to tune pump pulses which have sub-optimal turning angles at the frequency of the pump pulses.

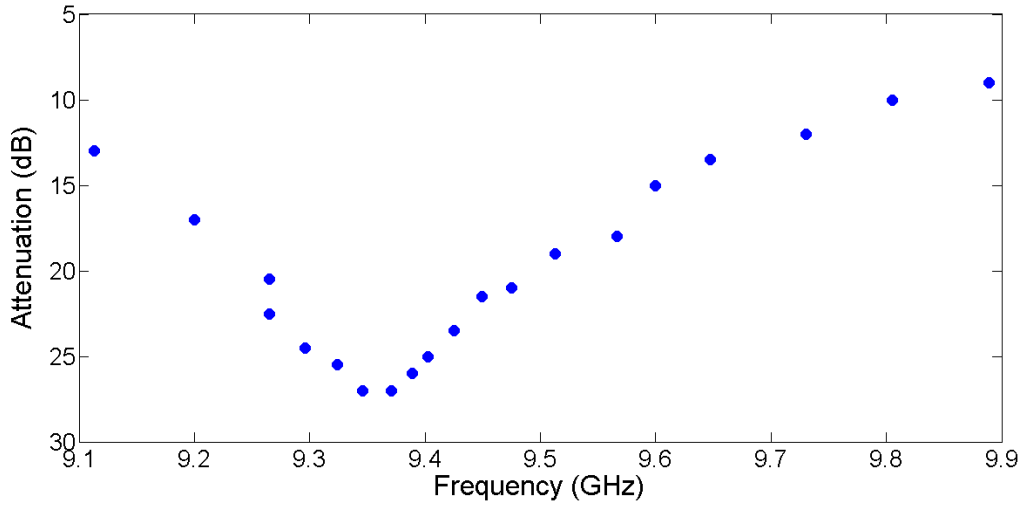


Figure 7.26: A plot of the resonator bandwidth of the MS2 resonator, measured experimentally by recording the high power attenuation (in dB) necessary to record the maximum echo intensity for a Hahn echo using 16 and 32 ns pulses with a τ value of 200 ns. (The high power attenuation is plotted on a negative axis to give the characteristic bandwidth 'dip'.)

If it is possible to tune two pump pulses such that they cancel one another at the experimental detection frequency, the experiment is still unlikely to be feasible with a single TWT, since applying three overlapping pulses is not possible within linear regime of a 1 kW TWT. It would therefore be necessary to collect two spectra with pump pulses in equal but opposite points and sum them. However, linear addition of two spectra should provide a better signal-to-noise ratio in the resultant spectra compared with dividing two spectra, as used in the phase shift correction of Milov et al.[16]

7.6 Conclusions

In this chapter, it has been shown that it is possible experimentally to record three-pulse DEER traces, which after simple manipulation, taking the absolute of the real and imaginary parts, are effectively dead-time free. This was achieved by recording spectra within the linear regime of the TWT using low-

power pulses. The use of low-power pulses also reduced the observed dynamic phase shift. Simulations using density matrix formalisms allowed further study of the source of the dynamic phase shift in three-pulse DEER and also the position of the zero-time for both three- and four-pulse DEER, which is seen to vary from an idealized value (found using delta pulses), due to the finite lengths and strengths of the pulses used.

The dynamic phase shift observed in three-pulse DEER data is a result of the cross-excitation of the detection spins by the pump pulse. The reverse effect, excitation of the pump spins by the detection pulses, results in differences in modulation depth between three- and four-pulse DEER data.

In many cases, the dynamic phase shift is most prominent in the x-y plane. For such cases, a theoretical method to correct the dynamic phase shift has been proposed, whereby two pump pulses at equal but opposite offset from the detection frequency are used. Each pulse causes its own dynamic phase shift in the x-y plane. However, the $\mathbf{B}_1$ fields are equal in magnitude, but occur in opposite directions, and thus application of the two pulses together cancels out the phase shift.

Although this method is seen to work theoretically, the asymmetry in the resonator bandwidth and also the limits of the TWT linear regime present difficulties in the applicability of this method for experiments.

It is likely that four-pulse DEER will still remain the method of choice for measuring short inter-spin distances. However, three-pulse DEER is a valuable technique for measuring longer inter-spin distances, particularly in systems where the relaxation conditions are less favourable. In the measurement of longer distances, the definition of t_0 is less important and therefore longer pulses of lower power can be used, which allow measurements to be recorded within the linear regime of the TWT amplifier. Although the dynamic phase shift in the x-y plane can be corrected by taking the absolute value, it would be possible to remove the phase shift entirely, including the component in the z-direction, using optimal control or shaped pulses, such as those frequently used in NMR. Work to use optimal control at X-band frequencies has recently been published,[207] and the next generation of commercial Bruker spectrometers will include pulse generators suitable to form shaped pulses as standard.[m]

[m] News of these spectrometers has been announced at several conferences including the 53rd Rocky Mountain Conference, July 24–28th, 2011 in Snowmass, Colorado, USA.

Chapter 8

Application of chemically induced dynamic nuclear polarization to elucidate the surface structure of equine lysozyme with oleic acid complexes

Chemically Induced Dynamic Nuclear Polarization or CIDNP (pronounced 'kidnip' or 'kidnap') uses NMR to detect non-Boltzmann populations of nuclear spins, induced by the formation of a radical pair and interaction of the electronic spin states with one another and the surrounding nuclei. This in turn causes large positive or negative enhancements in the NMR signals detected.

Although initial observations of the CIDNP effect were a fortuitous accident resulting from NMR studies of reaction mechanisms that occurred via radical intermediates,[223] the technique was later harnessed in the form of photo-CIDNP, where light induced radical formation from a flavin dye provided the unpaired electrons necessary to induce the non-Boltzmann populations in the nuclear spins.

CIDNP has been somewhat of a niche technique. Recently however, as NMR reaches a limit in terms of sensitivity due to the significant cost and difficulty to continue to progress to higher field systems (currently the limit stands at 1 GHz for proton NMR in static fields[224] and 1.3 GHz for NMR in pulsed fields[225]), there has been a renewed interest in Dynamic Nuclear Polarization (DNP) techniques including CIDNP. The enhancements seen in the NMR signals from DNP and CIDNP allow

greater signal intensity to be observed over fewer scans.

Although the names of the two techniques are similar, the mechanisms causing the observed enhancement in the NMR spectrum are different (see Section 8.1 for more detail). In addition, the experimental equipment needed is different. DNP experiments use microwave radiation to saturate an electronic transition in order to cause the necessary electronic polarization, whereas the electronic polarization in CIDNP arises form the formation of a radical pair. The signs of the enhancement observed in CIDNP therefore also afford the possibility of providing information about the state in which a radical pair is born.

In this chapter, CIDNP is used to measure the surface accessibility and environment of various amino acids present in the protein equine lysozyme, which is extracted from horse milk, when the protein occupies various native, molten-globule and complexed states. The work presented here was carried out in collaboration with Dr Ludmilla Morozova-Roche from the Department of Medical Biochemistry and Biophysics, Umeå University, Sweden. Some results from the study were collected in Sweden by Dr Morozova-Roche and her collaborators and these have been summarized in this chapter for completeness where this is the case it is indicated.

This work has been published: V. Vukojevič, A. M. Bowen, K. Wilhelm, Y. Ming, Z. Ce, J. Schleucher, P. J. Hore, L. Terenius and L. A. Morozova-Roche, *Langmuir*, 2010, **26(18)**, 14782–14787.[19] Some of the results figures in this chapter are reprinted with permission from Lipoprotein Complex of Equine Lysozyme with Oleic Acid (ELOA) Interactions with the Plasma Membrane of Live Cells; V. Vukojevič, A. M. Bowen, K. Wilhelm, Y. Ming, Z. Ce, J. Schleucher, P. J. Hore, L. Terenius and L. A. Morozova-Roche, *Langmuir*, 2010, **26(18)**, 14782–14787.[19]. Copyright © 2010 American Chemical Society.

8.1 An introduction to the theory and methods of CIDNP

The acronym CIDNP is in fact a misnomer since the mechanism of CIDNP is not the same as that found in other dynamic nuclear polarization (DNP) experiments, whereby radiation is used to excite the electrons into non-Boltzmann spin states that then couple to the surrounding nuclei inducing non-

Boltzmann spin distributions in these nuclei that are detected as enhancements in the NMR spectrum. Rather than inducing a non-Boltzmann distribution in the nuclear spin states by first inducing one in the electronic ordering, in CIDNP the enhancements are due to a radical pair formation. Under the influence of a magnetic field, a radical pair can either recombine to form the starting molecules or diffuse apart to form escape products. Certain radical pair states favour recombination over formation of the escape products and thus the recombination products are formed with non-Boltzmann nuclear spin states. A description of the theoretical basis of the photo-CIDNP mechanism, where light induces the radical pair formation, is given in the following sections (Section 8.1.1 and Section 8.1.2).

8.1.1 Radical pairs and spin chemistry

An electron, as a spin-$\frac{1}{2}$ particle, will adopt one of two spin states when placed in a magnetic field: the spin vector can have a z-axis projection of $m_s = +\frac{1}{2}$ (the higher energy, α, state) or $m_s = -\frac{1}{2}$ (the lower energy β state). When a radical pair is formed the spin states of the two electrons interact to produce one of four possible combinations of the two states. These combinations are classified with respect to the symmetry of the spin states of the two electrons. The three triplet ($|T_{0,+,-}\rangle$) states are symmetric with respect to exchange of spin wavefunctions of the two electrons forming the state and the singlet state ($|S\rangle$) is antisymmetric. For a strongly coupled system of two equivalent spins, these states can be denoted as below:[a]

$$|T_+\rangle = |\alpha_1\alpha_2\rangle \tag{8.1a}$$

$$|T_0\rangle = \frac{1}{\sqrt{2}}\left(|\alpha_1\beta_2\rangle + |\beta_1\alpha_2\rangle\right) \tag{8.1b}$$

$$|S\rangle = \frac{1}{\sqrt{2}}\left(|\alpha_1\beta_2\rangle - |\beta_1\alpha_2\rangle\right) \tag{8.1c}$$

$$|T_-\rangle = |\beta_1\beta_2\rangle \tag{8.1d}$$

[a]The full form for the $|T_0\rangle$ and $|S\rangle$ states are: $|T_0\rangle = \cos(\theta)\,|\alpha_1\beta_2\rangle + \sin(\theta)\,|\beta_1\alpha_2\rangle$ and $|S\rangle = \sin(\theta)\,|\alpha_1\beta_2\rangle - \cos(\theta)\,|\beta_1\alpha_2\rangle$, where θ determines the strength of the coupling regime and is 0 in a weak coupling regime and π in the strong coupling regime.

In the absence of an external magnetic field, all three of the triplet states are degenerate with respect to their energies. The energy ordering of the singlet and triplet states is dependent on the sign of the exchange coupling constant J. As stated in the Introduction to this thesis (Chapter 1) the exchange interaction will be comprised of both ferromagnetic an antiferromagnetic contributions (see Section 1.4.4). Frequently for a radical pair where the electrons are each associated with a different nucleus, the singlet state lies marginally lower in energy than the triplet state, corresponding to a negative value of J. The reason for this is that the singlet state corresponds more closely to a bonding interaction.[b]

When a magnetic field is applied, the three triplet states become non-degenerate with their energies due to the Zeeman interaction. This causes the $|T_+\rangle$ state to rise in energy and the $|T_-\rangle$ state to fall by equal but opposite amounts. The $|T_0\rangle$ and $|S\rangle$ states do not change energy since they both have a total spin angular momentum quantum number (M_S) of zero and thus do not exhibit a Zeeman interaction. The separation in energy of the triplet states is dependent on the strength of the magnetic field applied. For a 600 MHz NMR spectrometer such as that used in for the CIDNP results in this thesis the magnetic field strength is c. 14.1 Tesla. This means that the $|T_+\rangle$ and $|T_-\rangle$ states are of such a different energy to the $|T_0\rangle$ state that interconversion between the three triplet states is no longer possible. In comparison, the energy gap between the $|T_0\rangle$ and $|S\rangle$ states is small and thus these electronic states are able to inter-convert, provided that the two electrons forming the states have different Larmor precession frequencies.[226]

8.1.2 The radical pair process in biological photo-CIDNP

In biological photo-CIDNP a laser is used to photochemically excite a photosensitizer, frequently an aromatic flavin molecule, promoting one of its valence electrons into a higher energy orbital resulting in a molecule with two unpaired electrons. Initially this is formed in the singlet state as spin flips with electronic excitations are forbidden by the electronic selection rules. The singlet state can quickly

[b]Since electrons are fermions, a bonding pair of electrons will have a spatial wave function that is symmetric with respect to electronic exchange and hence only the anti-symmetric spin configuration is allowed. This fulfils the overall requirement for the Hamiltonian of two fermions to be anti-symmetric.

undergo inter-system crossing to the triplet state. Certain aromatic amino acids; tryptophan, tyrosine and histidine, are of a suitable structure to either accept a proton from the excited photosensitizer to form a spin correlated radical pair via hydrogen abstraction, as is the case for tyrosine and histidine. Alternatively tryptophan residues have occupied orbitals that are of a suitable energy to donate an electron into the lower singly occupied molecular orbital (SOMO) on the flavin forming a spin correlated radical pair via electron transfer, as shown in Fig. 8.2. It is usually assumed that electron transfer takes place to the triplet state; however, there is some evidence that this is not always the case for intra-protein electron transfer.[227]

The rate of singlet-triplet interconversion is dependent on the hyperfine coupling constants of the electrons to the nuclei of the molecule to which they belong. The reason for this dependence stems from the coupling of the electron to both the α or β nuclear spin states of surrounding nuclei causing a splitting in the energy levels of the electrons and thus in the electron resonant frequencies. As the frequency of $|T_0\rangle$ to $|S\rangle$ interconversion is dependent on the difference in the electron resonant frequencies of the two unpaired electrons, it therefore also depends on the hyperfine coupling to the nuclei. The result is that some nuclear spin states lead to faster intersystem crossing than others. Since the CIDNP experiment occurs over a fixed timescale some interconversions will lead to a larger proportion of the singlet state than others.

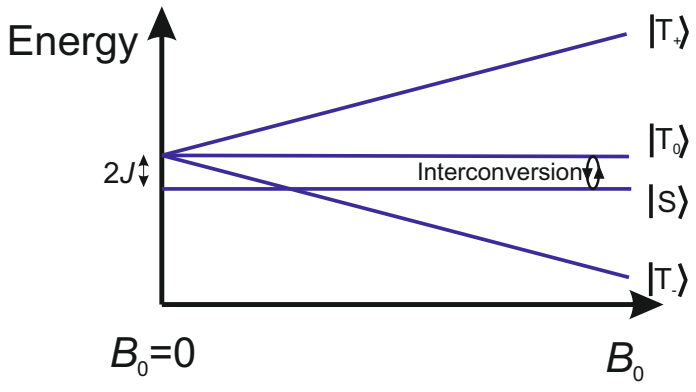


Figure 8.1: Schematic to show the dependence of the energy levels of the radical pair states on the strength of an external magnetic field, B_0. The size of the energy splitting between the levels $|T_0\rangle$ and $|S\rangle$ is dependent on the exchange coupling constant, J. The interconversion between the $|T_0\rangle$ and $|S\rangle$ levels which occurs during the CIDNP experiment is marked.

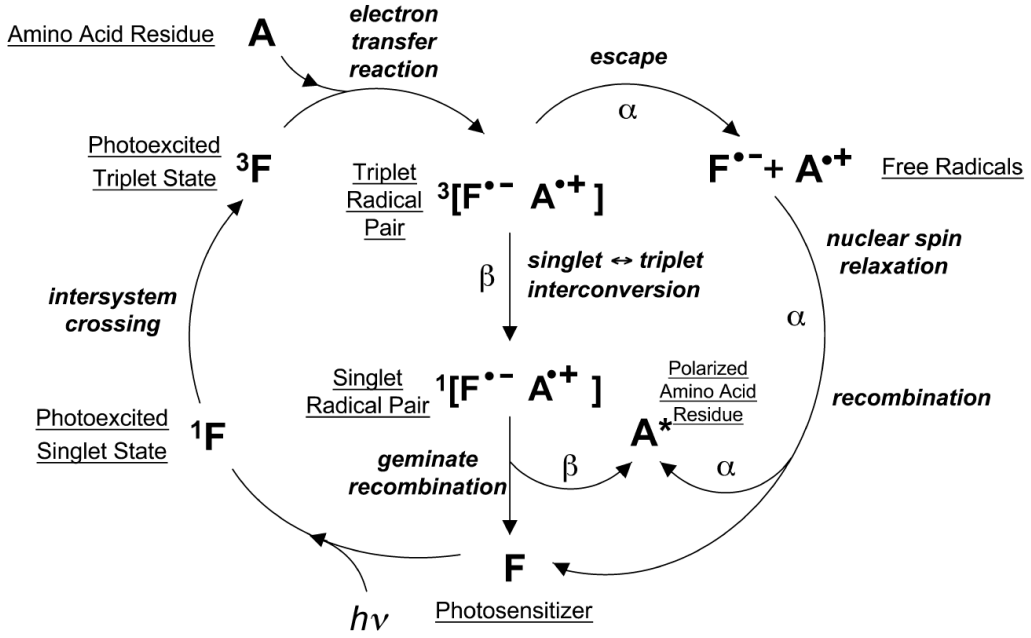


Figure 8.2: Pictorial representation of the radical pair process involved in CIDNP. **F** is the flavin, **A** is the amino acid and a spin correlated radical pair is shown in square brackets. The underlined text describes the different chemical species involved in the cycle and bold text indicates physical processes occurring. This figure is reprinted from *Methods*, **34(1)**, K. H. Mok and P. J. Hore, Photo-CIDNP NMR methods for studying protein folding, 75–87. Copyright © 2004, with permission from Elsevier.[17] After a figure in *Progress in NMR Spectroscopy*, **25(4)**, P. J. Hore and R. W. Broadhurst, Photo-CIDNP of biopolymers, 345–402. Copyright © 1993.[18]

The singlet state may then undergo back electron transfer (recombination), leading to the regeneration of the original amino acid with a non-Boltzmann nuclear spin state distribution. Under favourable tumbling conditions, so that the rotational correlation time does not lie within the range where modulations of the nuclear coupling due to rotation cause fast relaxation of the spin states back to equilibrium Boltzmann states, an enhancement is seen in the NMR spectrum.[228]

In cases where a higher population of the $|T_0\rangle$ state exists, the formation of the escape products is favoured. This would theoretically lead to a polarization of opposite phase to that of the recombination product. As can be seen in Fig. 8.2, where a pictorial representation of the radical pair process involved in CIDNP is given, in this case the geminate and escape products are the same. However, as the nuclear spin relaxation time is much faster in the paramagnetic free radicals than in any non-radical species,

since on average the escape products take longer to form than the geminate recombination products, very little nuclear polarization is observed from the escape products. Therefore there is very little cancellation effect of the geminate product signal even if the reaction process is cyclic.

In reality the reaction scheme is not perfectly cyclic since each laser flash results in a small amount of the flavin present being reduced (photo-bleached) limiting the number of laser flashes that can be applied to each sample.

The sign of the NMR enhancement

The sign of the NMR enhancement observed in the CIDNP spectrum can be predicted using Kaptein's sign rules, which are described by the equation below:[228,229]

$$\Gamma_i = \mu.\epsilon.\Delta g.a_i \tag{8.2}$$

The key to the symbols used in Equation 8.2 is given in Table 8.1.

Table 8.1: The key for Kaptein's sign rules.

Symbol	+	−
Γ_i	Absorpative enhancement	Emissive enhancement
μ	Triplet precursor	Singlet precursor
ϵ	Recombination product	Escape product
Δg	$g_F > g_A$	$g_F < g_A$
a_i	Positive hyperfine coupling constant	Negative hyperfine coupling constant

8.1.3 Representative CIDNP data

Although the chemical shifts of the nuclei in amino acids are dependent on the surrounding matrix (either protein structure or solution), provided that the radical pair causing the CIDNP enhancement is formed in the same state the signs of the CIDNP enhancements will not change.

In the case of the experiments performed here, the radical formation occurs via reaction with a photoexcited flavin dye and thus the mechanism of radical formation is not dependent on the envi-

ronment of the amino acid. For this reason, CIDNP enhancements observed from a solution of the N-acetyl form of the amino acids that form a radical pair with the flavin are very useful as benchmarks with which to compare CIDNP enhancements from proteins and can help with in the identification of the specific amino acids responsible for individual CIDNP signals in the protein spectrum.

For representative purposes, the light, dark and difference (light-dark) ^{1}H-NMR detected photo-CIDNP spectra are given in Fig. 8.3 for the three amino acids known to interact with the photosensitizer Flavin MonoNucleotide (FMN): tyrosine, tryptophan and histidine.

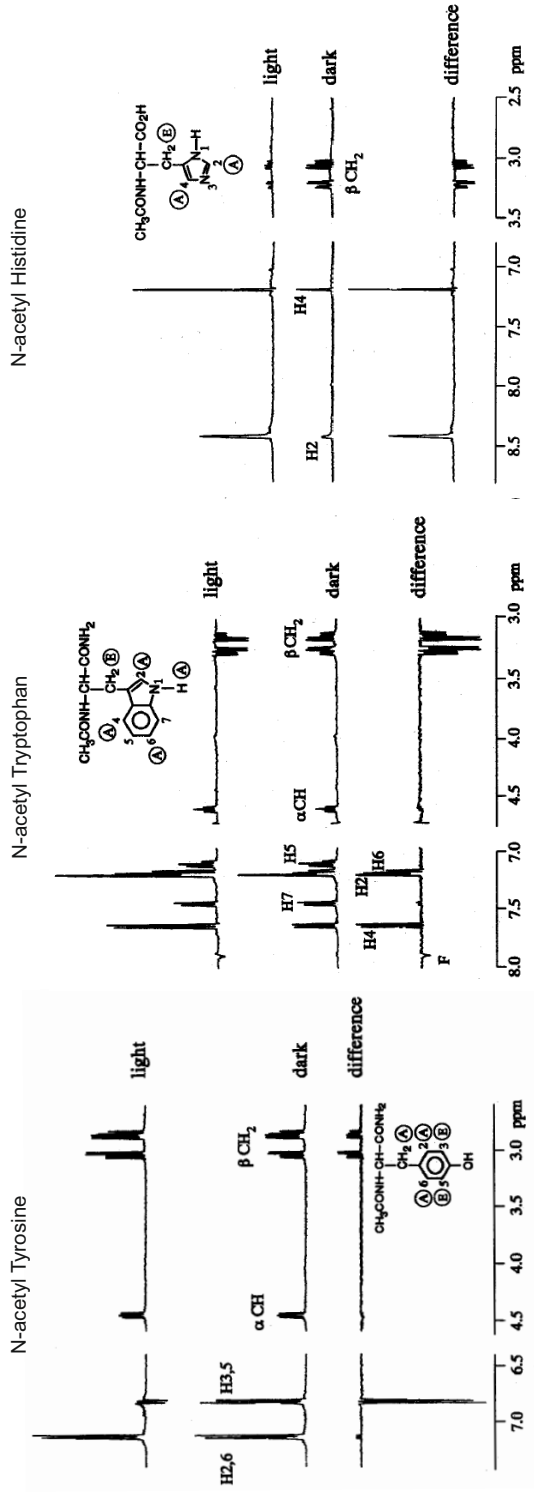


Figure 8.3: Representative ^{1}H-NMR detected photo-CIDNP for solution state N-acetyl tyrosine, tryptophan and histidine. This figure is adapted and reprinted from *Progress in NMR Spectroscopy*, **25(4)**, P. J. Hore and R. W. Broadhurst, Photo-CIDNP of biopolymers, 345–402. Copyright © 1993, with permission from Elsevier.[18]

8.2 A brief review equine lysozyme complexes with oleic acid (ELOA) as a model system and other related complexes

Protein aggregates form from unfolded or partially folded proteins due to hydrophobic interactions.[230] Many protein aggregates are associated with diseases, in particular, neurodegenerative and age-related diseases.[230] For example, amyloid oligomeric assemblies are known to lead to the death and dysfunction of neuronal cells in Alzheimer's and Parkinson's diseases.[231,232]

Although it is the formation of large fibrils which is commonly observed under disease conditions, there is mounting evidence to suggest that it is in fact early-stage aggregates of protein and lipoprotein oligomers which are responsible for cytotoxicity and cell death.[231,232] Although cytotoxicity in healthy cells in undesirable, when cells become diseased or multiply too rapidly, as is the case with many forms of cancer, harnessing the cytotoxicity of early protein aggregates becomes an attractive potential method of destroying such cells.

HAMLET (human α-lactalbumin made lethal to tumour cells) is a small aggregate of human α-lactalbumin with oleic acid, which occurs naturally in human milk and has been shown to induce cell death in cancerous cells via an apoptosis-like mechanism.[233] Although the original discovery was somewhat serendipitous, HAMLET has since been prepared in the laboratory by removal of the bound Ca^{2+} ion from human α-lactalbumin followed by complexation with oleic acid [$CH_3(CH_2)_7CH{=}CH(CH_2)_7COOH$].[234] The complex is now well characterized and is believed to form a state with some similarities to that of the molten-globule state formed by the apo-protein at low pH,[235] with approximately 5 oleic acid molecules per protein.[236] HAMLET has a very different cytotoxic activity to the proteinaceous compound alone. The unfolded protein alone does not show any cytotoxicity,[237] whereas protein modified to be non-native and inactive, by removal of cysteines involved in disulphide bonding in the native fold, will also form cytotoxic aggregates with oleic acid.[238] Further studies have also shown that for human α-lactalbumin, the cytotoxic properties are also specific to oleic acid.[239]

In addition to demonstrating the cytotoxic nature of HAMLET towards tumour cells *in-vitro*, three

in-vivo studies have also been published. The first showed that HAMLET was able to induce apoptosis in human glioblastoma cells in the brains of nude rats, but not in the surrounding healthy tissue.[240] Furthermore, topical application of HAMLET to skin papillomas resistant to conventional treatments in human patients was seen to have beneficial and lasting effects by reducing the size of lesions by 75% or more.[241] Finally, intravesical HAMLET treatment has been seen to rapidly reduce the size of human bladder cancer in mice affecting only the tumour tissue but not the adjacent healthy tissue.[242]

A similar complex has also been formed with bovine α-lactalbumin and oleic acid, BAMLET (bovine α-lactalbumin made lethal to tumour cells), which has also been shown to display similar cytotoxicity to HAMLET.[237] However, unlike human α-lactalbumin, bovine α-lactalbumin also forms aggregates with linoleic acid and steric acid. Furthermore, the linoleic acid aggregate also shows cytotoxic properties.[243]

Both human α-lactalbumin and bovine α-lactlabumin form molten-globule states at low pH. NMR and CIDNP experiments have shown significant changes in the solvent accessibility of protein side chains between the native folds and the molten-globule states.[244,245] However, there are some similarities between the molten-globule state, an apo-state without Ca^{2+} bound and a partially denatured state in 2.0 M guanidine chloride.[245] This illustrates the disordered nature of the molten-globule state, which is a precursor to the formation of the HAMLET and BAMLET aggregates.[234]

A third similar complex is formed between equine lysozyme, a protein found in horse milk, and oleic acid (referred to as ELOA); it is this complex that is used in this study. ELOA consists of c. 4–30 lysozyme molecules, each of which can bind anywhere from 11–48 molecules of oleic acid, considerably more than either HAMLET or BAMLET.[246] It has also been shown that the oleic acid bound in ELOA complexes is in equilibrium with free oleic acid and tends to dissociate at low concentrations.[247]

Although ELOA bears some structural similarities to HAMLET and BAMLET, and shares their cytotoxic properties, it also exhibits properties akin to those of the larger amyloid oligomers.[248] ELOA can bind the amyloid-marker thioflavin-T and forms ring shaped assemblies similar in appearance to the Aβ and α-synuclein oligomers observed in patients with Alzheimer's and Parkinson's diseases respectively.[249] Experiments have been attempted to form larger amyloid oligomers from HAMLET.

However, thus far it has proved impossible to do so.[250]

It is therefore believed that ELOA can be used as a model system, linking the two types of cytotoxic proteinaceous species.[246] It is hoped that by understanding the ELOA induced cell-toxicity better, light may be shed on the cell-toxicity of both small HAMLET and BAMLET-like complexes and larger amyloid assemblies.

8.2.1 Existing literature on the interaction of oleic acid complexes with cells and membranes

Although the role of complexes such as HAMLET, BAMLET and ELOA in cell apoptosis is now recognized, the molecular mechanisms of interaction between the complex and the surface of the cell are still not fully understood.[232]

Fluorescence measurements have shown that HAMLET can selectively enter tumour cells and then accumulates in the cell nuclei before inducing apoptosis. Furthermore, it has been possible to identify the histones (H3, H4 and H2B) as targets for HAMLET, where the binding of HAMLET to these proteins impairs their deposition on DNA and perturbs the chromatin structure, preventing transcription, translation and replication from occurring thus leading to cell death.[251] This is an additional mechanism of cell death to the apoptosis reported previously, which involves mitochondria.[252] The presence of multiple mechanisms helps to explain why HAMLET is cytotoxic to many different types of cancer cell.

In order for the HAMLET to enter the cell, it must penetrate the phospholipid bilayer forming the cell membrane. A study looking at the interaction of human α-lactalbumin and HAMLET with cell membranes, showed that HAMLET was able to bind to phospholipid bilayers at physiological pH.[253] However, native state α-lactalbumin did not show any interactions with the membranes and molten-globule α-lactalbumin[c] showed a much smaller affinity.[253] In addition, HAMLET accumulated in the membrane, perturbing the membrane structure, and resulting in increased membrane fluidity.[253] It has been hypothesized that the binding of partially unfolded proteins to membranes is driven

[c]Molten-globule α-lactalbumin was formed using a mutant, where all the cysteine residues forming structural disulphide bonds in the native fold have been replaced by alanine residues.

thermodynamically by access to partially folded intermediates.[253]

In comparison, fluorescence experiments investigating the interaction of BAMLET with cancer cells showed rapid translocation of the BAMLET to the endolysosomal compartment and very little nuclear uptake was observed.[254] The BAMLET induced an early leakage of lysosomal cathepsins (proteases) into the cytoplasmic matrix leading to apoptosis.[254]

Initial fluorescence studies of the interaction of ELOA with cells showed that an accumulation of ELOA on the cell membrane preceded ELOA apoptosis and thus it was hypothesized that the interaction of ELOA with the cell membrane triggers apoptosis.[246] Further studies of the interaction of ELOA with lipid vesicles have shown a considerable structural change on the binding of ELOA to the lipid membrane, characterized by a red shift in the fluorescence spectrum.[247] This has been interpreted as an increase in the solvent accessibility of tryptophan residues within the ELOA upon interaction of the ELOA with the membrane.[247] Furthermore, when ELOA is not complexed with a membrane, a blue shift in the fluorescence maxima, compared to native state equine lysozyme, is indicative of tryptophan residues being constrained within the molten-globule.[247] Nuclear Overhauser Enhancements (NOEs) measured by NMR spectroscopy have indicated interactions of aromatic residues within the equine lysozyme with the oleic acid in the complex.[246]

It has therefore been hypothesized that interaction of the ELOA with phospholipid vesicles may disrupt the interaction of the equine lysozyme with the oleic acid and thus allow the tryptophans to adopt a more native-like fold.[247] In combination with the knowledge that free oleic acid exists in equilibrium with the bound form in ELOA, it has been hypothesized that ELOA may facilitate transport of oleic acid to the membrane in a cargo off-loading mechanism.[247]

The experiments included in this chapter were devised to further probe the interaction of ELOA with plasma membranes. In particular, CIDNP was chosen as a direct probe for the solvent accessibility of tryptophan residues within the native state of equine lysozyme, the molten-globule state of the protein and ELOA.

8.2.2 Previous NMR studies of equine lysozyme and ELOA

The ^{1}H resonances have been assigned for 125 of the 129 residues in equine lysozyme in the native state.[20] In order to make these assignments it was necessary to use an array of two-dimensional NMR techniques, including COSY,[255] NOESY,[40,256] and TOCSY.[257,258] Assignments were made using samples of concentrations 1 to 5 mM, prepared at pH 4.5, with 10 mM $CaCl_2$ used to provide the Ca^{2+} that binds to the equine lysozyme. Dioxane was added to these samples to be used as a chemical shift standard, and NMR measurements were recorded at 35 °C.[20] In the same study hydrogen exchange NMR experiments were used to probe the dynamics of the protein and solvent accessibility of specific residues.[20]

Preliminary NMR measurements on the ELOA complex have also been conducted as part of a previous study.[247] These measurements allowed the ratio of equine lysozyme to oleic acid in the samples to be determined.[247] These NMR measurements of ELOA used samples with much lower protein concentrations, compared to those used in the NMR study of the native state equine lysozyme, of c. 50 μM prepared in 10 mM Tris.[247]

The observed chemical shifts for amino acids in proteins are dependent on the state of the protein, which in turn is dependent upon the conditions in which the protein sample is prepared. For this reason, in order to use the ^{1}H assignments determined previously in the analysis of NMR and CIDNP data from this study, it was necessary to record NMR and CIDNP experiments under conditions similar to those used in the assignment experiments.[20]

8.3 Experiments conducted on the equine lysozyme oleic acid complex (ELOA): experimental procedure and theory

In order to probe the cell-toxicity of ELOA, the interaction of fluorescently labelled ELOA complexes with live cells was monitored in real time, using confocal laser scanning microscopy and fluorescence correlation spectroscopy (FCS). Furthermore, in an attempt to identify possible sites of interaction on the ELOA surface, a combination of NMR and photo-CIDNP experiments were used to monitor the

surface accessibility of the aromatic amino acid side chains of histidine, tyrosine and tryptophan.

The experiments in this chapter were conducted in collaboration with Dr Ludmilla Morozova-Roche. CIDNP and NMR experiments were performed in Oxford and the production and characterization of protein and all the fluorescence experiments were carried out by Dr Ludmilla Morozova-Roche and her collaborators at Umeå in Sweden. Although the protein characterization and fluorescence experiments are summarized in this chapter, full details are given in Appendix L.

8.3.1 Production and characterization of ELOA complexes

ELOA was produced in a controlled manner by partial, oleic acid-induced protein unfolding at the solid-liquid interface in a chromatographic column; cell toxicity was then assayed.[246] Individual, round-shaped ELOA complexes were visualized and characterized by atomic force microscopy (AFM); the distribution of different sizes of ELOA complex present in the samples is shown in Fig. 8.4.

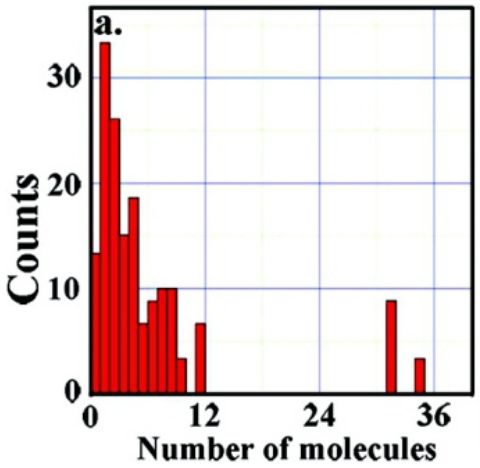


Figure 8.4: Distribution of equine lysozyme molecules contained in ELOA oligomers derived from AFM measurements of particle volumes. This figure is reprinted with permission from Lipoprotein Complex of Equine Lysozyme with Oleic Acid (ELOA) Interactions with the Plasma Membrane of Live Cells; V. Vukojevič, A. M. Bowen, K. Wilhelm, Y. Ming, Z. Ce, J. Schleucher, P. J. Hore, L. Terenius, and L. A. Morozova-Roche, *Langmuir*, 2010, **26(18)**, 14782–14787. Copyright © 2010 American Chemical Society.[19]

The size of ELOA complexes decreased upon dilution. At low concentrations (< 1.5 μM), ELOA is predominantly present in the form of low molecular weight complexes, monomers to pentameters, with

some larger aggregates also present in a lower quantity. This is important as the rotational correlation tumbling time of large complexes is generally too slow to average out the anisotropic interactions in solution state NMR, resulting in broad NMR lines and very complex spectra. Therefore, in order to measure distinct NMR transitions it is important to have a sample containing predominantly smaller complexes with lower molecular weights and faster rotational correlation times.

Fluorescence Correlation Spectroscopic analysis revealed that the average residence time of the fluorescently labelled ELOA complex in the observation volume element is shorter for ELOA complexes ($\tau_D^{\mathrm{ELOA}} = 120 \pm 20$ μs) compared to the standard Rhodamine 6G ($\tau_D^{\mathrm{Rh6G}} = 35 \pm 3$ μs). The average residence time reflects the diffusion properties of the investigated molecules. Hence the molecular weight of labelled ELOA could be estimated from the average residence time of ELOA as compared to the residence time of the reference fluorescent dye.[259]

$$\frac{\tau_D^{\mathrm{ELOA}}}{\tau_D^{\mathrm{Rh6G}}} = \left(\frac{M_{\mathrm{ELOA}}}{M_{\mathrm{Rh6G}}}\right)^{\frac{1}{3}} \tag{8.3}$$

A derivation of this formula is given in Appendix L. The molecular weight for an equine lysozyme monomer is 14.7 kDa, compared to the estimated value of the molecular weight of ELOA complexes (M_{ELOA}) for low concentration solutions (< 1.5 μM), which is is 20–30 kDa. This provides further evidence that ELOA is predominantly present as low molecular weight complexes under these conditions. This is in agreement with previously reported Atomic Force Microscopy and NMR experiments performed on the complex.[247] For the experiments conducted in this study the most populated states of the ELOA complex contained on average 1–5 protein molecules.

The number of oleic acid molecules per equine lysozyme was also measured using NMR spectra recorded at high, near-mM, concentrations. This is achieved by comparing the relative sizes of oleic acid and protein signals in the spectra. The average number of oleic acid molecules bound per molecule of equine lysozyme was found to be 16. At lower concentrations, a fraction of oleic acid dissociates from the complex, yielding a reduced number of oleic acid molecules bound to each equine lysozyme molecule.[247]

8.3.2 Fluorescence imaging and fluorescence correlation spectroscopy

The fluorescent label Alexa Fluor 488 was attached to equine lysozyme both alone and in complex with oleic acid, following the prescribed procedure. In addition, the plasma membrane of PC12 cells, from rat adrenal pheochromocytoma, was visualized using the lipophilic carbocyanine dye $DiIC_{18}(5)$. The Alexa Fluor 488 label gives rise to a green fluorescence and the $DiIC_{18}(5)$ fluoresces in the red region of the visible spectrum. It was therefore possible to conduct both double and single colour fluorescence studies.

Two types of fluorescence measurement were taken: avalanche photodiode (APD) imaging and fluorescence correlation spectroscopy (FCS). These experiments allowed the interaction of ELOA with PC12 cells to be studied. Details on the methodology of these measurements is given in Appendix L.

8.3.3 NMR and CIDNP experimental setup

NMR measurements were carried out on a 600 MHz (14.1 T) Varian INOVA NMR spectrometer with a triple-resonance (^{1}H, ^{13}C, ^{15}N) 5 mm probe.

In addition, the photo-CIDNP experimental set-up used a Spectra Physics BeamLok 2080 argon ion laser operating in multiline mode (488/514 nm), with 7 W output power to cause photoexcitation and radical pair formation. The illumination was gated with an NM Laser Products LS200 mechanical shutter, controlled by the spectrometer. A laser flash length of 80 ms was found to strike a good balance between the size of the CIDNP enhancements observed and the rate of bleaching of the sample.[260] The laser beam is focused into a fibre optic, which is fed into the bore of the NMR spectrometer and positioned within the sample using an internal calibration NMR co-axial insert from Wilmad (WGS-5BL 5mm). The insert is positioned so that the tip of the fibre optic lies 2 mm above the coil region of the probe. This position allows the region of the sample within the NMR detection coils to be exposed to the laser flash, without the fibre optic tip causing too much field inhomogeneity within the sample that is detected. This apparatus is illustrated in Fig. 8.5.[17]

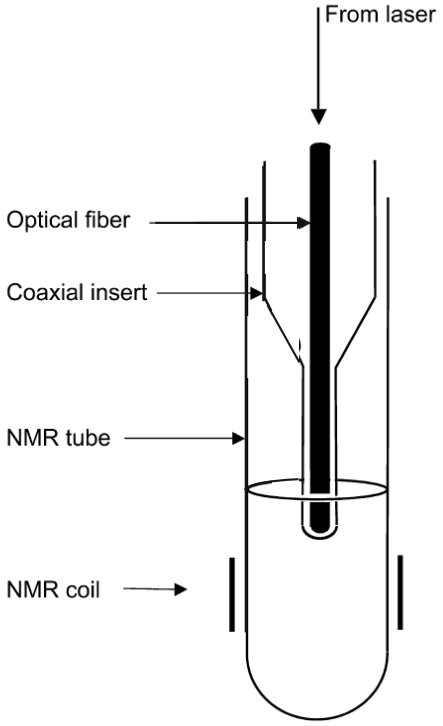


Figure 8.5: A diagram of the fibre optic insert used to direct the laser light into the sample while in the NMR bore. This figure is adapted and reprinted from *Methods*, **34(1)**, K. H. Mok and P. J. Hore, Photo-CIDNP NMR methods for studying protein folding, 75–87. Copyright © 2004, with permission from Elsevier.[17]

The CIDNP ^{1}H NMR pulse sequence

The pulse sequence used for ^{1}H NMR detection of CIDNP results is given in Fig.8.6. It includes an initial multiple pulse train to pre-saturate and suppress the NMR spectrum. This is followed by a laser flash (the shutter of the laser is controlled by the NMR console) and finally a Double Pulsed Field Gradient Spin-Echo Excitation (DPFGSE) solvent suppression sequence,[261] before the free induction decay (FID) is is detected and Fourier transformed to give the spectra in the frequency domain.

An initial delay time of 30 s (D1 in Fig. 8.6) was used to prevent localized heating in the sample from the laser light flash. The laser pulse length was 80 ms, and tuning the radio frequency pulses found that, for a $\frac{\pi}{2}$ pulse, 6.5 μs was optimal.

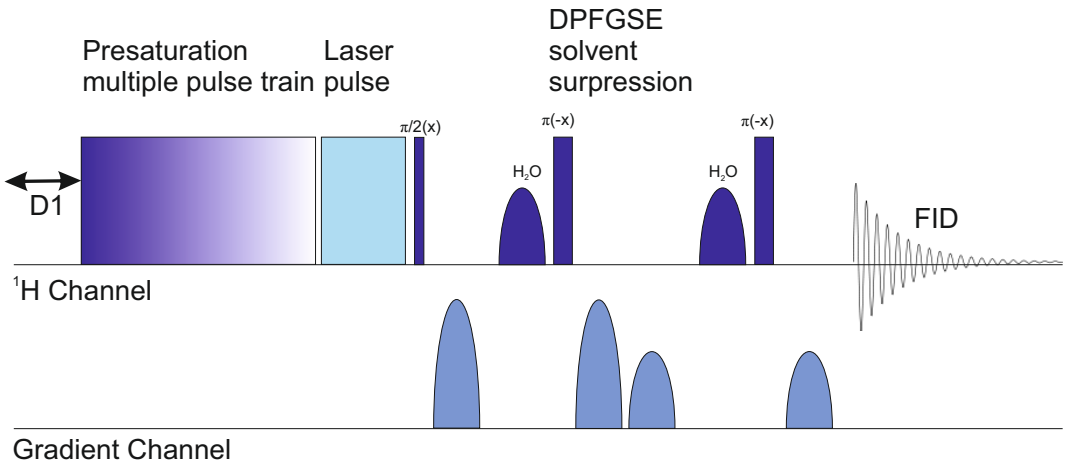


Figure 8.6: The pulse sequence used for the acquisition of ^{1}H CIDNP data, spectra are recorded both with ('light') and without ('dark') the initial laser flash so that 'light'−'dark' spectra, or difference spectra, can be calculated, which show purely the CIDNP enhancement signals. The DPFGSE sequence is used to suppress the solvent signal and to excite the FID signal.[261] This sequence requires both hard, non-selective, proton pulses (rectangular ^{1}H channel pulses) and proton pulses selective to the water signal (rounded ^{1}H channel pulses). Strong gradient fields (pulses in the gradient channel) are applied to encode the transverse magnetization and to dephase the solvent signal.

Suppression of the NMR spectrum is not complete. For this reason, spectra are collected both under 'light' (with the laser flash) and 'dark' (without the laser flash) conditions. Light-minus-dark difference spectra are free from the NMR signals that have no CIDNP enhancements; these are referred to as CIDNP spectra. For both the light and dark spectra 16 scans were recorded.

Although the samples were prepared in D_2O, DPFGSE solvent suppression was used at the resonance frequency of HDO to remove any residual solvent signal from the spectra.[d] The DPFGSE sequence uses an initial broadband $\frac{\pi}{2}$ pulse to generate transverse magnetization, before a strong field gradient, which phase encodes the transverse magnetization. The H_2O resonance is next selectively excited using a π, followed by a hard, non-selective, π pulse is used to excite the whole system. The following strong field gradients add to the dephasing of the solvent signal. A second gradient echo and non-selective π pulse are applied to complete the dephasing of the solvent signal and care is taken not to refocus the effects of the previous set of gradient pulses.[261,262] All components of the spectrum that

[d] In D_2O, solvent exchange of hydrogen and deuterium causes HDO to be the second most common water species ahead of H_2O.

are not excited by the selective π pulses are refocused by the gradient echoes to give an NMR spectrum where the solvent signal is suppressed.NMR spectra without the laser flash and the NMR suppressing pulse train were also collected.

NMR and CIDNP sample preparation

For both the NMR and CIDNP experiments presented in this chapter, ELOA and equine lysozyme samples were prepared at a protein concentration of 0.4 mM in D_2O. The use of D_2O reduced the size of the residual proton signal from the solvent, allowing a higher receiver gain to be used and increasing the sensitivity of the measurement.

The reaction scheme in Fig. 8.2 shows that a photosensitizer is required in order to generate a radical pair in the photo-CIDNP experiment. As neither equine lysozyme nor oleic acid have the correct photochemical properties to fulfil this role, it is necessary to add the photosensitizer Flavin MonoNucleotide (FMN) to solutions of the proteins. Samples for use in CIDNP experiments were therefore prepared with a 0.2 mM concentration of FMN. The structure of FMN is shown in Fig. 8.7.

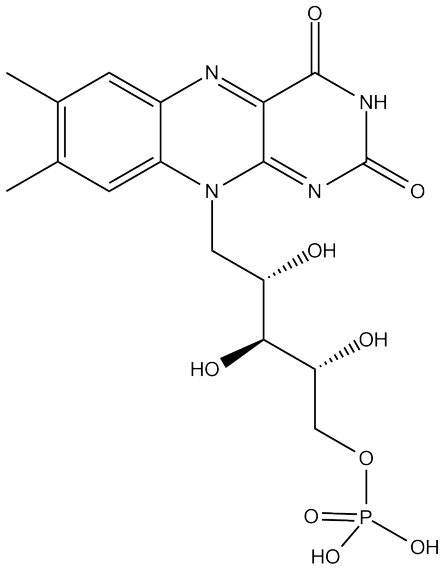


Figure 8.7: The chemical structure of the photosensitizer Flavin MonoNucleotide (FMN).

Furthermore, since the photochemical reaction occurring during a CIDNP experiment is not completely cyclic, as reduction occurs; 10 mM H_2O_2 was included in the CIDNP samples to re-oxidize photo-reduced flavin.[260] Both NMR and CIDNP samples were prepared with 20 mM dioxane. This is used as an internal chemical shift reference (3.73 ppm) during the analysis of the NMR spectra.[263]

Previous NMR studies of equine lysozyme and ELOA have used protein concentrations of 5 mM and 0.05 mM respectively (see Section 8.2.2). For the CIDNP experiments and the associated NMR carried out in this study, an intermediate protein concentration of 0.4 mM was chosen for the samples. This allowed CIDNP data with a sufficient signal-to-noise ratio to be collected in the limited number of scans procurable before the flavin sensitizer became bleached. Also, this concentration was sufficiently low that the dominant ELOA species were of low molecular weight and thus the degree of formation of large protein aggregates was low. The presence of large protein aggregates would cause spectral broadening of the NMR signals, which could hamper data interpretation.

Since ^{1}H resonances for amino acids in proteins are known to be dependent on sample conditions, NMR and CIDNP experiments were performed on equine lysozyme samples in the native state, at pH 4.5, 6.9 and 9.0, and molten-globule state, at pH 2. In these samples, the pH was adjusted using DCl and NaOD solutions. Measurements were also recorded for ELOA solution, which was buffered to pH 9 using sodium phosphate in D_2O. $CaCO_3$ was added to the native state protein solutions, at a concentration of 1 mM, to ensure correct folding of the holo structure. It was not added to the molten-globule or ELOA samples, for which Ca^{2+} binding is known to be less important.[20,246]

NMR and CIDNP spectra of the molten-globule at pH 2.0, ELOA buffered to pH 9.0, and native state at pH 9.0, were recorded at 20 °C. An additional three sets of spectra of the native state, at pH 4.5, 6.9 and 9.0, were obtained at 37 °C. The spectrum recorded at 37 °C and pH 4.5 is comparable to the conditions at which the ^{1}H assignments were made allowing for identification of the residues responsible for CIDNP enhancements in this spectrum.

Analysis of NMR spectra

A previous study has used NMR to characterize the native and A-state (the partially folded moleten globule state found to be stable at low pH values c. pH 2) [264,265] of equine lysozyme and resulted in the assignment of the ^{1}H NMR resonances for the native state. [20] In combination with the representative CIDNP spectra presented in Section 8.1.3, the ^{1}H NMR assignments from this study were used to aid in the identification of residues responsible for enhanced signals in the CIDNP spectrum.

NMR and CIDNP data was processed using ACD 1D Processor and Specmanager. [266] This program also allowed the subtraction of the spectra from CIDNP experiments recorded under 'light' and 'dark' conditions, to give the resultant CIDNP spectra.

8.4 Experiments conducted on the equine lysozyme oleic acid complex (ELOA): experimental results, analysis and discussion

CIDNP and NMR experiments were performed in Oxford and fluorescence experiments were carried out by Dr Ludmilla Morozova-Roche and her collaborators at Umeå in Sweden. The fluorescence work was therefore not directly carried out as part of this thesis. However, the results are summarized below in support of the CIDNP data. Further details on the fluorescent experiments and their results are given in Appendix L.

8.4.1 Summary of the results from fluorescence experiments

The fluorescence experiments studied the interaction of ELOA with the plasma membrane of PC12 cells. Three different scenarios were studied: the interaction of fluorescently labelled ELOA with unlabelled PC12 cells, the interaction of unlabelled ELOA with fluorescently labelled PC12 cells and the interaction of labelled ELOA with labelled PC12 cells. A summary of the results is given below; the results are presented in more detail in Appendix L.

ELOA was labelled with the fluorescent dye Alexa Flour 488. Observing the interaction of this labelled complex with PC12 cells, using fluorescence imaging, showed that ELOA initially accumulated

on the plasma membrane for c. 60 minutes before the cell membrane ruptured and ELOA flooded into the cell, showing particular affinity for the nucleus of the cell. Control experiments performed using investigating the interactions of equine lysozyme, oleic acid, or the dye Alexa Fluor 488 alone with PC12 cells, did not show this behaviour. These results were also supported by fluorescence correlation spectroscopy measurements, which were used to measure the relative concentrations of fluorescently labelled ELOA in different regions of the cell and surrounding matrix. It should be noted that this behaviour is different from that previously observed for the HAMLET complexes, which are taken up by the cells they kill.[237]

Adding the lipid based fluorescent membrane stain, $DiIC_{18}(5)$, to PC12, cells and observing the location of this stain using fluorescence imaging and fluorescence correlation spectroscopy, showed that the lipid probe localized to specific regions of the membrane when cells were exposed to ELOA. In cells labelled with $DiIC_{18}(5)$, in the absence on ELOA, the stain was seen to be evenly distributed over the cell membrane.

Dual fluorescence measurements using both fluorescently labelled ELOA and fluorescently labelled cells showed that the $DiIC_{18}(5)$ stain localized at sites of ELOA interaction. This is consistent with other experimental findings, which have shown that $DiIC_n$ probes with long aliphatic chains ($n = 18$) are preferentially located at the gel/fluid interface, showing particular affinity for areas rich in defects.[267]

8.4.2 Results of NMR and photo-CIDNP to probe the surface and structure of ELOA in relation to the native and molten-globule states of equine lysozyme

In light of the fluorescence results, which showed an accumulation of ELOA at the plasma membrane of the PC12 cells before the membrane was ruptured, it was decided to use CIDNP to help identify possible sites on the surface of the ELOA complex that could interact with plasma membranes. Control experiments showed that equine lysozyme alone did not accumulate on the membrane surface. Therefore, the mechanism of interaction must be specific to ELOA and is likely due to the difference in structure of the ELOA complex compared to the native state protein.

Biochemical literature has shown many examples of the affinity of the amino acid tryptophan for protein membrane interfaces, including examples of its frequent occurrence at the membrane protein interface in the structure of membrane proteins.[268] It has therefore been hypothesized that the exposure of tryptophan and other hydrophobic residues on the surface of a protein forms the basis for one mechanism of interaction of proteins with membrane surfaces.

CIDNP performed on a protein where a flavin photosensitizer is added to the solution provides a probe for the surface accessibility of tryptophan, tyrosine and histidine residues. It was therefore hoped that comparison of the CIDNP spectrum of the native state,[20] where the residues giving rise to the CIDNP effect could be determined from existing NMR assignments, with those of ELOA, may shed light on the surface structure of the ELOA complex and thus on the mechanism that allows interaction with the cell membrane.

ELOA was prepared by partial unfolding of equine lysozyme on an anion-exchange matrix within the column, preloaded with oleic acid, and followed by salt gradient elution. Partial unfolding of the equine lysozyme to form a molten-globule state is achieved by adjustment of the pH to approximately pH 2.[265] Due to the method of formation of the ELOA complex, it is expected that the equine lysozyme in the ELOA complex will retain a partially unfolded structure. NMR and CIDNP spectra of equine lysozyme at pH 2 in the molten-globule were therefore also recorded.

In order for an NMR signal to be observed for a specific amino acid, the dynamic of the protein or protein aggregate in the region of the amino acid must be static on the timescale of the NMR experiment. This allows the NMR and photo-CIDNP experiments to be used as a probe of structural stability for the ELOA, in relation to the native and molten-globule states.

The CIDNP results are given in Fig. 8.8 and the NMR data is presented in Fig. 8.9. The photo-CIDNP spectrum of the equine lysozyme native state is well-resolved; the polarized resonances were identified as originating from the amino acids Trp 63, Trp 64, Tyr 34, Tyr 54 and His 114, which indicates that these residues must be solvent accessible in the native state. Solvent accessibility calculations conducted on a crystal structure of the native state, see section 8.4.3, confirm that these residues appear to be solvent accessible in the native state.

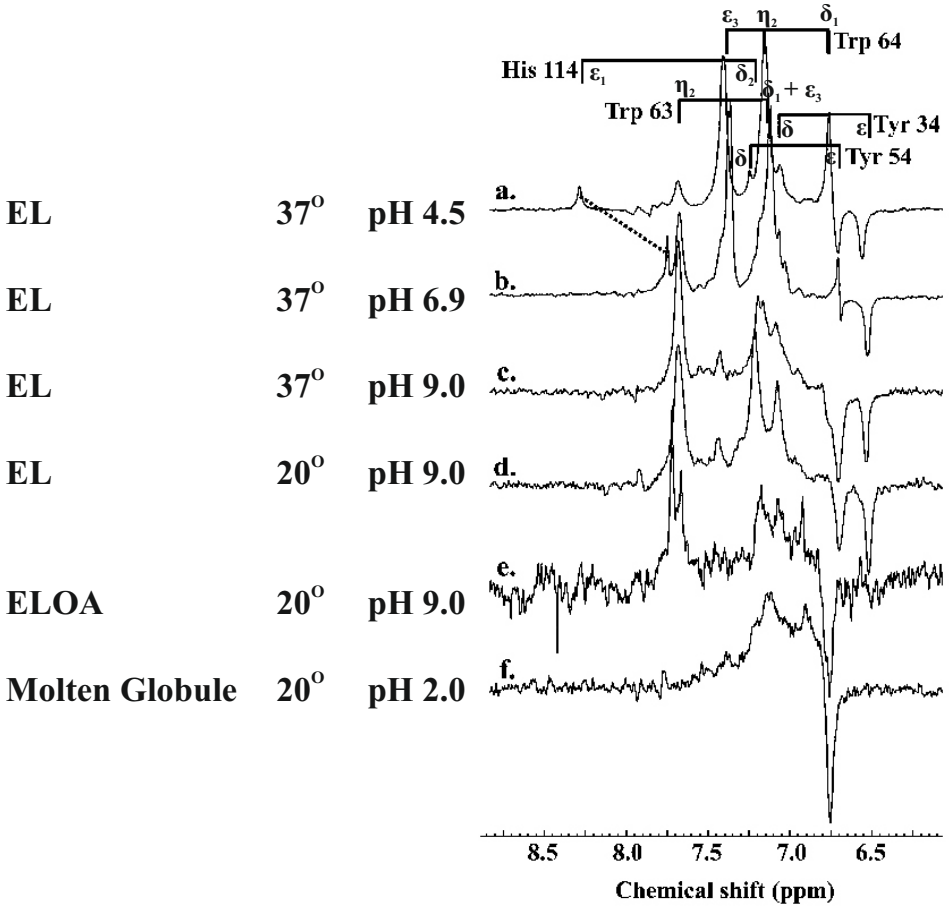


Figure 8.8: Identification of possible ELOA interaction sites by photo-CIDNP. ^{1}H photo-CIDNP difference spectra of the ELOA complex and of native and molten-globule states of equine lysozyme (EL). Native equine lysozyme state at (a) pH 4.5 and 37 °C, (b) pH 6.9 and 37 °C, (c) pH 9.0 and 37 °C and (d) pH 9.0 and 20 °C. (e) ELOA at pH 9.0 and 20 °C. (f) Molten-globule state at pH 2.0 and 20 °C. This figure is reprinted with permission from Lipoprotein Complex of Equine Lysozyme with Oleic Acid (ELOA) Interactions with the Plasma Membrane of Live Cells; V. Vukojevič, A. M. Bowen, K. Wilhelm, Y. Ming, Z. Ce, J. Schleucher, P. J. Hore, L. Terenius and L. A. Morozova-Roche, *Langmuir*, 2010, **26(18)**, 14782–14787. Copyright © 2010 American Chemical Society.[19]

The CIDNP and NMR spectra of ELOA and the equine lysozyme molten-globule state are much less well resolved, consistent with millisecond conformational fluctuations, but still allow one to distinguish solvent-exposed tyrosine and tryptophan/histidine residues, giving rise to a CIDNP effect based on their emissive and absorptive polarizations respectively. Both the molten-globule state and the ELOA show a pronounced emissive peak from one or more Tyr residues (c. 6.75 ppm). However, the ELOA

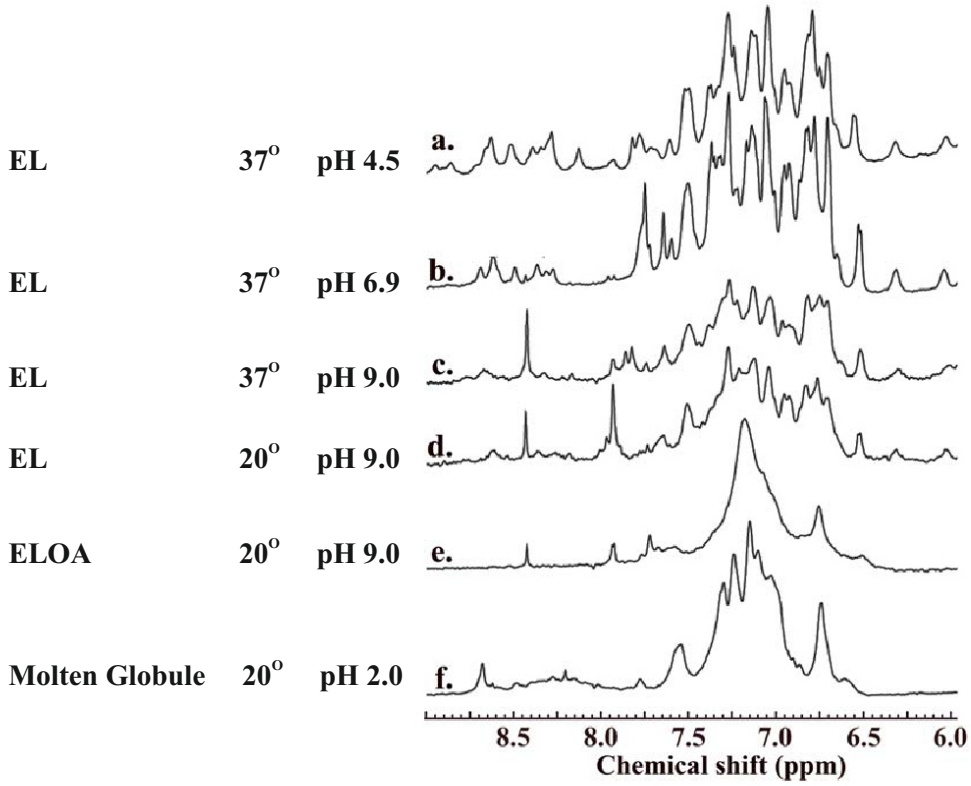


Figure 8.9: Comparison of ^{1}H NMR spectra of native and molten-globule states of equine lysozyme (EL) and ELOA. Native equine lysozyme state at (a) pH 4.5 and 37 °C, (b) pH 6.9 and 37 °C, (c) pH 9.0 and 37 °C and (d) pH 9.0 and 20 °C. (e) ELOA at pH 9.0 and 20 °C. (f) Molten-globule state at pH 2.0 and 20 °C. This figure is reprinted with permission from the Supporting Information of Lipoprotein Complex of Equine Lysozyme with Oleic Acid (ELOA) Interactions with the Plasma Membrane of Live Cells; V. Vukojevič, A. M. Bowen, K. Wilhelm, Y. Ming, Z. Ce, J. Schleucher, P. J. Hore, L. Terenius and L. A. Morozova-Roche, *Langmuir*, 2010, **26(18)**, 14782–14787. Copyright © 2010 American Chemical Society.[19]

also displays absorptivity polarized solvent-exposed resonances (c. 7.70 ppm), probably from Trp 63 or His 114, which are observed in the spectrum of the native state at the same pH, but not that of the molten-globule state.

The CIDNP spectra show that although there are clear similarities between the equine lysozyme molten-globule and ELOA, ELOA also appears to have some similarities with the native state, suggesting the existence of more structured regions, arising from binding the oleic acid. It may be that exposed hydrophobic residues in these regions promote the interaction of the ELOA complex with cell

membranes.

Analysis of the CIDNP spectra using existing NMR assignments

The CIDNP spectrum of the native state at pH 4.5 was assigned by comparison with published chemical shift data recorded at pH 4.5.[20]

In the native state CIDNP spectrum at pH 4.5 (Fig. 8.8 a), emissive peaks are clearly seen for Tyr 34 and Tyr 54 ϵ protons at 6.54 and 6.70 ppm respectively; the corresponding δ proton peaks fall at 7.05 and 7.24 ppm. Although Tyr 23 shares an ϵ proton chemical shift with Tyr 54, the absence of a Hδ peak for this residue indicates that it is unlikely to contribute to the negative peak at 6.70 ppm. Although all of the absorptive peaks occur at frequencies that could correspond to two or more protons susceptible to CIDNP, their relative intensities can be used to identify the major contributors, although there is some overlap in the region 7.05–7.25 ppm.

At pH 4.5, a clear triplet of peaks originating from Trp 64 can be seen at 6.83 ppm (δ_1), 7.14 ppm (η_2) and 7.39 ppm (ϵ_3). As the pH becomes more alkaline (Fig. 8.8 b and c), the positions of these peaks shift slightly and their intensities decrease, possibly indicating a change in conformation whereby Trp 64 becomes less solvent-exposed, so that it makes a smaller contribution to the pH 9 spectrum. The shift in the Trp 64 δ_1 peak causes this absorptive signal to overlap with the emissive resonance from the Tyr 54 ϵ protons, causing partial cancellation of the two peaks at pH 6.9 (Fig. 8.8 b).

The smaller peak at 7.68 ppm in the pH 4.5 spectrum can be attributed to Trp 63 δ_1 and ϵ_3 protons, with the η_2 peak completing the triplet at 7.15 ppm and therefore overlapping with the Trp 64 signal. At higher pH, the relative intensity of the Trp 63 peaks increases with respect to Trp 64, providing further evidence for a pH-dependent conformational change in the β-domain (possibly a rotation of the loop in which Trp 64 and 63 are located).

It is straightforward to assign the signal at 8.28 ppm to a His ϵ_1 resonance since it undergoes considerable shift with pH between 4.5 and 6.9 (shown by the dotted line in Fig. 8.8). The shift between pH 6.9 and 9.0 is less pronounced because His is almost fully deprotonated by pH 6.9. It seems likely that the His ϵ resonance overlaps with the Trp 63 δ_1 and ϵ_3 resonances at pH 9.0. Due to

its initial position, the signal at 8.28 ppm probably originates from the His 114 ϵ_1 proton, with the δ_2 proton resonance obscured by the large number of signals around 7.20 ppm.

The chemical shifts of the peaks in the CIDNP spectra at pH 4.5 differ slightly from the published NMR assignments;[20] this is believed to be due to slight differences in sample preparation.

Table 8.2: NMR assignments for the aromatic protons of tryptophan, tyrosine and histidines in native state equine lysozyme recorded at pH 4.5 and 37 °C. See Fig. 8.10 for structures with the proton positions labelled. This table is adapted and reprinted from the Supporting Information of *Journal of Molecular Biology*, **268(5)**, L. A. Morozova-Roche, C. C. Arico-Muendel, D. T. Haynie, V. I. Emelyanenko, H. van Dael, C. M. Dobson, Structural characterisation and comparison of the native and A-states of equine lysozyme, 903–921. Copyright © 1997, with permission from Elsevier.[20]

Residue	Chemical shifts for the aromatic protons (ppm)
Trp 28	δ_1 7.28, ϵ_1 9.65, ϵ_3 6.67, ξ_3 6.01, η_2 6.80, ξ_2 7.50
Trp 63	δ_1 7.61, ϵ_1 10.32, ϵ_3 7.77, ξ_3 6.77, η_2 7.15, ξ_2 7.28
Trp 64	δ_1 6.84, ϵ_1 10.01, ϵ_3 7.47, ξ_3 7.10, η_2 7.20, ξ_2 7.45
Trp 108	δ_1 7.01, ϵ_1 10.65, ϵ_3 7.51, ξ_3 6.34, η_2 7.18, ξ_2 6.84
Trp 111	δ_1 7.00, ϵ_1 10.51, ϵ_3 7.27, ξ_3 6.93, η_2 7.28, ξ_2 7.39
Tyr 23	δ 6.83, ϵ 6.71
Tyr 34	δ 6.98, ϵ 6.58
Tyr 54	δ 7.23, ϵ 6.71
Tyr 123	δ 7.12, ϵ 6.96
His 10	δ_2 7.37, ϵ_1 8.67
His 114	δ_2 7.19, ϵ_1 8.57

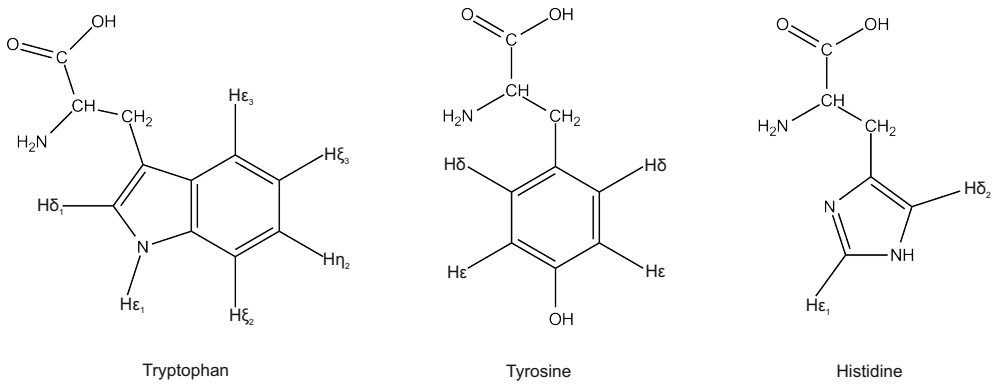


Figure 8.10: The amino acid structures of tryptophan, tyrosine and histidine with the aromatic protons labelled.

ELOA (Fig. 8.8 e) and the molten-globule state of equine lysozyme (Fig. 8.8 f) displayed less

well resolved CIDNP spectra, although it is still straightforward to distinguish tyrosine and tryptophan/histidine residues, based on their emissive (negative) and absorptive (positive) polarizations respectively. In the molten-globule state, the characteristic emissive peak corresponding to the Tyr ϵ protons is the dominant feature, while the other peaks observed for the native state are not present, indicating that these residues are not surface-accessible or occur in a region of the protein that is structurally flexible on the timescale of the NMR experiments, such that the resonances are broadened and therefore not observed. The ELOA spectrum contains the same emissive Tyr peak as seen for the molten-globule state, together with absorptive peaks in the region of 7.7 ppm, resembling those of Trp 63 and possibly His 114. For both of these residues, the other expected signals peaks fall between 6.9 and 7.2 ppm. The NMR assignments for the CIDNP-active amino acids in the native state of equine lysozyme are given in Table 8.2. Structures, with the corresponding proton positions marked, are given in Fig. 8.10.

The photo-CIDNP measurements suggest that structured regions in ELOA and the exposed side groups may be important for ELOA interaction with the plasma membrane. However, it should be noted that for technical reasons the ELOA surface structure was determined at a concentration which is considerably higher than that in live cell measurements, 0.4 mM as compared to 500 nM.

8.4.3 Solvent accessibility calculations

Solvent accessibility calculations were made using an X-ray structure of equine lysozyme in its native state from the PDB (*2EQL.pdb*).[269] Calculations were made using the program Accelerys DS visualizer.[163] Solvent accessibility was calculated for a probe of radius 1.4 Å, corresponding to a water molecule, and 4 Å, corresponding to the size of the FMN used in the CIDNP experiment.

8.4.4 Interpretation of the CIDNP data in light of the solvent accessibility data, hydrogen exchange data and protein structures

Residues with high solvent accessibility are normally expected to show strong CIDNP effects. For the equine lysozyme native state at pH 4.5, Trp 64 is more strongly polarized than Trp 63, while the

Table 8.3: Solvent accessibilities for the CIDNP active residues in equine lysozyme in its native fold using the PDB structure 2EQL. The H_2O solvent accessibility uses a probe of 1.4 Å and the FMN solvent accessibility uses a probe of 4.0 Å. Solvent accessibilities are expressed as a percentage solvent accessibility, with respect to the solvent accessibility of the amino acid in a short peptide fragment. This table is reprinted with permission from the Supporting Information of Lipoprotein Complex of Equine Lysozyme with Oleic Acid (ELOA) Interactions with the Plasma Membrane of Live Cells; V. Vukojevìc, A. M. Bowen, K. Wilhelm, Y. Ming, Z. Ce, J. Schleucher, P. J. Hore, L. Terenius and L. A. Morozova-Roche, *Langmuir*, 2010, **26(18)**, 14782–14787. Copyright © 2010 American Chemical Society.[19]

Residue	Percentage solvent accessibility (H_2O)	Percentage solvent accessibility (FMN)	CIDNP signal seen for native state protein
Trp 28	0	0	No
Trp 63	57.007	28.198	Yes
Trp 64	13.049	0	Yes
Trp 108	3.246	0	No
Trp 111	5.673	0	No
Tyr 23	22.396	7.994	No
Tyr 34	42.274	19.295	Yes
Tyr 54	11.899	0.198	Yes
Tyr 123	13.618	1.488	No
His 10	48.033	30.37	No
His 114	40.641	26.534	Yes

crystal structure predicts a substantially larger accessibility for Trp 63 than for Trp 64. The crystal structure appears to have been recorded in the absence of Ca^{2+}; differences from the solution structure of the Ca^{2+}-bound protein are therefore not unexpected. One interpretation is that in solution, the domain that contains both Trp 63 and Trp 64 (β-domain) has a different position with respect to the remainder of the protein (α-domain that includes all major α-helices), so reducing the accessibility of Trp 63 and possibly opening up the cleft between the two domains (see Fig. 8.11).

The solvent accessibility trend for the two Trp residues inferred from the CIDNP intensities is reversed in CIDNP measurements of the native state at higher pH, removing the discrepancy with the crystal structure. Since the latter was determined at pH 5.6, this may support the idea of a conformational change in the protein at lower pH.

Previously reported hydrogen-deuterium exchange data for the native state equine lysozyme recorded

at pH 4.5 and 25 °C show a much faster rates of exchange for Trp 64 (1.4×10^{-4} s^{-1}) compared to Trp 63 (1.1×10^{-6} s^{-1}).[20] As with the CIDNP data, this suggests greater surface accessibility for Trp 64 in solution at pH 4.5 compared to Trp 63, supporting the idea of a slight change in structure between that observed in the crystal structure and that found in weakly acidic solutions.

Although CIDNP enhancements were observed for His 114 in the equine lysozyme native state, no CIDNP enhancements were seen for His 10, despite its high calculated solvent accessibility, which is very similar to that of His 114. This might indicate the existence of small equine lysozyme oligomers under the conditions of the NMR experiments, with His 10 located in the protein-protein interface.

Comparing the NMR and CIDNP spectra of the ELOA complex with those of the molten-globule and protein native state at pH 9.0 (Fig. 8.9(d–f) and Fig. 8.8(d–f)) provides some information about the strucutre of ELOA with respect to these two states. The NMR spectrum of ELOA has a shape that is similar to the spectrum recorded for the molten-globule, indicating that ELOA adopts a molten-globule-like structure as suggested in previous studies.[236] Comparison of CIDNP spectra for these three species (Fig. 8.8(d–f)) shows a large emissive resonance, resulting from a tyrosine residue in the spectra from ELOA and the molten-globule equine lysozyme, indicating that both states have a tyrosine residue located within a region of the protein, which is structurally rigid. However, in addition there is a narrow photo-CIDNP signal for the ELOA complex, which is not present in the spectrum of the molten-globule state. This signal has been assigned to either His 114 or Trp 63 or potentially both. A similar signal is also observed in the CIDNP spectrum for the native state equine lysozyme at pH 9.0. Although ELOA is believed to possess a molten-globule-like structure, a previous study of ELOA has hypothesized that ELOA may adopt a more native-like fold on interaction with a plasma membrane.[247] The CIDNP results show that even in the absence of a plasma membrane, ELOA in solution shares characteristics with both the native fold and the molten-globule state.

Both His 114 and Trp 63 occur close to the inter-domain cleft (see Fig. 8.11). The sharp nature of the signal resulting from one or both of these residues in the ELOA CIDNP spectrum indicates limited conformational mobility of the protein in this region of the ELOA complex compared to the rest of the protein. Hence it appears that this region of the protein is structurally stable in the presence of oleic

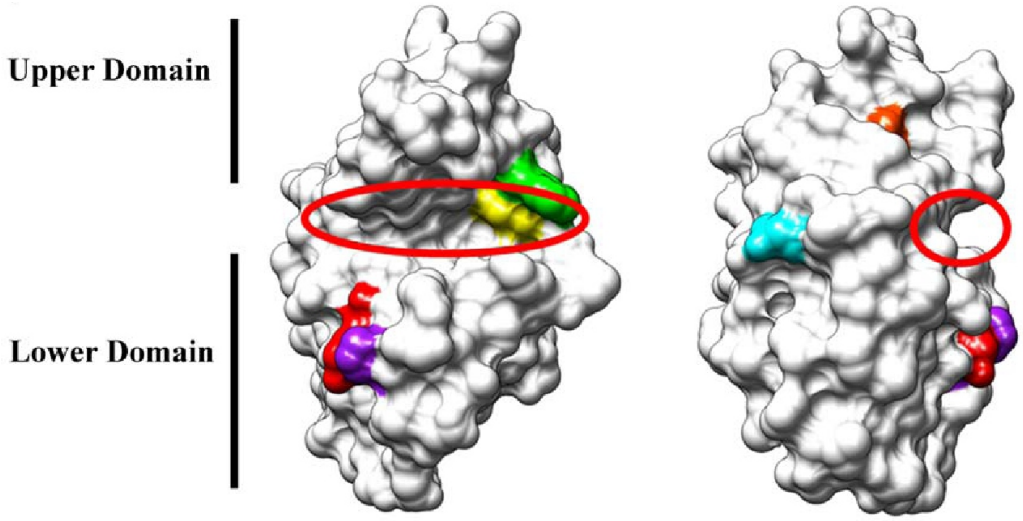


Figure 8.11: Solvent accessible surface of equine lysozyme (RCSB PDB, 2EQL). Residues giving rise to the CIDNP effect in the native state samples: Tyr 34 (red), Tyr 54 (orange), Trp 63 (green), Trp 64 (yellow) and His 114 (purple). The Ca^{2+} binding site has been identified as adjacent to residue 87 (cyan). A potential binding cleft or dynamic opening and closing cleft is circled in red. This figure is reprinted with permission from the Supporting Information of Lipoprotein Complex of Equine Lysozyme with Oleic Acid (ELOA) Interactions with the Plasma Membrane of Live Cells; V. Vukojevič, A. M. Bowen, K. Wilhelm, Y. Ming, Z. Ce, J. Schleucher, P. J. Hore, L. Terenius and L. A. Morozova-Roche, *Langmuir*, 2010, **26(18)**, 14782–14787. Copyright © 2010 American Chemical Society.[19]

acid. This result appears to be consistent with previous fluorescence measurements, which indicated the presence of constrained tryptophans in ELOA.[247]

It is possible to imagine that oleic acid may bind close to or in this cleft, allowing short-range order to be maintained, while simultaneously inducing further large-scale changes in the relative positions of the two domains, possibly lowering the affinity of the Ca^{2+} binding site and inducing a molten-globule-like structure for the remaining portion of the protein. ELOA is an early-stage aggregate. Therefore it is possible that binding of oleic acid alone is not responsible for stabilizing these residues and that aggregation of multiple equine lysozyme proteins may allow for regions of structural stability. Finally, it is not unknown for lysozymes to have dynamic clefts that open and close, for example such behaviour is observed in lysozyme from bacteriophage lambda. For bacteriophage lambda lysozyme both an open and closed structure have been crystallized,[270] and the closed structure appears to be

favoured upon substrate binding within the cleft.[271] In ELOA, formation of a state with a closed cleft could potentially stabilize the protein structure around this cleft.

Furthermore, the identification of a CIDNP enhancement in the spectrum of ELOA, which can potentially be attributed to Trp 63, shows that this amino acid is surface accessible. Since it is known that tryptophans are frequently involved in the interactions of proteins with membranes (see Section 8.4.2), it is possible that Trp 63 may play a role in the interactions of ELOA with cell membranes. To investigate this, it would be necessary to culture equine lysozyme, where Trp 63 is mutated to another residue, and study the interaction of ELOA formed from this mutated protein with cell membranes in comparison to the naturally occurring ELOA.

8.5 Conclusions

Although the results from these experiments show that interactions between ELOA and a plasma membrane are important for cell cytoxicity and also the CIDNP results yield an interesting insight into the nature of the amino acids on the surface of the ELOA complex, which may allow for this interaction, it should be remembered that ELOA interaction with the plasma membrane is a two-partner event. In this encounter the plasma membrane, a complex and dynamic mosaic of lipids, proteins and carbohydrates is not an inert partner, but rather an 'active' one. Polyelectrostatic interactions between ELOA and the plasma membrane constituents may induce conformational changes in ELOA, thereby promoting its subsequent fusion with the plasma membrane.[272]

Chapter 9

Conclusions and further work

This thesis has examined the application of magnetic resonance techniques, in particular Electron Paramagnetic Resonance (EPR) and Chemically Induced Dynamic Nuclear Polarisation (CIDNP), to an array of different biological and model systems. The primary EPR technique utilized was Double Electron-Electron Resonance (DEER), which measures the interaction of two spins as a modulation in the response of one spin when the second spin is inverted by a π pump pulse. Although this technique is currently widely used in the analysis of inter-spin distances between conformationally mobile nitroxide centres, its application to more complex spin systems such as metal centres is currently limited. The primary reason for this is the more complex data analysis required to take into account the achievable frequency bandwidth of the excitation pulses in relation to the spectra, which for most metal centres results in each pulse only exciting a small portion of the centres EPR spectrum. This leads to orientational selectivitly.

Chapter 2 presented a generalized method of modelling this orientational selectivity in DEER spectra. This modelling method has been realized as a custom-written MATLAB-based program that requires as input the EPR parameters describing the two centres (g-values, hyperfine couplings and strain parameters), the relative positions of the two centres, and experimental parameters (such as the pulse lengths, experimental field position, and pulse frequencies).

Previous methods to analyse quantitatively the orientational dependence of DEER spectra, in order to extract both distance and angular information, have purported to be model-free. However, the presence of different conformational flexibility in systems can produce large variations in the relative

spatial distribution of two spin centres. Therefore, in order to model the DEER spectrum resulting from two centres accurately, it is necessary to have some prior knowledge of this distribution, since the model used can have a dramatic effect on the spectrum simulated.

This modelling method has been applied to a variety of different systems containing metal centres. Chapter 3 shows applications based on copper centres; the method was initially tested on model systems where a distribution of the two centres was modelled using DFT and the results compared to similar nitroxide-based systems which could be analysed by existing methods using the DeerAnalysis program.[45] Secondly, a homodimer of the copper containing protein, copper amine oxidase from *Arthrobacter globiformis* (AGAO), was used as a biological model system. Crystal structures for this protein are available in the literature and the rigidity of the backbone structure limits the number of conformations that the two copper centres can adopt with respect to one another. This made AGAO an ideal candidate to provide a proof of method for the analysis of biological systems.

Having demonstrated that the methodology was correct, it was possible to apply this orientationally selective modelling to solve the unknown structures of docked protein complexes. The system chosen for this investigation was that of ferredoxin in complex with both ferredoxin reductase and cytochrome P450. It has proved impossible to crystallize any docked complexes of ferrexodins with P450 and the literature contains only one non-native tethered structure of ferredoxin docked to ferredoxin reductase.[139] The lack of published crystallographic structures is not due to an absence of studies on these systems (P450 is very well characterized, since it is almost ubiquitous throughout nature and important in the catalytic hydroxylation of many organic substrates), but rather to inherent difficulties associated with the crystallization of large proteins.

Orientationally selective DEER traces were measured between the $[Fe_2S_2]^+$ cluster in ferredoxin and nitroxide labelling sites on the partner protein. To allow analysis of these traces with respect to the molecular structures, it was necessary to know the orientation of the g-tensor of the $[Fe_2S_2]^+$ cluster within the molecular environment. This was determined for the ferredoxin protein PuxB using a combination of X-band HYSCORE (HYperfine Sublevel CORrElation) and W-band ENDOR (Electron Nuclear DOuble Resonance); see Chapter 5. The orientation attained was found to be in

good agreement with several published results for similar ferredoxin proteins with axial g-matrices. Therefore, it appears that this g-matrix orientation is a general result for this type of protein.

By direct fitting of orientationally selective DEER data measured between $[Fe_2S_2]^+$–$NO^\bullet$, with a few $NO^\bullet - NO^\bullet$ restraints to confirm the structures, it has been possible to determine the first solution based structure for the ferredoxin–ferredoxin reductase complex and the first structure ferredoxin–P450 complex (see Chapter 4). The initial structures underwent initial geometrical refinement and contact analysis; however, before a final structure can be published, a full molecular dynamics refinement will be required. This simulation is on-going at present.

Expansion of DEER spectroscopy to more complex systems has highlighted some shortcomings of the existing three- and four-pulse methods. To address some of the problems, in particular low modulation depths and fast relaxation times, method development was pursued, which resulted in two amendments to the existing DEER sequences. These have been named REINDEER (Repeated excitation IN DEER) and dead-time free three-pulse DEER.

REINDEER (Chapter 6) uses the application of two (or more) pump pulses simultaneously at different frequencies to increase the bandwidth of the pump pulse excitation profile. This has important benefits when applied to metal centres with broad EPR spectra, since it allows a larger portion of the spectrum to be excited by the pump pulse(s), thus effectively increasing the pump pulse efficiency and resulting in the observation of a corresponding increase in modulation depth. This technique will become much more easily applicable with the next generation of commercially available Bruker spectrometers which will allow the generation of pulses containing multiple frequencies without the need for an additional external frequency source.

The shorter three-pulse DEER sequence has advantages over the four-pulse technique, since the size of the echo detected is larger. This result is due not only from the generally shorter sequence (there is no τ_1 period required) but also from the lower number of detection pulses used, which reduces the level of spectral diffusion. However, three-pulse DEER set up under normal high power conditions suffers from a dead-time around the zero-time (t_0). This occurs due to a combination of the crossing pulses pushing the TWT (Traveling-Wave Tube) amplifier into a non-linear regime and a dynamic Bloch-Siegert phase

shift. The experiments in Chapter 7 show that by reducing the power of the pulses, it is possible to restrain the pulse crossing within the linear regime of a 1 kW TWT amplifier. In addition, this reduction in power also satisfactorily constrains the dynamic Bloch-Siegert phase shift to the x-y plane, where it can be corrected by taking the absolute value of the real and imaginary parts of the signal collected. Prior knowledge of the experimental pulse lengths and delays is required to accurately determine t_0, as unlike four-pulse DEER the three-pulse DEER trace is not symmetric about t_0. However, once this is known, it is possible to process the absolute of the data using DeerAnalysis without the formation of any artefacts in the determined distance distribution. Dead-time free three-pulse DEER has already found applications among other members of the CÆSR (Centre for Advanced Electron Spin Resonance) community at Oxford University for the study of membrane proteins with particularly short T_m times. Although it is possible to extend the relaxation times and thus measurement times of such systems by deuteration of both the matrix and protein,[273] this is a costly procedure and therefore an experimental method to increase the quality of the signals gained from systems with short relaxation times is still of value.

The final experimental chapter (Chapter 8) explores a different magnetic resonance technique, CIDNP. Although this is a powerful technique and has been used to study topics as diverse as protein folding[17] and the different states in which radical pairs are formed,[229] here is it used to examine the solvent accessibility and thus surface properties of the tryptophan, tyrosine and histidine residues in equine lysozyme and its early stage oligomer ELOA (Equine Lysozyme with Oleic Acid). ELOA has been shown to induce apoptosis in tumour cells and thus, along with the closely related aggregates of HAMLET and BAMLET (Human and Bovine α-lactalbumin Made LEthal to Tumour cells), shows promise as an anti-cancer agent of the future. The study revealed that ELOA shares characteristics with both the native fold of equine lysozyme and also the molten globule state induced at low pH. The shared characteristics with the native state indicated that the ELOA fold is more ordered than previous experiments had indicated and also allowed identification of potential interaction sites of the oleic acid with the protein. In addition, ELOA was shown to have surface-exposed tryptophan residues, which may play a role in the interaction of the protein with cell membranes. Further work, in the form of

mutagenesis studies, would be required to further probe the action of these tryptophans in relation to the interaction with plasma membranes.

Magnetic resonance forms a vast area for research, within which EPR is an exciting and fast growing topic. It is hoped that this thesis can contributed in some small way to the advances in this fascinating research field.

Bibliography

[1] E. F. Pettersen, T. D. Goddard, C. C. Huang, G. S. Couch, D. M. Greenblatt, E. C. Meng and T. E. Ferrin, *Journal of Computational Chemistry*, 2004, **25**, 1605–1612.

[2] University of Hamburg Department of Chemistry, *Dipolar coupling,* http://www.chemie.uni-hamburg.de/nmr/insensitive/tutorial/en.lproj/dipolar_coupling.html.

[3] E. Bordignon, *Nitroxide Spectrum Analysis Tutorial, EPR Summer School, Constance*, 2010.

[4] G. W. Reginsson, R. I. Hunter, P. A. S. Cruickshank, D. R. Bolton, S. T. Sigurdsson, G. M. Smith and O. Schiemann, *Journal of Magnetic Resonance*, 2012, **216**, 175–182.

[5] J. E. Lovett, A. M. Bowen, C. R. Timmel, M. W. Jones, J. R. Dilworth, D. Caprotti, S. G. Bell, L. L. Wong and J. Harmer, *Physical Chemistry Chemical Physics*, 2009, **11**, 6840–6848.

[6] G. Jeschke, in *Biological Magnatic Resonance, Volume 27: ESR Spectroscopy in Membrane Biophysics*, ed. M. Hemminga and L. J. Berliner, Springer, 2007, ch. 2, pp. 17–47.

[7] S. Stoll and A. Schweiger, *Journal of Magnetic Resonance*, 2006, **178**, 42–55.

[8] B. E. Bode, J. Plackmeyer, T. F. Prisner and O. Schiemann, *Journal of Physical Chemistry A*, 2008, **112**, 5064–5073.

[9] Z. Yang, D. Kise and S. Saxena, *The Journal of Physical Chemistry B*, 2010, **114**, 6165–6174.

[10] Z. Yang, J. Becker and S. Saxena, *Journal of Magnetic Resonance*, 2007, **188**, 337–343.

[11] N. Andrusier, R. Nussinov and H. J. Wolfson, *Proteins*, 2007, **69**, 139–159.

[12] S. G. Bell, F. Xu, E. O. D. Johnson, I. M. Forward, M. Bartlam, Z. Rao and L.-L. Wong, *Journal of Biological Inorganic Chemistry*, 2010, **15**, 315–328.

[13] B. Epel, P. Manikandan, P. M. H. Kroneck and D. Goldfarb, *Applied Magnetic Resonance*, 2001, **21**, 287–297.

[14] C. Calle, A. Sreekanth, M. V. Fedin, J. Forrer, I. Garcia-Rubio, I. A. Gromov, D. Hinderberger, B. Kasumaj, P. Leger, B. Mancosu, G. Mitrikas, M. G. Santangelo, S. Stoll, A. Schweiger, R. Tschaggelar and J. Harmer, *Helvetica Chimica Acta*, 2006, **89**, 2495–2521.

[15] J. A. B. Abdalla, A. M. Bowen, S. G. Bell, L. L. Wong, C. R. Timmel and J. Harmer, *Physical Chemistry Chemical Physics*, 2012, **14**, 6526–6537.

[16] A. D. Milov, Y. A. Grishin, S. A. Dzuba and Y. D. Tsvetkov, *Applied Magnetic Resonance*, 2011, **41**, 59–67.

[17] K. H. Mok and P. J. Hore, *Methods*, 2004, **34**, 75–87.

[18] P. J. Hore and R. Broadhurst, *Progress in NMR Spectroscopy*, 1993, **25**, 345–402.

[19] V. Vukojević, A. M. Bowen, K. Wilhelm, Y. Ming, Z. Ce, J. Schleucher, P. J. Hore, L. Terenius and L. A. Morozova-Roche, *Langmuir*, 2010, **26**, 14782–14787.

[20] L. A. Morozova-Roche, C. C. Arico-Muendel, D. T. Haynie, V. I. Emelyanenko, H. van Dael and C. M. Dobson, *Journal of Molecular Biology*, 1997, **268**, 903–921.

[21] J. R. Blume, *Physical Review*, 1958, **109**, 1867–1873.

[22] J. T. Arnold, S. S. Dharmatti and M. E. Packard, *The Journal of Chemical Physics*, 1951, **19**, 507.

[23] Y. K. Zavoisky, *Ph.D. thesis*, Kazan State University, 1944.

[24] F. Bloch, *Physical Review*, 1946, **70**, 460 –474.

[25] E. M. Purcell, H. C. Torrey and R. V. Pound, *Physical Review*, 1946, **69**, 37–38.

[26] P. A. M. Dirac, *Proceedings of the Royal Society A: Mathematical, Physical and Engineering Sciences*, 1928, **117**, 610–624.

[27] P. A. M. Dirac, *Proceedings of the Royal Society A: Mathematical, Physical and Engineering Sciences*, 1928, **118**, 351–361.

[28] P. W. Atkins and R. Friedman, *Molecular Quantum Mechanics*, Oxford University Press, 4th edn., 2005.

[29] A. Schweiger and G. Jeschke, *Principles of Pulse Electron Paramagnetic Resonance*, Oxford University Press, 2001.

[30] A. Landé, *Zeitschrift für Physik*, 1921, **5**, 231–241.

[31] M. Symons, *Chemical and Biochemical Aspects of Electron Spin Resonance Spectroscopy*, John Wiley and Sons, 1978.

[32] P. Zeeman, *Nature*, 1897, **55**, 347.

[33] P. Zeeman, *Philosophical Magazine Series 5*, 1897, **43**, 226–239.

[34] P. Zeeman, *Philosophical Magazine Series 5*, 1897, **44**, 55–60.

[35] P. Zeeman, *Philosophical Magazine Series 5*, 1897, **44**, 255–259.

[36] G. Uhlenbeck and S. Goudsmit, *Nature*, 1926, **117**, 264–265.

[37] J. R. Norris, M. C. Thurnauer and M. K. Bowman, *Advances in Biological and Medical Physics*, 1980, **17**, 365–416.

[38] B. E. Bode, J. Plackmeyer, M. Bolte, T. F. Prisner and O. Schiemann, *Journal of Organometallic Chemistry*, 2009, **694**, 1172–1179.

[39] A. W. Overhauser, *Physical Review*, 1953, **92**, 411–415.

[40] A. Kumar, R. Ernst and K. Wuthrich, *Biochemical and Biophysical Research Communications*, 1980, **95**, 1–6.

[41] R. R. Ernst and W. A. Anderson, *Review of Scientific Instruments*, 1966, **37**, 93–102.

[42] W. Heisenberg, *Zeitschrift für Physik A: Hadrons and Nuclei*, 1927, **43**, 172–198.

[43] S. A. Dzuba and A. Kawamori, *Concepts in Magnetic Resonance*, 1996, **8**, 49–61.

[44] A. D. Milov, K. M. Salikhov and M. D. Shchirov, *Soviet Physics, Solid State*, 1981, **23**, 565–569.

[45] G. Jeschke, V. Chechik, P. Ionita, A. Godt, H. Zimmermann, J. Banham, C. R. Timmel, D. Hilger and H. Jung, *Applied Magnetic Resonance*, 2006, **30**, 473–498.

[46] T. Prisner, M. Rohrer and F. MacMillan, *Annual Review of Physical Chemistry*, 2001, **52**, 279–313.

[47] L. J. Berliner, J. Grunwald, H. O. Hankovszky and K. Hideg, *Analytical Biochemistry*, 1982, **119**, 450–455.

[48] G. L. Kenyon and T. W. Bruice, in *Methods in Enzymology, Volume 47: Enzyme Structure, Part E*, ed. C. Hirs and S. N. Timasheff, Elsevier, 1977, ch. 40, pp. 407–430.

[49] A. P. Todd, J. Cong, F. Levinthal, C. Levinthal and W. L. Hubbell, *Proteins*, 1989, **6**, 294–305.

[50] W. L. Hubbell, D. S. Cafiso and C. Altenbach, *Nature Structural Biology*, 2000, **7**, 735–739.

[51] R. G. Larsen and D. J. Singel, *The Journal of Chemical Physics*, 1993, **98**, 5134–5146.

[52] P. J. Hore, *Dipole-dipole and exchange coupling - Lecture 13, EPR Summer School, Constance*, 2010.

[53] G. Jeschke and Y. Polyhach, *Physical Chemistry Chemical Physics*, 2007, **9**, 1895–1910.

[54] A. Weber, O. Schiemann, B. Bode and T. F. Prisner, *Journal of Magnetic Resonance*, 2002, **157**, 277–285.

[55] C. Riplinger, J. P. Y. Kao, G. M. Rosen, V. Kathirvelu, G. R. Eaton, S. S. Eaton, A. Kutateladze and F. Neese, *Journal of the American Chemical Society*, 2009, **131**, 10092–10106.

[56] G. Jeschke, *Macromolecular Rapid Communications*, 2002, **23**, 227–246.

[57] G. Jeschke, *Annual Review of Physical Chemistry*, 2012, **63**, 419–446.

[58] J. E. Banham, C. M. Baker, S. Ceola, I. J. Day, G. H. Grant, E. J. J. Groenen, C. T. Rodgers, G. Jeschke and C. R. Timmel, *Journal of Magnetic Resonance*, 2008, **191**, 202–218.

[59] C. Elsässer, B. Monien, W. Haehnel and R. Bittl, *Magnetic Resonance in Chemistry*, 2005, **43**, S26–S33.

[60] M. Pannier, S. Veit, A. Godt, G. Jeschke and H. W. Spiess, *Journal of Magnetic Resonance*, 2000, **142**, 331–340.

[61] R. E. Martin, M. Pannier, F. Diederich, V. Gramlich, M. Hubrich and H. W. Spiess, *Analytical Biochemistry*, 1998, **37**, 2834–2837.

[62] P. P. Borbat, E. R. Georgieva and J. H. Freed, *The Journal of Physical Chemistry Letters*, 2013, **4**, 170–175.

[63] D. Margraf, B. E. Bode, a. Marko, O. Schiemann and T. F. Prisner, *Molecular Physics*, 2007, **105**, 2153–2160.

[64] Y. Polyhach, A. Godt, C. Bauer and G. Jeschke, *Journal of Magnetic Resonance*, 2007, **185**, 118–129.

[65] S. Kuroiwa, M. Tonaka, A. Kawamori and K. Akabori, *Biochimica et Biophysica Acta*, 2000, **1460**, 330–337.

[66] M. M. Hertel, V. P. Denysenkov, M. Bennati and T. F. Prisner, *Magnetic Resonance in Chemistry*, 2005, **43 Spec no**, S248–S255.

[67] V. P. Denysenkov, T. F. Prisner, J. Stubbe and M. Bennati, *Proceedings of the National Academy of Sciences of the United States of America*, 2006, **103**, 13386–13390.

[68] V. P. Denysenkov, D. Biglino, W. Lubitz, T. F. Prisner and M. Bennati, *Angewandte Chemie (International ed.)*, 2008, **47**, 1224–1227.

[69] I. M. C. van Amsterdam, M. Ubbink, G. W. Canters and M. Huber, *Angewandte Chemie (International ed.)*, 2003, **42**, 62–64.

[70] C. W. M. Kay, H. El Mkami, R. Cammack and R. W. Evans, *Journal of the American Chemical Society*, 2007, **129**, 4868–4869.

[71] Z. Yang, M. Ji and S. Saxena, *Applied Magnetic Resonance*, 2010, **39**, 487–500.

[72] E. Narr, A. Godt and G. Jeschke, *Angewandte Chemie (International ed.)*, 2002, **41**, 3907–3910.

[73] R. Codd, A. V. Astashkin, A. Pacheco, A. M. Raitsimring and J. H. Enemark, *Journal of Biological Inorganic Chemistry*, 2002, **7**, 338–350.

[74] A. Savitsky, A. A. Dubinskii, M. Flores, W. Lubitz and K. Möbius, *The Journal of Physical Chemistry B*, 2007, **111**, 6245–6262.

[75] A. Marko, D. Margraf, H. Yu, Y. Mu, G. Stock and T. Prisner, *The Journal of Chemical Physics*, 2009, **130**, 064102.

[76] A. Marko, D. Margraf, P. Cekan, S. T. Sigurdsson, O. Schiemann and T. F. Prisner, *Physical Review E*, 2010, **81**, 1–9.

[77] L. Song, M. Larion, J. Chamoun, M. Bonora and P. G. Fajer, *European Biophysics Journal*, 2010, **39**, 711–719.

[78] Y. Kawahashi, G. Maruta and S. Takeda, *Polyhedron*, 2009, **28**, 2063–2069.

[79] O. Schiemann, P. Cekan, D. Margraf, T. F. Prisner and S. T. Sigurdsson, *Angewandte Chemie (International ed.)*, 2009, **48**, 3292–3295.

[80] Y. Polyhach, E. Bordignon and G. Jeschke, *Physical Chemistry Chemical Physics*, 2011, **13**, 2356–2366.

[81] Y. Polyhach and G. Jeschke, *Journal of Spectroscopy*, 2010, **24**, 651–659.

[82] P. A. S. Cruickshank, D. R. Bolton, D. A. Robertson, R. I. Hunter, R. J. Wylde and G. M. Smith, *Review of Scientific Instruments*, 2009, **80**, 103102.

[83] D. Goldfarb, Y. Lipkin, A. Potapov, Y. Gorodetsky, B. Epel, A. M. Raitsimring, M. Radoul and I. Kaminker, *Journal of Magnetic Resonance*, 2008, **194**, 8–15.

[84] A. Potapov, Y. Song, T. J. Meade, D. Goldfarb, A. V. Astashkin and A. Raitsimring, *Journal of Magnetic Resonance*, 2010, **205**, 38–49.

[85] Y. Song, T. J. Meade, A. V. Astashkin, E. L. Klein, J. H. Enemark and A. Raitsimring, *Journal of Magnetic Resonance*, 2011, **210**, 59–68.

[86] A. Potapov, H. Yagi, T. Huber, S. Jergic, N. E. Dixon, G. Otting and D. Goldfarb, *Journal of the American Chemical Society*, 2010, **132**, 9040–9048.

[87] H. Yagi, D. Banerjee, B. Graham, T. Huber, D. Goldfarb and G. Otting, *Journal of the American Chemical Society*, 2011, **133**, 10418–10421.

[88] G. Jeschke, M. Pannier, A. Godt and H. W. Spiess, *Chemical Physics Letters*, 2000, **331**, 243–252.

[89] G. Jeschke, A. Bender, H. Paulsen, H. Zimmermann and A. Godt, *Journal of Magnetic Resonance*, 2004, **169**, 1–12.

[90] P. P. Borbat and J. H. Freed, in *Biological Magnatic Resonance, Volume 19: Distance Measurments in Biological Systems by EPR*, ed. L. J. Berliner, G. R. Eaton and S. S. Eaton, Springer, 2000, ch. 9, pp. 383–456.

[91] A. Blank and H. Levanon, *Spectochemical Acta, Part A*, 2002, **58**, 1329–1335.

[92] P. Höfer and P. Carl, *Spin Report*, 2006, **157**, 52–56.

[93] S. Milikisyants, E. J. J. Groenen and M. Huber, *Journal of Magnetic Resonance*, 2008, **192**, 275–279.

[94] W. B. Mims, in *Electron Paramagnetic Resonance*, ed. S. Gecshwind, Plenum, 1972, ch. 4, pp. 263–351.

[95] A. L. Bloom, *Physical Review*, 1946, **98**, 1105–1111.

[96] S. Stoll and A. Schweiger, in *Biological Magnatic Resonance, Volume 27: ESR Spectroscopy in Membrane Biophysics*, ed. M. Hemminga and L. J. Berliner, Springer, Springer edn., 2007, ch. Appendix 6, pp. 299–321.

[97] S. Lyubenova, M. K. Siddiqui, M. J. M. Penning de Vries, B. Ludwig and T. F. Prisner, *The Journal of Physical Chemistry B*, 2007, **111**, 3839–3846.

[98] G. Jeschke, M. Sajid, M. Schulte and A. Godt, *Physical Chemistry Chemical Physics*, 2009, **11**, 6626–6637.

[99] A. D. Milov, Y. D. Tsvetkov, F. Formaggio, M. Crisma, C. Toniolo and J. Raap, *Journal of the American Chemical Society*, 2000, **122**, 3843–3848.

[100] A. D. Milov, A. B. Ponomarev and Y. D. Tsvetkov, *Chemical Physics Letters*, 1984, **110**, 67–72.

[101] G. Jeschke, *DeerAnalysis2011 User Manual*, 2012.

[102] G. Jeschke, in *Structure and Bonding, Volume 151: Spin-labels and intrinsic paramagnetic centres in the Biosciences: Structural information from distance measurements*, ed. C. R. Timmel and J. Harmer, SpringerLink, 2012, ch. 1, pp. 1–38.

[103] C. Abé, D. Klose, F. Dietrich, W. H. Ziegler, Y. Polyhach, G. Jeschke and H.-J. Steinhoff, *Journal of Magnetic Resonance*, 2012, **216**, 53–61.

[104] M. Ubbink, J. A. R. Worrall, G. W. Canters, E. J. J. Groenen and M. Huber, *Annual Review of Biophysics and Biomolecular Structure*, 2002, **31**, 393–422.

[105] J. S. Becker and S. Saxena, *Chemical Physics Letters*, 2005, **414**, 248–252.

[106] J. E. Lovett, B. Lovett and J. Harmer, *Journal of Magnetic Resonance*, 2012, **223**, 98–106.

[107] N. Miyaura, K. Yamada and A. Suzuki, *Tetrahedron Letters*, 1979, **36**, 3437–3440.

[108] SCM, *Amsterdam Density Functional (ADF)*, http://www.scm.com/.

[109] G. te Velde, F. M. Bickelhaupt, E. J. Baerends, C. Fonseca Guerra, S. J. A. van Gisbergen, J. G. Snijders and T. Ziegler, *Journal of Computational Chemistry*, 2001, **22**, 931–967.

[110] F. Neese and E. I. Solomon, in *Magnetism : Molecules to Materials IV*, ed. J. S. Miller and M. Drillon, Wiley-VCH, 2002, ch. 9, pp. 345–482.

[111] E. Ruiz, J. Cirera and S. Alvarez, *Coordination Chemistry Reviews*, 2005, **249**, 2649–2660.

[112] K. Mobius and A. Stavitsky, *High-Field EPR Spectroscopy on Proteins and their Model Systems*, RSC Publishing, 2009.

[113] L. N. Ikryannikova, L. Y. Ustynyuk and A. N. Tikhonov, *Magnetic Resonance in Chemistry*, 2010, **48**, 337–349.

[114] J. Cosier and A. M. Glazer, *Journal of Applied Crystallography*, 1986, **19**, 105–107.

[115] Z. Otwinowski and W. Minor, in *Methods in Enzymology, Volume 276: Macromolecuar Crystallography, Part A*, ed. C. W. Carter, Elsevier, 1997, pp. 306–315.

[116] A. Altomare, G. Cascarano, C. Giacovazzo and A. Guagliardi, *Journal of Applied Crystallography*, 1994, **27**, 1045–1050.

[117] P. W. Betteridge, J. R. Carruthers, I. Richard, K. Prout and D. J. Watkin, *Journal of Applied Crystallography*, 2003, **36**, 1487.

[118] G. A. Juda, J. A. Bollinger and D. M. Dooley, *Protein Expression and Purification*, 2001, **22**, 455–461.

[119] S. Kishishita, T. Okajima, M. Kim, H. Yamaguchi, S. Hirota, S. Suzuki, S. Kuroda, K. Tanizawa and M. Mure, *Journal of the American Chemical Society*, 2003, **125**, 1041–1055.

[120] A. C. Wallace, R. A. Laskowski and J. M. Thornton, *Protein Engineering*, 1995, **8**, 127–134.

[121] R. A. Laskowski and M. B. Swindells, *Journal of Chemical Information and Modeling*, 2011, **51**, 2778–2786.

[122] D. B. Langley, A. P. Duff, H. C. Freeman and J. M. Guss, *Acta Crystallographica, Section F: Structural Biology and Crystallization Communications*, 2006, **62**, 1052–1057.

[123] R. H. Moore, M. A. Spies, M. B. Culpepper, T. Murakawa, S. Hirota, T. Okajima, K. Tanizawa and M. Mure, *Journal of the American Chemical Society*, 2007, **129**, 11524–11534.

[124] A. P. Duff, D. M. Trambaiolo, A. E. Cohen, P. J. Ellis, G. A. Juda, E. M. Shepard, D. B. Langley, D. M. Dooley, H. C. Freeman and J. M. Guss, *Journal of Molecular Biology*, 2004, **344**, 599–607.

[125] M. Kim, T. Okajima, S. Kishishita, M. Yoshimura, A. Kawamori, K. Tanizawa and H. Yamaguchi, *Nature Structural Biology*, 2002, **9**, 591–596.

[126] M. C. Wilce, D. M. Dooley, H. C. Freeman, J. M. Guss, H. Matsunami, W. S. McIntire, C. E. Ruggiero, K. Tanizawa and H. Yamaguchi, *Biochemistry*, 1997, **36**, 16116–16133.

[127] Y.-C. Chiu, T. Okajima, T. Murakawa, M. Uchida, M. Taki, S. Hirota, Y. Yamamoto and K. Tanizawa, *Biochemistry*, 2006, **45**, 4105–4120.

[128] J. E. Lovett, M. Hoffmann, A. Cnossen, A. T. J. Shutter, H. J. Hogben, J. E. Warren, S. I. Pascu, C. W. M. Kay, C. R. Timmel and H. L. Anderson, *Journal of the American Chemical Society*, 2009, **131**, 13852–13859.

[129] R. Ahlrichs, F. Furche, C. Hättig, W. M. Klopper, M. Sierka and F. Weigend, *TurboMol*, http://www.turbomole.com/.

[130] J. K. Sprafke, D. V. Kondratuk, M. Wykes, A. L. Thompson, M. Hoffmann, R. Drevinskas, W.-H. Chen, C. K. Yong, J. Kärnbratt, J. E. Bullock, M. Malfois, M. R. Wasielewski, B. Albinsson, L. M. Herz, D. Zigmantas, D. Beljonne and H. L. Anderson, *Journal of the American Chemical Society*, 2011, **133**, 17262–17273.

[131] G. E. Pake, *The Journal of Chemical Physics*, 1948, **16**, 327–336.

[132] B. Joseph, G. Jeschke, B. A. Goetz, K. P. Locher and E. Bordignon, *The Journal of Biological Chemistry*, 2011, **286**, 41008–41017.

[133] J. Banham, R. Abbott, J. Caesar, P. Roversi, G. Jeschke, C. Timmel and S. Lea, *Molecular Immunology*, 2008, **45**, 4122.

[134] J. Bhatnagar, J. H. Freed and B. R. Crane, in *Methods in Enzymology, Volume 423: Two-Component Signalling Systems, Part B*, ed. M. I. Simon, B. R. Crane and A. Crane, 2007, pp. 117–133.

[135] P. P. Borbat and J. H. Freed, in *Methods in Enzymology, Volume 423: Two-Component Signalling Systems, Part B*, ed. M. I. Simon, B. R. Crane and A. Crane, Elsevier, 2007, pp. 52–116.

[136] D. Hilger, Y. Polyhach, E. Padan, H. Jung and G. Jeschke, *Biophysical Journal*, 2007, **93**, 3675–3683.

[137] R. Cammack and F. MacMillan, in *Biological Magnatic Resonance, Volume 29: Metals in Biology*, ed. G. Hanson and L. Berliner, Springer, 2010, ch. 2, pp. 11–44.

[138] M. M. Roessler, M. S. King, A. J. Robinson, F. A. Armstrong, J. Harmer and J. Hirst, *Proceedings of the National Academy of Sciences of the United States of America*, 2010, **107**, 1930–1935.

[139] I. F. Sevrioukova, T. L. Poulos and I. Y. Churbanova, *The Journal of Biological Chemistry*, 2010, **285**, 13616–13620.

[140] J. J. Müller, A. Lapko, G. Bourenkov, K. Ruckpaul and U. Heinemann, *The Journal of Biological Chemistry*, 2001, **276**, 2786–2789.

[141] I. F. Sevrioukova and T. L. Poulos, *Archives of Biochemistry and Biophysics*, 2011, **507**, 66–74.

[142] H. Farhan, K. Wähälä, H. Adlercreutz and H. S. Cross, *Journal of Chromatography B*, 2002, **777**, 261–268.

[143] F. P. Guengerich, *Critical Reviews in Biochemistry and Molecular Biology*, 1990, **25**, 97–153.

[144] F. P. Guengerich, *Chemical Research in Toxicology*, 2008, **21**, 70–83.

[145] Y.-R. Lou, S. Qiao, R. Talonpoika, H. Syvälä and P. Tuohimaa, *The Journal of Steroid Biochemistry and Molecular Biology*, 2004, **92**, 317–325.

[146] T. Sakaki, N. Sawada, Y. Nonaka, Y. Ohyama and K. Inouye, *European Journal of Biochemistry*, 1999, **262**, 43–48.

[147] S. G. Bell, E. Orton, H. Boyd, J.-A. Stevenson, A. Riddle, S. Campbell and L.-L. Wong, *Dalton Transactions*, 2003, 2133–2140.

[148] S. G. Bell, J.-A. Stevenson, H. D. Boyd, S. Campbell, A. D. Riddle, L. Erica and L.-L. Wong, *Chemical Communications*, 2002, **5**, 490–491.

[149] F. Xu, S. G. Bell, J. Lednik, A. Insley, Z. Rao and L.-L. Wong, *Angewandte Chemie (International ed.)*, 2005, **44**, 4029–4032.

[150] F. Xu, S. G. Bell, Y. Peng, E. O. D. Johnson, M. Bartlam, Z. Rao and L.-L. Wong, *Proteins*, 2009, **77**, 867–880.

[151] S. G. Bell, F. Xu, I. Forward, M. Bartlam, Z. Rao and L.-L. Wong, *Journal of Molecular Biology*, 2008, **383**, 561–574.

[152] S. G. Bell, N. Hoskins, F. Xu, D. Caprotti, Z. Rao and L.-L. Wong, *Biochemical and Biophysical Research Communications*, 2006, **342**, 191–196.

[153] S. G. Bell, W. Yang, A. B. H. Tan, R. Zhou, E. O. D. Johnson, A. Zhang, W. Zhou, Z. Rao and L.-L. Wong, *Dalton Transactions*, 2012, **41**, 8703–8714.

[154] S. G. Bell, A. B. H. Tan, E. O. D. Johnson and L.-L. Wong, *Molecular Biosystems*, 2009, **6**, 206–214.

[155] J. E. Banham, *Ph.D. thesis*, University of Oxford, 2006.

[156] J. E. D. Lillington, J. E. Lovett, S. Johnson, P. Roversi, C. R. Timmel and S. M. Lea, *Journal of Molecular Biology*, 2011, **405**, 427–435.

[157] D. Duhovny, R. Nussinov and H. J. Wolfson, in *Proceedings of the 2nd Workshop on Algorithms in Bioinformatics (WABI). Lecture Notes in Computer Science 2452*, ed. D. Gusfield, Springer, 2002, pp. 185–200.

[158] D. Schneidman-Duhovny, Y. Inbar, V. Polak, M. Shatsky, I. Halperin, H. Benyamini, A. Barzilai, O. Dror, N. Haspel, R. Nussinov and H. J. Wolfson, *Proteins*, 2003, **52**, 107–112.

[159] E. Mashiach, D. Schneidman-Duhovny, N. Andrusier, R. Nussinov and H. J. Wolfson, *Nucleic Acids Research*, 2008, **36**, W229–W232.

[160] C. Zhang, G. Vasmatzis, J. L. Cornette and C. DeLisi, *Journal of Molecular Biology*, 1997, **267**, 707–726.

[161] C. Dominguez, R. Boelens and A. M. J. J. Bonvin, *Journal of the American Chemical Society*, 2003, **125**, 1731–1737.

[162] K. Harada, K. Sakurai, K. Ikemura, T. Ogura, S. Hirota, H. Shimada and T. Hayashi, *Journal of the American Chemical Society*, 2008, **130**, 432–433.

[163] Accelrys, *Accelrys Discovery Studio*, http://accelrys.com/products/discovery-studio/.

[164] R. Kappl, G. Bracic and J. Hüttermann, in *Biological Magnetic Resonance Volume 28: High Resolution EPR,*, ed. G. Hanson and L. Berliner, Springer, 2009, pp. 63–103.

[165] R. Kappl, M. Ebelsh, F. Hannemann, R. Bernhardt and J. Hüttermann, *Applied Magnetic Resonance*, 2006, **30**, 427–459.

[166] R. Kappl, S. Ciurli and C. Luchinat, *Journal of the American Chemical Society*, 1999, **121**, 1925–1935.

[167] A. Müller, I. Tscherny, R. Kappl, E. C. Hatchikian, J. Hüttermann and R. Cammack, *Journal of Biological Inorganic Chemistry*, 2002, **7**, 177–194.

[168] R. Kappl, L. D. Eltis, M. B. Caspersen, H. E. M. Christensen and J. Hüttermann, *Applied Magnetic Resonance*, 2007, **31**, 483–507.

[169] T. Iwasaki, R. Kappl, G. Bracic, N. Shimizu, D. Ohmori and T. Kumasaka, *Journal of Biological Inorganic Chemistry*, 2011, **16**, 923–935.

[170] D. Goldfarb, *Pulsed ENDOR Methods - Lecture 11, EPR Summer School, Constance*, 2010.

[171] W. B. Mims, *Proceedings of the Royal Society A: Mathematical, Physical and Engineering Sciences*, 1965, **283**, 452–457.

[172] E. Davies, *Physics Letters A*, 1974, **47**, 1–2.

[173] Bruker-Biospin, *Stochastic ENDOR*, 2012, http://www.bruker-biospin.com/sto_endor.html.

[174] B. Epel, A. Pöppl, P. Manikandan, S. Vega and D. Goldfarb, *Journal of Magnetic Resonance*, 2001, **148**, 388–397.

[175] S. Van Doorslaer, *Correlation Peaks and 2D HYSCORE - Lecture 21, EPR Summer School, Constance*, 2010.

[176] P. Höfer, A. Grupp, H. Nebenfuhr and M. Mehring, *Chemical Physics Letters*, 1986, **132**, 279–282.

[177] J. Fritz, H. Anderson, J. Fee, C. Palmer, R. H. Sands, J. C. M. Tsibris, I. C. Gunsalus, W. H. Orme-Johnson and H. Beinert, *Biochimica et Biophysica Acta*, 1971, **253**, 110–133.

[178] M. M. Dicus, A. Conlan, R. Nechushtai, P. A. Jennings, M. L. Paddock, R. D. Britt and S. Stoll, *Journal of the American Chemical Society*, 2010, **132**, 2037–2049.

[179] W. Dunham and R. H. Sands, *Biochemical and Biophysical Research Communications*, 2003, **312**, 255–261.

[180] C. Canne, M. Ebelshäuser, E. Gay, J. K. Shergill, R. Cammack, R. Kappl and J. Hüttermann, *Journal of Biological Inorganic Chemistry*, 2000, **5**, 514–526.

[181] M. K. Bowman, E. A. Berry, A. G. Roberts and D. M. Kramer, *Biochemistry*, 2004, **43**, 430–436.

[182] R. J. Gurbiel, P. E. Doan, G. T. Gassner, T. J. Macke, D. A. Case, T. Ohnishi, J. A. Fee, D. P. Ballou and B. M. Hoffman, *Biochemistry*, 1996, **35**, 7834–7845.

[183] A. Bencini and D. Gatteschi, *EPR of Exchange Coupled Systems*, Springer-Verlag, Berlin, 1990.

[184] I. F. Sevrioukova, *Journal of Molecular Biology*, 2005, **347**, 607–621.

[185] N. U. Jain, E. Tjioe, A. Savidor and J. Boulie, *Biochemistry*, 2005, **44**, 9067–9078.

[186] J. Mouesca, L. Noodleman, D. A. Case and B. Lamottes, *Inorganic Chemistry*, 1995, **34**, 4347–4359.

[187] J.-M. Mouesca and B. Lamotte, *Coordination Chemistry Reviews*, 1998, **178-180**, 1573–1614.

[188] W. R. Dunham, G. Palmer, R. H. Sands and A. J. Bearden, *Biochimica et Biophysica Acta*, 1971, **253**, 373–384.

[189] W. R. Dunham, A. J. Bearden, I. T. Salmeen, G. Palmer, R. H. Sands, W. H. Orme-Johnson and H. Beinert, *Biochimica et Biophysica Acta*, 1971, **253**, 134–152.

[190] J. T. Sage, Y.-M. Xia, P. G. Debrunner, D. T. Keough, J. de Jersey and B. Zerner, *Journal of the American Chemical Society*, 1989, **111**, 7239–7247.

[191] B. Guigliarelli, P. Bertrand and J.-P. Gayda, *The Journal of Chemical Physics*, 1986, **85**, 1689–1692.

[192] L. Noodleman, C. Y. Peng, D. A. Case and J. M. Mouesca, *Coordination Chemistry Reviews*, 1995, **144**, 199–244.

[193] P. Bertrand, C. More, B. Guigliarelli, A. Fournel, B. Bennett and B. Howed, *Journal of the American Chemical Society*, 1994, **116**, 3078–3086.

[194] P. Bertrand, P. Camensuli, C. More and B. Guigliarelli, *Journal of Physical Chemistry A*, 1996, **118**, 1426–1434.

[195] J. Owen and J. H. M. Thornley, *Reports on Progress in Physics*, 1966, **29**, 675–728.

[196] M. van Gastel, W. Lubitz, G. Lassmann and F. Neese, *Journal of the American Chemical Society*, 2004, **126**, 2237–2246.

[197] C. Schulz and P. G. Debrunner, *Physics Letters A*, 1979, **69**, 360–363.

[198] I. Moura, B. H. Huynh, R. P. Hausinger, J. Le Gall, A. V. Xavier and E. Münck, *Journal of Biological Chemistry*, 1980, **255**, 2493–2498.

[199] B. Epel, J. Niklas, M. L. Antonkine and W. Lubitz, *Applied Magnetic Resonance*, 2006, **30**, 311–327.

[200] F. Moriaud, S. Gambarelli, B. Lamotte and J. M. Mouesca, *Journal of Magnetic Resonance*, 2001, **153**, 238–245.

[201] F. Moriaud, S. Gambarelli, B. Lamotte and J.-M. Mouesca, *The Journal of Physical Chemistry B*, 2001, **105**, 9631–9642.

[202] M. Orio and J.-M. Mouesca, *Inorganic Chemistry*, 2008, **47**, 5394–5416.

[203] S. Gambarelli and J.-m. Mouesca, *Inorganic Chemistry*, 2004, **43**, 1763–1773.

[204] P. Bertrand, B. Guigliarelli, J.-P. Gayda, P. Beardwood and J. F. Gibson, *Biochimica et Biophysica Acta*, 1985, **831**, 261–266.

[205] P. Bertrand and B. Guigliarelli, *Advances in Inorganic Chemistry*, 1999, **47**, 421–497.

[206] Y. Asada, R. Mutoh, M. Ishiura and H. Mino, *Journal of Magnetic Resonance*, 2011, **213**, 200–205.

[207] P. E. Spindler, Y. Zhang, B. Endeward, N. Gershernzon, T. E. Skinner, S. J. Glaser and T. F. Prisner, *Journal of Magnetic Resonance*, 2012, **218**, 49–58.

[208] A. Godt, M. Schulte, H. Zimmermann and G. Jeschke, *Angewandte Chemie (International ed.)*, 2006, **45**, 7560–7564.

[209] I. Kaminker, M. Florent, B. Epel and D. Goldfarb, *Journal of Magnetic Resonance*, 2011, **208**, 95–102.

[210] G. Jeschke, M. Sajid, M. Schulte, N. Ramezanian, A. Volkov, H. Zimmermann and A. Godt, *Journal of the American Chemical Society*, 2010, **132**, 10107–10117.

[211] F. Bloch and A. Siegert, *Physical Review*, 1940, **57**, 522–527.

[212] M. K. Bowman and A. G. Maryasov, *Journal of Magnetic Resonance*, 2007, **185**, 270–282.

[213] A. D. Milov, A. G. Maryasov, Y. D. Tsvetkov and J. Raap, *Chemical Physics Letters*, 1999, **303**, 135–143.

[214] A. D. Milov, Y. D. Tsvetkov, E. Y. Gorbunova, L. G. Mustaeva, T. V. Ovchinnikova and J. Raap, *Biopolymers*, 2002, **64**, 328–336.

[215] B. E. Bode, R. Dastvan and T. F. Prisner, *Journal of Magnetic Resonance*, 2011, **211**, 11–17.

[216] P. P. Borbat and J. H. Freed, *Chemical Physics Letters*, 1999, **313**, 145–154.

[217] M. Nectschein and J. S. Hyde, *Physical Review Letters*, 1970, **24**, 672–674.

[218] L. Emsley and G. Bodenhauser, *Chemical Physics Letters*, 1990, **168**, 297–303.

[219] R. H. Crepeau, A. Dulic, J. Gorcester, T. R. Saarinen and J. H. Freed, *Journal of Magnetic Resonance*, 1989, **84**, 184–190.

[220] A. G. Maryasov and Y. D. Tsvetkov, *Applied Magnetic Resonance*, 2000, **18**, 583–605.

[221] O. W. Sorensen, G. W. Eich, M. H. Levitt, G. Bodenhausen and R. R. Ernst, *Progress in NMR Spectroscopy*, 1983, **16**, 163–192.

[222] A. D. Milov, B. D. Naumov and Y. D. Tsvetkov, *Applied Magnetic Resonance*, 2004, **26**, 587–599.

[223] H. R. Ward and R. G. Lawler, *Journal of the American Chemical Society*, 1967, **89**, 5518–5519.

[224] A. Bhattacharya, *Nature (News Feature)*, 2010, **463**, 605–606.

[225] J. Haase, M. Kozlov, K.-H. Müller, H. Siegel, B. Büchner, H. Eschrig and A. G. Webb, *Journal of Magnetism and Magnetic Materials*, 2005, **290-291**, 438–441.

[226] B. Brocklehurst, *Chemical Society Reviews*, 2002, **31**, 301–311.

[227] K. B. Henbest, K. Maeda, P. J. Hore, M. Joshi, A. Bacher, R. Bittl, S. Weber, C. R. Timmel and E. Schleicher, *Proceedings of the National Academy of Sciences of the United States of America*, 2008, **105**, 14395–14399.

[228] I. Kuprov, T. D. Craggs, S. E. Jackson and P. J. Hore, *Journal of the American Chemical Society*, 2007, **129**, 9004–9013.

[229] R. Kaptein, *Chemical Communications*, 1971, **14**, 732–733.

[230] F. Chiti and C. M. Dobson, *Annual Review of Biochemistry*, 2006, **75**, 333–366.

[231] S. Baglioni, F. Casamenti, M. Bucciantini, L. M. Luheshi, N. Taddei, F. Chiti, C. M. Dobson and M. Stefani, *The Journal of Neuroscience*, 2006, **26**, 8160–8167.

[232] M. Stefani, *The Neuroscientist*, 2007, **13**, 519–531.

[233] A. Hå kansson, B. Zhivotovsky, S. Orrenius, H. Sabharwal and C. Svanborg, *Proceedings of the National Academy of Sciences of the United States of America*, 1995, **92**, 8064–8068.

[234] M. Svensson, A. Hå kansson, A. K. Mossberg, S. Linse and C. Svanborg, *Proceedings of the National Academy of Sciences of the United States of America*, 2000, **97**, 4221–4226.

[235] M. Svensson, H. Sabharwal, A. Hå kansson, A. K. Mossberg, P. Lipniunas, H. Leffler, C. Svanborg and S. Linse, *The Journal of Biological Chemistry*, 1999, **274**, 6388–6396.

[236] A.-K. Mossberg, K. Hun Mok, L. A. Morozova-Roche and C. Svanborg, *The FEBS Journal*, 2010, **277**, 4614–4625.

[237] M. Svensson, J. Fast, A.-K. Mossberg, L. Gustafsson, O. Hallgren, C. Du, C. L. Brooks, L. Berliner, S. Linse and C. Svanborg, *Protein Science*, 2003, **12**, 2794–2804.

[238] J. Pettersson-Kastberg, A.-K. Mossberg, M. Trulsson, Y. J. Yong, S. Min, Y. Lim, J. E. O'Brien, C. Svanborg and K. H. Mok, *Journal of Molecular Biology*, 2009, **394**, 994–1010.

[239] M. Svensson, A.-K. Mossberg, J. Pettersson, S. Linse and C. Svanborg, *Protein Science*, 2003, **12**, 2805–2814.

[240] W. Fischer, *Cancer Research*, 2004, **64**, 2105–2112.

[241] L. Gustafsson, R. N. Leijonhufvud, A. Aronsson, A.-K. Mossberg and C. Svanborg, *The New England Jornal of Medicine*, 2004, **350**, 2663–2672.

[242] A.-K. Mossberg, Y. Hou, M. Svensson, B. Holmqvist and C. Svanborg, *The Journal of Urology*, 2010, **183**, 1590–1597.

[243] M. Zhang, F. Yang, J. Chen, C.-Y. Zheng and Y. Liang, *Chemico-Biological Interactions*, 2009, **180**, 131–142.

[244] O. B. Morozova, A. V. Yurkovskaya, R. Z. Sagdeev, K. H. Mok and P. J. Hore, *The Journal of Physical Chemistry B*, 2004, **108**, 15355–15363.

[245] K. H. Mok, T. Nagashima, I. J. Day, P. J. Hore and C. M. Dobson, *Proceedings of the National Academy of Sciences of the United States of America*, 2005, **102**, 8899–8904.

[246] K. Wilhelm, A. Darinskas, W. Noppe, E. Duchardt, K. H. Mok, V. Vukojević, J. Schleucher and L. A. Morozova-Roche, *The FEBS Journal*, 2009, **276**, 3975–3989.

[247] S. B. Nielsen, K. Wilhelm, B. Vad, J. Schleucher, L. A. Morozova-Roche and D. Otzen, *Journal of Molecular Biology*, 2010, **398**, 351–361.

[248] L. A. Morozova-Roche, *FEBS Letters*, 2007, **581**, 2587–2592.

[249] H. A. Lashuel, D. Hartley, B. M. Petre, T. Walz, P. T. Lansbury Jr., J. Turner, J. C. King, T. A. Lachlan-cope and P. D. Jones, *Nature*, 2002, **418**, 4–5.

[250] J. Pettersson-Kastberg, S. Aits, L. Gustafsson, A. Mossberg, P. Storm, M. Trulsson, F. Persson, K. H. Mok and C. Svanborg, *Annals of Medicine*, 2009, **41**, 162–176.

[251] C. Düringer, A. Hamiche, L. Gustafsson, H. Kimura and C. Svanborg, *The Journal of Biological Chemistry*, 2003, **278**, 42131–421315.

[252] S. Min, J. Meehan, L. M. Sullivan, N. P. Harte, Y. Xie, G. P. Davey, C. Svanborg, A. Brodkorb and K. H. Mok, *Biochemical Society Transactions*, 2012, **40**, 746–751.

[253] A.-K. Mossberg, M. Puchades, O. Halskau, A. Baumann, I. Lanekoff, Y. Chao, A. Martinez, C. Svanborg and R. Karlsson, *PloS one*, 2010, **5**, e9384.

[254] P. Rammer, L. Groth-Pedersen, T. Kirkegaard, M. Daugaard, A. Rytter, P. Szyniarowski, M. Hoyer-Hansen, L. K. Povlsen, J. Nylandsted, J. E. Larsen and M. Jäättelä, *Molecular Cancer Therapeutics*, 2010, **9**, 24–32.

[255] W. P. Aue, E. Bartholdi and R. R. Ernst, *The Journal of Chemical Physics*, 1976, **64**, 2229–2246.

[256] J. Jeener, B. H. Meier, P. Bachmann and R. R. Ernst, *The Journal of Chemical Physics*, 1979, **71**, 4546–4553.

[257] A. Bax and D. G. Davis, *Journal of Magnetic Resonance*, 1985, **65**, 355–360.

[258] C. Griesinge, G. Otting, K. Wuthrich and R. R. Ernst, *Journal of the American Chemical Society*, 1988, **110**, 7870–7872.

[259] E. L. Elson and D. Magde, *Biopolymers*, 1974, **13**, 1–27.

[260] K. Maeda, C. E. Lyon, J. J. Lopez, M. Cemazar, C. M. Dobson and P. J. Hore, *Journal of Biomolecular NMR*, 2000, **16**, 235–244.

[261] T.-L. Hwang and A. Shaka, *Journal of Magnetic Resonance, Series A*, 1995, **112**, 275–279.

[262] P. Stilbs, *Progress in NMR Spectroscopy*, 1987, **19**, 1–45.

[263] H. E. Gottlieb, V. Kotlyar and A. Nudelman, *Journal of Organic Chemistry*, 1997, **62**, 7512–7515.

[264] L. A. Morozova, D. T. Haynie, C. Arico-Muendel, H. Van Dael and C. M. Dobson, *Nature Structural Biology*, 1995, **2**, 871–875.

[265] H. Van Dael, P. Haezebrouck, L. Morozova, C. Arico-Muendel and C. M. Dobson, *Biochemistry*, 1993, **32**, 11886–11894.

[266] ACD/Labs, *ACD/SpecManager*, http://www.acdlabs.com/products/km/ackm/specman/.

[267] L. M. Loura, A. Fedorov and M. Prieto, *Biochimica et Biophysica Acta*, 2000, **1467**, 101–112.

[268] H. Sun, D. V. Greathouse, O. S. Andersen and R. E. Koeppe, *The Journal of Biological Chemistry*, 2008, **283**, 22233–22243.

[269] H. Tsuge, H. Ago, M. Noma, K. Nitta, S. Sugai and M. Miyano, *Journal of Biochemistry*, 1992, **111**, 141–143.

[270] C. Evrard, J. Fastrez and J. P. Declercq, *Journal of Molecular Biology*, 1998, **276**, 151–164.

[271] A. K. Leung, H. S. Duewel, J. F. Honek and A. M. Berghuis, *Biochemistry*, 2001, **40**, 5665–5673.

[272] K. A. Dunker, C. J. Oldfield, J. Meng, P. Romero, J. Y. Yang, J. W. Chen, V. Vacic, Z. Obradovic and V. N. Uversky, *BMC Genomics*, 2008, **9 Suppl 2**, S1.

[273] R. Ward, A. Bowman, E. Sozudogru, H. El-Mkami, T. Owen-Hughes and D. G. Norman, *Journal of Magnetic Resonance*, 2010, **207**, 164–167.

[274] A.-M. Ampere, *Memoires de l'academie royale des sciences de l'institut de france*, 1823, **6**, 175–387.

[275] J. Thomson, *Philosophical Magazine Series 5*, 1897, **44**, 293–316.

[276] J. Thomson, *Philosophical Magazine Series 6*, 1904, **7**, 237–265.

[277] H. Geiger and E. Marsden, *Proceedings of the Royal Society A: Mathematical, Physical and Engineering Sciences*, 1909, **82**, 495–500.

[278] N. Bohr, *Philosophical Magazine Series 6*, 1913, **26**, 1–25.

[279] O. Stern and W. Gerlach, *Zeitschrift für Physik A: Hadrons and Nuclei*, 1922, **9**, 353–355.

[280] W. Pauli, *Zeitschrift für Physik A: Hadrons and Nuclei*, 1925, **31**, 765–783.

[281] W. Pauli, *Zeitschrift für Physik A: Hadrons and Nuclei*, 1925, **31**, 373–385.

[282] I. I. Rabi, S. Millman and P. Kusch, *Physical Review*, 1939, **55**, 526–535.

[283] G. Feher, *Physical Review*, 1956, **103**, 834–835.

[284] W. B. Mims, K. Nassau and J. D. McGee, *Physical Review*, 1961, **123**, 2059–2069.

[285] W. Pauli, *Zeitschrift für Physik A: Hadrons and Nuclei*, 1926, **36**, 336–363.

[286] R. Frisch, T. E. Phipps, E. Segre and O. Stern, *Nature*, 1932, **130**, 892–893.

[287] F. Bloch and I. I. Rabi, *Reviews of Modern Physics*, 1945, **17**, 237 –244.

[288] W. D. Knight, *Physical Review*, 1949, **76**, 1259 –1260.

[289] E. L. Hahn, *Physical Review*, 1950, **80**, 580–594.

[290] G. Wagner, A. Kumar and K. Wuthrich, *European Journal of Biochemistry*, 1981, **114**, 375–384.

[291] R. G. Lawler, *Journal of the American Chemical Society*, 1967, **89**, 5519–5521.

[292] H. Bargon, J. Fischer and U. Johnsen, *Zeitschrift für Naturforschung A: Astrophysik, Physik und Physikalische Chemie*, 1967, **A 22**, 1551.

[293] H. Bargon and J. Fischer, *Zeitschrift für Naturforschung A: Astrophysik, Physik und Physikalische Chemie*, 1967, **A 22**, 1556.

[294] R. Kaptein and J. L. Oosterhoff, *Chemical Physics Letters*, 1969, **4**, 195–197.

[295] R. Kaptein and J. L. Oosterhoff, *Chemical Physics Letters*, 1969, **4**, 214–216.

[296] S. Schaublin, A. H. Hener and R. R. Ernst, *Journal of Magnetic Resonance*, 1974, **13**, 196–216.

[297] R. Kaptein, K. Dijkstra, F. Muller, C. G. van Schagen and A. J. W. G. Visser, *Journal of Magnetic Resonance*, 1978, **31**, 171–176.

[298] R. Kaptein, K. Dijkstra and K. Nicolay, *Nature*, 1978, **274**, 293–294.

[299] C. L. Kingsford, B. Chazelle and M. Singh, *Bioinformatics*, 2005, **21**, 1028–1036.

Appendix A

A historical review of EPR and NMR

The development of magnetic resonance techniques was driven by the desire of the early-modern physicists to understand quantum mechanics. Early observations of magnetic resonance transitions occurred in experiments designed to illustrate the presence of quantum mechanical properties.

A.1 A brief time-line of EPR and quantum mechanics

The first observation of magnetism associated with the motion of electronic charge was made almost 200 years ago by André-Marie Ampère in 1823.[274] Despite that, it was not until 1891 that the electron was 'named' as a unit of electricity by George Johnstone Stoney and it was a full six years later that the electron was formally 'discovered' and its charge to mass ratio measured by J. J. Thompson using cathode rays.[275] Thompson also understood that the electron formed part of the atomic structure and in 1904 suggested the plum pudding atomic model, whereby all of the electrons are free to move within a cloud of positive substance.[276] In 1909, this structure was disproved by Rutherford, Marsden and Geiger, who showed that the scattering patterns of alpha particles fired at a sheet of gold leaf inferred the presence of a dense positively charges nucleus surrounded by an electron cloud.[277]

The Rutherford model was further modified in 1913 by Niels Bohr, who suggested that the electrons formed circular orbits around the centrally charged nucleus which had specific energies, allowing the spacing of the spectral lines of hydrogen to be explained via the Rydberg formula:[278]

$$\frac{1}{\lambda} = R\left(\frac{1}{n_1^2} - \frac{1}{n_2^2}\right) \tag{A.1}$$

where λ is the wavelength of the lines in the hydrogen spectrum, n_1 and n_2 are the quantum numbers of the two electronic energy levels and R is the Rydberg constant, itself a collection of other constants: $R = \frac{m_e e^4}{8\epsilon_0^2 h^3 c}$ with m_e as the mass of an electron, e, the electronic charge, ϵ_0 is the permittivity of free space, h is Planks constant and c is the speed of light in a vacuum.

A.1.1 The Stern-Gerlach experiment, hydrogen fine structure and Zeeman splittings

Although the Bohr model quantized the energy levels of the electron within the atom which accounted for the main structure of the hydrogen spectrum, quantified by the Rydberg formula, it could not account for the observation of closely spaced splitting within hydrogen spectral lines, known as fine structure. The explanation for this came in 1921, following a surprising result for the deflection of electronically neutral silver atoms in an inhomogeneous magnetic field. This is known as the Stern-Gerlach experiment and the experimental apparatus is shown in Fig. A.1.[279]

In 1897, J. J. Thompson had already show that streams of electrons in a vacuum, known as cathode rays, could be deflected by a magnetic field.[275] However, whereas the cathode rays were spread by the magnetic field from a fine beam to a broad fan shape, the beam of silver atoms was split into two discrete bands with equal but opposite positive and negative deflections. This result suggested the existence of another form of quantization within the atom; this was defined as the spin angular momentum. Silver atoms have the electronic structure [Kr] $4\,\mathrm{D}^{10}\ 5\,\mathrm{S}^1$ and as such contain a single unpaired electron in the outer 5S shell. Therefore, the behaviour of the atom in the magnetic field is determined by the state of this unpaired electron. If the silver atoms or the unpaired electron within them were classically spinning particles, their spin angular momentum vectors would be expected to be random and continuous, so

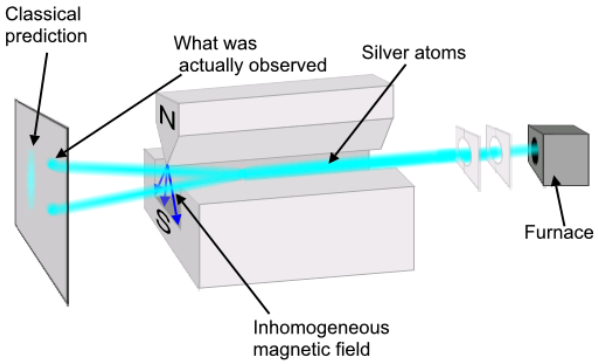


Figure A.1: The experimental apparatus used in the Stern-Gerlach experiment. Figure made by Theresa Knott for *www.wikipedia.org*. This figure is licensed under the GNU Free Documentation License.

that each atom would be deflected by a different amount, producing a distribution on the detection screen. The observation of two discrete paths can be explained by invoking the concept of quantization in angular momenta, which had already been predicted theoretically by Goudsmit and Uhlenbeck, who are credited with the discovery of an electron's spin in 1925.[36] These two scientists were the first to recognize that by allowing the electron to 'spin'. The angular momentum associated with the 'spinning' electron, which they designated m_s, couples to the angular momentum of the electrons motion around the nucleus, designated by m_l. This coupling explains the fine structure seen in the emission spectra of a hydrogen atom, as well as the splittings in spectral lines induced by exposure to a static external magnetic field, first observed by Zeeman in 1897.[32–35] The presence of two spin states of the electron also explains the discrete spectrum observed in the Stern-Gerlach experiment; quantum mechanical explanation of these phenomena is given in Appendix C.

It should be noted that the discrete spectra can also be observed in a stream of electrons; however, due to the charge on the particles, a Lorentz force is induced as the stream passes through a magnetic field, which causes the electron beam to bend. The magnitude of this deflection is much larger than that due to the spin angular momentum and therefore obscures the observation of the spin angular momentum. The Lorentz force can be counteracted with an electric field and, once this is achieved, the splitting due to the discrete angular momenta can be seen.

1925 also saw Pauli publish the exclusion principle, which stated that within an atom no two fermions could occupy the same quantum state simultaneously.[280,281] This allowed the electronic structure of an atom to be defined.

A.1.2 Progression towards modern EPR techniques

After the Stern-Gerlach experiment, many other advancements, both theoretical and experimental, were made in fairly rapid succession. These included Dirac's equation of 1928, which showed that the spin of an electron could be predicted theoretically from the relativistic Hamiltonian.[26,27] In 1939, the experimental advancements cumulated in the first measurements of magnetic resonance by Rabi and co-workers,[282] and developments made during the World War II in microwave technology for use in radar allowed the first measurements of EPR in 1944 by Zavoisky.[23]The next major breakthrough in EPR techniques came in 1956, when George Ferher used a radio frequency source in conjunction with an EPR experiment to simultaneously excite nuclear spin state transitions, a technique that was dubbed Electron Nuclear DOuble Resonance (ENDOR).[283] These measurements were all continuous wave, whereby a single frequency microwave excitation source is used and the magnetic field strength can be changed to allow detection of a complete spectrum.

In 1958, R. J. Blume measured the first electron spin echo (shown in Fig. A.2), which paved the way for the modern pulsed EPR techniques utilized in this thesis.[21]

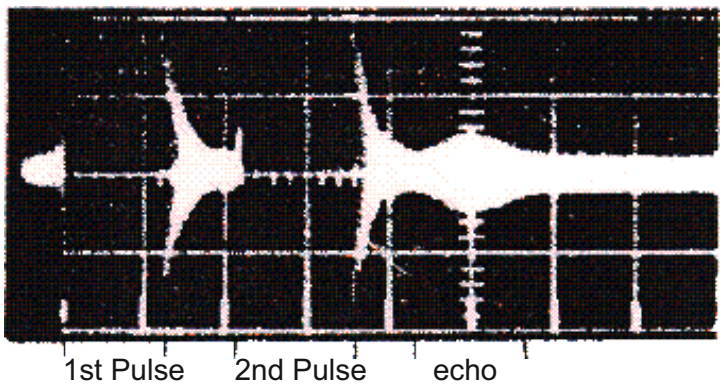


Figure A.2: The first electron spin echo reported by R. Blume in 1958. This figure is reprinted from *Physical Review*, **109(6)**, J. Blume, Electron spin relaxation times in sodium-ammonia solutions, 1867-1873.[21]

The development of pulsed EPR was progressed in the group of W. B. Mims during the 1960s resulting in the development of two important pulse techniques: Electron Spin Envelope Echo Modulation (ESSEM) in 1961[284] and Pulsed ENDOR in 1965.[171] The main pulse sequences utilized in this thesis are: Davies ENDOR, originated by E. R. Davies in 1974;[172] HYSCORE, proposed in 1986 by Peter Höfer et al.;[176] and DEER (or PELDOR), originally formulated as a three-pulse sequence by Milov and Salikov in 1981 and later modified to a four-pulse technique by Jeschke and Spiess in 2000.[44,60]

A.2 A brief time-line of NMR and CIDNP

The year after the discovery of the spin angular momentum of an electron in 1925 by Goudsmit and Uhlenbeck, and the publication of his exclusion principle, Pauli extended the idea to the nucleus and made the prediction of nuclear spin angular momentum.[285] In 1932, Otto Stern was able to make the first experimental measurements of this phenomenon using molecular beams.[286] The first recognizable NMR experiments were conducted in 1945 independently by Bloch, using water,[24,287] and by Purcell, using paraffin.[25] However, the chemical importance of NMR did not become apparent until 1949, with the discovery of NMR chemical shifts. It was initially thought that each type of atom would have its own resonant frequency, which was believed to be independent of the chemical environment. Walter David Knight showed that this hypothesis was incorrect when he was able to measure different resonant frequencies for atoms in metallic and non-metallic environments.[288] The following year, it was shown that this principle also applied for atoms of the same type with different chemical environments within the same molecule, when the ^{1}H for ethanol was recorded.[22] The resulting spectrum is shown in Fig. A.3.

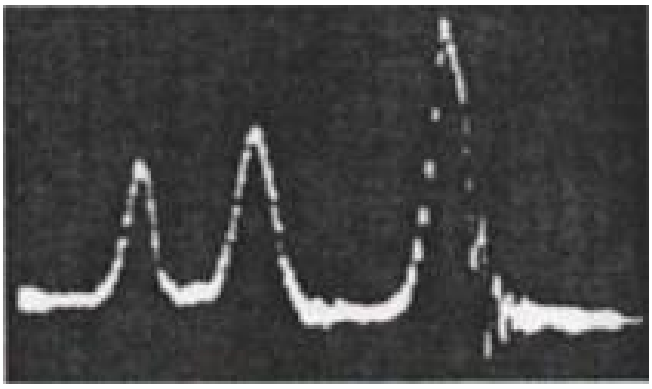


Figure A.3: The first NMR signal observed from ethanol in 1950.[22] The peaks from left to right correspond to the hydroxyl proton, the ethyl protons and the methyl protons. This figure is reprinted with permission from *The Journal of Chemical Physics*, **19(4)**, J. T. Arnold, S. S. Dharmatti and M. E. Packard, Chemical Effects on Nuclear Induction Signals from Organic Compounds, 507. Copyright © 1951, AIP Publishing LLC.

The fact that environmental factors affect the resonant nuclear frequency of an atom made the technique very attractive to chemists, who wished to use it as a non-invasive analytical method for determining the structure and identity of different molecules. It was this demand for NMR that drove the rapid development of the technique. In 1950, Hahn recorded the first nuclear spin echo,[289] eight years in advance of the same experiment on electrons, conducted by Blume.[21] The observation of the spin echo opened the way for all of the modern pulsed NMR techniques.

As with EPR, the early experiments were all continuous wave and carried out at low magnetic fields, easily achievable using electromagnets. However, it was soon realized that in order to gain greater resolution in the spectra, it was necessary to go to higher magnetic fields. This was facilitated by the introduction of superconducting magnets.

The next major improvement was the advent of Fourier Transform methods (FT-NMR). This technique allows a broad band of frequencies to be excited simultaneously and those that are resonant with the sample can be found from the Fourier transform of the time-domain signal, which is a direct response to the applied pulse(s).[41] This negates the need for either the frequency source or the magnetic field to be swept, which makes the experiment far more robust and allows for complex pulse sequences, such as the double resonance techniques required to elucidate the structure of proteins using NMR. The

first solution state protein structure produced using NMR was that of a pancreatic trypsin inhibitor in 1981 by Wagner et al.[290]

A.2.1 Chemically Induced Dynamic Nuclear Polarisation

Chemically Induced Dynamic Nuclear Polarization (CIDNP) uses NMR to detect non-Boltzmann distributions of nuclear spin states, which are induced by thermal or photochemical reactions. The non-Boltzmann states give rise to enhancements in the NMR signals detected, which can either be absorptive or emissive. The first CIDNP effects were seen in 1967 by Bargon and Fischer, and, independently, by Ward and Lawler.[223,291–293] The initial theory utilized to explain the observed enhancements was based on Dynamic Nuclear Polarization; however, it was soon found that in many cases this fails to explain the phase of the CIDNP effect. Thus, CIDNP is actually a misnomer and in 1969 a second mechanism was proposed by Closs and independently by Kaptein and Oosterhoff.[294,295] This invoked the formation of a radical pair, the recombination of which produces a molecule with a non-Boltzmann distribution of spin states.

As with early NMR experiments, the first CIDNP experiments were performed on a continuous wave NMR spectrometer and it was not until the 1970s that Fourier Transform NMR was used in conjunction with a CIDNP experiment.[296]

Although CIDNP remains a somewhat niche technique, within broader magnetic resonance research it has found applications in characterizing transient free radicals and their reaction mechanisms.

The photo-CIDNP technique utilized in this thesis originated in the group of Kaptein in 1978.[297] This adaptation uses light to induce the formation of a radical pair between a dye molecule and an electron transfer partner, commonly an electron donor. It has allowed the use of CIDNP in conjunction with protein NMR. The large size of proteins leads inherently to complex NMR spectra, as we have already seen, it was not until 1981 that the first protein structure was solved using NMR. Since the enhancements seen in CIDNP are localized to the nuclei, which can couple to the unpaired electron formed via the hyperfine mechanism, in the case of proteins this is limited to tyrosine, tryptophan and histidine amino acids that can form radical pairs with a photo-excited flavin dye molecule. In this way,

CIDNP can be used to simplify the spectrum for a large protein, by only highlighting part of it. For a protein sample where a flavin is added to the solution as a photo-sensitizer, only those amino acids on the surface of the protein will interact with the flavin and thus the CIDNP signals can be used as a probe of surface accessibility. This application was first used by Kaptein in 1978.[298]

Further experimental and theoretical detail about photo-CIDNP are given in Chapter 8.

Appendix B

The classical description of magnetic resonance

Just as a charged rotating particle in classical electrodynamics possesses a magnetic dipole moment. so the spin of an electron and its motion within an orbital cause it to possess magnetic dipole moments. Classically, the magnetic dipole moment is given by:

$$\mu = IA \tag{B.1}$$

where I is the current flowing and A is the area within the loop. The direction of the magnetic moment is normal to the loop of current (see Fig. B.1). If an external magnetic field of magnitude B is applied, the torque, τ, on the current loop is given by:

$$\tau = \mu B sin\theta \tag{B.2}$$

where θ is the angle between the magnetic dipole moment and the external magnetic field (see Fig. B.1).

The torque has a direction and acts perpendicularly to the magnetic moment, $\boldsymbol{\mu}$, and the external magnetic field, $\mathbf{B}$; thus it can also be written as a vector product:

$$\boldsymbol{\tau} = \boldsymbol{\mu} \times \mathbf{B} \tag{B.3}$$

The action of the torque will cause the magnetic moment to precess around the direction of the external magnetic field at a characteristic frequency, which is known as the Larmor frequency.

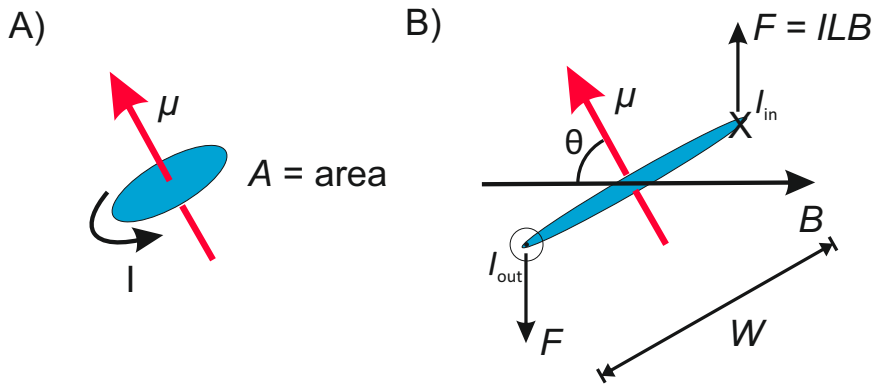


Figure B.1: **A)** The magnetic dipole moment, μ, originating from the flow of current, I, in a loop. **B)** The torque active on the same loop of current, when placed in an external static magnetic field. The force acting on the loop, F, is equal to the product of the current, I, the magnetic field, B, and the length of the wire in the field, L. The force is related to the torque as follows: $\tau = FW \sin\theta$, where W is the width of the wire loop (such that area $= A = WL$) and θ is the angle shown in the figure. The torque, $\boldsymbol{\tau}$, acts perpendicularly to the magnetic moment, causing the magnetic moment to precess around the magnetic field.

B.1 The magnetic dipole for orbital angular momentum

The motion of an electron within an orbital is akin to the classical motion of a current in a wire. If we consider the motion in an orbital to be circular, the current caused by this motion is given by:

$$I = \frac{-e}{T} = \frac{-ev}{2\pi r} \tag{B.4}$$

where T is the period of the orbit, e is the electronic charge, v is the velocity of the electron and r is

the radius of the orbit. The orbital magnetic dipole moment is therefore:

$$\mu_l = IA = \frac{-ev}{2\pi r}.\pi r^2.\frac{m_e}{m_e} = \frac{-e}{2m_e}L \tag{B.5}$$

where m_e is the mass of the electron and L is the magnitude of the orbital angular momentum, which is given classically for an electron by: $L = m_e vr$. For the quantized picture, we must replace the classical angular momentum L with the quantized magnitude of the orbital angular momentum quantum number, l. So μ_l becomes:

$$\mu_l = \frac{-e}{2m_e}\sqrt{l(l+1)}\hbar = -\sqrt{l(l+1)}\mu_B \tag{B.6}$$

where μ_B is known as the Bohr Magneton and is a collection of constants, $\frac{e\hbar}{2m_e} = -9.27 \times 10^{-24}\mathrm{JT}^{-1}$.

Orbital angular momentum is a vector property. $\mathbf{l}$ and therefore the vector form of $\boldsymbol{\mu}_\mathbf{l}$ is given by:

$$\boldsymbol{\mu}_\mathbf{l} = -\mu_B\frac{\mathbf{l}}{\hbar} \tag{B.7}$$

When a set of axes can be defined through the application of an external static magnetic field, which is chosen to be in alignment with the z-axis, the z-component of the orbital magnetic moment is defined as:

$$\mu_{l,z} = -m_l\mu_B \tag{B.8}$$

where m_l is the magnetic quantum number.

Appendix C

Experimental evidence for spin angular momentum

Before magnetic resonance spectroscopy was established as an experimental technique, there were three important experimental observations that led to our modern understanding of the role that angular momentum plays on the subatomic level. These were the Zeeman effect, the Stern-Gerlach experiment and the observation of fine structure in the emission spectrum of hydrogen.

The explanations for all three of these experiments rely on the interaction of the magnetic dipole moments, generated by spin and orbital angular momenta, either with each other, such as in the fine splittings observed in hydrogen spectra, or with an external magnetic field, as is the case in the anomalous Zeeman effect and in the Stern-Gerlach experiment.

C.1 The interactions or coupling of angular momenta with one another and external magnetic fields

Like the classical case of placing two small magnets close to one another or a smaller bar magnet in a larger external magnetic field, different energy states for the magnets are possible, which are dependent on the orientation of the magnets with respect to one another and the magnetic fields they produce.

For a bar magnet in a larger external magnetic field, the lowest energy state is when the magnet is aligned with the external magnetic field and the highest energy state occurs when the magnet is aligned against the field. In the classical case, there are an infinite number of intermediate energy states possible, when the magnet is at a given angle to the external field. Similarly for two smaller magnets, there will be an infinite number of orientational configurations, some of higher energy than others. For cases with a large external magnetic field, it is the direction of the magnetic field that prescribes the energy of a given orientation of a magnet with respect to this external field and, for two smaller magnets, it is their relative orientation with respect to one other that dictates the energy of the system. It is common practice to notate the direction of the largest magnetic dipole or the external field as the z-direction, to provide an arbitrary set of axes with which to view the system and its energy.

In the quantum mechanical case with magnetic dipoles originating from angular momenta, the number of angular momenta states is quantized and thus the number of orientations of the magnetic dipole with respect to the external magnetic field is also quantized. For a spin-$\frac{1}{2}$ particle, we have already seen that there are two possible orientations of the magnetic dipole moment with respect to an external magnetic field, providing two possible energy levels; and for a spin-1 particle there are three (see Fig. 1.1). It is important to remember at this point that the direction of the spin and orbital angular momentum vectors for an electron lie anti-parallel to the corresponding magnetic dipole moment vectors, due to the negative charge on the electron. For nuclei the two vectors can either lie in the same direction or in opposite directions depending on the sign of the gyromagnetic ratio.

Both the spin and orbital angular momenta are in possession of a magnetic dipole moment, therefore they will interact with one another and also with external magnetic fields. The interaction or coupling of the spin and orbital angular momenta results in an overall coupled magnetic moment vector, $\boldsymbol{\mu}_{\mathbf{J}}$, and a corresponding angular momentum vector, $\mathbf{J}$. A pictorial representation of this coupling, known as spin-orbit coupling, is given in Fig. C.1. The conical shapes are the precession cones of the spin and orbital angular momentum vectors about the combined total angular momentum vector.

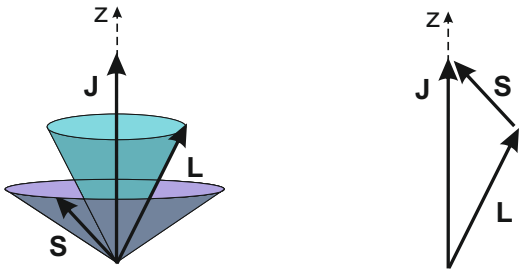


Figure C.1: The spin (**S**) and orbital (**L**) angular momentum vectors couple to give an overall angular momentum vector (**J**).

In the presence of a weak magnetic field, this coupled spin-orbit angular momentum will also further couple to the external magnetic field. In addition, the spin and orbital angular momentum vectors will continue to precess about the total angular momentum vector, which in turn precesses about the magnetic field vector. A representation of this is shown in Fig. C.2

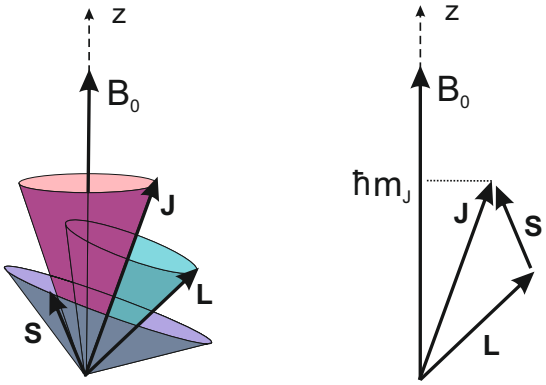


Figure C.2: The spin (**S**) and orbital (**L**) angular momentum vectors couple to give an overall angular momentum vector (**J**), which further interacts with the external magnetic field, B_0.

When the applied static magnetic field is much larger than the spin orbit coupling interaction, the spin-orbit coupling breaks down and both the spin and orbital angular momenta couple to the external field independently, both vectors now precess about the applied external magnetic field vector. This is shown in Fig. C.3. In EPR and NMR, it is normally the case that the external magnetic field can be considered to be in the strong magnetic field regime.

The result of these couplings is to allow different possible energy levels for the system. It was the differences in these energy levels that were observed in the fine-structure of hydrogen spectra, the

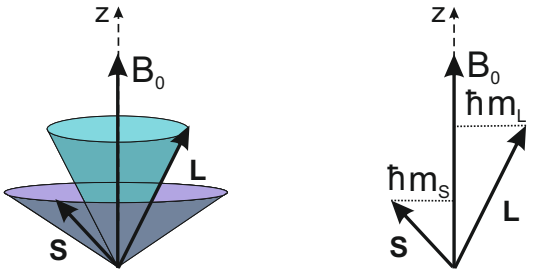


Figure C.3: In the strong magnetic field limit he spin (**S**) and orbital (**L**) angular momentum vectors interact independently with the external magnetic field B_0.

Zeeman effect and the Stern-Gerlach experiment. In each case, the spin angular momentum is coupled to either to the orbital angular momentum (hydrogen spectra fine structure), an external magnetic field (Stern-Gerlach experiment) or both (the anomalous Zeeman effect). In order to explain the results of these experiments, it was necessary to invoke spin angular momentum and thus the explanation of these experiments lead to the discovery of an electron's spin and subsequently the spin of nuclei.

C.2 The quantum mechanics of hydrogen spectra fine structure

If we consider the transition in the hydrogen spectrum from 2P to 1S, when the electron is in the upper 2P level, the spin angular momentum of the electron couples to the orbital angular momentum of the 2P orbital to give an overall angular momentum of either $\frac{3}{2}$ or $\frac{1}{2}$ (found by coupling the two momenta together using a Clebsch-Gordan series). Hence, the electron in the 2P orbital has two possible energy levels and thus there are two possible transition energies for the 2P to 1S emissive transition, or 1S to 2P absorptive transition. The two possible transitions are illustrated in Fig. C.4. Although the average in energy between the 2P and 1S energy levels is much smaller than the difference between the energy levels within the 2P orbital, this minor difference manifests itself as a small splitting in the 2P to 1S emission band of the hydrogen spectrum.

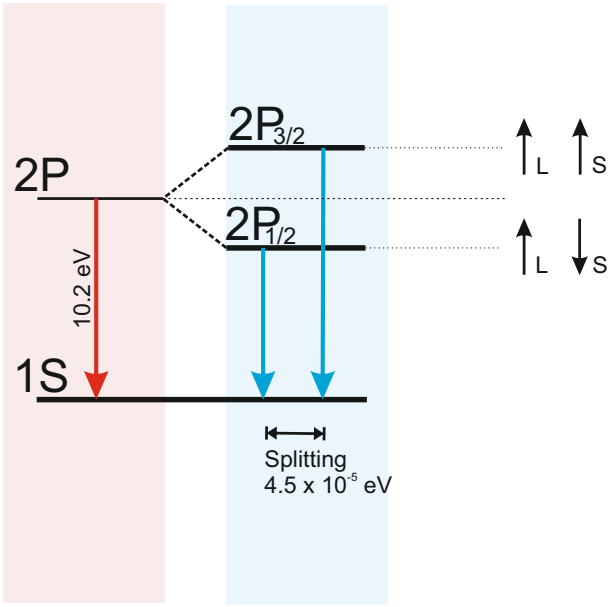


Figure C.4: The Rydberg formula predicts only one energy transition for the 2P $\rightarrow$ 1S transition with an energy of 10.2 eV (red arrow) and only one possible energy state for the 2P orbitals (pink box). However, spin-orbit coupling causes the 2P energy level to split into two possible states $2P_{2/3}$ and $2P_{1/2}$, which are not degenerate in energy (blue box). Two 2P $\rightarrow$ 1S transitions of different energies are therefore possible (blue arrows), which have an energy difference of 4.5×10^{-5} eV, and thus a splitting of this size is observed in the 2P $\rightarrow$ 1S line of the hydrogen spectrum.

C.3 The quantum mechanics of the Zeeman effect

In 1897, Pieter Zeeman published three papers and a letter in *Nature* on the effect of magnetism on visible spectra. The magnetic field caused single lines in the spectra to split into doubles or triples.[32–35] Although it was recognized at the time that the primary effect causing this was the coupling of the electronic orbital angular momentum to the external field, termed the primary or normal Zeeman effect, this did not explain all of the splittings observed. The remainder of the splittings were assigned to the anomalous Zeemen effect and this could not be fully explained for almost 30 years, until Goudsmit and Uhlenbeck were able to propose an explanation invoking the spin angular momentum of an electron.[36]

The primary or normal Zeeman effect involves the coupling of orbital angular momenta to an external magnetic field. This lifts the degeneracy of the orbitals with the same orbital angular momentum quantum number, l, but different magnetic quantum numbers, m_l. For orbitals within a sub-shell with

non-zero orbital angular momentum, this causes a splitting in the energy levels (see Fig. C.5). In the normal Zeeman effect, the splitting of a single line in the spectrum will result in $(2l+1)$ levels, where l is the orbital angular momentum quantum number. Since l is always an integer value the normal Zeeman effect will always result in an odd number of energy levels.

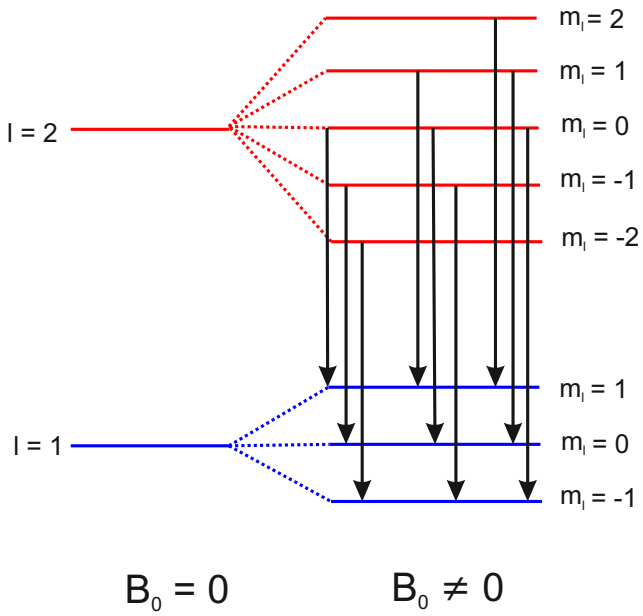


Figure C.5: **The normal Zeeman effect**. For electronic energy states where there is no spin angular momentum, a magnetic field splits a single energy level into $(2l+1)$ levels, by lifting the degeneracy of the different m_l states with the same l number. In the case of a transition from an $l=2$ state to an $l=1$ state with the selection rules for electronic transitions of $\Delta m_l = 0, \pm 1$ and $\Delta l = \pm 1$ there are nine allowed transitions of three distinct energies.

The anomalous Zeeman effect occurs when a single energy level splits into an even number of energy levels in the presence of a magnetic field. The splitting into an even number of possible energy levels gave direct experimental evidence for the existence of a magnetic property with a half integer value. This was identified as the spin angular momentum of an electron. In the case of the anomalous Zeeman effect, it is not the orbital angular momentum, l, which couples to the external magnetic field, instead it is the total angular momentum, j, which is formed by the coupling of the spin and orbital angular momenta (see Fig. C.6).

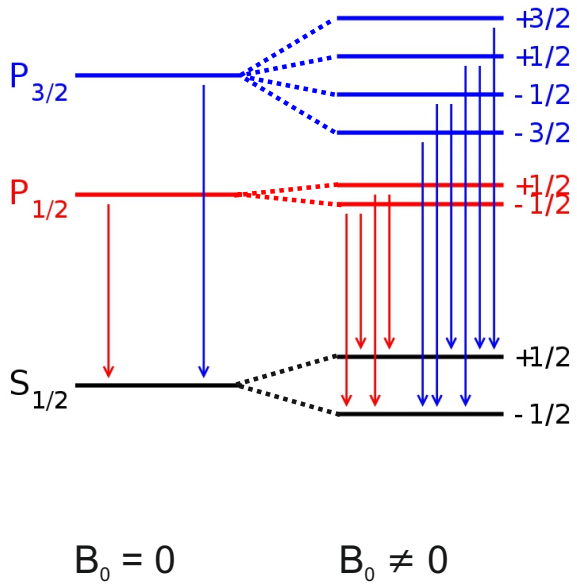


Figure C.6: **The anomalous Zeeman effect**. The left side of the figure above and Fig. C.4 show the splitting in the 2P level of hydrogen due to spin orbit coupling in the absence of a magnetic field ($B_0 = 0$). When hydrogen is placed in a magnetic field ($B_0 \neq 0$), both the 1S and 2P levels split further, due to the non-zero spin angular momentum of these states when they are occupied by a single electron. This therefore gives rise to a total of ten 2P $\rightarrow$ 1S possible transitions of different energies.

The anomalous Zeeman effect is only valid under conditions of weak static fields, where spin-orbit coupling is still valid. In strong magnetic fields, where the applied static magnetic field is much larger than the spin-orbit coupling interaction, the orbital and spin angular momenta interact with the applied magnetic field independently giving rise to the Paschen-Back effect, where the expectation values of L_z and S_z can be evaluated independently.

C.4 The quantum mechanics of the Stern-Gerlach experiment

As previously described in Section A.1.1 of Appendix A, this experiment involved passing a stream of silver atoms through an inhomogeneous magnetic field. This resulted in the atoms being either deflected in a positive or negative direction by equal but opposite values. This result can be explained though the inherent property of spin, possessed by the electronically neutral silver atoms.

Both electrons and silver atoms are spin-$\frac{1}{2}$ particles. The magnitude of their angular momenta is either $+\hbar/2$ or $-\hbar/2$, measured against a z-axis defined by the direction of the applied magnetic field. Since the state of the angular momentum of a particle is unknown until an observation is taken, the two states are said to form a superposition within the wave function, for a spin-$\frac{1}{2}$ particle this takes the form:

$$|\Psi\rangle = c_1 \left|\psi_{j=+\frac{\hbar}{2}}\right\rangle + c_2 \left|\psi_{j=-\frac{\hbar}{2}}\right\rangle \tag{C.1}$$

where $|c_1|^2 + |c_2|^2 = 1$. When a magnetic field is applied to a spin-$\frac{1}{2}$ particle, the two possible angular momenta couple to the external magnetic field in different ways. Thus, the two states have two different energies and interact differently with the inhomogeneous magnetic field, causing the opposite deflections observed in the Stern-Gerlach experiment. Whereas the Zeeman effect spectra and the fine splitting in hydrogen spectra measure the difference in energy of two different energy states, the Stern-Gerlach experiment is a direct measurement of the superposition of two energy states, since the particle does not change state in order to be observable.

Appendix D

The Landé *g*-factor

In systems such as single light atoms in a weak magnetic field, it is possible to predict the g-factor via the Landé formula to give the Landé g-factor, g_J.[30]

$$g_J = g_L \frac{J(J+1) - S(S+1) + L(L+1)}{2J(J+1)} + g_S \frac{J(J+1) + S(S+1) - L(L+1)}{2J(J+1)} \tag{D.1}$$

If we take $g_S \approx 2$ and $g_L = 1$ then the Landé g-factor becomes:

$$g_J \approx \frac{3}{2} + \frac{S(S+1) - L(L+1)}{2J(J+1)} = 1 + \frac{J(J+1) + S(S+1) - L(L+1)}{2J(J+1)} \tag{D.2}$$

It should be noted that the Landé g-formula is only valid in the case of Russell-Saunders coupling of spin and orbital angular momenta. Furthermore, it breaks down in high magnetic fields and also when the ion containing the electron being considered interacts with ligands, which change the symmetry of the system and quench the spin-orbit coupling. It can therefore be very difficult to predict the size of the g-value for unpaired electrons found within a molecule, since there are many potential sources of magnetic dipoles that couple to one another.

Appendix E

Interactions that contribute to the structure of magnetic resonance spectra for nuclei $S > \frac{1}{2}$

In Section 1.4 we have already considered interactions arising from the coupling of spin vectors to one another and to an external magnetic field for spin-$\frac{1}{2}$ particles. For systems with $S > \frac{1}{2}$, two other interactions, the nuclear quadrupole interaction and zero field splitting, must be considered, which are a result of this higher spin state. This thesis concentrates primarily on systems with a spin state or ground spin state of $\frac{1}{2}$. However, a brief description of these effects is included here for completeness.

E.1 Nuclear quadrupole interaction

For nuclei with spin $I \geq 1$, the charge distribution in the nucleus is not spherical; this gives rise to the nuclear quadrupole moment, Q. The quadrupole moment does not interact directly with other spin vectors or the applied magnetic field, but instead with the electric field gradient caused by the electrons and nuclei in close proximity to the nucleus.

This interaction is described by the Hamiltonian:

$$\hat{\mathbf{H}}_{NQ} = \tilde{\hat{\mathbf{I}}}\mathbf{P}\hat{\mathbf{I}} \tag{E.1}$$

where $\mathbf{P}$ is the nuclear quadrupolar tensor. In EPR, the nuclear quadrupolar interactions manifest themselves as shifts in the resonance frequencies and also in the appearance of forbidden transitions, where both the electron and the nuclear spin are flipped. In most magnetic resonance spectra, the primary contribution of the quadrupolar interaction is to cause fast relaxation of the nuclear spins and any associated electron spins. Other relaxation mechanisms are discussed in Section 1.8.

E.2 Zero field splitting

For electron spin systems with $S > \frac{1}{2}$ in symmetry environments that are non-cubic, the $(2S + 1)$ degeneracy of the ground state is removed. This is a consequence of molecular electronic structure and/or spin density distribution. The splitting is not dependent on the interaction of a magnetic field and is present even when the molecule is not in a magnetic field. This interaction is therefore termed zero field splitting and can be given in Hamiltonian form by:

$$\hat{\mathbf{H}}_{ZFS} = \tilde{\hat{\mathbf{S}}}\mathbf{D}\hat{\mathbf{S}} \tag{E.2}$$

$\mathbf{D}$ is the interaction tensor and it is symmetric and traceless. In the principal axes of the $\mathbf{D}$ tensor, the Hamiltonian becomes:

$$\hat{\mathbf{H}}_{ZFS} = D_x\hat{S}_x^2 + D_y\hat{S}_y^2 + D_z\hat{S}_z^2 = D\left[\hat{S}_z^2 - \frac{1}{3}\hat{S}(\hat{S}+1)\right] + E\left(\hat{S}_x - \hat{S}_y^2\right) \tag{E.3}$$

where $D = \frac{3D_z}{2}$ and $E = \frac{D_x - D_y}{2}$. It should be noted that in a cubic symmetry $D = E = 0$ and zero field splitting is not present.

Appendix F

The vector model for four-pulse DEER

Like the model shown for three-pulse DEER in chapter 2, by considering motion of the spin packets under the influence of the applied pulses during a DEER sequence, it is clear how the echo is formed and also how the application of the pump pulse disrupts the spin packets, so that the final echo does not refocus fully.

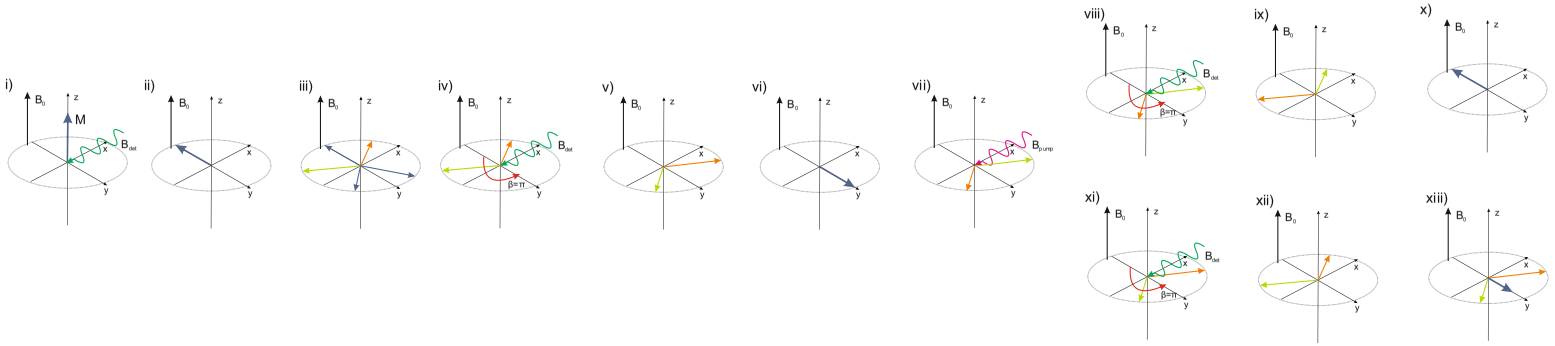


Figure F.1: **Vector diagram for four-pulse DEER in the rotating frame**. The movement of the vectors is very similar to that seen for three-pulse DEER in Fig. 2.6. Application of an initial $\frac{\pi}{2}$ pulse on-resonance with the rotating frame and the detection spins (i) moves these spins from the z-axis to be aligned with the $-y$-axis (ii). The components of the magnetization with slightly differing resonant frequencies spread out into the x-y plane (iii). Considering only a 'fast' (orange) and a 'slow' component from this distribution of frequencies (iv) after a time τ_1, a π detection pulse is applied during the distribution of components in the x-y plane about the x-axis (v). After another time delay of length τ_1, the components refocus along the $+y$-axis (vi). The components are allowed to continue to precess and begin to dephase again (vii). During this precession, a π pulse, off-resonance with the detection spins, is applied, this is the pump pulse. If this has no effect on the system, the components continue to precess until a π pulse on-resonance with the spins is applied (viii) causing them to turn about the x-axis (ix). Allowing the spins to continue to precess, they will refocus to form an echo along the $-y$-axis at a time τ_2 after the final π detection pulse. This time interval τ_2 is the same as that between the first echo (vi) and the application of the final π detection pulse. If the applied pump pulse is on-resonance with a spin coupled to the detection spin, this causes interconversion of the Larmor speeds for the 'fast' and 'slow' components previously described (xi). Application of a detection π pulse on-resonance with the rotating frame turns the spins in the x-y plane about the x-axis (xii). However, unlike the first case described, due to the new different Larmor speeds of the components, these do not refocus completely along the $+y$ axis at a time τ_2 after the π detection pulse. Thus, the size of the echo observed is reduced. The degree of the reduction is dependent on when the π pump pulse occurs within the delay between the two π detection pulses. No reduction in the size of the observed echo is seen if the application of the pump pulse is coincident with the initial echo. This is known as the zero time.

Appendix G

Synthetic schemes for copper and nitroxide model systems

All reagents and solvents were obtained from commercial sources (SigmaAldrich and Alfa Aesar) and, unless otherwise stated, were used as received. Where appropriate, solvents were purified by using the procedures described by A. B. Pangborn, M. A. Giardello, R. H. Grubbs, R. K. Rosen and F. J. Timmers, *Organometallics*, 1996, **15**, 1518–1520.

Scheme 1

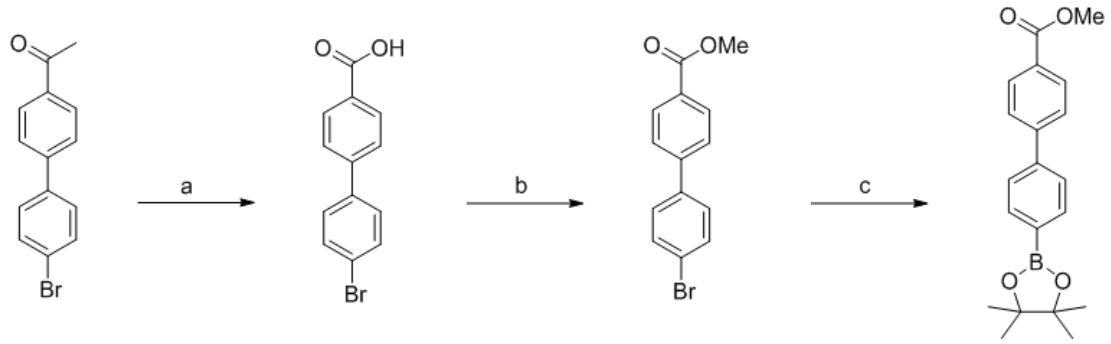


Figure G.1: **a)** Br_2, NaOH, H_2O, dioxane, 35-40°C; **b)** (i) $SOCl_2$, PhMe, reflux, 1 h (ii) MeOH; **c)** Bis(pinacolato)diboron, $PdCl_2(PPh_3)_2$, K_2CO_3, THF, reflux, 20 h.

The oxidation of the acetyl motif was achieved using NaOBr, generated in situ, according to the preparation of D. J. Byron, G. W. Gray and R. C. Wilson, *Journal of the Chemical Society C*, 1966,

840–845.

The methylation of the carboxylic acid was achieved according to the procedure of D. I. Fletcher et al. *Bioorganic and Medicinal Chemistry*, 2007, **15**, 5457–5479.

Other methods to prepare the boronate coupling partner were investigated (e.g. lithiation using *n*-BuLi and then quenching this with a range of boron sources), but these were either found to not work or to give unacceptably low yields of the product.

Scheme 2

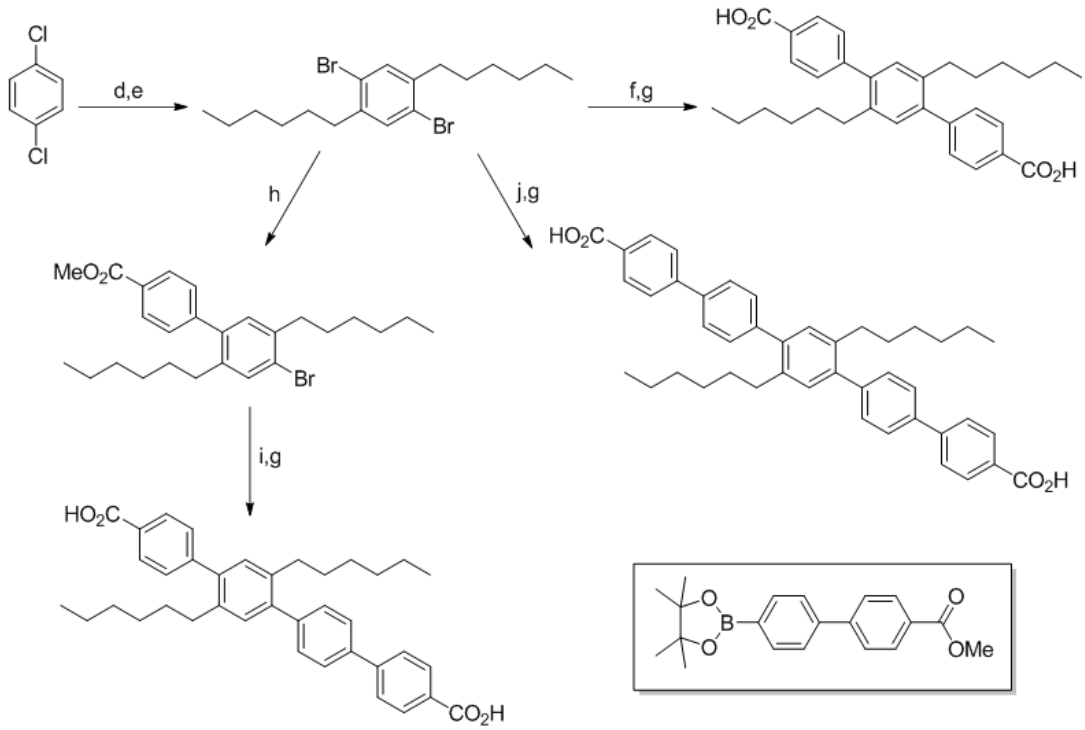


Figure G.2: **d)** : *n*-Hexylbromide, $Mg_{(s)}$, cat. $BrCH_2CH_2Br$, $[Ni(dppp)Cl_2]$, THF, reflux; **e)** Br_2, cat. I_2 0°C→RT; **f)** excess 4-(CO_2Me)−phenyl−$B(OH)_2$, $PdCl_2(PPh_3)_2$, K_2CO_3, THF, reflux; **g)** $LiOH{\cdot}H_2O$, THF, H_2O, reflux; **h)** 1 mol equiv. 4-(CO_2Me)−phenyl−$B(OH)_2$, $PdCl_2(PPh_3)_2$, K_2CO_3, THF, reflux; **i)** 1,1'-biphenyl boronate (see inset), $PdCl_2(PPh_3)_2$, K_2CO_3, THF, reflux; **j)** excess 1,1'-biphenyl boronate (see inset), $PdCl_2(PPh_3)_2$, K_2CO_3, THF, reflux.

The first two steps (**d** and **e**) were in line with the protocol of M. Rehahn et al. *Synthesis*, 1988, (5), 386–388. (NB: $[Ni(dppp)Cl_2]$ = [1,3-bis(diphenylphosphino)propane]-dichloro-nickel(II)).

The Suzuki-Miyaura coupling reaction (N. Miyaura and A. Suzuki, *Chemical Review* 1979, **95**, 2457–2483) was employed successfully for all of the boronate/boronic acid to bromide coupling reactions which proceeded in moderate to high yields.

The saponification of the esters was performed in a procedure adapted from M. W. Jones et al. *Dalton Transactions*, 2012, **41**, 14068-14086, and was essentially quantitative for each of the diacids.

Scheme 3

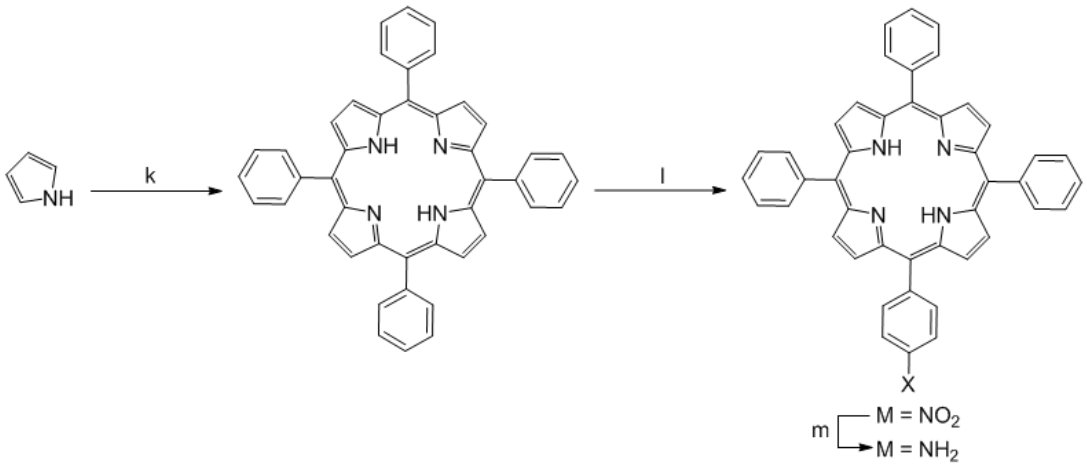


Figure G.3: **k)** benzaldehyde, propionic acid, reflux, 0.5 h; **l)** *(i)* $NaNO_2$, CF_3CO_2H, 5°C, 3 min *(ii)* H_2O, CH_2Cl_2, $NaHCO_{3(aq)}$; **m)** *(i)* $SnCl_2{\cdot}2H_2O$, conc. HCl, 65°C, 2 h *(ii)* NH_4OH, CH_2Cl_2.

The preparation of the 5-(4-aminophenyl)-10,15,20-triphenylporphyrin was performed according to the literature report of R. Luguya, L. Jaquinod, F. R. Fronczek, M. G. H. Vicente and K. M. Smith, *Tetrahedron*, 2004, **60**, 2757–2763 whereby meso-tetraphenylporphyrin (as prepared by the method of A. D. Adler, F. R. Longo, J. D. Finarelli, J. Goldmacher, J. Assour and L. Korsakoff, *Journal of Organic Chemisty*, 1966, **32**, 476.) was mono-nitrated selectively on the para position of a phenyl ring, and subsequently reduced to the amine using $SnCl_2$.

Scheme 4

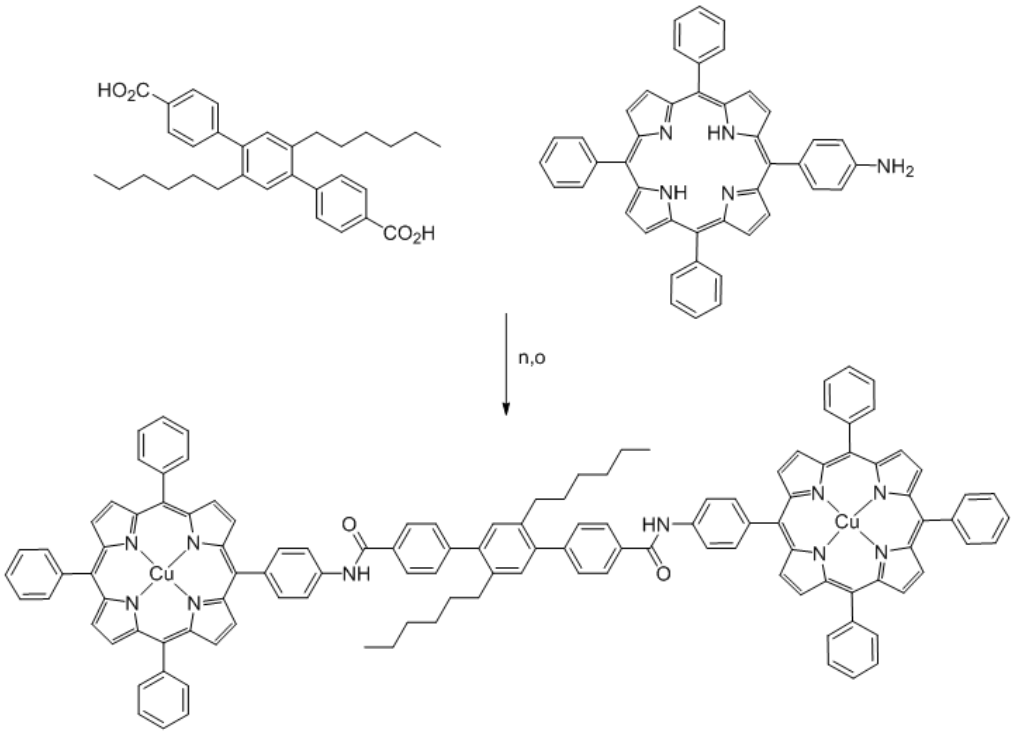


Figure G.4: **n)** BOP, DIPEA, DMF, room temperature. 4 days; **o)** $Cu(OAc)_2 \cdot H_2O$, $CHCl_3$, MeOH, reflux 3 h.

Peptide coupling employing BOP ((benzotriazol-1-yloxy)tris(dimethylamino)phosphonium hexafluorophosphate) under standard peptide coupling conditions to couple the requisite diacid with the 5-(4-aminophenyl)-10,15,20-triphenylporphyrin. To ensure that all of the diacid was coupled, a slight excess of the highly visible amino porphyrin was used, which was later removed by column chromatography. The respective 1- and 2-phenyl linkers were commercially available and subjected to the same conditions as illustrated in scheme 4. Metallation of the porphyrin with copper(II) was trivially accomplished using an excess of $Cu(OAc)_2 \cdot H_2O$ in refluxing $CHCl_{3/}$MeOH.

Scheme 5

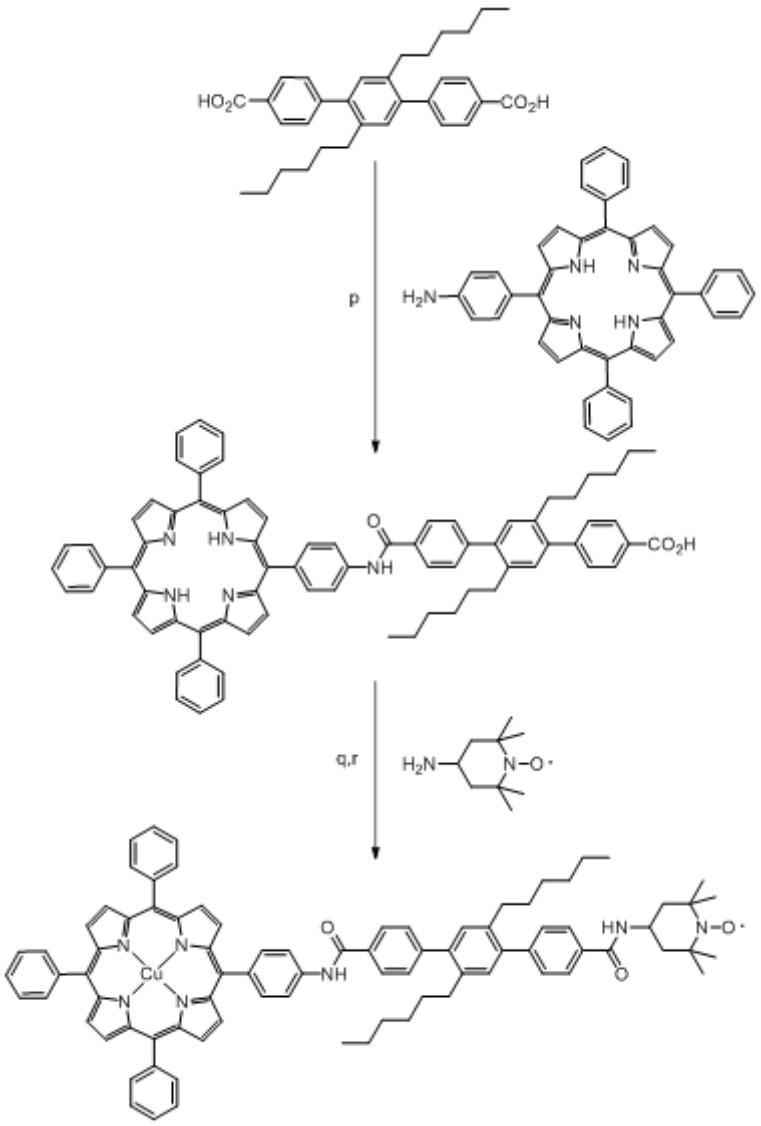


Figure G.5: **p)** BOP, DIPEA, DMF, room temperature. 2 days; **q)** BOP, DIPEA, DMF, room temperature. 2 days **r)** $Cu(OAc)_2 \cdot H_2O$, $CHCl_3$, MeOH, reflux 3 h.

Monofunctionalization with 5-(4-aminophenyl)-10,15,20-triphenylporphyrin and either 1,4-benzene dicarboxylic acid or the 3-phenyl diacid was achieved under BOP mediated peptide coupling conditions, using 1:1 stoichiometry of the reagents, shorter reaction time and higher dilution of the reaction mixture. Facile purification, owing to the vastly different polarities of the products using column

chromatography, lead to the isolation of the desired monoadducts in moderate yield. Attachment of the nitroxide was again performed with a BOP peptide coupling procedure and to 4-amino-2,2,6,6-tetramethylpiperidine-1-oxyl which gave the porphyrin-nitroxide species. Metallation using analogous conditions to above in order to give the Cu−$NO^{\bullet}$ species, which were characterized by mass spectrometry, thin layer chromatography, UV-vis and CW-EPR at X-band.

Appendix H

The catalytic cycle of cytochrome P450

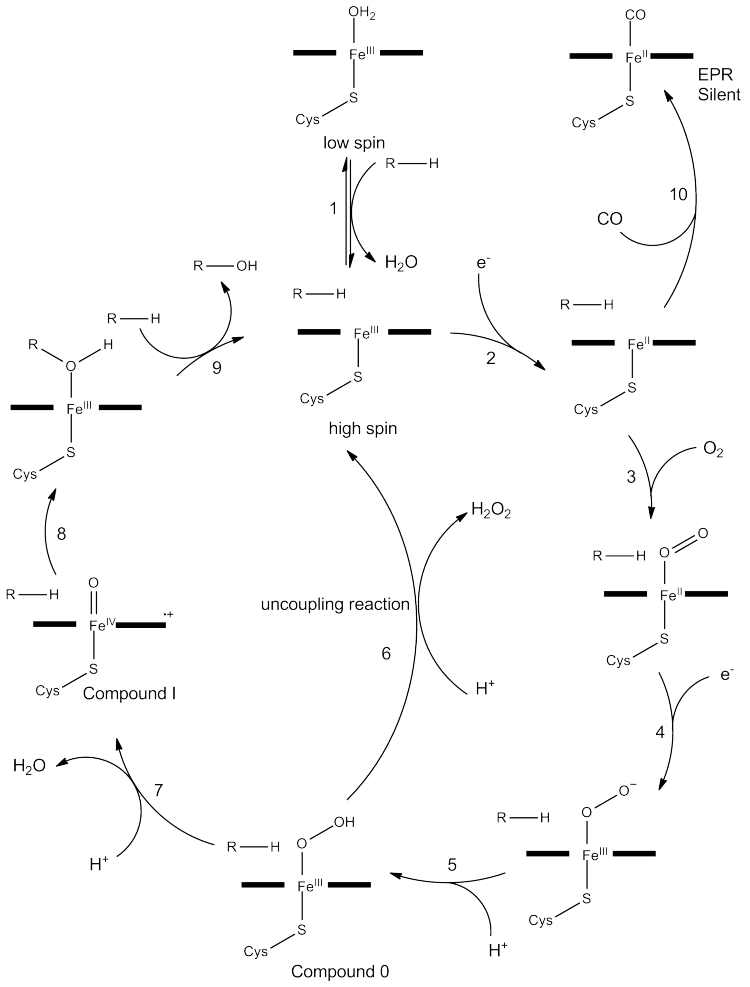


Figure H.1: The complete reaction cycle for the P450 family of enzymes.

Appendix I

The experimental parameters used for DEER experiments on the ferredoxin reductase−ferredoxin and ferredoxin−P450 protein systems

Details of the pump frequencies, detection frequencies and field positions used for DEER experiments on the ferredoxin reductase−ferredoxin and ferredoxin−P450 protein complexes.

Table I.1: Pump frequencies, detection frequencies and field positions, for the experiments on each of the nitroxide labelling sites in the PuxB-PuR system.

PuR labelling site	PuR mutation	DEER detection frequency (GHz)	DEER pump frequency (GHz)	DEER field position (mT)	DEER pulse separation (MHz)	Exp. number for simulation
82	Ser to Cys	9.5199	9.1800	338.4	+340	1
		9.4302	9.1900	335.30	+240	2
		9.3403	9.1900	332.00	+150	3
		9.3091	9.2342	330.85	+75	4
		9.3605	9.4250	332.70	−65	5
135	Val to Cys	9.2250	9.5554	340.26	+330	1
		9.2234	9.3738	333.75	+150	3
		9.2244	9.1583	326.07	-66	5
164	Ala to Cys	9.2127	9.5382	339.7	+325	1
		9.2185	9.3650	333.46	+147	3
		9.2143	9.1497	325.78	−65	5
196	Ser to Cys	9.5201	9.180	338.40	+340	1
		9.4201	9.1800	334.90	+240	2
		9.5201	9.3700	338.40	+150	3
		9.2900	9.2150	330.20	+75	4
		9.2899	9.3550	330.20	−65	5
249	Ala to Cys	9.5452	9.2076	339.40	+338	1
		9.5448	9.3950	339.30	+150	3
		9.5448	9.6111	339.30	-66	5
281	Glu to Cys	9.5250	9.185	338.70	+345	1
		9.3549	9.1850	332.60	+170	3
		9.3672	9.4320	332.90	−65	5
303	Wild Type	9.6303	9.300	342.20	+330	1
		9.5114	9.3315	338.1	+180	3
		9.2464	9.3315	328.6	−85	5
309	Thr to Cys	9.5200	9.1800	338.4	+340	1
		9.5200	9.2750	338.40	+245	2
		9.5200	9.3700	338.40	+150	3
		9.3903	9.3100	333.75	+80	4
		9.3006	9.3650	330.60	−62	5
347	Ser to Cys	9.8059	9.4734	349.18	+333	1
		9.6230	9.4723	342.64	+150	3
		9.4072	9.4713	334.96	−64	5

Table I.2: Pump frequencies, detection frequencies and field positions, for the experiments on each of the nitroxide labelling sites in the HaPux-P450 system.

P405 labelling site	P450 mutation	DEER detection frequency (GHz)	DEER pump frequency (GHz)	DEER field position (mT)	DEER pulse separation (MHz)	Exp. number for simulation
42	Thr to Cys	9.5650	9.2350	340.10	+330	1
		9.4826	9.2350	340.10	+248	2
		9.4001	9.2350	334.23	+165	3
		9.3148	9.2350	331.16	+80	4
		9.1703	9.2350	326.06	−65	5
226	Wild Type	9.5650	9.2355	340.10	+335	1
		9.4824	9.2355	337.17	+248	2
		9.4500	9.2855	336.01	+165	3
		9.4603	9.3800	336.36	+80	4
		9.3151	9.3800	331.21	−65	5
315	Thr to Cys	9.5648	9.2350	340.10	+335	1
		9.4826	9.2350	337.17	+248	2
		9.4002	9.2350	334.23	+165	3
		9.4599	9.3800	336.36	+80	4
		9.2349	9.3000	328.37	−65	5
345	Thr to Cys	9.5651	9.2350	340.10	+335	1
		9.4826	9.2350	337.17	+248	2
		9.3999	9.2350	334.23	+165	3
		9.4600	9.3800	336.36	+80	4
		9.3949	9.4600	334.06	−65	5
404	Ser to Cys	9.5649	9.2350	340.10	+335	1
		9.4827	9.2350	337.17	+248	2
		9.3999	9.2350	334.23	+165	3
		9.4602	9.3800	336.36	+80	4
		9.2350	9.3000	328.37	−65	5

Appendix J

PatchDock and FireDock

PatchDock[157,158] and FireDock[11,159] form a suite of docking programs that can be used to predict possible structures for protein-protein complexes. PatchDock reads in the coordinates of the independently found structures for two proteins and uses rigid-body docking to produce initial docked structures. These structures can be refined using side-chain optimization in FireDock. Knowledge of the binding interfaces was included in the calculation, by specifying residues that are known to lie in the binding interface. Details of the method of docking and refinement are given in the following sections.

J.1 PatchDock

PatchDock[157,158] uses object recognition and image segmentation techniques in order to create docked complexes. Initially, surfaces are generated for both the receptor and the ligand proteins. These surfaces are then classified in to areas or 'patches' according to their shape; concave, flat or convex. These patches are next superimposed using shape matching algorithms, so concave patches are matched with convex and flat patches with any type of patches. This is very much like solving a jigsaw puzzle; the shape of one surface is considered and the program looks for regions on the second protein with complementary surface patches. Finally, the potential docked complexes are filtered and scored; all complexes with unacceptable penetrations of the atoms of the receptor into the atoms of the ligand are disregarded and the remaining structures are ranked according to a geometric shape complementarity

score. PatchDock is an example of rigid body docking since it does not take into account any movement of the proteins, particularly that of the side chains, which is likely to occur when two proteins dock.

Residues in the active site can be specified in PatchDock and these are included by only considering patches that contain one or more of these residues in the shape matching algorithm. The scoring in PatchDock uses hydrophobicity and atomic contact energies (ACE),[160] in addition to the contact surface sizes.

PatchDock is available via an online server (*http://bioinfo3d.cs.tau.ac.il/PatchDock*) and also as a free download from the same website.

J.2 FireDock

FireDock[11,159] targets the problem of flexibility in the solutions produced through rigid-body docking by refining and re-scoring pre-docked structures. The output structures from PatchDock were used as the input structures for FireDock.

Each candidate structure was refined in two ways: a restricted interface side-chain optimization (RISCO) and a full interface side-chain optimization (FISCO). The side-chain flexibility is modelled by rotamers and the combinatorial optimization problem obtained is solved by integer linear programming.[299] The restricted side-chain refinement used an atomic radii scaling of 0.8, which allowed for some side chain clashes, whereas the full refinement used a side-chain scaling factor of 0.85 in order to reduce the number of clashes.

In each case, following rearrangement of the side-chains, the relative position of the two docking partners is refined by Monte Carlo minimization of the program's inbuilt binding score function (as detailed in Chapter 4).

Usually the full side-chain refinement would be carried out only on the top structures from the restricted side-chain refinement. For the research described in Chapter 4, both techniques were performed on all of the output structures from PatchDock. The reason for this was simply to create a larger number of possible structures to test for agreement with the experimental DEER data.

Appendix K

Derivation of the rotating frame Hamiltonians and the time-dependent Hamiltonians for the pump pulse in regions of pulse overlap

The form of the time-dependent Hamiltonians given in Chapter 7, Section 7.4.1 can be derived from the time-dependence of Hamiltonians in the laboratory frame. The propagating Hamiltonian for the two spins, a and b, with Larmor frequencies ω_a and ω_b, is:

$$\hat{H}_{0,lab} = \omega_a \hat{S}_a^z + \omega_b \hat{S}_b^z + \omega_\perp (3\cos^2\theta - 1)\hat{S}_a^z \hat{S}_b^z \tag{K.1}$$

In the laboratory frame, all pulses are time-dependent and the Hamiltonian for the application of a pulse of frequency ω_{pulse} is given by:

$$\hat{H}_{1,lab} = -2\omega_1 \left(\hat{S}_a^x + \hat{S}_b^x\right) \cos\omega_{pulse} t + \hat{H}_{0,lab} \tag{K.2}$$

The radiation forming the excitation pulse is linearly polarized. Therefore, in order to move this pulse into the rotating frame, it is necessary to consider the pulse as a rotating field that is formed by the sum of two counter-rotating fields. The counter-rotating nature of the fields means that only one of these fields will be on or near resonant with any rotating frame chosen. It can thus be assumed that the off-resonant component will not cause any excitations and thus only the component of the rotating

field on or near resonance with the rotating frame chosen needs to be considered.[a] The Hamiltonian for the pump pulse therefore becomes:

$$\hat{H}_{1,field} = -\omega_1 \left[\left(\hat{S}_a^x + \hat{S}_b^x \right) \cos \omega_{pulse} t + \left(\hat{S}_a^y + \hat{S}_b^y \right) \sin \omega_{pulse} t \right] + \hat{H}_{0,lab} \tag{K.3a}$$

$$= -\omega_1 \left[\hat{S}^x \cos \omega_{pulse} t + \hat{S}^y \sin \omega_{pulse} t \right] + \hat{H}_{0,lab} \tag{K.3b}$$

where $S_a^i + S_b^i = S^i$. It should be noted that a factor of two is lost compared to Equation K.2, since only one of the rotating fields contributes. The transformation of this Hamiltonian into the rotating frame requires the use of the cyclic commutation relationship of spin operators:

$$\left[\hat{S}^x, \hat{S}^y \right] = i\hat{S}^z \quad \text{(K.4a)} \qquad \left[\hat{S}^y, \hat{S}^x \right] = -i\hat{S}^y \quad \text{(K.5a)} \qquad \left[\hat{S}^x, \hat{S}^x \right] = 0 \quad \text{(K.6a)}$$

$$\left[\hat{S}^y, \hat{S}^z \right] = i\hat{S}^x \quad \text{(K.4b)} \qquad \left[\hat{S}^z, \hat{S}^y \right] = -i\hat{S}^y \quad \text{(K.5b)} \qquad \left[\hat{S}^y, \hat{S}^y \right] = 0 \quad \text{(K.6b)}$$

$$\left[\hat{S}^z, \hat{S}^x \right] = i\hat{S}^y \quad \text{(K.4c)} \qquad \left[\hat{S}^x, \hat{S}^z \right] = -i\hat{S}^y \quad \text{(K.5c)} \qquad \left[\hat{S}^z, \hat{S}^z \right] = 0 \quad \text{(K.6c)}$$

[a] The breakdown of this approximation leads to a Bloch-Siegert shift as originally defined in Bloch and Siegert's paper of 1940.[211] The definition of a Bloch-Siegert shift used in this chapter considers a phase shift caused by the application of any off-resonance excitation, rather than that caused only by the off-resonant component of a linearly polarized field.

These can be used to simplify the form of the matrix representation of the Euler relation for the Pauli spin operators. The general form of the matrix representation of the Euler relation is given as:[29]

$$e^{-i\Phi B}Ae^{+i\Phi B} = A\left(1 - \frac{\Phi^2}{2!} + \frac{\Phi^4}{4!} - \ldots\right) - i\,[B, A]\left(\Phi - \frac{\Phi^3}{3!} + \frac{\Phi^5}{5!} - \ldots\right) \tag{K.7}$$

For the case $A \neq B$, this simplifies to give:

$$e^{-i\Phi B}Ae^{+i\Phi B} = A\cos\Phi - i\,[B, A]\sin\Phi \tag{K.8}$$

or for the case $A = B$:

$$e^{-i\Phi B}Ae^{+i\Phi B} = A \tag{K.9}$$

Applying this relation to the Pauli spin operators and using the cyclic commutator relationships gives:

$$e^{-i\theta S^z}S^x e^{+i\theta S^z} = S^x\cos\theta + S^y\sin\theta \tag{K.10a}$$

$$e^{-i\theta S^z}S^y e^{+i\theta S^z} = S^y\cos\theta + S^x\sin\theta \tag{K.10b}$$

$$e^{-i\theta S^z}S^z e^{+i\theta S^z} = 0 \tag{K.10c}$$

These relationships can be used to transform the Hamiltonian of a time-dependent pulse in the laboratory frame (comprised of Pauli spin operators) into the rotating frame. The transformation from the laboratory frame is equivalent to a rotation about the z-axis.

Therefore, considering only the time-dependent part of Equation K.3b, $\hat{H}_{1,red}$, the transformation into a rotating frame of frequency ω_{rot} is formulated in the following fashion, by application of a rotation about the z-axis. The angle of rotation, θ, in Equations K.10a to K.10c, is set to $\omega_{rot}t$.

$$
\begin{aligned}
&e^{-i\omega_{rot}t\hat{S}^z}\hat{H}_{1,red}e^{+i\omega_{rot}t\hat{S}^z} \\
&\quad= e^{-i\omega_{rot}t\hat{S}^z}\left[-\omega_1\left(\hat{S}^x\cos\omega_{pulse}t-\hat{S}^y\sin\omega_{pulse}t\right)\right]e^{+i\omega_{rot}t\hat{S}^z} && \text{(K.11a)}\\
&\quad= -\omega_1\Big[e^{-i\omega_{rot}t\hat{S}^z}\hat{S}^x e^{+i\omega_{rot}t\hat{S}^z}\cos\omega_{pulse}t \\
&\qquad\qquad -e^{-i\omega_{rot}t\hat{S}^z}\hat{S}^y e^{+i\omega_{rot}t\hat{S}^z}\sin\omega_{pulse}t\Big] && \text{(K.11b)}\\
&\quad= -\omega_1\Big[\left(\hat{S}^x\cos\omega_{rot}t+\hat{S}^y\sin\omega_{rot}t\right)\cos\omega_{pulse}t \\
&\qquad\qquad -\left(\hat{S}^y\cos\omega_{rot}t-\hat{S}^x\sin\omega_{rot}t\right)\sin\omega_{pulse}t\Big] && \text{(K.11c)}
\end{aligned}
$$

To obtain the full Hamiltonian for the application of a pump pulse in a rotating frame, we must also consider the form that the propagating Hamiltonian, $\hat{H}_0$, takes in the rotating frame. This can be found by evaluating the expression $\hat{H}_{0,rot} = e^{-i\omega_{rot}\hat{S}^z}\hat{H}_0 e^{+i\omega_{rot}\hat{S}^z}$. However, an alternative derivation for $\hat{H}_{0,rot}$ comes directly from the Schrödinger equation; the Schrödinger equation in the laboratory frame can be given as:

$$\frac{d\left|\psi\right\rangle}{dt} = -i\hat{H}_0\left|\psi\right\rangle \tag{K.12}$$

The transformation of the wave function into the rotating frame is achieved using: $\left|\psi\right\rangle_{rot} = e^{+i\omega_{rot}\hat{S}^z t}\left|\psi\right\rangle$. Therefore, substitution of this into the Schrödinger equation gives:

$$
\begin{aligned}
\frac{d\left|\psi\right\rangle_{rot}}{dt} =& i\omega_{rot}\hat{S}^z e^{+i\omega_{rot}\hat{S}^z t}\left|\psi\right\rangle + e^{+i\omega_{rot}\hat{S}^z t}\frac{d\left|\psi\right\rangle}{dt} && \text{(K.13a)}\\
=& i\omega_{rot}\hat{S}^z\left|\psi\right\rangle_{rot} - ie^{+i\omega_{rot}\hat{S}^z t}\hat{H}_0\left|\psi\right\rangle && \text{(K.13b)}
\end{aligned}
$$

This equation can further be simplified using the identity $e^{-i\omega_{rot}\hat{S}^z t}e^{+i\omega_{rot}\hat{S}^z t} = 1$ and the fact that $\hat{H}_0$ only contains the operators $\hat{S}_a^z$ and $\hat{S}_b^z$, both of which commute with $\hat{S}^z$. This therefore implies that $\hat{H}_0$ also commutes with $\hat{S}^z$. Hence:

$$\frac{d\left|\psi\right\rangle_{rot}}{dt} = i\omega_{rot}\hat{S}^z e^{+i\omega_{rot}\hat{S}^z t}\left|\psi\right\rangle - ie^{+i\omega_{rot}\hat{S}^z t}\hat{H}_0 e^{-i\omega_{rot}\hat{S}^z t}e^{+i\omega_{rot}\hat{S}^z t}\left|\psi\right\rangle \tag{K.14a}$$

$$= i\omega_{rot}\hat{S}^z e^{+i\omega_{rot}\hat{S}^z t}\left|\psi\right\rangle - ie^{+i\omega_{rot}\hat{S}^z t}e^{-i\omega_{rot}\hat{S}^z t}\hat{H}_0 e^{+i\omega_{rot}\hat{S}^z t}\left|\psi\right\rangle \tag{K.14b}$$

$$= i\omega_{rot}\hat{S}^z e^{+i\omega_{rot}\hat{S}^z t}\left|\psi\right\rangle - ie^{+i\omega_{rot}\hat{S}^z t}e^{-i\omega_{rot}\hat{S}^z t}\hat{H}_0\left|\psi\right\rangle_{rot} \tag{K.14c}$$

$$= i\omega_{rot}\hat{S}^z e^{+i\omega_{rot}\hat{S}^z t}\left|\psi\right\rangle - i\hat{H}_0\left|\psi\right\rangle_{rot} \tag{K.14d}$$

Comparison of Equation K.14d for the propagating Hamiltonian in the rotating frame with that for the same Hamiltonian in the laboratory frame, Equation K.12, shows that $\hat{H}_0$ from the laboratory frame becomes $\hat{H}_0 - \omega_{rot}\hat{S}^z$ in the rotating frame.

The full Hamiltonian for a pulse in the rotating frame is therefore:

$$\begin{aligned}\hat{H}_{1,rot} = \quad & -\omega_1\Big[\Big(\hat{S}^x\cos\omega_{rot}t + \hat{S}^y\sin\omega_{rot}t\Big)\cos\omega_{pulse}t \\ & -\Big(\hat{S}^y\cos\omega_{rot}t - \hat{S}^x\sin\omega_{rot}t\Big)\sin\omega_{pulse}t\Big] \\ & +\hat{H}_{0,lab} - \omega_{rot}\left(\hat{S}^z\right)\end{aligned} \tag{K.15}$$

If the frequency of the pulse, ω_{pulse}, is on-resonance with the rotating frame, ω_{rot}, Equation K.15 transforms to give Equation 7.5.

The DEER experiment requires pulses at two different frequencies; therefore performing a similar transformation into the rotating frame for the Hamiltonian in the laboratory frame is necessary. The Hamiltonian for the application of the pulse in the laboratory frame is:

$$\hat{H}_{2,lab} = -2\omega_1 \left(\hat{S}_a^x + \hat{S}_b^x\right) \cos\left(\omega_{pulse,2}\right) t + \hat{H}_{0,lab} \tag{K.16a}$$

$$= -2\omega_2 \left(\hat{S}_a^x + \hat{S}_b^x\right) \cos\left(\omega_{pulse,1} + \xi\right) t + \hat{H}_{0,lab} \tag{K.16b}$$

where ω_2 is the strength of the pulse applied at $\omega_{pulse,2}$. Ω corresponds to the separation in frequency between the two pulses; $\Omega = \omega_{pulse,2} - \omega_{pulse,1}$. Like the pulse at frequency $\omega_{pulse,1}$, the pulse at $\omega_{pulse,2}$ is also composed of two counter-rotating fields and provided that, in the rotating frame, one field can be considered so far off-resonance so it does not cause any excitations, only the field near resonance with the rotating frame need be considered.

$$\hat{H}_{2,field} = -\omega_2 \left[\hat{S}^x \cos\omega_{pulse} t + \hat{S}^y \sin\omega_{pulse} t\right] + \hat{H}_{0,lab} \tag{K.17}$$

Transforming this into the rotating frame gives:

$$\begin{aligned} \hat{H}_{2,rot} \quad = -\omega_2 \Big[& \left(\hat{S}^x \cos\omega_{rot} t + \hat{S}^y \sin\omega_{rot} t\right) \cos\left(\omega_{pulse,1} + \xi\right) t \\ & - \left(\hat{S}^y \cos\omega_{rot} t - \hat{S}^x \sin\omega_{rot} t\right) \sin\left(\omega_{pulse,1} + \xi\right) t \Big] \\ & + \hat{H}_{0,lab} - \omega_{rot} \left(\hat{S}^z\right) \end{aligned} \tag{K.18}$$

This can be expanded using the sum and difference trigonometric identities to give:

$$\begin{aligned}\hat{H}_{2,rot} &= -\omega_2 \Big[\hat{S}^x \left(\cos\omega_{rot}t\cos\omega_{pulse,1}t\cos\xi t - \cos\omega_{rot}t\sin\omega_{pulse,1}t\sin\xi t\right.\\ &\quad \left.+\sin\omega_{rot}t\cos\omega_{pulse,1}t\sin\xi t + \sin\omega_{rot}t\sin\omega_{pulse,1}t\cos\xi t\right)\\ &\quad +\hat{S}^y \left(\sin\omega_{rot}t\cos\omega_{pulse,1}t\cos\xi t + \sin\omega_{rot}t\sin\omega_{pulse,1}t\sin\xi t\right.\\ &\quad \left.-\cos\omega_{rot}t\cos\omega_{pulse,1}t\sin\xi t - \cos\omega_{rot}t\sin\omega_{pulse,1}t\cos\xi t\right)\Big]\\ &\quad +\hat{H}_{0,lab} - \omega_{rot}\left(\hat{S}^z\right) \qquad \text{(K.19)}\end{aligned}$$

Setting the frequency of the rotating frame equal to that of the first pulse, $\omega_{rot} = \omega_{pulse,1}$, and using the trigonometric Pythagorean identities to simplify the result yields Equation 7.6, without the '$+\alpha$' term, which is included only to make the pump pulse at frequency $\omega_{pulse,2}$ non-coherent.

Appendix L

Fluorescence experiments performed on equine lysozyme with oleic acid bound (ELOA)

Fluorescence imaging measurements allow the visualization of the location of a fluorescently labelled particle within a given system. They are therefore very useful for visualizing the uptake of a protein by a cell over an extended time window.

Fluorescence correlation spectroscopy measures the amplitude of fluorescence intensity fluctuations in a very small diffraction limited volume element (N). These can be analysed using statistical methods to derive molecular numbers and diffraction transport coefficients.[259]

In this study, fluorescence measurements are used to investigate the interaction of the ELOA lipid-protein oligomer with cells.

L.1 Fluorescence experimental procedures and theory

Two types of fluorescence measurement were performed on the ELOA complex: avalanche photodiode (APD) imaging and fluorescence correlation spectroscopy (FCS). Both were performed on a modified ConfoCor3 instrument consisting of an inverted microscope for transmitted light and epifluorescence (Axiovert 200 M): a VIS-laser module comprising the Ar/ArKr (458, 477, 488 and 514 nm), HeNe 543 nm and HeNe 633 nm lasers; and the scanning module LSM 510 META. The instrument was

modified to enable detection using silicon avalanche photodiodes (SPCM-AQR-1X; PerkinElmer) for imaging and FCS. Images were recorded at a 512 × 512 pixel resolution. The C-Apochromat 40×/1.2 W UV-vis-IR objective was used throughout. Fluorescence intensity fluctuations were recorded in arrays of 5–10 consecutive measurements, each measurement lasting 5–10 s.

L.1.1 Fluorescence imaging

Fluorescence imaging was achieved using avalanche photodiodes. It provides a complete picture of the location of fluorescent particles in real time. The images collected here show one or more PC12 cells in a solution of ELOA, over a time period of several hours, where one or both of the types of molecule are fluorescently labelled.

L.1.2 Fluorescence correlation spectroscopy (FCS)

The experiments carried out on the PC12 cells with ELOA measured the fluorescence intensity fluctuation at distinct locations: in the bulk culturing medium, at the plasma membrane and inside the cell. The measurements were analysed to determine the average number of fluorescent molecules in the observation volume element (N) and the average time each molecule spent within this element (τ_D).

Three-dimensional diffusion can be described using the following formula for the autocorrelation function $G(\tau)$:

$$G(\tau) = 1 + \frac{1}{N} \frac{1}{\left(1 + \frac{\tau}{\tau_D}\right) \sqrt{1 + \frac{w_{xy}^2}{w_z^2} \frac{\tau}{\tau_D}}} \tag{L.1}$$

$\frac{w_{xy}^2}{w_z^2}$ represents the square of the ratio of the radial and axial radii of a three-dimensional Gaussian intensity profile at $\frac{1}{e^2}$ of its maximal intensity. This value was determined experimentally in calibration measurements using Rhodamine 6G.

The amplitude of the autocorrelation function $G(\tau)$, at τ times close to 0, is inversely proportional to the absolute concentration of fluorescently labelled molecules in the system. $G(\tau)$ also has a characteristic decay time τ_D, which is related to the diffusion coefficient, D.

$$\tau_D = \frac{w_{xy}^2}{4D} \tag{L.2}$$

The value of the diffusion coefficient is related to the size of the molecule via the Stokes-Einstein equation:

$$D = \frac{k_B T}{6\pi\eta R} \tag{L.3}$$

where k_B is the Boltzmann constant, T is the temperature, η is the solvent viscosity and R is the hydrodynamic radius of the protein complex.

It is therefore possible to estimate the molecular mass, M, of a species from FCS measurements via the relationship:

$$\frac{1}{D} \propto \frac{6\pi\eta}{k_B T} \sqrt[3]{M} \tag{L.4}$$

For the system of ELOA with PC12 cells, there was not only free three-dimensional diffusion but also interactions of the ELOA with the surface membrane of the PC12 cells. A different model for taking into account these two contributions was therefore needed for these systems.

$$G(\tau) = 1 + \frac{1}{N}\left(\frac{1-y}{\left(1+\frac{\tau}{\tau_{D1}}\right)\sqrt{1+\frac{w_{xy}^2}{w_z^2}\frac{\tau}{\tau_D}}} + \frac{y}{1+\frac{\tau}{\tau_{D2}}}\right) \tag{L.5}$$

This has a similar form to Equation L.1, but an additional component to describe the interactions with the membrane surface is present. N is the average number of ELOA molecules in the observation volume element and y is the fraction of ELOA molecules associated with the plasma membrane. τ_{D1} and τ_{D2} are the characteristic diffusion times for ELOA diffusion in the bulk medium and the plasma membrane.

L.2 Fluorescence results for ELOA and PC12 cells

Fluorescence experiments were used to study the interaction of ELOA with PC12 cells. Three experimental systems were studied: the interaction of fluorescently labelled ELOA with unlabelled PC12 cells (Section L.2.1), the interaction of fluorescently labelled PC12 cells with unlabelled ELOA (Section L.2.2) and the interaction of fluorescently labelled ELOA with fluorescently labelled PC12 cells (Section L.2.3).

L.2.1 Single colour fluorescence studies with fluorescently labelled ELOA

Labelling only the ELOA and fluorescence imaging showed how, over time, there is initially an accumulation of ELOA on the plasma membrane of the PC12 cells, compared to the cell interior and the surrounding bulk medium. For just over an hour, ELOA is not seen to enter into the PC12 cells, which appear resistant to 'ELOA attacks'. However, after this period of resistance, the PC12 cell membranes ruptured and ELOA streamed into the cell interior very quickly, showing particular affinity for the nucleus of the cell. Fluorescent images over time are shown in Fig. L.1.

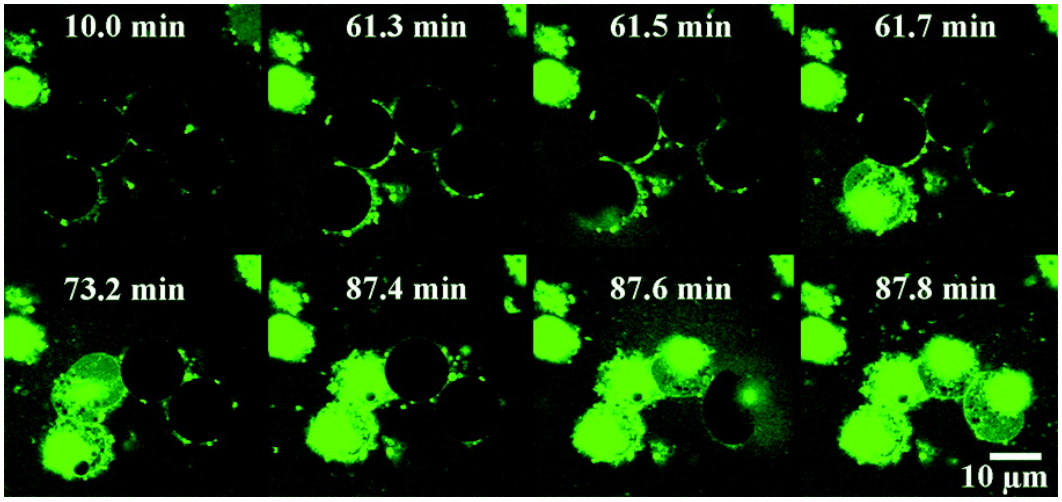


Figure L.1: Cellular uptake of ELOA complexes studied by fluorescence imaging. Time-lapse avalanche photodiode image capture shows that fluorescently labelled ELOA complexes are not gradually taken up by PC12 cells. The concentration of ELOA complexes in the immediate cellular surroundings progressively increases, reaching a local concentration that is several times higher than the concentration in the bulk medium. At a critical time point (61.5 min), the plasma membrane ruptures. Only then do the ELOA complexes 'stream in' and swiftly distribute in the cellular interior, preferring the cell nucleus in particular. The scale bar is 10 μm. This figure is reprinted with permission from Lipoprotein Complex of Equine Lysozyme with Oleic Acid (ELOA) Interactions with the Plasma Membrane of Live Cells; V. Vukojevič, A. M. Bowen, K. Wilhelm, Y. Ming, Z. Ce, J. Schleucher, P. J. Hore, L. Terenius and L. A. Morozova-Roche, *Langmuir*, 2010, **26(18)**, 14782–14787. Copyright 2010 American Chemical Society.[19]

Control experiments using equine lysozyme, oleic acid or the dye Alexa Fluor 488 alone did not show this behaviour. It is therefore believed that interactions between the ELOA and the membrane must be the trigger to cause the membrane to rupture.

The relative concentrations of fluorescently labelled ELOA were measured using FCS; results are shown in Fig. L.2. The results from these experiments mirror those from the fluorescence imaging experiments.

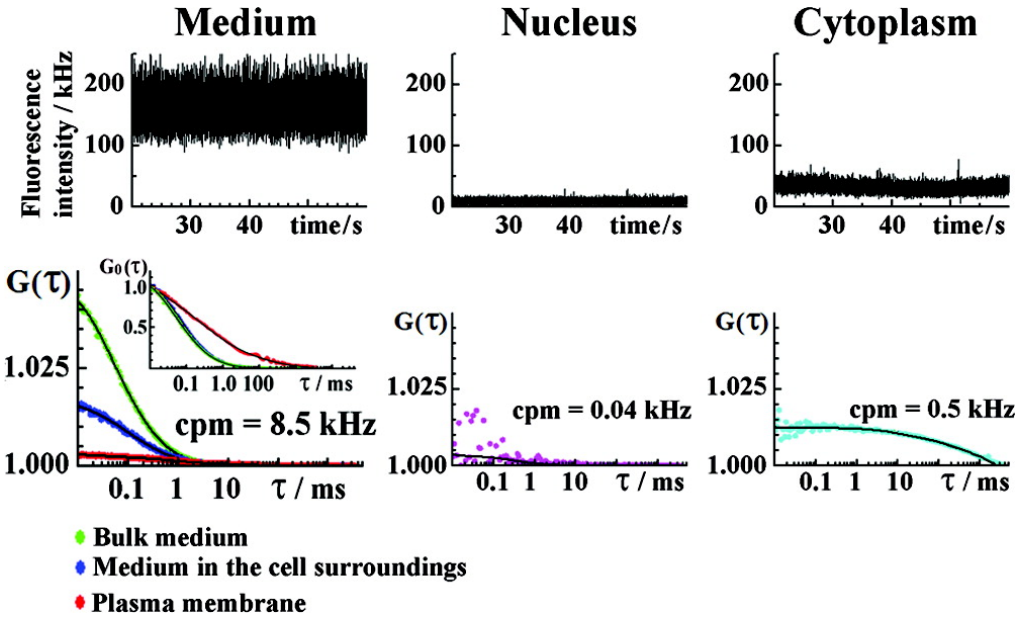


Figure L.2: Cellular uptake of ELOA complexes studied by single colour FCS. Fluorescence intensity fluctuations (upper row) and autocorrelation curves (bottom row), recorded at different locations, in the medium (left column), the cell nucleus (middle column), and the cytoplasm (right column), 40–45 minutes after exposing the PC12 cells to fluorescently labelled ELOA. The concentration of ELOA in the bulk medium, c^{bulk}_{medium} = 240 nM, was much lower than in the immediate cell surroundings, c^{cell}_{medium} = 670 nM, and the plasma membrane, $c^{plasmamembrane}_{medium}$ = 2.5 μM. Autocorrelation curves normalized to the same amplitude (inset in the lower graph of the left column) show that lateral mobility of ELOA in the plasma membrane is significantly reduced. No presence of ELOA in the cell nucleus or the cytoplasm was detected. This figure is reprinted with permission from Lipoprotein Complex of Equine Lysozyme with Oleic Acid (ELOA) Interactions with the Plasma Membrane of Live Cells; V. Vukojevič, A. M. Bowen, K. Wilhelm, Y. Ming, Z. Ce, J. Schleucher, P. J. Hore, L. Terenius and L. A. Morozova-Roche, *Langmuir*, 2010, **26(18)**, 14782–14787. Copyright 2010 American Chemical Society.[19]

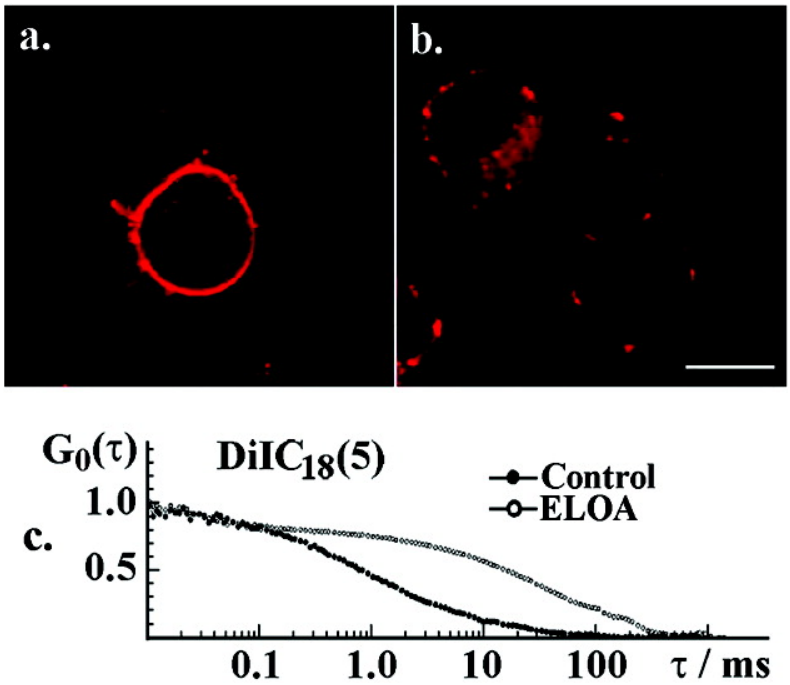


Figure L.3: ELOA interactions with the plasma membrane of PC12 studied by single-colour fluorescence imaging and FCS. (a) Uniform distribution of the fluorescent lipid marker $DiIC_{18}(5)$ in control cells not exposed to ELOA. (b) In cells exposed to ELOA, the distribution of $DiIC_{18}(5)$ becomes patchy and regions of local accumulation could be observed. The scale bar is 10 μm. (c) The autocorrelation curve shifts to longer characteristic times in cells treated with ELOA, which is consistent with a non-uniform distribution. This figure is reprinted with permission from Lipoprotein Complex of Equine Lysozyme with Oleic Acid (ELOA) Interactions with the Plasma Membrane of Live Cells; V. Vukojevič, A. M. Bowen, K. Wilhelm, Y. Ming, Z. Ce, J. Schleucher, P. J. Hore, L. Terenius and L. A. Morozova-Roche, *Langmuir*, 2010, **26(18)**, 14782–14787. Copyright 2010 American Chemical Society.[19]

L.2.2 Single colour fluorescence studies with fluorescently labelled plasma membrane

Having established that the interactions of ELOA with the surface membrane seem to induce membrane rupture and consequently apoptosis, these interactions were further probed using the fluorescent membrane stain $DiIC_{18}(5)$. The stain was added to PC12 cells that had been exposed to ELOA and, as a control experiment, those that had not. Fluorescence imaging and FCS showed that the distribution and dynamics (rate of diffusion) of the lipid probe are affected by the presence of ELOA. For the cells without ELOA present, uniform staining of the cell plasma membrane was seen; however, in cells that had been exposed to ELOA there was a 'patchy' non-uniform distribution of the stain. FCS showed that the characteristic diffusion time became longer for the PC12 cells where ELOA was present, which is consistent with a non-uniform distribution of the accumulated stain on the membrane. The experimental data are shown in Fig. L.3.

L.2.3 Dual colour fluorescence studies with fluorescently labelled ELOA and plasma membrane

Results from the dual-staining experiments, where both ELOA was fluorescently labelled and the membrane was stained, supported those of the single-colour experiments. They also showed that the $DiIC_{18}(5)$ stain accumulated at the site of ELOA interaction with the plasma membrane. This is consistent with other experimental findings, which have shown that $DiIC_n$ probes with long aliphatic chains ($n = 18$) are preferentially located at the gel/fluid interface, showing particular affinity for areas rich in defects.[267] Dual-colour results are shown in Fig. L.4.

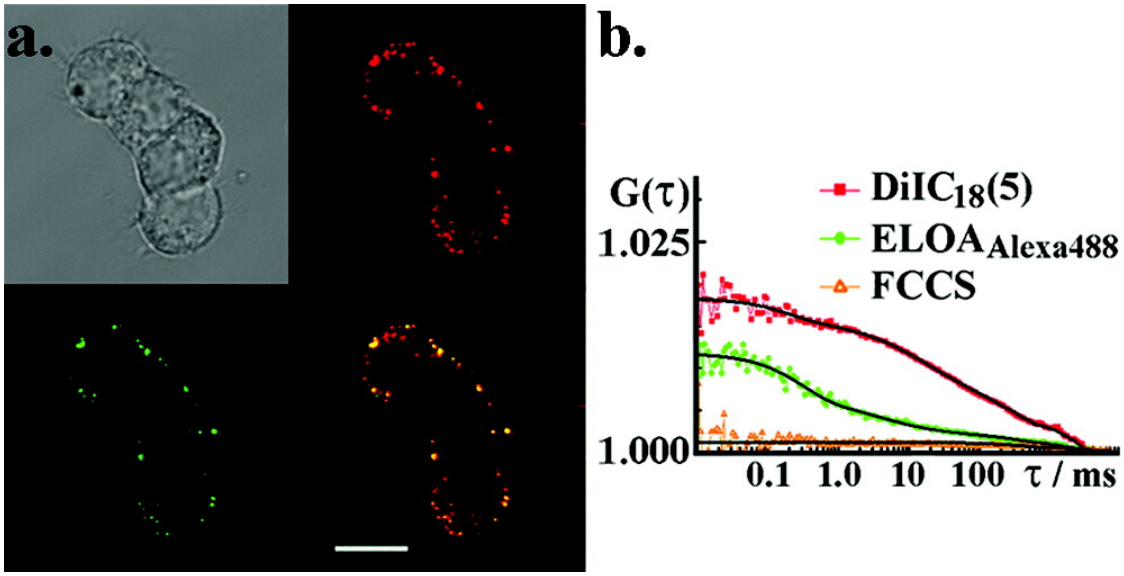


Figure L.4: ELOA interactions with the plasma membrane by dual colour fluorescence imaging and FCS. (a) Confocal images of PC12 cells immediately after exposure to ELOA (upper row) and 40 minutes later (lower row). The transmitted light images show the cellular morphology. Plasma membrane lipids, visualized by staining with the general lipophilic carbocyanine dye $DiIC_{18}(5)$ (red) and fluorescently labelled ELOA complexes (green), indicate that ELOA is not taken up by the cells. Co-localization analysis shows that plasma membrane lipids accumulated at the sites where ELOA associated with the plasma membrane. The scale bar is 10 μm. (b) Autocorrelation curves reflecting the dynamics of ELOA (green) and the lipid probe $DiIC_{18}(5)$ (red) at the plasma membrane of PC12 cells. Cross-correlation was observed for long correlation times. Figure reproduced from V. Vukojevič, A. M. Bowen, K. Wilhelm, Y. Ming, Z. Ce, J. Schleucher, P. J. Hore, L. Terenius and L. A. Morozova-Roche, *Langmuir*, 2010, **26(18)**, 14782–14787.[19]